

# Fragmentation Dependence of Level 1 Jet Trigger Efficiencies

Brent J. May  
Geoffrey E. Forden

University of Arizona  
September 4, 1992

## Abstract

The current Level 1 jet triggers depend on transverse energy deposited in one to four calorimeter "trigger towers" each with a size of  $\Delta\eta \times \Delta\phi = 0.2 \times 0.2$ . Since the trigger towers are considerably smaller than a jet, the Level 1 jet triggers may be sensitive to differences in fragmentation of the hard final state partons. We study this dependence by looking for biases in the quark and gluon jet subpopulations induced by the trigger. We use a fragmentation scheme that is consistent with data to show that there are indeed systematic biases but that the current triggers produce unbiased sample populations in their accepted  $p_T$  regimes.

# 1 Introduction

A *calorimeter trigger tower* is defined as a  $2 \times 2$  block of calorimeter towers measuring  $0.2 \times 0.2$  in  $\eta$ - $\phi$  space. In contrast, an average jet with a radius of  $R = \sqrt{\Delta\phi^2 + \Delta\eta^2} = 0.7$  is approximately 40 times larger. This suggests that the trigger towers should be responsive to the structure of a jet. As a result, the current jet triggers may be very sensitive to fragmentation differences between quark jets and gluon jets and consequently systematically bias the quark and gluon hard subprocesses.

Various studies of quark and gluon fragmentation have been done, all indicating a marked difference between quark and gluon jets. Gluon jets tend to be much wider and softer than quark jets of the same energy. This has been shown in both  $e^+e^-$  and  $p\bar{p}$  collisions indicating a universal fundamental difference in the way that quarks and gluons fragment [1, 2].

We have chosen the Lund monte carlo program JETSET 7.3 for our study since it is reasonably consistent with the observed differences between quark and gluon fragmentation. Figure 1a shows the ratio of gluon jet to quark jet energy fraction  $z = E/E_{jet}$  distribution which is consistent with UA1[1] (Fig. 1b) and OPAL[2] (Fig. 1c). The inclusive angular multiplicity distributions shown in Figures 2a–b illustrate the broadness of gluon jets as opposed to quark jets. From these properties, we would expect these differences to be apparent in the trigger efficiencies since the trigger towers are on the order of a typical hadronic calorimeter shower (i.e. calorimeter particle resolution).

to give full calorimeter simulation.<sup>2</sup>

We used the D-Zero Level 1 trigger simulator to obtain single-jet efficiencies for each of the 10  $p_T$  values. We selected several of the current jet triggers contained in Trigger menu 5.1, namely JT(1,3), JT(1,7), JT(2,7) and JT(3,7). (This is the standard jet trigger terminology. Thus JT(2,7) means two calorimeter trigger towers each with transverse energy  $E_T$  above 7 GeV.) Efficiencies were extracted for each type of single-jet event and each trigger to give single-jet efficiencies as a function of parton  $p_T$  as shown in Figures 3–4. It is important to note that these are *parton*→*jet* efficiencies dependent on *parton*  $p_T$  as opposed to *jet* efficiencies dependent on *jet*  $p_T$ . Thus, these efficiencies should be applied to events at the *hard parton level* before any “soft” parton showering or fragmentation.

## Dijet Efficiencies

It is relatively straightforward to calculate dijet trigger efficiencies from single-jet efficiencies. First, the single-jet efficiencies are interpolated between  $p_T$  values to give a smooth continuous function. We use a cubic spline interpolation which produces smooth monotonically increasing efficiency curves. Next, the  $qq$  ( $=q\bar{q}=\bar{q}\bar{q}$ ),  $gg$ , and  $qg$  ( $=\bar{q}g$ ) dijet efficiencies are calculated using conditional probability, where the efficiency  $\epsilon$  represents a probability that a trigger will pass[3].

---

<sup>2</sup>We did not use the D0Geant shower library because it seems unreliable for very low  $p_T$  showers. The shower library produces much larger high energy fluctuations (out to  $10\sigma$ ) than the standard D0Geant.

Table 1: Subprocess dijet trigger turn-on  $p_T$  at 95% and 99% efficiency.

Trigger Turn-on $p_T$ (GeV)						
Trigger	95% Efficiency			99% Efficiency		
	$qq$	$qg$	$gg$	$qq$	$qg$	$gg$
JT(1,3)	17.	20.	24.	21.	24.	31.
JT(1,7)	32.	39.	49.	39.	51.	59.
JT(2,7)	45.	55.	60.	60.	66.	72.
JT(3,7)	72.	75.	77.	97.	93.	91.

### 3 Results

#### Jet Trigger Bias

It is evident from both Figures 5–7 and Table 1 that  $\epsilon_{qq}$ ,  $\epsilon_{gg}$ , and  $\epsilon_{qg}$  are different for the same jet trigger. Hard inclusive *quark* subprocesses ( $qq$  and  $qg$  dijets) become efficient at lower  $p_T$  than hard pure *gluon* subprocesses ( $gg$  dijets). In fact,  $\epsilon_{qq} \geq \epsilon_{qg} \geq \epsilon_{gg}$  for almost all triggers and  $p_T$  indicating that the triggers are indeed sensitive to the fragmentation differences between quarks and gluons.

#### Bias in the Measured Dijet Cross Section

The *measured differential cross section*  $\sigma_{\text{exp}}$  is defined as the actual cross section  $\sigma_{\text{QCD}}$  times the experimental efficiency  $\epsilon_{\text{exp}}$ . In addition, the measured cross section can be expressed as the sum of the subprocess cross sections



tion. A plot of the total and contributing subprocess cross sections (eq. (3)) as generated by the Monte Carlo HERWIG is shown in Figure 8. (The total dijet cross section for  $p_T > 2$  GeV is 33 mb.) The ratios  $\hat{\sigma}_{gg}/\hat{\sigma}_{\text{QCD}}$ ,  $\hat{\sigma}_{qg}/\hat{\sigma}_{\text{QCD}}$ , and  $\hat{\sigma}_{qq}/\hat{\sigma}_{\text{QCD}}$  are shown in Figure 9 indicating the relative subprocess contributions to the total cross section.

### Quark vs. Gluon Subprocess Bias

To get a measure of the difference in the efficiencies due to different subprocesses, we define a *bias-measure*  $\beta$  of a trigger towards one subpopulation  $i$  with respect to another subpopulation  $j$  as the ratio of the efficiencies or

$$\beta_j^i = \frac{\epsilon_i}{\epsilon_j}. \quad (5)$$

Since  $\epsilon_{gg}$  is the smallest in general for each trigger, we determine the  $qq$  and  $qg$  dijet efficiency bias-measure relative to  $gg$  as shown in Figures 10–11. We use only the 10 original  $p_T$  values for this ratio since these points are fixed: spline interpolation introduces small artificial fluctuations in the bias between data points. These fluctuations are exacerbated by taking ratios of the efficiencies especially at small efficiency. In addition, we plot only those points for which the  $gg$  efficiency is non-zero so that the bias is well-defined.

These plots dramatically demonstrate a systematic trigger bias towards inclusive quark ( $qq$  and  $qg$ ) subprocesses. For each trigger there is a  $p_T$  range where the  $qq$  and  $qg$  dijets are much more likely to pass than the  $gg$  dijets. Not surprisingly,  $\beta$  approaches unity (no bias) as both triggers approach 100%.

Table 2: Quark-gluon trigger bias and  $p_T$  at 95% and 99% efficiency.

Trigger Bias and Turn-on				
Trigger	95% Efficiency		99% Efficiency	
	$\delta$	$p_T(\text{GeV})$	$\delta$	$p_T(\text{GeV})$
JT(1,3)	7%	22.	1%	28.
JT(1,7)	7%	46.	1%	56.
JT(2,7)	6%	59.	1%	69.
JT(3,7)	2%	76.	-1%	93.

and  $qg$  (positive) biasing, and an additional suppression (negative biasing) of the  $gg$  subprocess with respect to the measured efficiency. The dotted vertical lines represent the  $p_T$  at which the total efficiency becomes 95% and 99%.

It is clear from Figures 16–19 that *there is not a significant bias* in any of the jet triggers due to differences in quark and gluon fragmentation when the triggers become efficient ( $\epsilon \geq 95\%$ ). In fact, the largest quark-gluon *bias*, defined as  $\delta = (1 - \beta) \cdot 100\%$ , is about 7% at 95% efficiency and 1% at 99% efficiency. The quark-gluon bias at 95% and 99% total efficiency for each jet trigger is summarized in Table 2.

It is easy to understand why the largest bias is only on the order of  $100\% - \epsilon_{\text{exp}}$  opposed to a much larger value. Since the total efficiency gets a large contribution from the  $gg$  subprocess (Figures 12–15), the total efficiency can be roughly approximated by the  $gg$  efficiency. Furthermore, in general  $qq$  dijets are more efficient than  $gg$  dijets; as a worst case we assume the  $qq$  dijet efficiency is 100% when the total efficiency is  $\geq 95\%$ . Thus, the

---

ures 10–11.

- Parton fragmentation can be “factorized” to obtain single parton trigger efficiencies. Thus gluon fragmentation is the same in  $qg$  and  $gg$  events.
- A parton-parton subsystem fragments purely into dijets; i.e. there is no NLO contribution giving three jets except due to LLA parton showering.

There is an uncertainty inherent in each of these assumptions, but the qualitative aspects of the physics should be the same as a fully rigorous analysis.

Of course, one of the largest uncertainties in our analysis is fragmentation. Unfortunately since fragmentation is not fully understood it can only be approximated using phenomenological models. These models have an inherent uncertainty that can only be rectified by experiment. However, the uncertainties in fragmentation measurements are generally large, implying that only intelligent guesses can be made at the proper shape and normalization of fragmentation functions.

We have used the JETSET Monte Carlo because it is “consistent” (i.e. generally within the error bars) with fragmentation data. However, since fragmentation functions in general are not well defined, there is an infinite number of functions that are “consistent” with data. A truly rigorous trigger bias study should determine the *range* of biasing consistent with data. Fortunately, since gluons fragment more softly than quarks, biasing has an upper limit because of the subprocess cross section distributions.

## List of Figures

**Figure 1a.** The ratio of quark to gluon energy fraction spectrum from JETSET ( $E_{jet} = 25$  GeV).

**Figure 1b.** The scaled inclusive energy spectrum ratio of quarks to gluons as determined by OPAL.

**Figure 1c.** The ratio of quark to gluon fragmentation functions as determined by UA1.

**Figure 2a.** The quark and gluon inclusive angular multiplicity distributions from JETSET ( $E_{jet} = 25$  GeV).

**Figure 2b.** The quark and gluon inclusive angular multiplicity distributions for 3-jet events from OPAL.

**Figure 3.** Level 1 Single *Gluon* Jet Efficiencies for JT(1,3), JT(1,7), JT(2,7), JT(3,7).

**Figure 4.** Level 1 Single *U-Quark* Jet Efficiencies for JT(1,3), JT(1,7), JT(2,7), JT(3,7).

**Figure 5.** Level 1 *qq* Dijet Trigger Efficiencies.

**Figure 6.** Level 1 *qg* Dijet Trigger Efficiencies.

**Figure 7.** Level 1 *gg* Dijet Trigger Efficiencies.

**Figure 8.** Total and subprocess fitted cross sections from HERWIG.

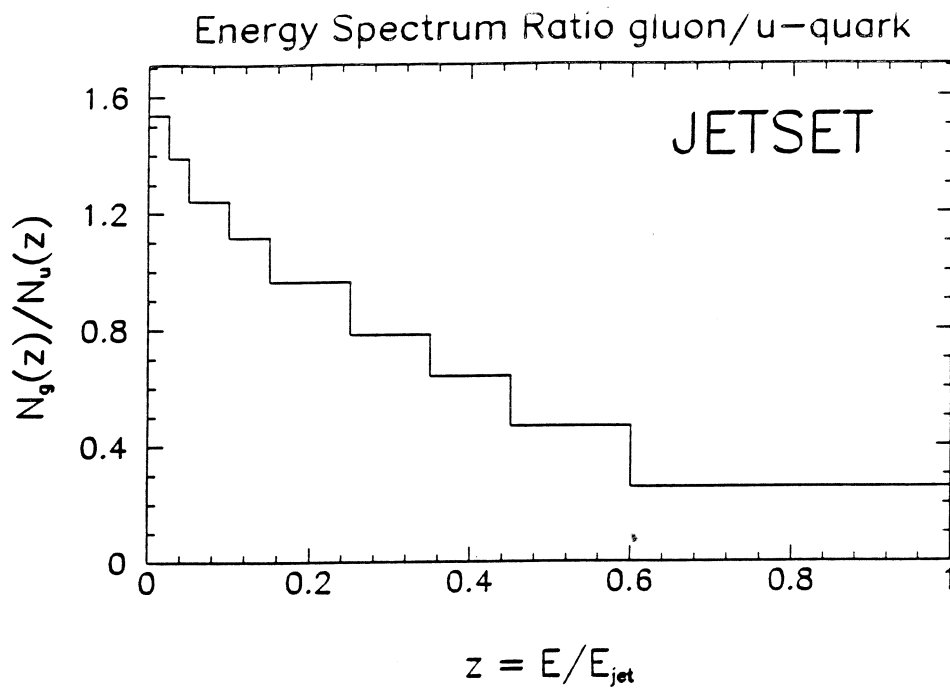


Figure 1a.

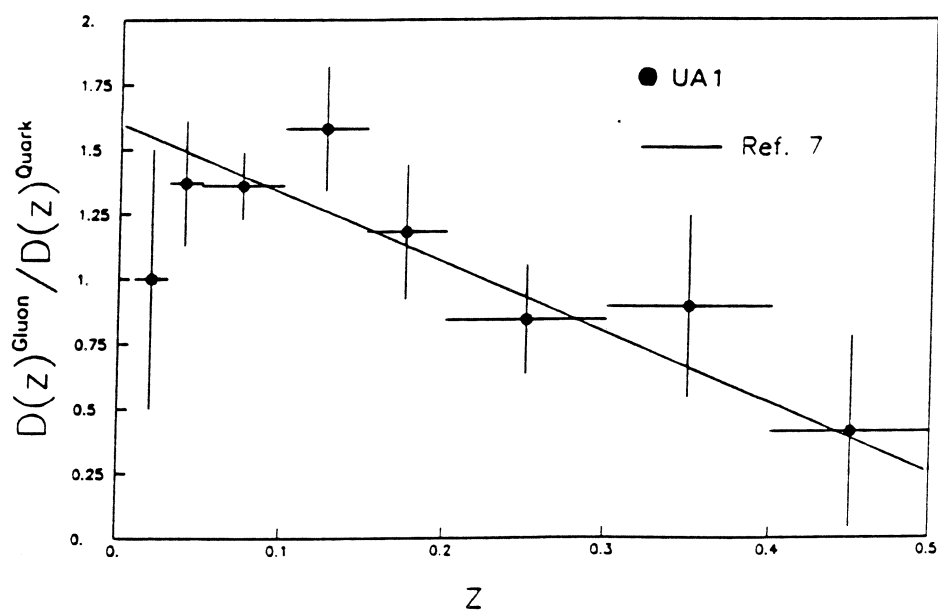


Figure 1b.

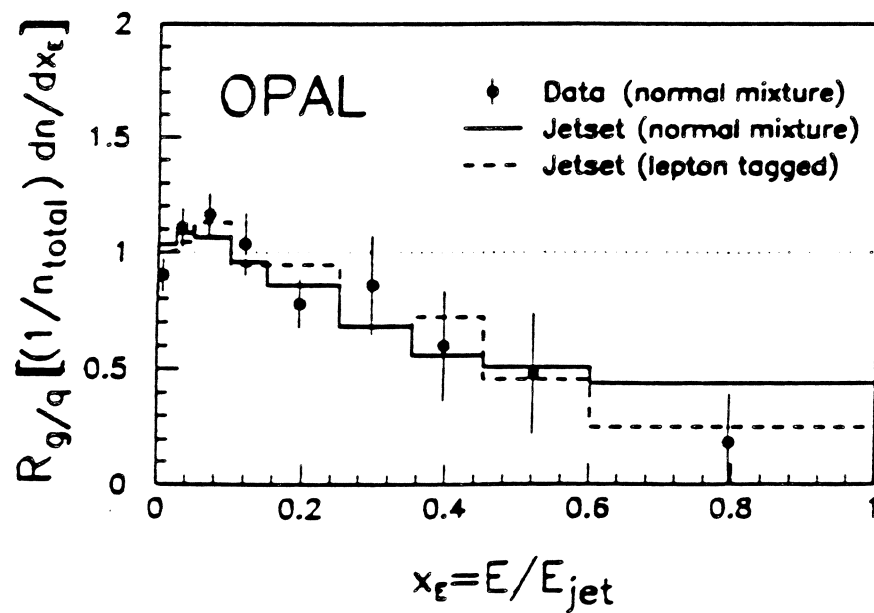


Figure 1c.

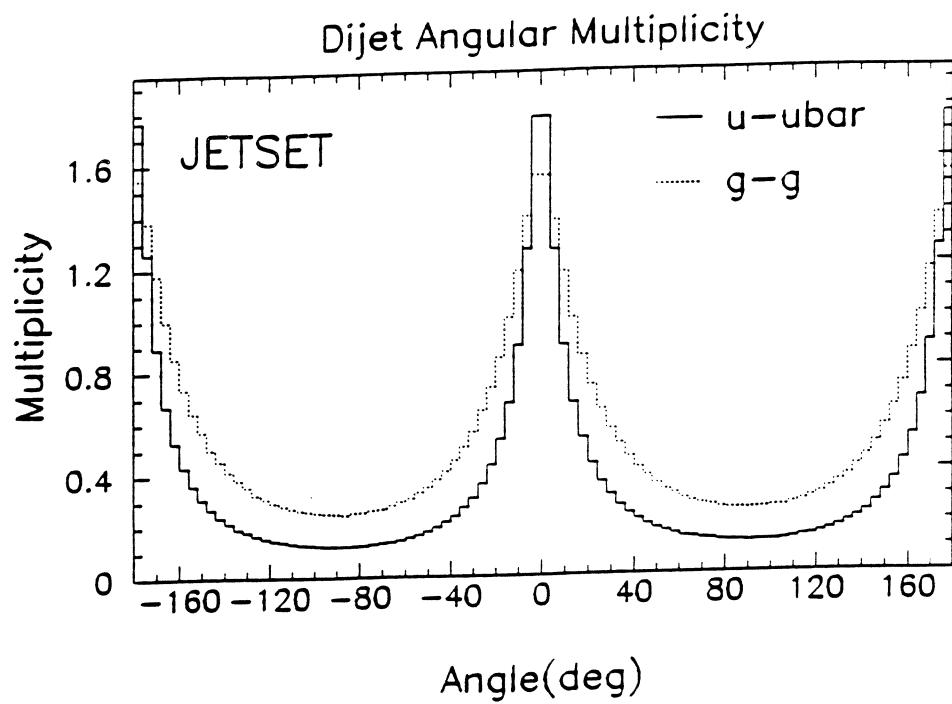


Figure 2a.

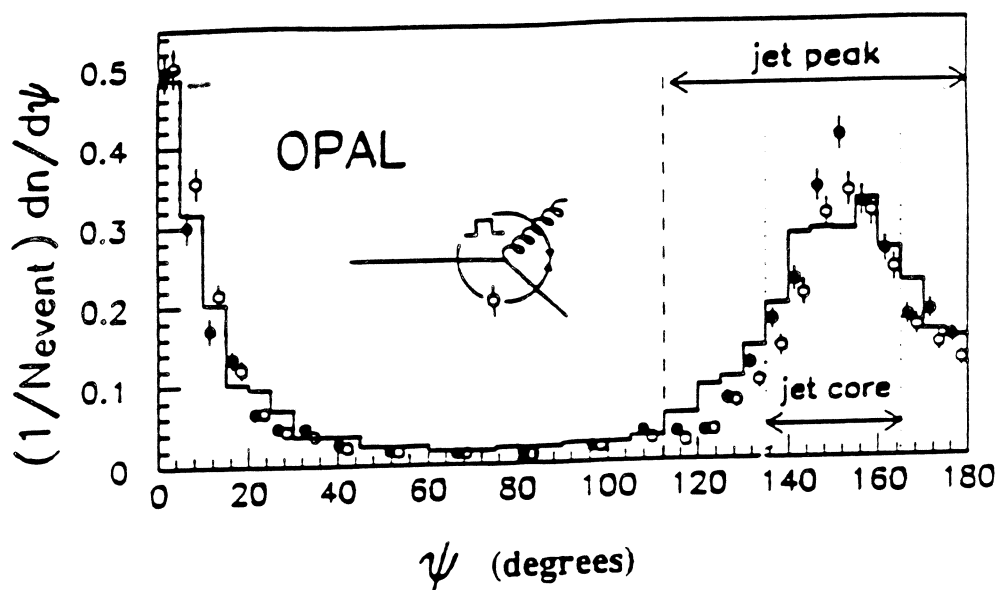


Figure 2b.

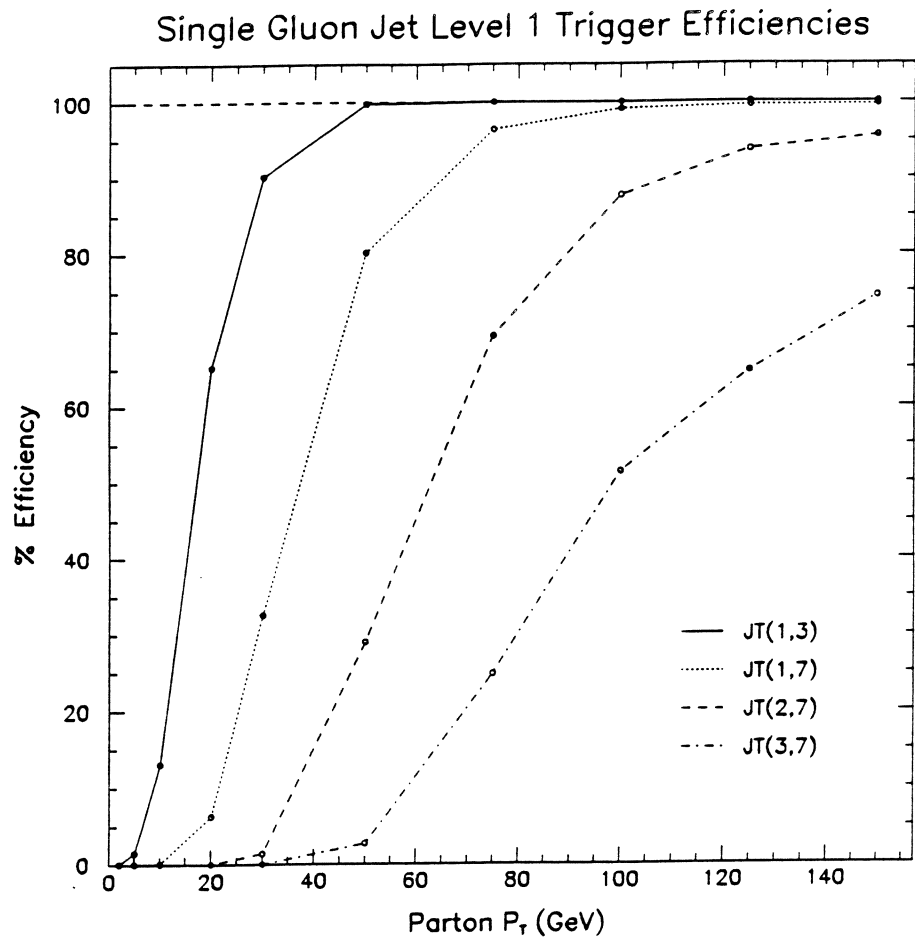


Figure 3.

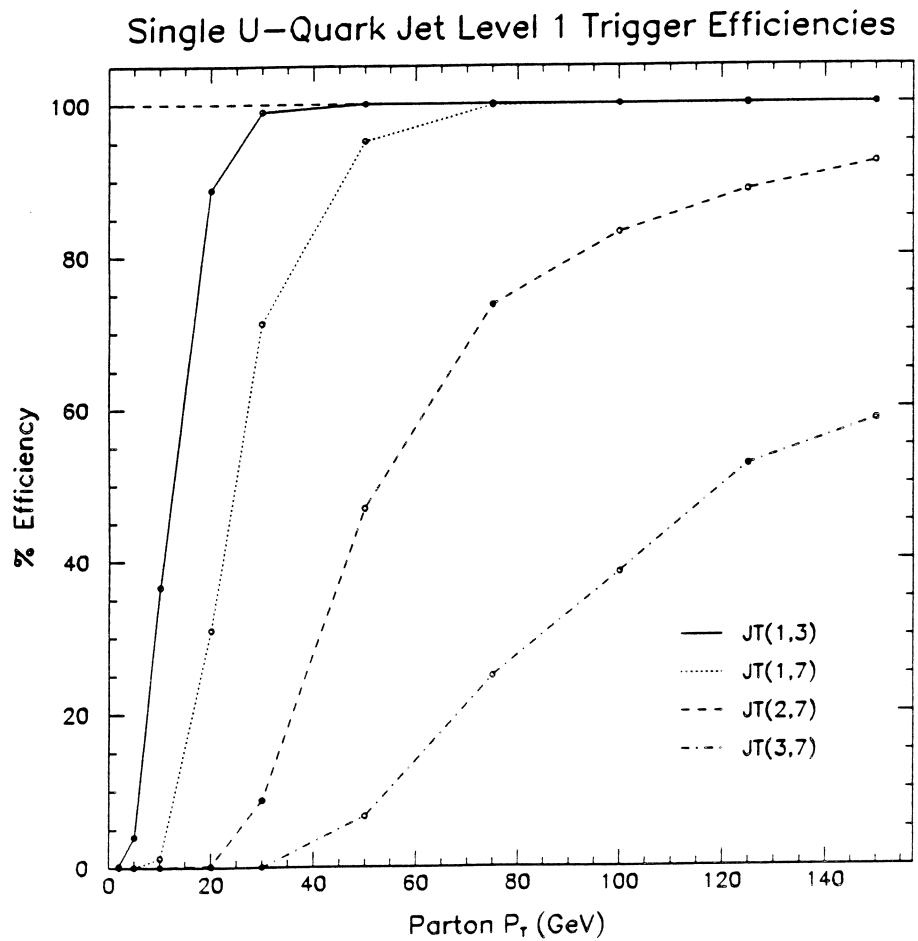


Figure 4.

## qq Dijet Level 1 Trigger Efficiencies

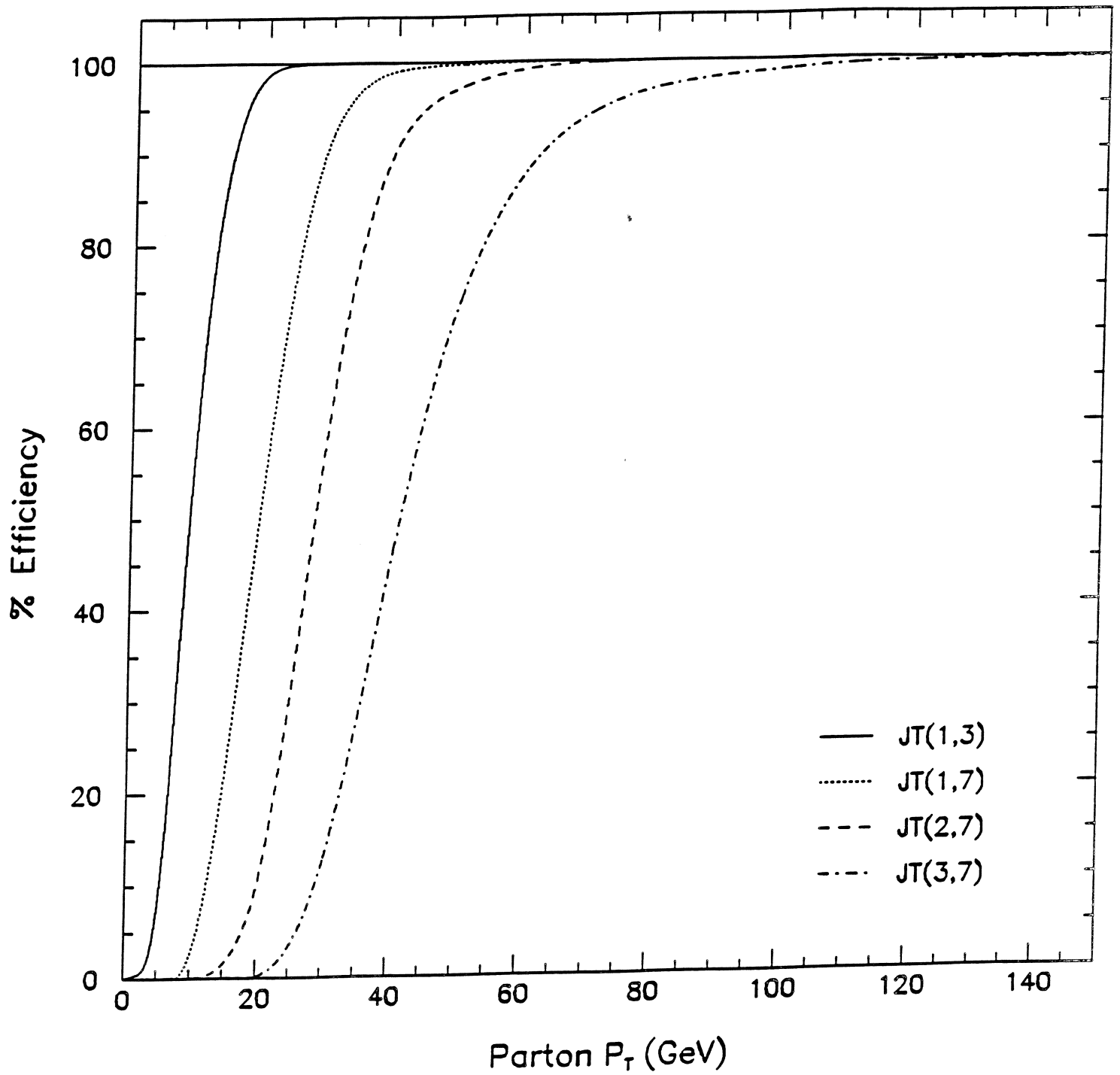


Figure 5.



## qg Dijet Level 1 Trigger Efficiencies

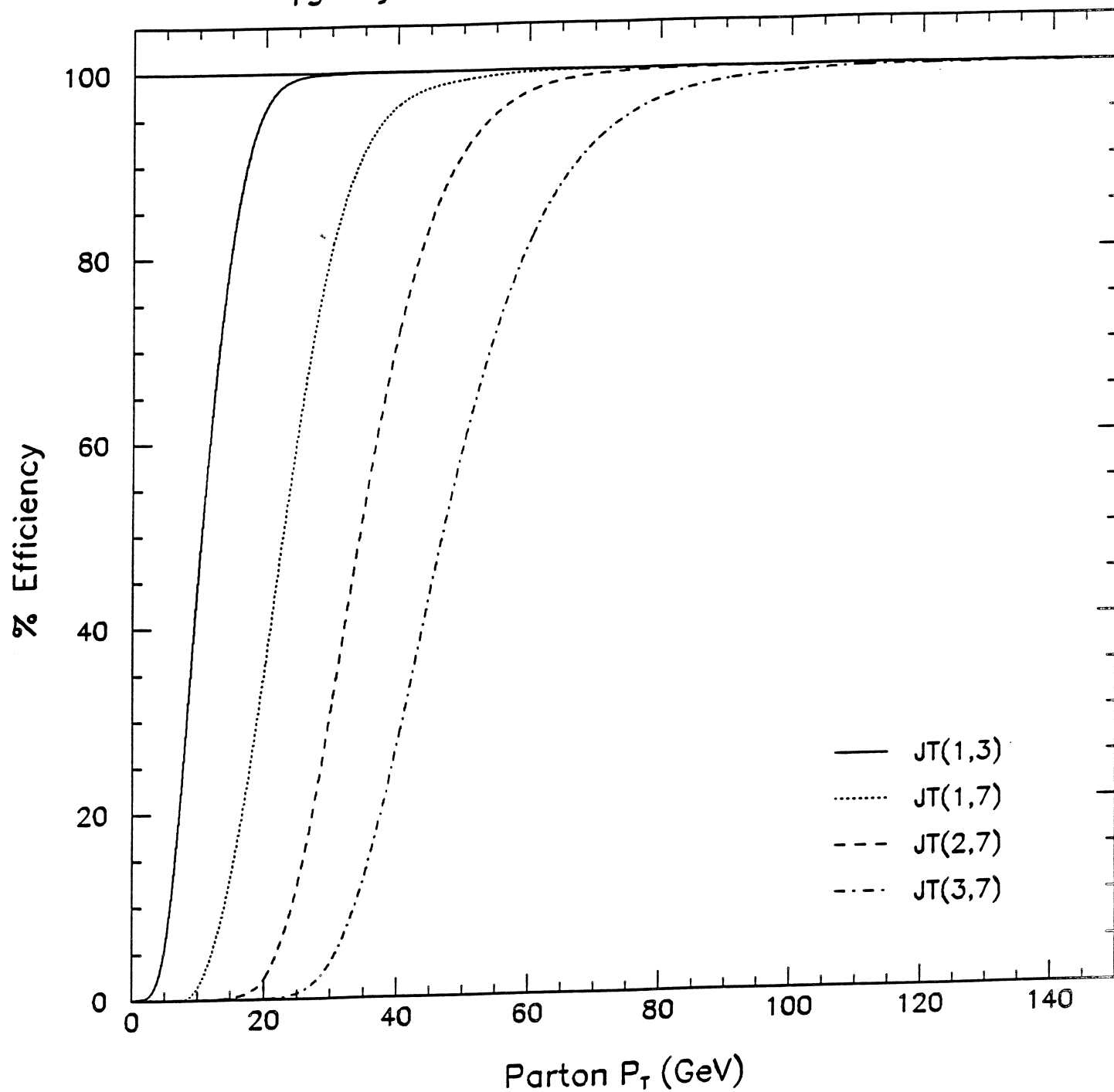


Figure 6.

# gg Dijet Level 1 Trigger Efficiencies

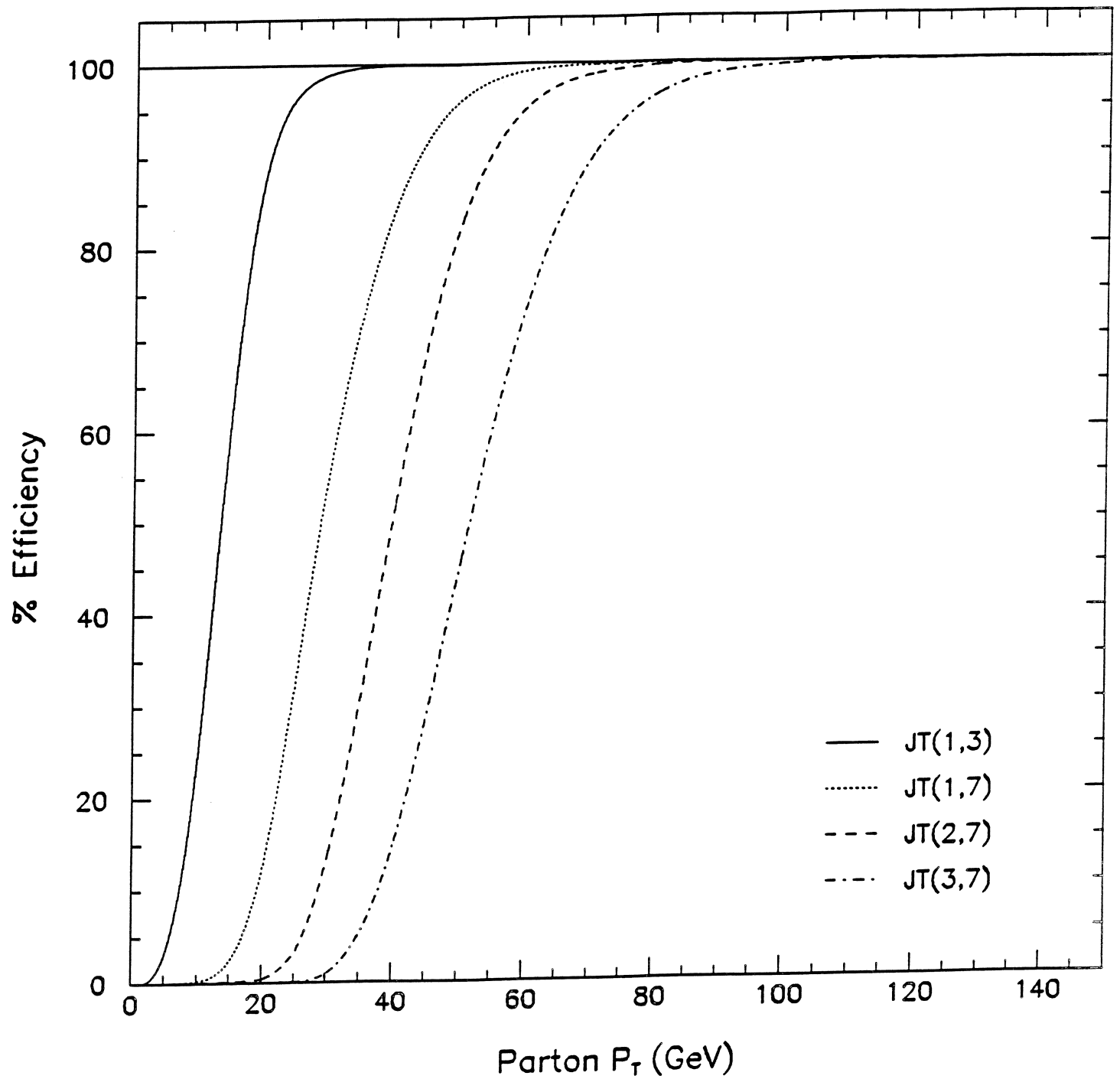


Figure 7.

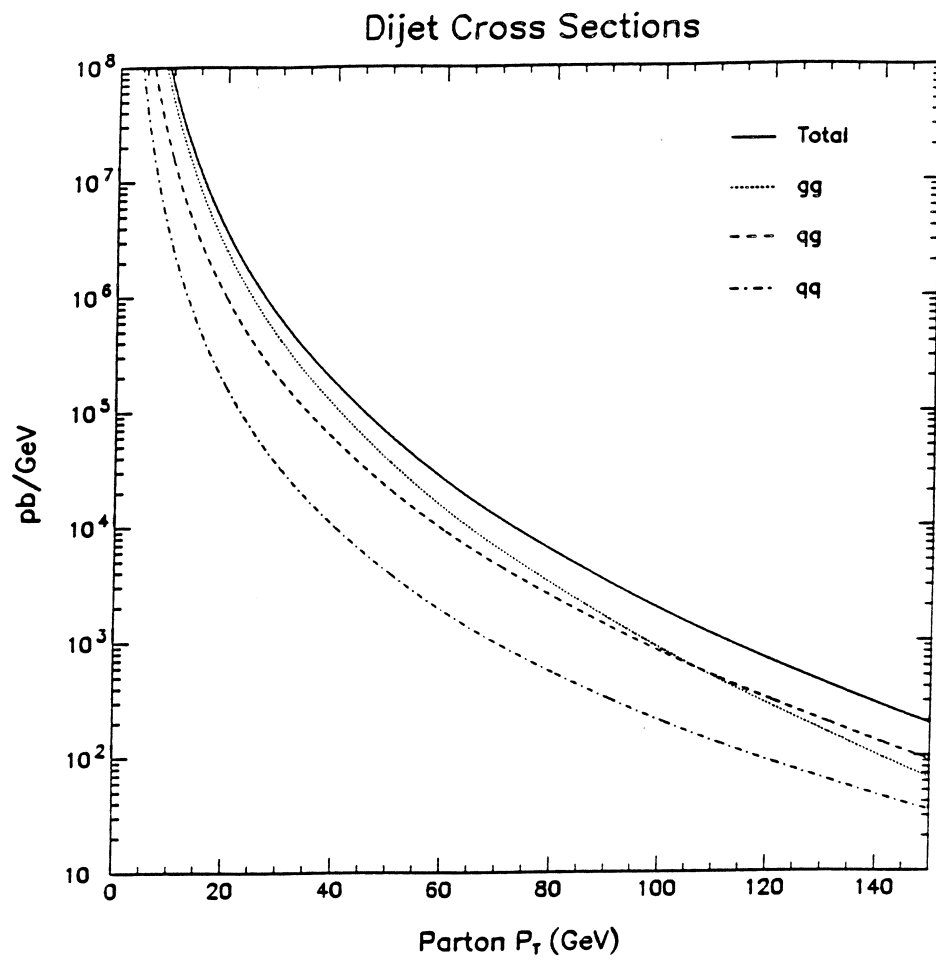


Figure 8.

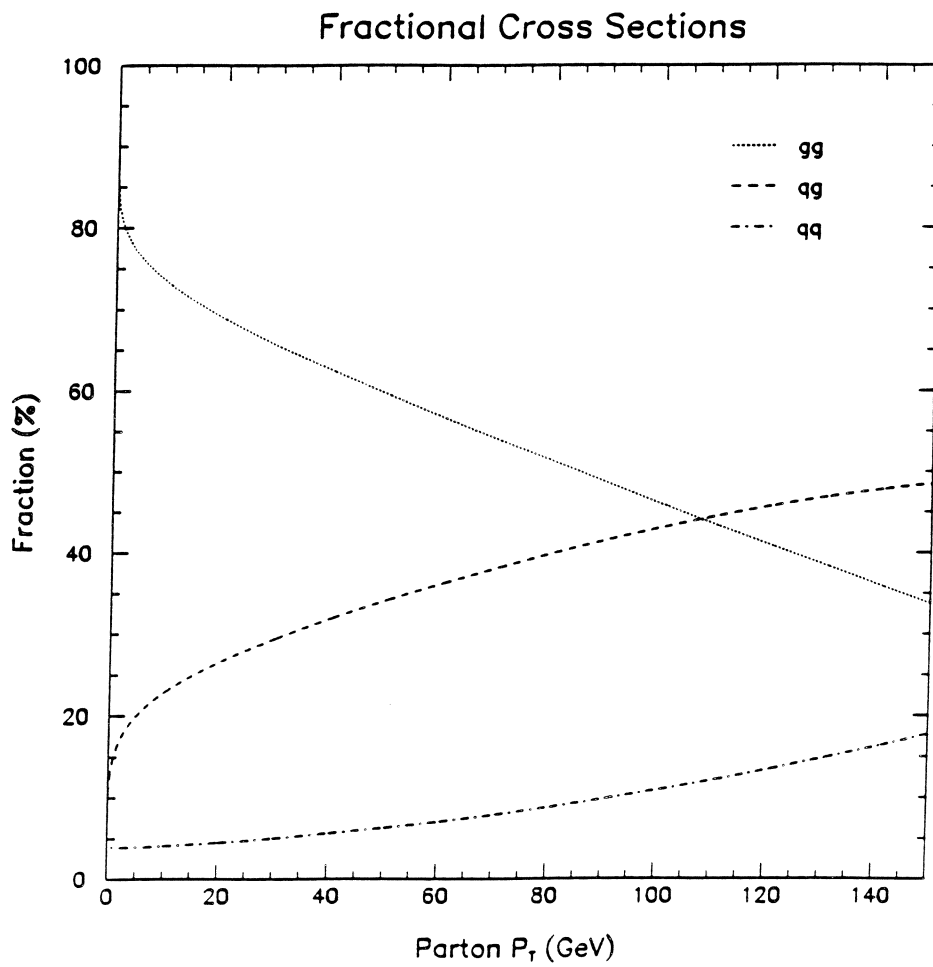


Figure 9.

# qq/gg Trigger Efficiency Bias

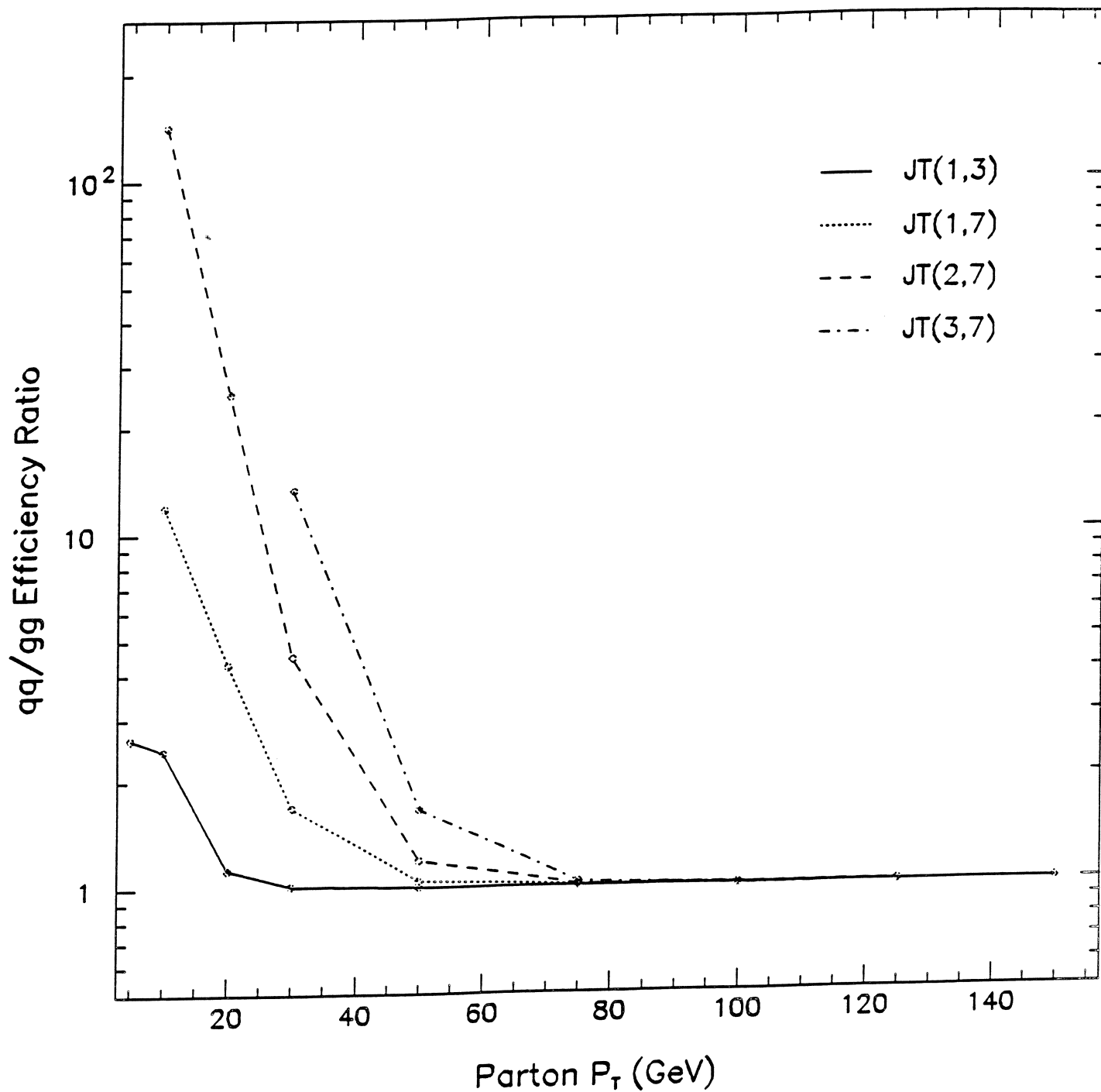


Figure 10.

# qg/gg Trigger Efficiency Bias

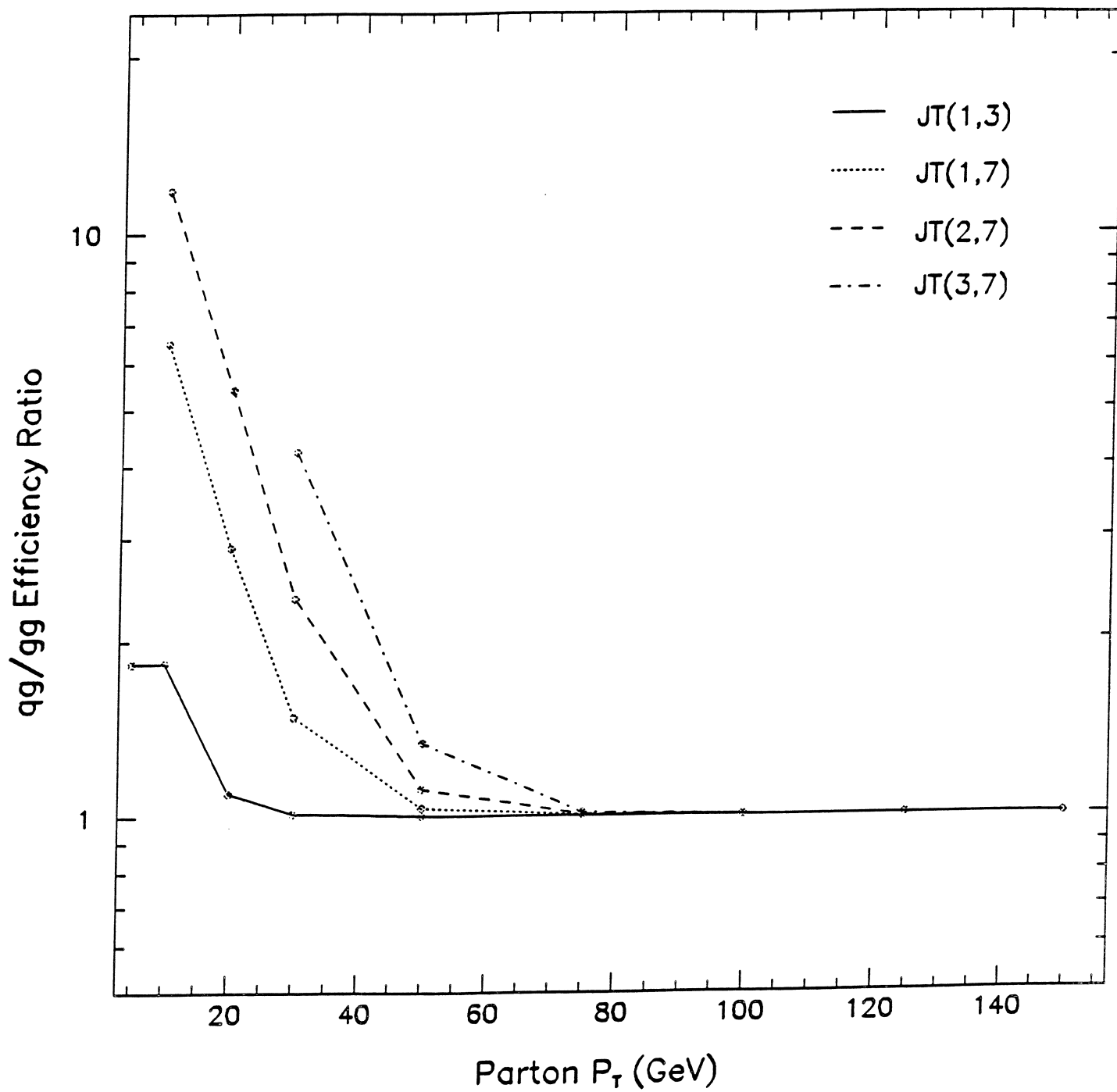


Figure 11.

# JT(1,3) Subprocess Contributions to Efficiency

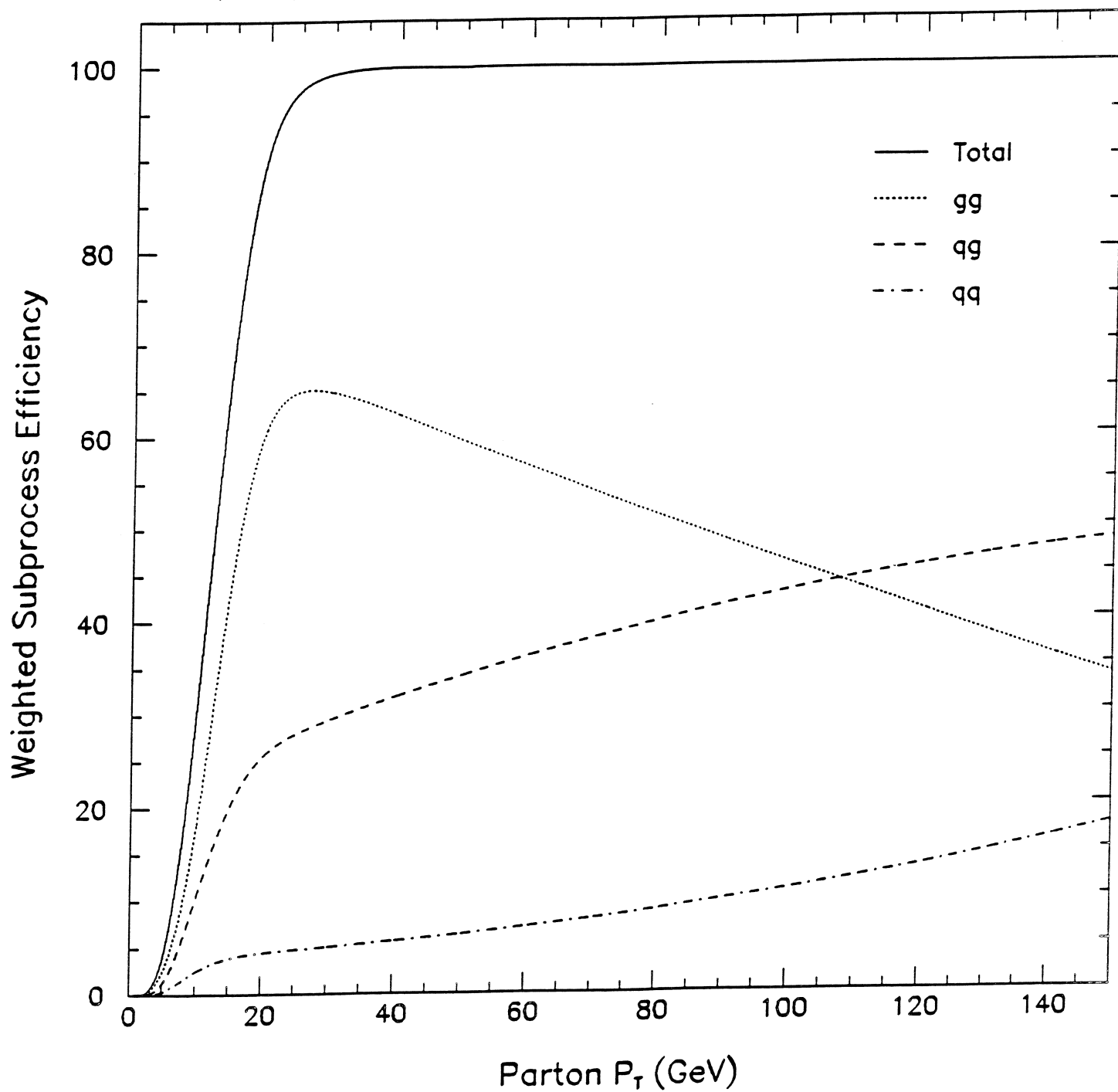


Figure 12.

# JT(1,7) Subprocess Contributions to Efficiency

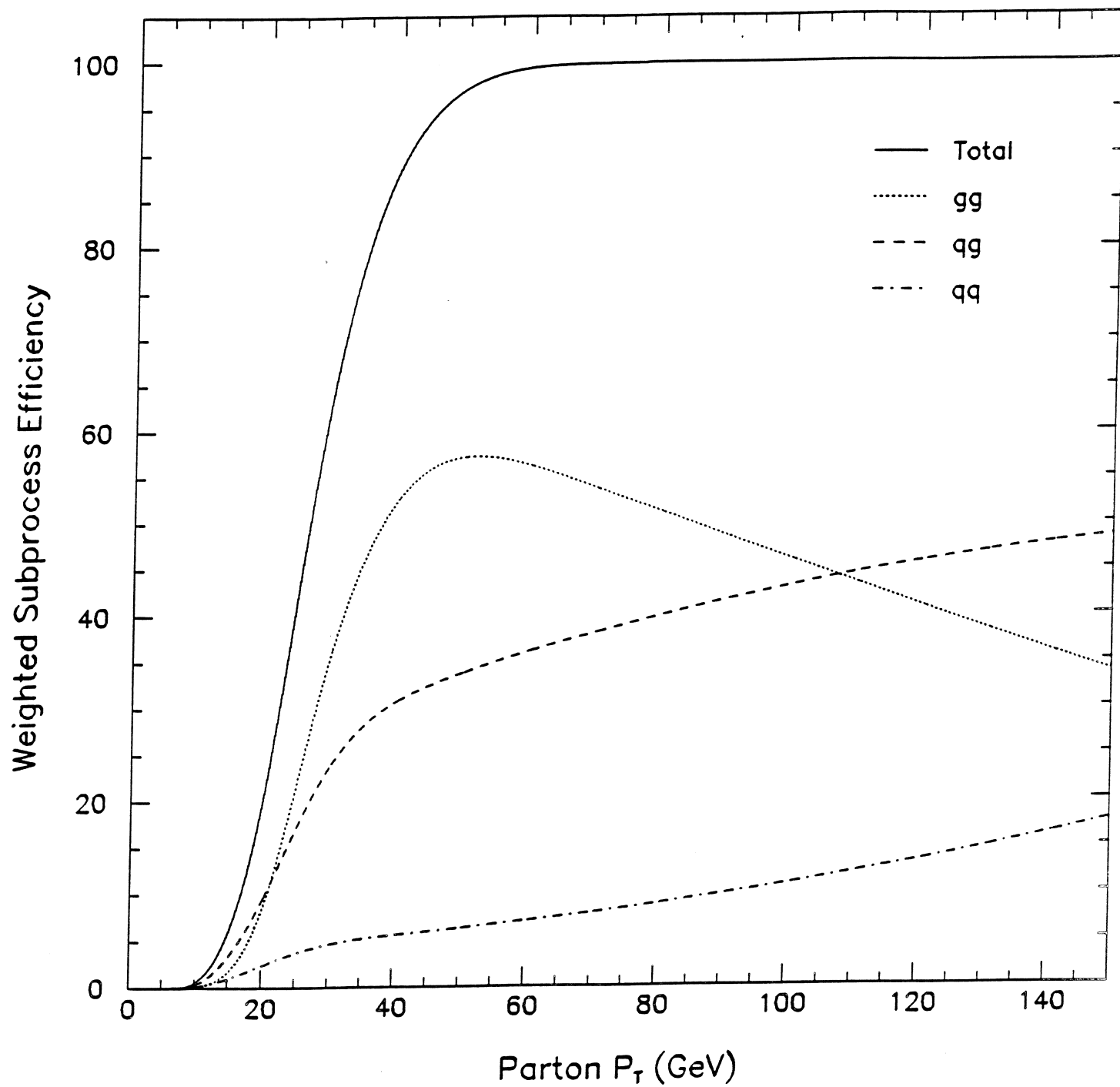


Figure 13.

# JT(2,7) Subprocess Contributions to Efficiency

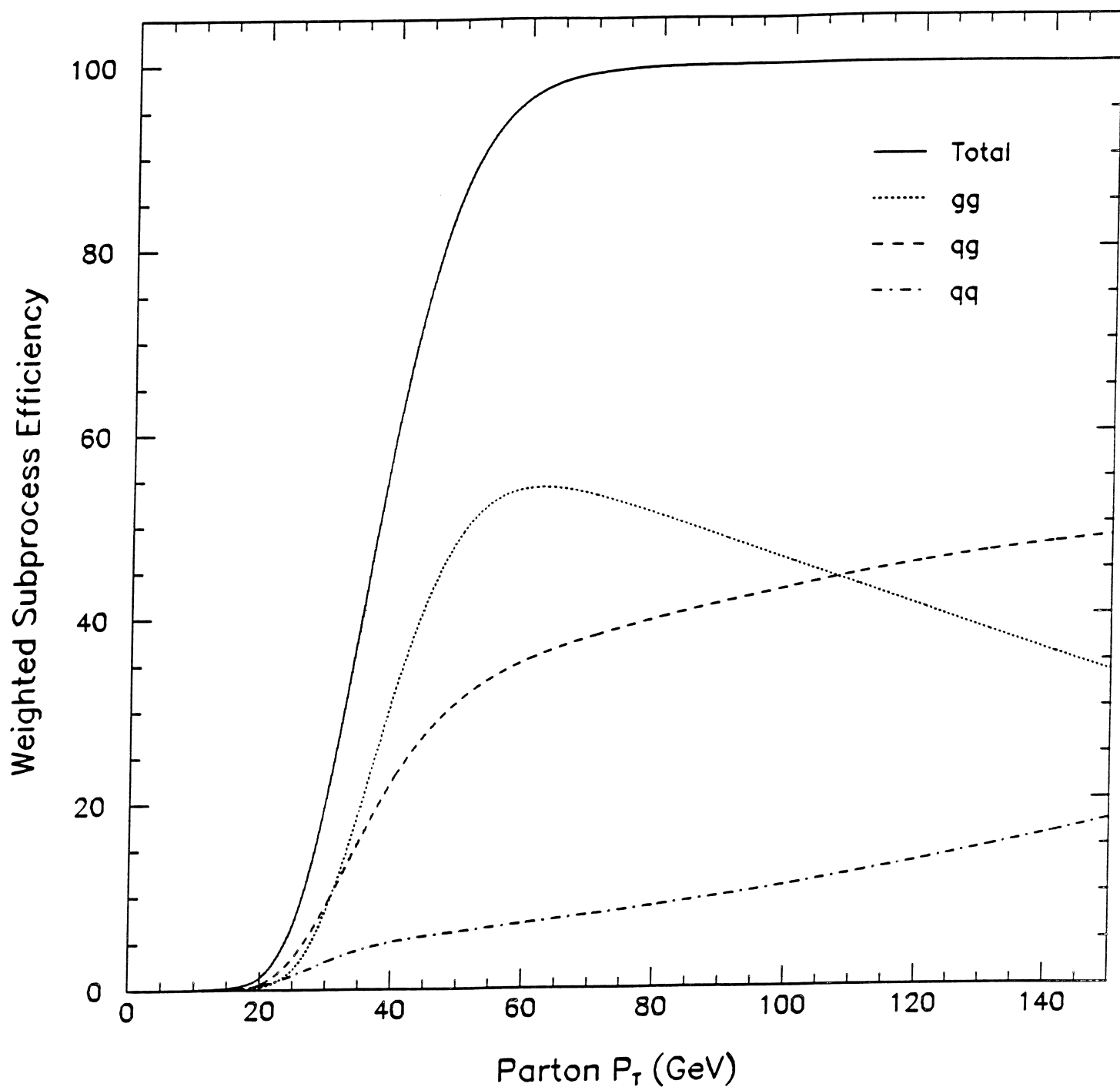


Figure 14.



# JT(3,7) Subprocess Contributions to Efficiency

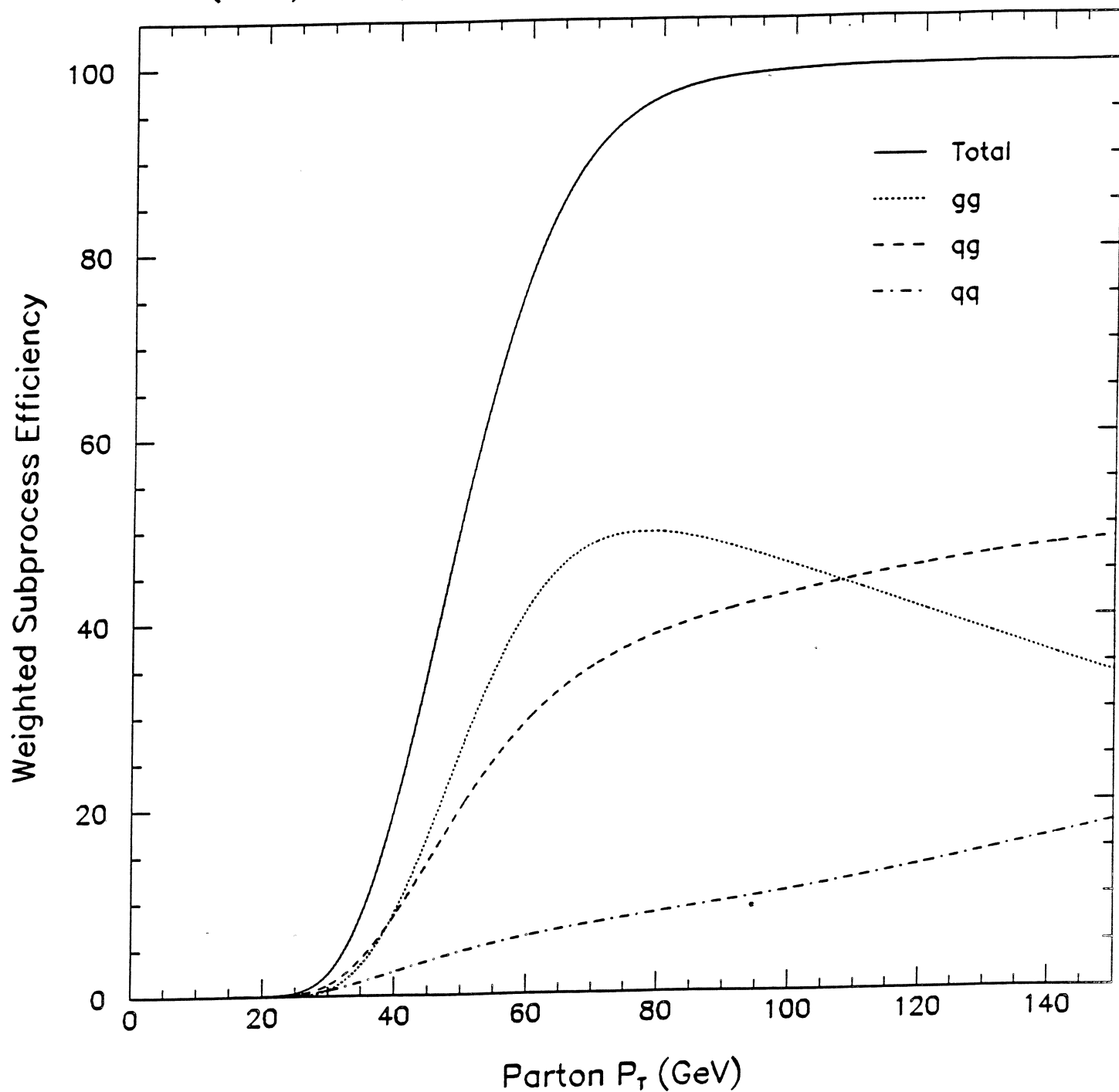


Figure 15.

# JT(1,3) Trigger Efficiency Bias

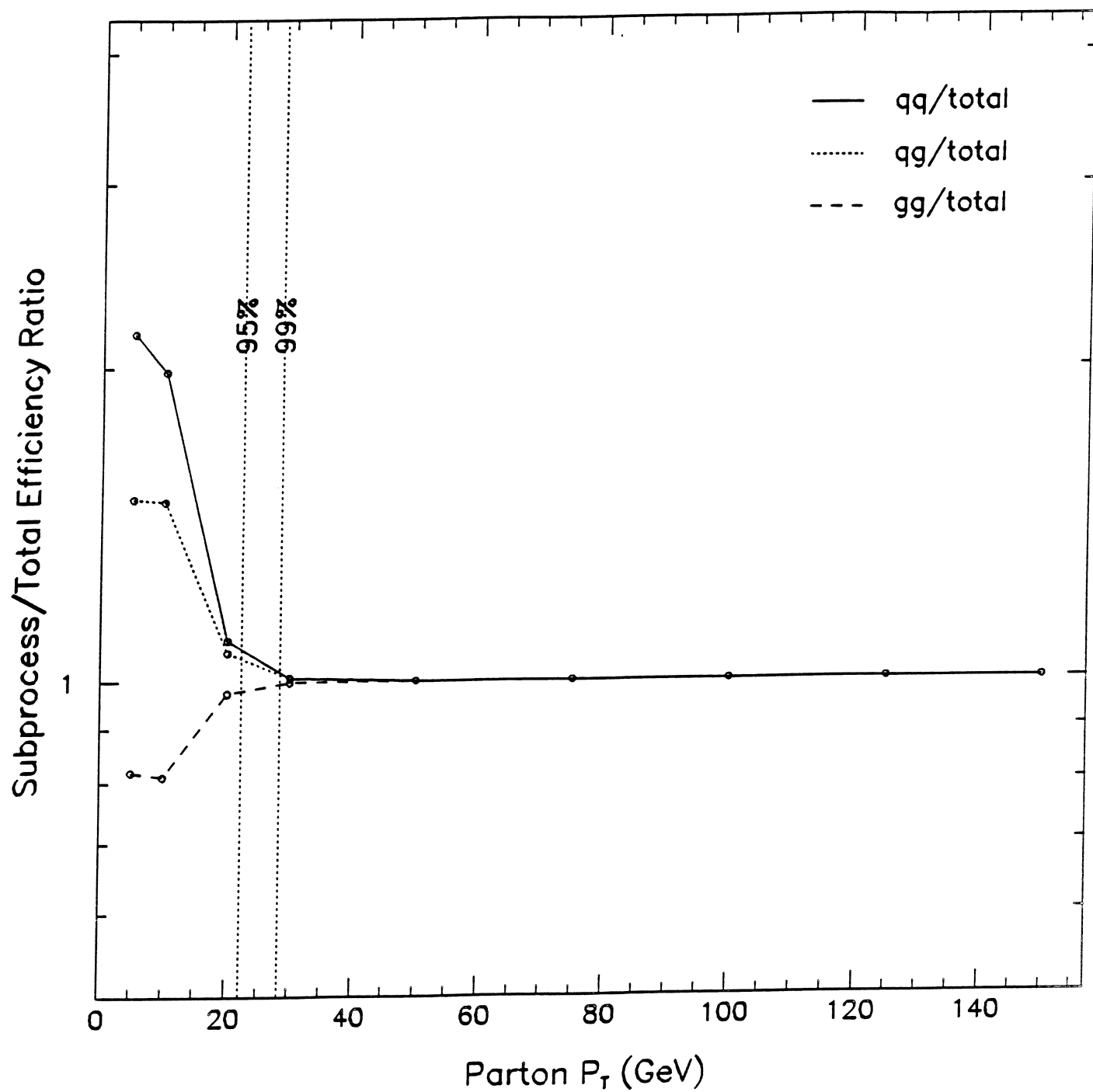


Figure 16.

# JT(1,7) Trigger Efficiency Bias

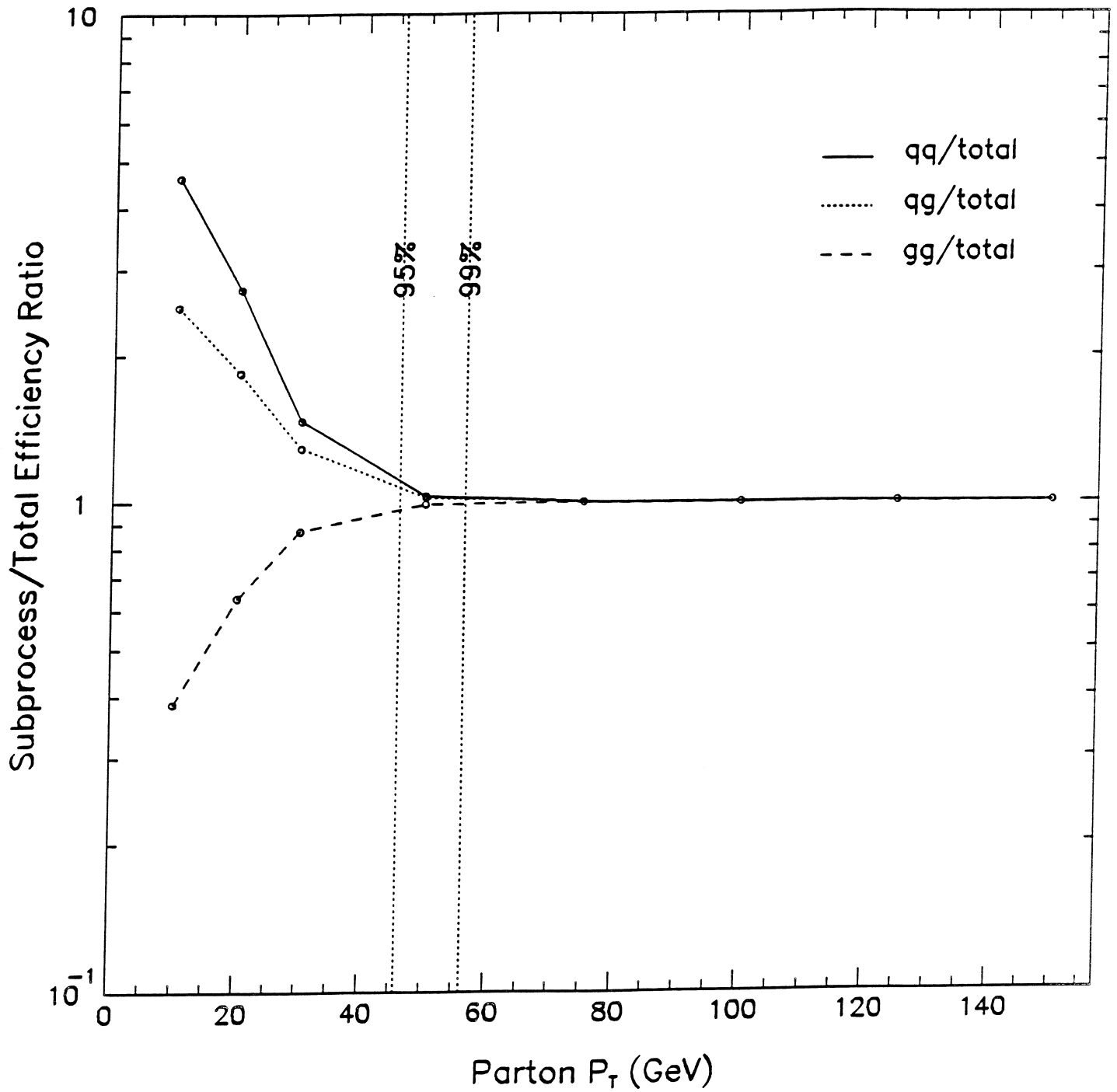


Figure 17.

# JT(2,7) Trigger Efficiency Bias

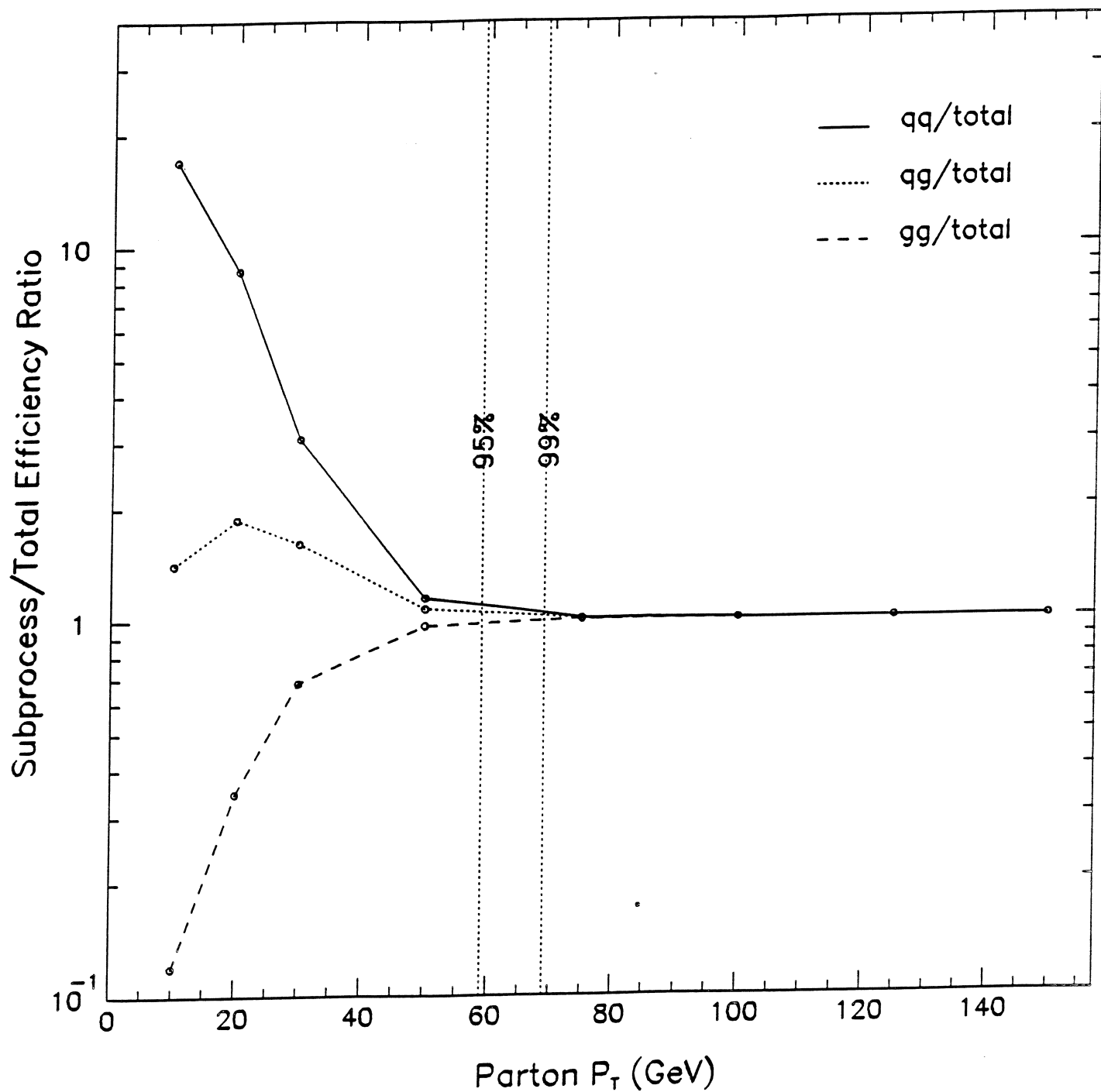


Figure 18.

# JT(3,7) Trigger Efficiency Bias

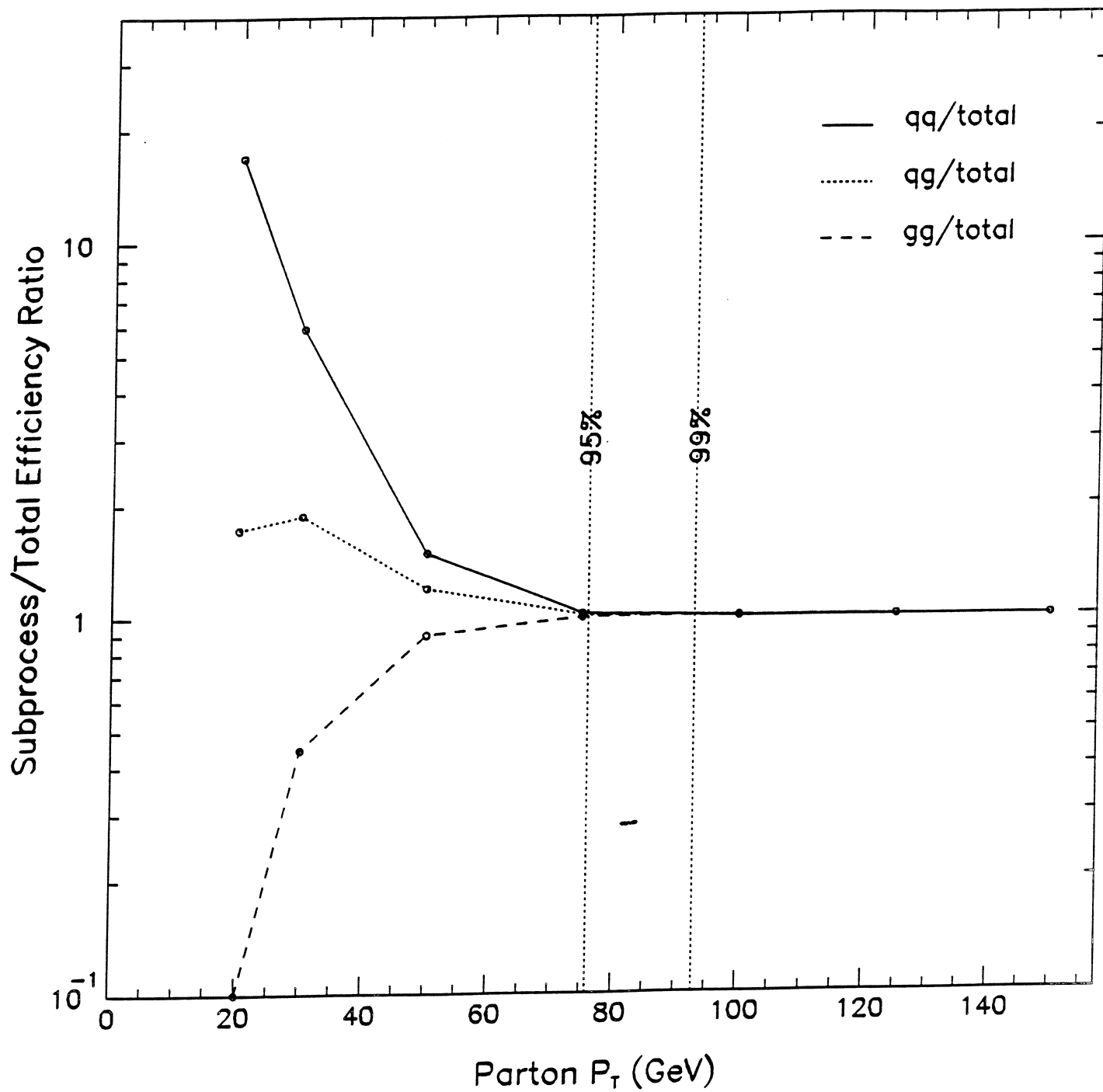


Figure 19.

**D0 END CALORIMETER RESPONSE TO MUONS AND  
“ $\mu$ ” RATIO - TEST BEAM LOAD 1**

**W. G. D. Dharmaratna, Mark Goforth, Robert Madden  
and Henryk Piekarz**

*Florida State University, Tallahassee, FL 32306*

**Abstract**

D0 End calorimeter modules response to muons is studied during the test beam load 1(1990). The calorimeter uniformity in depth is studied by using the low energy(15 GeV) muons. The energy dependance of the response is studied by using four different beam energies, 15, 50, 100 and 150 GeV. Both the most probable value and the mean value of the signal increase with energy as expected. By comparing the data with the monte carlo the expected signal for a minimum ionizing particle(MIP) is extracted. The “ $\mu$ ” ratio, which is energy dependent, is obtained at each energy. An energy independent quantity, “ $\frac{mip}{\mu}$ ” ratio, is calculated by using the deduced MIP signal.

Using the small fraction of muons (originating from pion decay) in the pion beam, the end calorimeter, electromagnetic (ECEM) and inner hadronic (ECIH), module response to muons was studied under the same experimental conditions as for electrons and pions. The arrangement of the calorimeter modules and the muon beam counters is shown in Fig.1. The muon beam passing through the calorimeter tower is identified by a coincident signal in the S1, S2 and S3 scintillation counters. The ECEM and ECIH calorimeter modules constitute about 20 radiation lengths and 8.5 interaction lengths thus being able to contain, both the electromagnetic and hadronic showers from the electron and pion beams of the 10-150 GeV/c momentum range used in the study. The 3m long steel block corresponding to about 17.9 interaction lengths was placed behind the cryostat (and between the S2 and S3 counters) in order to absorb any "leaking through" energy from hadronic showers. On the other hand, for the muon beam the ionization energy loss in the calorimeter modules, in the liquid argon space behind them and in the steel block set the passing muon momentum threshold at about 4.78 GeV/c. The S1.S2.S3 coincident signal was included in the standard beam trigger system with randomly interspersed pedestal triggers during the beam spill. Data were taken at four different momenta: 15, 50, 100 and 150 GeV/c.

In contrast with electrons or pions, the muons deposit only a very small fraction of their energy in the calorimeter, and only a small fraction of that (the "sampling fraction") is in the active medium and thus observable. A 15 GeV/c muon, e.g., deposits about 2% of its energy in the electromagnetic section of the ECEM and only about 8% of that is in the sensitive medium. Hence the observed signal is much smaller for muons than for electrons or pions. Therefore any contribution from noise could constitute a significant fraction of the observed muon signal. To minimize this effect, the analysis of muon data was performed slightly differently from that of the pion and electron data. Firstly, pedestals interspersed with data events were used to calculate the mean and the sigma of the pedestal values of each cell independently for each data file and then these values were used in the pedestal subtraction and in the zero suppression when analysing data. Secondly, only the cells adjacent to the projected track (obtained by extrapolating the beam track found using the beam PWC information) in the modules were used in

obtaining the signal. It was found that four projective towers (two nearest  $\phi$  and two nearest  $\eta$ ), were sufficient to collect the muon signal at  $\eta = 2.3$ .

Two properties of the calorimeter modules were studied by using muon data, the uniformity in depth and the “ $\frac{\mu}{e}$ ” ratio for ECEM. It has been known experimentally[1] as well as theoretically[2] that, especially at high energies, the energy loss of a muon is energy and material dependent. This is due to the fact that at higher energies the relativistic rise becomes important and eventually the other sources of muon energy loss,  $e^+e^-$  pair production, bremsstrahlung and nuclear interaction, dominate over ionization. The energy dependence of the energy loss by a relativistic muon is significantly different for passive (high Z) and active (low Z) layers in a sampling calorimeter[3]. As a result, the observed signal becomes more complicated, and a more careful treatment is required for muons compared with a fictitious minimum ionizing particle (MIP) traversing a bulk material. Taking these complications into account, it has been suggested[4] that it is preferable to measure “ $\frac{\mu}{e}$ ” ratios at a well-defined energy or to convert the measured “ $\frac{\mu}{e}$ ” ratio to  $\frac{mip}{e}$  ratio, in order to make comparison with other data possible.

## 1 Uniformity in Depth

At low energies where the radiative processes are not significant, one could use the muon signal to study the uniformity in the calorimeter modules. If it is assumed that the energy of the  $\delta$ -electrons is deposited locally in each argon layer, then one would expect the observed signal per unit thickness of active medium to be the same anywhere in the calorimeter regardless of the number of active/passive layers and their thicknesses. Under this assumption, we have made an attempt to study the uniformity in depth, i.e. to compare the muon signal on individual layers of ECEM and ECIH modules at  $\eta = 2.3$ , by using the data at the lowest available energy (15 GeV/c).

The pulse height distribution measured in some of the ECEM and ECIH layers with their pedestal distributions are shown in Fig.2 (a),(b),(c) and (d). The data points are fitted with the Moyal function[5],[6] (an approximate analytic expression of the Landau distribution), convoluted with a Gaussian resolution function.



The most probable values obtained from the fit are given in the figure. It is the mean value of the pulse height, not the most probable value, that is proportional to the thickness of the medium traversed by the muon[5]. The mean pulse heights, as calculated from the fit, per unit thickness of the argon gap( for EM layers measured gap thicknesses and for IH layers 85 mils gaps are used) for individual layers are shown in Fig.2(e). The result shows the expected uniformity between layers.

## 2 Signal-to-Noise ratio

In order to understand the significance of the noise, the electronics noise which is linearly depending on the cell capacitances and the Uranium noise due to radio active decay, we compare the interspersed pedestal distribution with the 15 GeV/c muon distribution. The muon distribution is obtained for a single tower( $\Delta\eta \times \Delta\Phi = 0.1 \times 0.1$ ), i.e. four cells in EM layer 3 and a single cell in each of the other layers, by selecting events with the projected PWC tracks centering the tower. The interspersed pedestal distribution (pedestal subtracted and gain corrected) is obtained for same cells as for the muon. The resultant distributions for the individual EM layers and for the total EM section, for the tower at  $\eta = 1.95$  and  $\Phi = 30.5$  are shown in Fig.3.

We define the Signal-to-Noise ratio as:

$$\frac{S}{N} = \frac{(PH)_{Peak}^{\mu} - (PH)_{Peak}^{ped}}{\sigma_{ped}}$$

where  $PH_{Peak}^{\mu}$  is the peak value of the muon signal and  $PH_{Peak}^{ped}$  and  $\sigma_{ped}$  are the peak value and the  $\sigma$  of the pedestal distribution. All quantities are measured in ADC counts. For the tower used the Signal-to-Noise ratio for individual EM layers and total EM section are:

Layer	S/N
1	$3.7 \pm 0.3$
2	$4.2 \pm 0.3$
3	$5.1 \pm 0.4$
4	$8.3 \pm 0.4$
EM total	$10.7 \pm 0.6$

### 3 “ $\frac{\mu}{e}$ ” Ratio

As discussed earlier the muon response is expected to be energy dependent. This can be seen in Fig.4 which shows the normalized pulse height distributions from muons of four different energies (15, 50, 100 and 150 GeV/c) in the ECEM, together with a fit to the function described above. Both the mean and the most probable value (both obtained from the fit), shown in Fig.4(e), increase with energy, the latter to a lesser degree, as expected [3]. Also, the spectrum becomes broader and more asymmetric at higher energies due to the contributions from radiative production.

The above results clearly indicate that the signal in the calorimeter for a realistic muon is always larger than that of a MIP. The minimum of the  $dE/dx$  curve for muon occurs around 300-400MeV. By comparing the observed signal with Monte Carlo results (Geant 3.14), we have estimated the MIP signal as follows. First, the Monte Carlo results for muons, traversing the same position in the calorimeter with same energies as data, were obtained. Then the most probable value (in MeV) of the MC spectrum is obtained by fitting the Moyal function. The MC results, converted to ADC counts by using a constant factor for all energies, agree very well with data as shown in Fig.4(e). In other words, the constant factor ( $4.0 \pm 0.1$  ADC/MeV) obtained here is the calibration of the active section of the EM calorimeter. Assuming that the MIP deposits energy according to the  $\frac{dE}{dx}$  table values[7], and knowing the MC result, we obtained the ratio of the energy scale between the two at each energy. Finally, the pulse height for MIP is obtained by reducing the measured pulse height according to the above scale factors. The result is included in the Fig.4(e) and is independent of energy as expected.

In order to compare the electromagnetic calorimeter response to muons with the response to electrons we consider the ratio,

$$\frac{\mu}{e} = \frac{PH_{\mu}/E_{\mu}}{PH_e/E_e}$$

where  $PH_{\mu}$  and  $PH_e$  are the measured pulse heights for muons and electrons respectively,  $E_e$  is the electron beam energy and  $E_{\mu}$  is the total energy loss by a muon traversing the ECEM. All quantities except  $E_{\mu}$  are measured experimentally. If one

assumes that the muon behaves as a MIP then  $E_\mu$  could be calculated by using the known[7]  $dE/dx$  values. The “ $\frac{e}{e}$ ” ratio obtained under such assumption is shown in Fig.5. The energy dependence of the “ $\frac{e}{e}$ ” is due to the energy dependence of  $PH_\mu$ , which becomes smaller if most probable value is used for  $PH_\mu$ . By using the corrected  $PH$  for MIPs we obtained the  $\frac{MIP}{e}$  ratio which is energy independent as it should be the case.

It should be pointed out that to estimate the pulse height for MIP from the experimental data one needs a reliable Monte Carlo simulation. Our study indicates that the best way to obtain an approximate value of the  $\frac{MIP}{e}$  ratio without such a simulation is to use the most probable value of the measured muon signal at the lowest possible energy. For the D0 ECEM the best estimate of the  $\frac{MIP}{e}$  ratio is  $1.41 \pm 0.05$ . It is important to note that the ECEM module is placed just behind a cryostat wall which could be acting as a part of the calorimeter especially for electromagnetic showers. If we treat the cryostat wall as a part of the calorimeter then the  $\frac{MIP}{e}$  ratio is  $1.22 \pm 0.05$ .

Similar behavior has been observed in sampling calorimeters in other experiments. A detailed comparison of the data with Monte Carlo results[4] has shown that this is due to the way in which low energy photons, which are abundantly produced in the electromagnetic shower development, interact with matter. Due to the strong  $Z$ -dependence of the photoelectric effect ( $\propto Z^5$ ), most of these photons will transfer their energies to electrons in the high  $Z$  absorber rather than the low  $Z$  sensitive medium. Therefore the observed fraction of the energy deposited by these low energy photons is much smaller than what could be expected from the sampling fraction based on the MIP energy loss. This causes the  $\frac{e}{MIP} < 1$ , which is an important factor in making the calorimeter response to electromagnetic and hadronic showers equal.

We would like to thank Anthony L. Spadafora for giving us information on the electron response.

## References

1. T. Åkesson *et al.*, Performance of the uranium/plastic scintillator calorimeter for the HELIOS experiment at CERN, Nucl. Instr. & Meth. **A262** (1987) 243.
2. W. Lohmann, R. Kopp and R. Voss, Energy loss of muons in the energy range 1-10000 GeV/c; CERN Report CERN 85-03 (1985)
3. B. Anders, U. Behrens and H. Brückmann, Nucl. Instr. & Meth. **A270** (1988) 140.
4. R. Wigmans, On the energy resolution of uranium and other hadron calorimeters, Nucl. Instr. & Meth. **A259** (1987) 389.
5. E. Bernardi, On the Optimization of the energy resolution of hadronic calorimeters, Dissertation, Universität Hamburg, Hamburg (1987)
6. J. E. Moyal, Theory of ionization fluctuations, Phil. Mag. **46** (1955) 263.
7. Review of Particle Properties, Phys. Lett. **B 170** (1986) 1.

## Figure Captions

Figure 1: The arrangement of the calorimeter modules and the muon beam counters

Figure 2: Response of individual calorimeter layers to 15 GeV/c muons. (a)-(d) the pulse height and the pedestal distributions in four layers. (e) Mean pulse height per unit Ar thickness vs layer index.

Figure 3: Response of EM module to 15 GeV/c muons at rapidity 1.95. (a)-(e) The pulse height and the pedestal distributions in four individual layers and the total EM section.

Figure 4: Energy dependence of the ECEM response to muons: (a)-(d) Pulse height fitted with the Moyal/Gaussian convolution at 15, 50, 100 and 150 GeV/c respectively. The most probable value (MPV) in ADC counts is indicated. (e) The mean value, the MPV (data and Monte Carlo) and the deduced MIP pulse height vs energy. (Monte Carlo numbers are converted to ADC counts.)

Figure 5: " $\frac{\mu}{e}$ " ratio vs energy. The ratio obtained by using the mean, the MPV and the MIP pulse height are included.

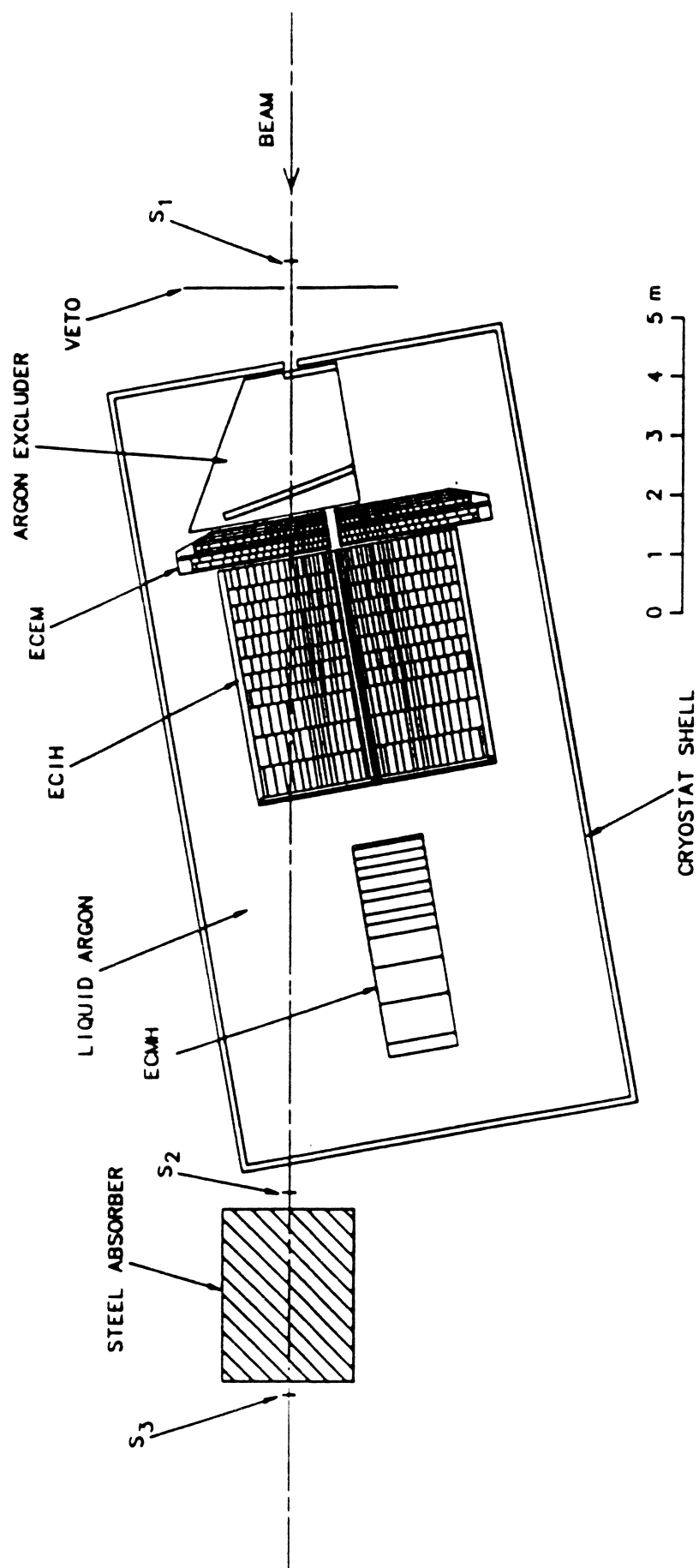


FIGURE 1

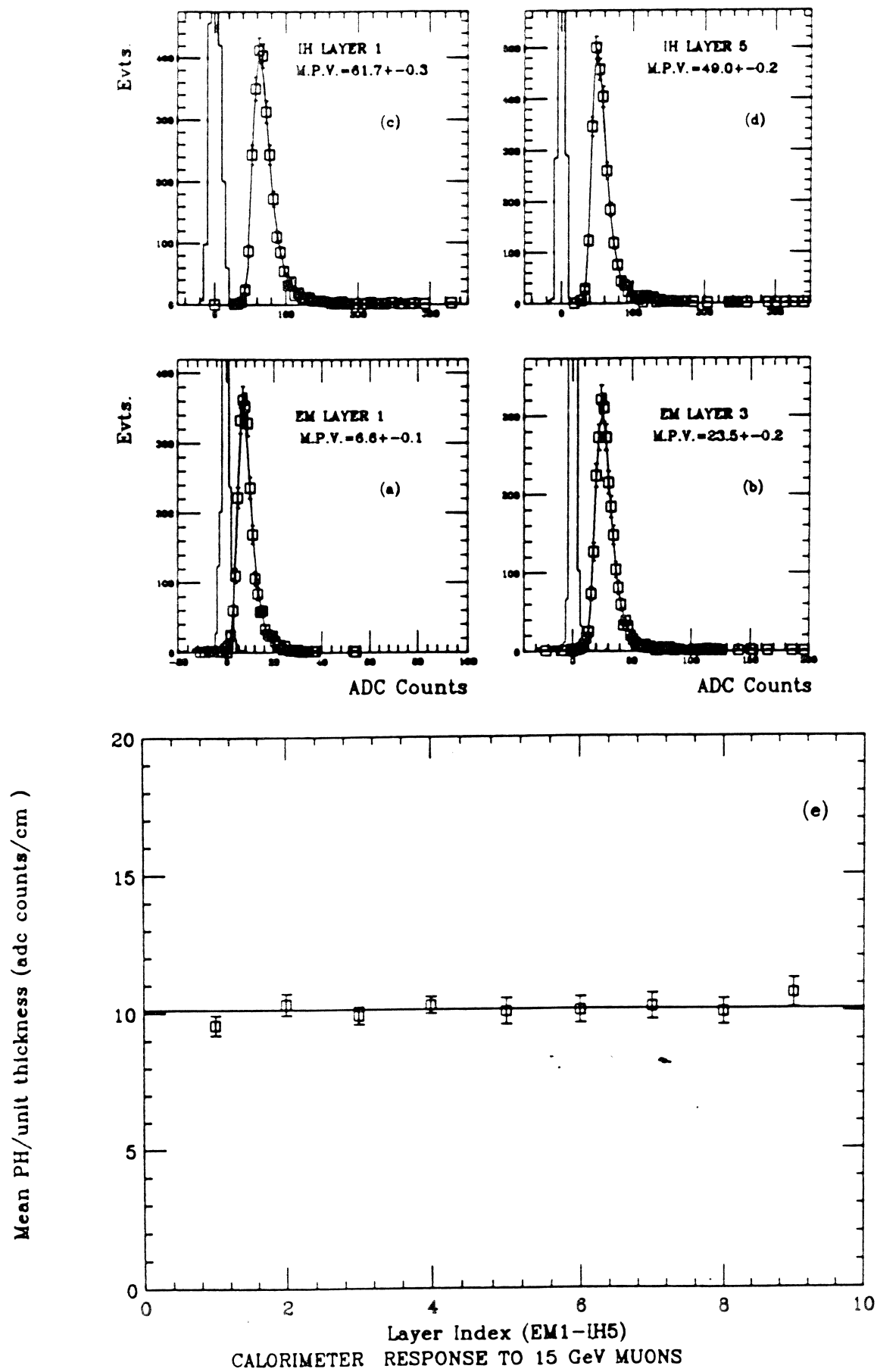


FIGURE 2

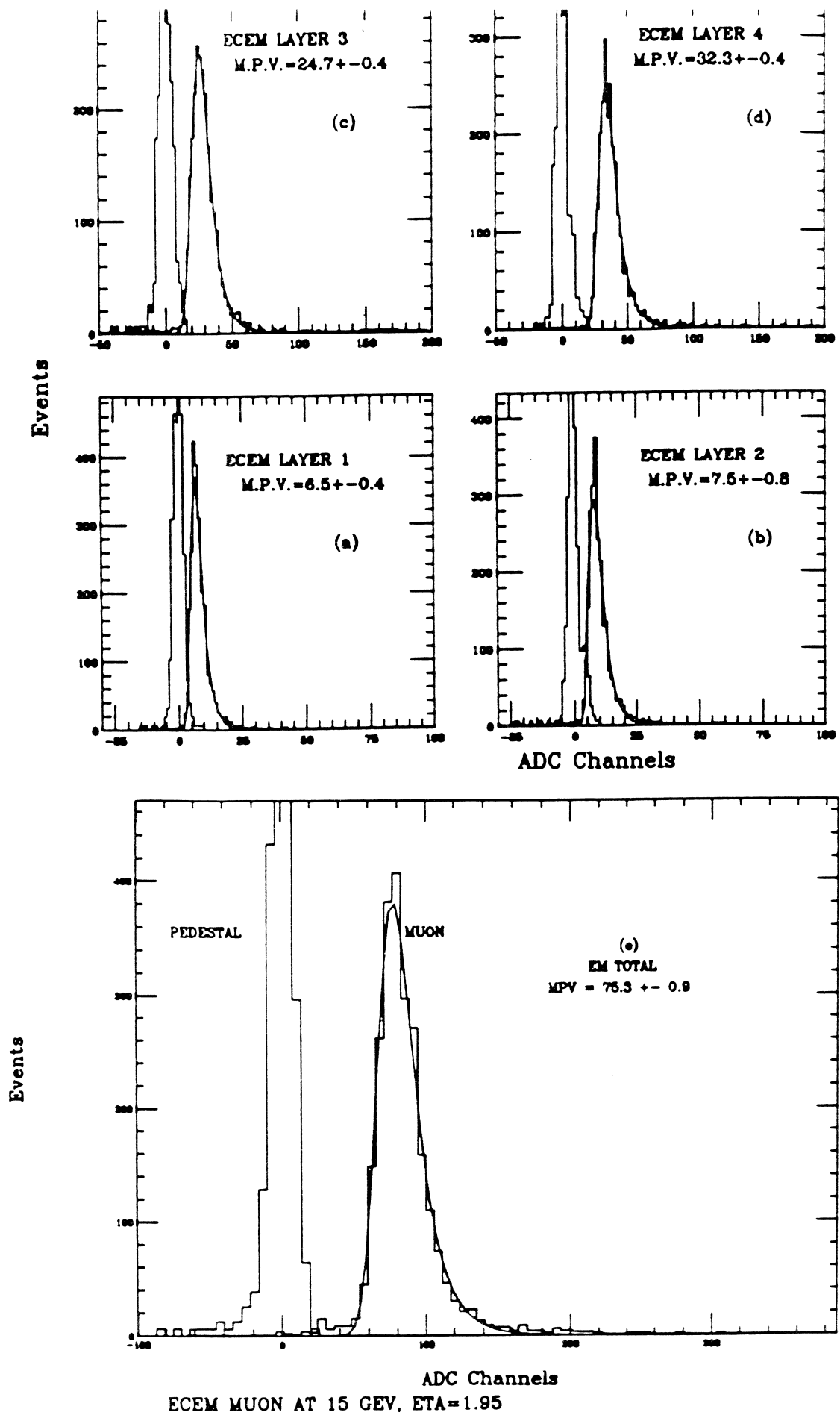


FIGURE 3



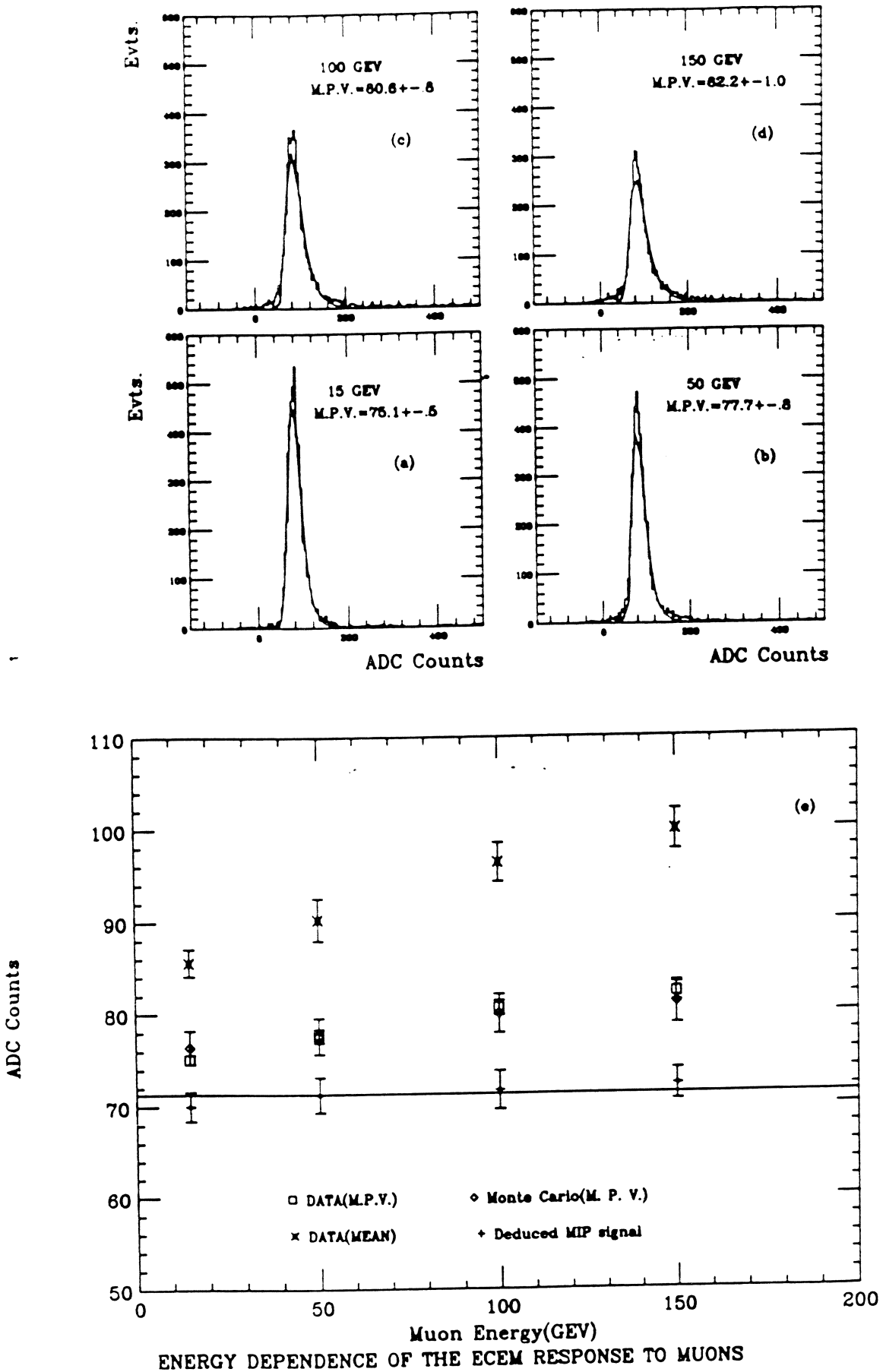


FIGURE 4

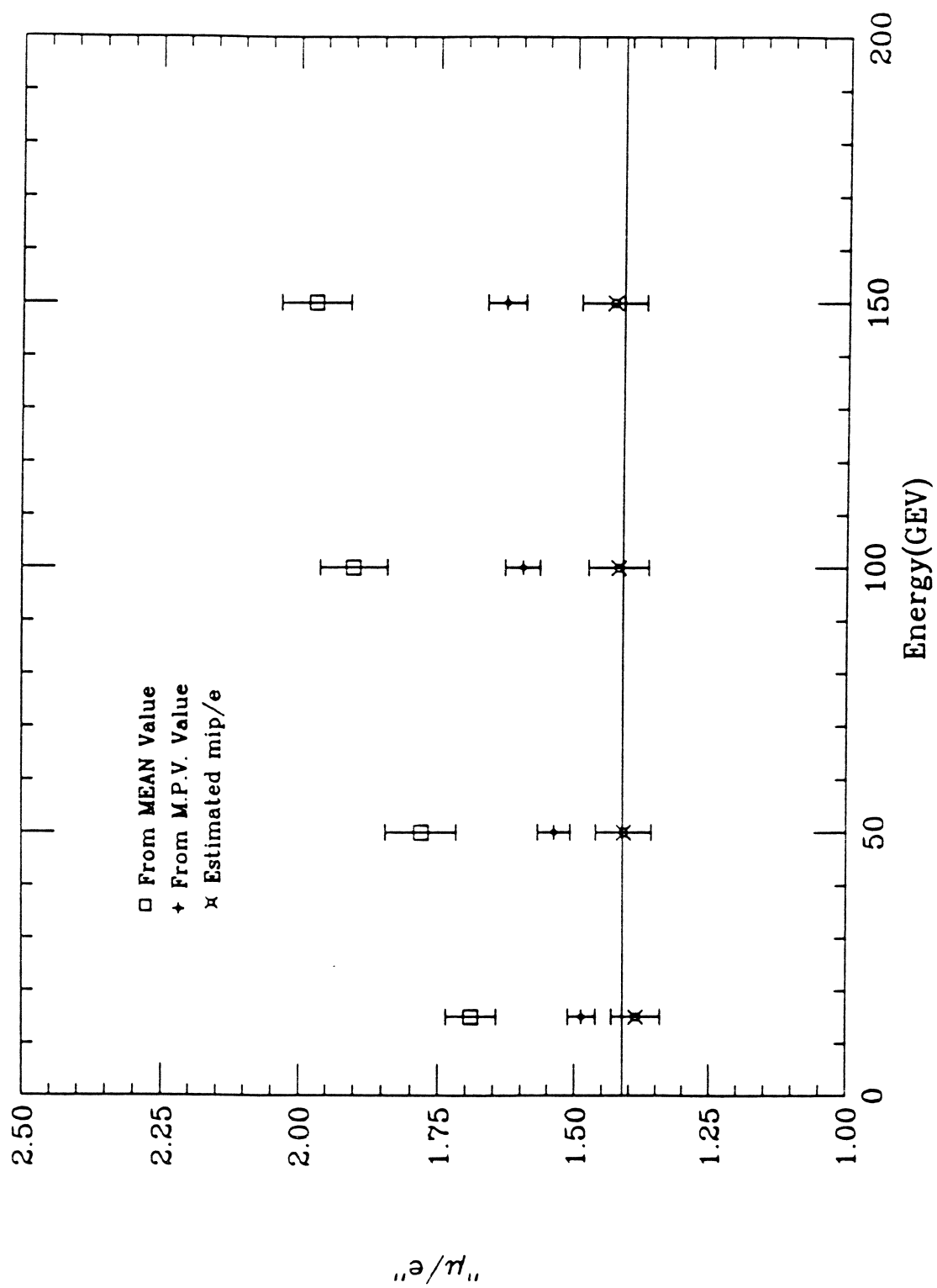


Fig. 5



DØ Note 1300

Dec. 5, 1991

TBM

**DØ CALORIMETER RESPONSE  
TO LOW ENERGY BEAM AT NWA  
AND  
IMPLICATIONS TO DØ PHYSICS**

**P. Bhat  
Fermilab**

CALORIMETRY in the present high energy collider era should provide good energy measurements of electrons, photons, hadronic jets, non-interacting particles neutrinos, (photons) by  $E_t$ .

Jets have large fraction of low energy hadrons.

Precision of  $E_t$  measurement critically depends on understanding the calorimeter response to low energy particles.

**\* LOW ENERGY RESPONSE IS VERY IMPORTANT \***

1. LOW ENERGY BEAM AT NWA

Making of the tertiary beam

2. RESULTS ON

- \* ELECTRON AND HADRON RESPONSE BELOW 10GEV
- \* LINEARITY
- \*  $e/\pi$

3. IMPLICATIONS TO DO PHYSICS

- A. JET ENERGY SCALE
- B. W BOSON PROPERTIES

**September, 1986**

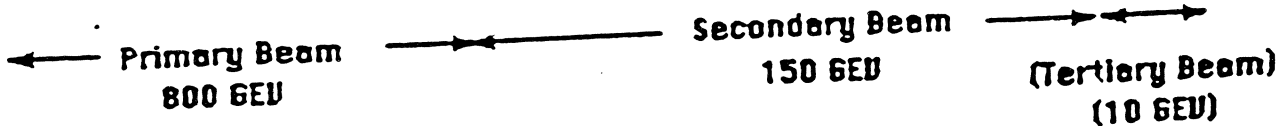
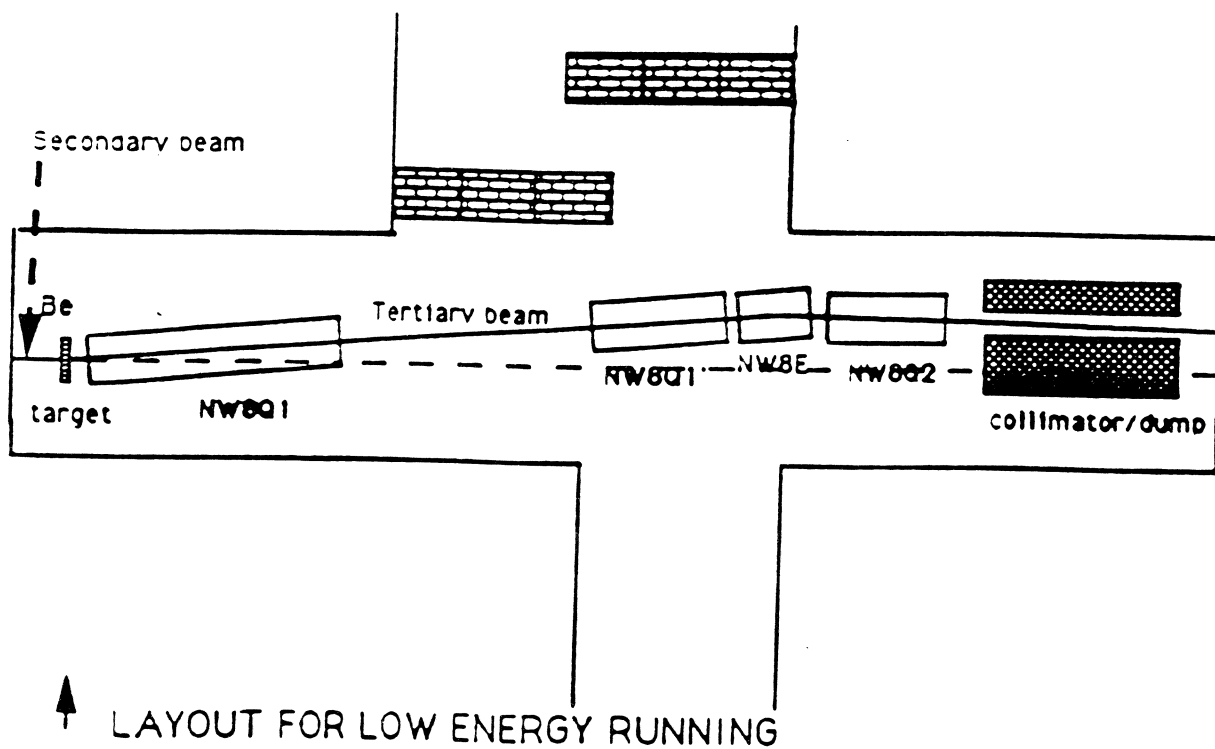
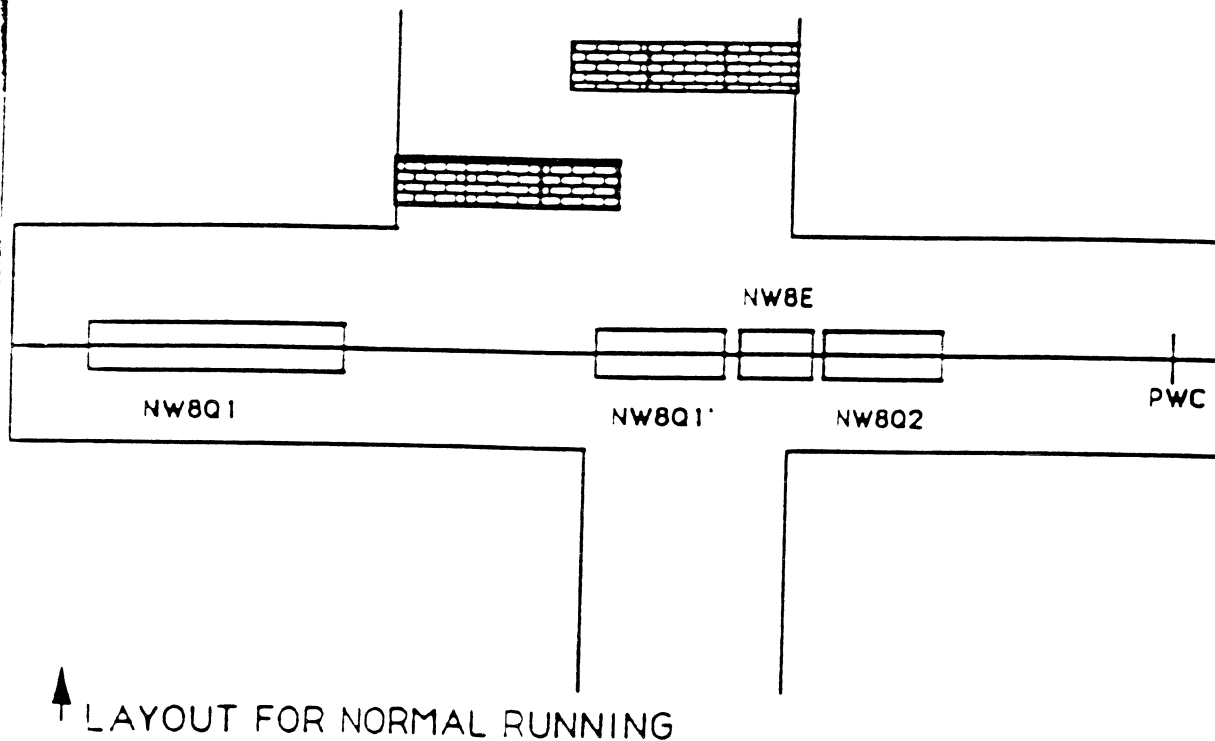


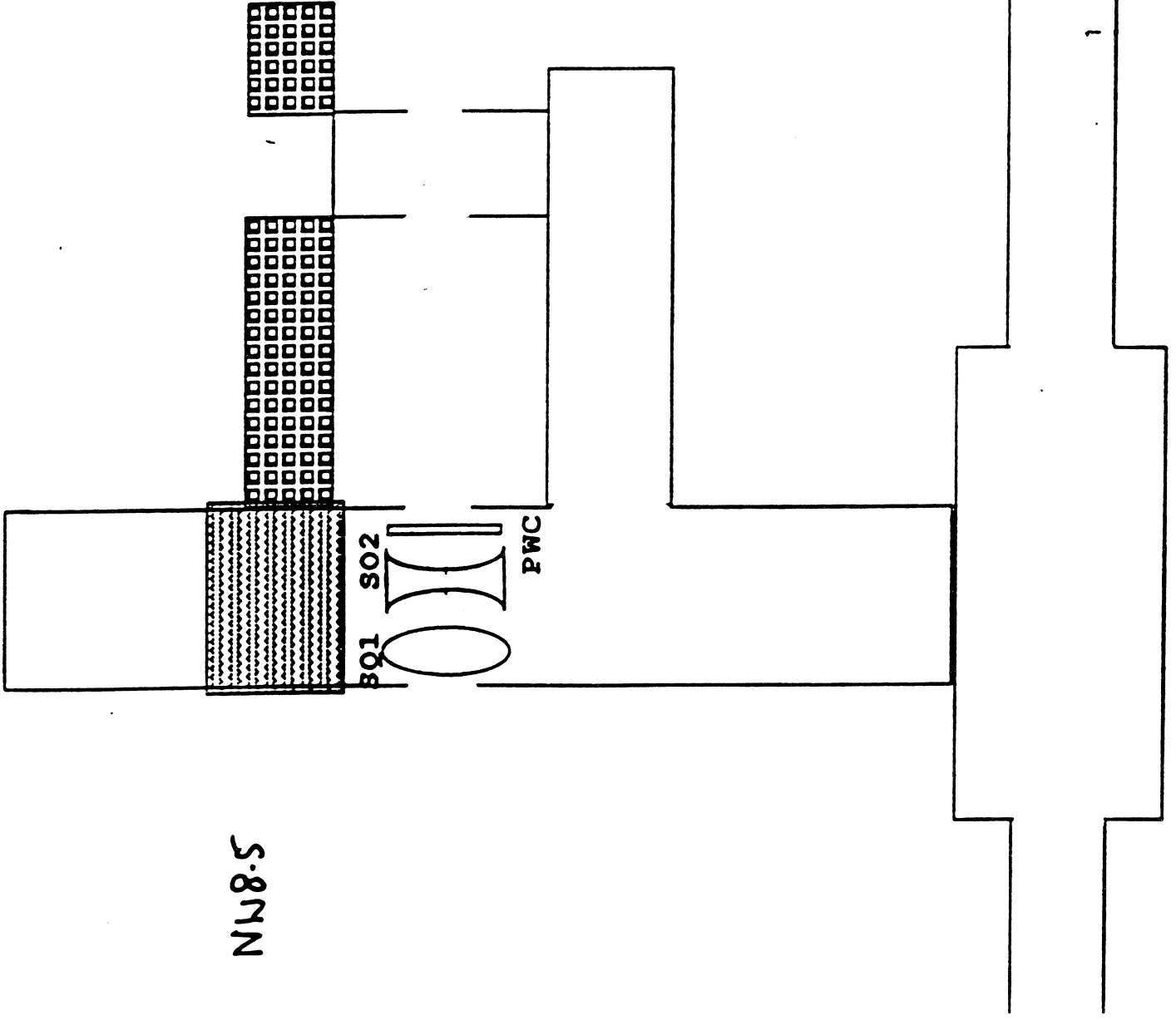
FIG. 6. NW8 ENCLOSURE LAYOUT AFTER UPGRADE:

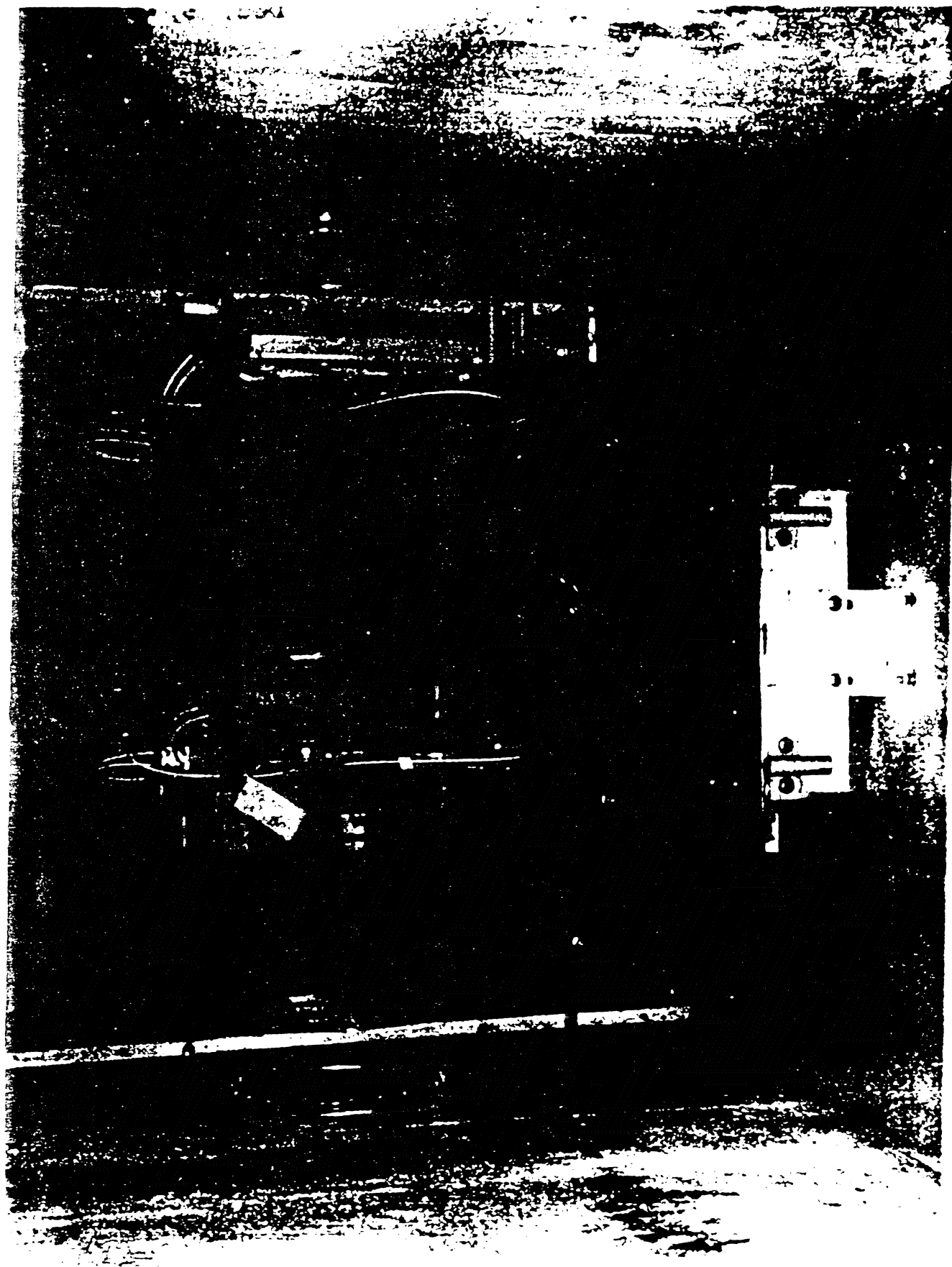


\* Figure is only schematic and the magnets are not shown with their full transverse dimensions.



NW8-5

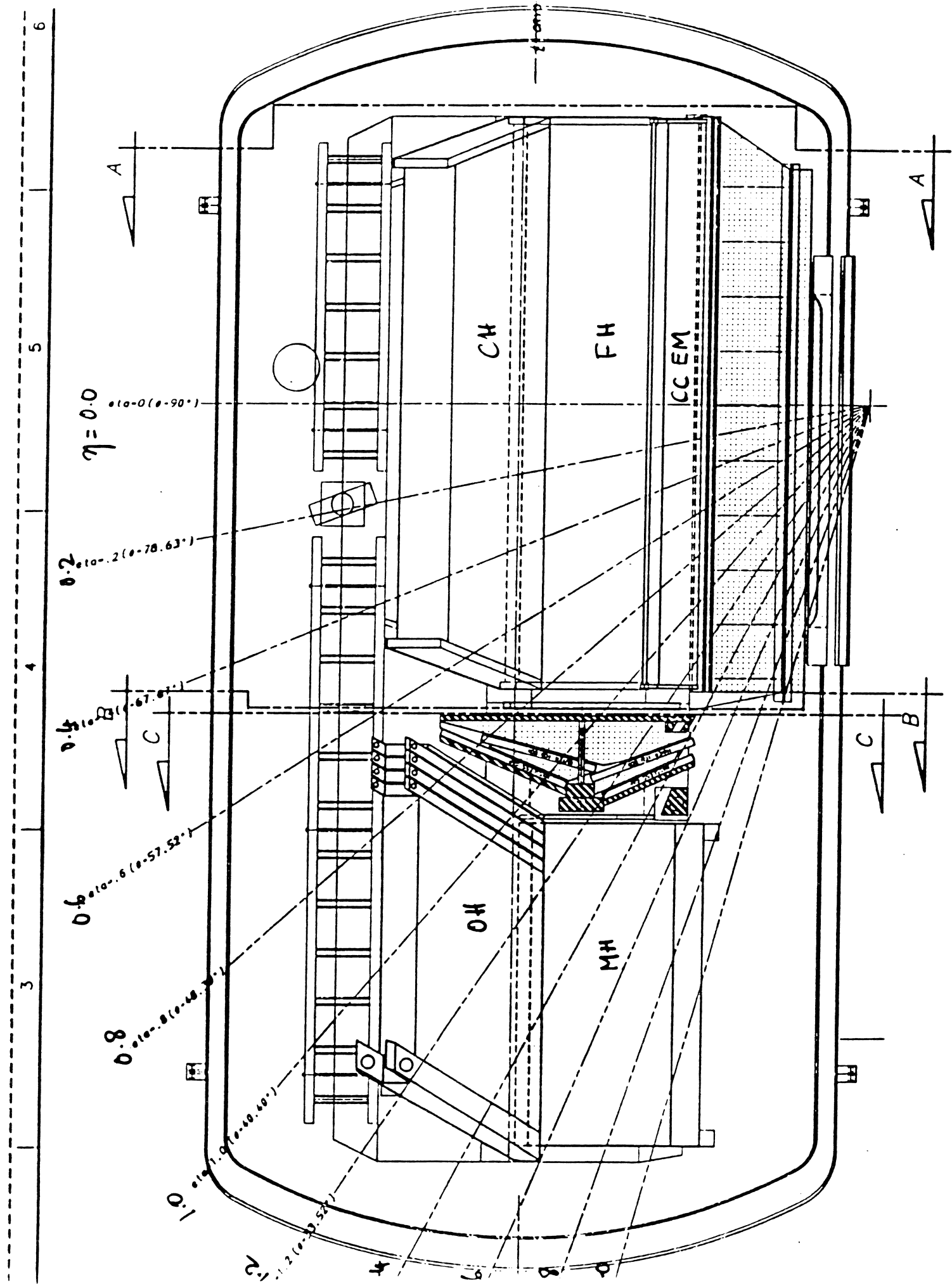


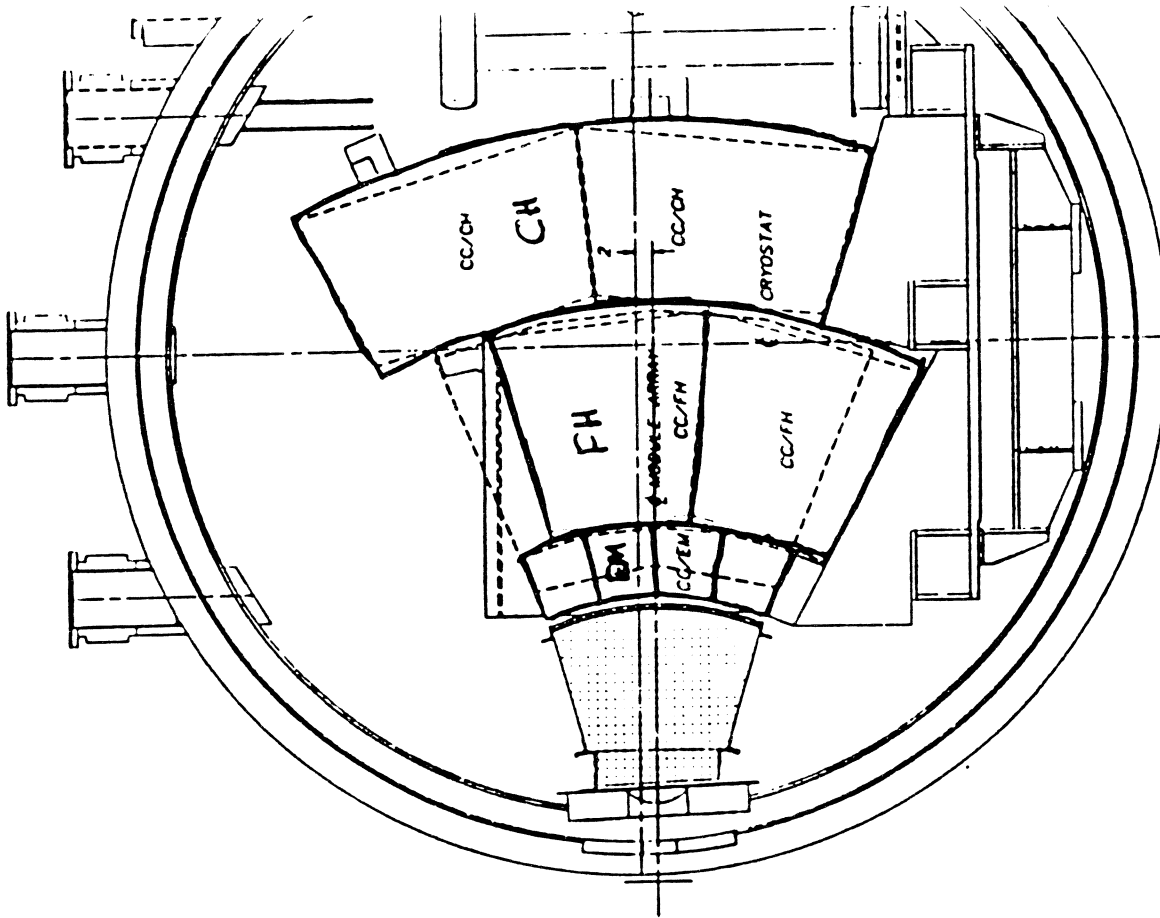


PB  
10/3/91

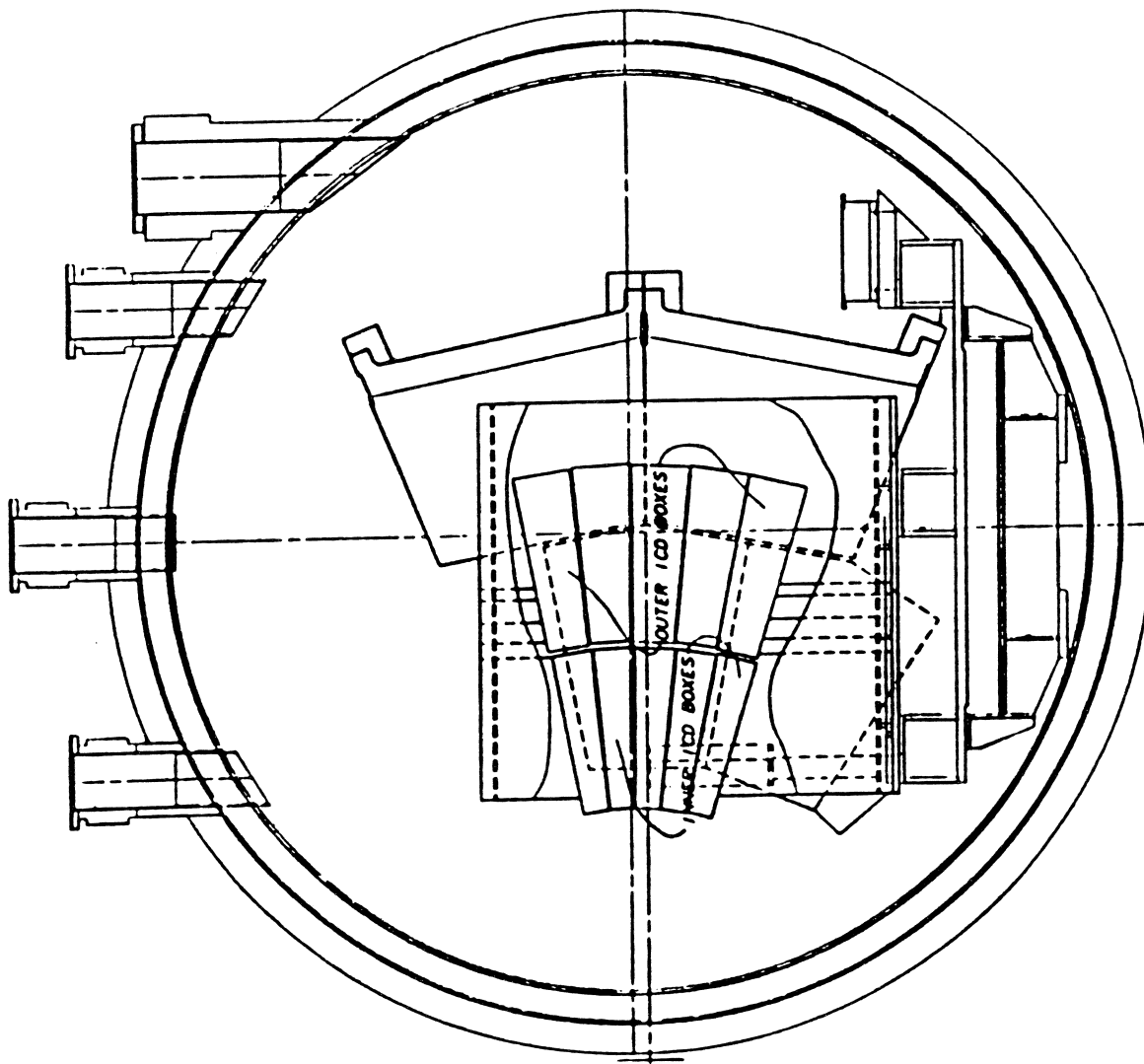
Pion rates

Energy	# of pions / spill of $1 E12$	Average # / hour	
10 GeV	100 / spill	5000	50% p
5 GeV	20	1000	12% p
3.5	6	300	
3	3	150	
2.5	1.5	75	
2	.7	35	~1%



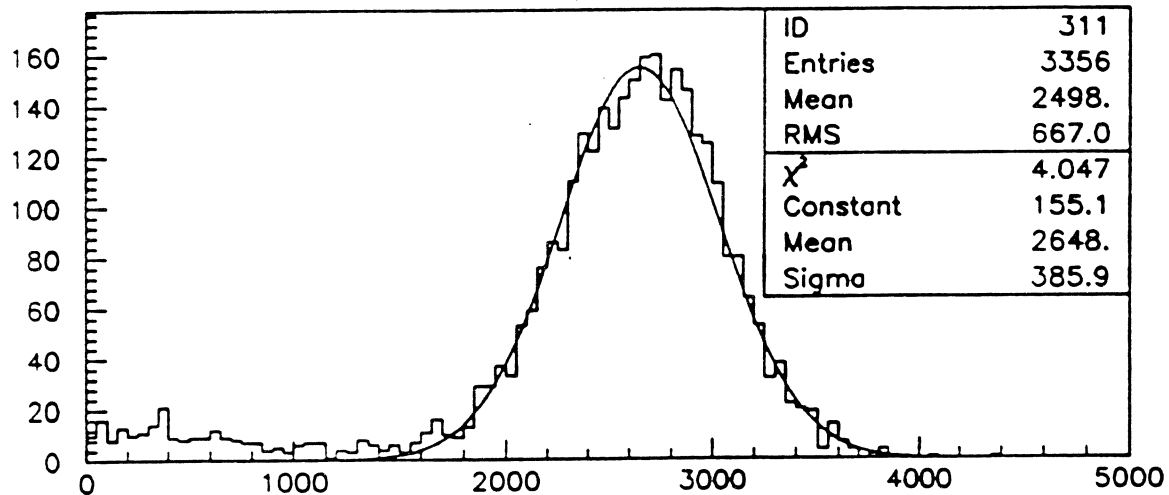


SECTION A-A

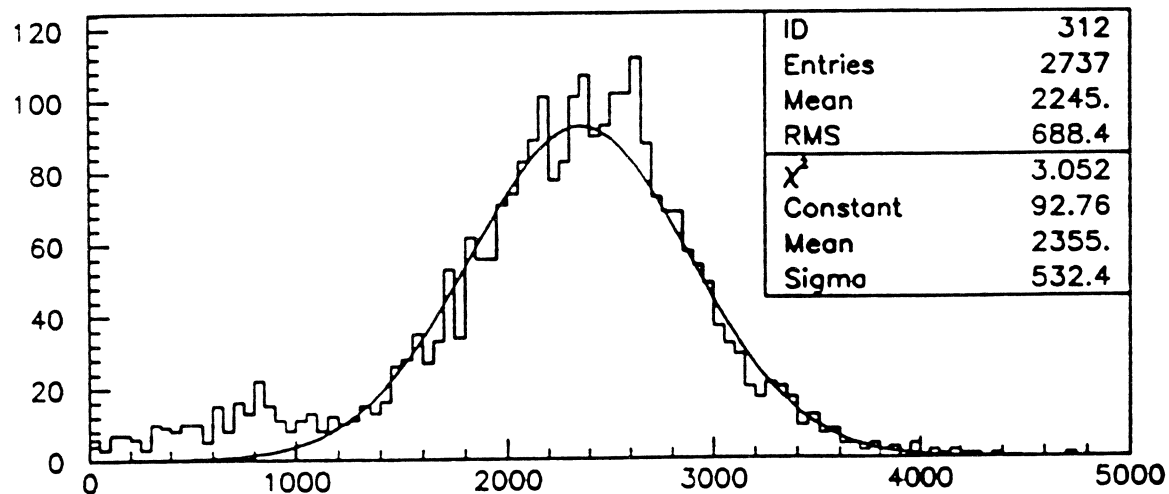


SECTION B-B

run1012513, 10GeV 0.05,31.6

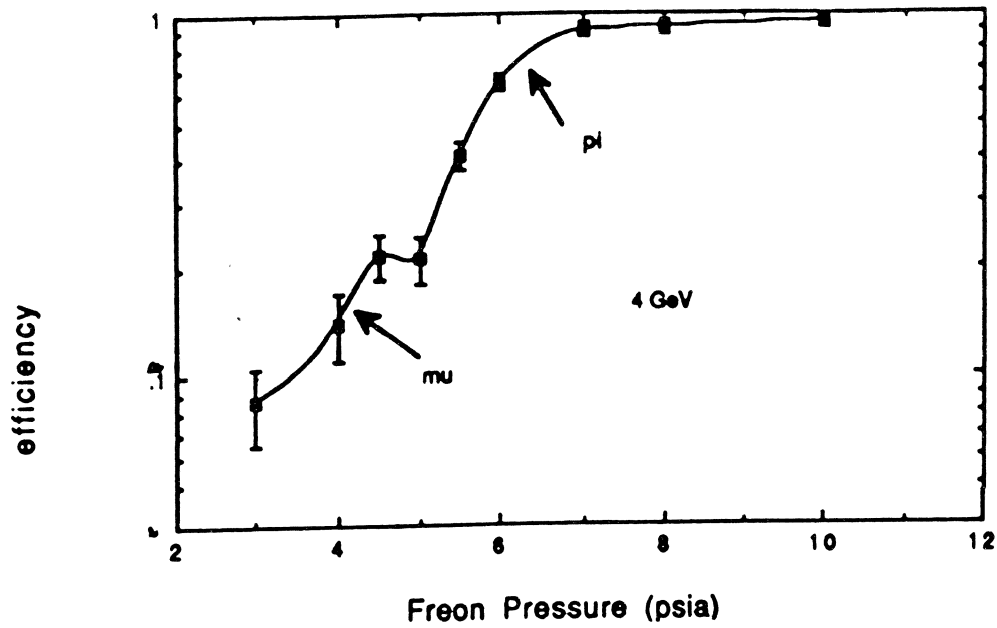


EMzW+.85\*FHzW+CHzW, ELECTRONS

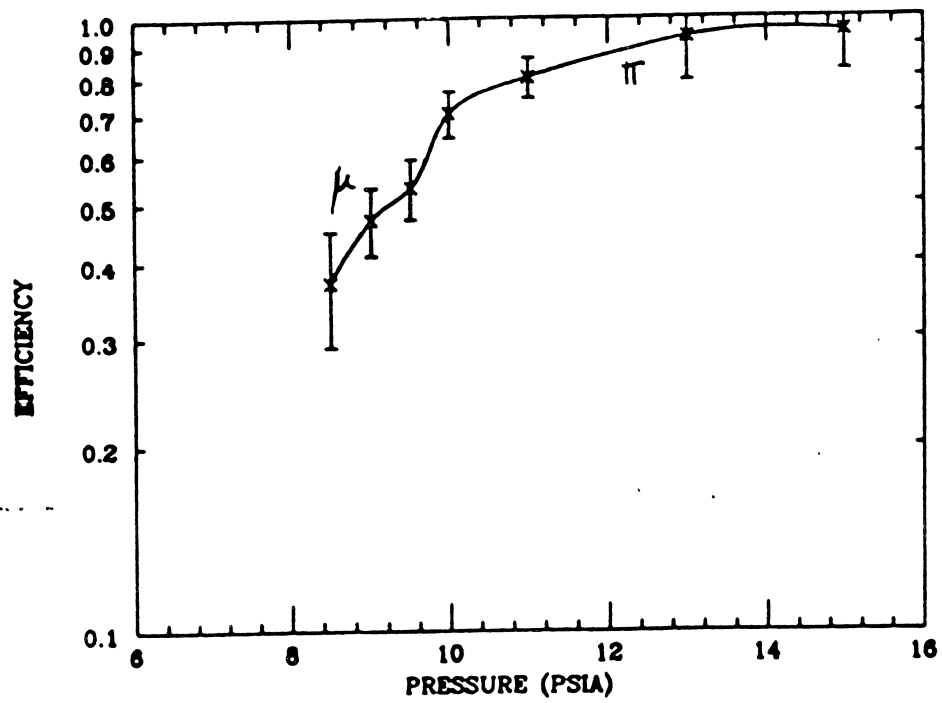


EMzW+.85\*FHzW+CHzW, PIONS

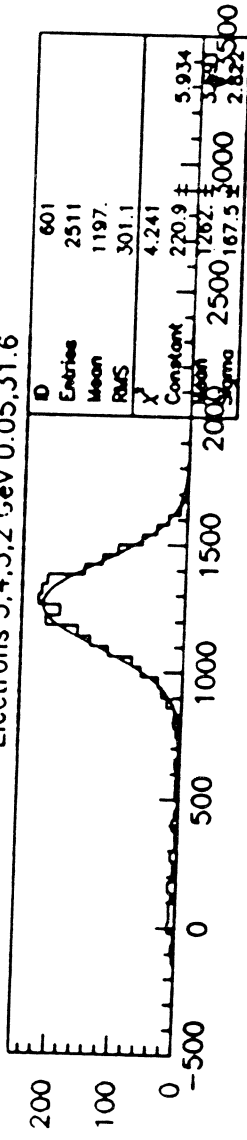
Freon-114 CC pressure curve



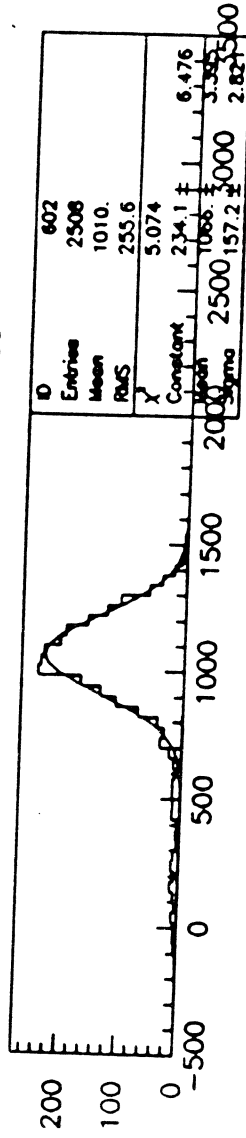
FREON-114 CERENKOV PRESSURE CURVE, 3 GEV



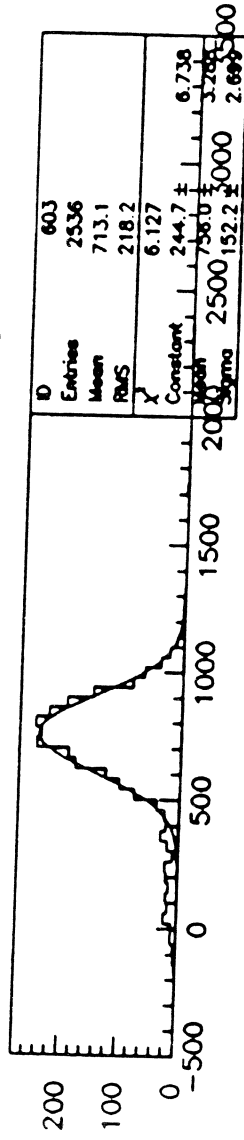
# Electrons 5.4,3.2 GeV 0.05,31.6



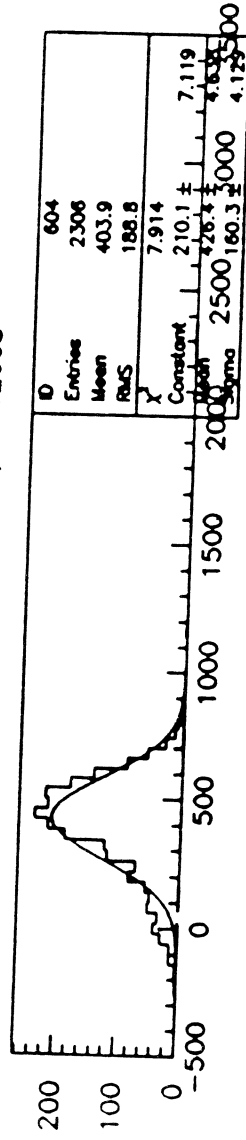
emztotzw+0.85\*fh1w, run12730



emztotzw+0.85\*fh1w, run12705



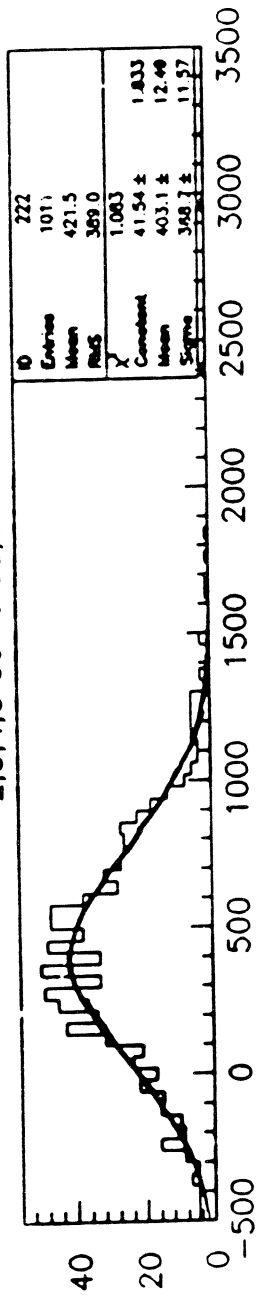
emztotzw+0.85\*fh1w, run12668



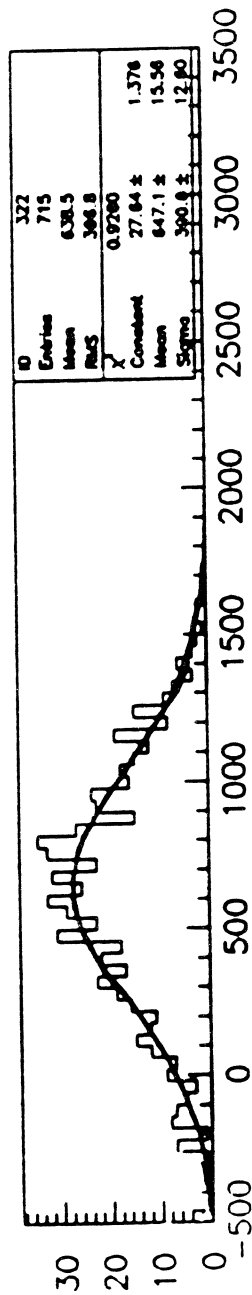
emztotzw+0.85\*fh1w, run12622



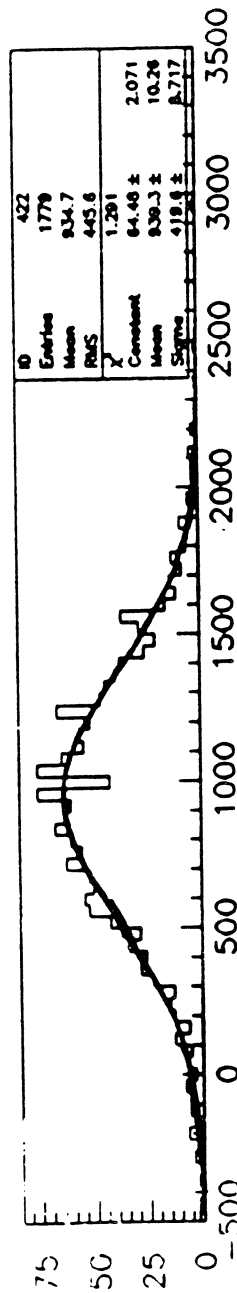
2,3,4,5 GeV 0.05,31.6



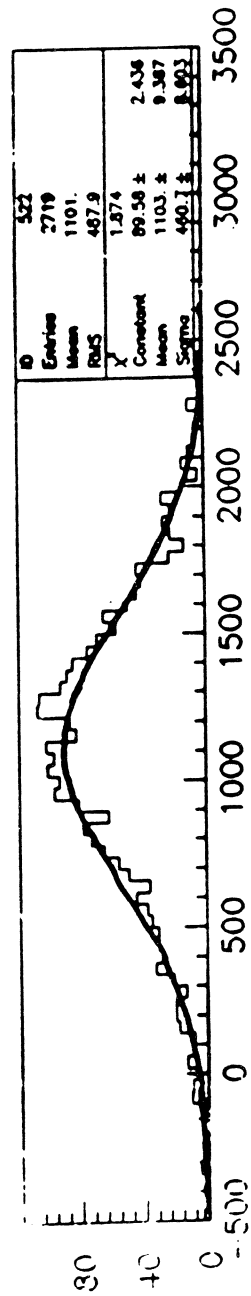
EMzW + .85\*FHZW + CHZW, PIONS



EMzW + .85\*FHZW + CHZW, PIONS

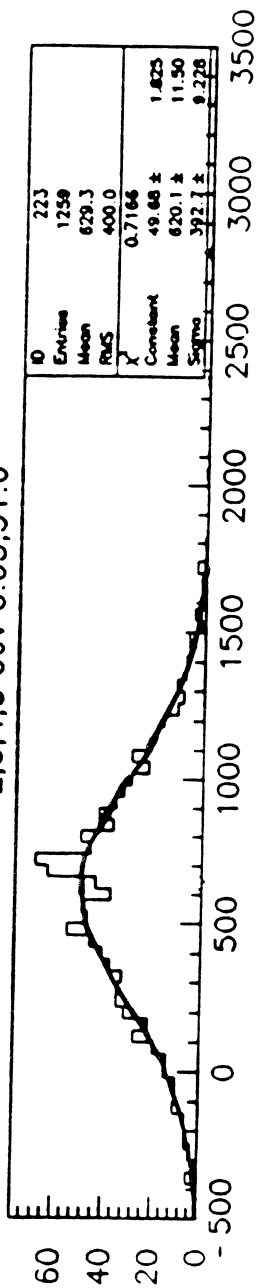


EMzW + .85\*FHZW + CHZW, PIONS

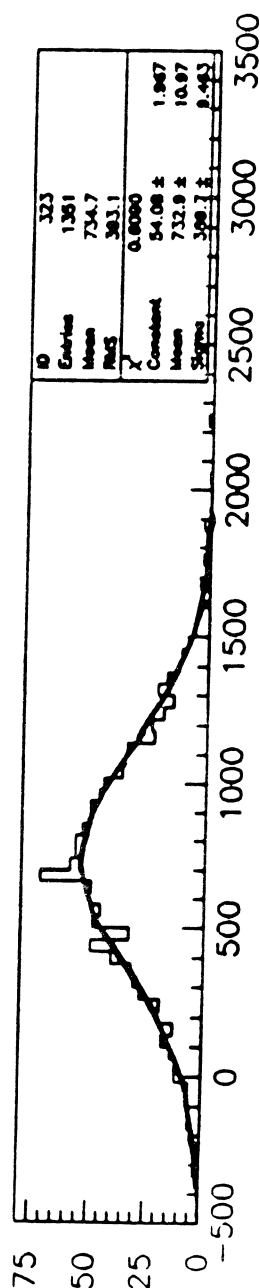


EMzW + .85\*FHZW + CHZW, PIONS

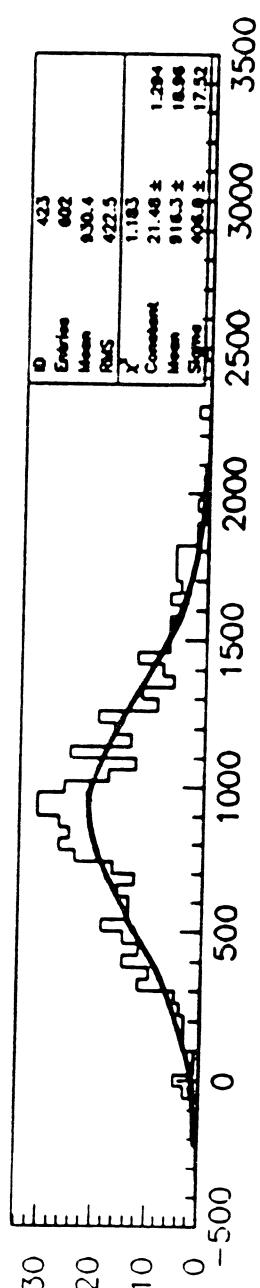
2,3,4,5 GeV 0.05,31.6



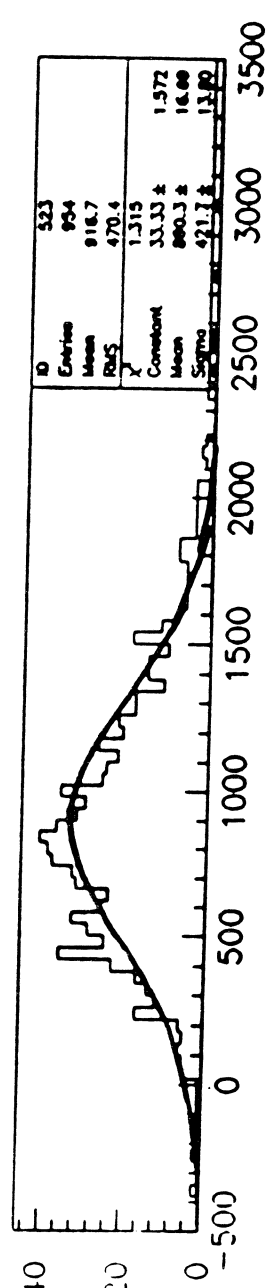
EMzW+.85\*FHZW+CHZW, MUONS



EMzW+.85\*FHZW+CHZW, MUONS

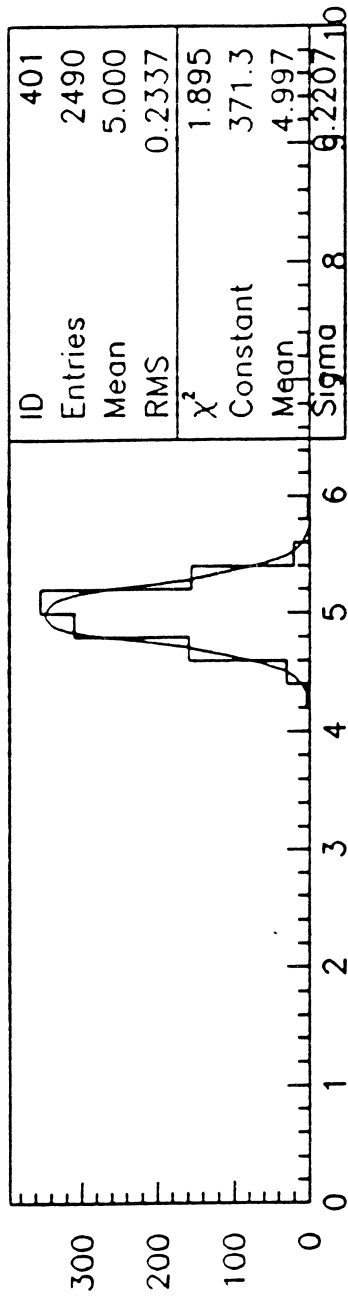


EMzW+.85\*FHZW+CHZW, MUONS

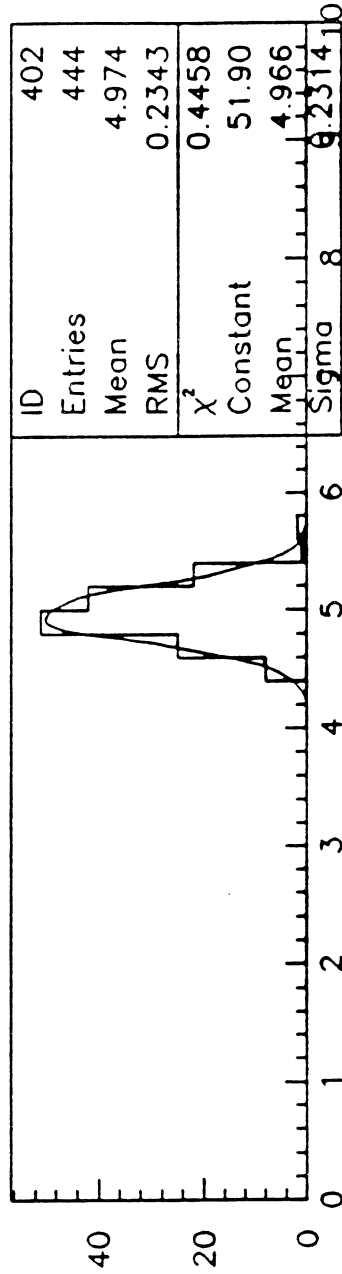


EMzW+.85\*FHZW+CHZW, MUONS

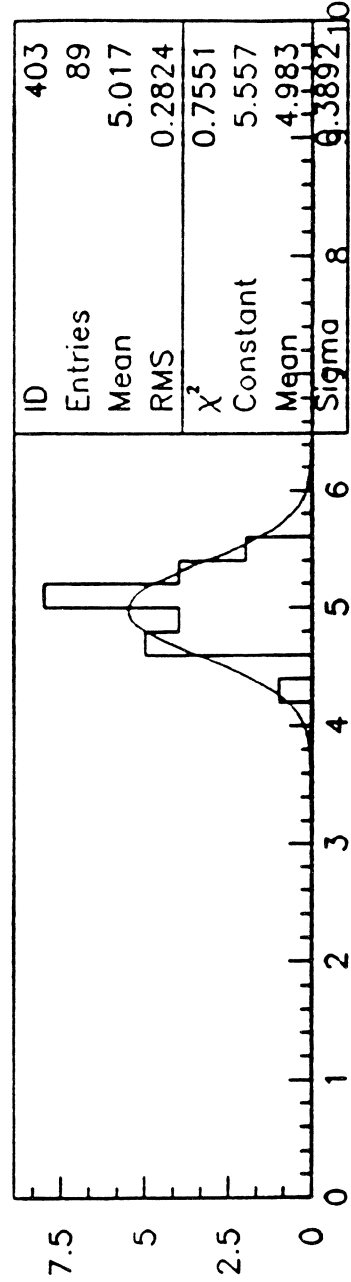
run1012442 5 GeV



beamzmom, electrons

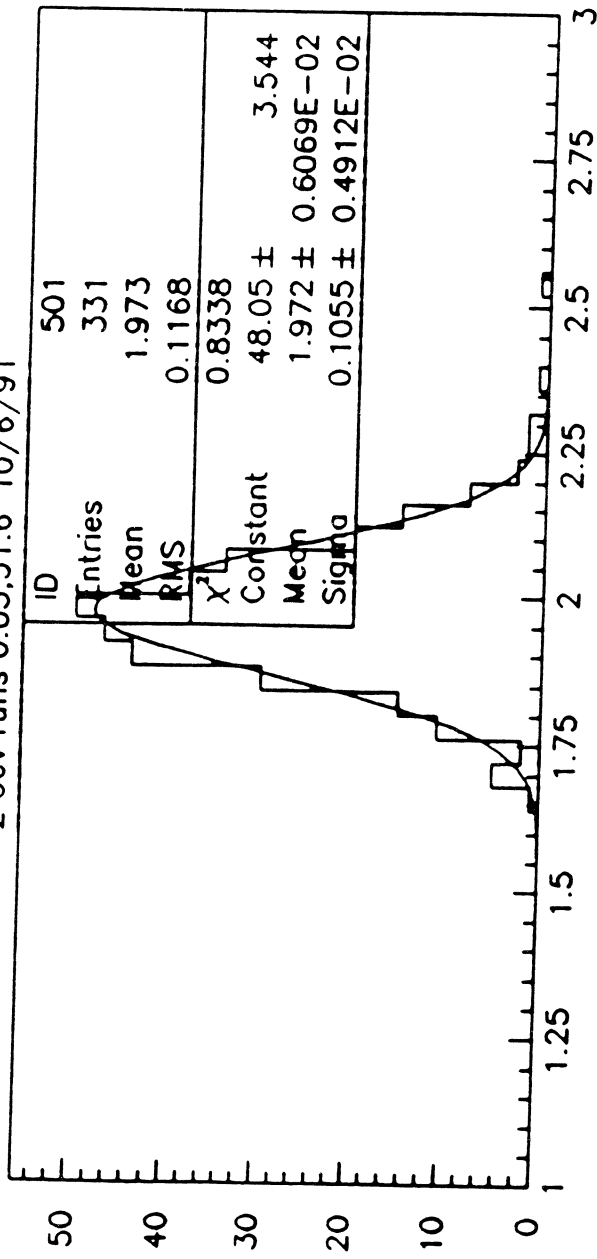


beamzmom, pions

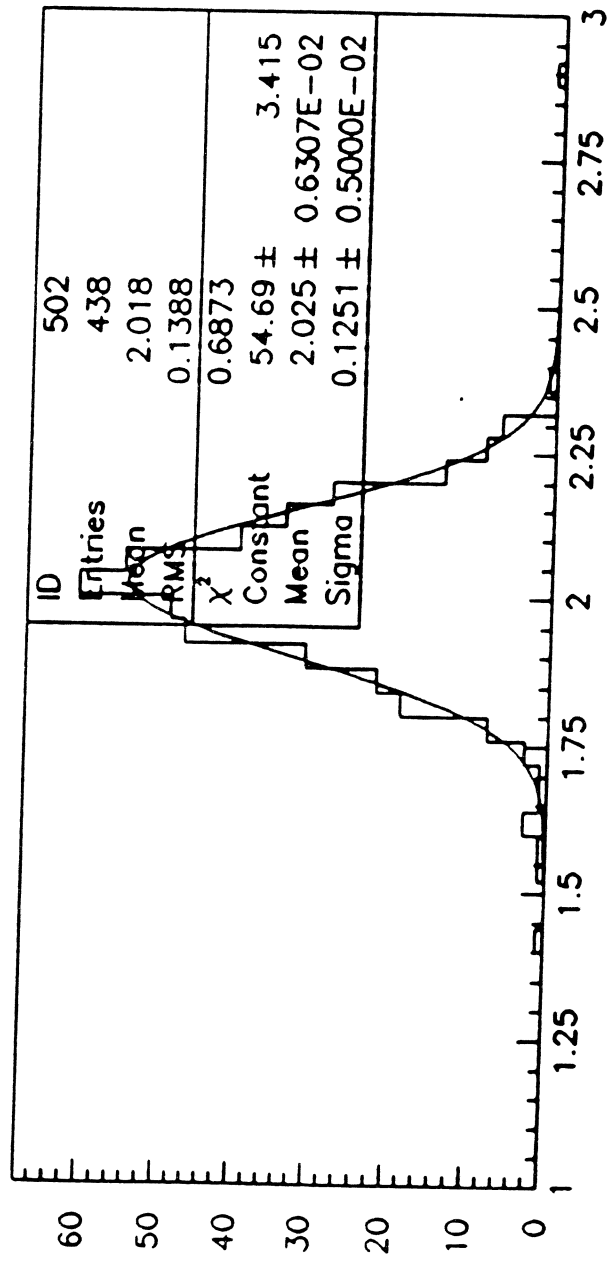


beamzmom, muons

2 GeV runs 0.05,31.6 10/6/91

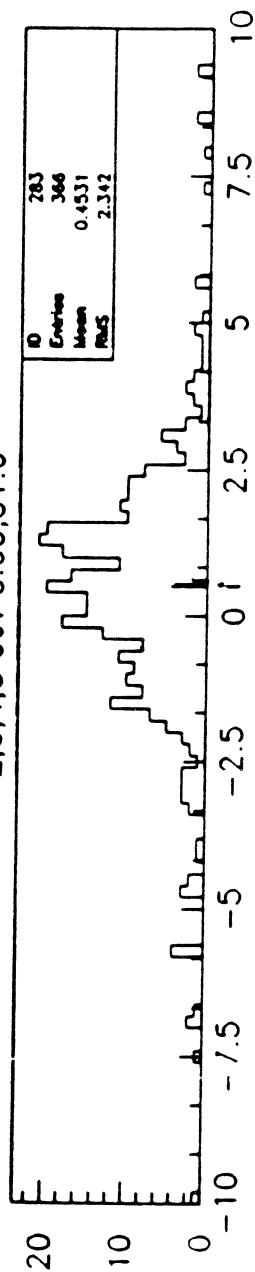


beamzmom, pions

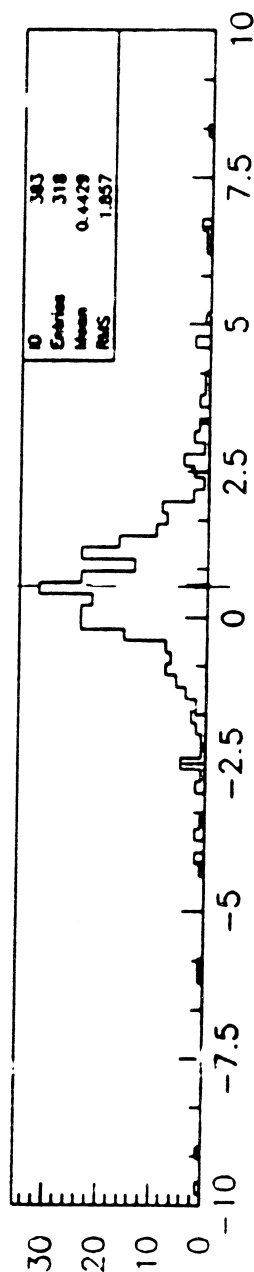


beamzmom, muons

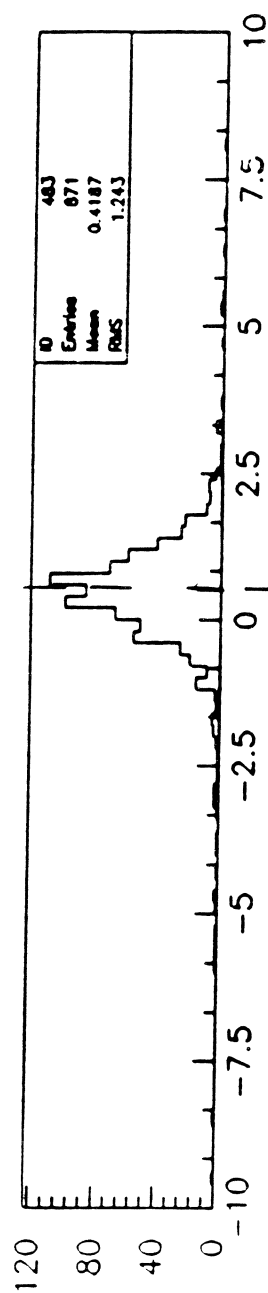
2,3,4,5 GeV 0.05,31.6



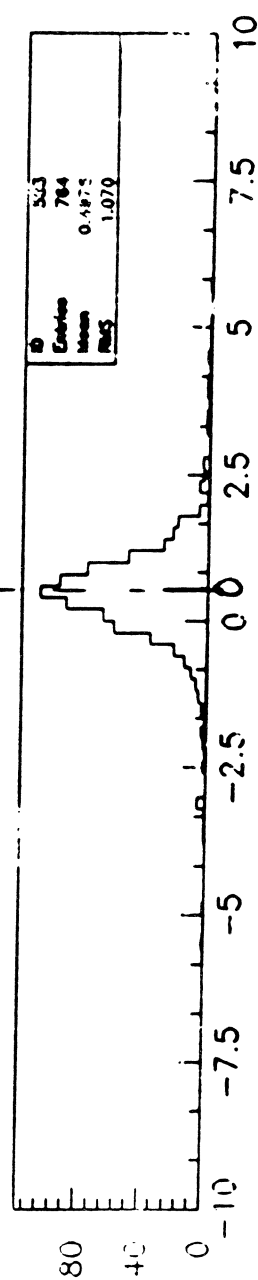
XUTK-XDTK, 2GeV



XUTK-XDTK, 3GeV



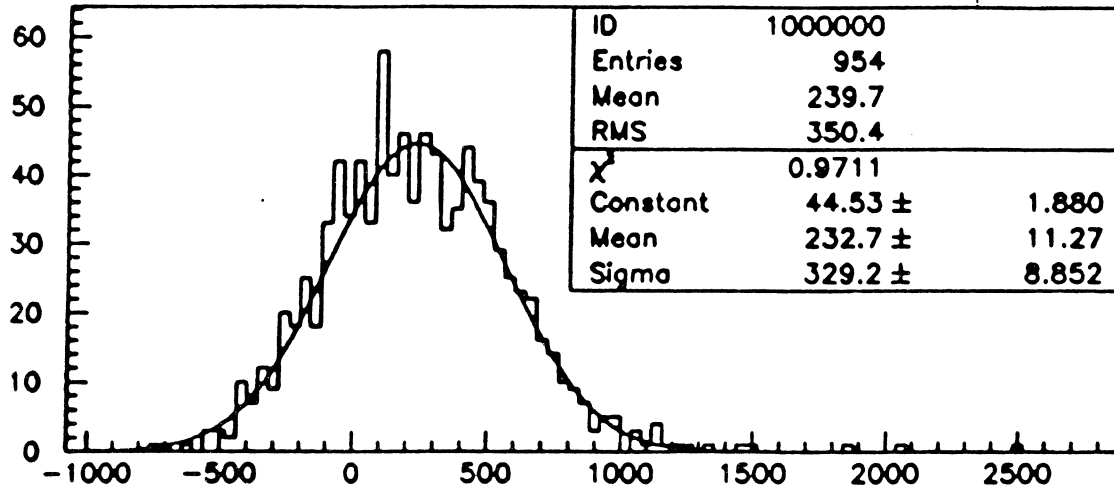
XUTK-XDTK, 4GeV



XUTK-XDTK, 5GeV

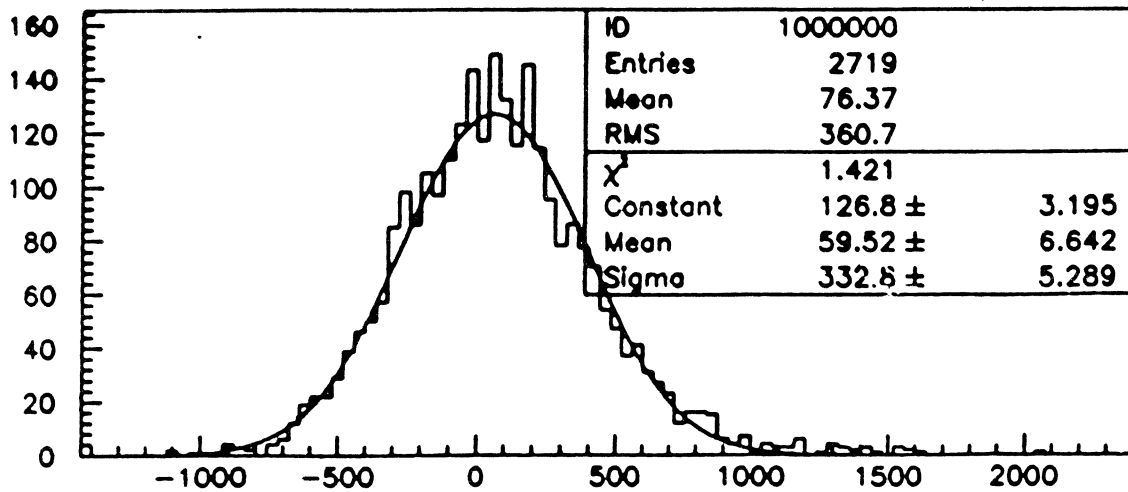
5 GeV

MUONS

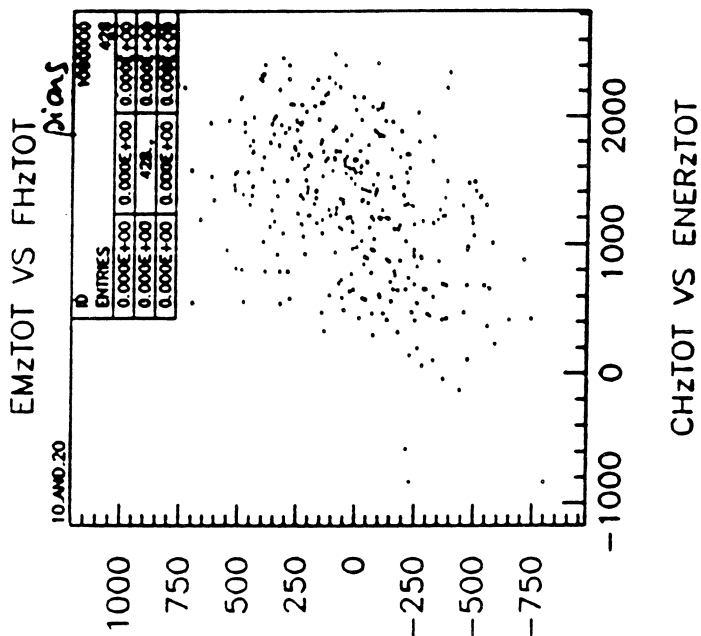
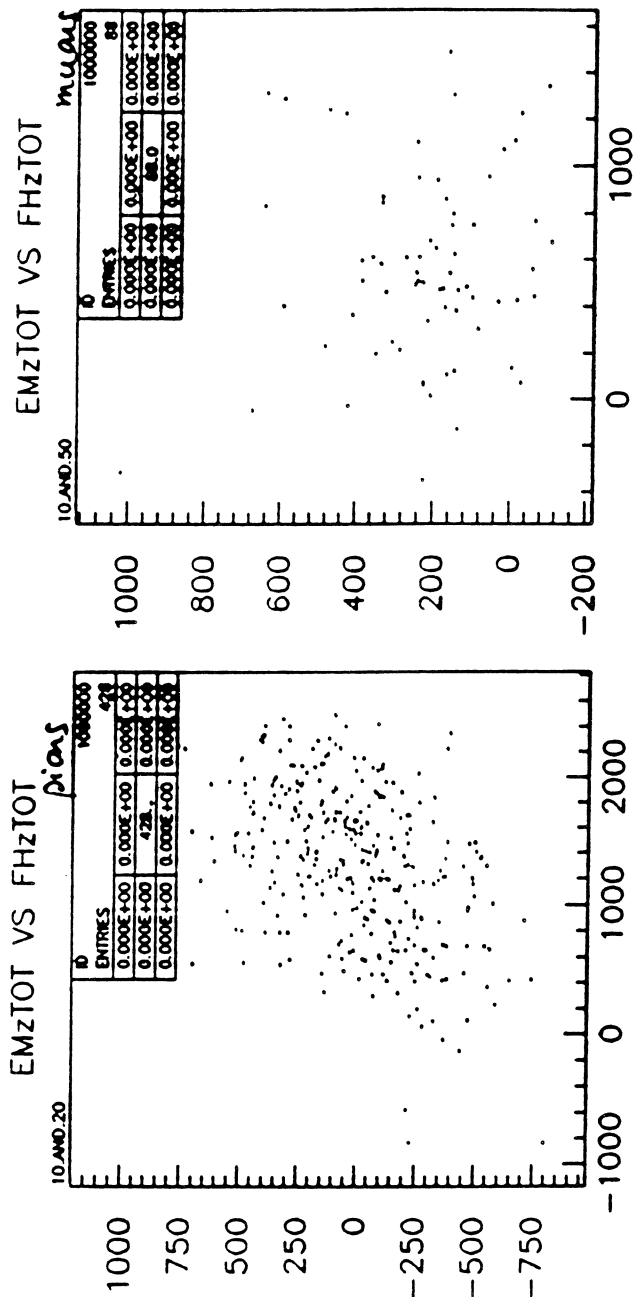
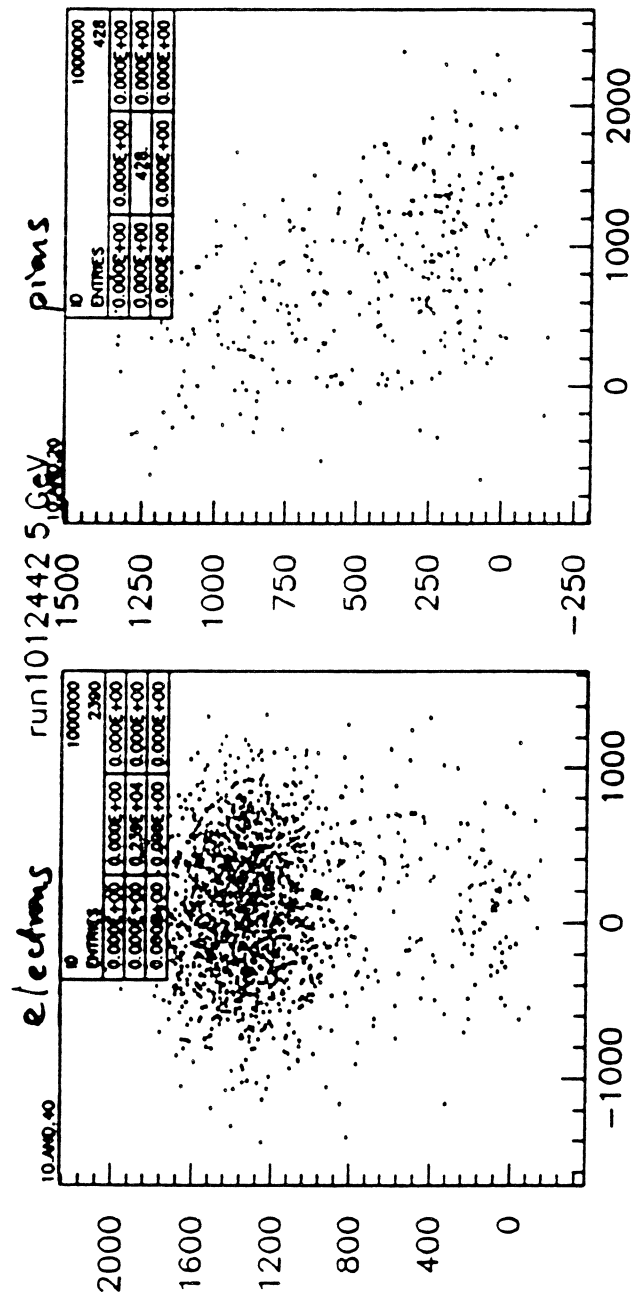


CHzTOT

PIONS



CHzTOT

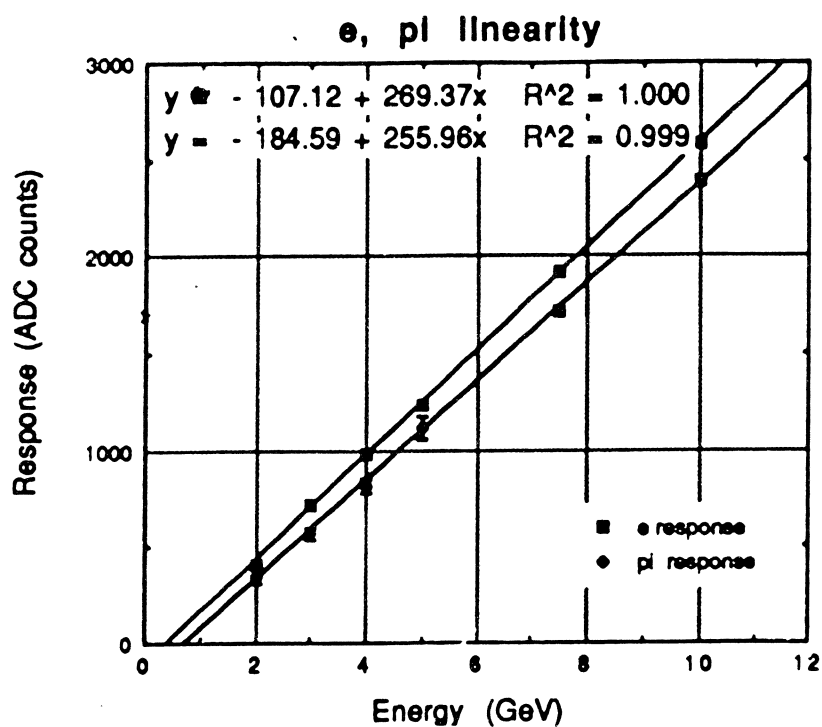


EMzTOT VS FHZTOT

EMzTOT VS FHZTOT

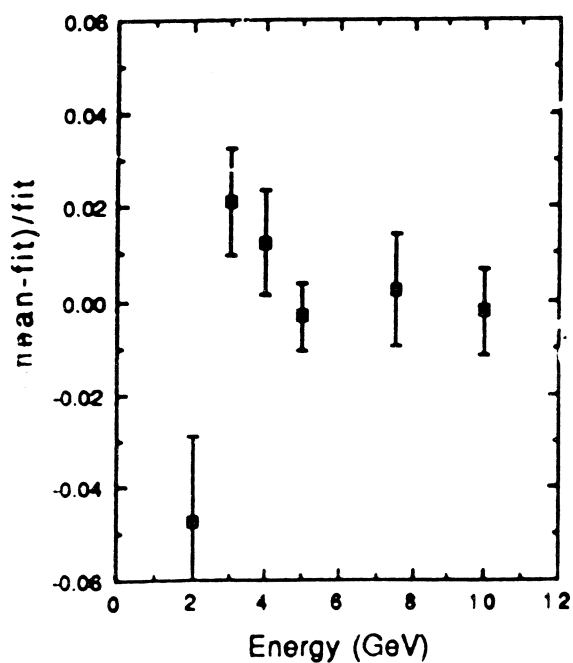
EMzTOT VS ENERzTOT

CHzTOT VS ENERzTOT

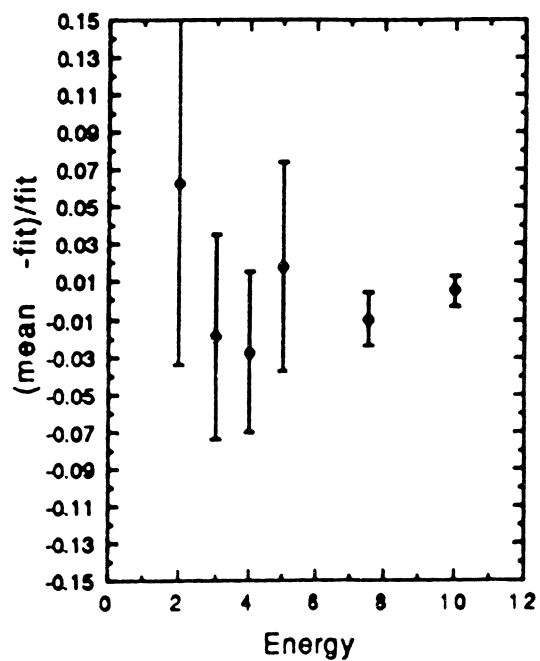


## Residuals from linear fit

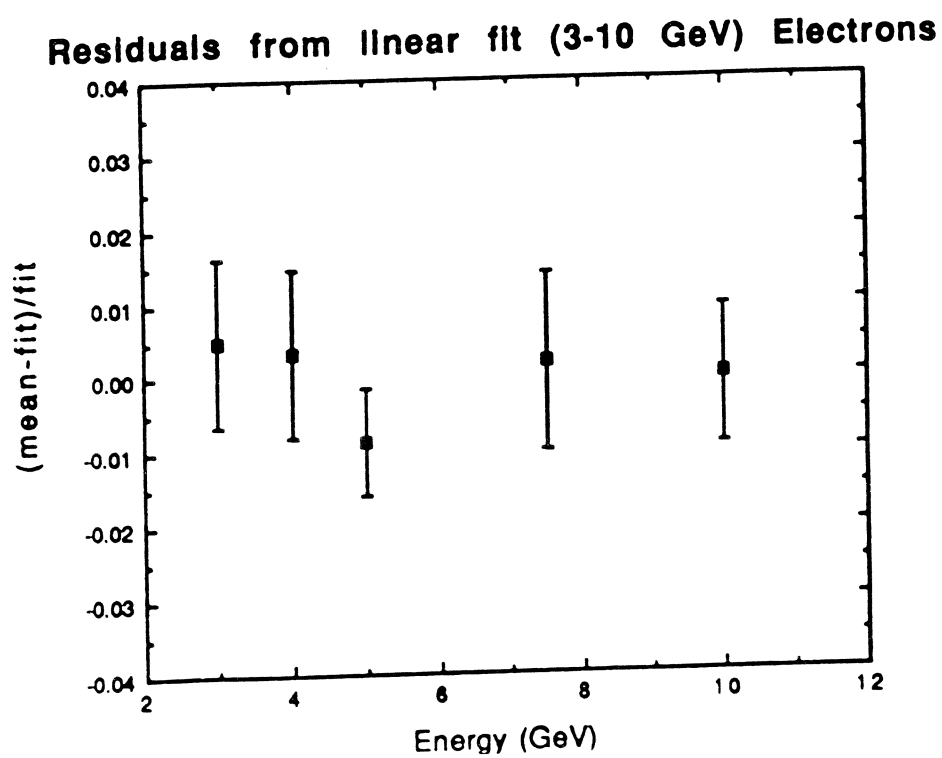
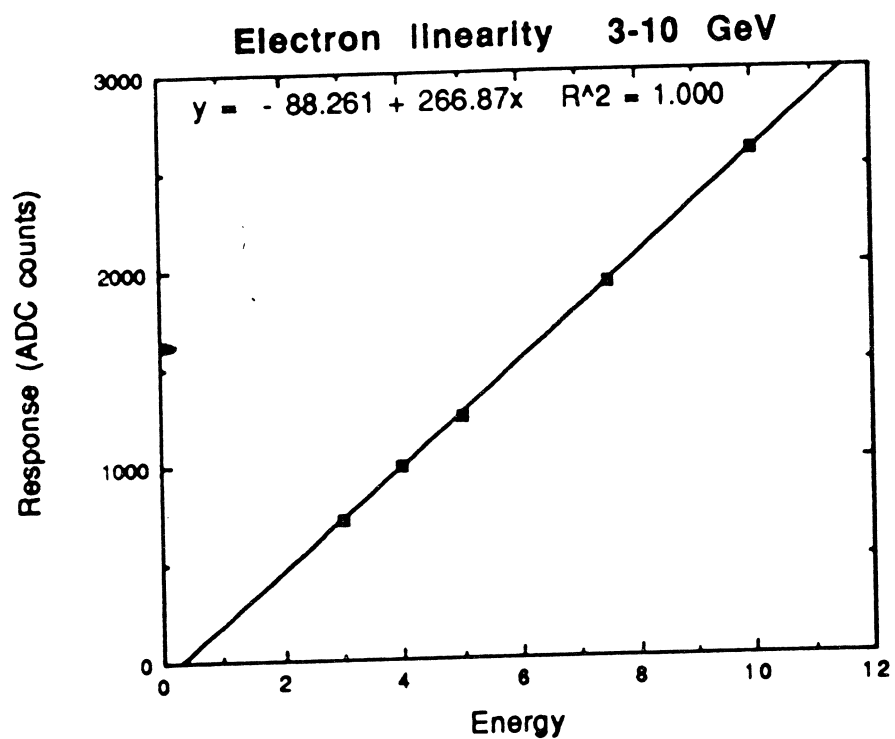
### Electrons

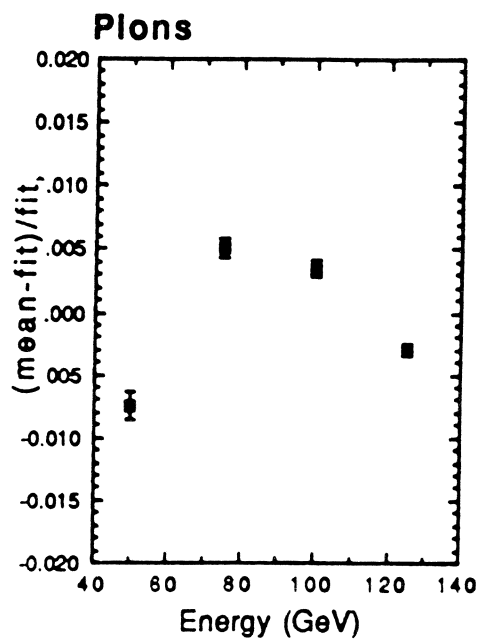
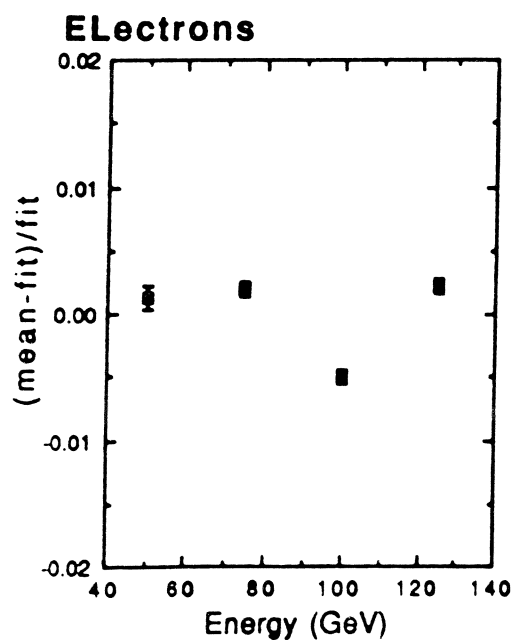
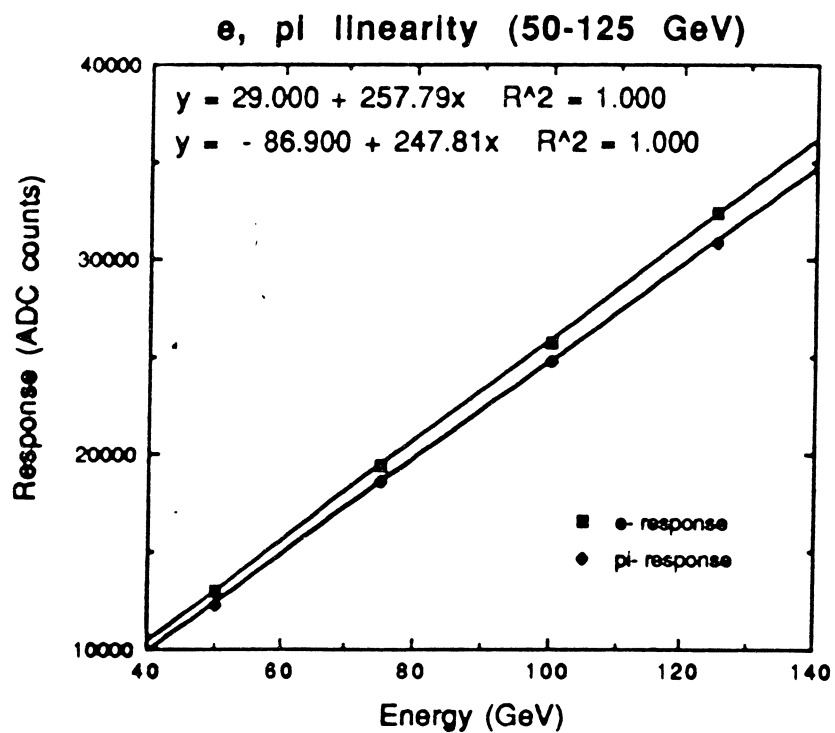


### Pions

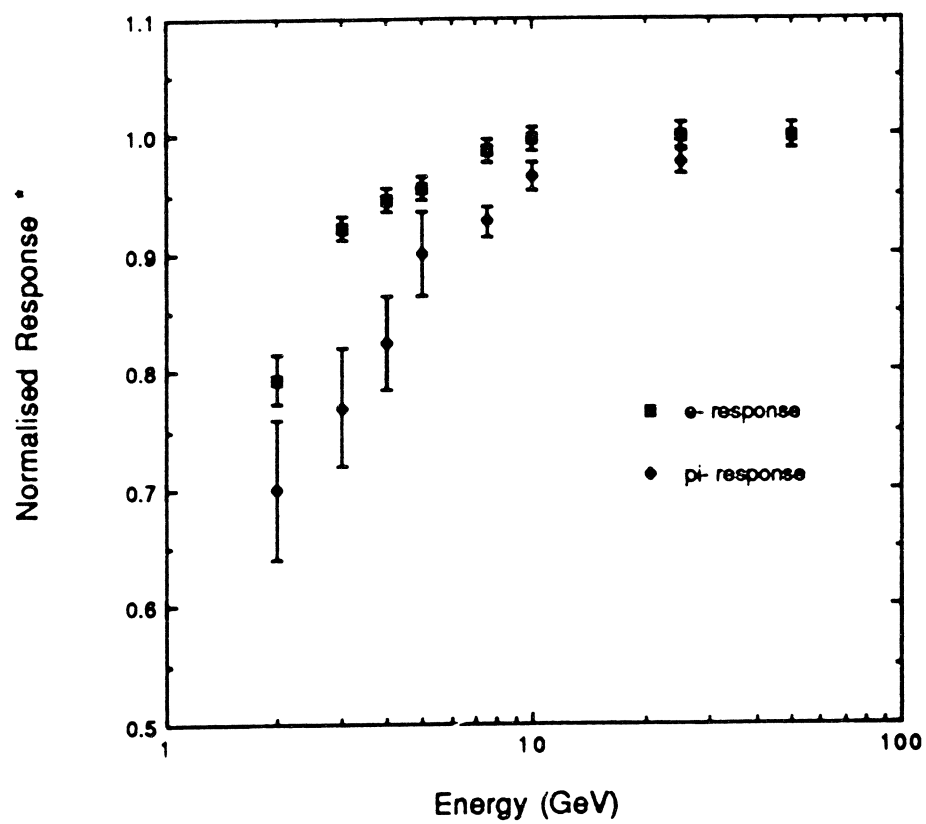






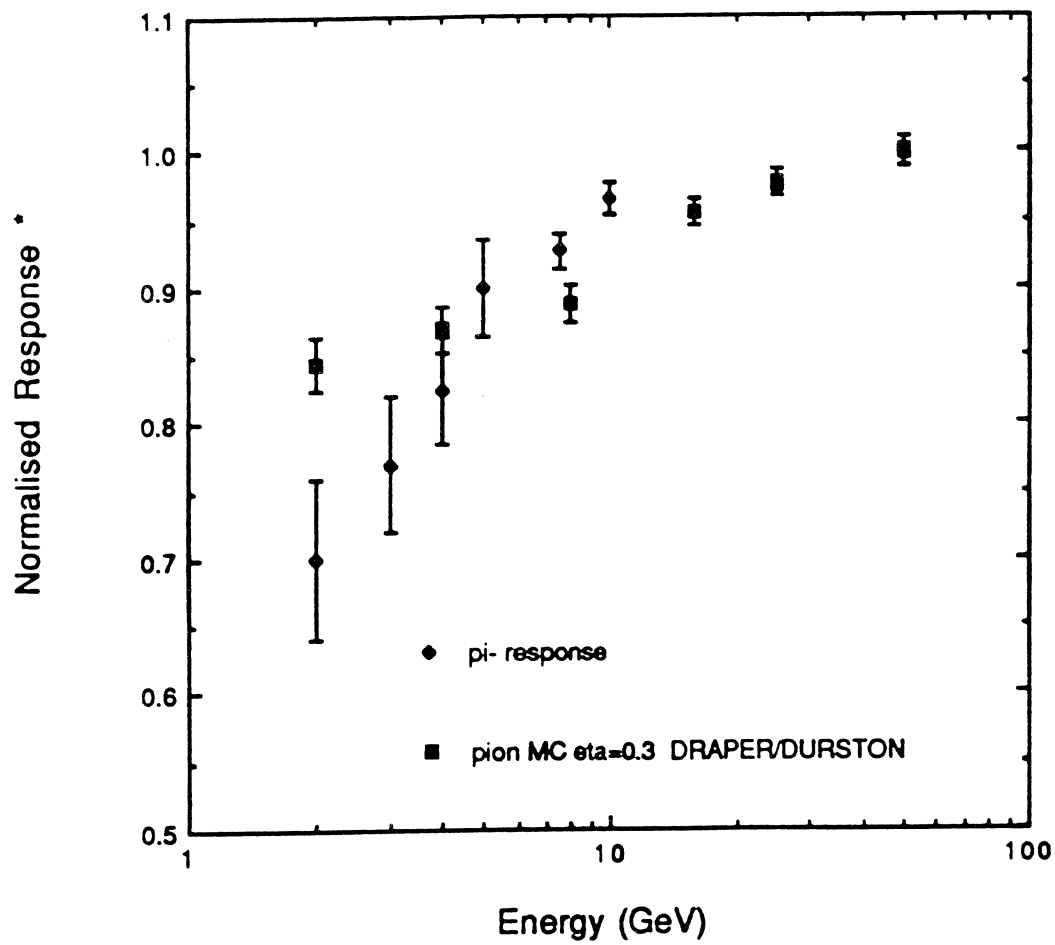


e, pi Normalised Response\*

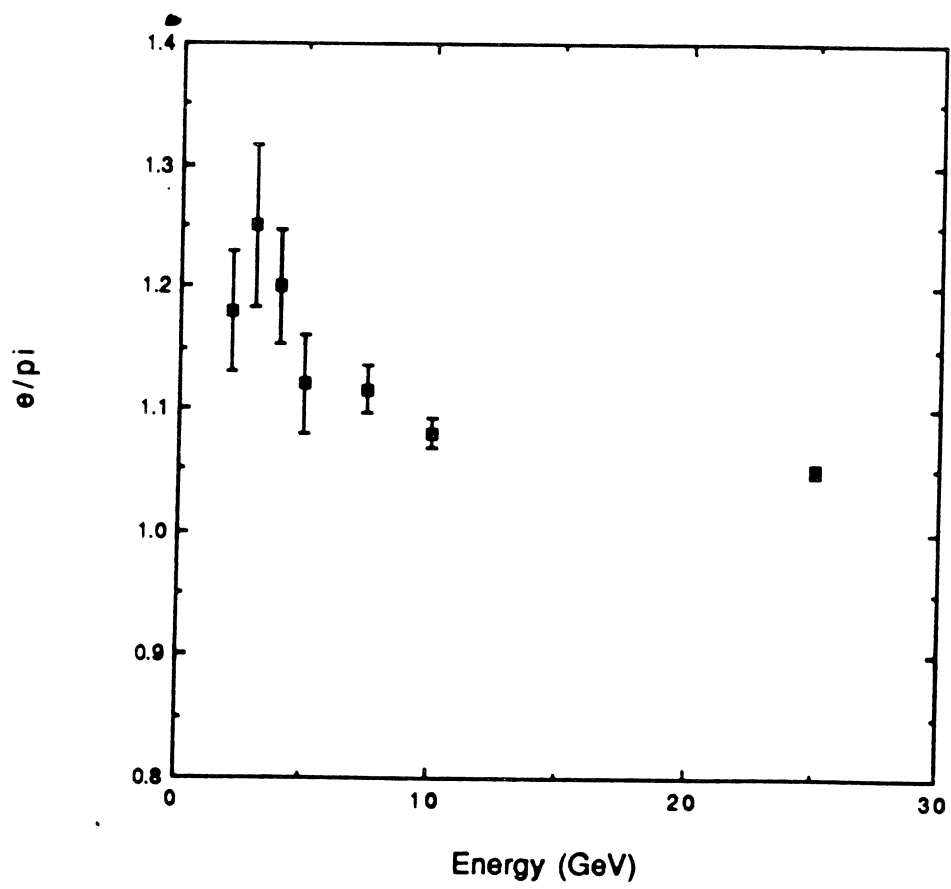


\* Normalised to 50 GeV response

# pi Normalised Response\*



\* Normalised to 50 GeV response



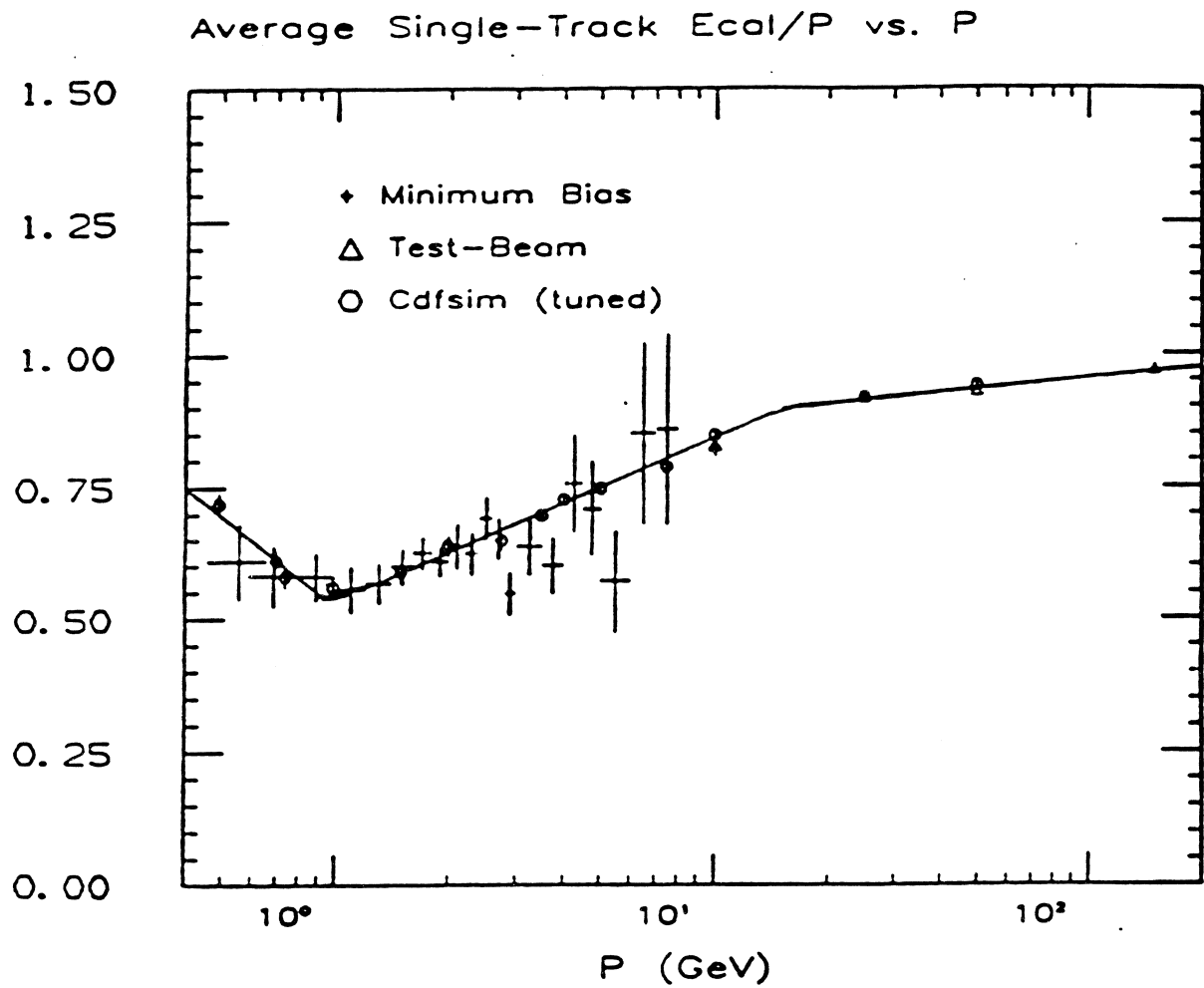


Fig:1 The CDF calorimeter calibration data; the measured ratio of calorimeter response to the true particle momentum.

# Systematic Uncertainty on Jet E vs. Corrected E

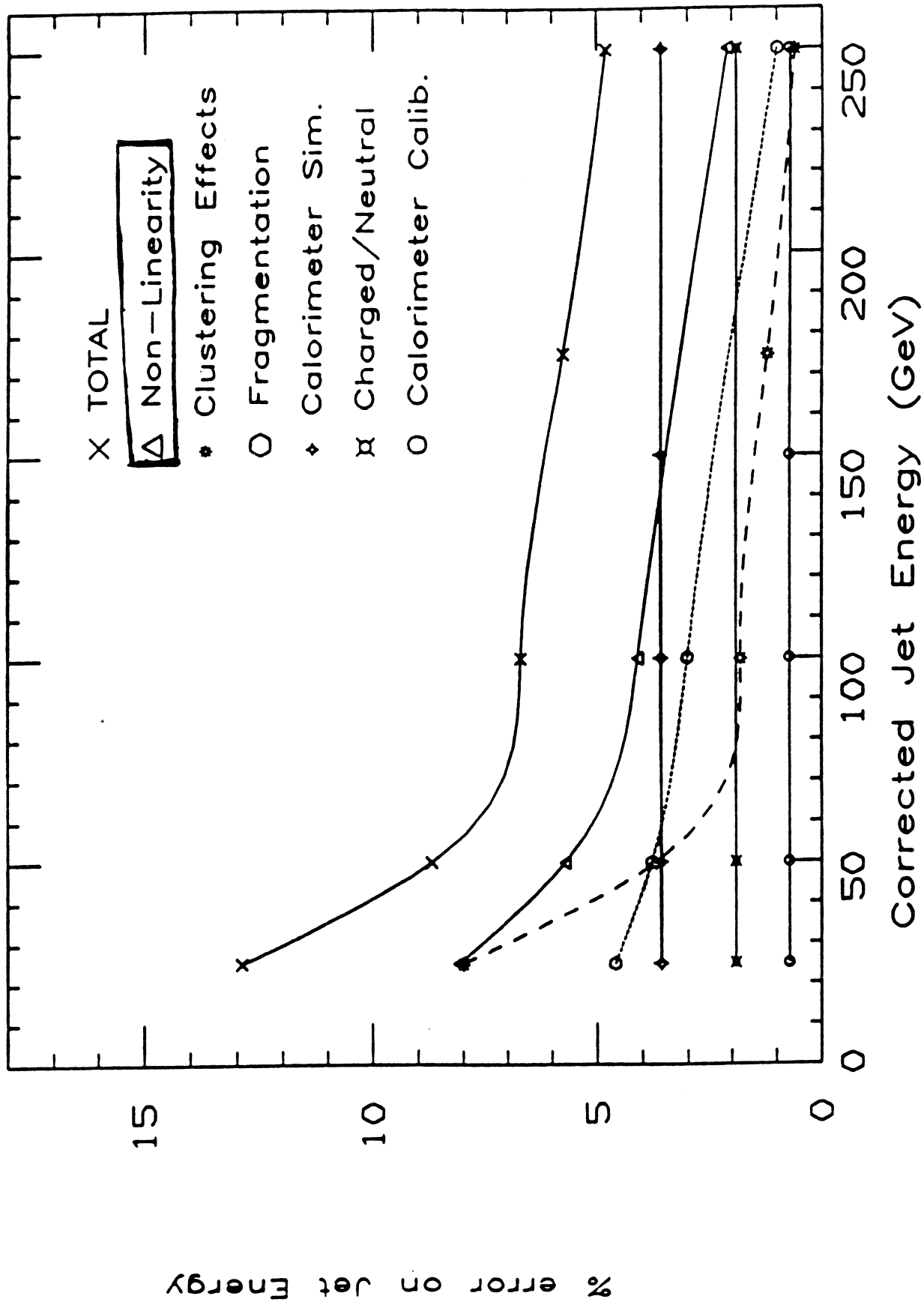


FIG. 11

Mesured Jet Et spectrum is affected  
(and distorted) by the following effects:

- a. non-uniform response and losses due to cracks and dead material in the calorimeter
- b. non-linear LOW ENERGY response of the calorimeter
- c. Convolution of single particle response (by MC) with the jet fragmentation spectrum.

So, to get the corrected jet Et spectrum model the response of the calorimeter including the effects of non-uniform response and correction for energy loss in the dead material, i.e.,

get  $R(E, \eta)$       RESPONSE FUNCTION

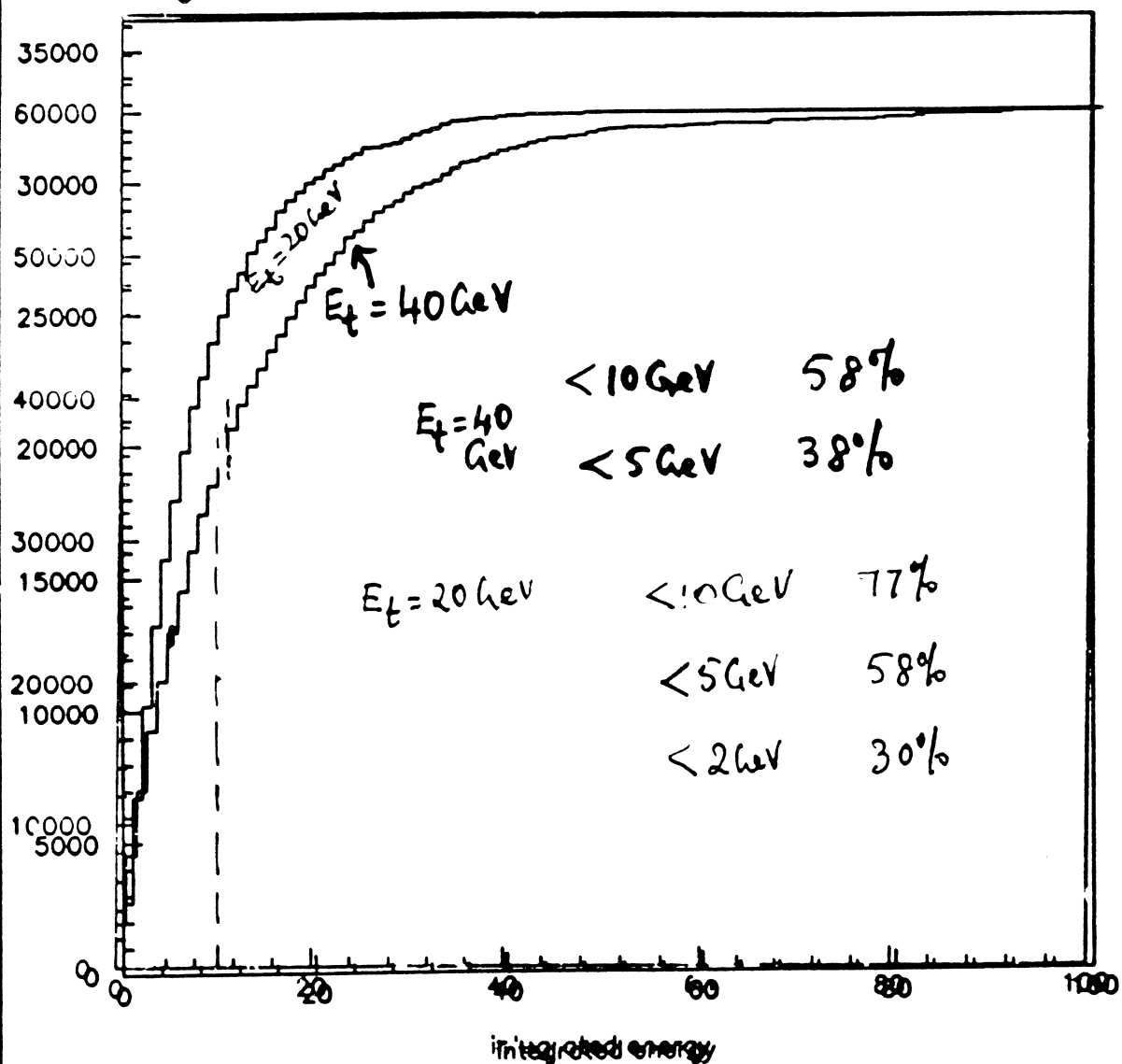
Combine with proper jet fragmentation spectrum

$$\int R(E, \eta) (E \cdot dn/dE) dE \quad \text{QCD group}$$

May require tuning the MC single particle response as seen by TB data



$$\int E \frac{dn}{dE} \cdot dE$$

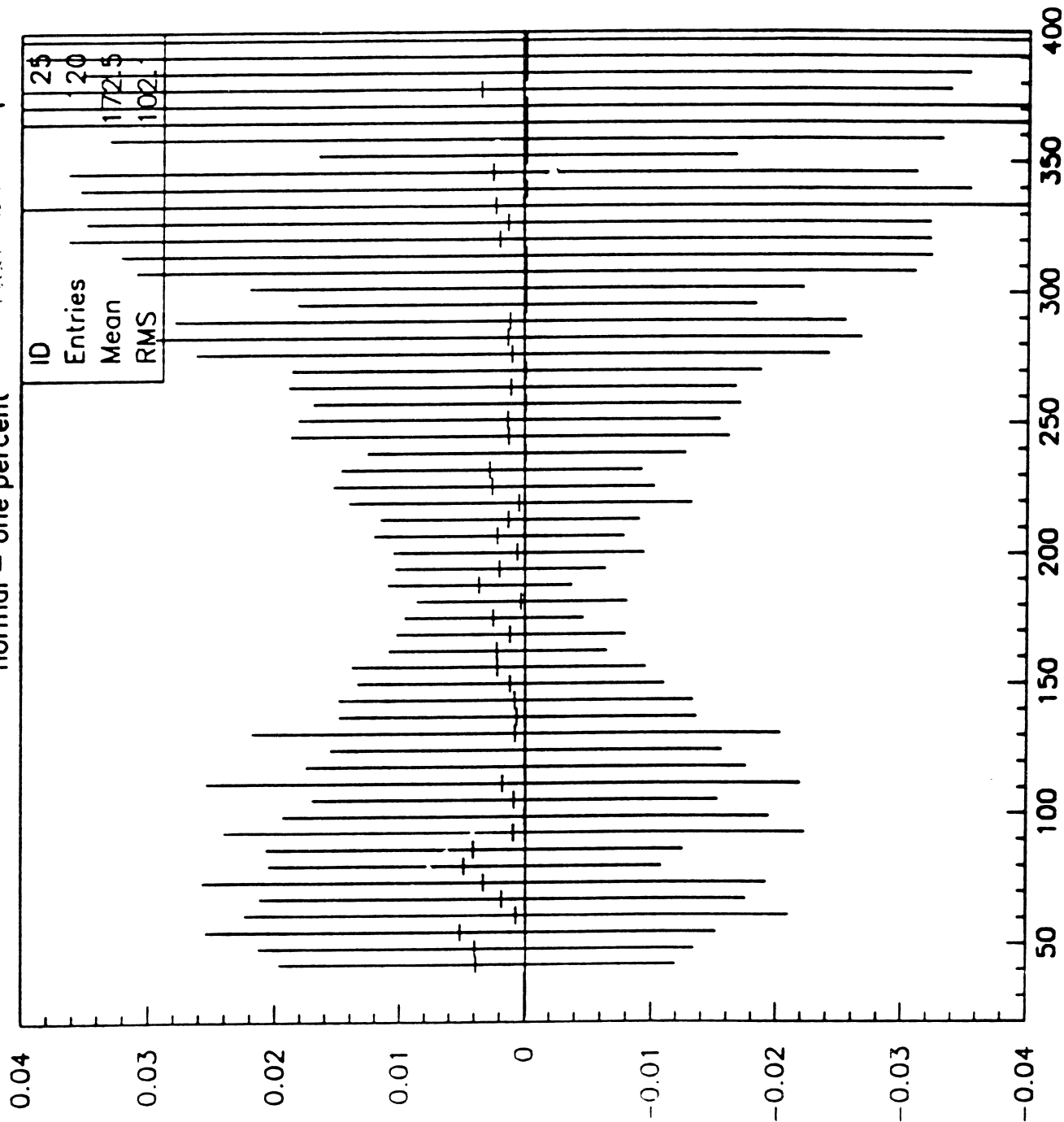


1991/09/27 12:40

2. above  
5. below

normal - one percent

absolute response by



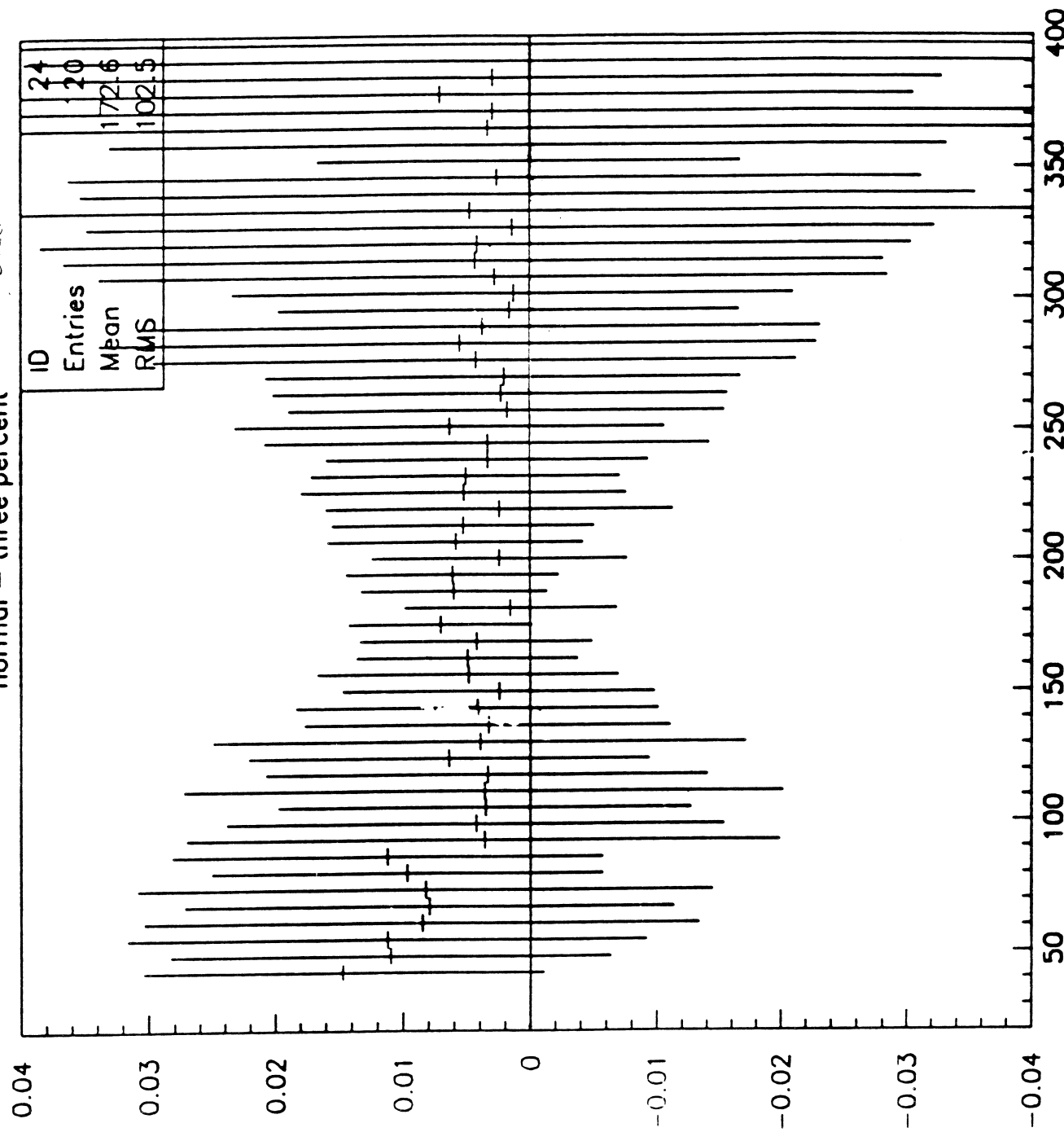
XH2AWY OF Et VS (PJET-CALIBJET)/PJET

1991/09/27 12:43

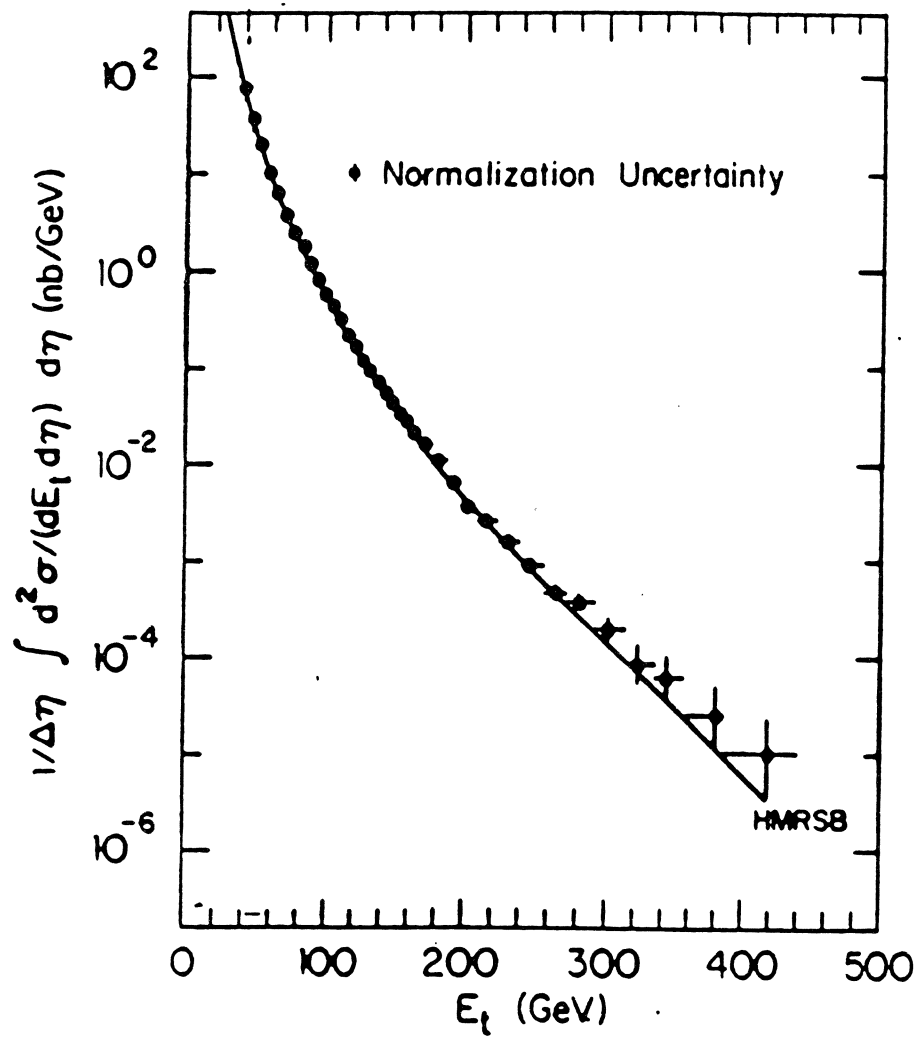
2 below  
5 (N)

show a response of 5

normal - three percent



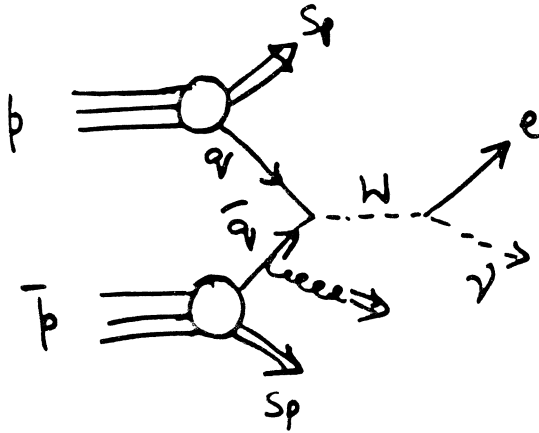
XH2AWY OF Et VS (PJET-CALIBJET)/PJET



10% reduction in response  $\Rightarrow$  4% shift in energy scale  
below 5 GeV @  $E_t = 40 \text{ GeV}$

$\Rightarrow$  26% error in cross-section

## W Boson



$M_T^W$  is sensitive to the measurement of the hadronic energy in the event.

$$\vec{p}_t = \vec{E}_t^{\text{had}} = -\vec{E}_t^e - \sum_i E_{ti} \cdot \hat{n}_i \quad (\text{excluding the lepton})$$

$$\vec{p}_t^W = -\sum_{\text{hadrons}} \vec{p}_t^i = \vec{p}_t^e + \vec{p}_t^{\nu}$$

good measurement of  $p_t^W$  important  
excess in high  $p_t^W$  tail should indicate heavy particles decaying to W

Control systematics / cross-check using Z sample

$$\vec{p}_t^Z = \vec{p}_t^{e_1} + \vec{p}_t^{e_2} = \sum \vec{p}_t^{\text{hadrons}}$$

## SUMMARY

\* Low energy test beam effort was successful.

We have useful data for 2 - 10 GeV pions  
1 - 10 GeV electrons

•  $\eta = 0.05$ ,  $\phi = 31.6$

2, 3, 4 GeV       $\sim 3000$  pions @ each energy

5 - 10 GeV       $> 10k$

•  $\eta = 0.45$ ,  $\phi = 31.6$       less statistics

• Crack-scan, ICD scan data.

\* Preliminary results show  $\sim 30\%$  reduction in the pion response compared to higher energies.

\* Low energy response very important for jet physics and H Physics

MC has to be tuned if needed.



# Test Beam Results from the D0 Liquid Argon End Calorimeter Electromagnetic Module

Anthony L. Spadafora\*  
Lawrence Berkeley Laboratory  
University of California  
Berkeley, California 94720 USA  
Representing the D0 collaboration<sup>†</sup>

August 12, 1991

*Presented at the 5<sup>th</sup> Pisa Meeting on Advanced Detectors  
Elba, Italy, May 26-31, 1991*

## Abstract

Results are presented from a test beam study of the D0 liquid argon end calorimeter electromagnetic module prior to its installation at the Fermilab Tevatron Collider. Using electron beams with energies ranging from 10 – 150 GeV we have obtained an energy resolution of  $15.7\%/\sqrt{E(\text{GeV})}$  with a small constant term of 0.3% and a linearity of better than  $\pm 0.5\%$ . The position resolution of the calorimeter is found to be approximately 1 mm for 100 GeV electrons.

---

\*This work was supported by the Director, Office of Energy Research of the U.S. Department of Energy under Contract No. DE-AC03-76SF00098.

<sup>†</sup>The D0 collaboration includes members from Universidad De Los Andes Colombia, University of Arizona, Brookhaven National Laboratory, Brown University, University of California Riverside, Columbia University, Centro Brasileiro de Pesquisas Fisicas Brazil, Fermi National Accelerator Laboratory, Florida State University, University of Florida, University of Hawaii, University of Illinois Chicago, Indiana University, Institute for High Energy Physics Serpukhov USSR, Iowa State University, Lawrence Berkeley Laboratory, University of Maryland, University of Michigan, Michigan State University, New York University, Northern Illinois University, Northwestern University, University of Notre Dame, Purdue University, Rice University, University of Rochester, CEN Saclay France, State University of New York - Stony Brook, Tata Institute of Fundamental Research Bombay India, Texas A&M University, University of Texas at Arlington and Yale University.



# 1 Introduction

The D0 experiment, which will begin taking physics data in the 1992 run of the Fermilab Tevatron Collider, features a uniform, fine-grained uranium liquid argon calorimeter which provides good energy resolution and hermetic coverage for electrons, photons and jets. A test beam facility has been established at Fermilab to study the response of the electromagnetic and hadronic modules that comprise the central (CC) and end (EC) calorimeters (Fig 1.) This paper will present results from the test beam study of the response of the end calorimeter electromagnetic module (ECEM) to electron beams. The response of the combined electromagnetic and hadronic modules to pion beams can be found in Ref.[1] and test beam results from CC modules in Ref.[2, 3].

## 2 The ECEM Module

The ECEM module, shown schematically in Fig. 2, provides full azimuthal ( $\phi$ ) coverage in the forward region ( $1.4 < \eta < 4.0$ )<sup>†</sup>. In order to minimize losses due to internal cracks, the module is built as a single unit: both the signal boards and the absorber plates are preassembled as disks of typically 1 m radius and then stacked to assemble the module. The basic sampling cell of the module consists of a 4 mm depleted uranium absorber plate, a 2.3 mm liquid argon gap, a NEMA G-10 signal board and another 2.3 mm liquid argon gap. A more detailed description of the module's construction can be found in Ref.[4]. Signals are read out in four longitudinal sections and transverse segmentation is provided by semi-projective towers of approximately square pads of  $\Delta\eta \times \Delta\phi = 0.1 \times \pi/32 (\approx 0.1)$ . In the third longitudinal section, which typically contains 65% of the electromagnetic shower, the transverse segmentation is doubled in both directions ( $0.05 \times 0.05$ ) to provide better shower

---

<sup>†</sup> $\eta$  is the pseudorapidity defined as  $\eta = -\ln \tan(\theta/2)$ , where  $\theta$  is the polar angle from the beam axis.

position resolution. See Table 1 for a summary of the readout segmentation.

### 3 Test Beam Setup

The D0 calorimeter test beam facility has been established in the Fermilab Neutrino-West beam line which provides electron and pion beams with momenta from 10 to 150 GeV/c. A system of proportional wire chambers (PWC's) and Cerenkov counters provides particle momentum and identification on an event-by-event basis. The spread of the beam momentum is typically 1.5% (measured to an accuracy of 0.2%) and the pion contamination in the electron beam is negligible (less than  $10^{-5}$ ). A set of scintillation counters provides the trigger.

The test beam run described here was performed with the final D0 ECEM and ECIH (end calorimeter inner hadronic) modules prior to their installation at the collider. The test beam cryostat has a thin window (two 1.6 mm thick steel plates) in the region illuminated by the beam and was configured with a liquid argon excluder, a 2.5 cm thick stainless steel plate to simulate the D0 cryostat walls, and a 4.4 cm thick aluminum plate at small angles to simulate the D0 vertex detector endplates and electronics. The test beam cryostat is equipped with a computer controlled transporter that orients the module so that the beam strikes it along projective towers as do particles at the collider. The region illuminated by the beam ( $\pm 15$  degrees in  $\phi$  and the full extent in  $\eta$ ) and a surrounding border zone were instrumented with the readout electronics (1452 channels in total) and internal cryostat cables which will be used in the final D0 detector. The overall sensitivity [5] of the electronics is  $\sim 0.57$  fC per ADC count or 3600 electrons per count.

## 4 Test Beam Results

The analysis of the calorimeter data proceeds by first correcting for the electronic channel pedestals and gains, which were measured once per eight hours and once per day, respectively. The pedestal widths vary with the channel capacitance but were about 8 MeV for a typical 2 nF cell. The spread in the beam momentum was corrected event-by-event using the momentum measured by the PWC system.

The energy of electromagnetic showers was reconstructed by summing all four longitudinal sections in the ECEM and the first section of the ECIH. Relative sampling fractions for each longitudinal section were obtained by simultaneously minimizing the energy resolution and the deviation from linearity for electron momenta ranging from 10 to 150 GeV/c. These optimized values, shown in the last column of Table 2, are not very different from the relative values calculated from minimum ionizing  $dE/dX$  losses. The analyses presented here used a single set of energy independent relative sampling fractions. The number of towers summed to contain an electromagnetic shower varies with  $\eta$ , corresponding to the variation of pad size with  $\eta$ . For example, for intermediate size pads of 5 cm square, 99.5% containment is achieved by summing an array of 5 by 5 towers, while for pads of 1 cm square an array of 9 by 9 towers is needed.

“Benchmark” runs at a selected point in the module ( $\eta = 1.95$ ) were repeated almost daily to monitor the stability of the apparatus. For the three month duration of the run the mean value of the response for 100 GeV electrons was found to be constant with an rms spread of 0.3%.

The results of a high voltage scan with 100 GeV electrons is shown in Fig. 3. Our operating voltage of 2.5 kV (11 kV/cm) is well located on the plateau. The curve in Fig. 3 is a fit to the form of Ref[6] and yields an estimate of the oxygen contamination of  $0.52 \pm 0.03$  ppm O<sub>2</sub>. Such scans were repeated approximately every ten days and

no measurable change was found.

Clear signals for muons were seen in the calorimeter arising from the approximately 3% muon component of the hadron beam. A muon peak is distinguishable above pedestal in all longitudinal sections of the calorimeter. The pulse height spectrum for 15 GeV muons in the third EM layer is shown in Fig. 4. From the fitted most probable value of the muon spectrum in each layer, we obtain an average value of  $9.8 \pm 0.1$  ADC counts/cm of liquid argon. Comparing the ratio of pulse height to deposited energy for electrons and muons, we find for 15 GeV muons:

$$e/\mu = \frac{PH(e)/E(e)}{PH(\mu)/E(\mu)} = 0.69 \pm .05$$

Pulse height distributions from electrons of various beam momenta are shown in Fig. 5. The mean value in ADC counts of the Gaussian fits are shown in Fig. 6a as a function of beam energy and, in Fig. 6b, the residuals from a linear fit of the form:

$$\mu(\text{cts}) = E_{\text{beam}}(\text{GeV}) \times (263.0 \pm 0.1) \text{ cts/GeV} - (23 \pm 4) \text{ cts}$$

The fractional energy resolution, calculated as  $\sigma/\mu$  from a Gaussian fit, is shown in Fig. 6c. We assume the energy dependence of the resolution is of the form  $(\sigma/\mu)^2 = C^2 + S^2/E + N^2/E^2$ , where  $E$  is the beam energy in GeV,  $C$  is a constant contribution from systematic errors such as remaining channel-to-channel variation in gain,  $S$  is due to the statistical error in sampling, and  $N$  represents energy independent contributions to  $\sigma$  such as electronic and uranium noise. The results of the fit are:  $C = 0.003 \pm 0.002$ ,  $S = 0.157 \pm 0.005(\sqrt{\text{GeV}})$ , and  $N = 0.329 \pm 0.030(\text{GeV})$ . The noise term,  $N$ , is consistent with the value obtained for an array of 5 by 5 towers from the pedestal widths.

The small pads (widths range from 1.4 cm square to 5 cm square) of the third EM layer are used to obtain a measurement of the shower transverse shape and impact position. The one-dimensional shower profile can be written as a sum of “core” and “tail” exponential terms:

$$\frac{dE}{dx} = a_1 e^{-|x-x_0|/b_1} + a_2 e^{-|x-x_0|/b_2}$$

where  $x_0$  is the shower impact position. The fraction of the shower energy that is found to one side of a pad edge is calculated from the double exponential form to be:

$$\frac{E_R}{E_{tot}} = \frac{\int_0^\infty \frac{dE}{dX}}{\int_{-\infty}^\infty \frac{dE}{dX}} = 1 - \frac{a_1 b_2 e^{-b_1|x_0|} + a_2 b_1 e^{-b_2|x_0|}}{2(a_1 b_2 + a_2 b_1)} \quad (x_0 > 0)$$

where  $E_R$  and  $E_{tot}$  are the energy to the right (i.e. increasing  $x$ ) of a pad edge and the total energy, respectively. Using the shower impact position projected from the track trajectories measured with the PWC system independently of the calorimeter, we fit for the double-exponential parameters and obtain the results given in Table 3.

For determination of the position resolution we use the center of gravity algorithm with a correction term to remove the bias with distance of the shower from a pad edge. Approximating the shower transverse shape by a single exponential term, the corrected center of gravity is given by[7]

$$x = x_c + b \sinh^{-1} \left( \frac{x_c - x_m}{\Delta} \sinh \frac{\Delta}{b} \right)$$

where  $x_c$  = the  $x$  coordinate of the shower center of gravity,  $x_m$  = pad center,  $\Delta$  = pad halfwidth, and  $b$  is the single-slope characteristic length for which we have found 5 mm to be the optimum value. This algorithm is somewhat simpler than the double exponential technique and yields the same value for the position resolution. The resolution obtained for 100 GeV electrons and pads 2.5 cm square in the third EM layer is shown in Fig. 7 as a function of  $x_e$ , the distance from the pad edge. The dependence of the resolution on  $x_e$  is fit by a quadratic form:  $\sigma = a_0 + a_2 x_e^2$  where  $a_0 = (0.081 \pm 0.001)$  cm and  $a_2 = (0.023 \pm 0.002)$  cm. Applying this analysis to data taken at varying beam energies, we obtain an energy dependence of the position resolution averaged over the pad of approximately:  $\sigma = (1.3 \pm 0.1) \text{ cm} \times E^{(-0.61 \pm 0.02)}$  where  $E$  is in GeV.

Although the above measurements of energy and position resolution were obtained at selected spots in the calorimeter, we have taken uniformity scans to verify that such performance can be achieved throughout the module. The results of a scan in azimuth ( $\phi$ ) at a constant  $\eta$  is shown in Fig.8. The mean response is constant to 0.5%. Data was also taken scanning the only two sources of non-uniformity in response: the tie-rods that penetrate the stack and the small crack between the uranium plates. The regions affected by these features comprise only a few percent of the active area of the module.

## 5 Conclusion

The performance of the D0 end calorimeter electromagnetic calorimeter module was studied using electrons with energy ranging from 10 to 150 GeV. The calorimeter response was found to be uniform across the instrumented area and stable for the duration of the run. The energy resolution is  $15.7\%/\sqrt{E \text{ (GeV)}}$  with a small constant term of 0.3% and the response is linear to better than  $\pm 0.5\%$ . A position resolution for the localization of electromagnetic showers of 1 mm is achieved for 100 GeV electrons impacting on a tower edge.

I would like to thank H. Aihara, W. Dharmaratna, and N. Roe for their contribution to the analyses presented in this paper. The D0 Calorimeter group would like to thank the Fermilab Accelerator Division and the staffs at our individual institutions for their contributions to the success of this project. This work was supported by the Director, Office of Energy Research of the U.S. Department of Energy under Contract No. DE-AC03-76SF00098.

## References

- [1] N.Amos, Proceedings of the International Conference on Calorimetry in High Energy Physics, Batavia, IL Oct. 29 – Nov. 1, 1990, to be published.
- [2] M.Abolins et al., Nucl. Instr. and Meth. **A280** (1989) 36.
- [3] P.Franzini, Nucl. Instr. and Meth. **A289** (1990) 438
- [4] A.Spadafora, Proceedings of the International Conference on Calorimetry in High Energy Physics, Batavia, IL Oct. 29 – Nov. 1, 1990, to be published.
- [5] M.Demarteau, Proceedings of the International Conference on Calorimetry in High Energy Physics, Batavia, IL Oct. 29 – Nov. 1, 1990, to be published.
- [6] J.Engler et. al., Nucl. Instr. and Meth. **120** (1974) 157.
- [7] G.A.Akopdjanov, et. al., Nucl.Instr.and Meth. **140** (1977) 441; A.DeAngelis and F.Mazzone, Nucl. Instr. and Meth. **A287** (1990) 397.

Table 1 : Longitudinal and transverse segmentation of the ECEM readout.

Layer	# Cells	Absorber		$\Delta\eta \times \Delta\phi$
EM1	2	1.6 mm Fe	$0.2X_0$	$.1 \times .1$
EM2	2	4 mm DU	$2.6X_0$	$.1 \times .1$
EM3	6	4 mm DU	$7.9X_0$	$.05 \times .05$
EM4	8	4 mm DU	$9.2X_0$	$.1 \times .1$

Table 2 : The sampling fractions calculated for a minimum ionizing particle, these values normalized to the third EM layer, and the relative values found from the resolution/linearity minimization. The values in parentheses were not varied in the fit.

	dE/dX		Fit
Layer	$SF$	$\frac{SF(3)}{SF(i)}$	$\frac{SF(3)}{SF(i)}$
EM1	.047	1.82	1.61
EM2	.090	0.96	0.96
EM3	.086	(1.0)	(1.0)
EM4	.081	1.06	1.10
IH1	.056	1.52	(1.52)

Table 3: The fitted shower shape parameters from the double exponential form. The amplitude of the second term,  $a_2$ , is set equal to 1.

$a_1$	$3.71 \pm .09$
$b_1$	$(2.87 \pm .7) \text{ mm}$
$a_2$	1.00
$b_2$	$(10.3 \pm .1) \text{ mm}$



## Figure Captions

**Fig.1** The D0 liquid argon calorimeters.

**Fig.2** The ECEM Module.

**Fig.3** High Voltage plateau curve of the ECEM taken with 100 GeV electrons.

**Fig.4** Pedestal subtracted pulse height spectrum for 15 GeV muons in the third EM layer.

**Fig.5** Pulse height distributions of electrons for various beam energies, normalized to the same number of events.

**Fig.6** a) Mean pulse height as a function of beam energy, b) residuals from a linear fit, and c) fractional energy resolution as a function of beam energy.

**Fig.7** Position Resolution of the ECEM as a function of the distance from edge of a pad.  $\sigma$  is the rms of the difference between the corrected center of gravity impact position in the third EM layer and that projected from the track reconstructed from the PWC's. The fit is the quadratic form given in the text.

**Fig.8** Mean pulse height for 100 GeV electrons runs at a fixed  $\eta$  but varying azimuth. The azimuth is given as the arc length at the calorimeter  $S = R \times \phi$  where R for this scan is 59 cm.

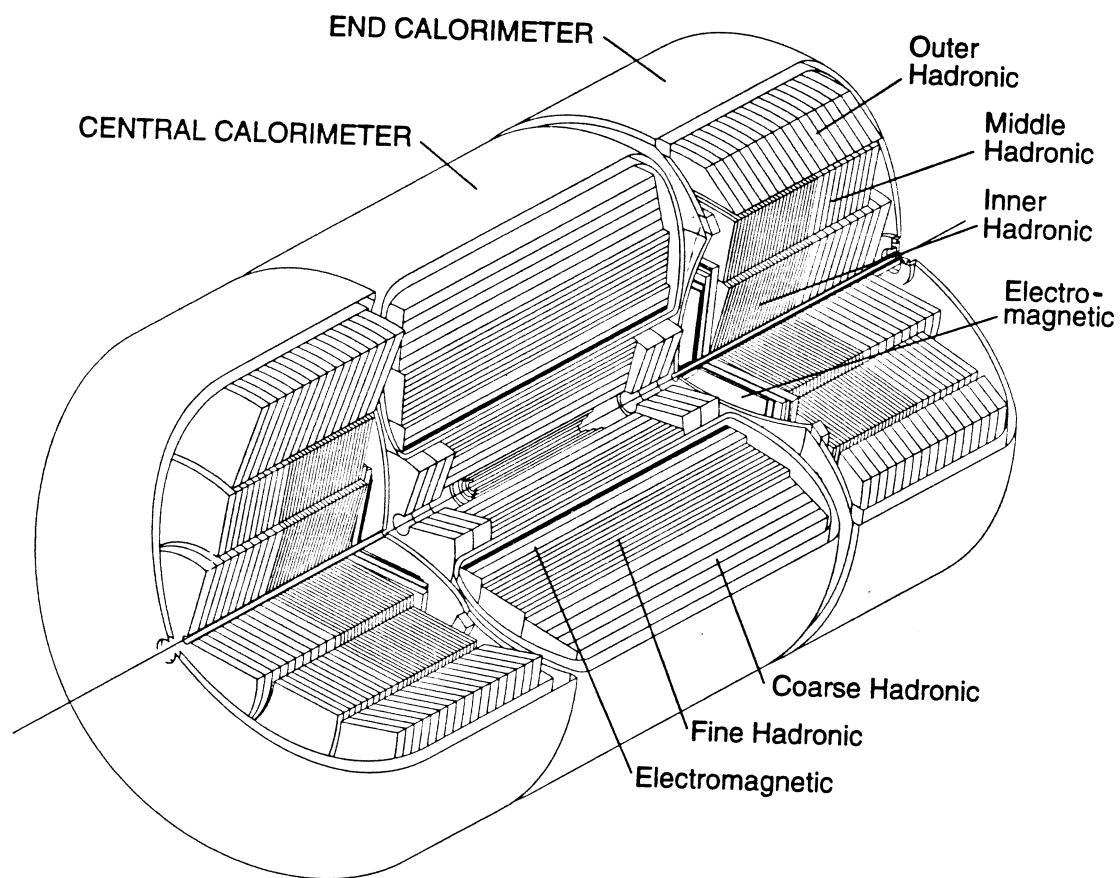


Figure 1:

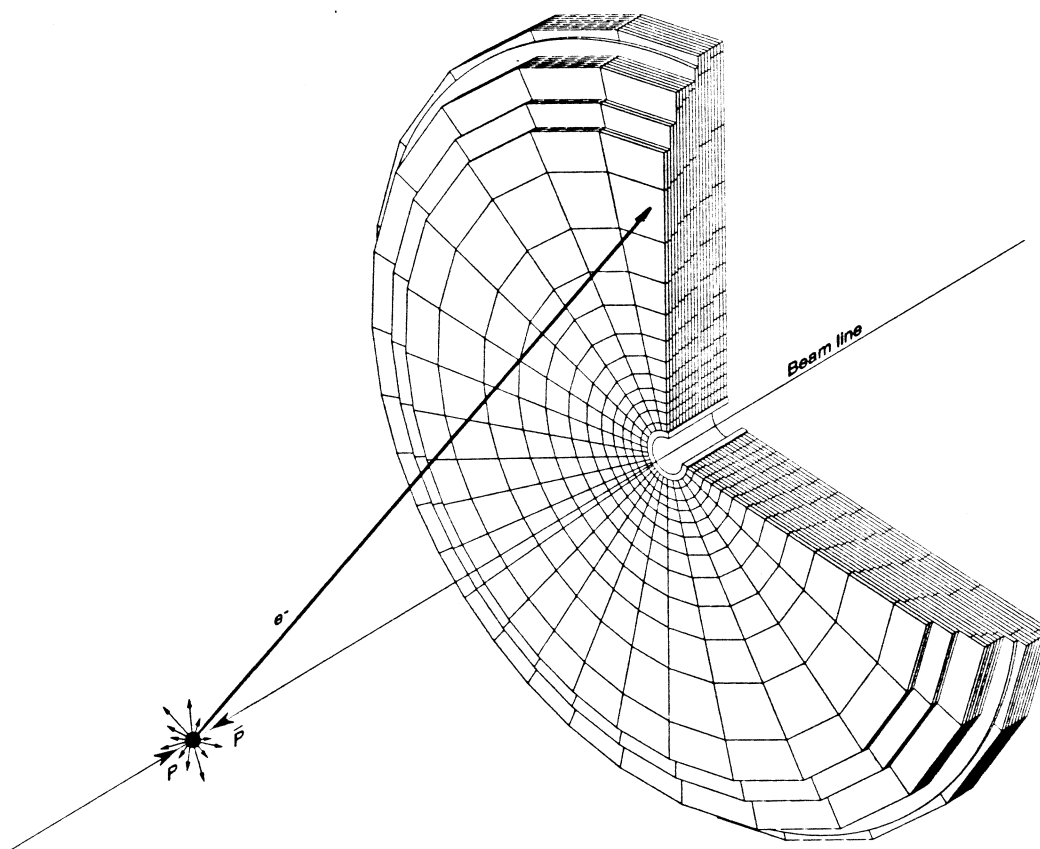


Figure 2:

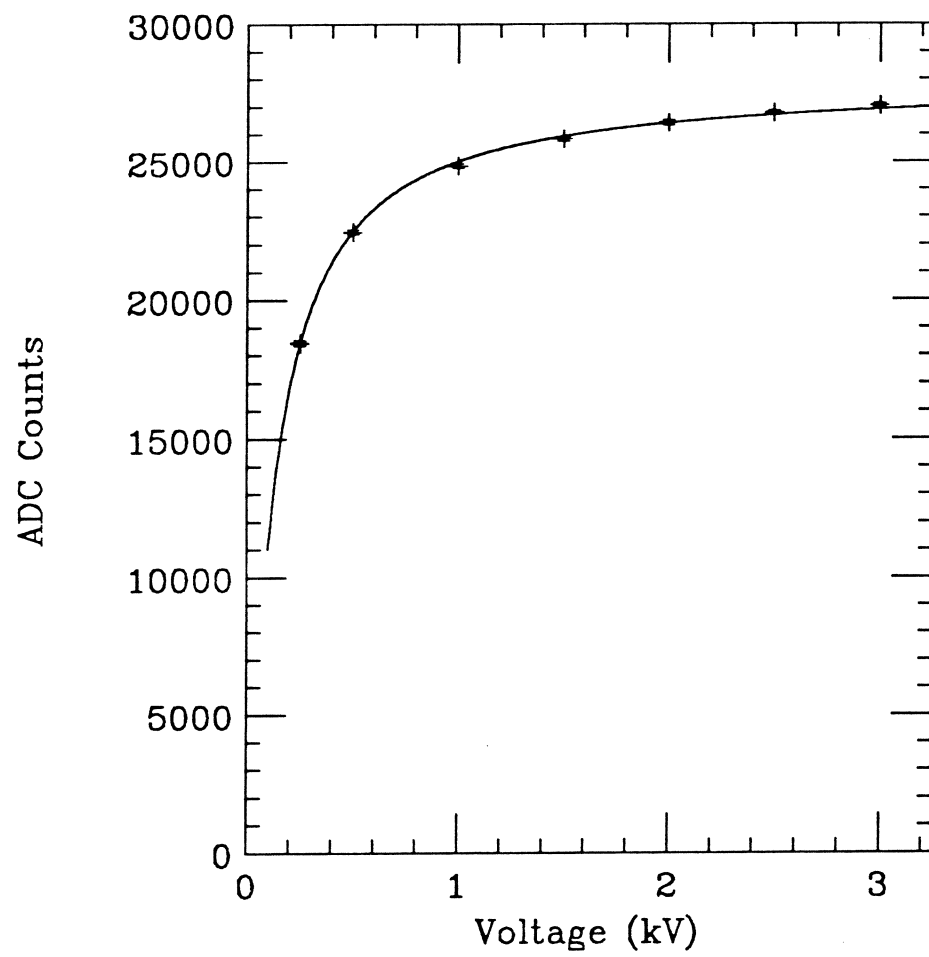


Figure 3:

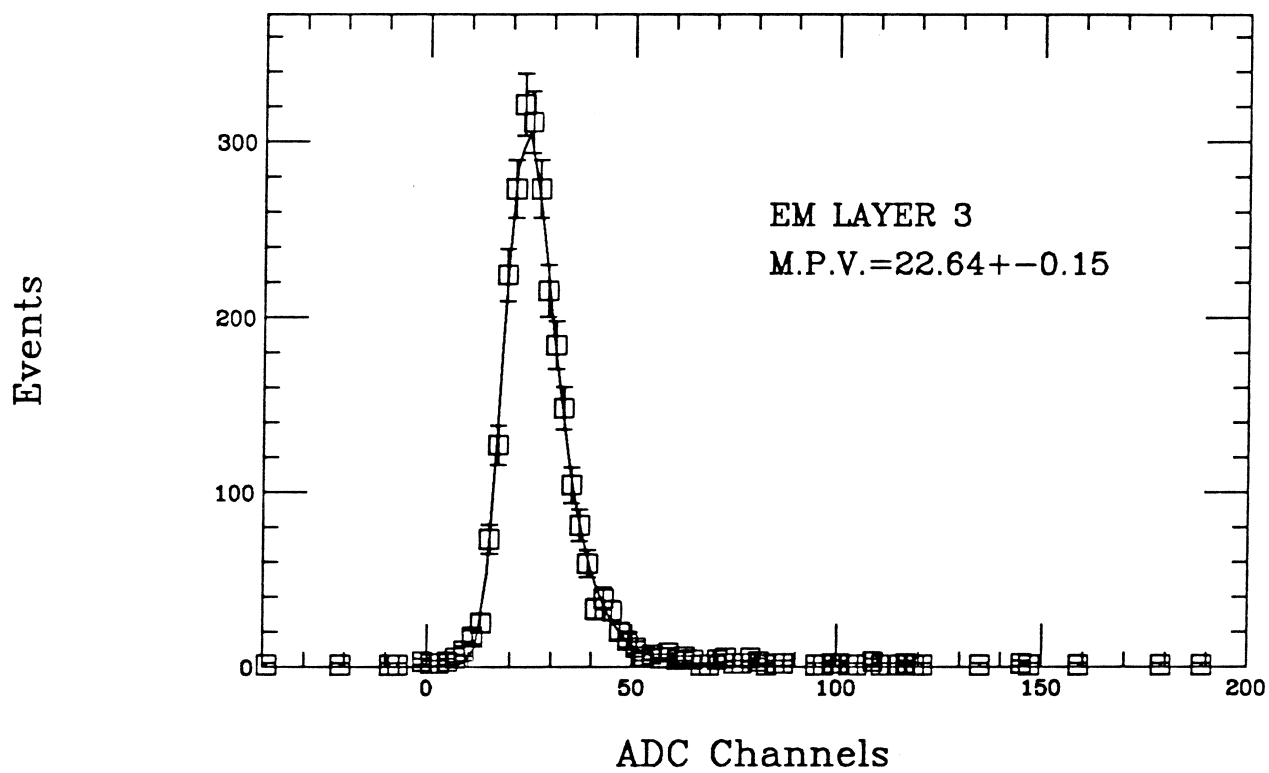


Figure 4:

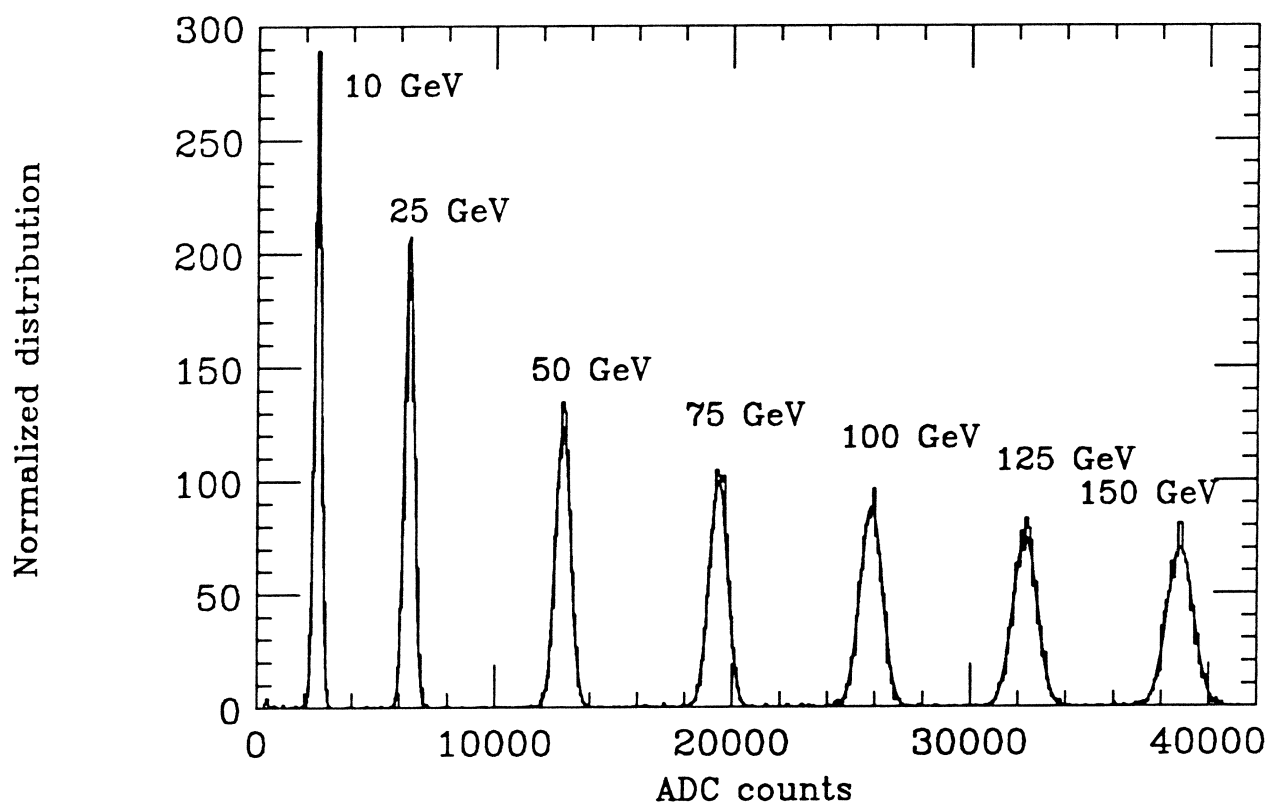


Figure 5:

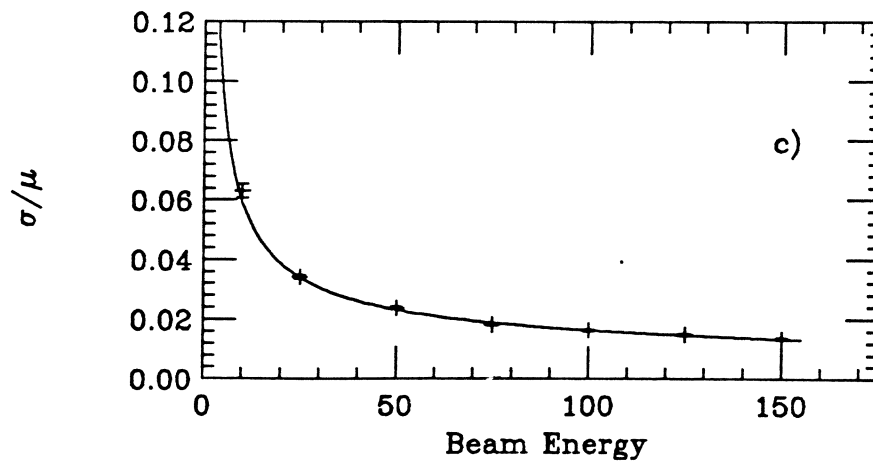
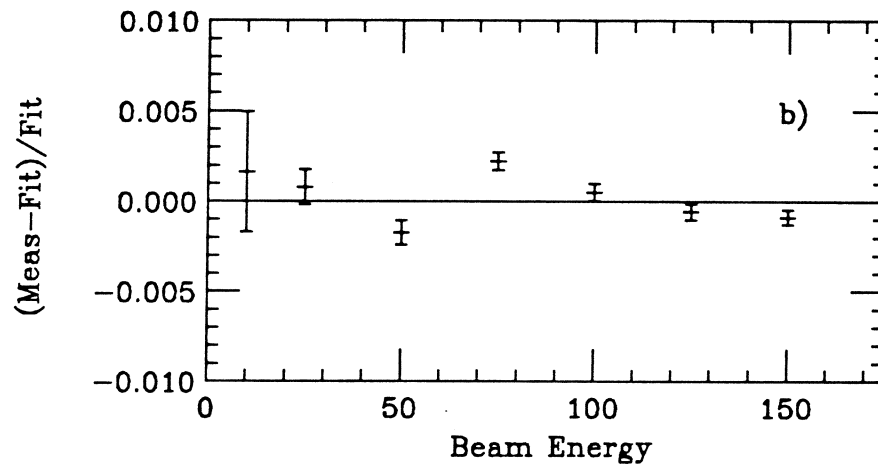
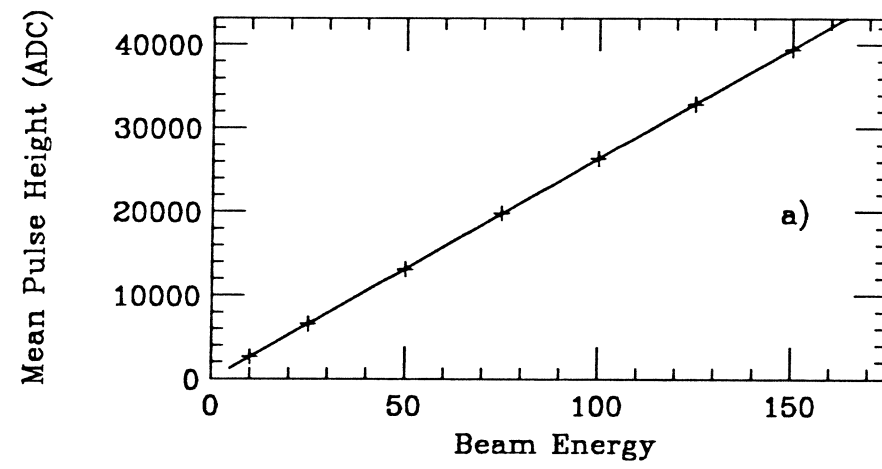


Figure 6:

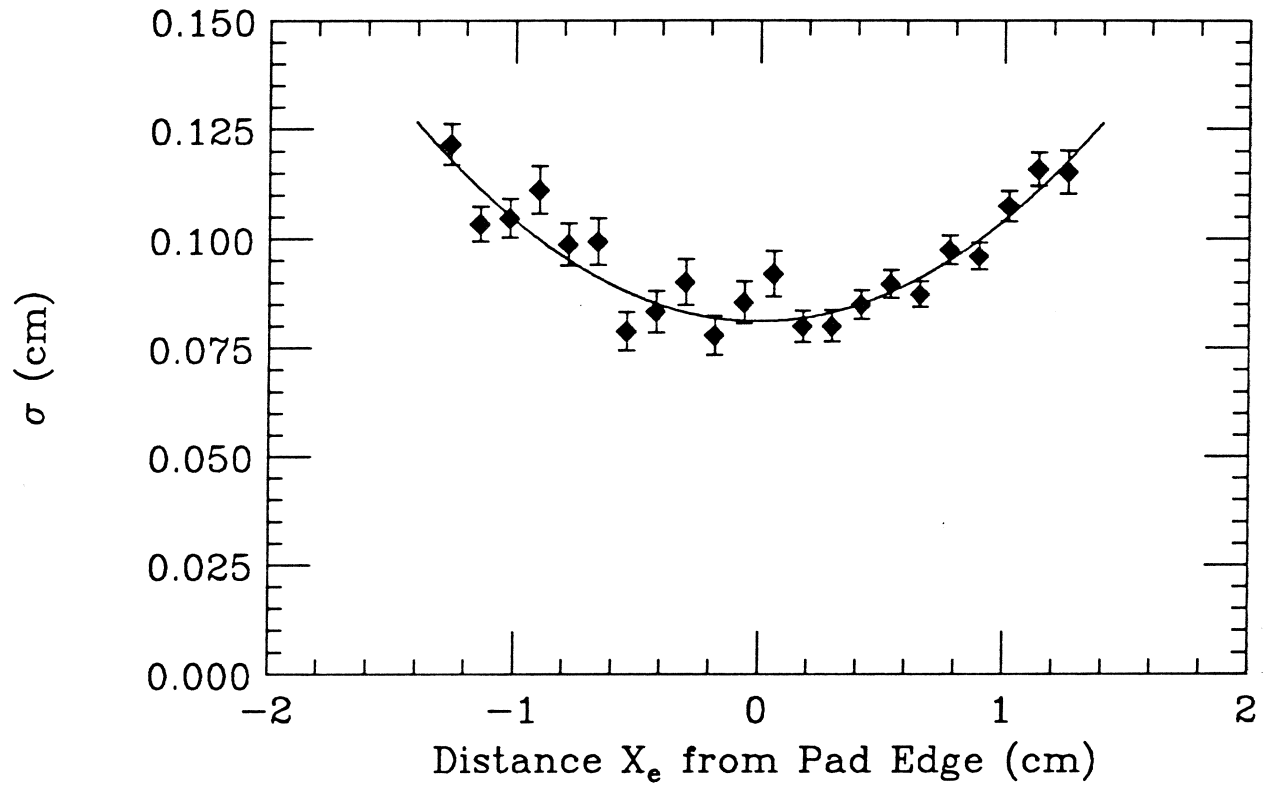


Figure 7:



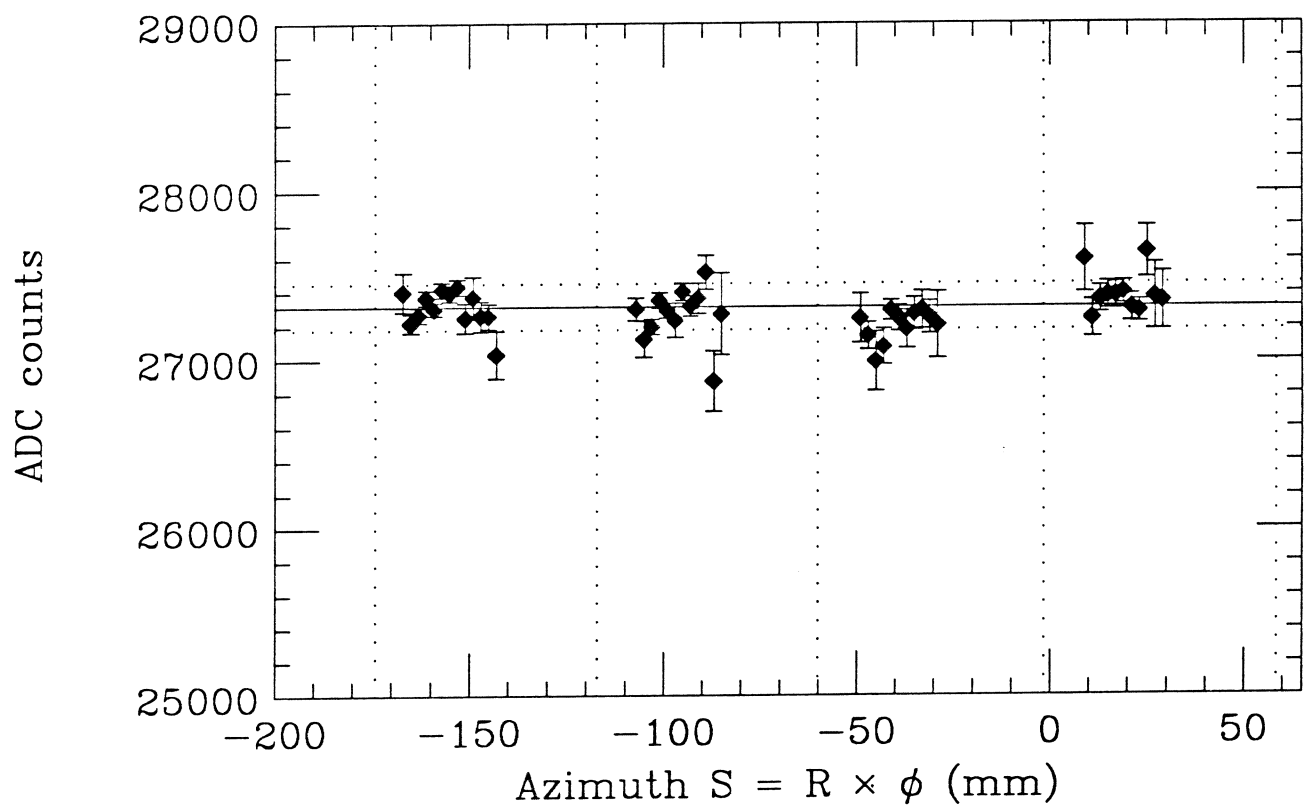


Figure 8:

Level 1 Jet Trigger and Level 2 Jet Tool  
Rates and Efficiencies.

Richard Astur  
Harry Weerts  
Michigan State University  
November 8, 1990

**Purpose:**

The D0 level 1 and level 2 trigger systems are complex in terms of what triggers should be defined at level 1, and how level 2 should respond to these triggers to best handle the event rate while optimizing the recording of interesting physics events. Trigger definitions on either level remain largely undefined and unstudied. In this note we investigate D0 triggering at its simplest level. We define a level 1 hardware trigger and a level 2 software filter which we require to be called if and only if the level 1 trigger is satisfied. Both 'triggers' are geared towards jet finding. We have investigated the jet finding efficiency of this combined trigger as a function of some adjustable parameters and calculated the corresponding event rates.

**Level 1 Jet trigger:**

The level 1 calorimeter trigger looks at the calorimeter in terms of trigger towers, each of which covers  $.2 \times .2$  in eta-phi space. The various layers of each tower are summed in hardware and then a vertex dependent sin theta table is used to produce transverse energy values (ETs) for both the electromagnetic (EM) and fine hadronic (FH) portion of that tower. At this point many possible quantities can be constructed. The most applicable quantity towards jets is the number of trigger towers with total (EM + FH) ET above a certain threshold; this is often referred to as 'the' level 1 jet trigger. For the purposes of this discussion we will define the level 1 jet trigger to fire if and only if there is at least ONE trigger tower whose ET value exceeds a threshold we denote as L1\_Et\_CUT. Level 1 enters all trigger towers that satisfy this condition into a 'hot' tower list in the TRGR zebra bank for use by level 2. Note it is very possible and probable for an energetic jet to cause more than one trigger tower to 'fire' in this manner. Hence the number of level 1 'hot' towers in no way is a good indicator of the number of jets.

### Level 2 Jet Tool: L2JETS.

Normally, for each of the 32 level 1 hardware triggers that can fire, level 2 defines one or more FILTERS that are called in response. Each of these FILTERS is a series of one or more software callable routines called TOOLS, each of which are given an adjustable PARAMETER SET of CUTS that are used in the TOOL'S analysis of the event. Each TOOL returns a TRUE or FALSE to indicate whether the event made the cuts established by the PARAMETER SET it was given. If all TOOLS called by a FILTER return a TRUE, then the FILTER passes the event and it will be written. L2JETS is a TOOL which finds jets. The usual PARAMETER SET it is given include L2\_JET\_NUMBER and L2\_Et\_CUT. L2JETS returns a TRUE if it finds at least L2\_JET\_NUMBER jets each with a minimum ET of L2\_Et\_CUT. We define a simple level 2 FILTER that gets called whenever the above level 1 trigger fires. The FILTER consists solely of one tool: L2JETS with L2\_JET\_NUMBER set equal to ONE and L2\_Et\_CUT left for us to adjust.

### Summary of our Jet Trigger:

In summary, we say that the level 1 jet trigger has 'triggered' if there is at least one trigger tower whose ET is above L1\_Et\_CUT. If the level 1 jet trigger fires, then the routine L2JETS is called. This routine finds jets in the event and we say that the level 2 jet trigger has 'triggered' if L2JETS finds at least one jet whose ET exceeds L2\_Et\_CUT. Note that level 2 cannot trigger unless level 1 does. We say that the event has 'triggered' or 'PASSED' if both level 1 and level 2 have triggered. It is upon this condition that we later define our 'trigger' efficiency and rate.

### How L2JETS works:

L2JETS does the following:

- 1) It first obtains a list of the 'hot' trigger towers that caused level 1 to trigger. These trigger towers are taken as possible jet seeds.
- 2) Starting with the highest ET 'hot' tower, L2JETS adds all the neighboring trigger towers that are within a cone of radius equal to .3 (ICON\_CEN=1) in eta-phi space around the seed tower. Any other 'hot' towers that are 'swallowed' up during this process are not considered further. Also a position for the jet centroid is obtained by doing an ET weighted average over all the contributing trigger towers in eta-phi space.

3) Now all jets are increased in size in .2 increments in eta-phi space until each jet has grown into a cone of radius equal to  $R=.7$  (ICON\_ENG=3). This is done to allow a more even distribution of energy between adjacent jets. Each tower is flagged when used so that it can not give its ET to more than one jet. Both these cone sizes are passed parameters that are user defined.

4) At this point the ET of each jet is multiplied by a calibration number which is meant to correct for energy losses in the calorimeter. We used 1.19 for the central and endcap region and 1.64 for the crack region. These numbers were chosen by comparing L2JETS found jets with the underlying parton jets from the event generator (ISAJET). These 3 calibration numbers are variable and meant to be user defined.

5) Finally all found jets are compared against L2\_Et\_CUT to see if at least one surpasses this threshold. If so, we say that the event has 'triggered'.

#### **Data Sets Used:**

Most of our studies were done using double blind events that have been passed through D0GEANT. Specifically the files: BLND09I.CRD, BLND10I.CRD & BLND11I.CRD were used. It is understood that the 'I' series of D0GEANT events had certain problems. Some of these had to do with the ICD and Massless gap which is not used by the LV1 trigger and not currently used by L2JETS as well. There was also a suppression of electromagnetic energy (by about 5%) in the endcap region. This was seen by analyzing files with 50 Gev electrons but did not show up in the endcap portion of our jet calibration. (see above).

#### **Software used:**

A variety of D0 software was used to obtain and check our results. We will describe some of them:

**PJET:** is an ISAJET output bank that contains the results of applying a fixed cone jet finding algorithm on the final state ISAJET partons. It is intended to try to give an indication of the 'real' underlying jet ET and position. PJET, for the double blind events we used, had a cone radius of .45 and an ET cut of 10. Gev.

**ISA\_CAEP:** is a routine that takes the underlying ISAJET event, calorimeter resolution and vertex information to form a 'FAKE' calorimeter bank comprised of ISAJET track information. This is useful for comparing to the 'REAL' calorimeter banks made by D0GEANT. This version of ISA\_CAEP had longitudinal energy deposition in only two layers.

**CAJETS:** is the offline calorimeter jet finding routine. In particular, we used the cone algorithm with a jet cone size of  $R=.7$  and a minimum jet ET cut of 4 GeV.

**Level 1 Calorimeter Trigger Simulator:** simulates the LV1 trigger. We used it to define our LV1 jet trigger and set the value of L1\_Et\_CUT. The simulator creates a TRGR bank as well as the list of 'hot' trigger towers that pass the L1\_Et\_CUT.

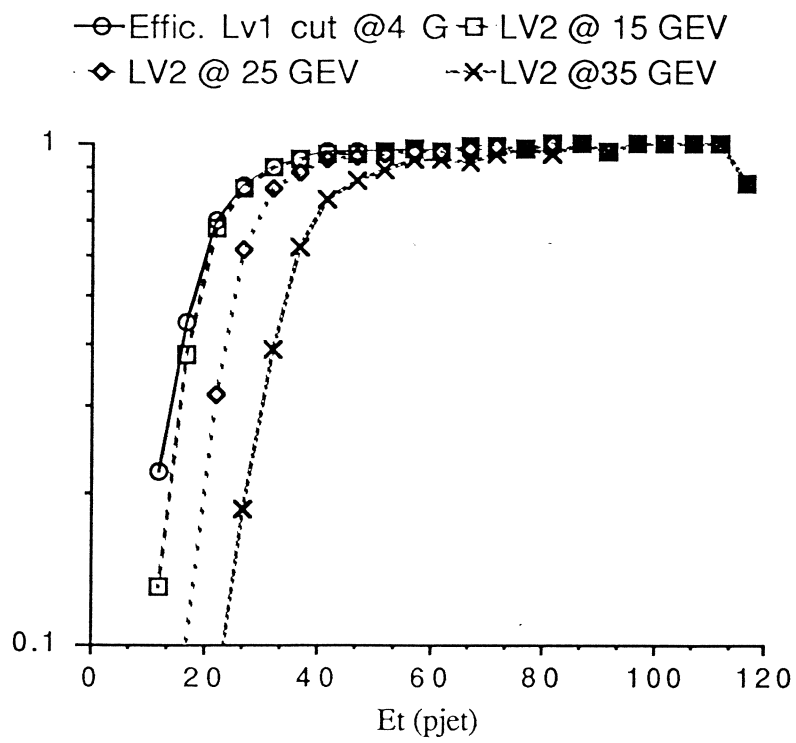
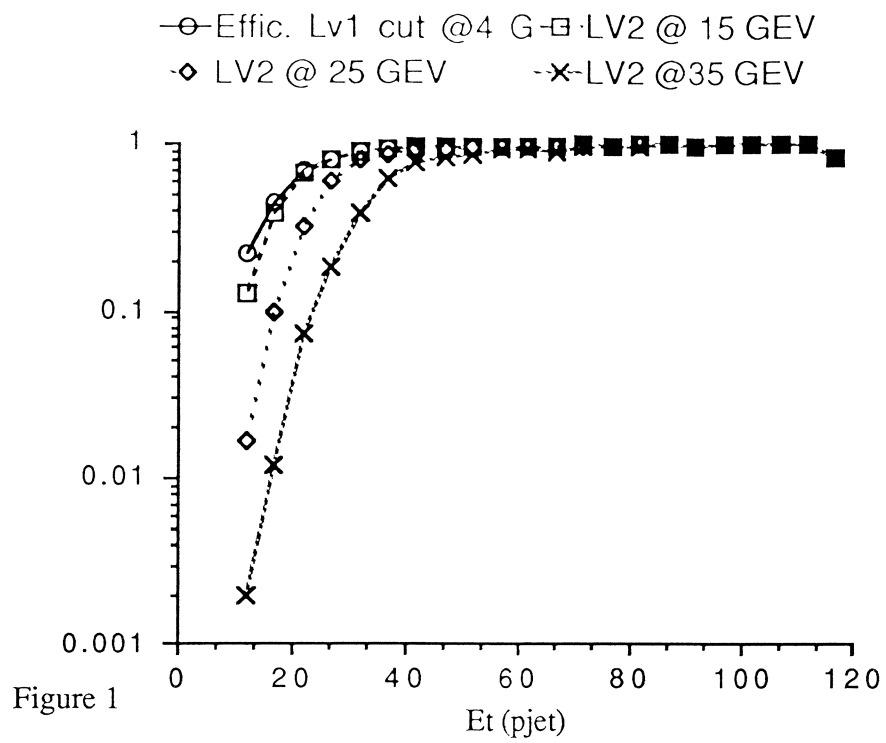
**VMS\_FILTER package and L2JETS:** to simulate the level2 jet finding. Here we are able to set L2\_Et\_CUT. Note that by setting L2\_Et\_CUT = 0.0, we are in fact investigating LV1 efficiencies and rates.

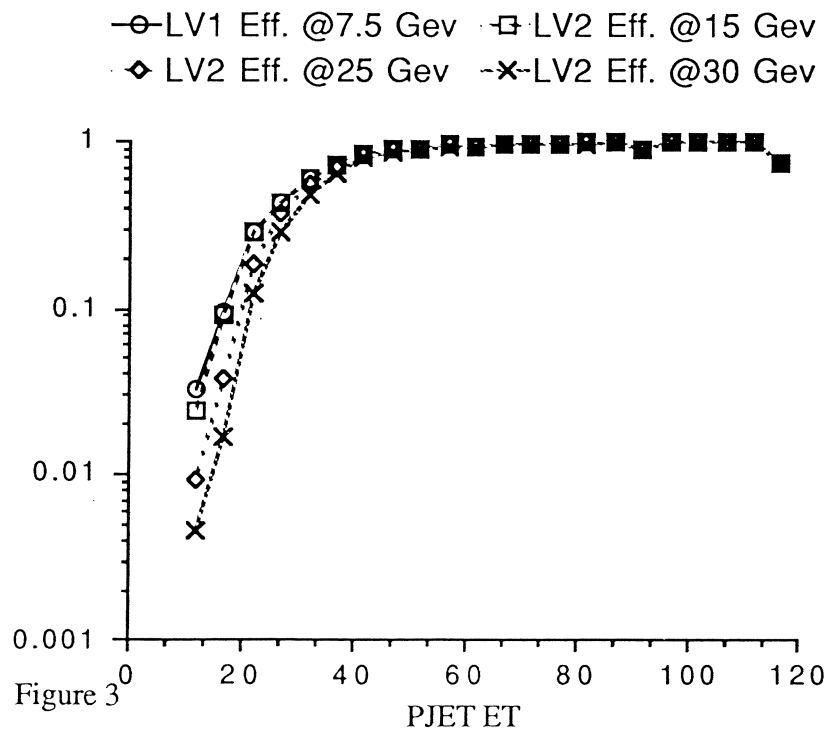
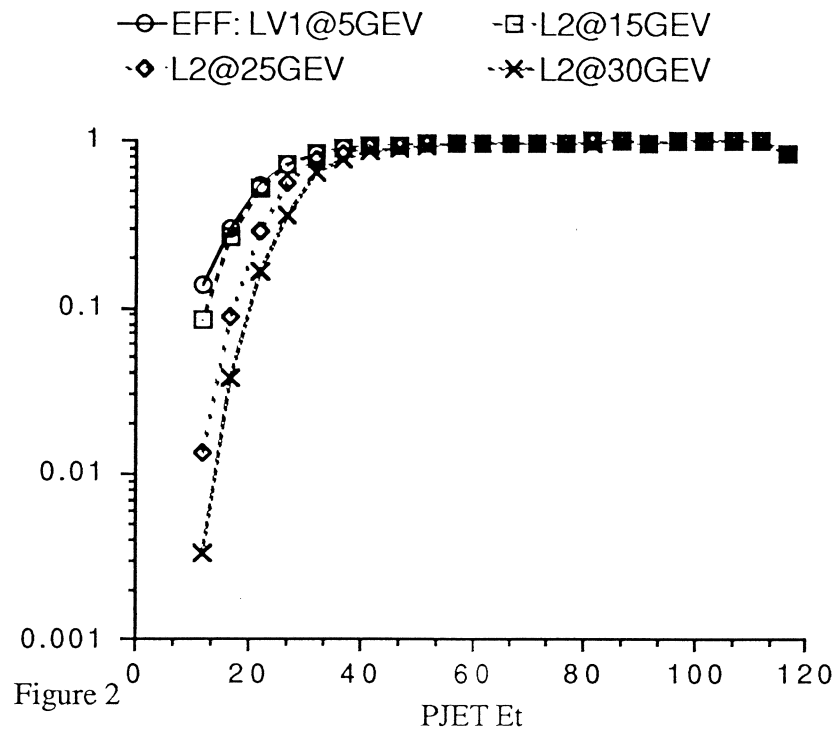
### **CALCULATION OF INDIVIDUAL JET EFFICIENCIES:METHOD 1.**

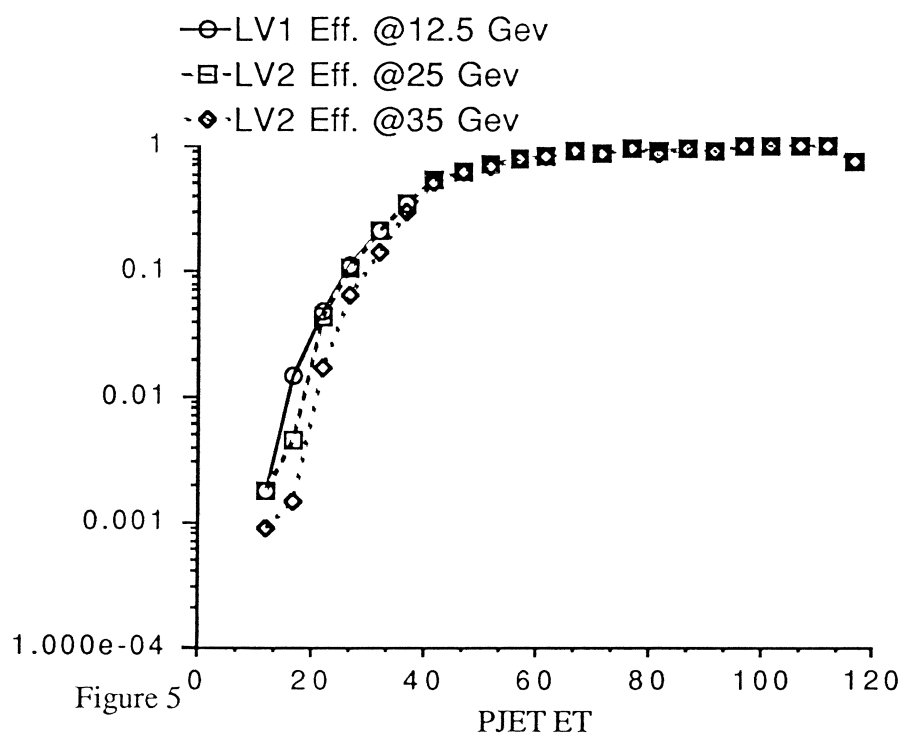
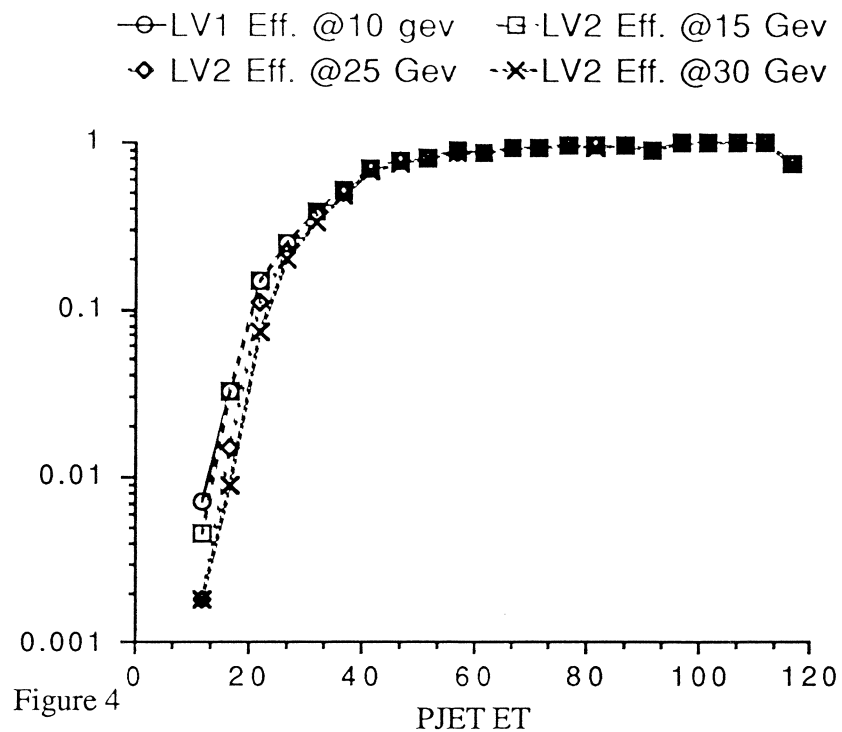
We ran the combined LV1 & LV2 jet trigger as defined above on the DOGEANT data files. We then tried to match PJETS ( ISAJET generated parton jets) with L2JETS ( jets found in the calorimeter via the LV1 and LV2 simulators). Each PJET was matched to a L2JET as follows: If there were no L2JETS within .5 of the PJET it was listed as having no match. If there was only 1 within that distance, then that one was taken as the correct match. If more than one PJET matched to a L2JET, those PJETS were clustered together and redefined as a larger ET parton jet. Most of the time there is no ambiguity between matching the PJET and the L2JET. In addition, histograms of the delta R between PJETs and L2JETS indicate that a cut of  $R=.5$  is still at least 96% efficient for PJETs greater than 40 GeV. Assuming our jet matching is ET independent, then we expect this number holds out in general.

Each PJET was binned by its ET. All PJETs that had a L2JET match were entered into another histogram as well. We calculate our efficiency simply by doing a division of the two histograms.

The following figures show the efficiency for triggering on a PJET as a function of the ET of the PJET. Each plot is the efficiency curve for a particular value of L1\_Et\_CUT. Figures 1-5 show results for L1\_Et\_CUT = 4,5,7.5,10 and 12.5 GEV. Each plot has various curves for different L2\_Et\_CUTs. The curve marked LV1 in each is simply when we set L2\_Et\_CUT=0.0 and so directly measures level 1 efficiencies.









### COMMENTS:

1) The efficiencies calculated were for 5 GeV bins. Since the points were not distributed evenly within the bin, the efficiency calculated does not correspond to the middle of the bin. Assuming an exponential behavior such that the number of PJETS fell by a factor of 9 over the 5 GeV bin, we determine that the calculated efficiency is more correctly placed at the end of the lower 1/3 of the bin. All the figures shown were adjusted this way.

2) Since the PJETS for the D0geant events used were created under an algorithm that required a minimum PJET ET of 10 GeV, we do not have any points in the first two bins and hence no efficiency numbers as well. We address this problem later.

3) Low statistics in the high ET bins causes some 'dips' in the plots at high ET. But the main intent of these curves was to emphasize the behavior up to the point where they become efficient. These curves reach 90% efficiency at 32,37,47,64 & 65 GeV and 99% efficiency at 77,77,77,96 & 96 GeV for the curves with L1\_Et\_CUT set at 4.,5.,7.5,10. & 12.5 GeV respectively. The 99% numbers are more uncertain as they involve the higher, less statistically sound, ET region.

4) It can be seen from figure 1 (L1\_Et\_CUT=4.0) that the efficiency curves start to flatten out the quickest. In this case the various LV2 cuts are rejecting much more of the lower ET jets than LV1 but rises quickly enough to become fully efficient at the same time LV1 does.

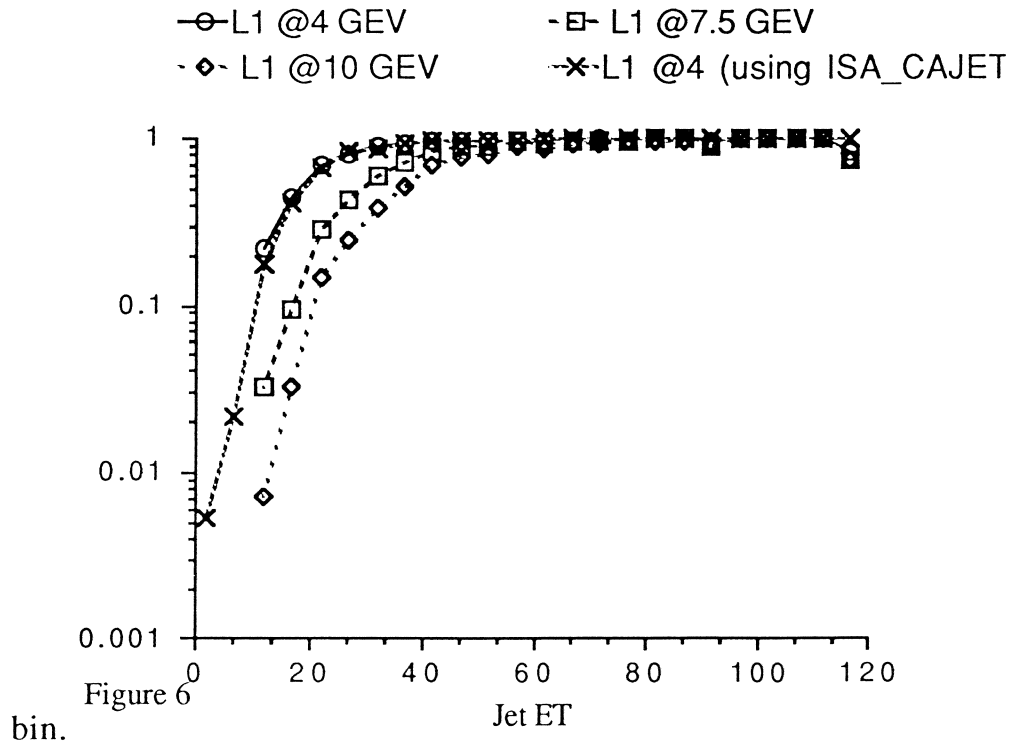
5) In contrast, figure 5 (L1\_Et\_CUT=12.5) shows little difference between the LV1 and LV2 curves.

## CALCULATION OF INDIVIDUAL JET EFFICIENCIES: METHOD 2

We again found montecarlo jets with our trigger as described above. But this time we compared our LV2 jets to an ISAJET particle level jet finder instead of PJETS. ISA\_CAEP was run on the ISAJET event and then CAJETS (the offline jet finder) was used to find jets. We used the official CAJET fixed cone algorithm set with  $R=.7$  and a minimum jet ET of 4 Gev. As before we calculate efficiencies by dividing a histogram of found L2JETS by a histogram of matching ISA\_CAJETS.

This method was desirable because 1) It allowed us to compare between two algorithms with the same cone size. 2) We were now able to calculate efficiencies for the 0-5 and 5-10 gev bin. & 3) The jet algorithm we compare to uses fragmented particles instead of partons.

Figure 6 show various efficiency curves made with the PJET method (Method 1) and one with the ISA\_CAEP/CAJET method (Method 2) described above. The two methods for  $L1\_Et\_CUT=4\text{Gev}$  agree fairly well except for the 10-15 Gev.

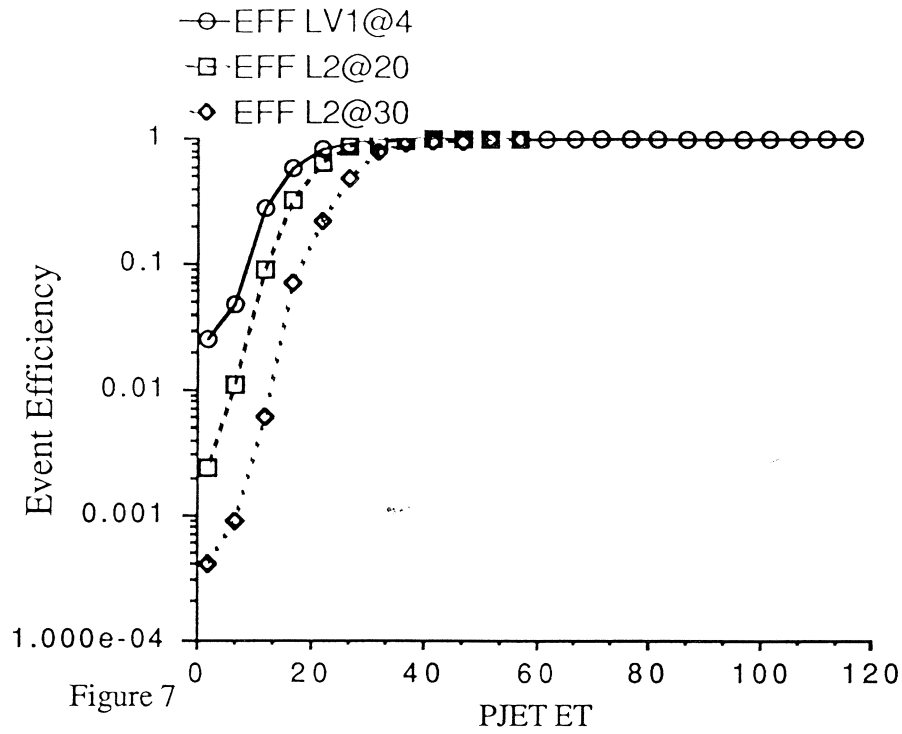


## CALCULATION OF EVENT JET EFFICIENCIES:

Up to now, we have been talking about individual jet efficiencies; in other words, the probability that a jet of a certain ET directly causes a 'trigger' as defined above. We will now look at the broader question of event efficiencies. Say we are interested in accepting jets of a certain ET value and above. Well we know the probability that it will cause a direct trigger because we can get that information from the efficiency curves given above. What's more, we can do linear interpolation between the points to obtain approximate efficiencies for any jet ET. However, even if the jet we are interested in does not trigger, there is a chance that the other ET balancing jets in the event WILL trigger. We calculate efficiencies and event rates for this as follows:

We generated ISAJET events in various ET bins running from 4 Gev to 80 Gev. We set the PJET parameters to have a cone size of  $R=.5$  and a minimum ET of 2 Gev. Then, for each event, we took the three highest ET PJETS and assigned each one a 'probability of triggering' derived from linear interpolation of the aforementioned efficiency curves. We used the curves made with the PJET method but we use the ISA\_CAJET efficiencies for the first 2 ET bins as the PJET method did not give us these numbers. We are then able to calculate the probability of one of the three PJETs causing a trigger. These 'event efficiency' numbers were histogrammed as a function of the ET of the highest ET PJET in the event. In addition, each event had a rate associated with it. This rate was found by taking the ISAJET cross section, multiplying by an assumed instantaneous luminosity of  $10^{30}$  /cm<sup>2</sup>/second and weighting this number with the event efficiency. In this way, we end up with bin averaged efficiencies and rates for accepting an event whose highest PJET has a certain ET.

Figure 7 shows the event efficiency for various L2\_Et\_CUT values assuming that L1\_Et\_CUT is set at 4 Gev.



#### COMMENTS:

The event efficiencies curves become saturated much quicker than the individual jet efficiency curves. All of the event efficiency curves reached 99% by ET = 37 GeV. This is in contrast to the corresponding number (77 GeV) for the individual jet curves.

## Appendix A

### Trigger rates from level-1

The event rate from the level-1 trigger as a function of the level-1  $E_t$  threshold ( $L1\_E_t\_CUT$ ) has been determined once in 1989. The event sample used for this exercise was the 10K two-jet events produced in ~1987 with a very preliminary version of DOGEANT and the level-1 trigger simulator. Trigger rates (based on a sample of two-jet events with  $5 < E_t < 140\text{GeV}$ ) were calculated in 1989 and are part of the D0 upgrade of the Breckenridge workshop (p. 263 in the proceedings of that workshop). The triggers used for that simulation were: total  $E_t$ , a jet trigger, an electromagnetic trigger and a missing  $E_t$  trigger. For reference the rates obtained in 1989 for total  $E_t$ , jet trigger and EM trigger are shown as part of Fig. A1, A2 and A3. These results are labelled "1989" and serve as a reference point for the rates determined this year.

Since we do not have a large sample of Monte Carlo events (at low  $E_t$ ) for determination of the rate from the jet trigger from level-1, we tried to estimate it using different techniques and comparing them to each other. As a reference we always use the "1989" results which are based on the above described sample.

One of the simplest approaches to calculating the jet rate is the use of the toy calorimeter in ISAJET (not the ISA\_CAEP version !). Here the energy of a particle is deposited in an  $\eta, \phi$  space on  $\Delta\eta = \Delta\phi = 0.1$  grid without any smearing whatsoever. We changed this grid to  $\Delta\eta = \Delta\phi = 0.2$  and simply plotted the  $E_t$  of the tower with the largest  $E_t$  in the event. We did this for two jet events with  $E_t$  in the range 5 - 150GeV. The resulting  $E_t$  spectrum leads to the rate curve labelled "Jet rate lev-1 toy" shown in Figs. A1 and A3. This simple simulation does not take into account: cracks, dead regions, shower spreading, resolutions, vertex smearing etc. Despite that it agrees rather well with the 1989 results.

In an attempt to be more accurate and take into account all detector effects, we used the efficiencies for the level-1 trigger as a function of  $L1\_E_t\_CUT$  derived in the previous part of this note. These efficiencies give us the probability that a jet (defined by the PJET algorithm, which sums parton energies in a cone of  $R=0.45$ ) with a given  $E_t$  passes the level-1 tower  $E_t$  cut-off ( $L1\_E_t\_CUT$ ). Fig A1 shows the rate (labelled Pjet rate) for two jet events ( $E_t \text{ jet} > 5\text{ GeV}$ ) if we were able to trigger on the jet energy determined by PJET. Again this is simply derived from the spectrum of the jet with the highest PJET  $E_t$  in each event. This rate is obviously larger than the level-1 rate, because level-1 only sees a fraction of the real jet energy (one trigger tower only). Using the L1 jet efficiencies, the correct ISAJET PJET jet spectrum and calculating the probability for each event (folding all PJET jets in the event with the appropriate probability) of being picked up by the level-1

as a function of  $L1_{E_t\_CUT}$  we find the rate of the level-1 jet trigger. This is the curve labeled "Jet rate level-1(1990)" in Fig. A3. This rate is lower than other estimated rates. Part of that is due to the energy scale in the current D0geant simulation. Comparing the energies of reconstructed jets to the underlying Pjets and comparing D0geant simulated 50GeV pions with the energy deposited in the calorimeter the "measured" energy in D0geant is smaller by 10-20%. This means that a  $L1_{E_t\_CUT}$  of 20GeV really corresponds to a cut of 22-24 GeV, which shifts the whole curve to the right and makes it agree better. This does not compensate for all the difference, but after all some difference is expected because this is the first time that a full simulation of detector AND the level-1 trigger was used.

In Fig. A2 some rates for the EM trigger from level-1 are shown. The interesting comparison here is between "EM rate level-1(1989)" and "EM rate lev-1 toy". Using the simple ISAJET toy calorimeter (not CAEP), we calculate the rate of the EM trigger due to two-jet events only taking into account the true electromagnetic component of the jets i.e. only primary  $\gamma$ 's,  $\pi^0$ 's,  $\eta$ 's, etc). Here the toy calorimeter was used in exactly the same way as for jets, but now only the EM part of the tower was taken into account. This illustrates what the minimal rate for the EM trigger is, based on two jet events ( $E_t > 5$  GeV) only.

Figure A1

Comparison of rates from level-1 estimated by  
different methods.

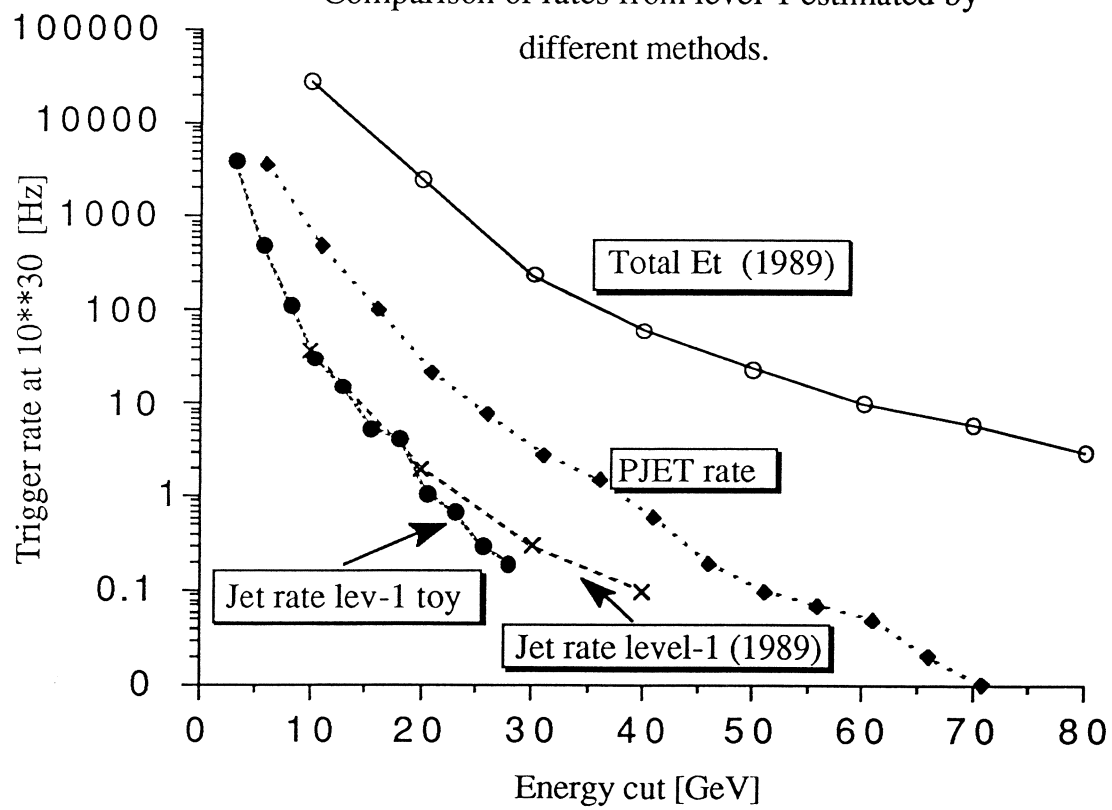


Figure A2

Comparison of rates from level-1 estimated by  
different methods.

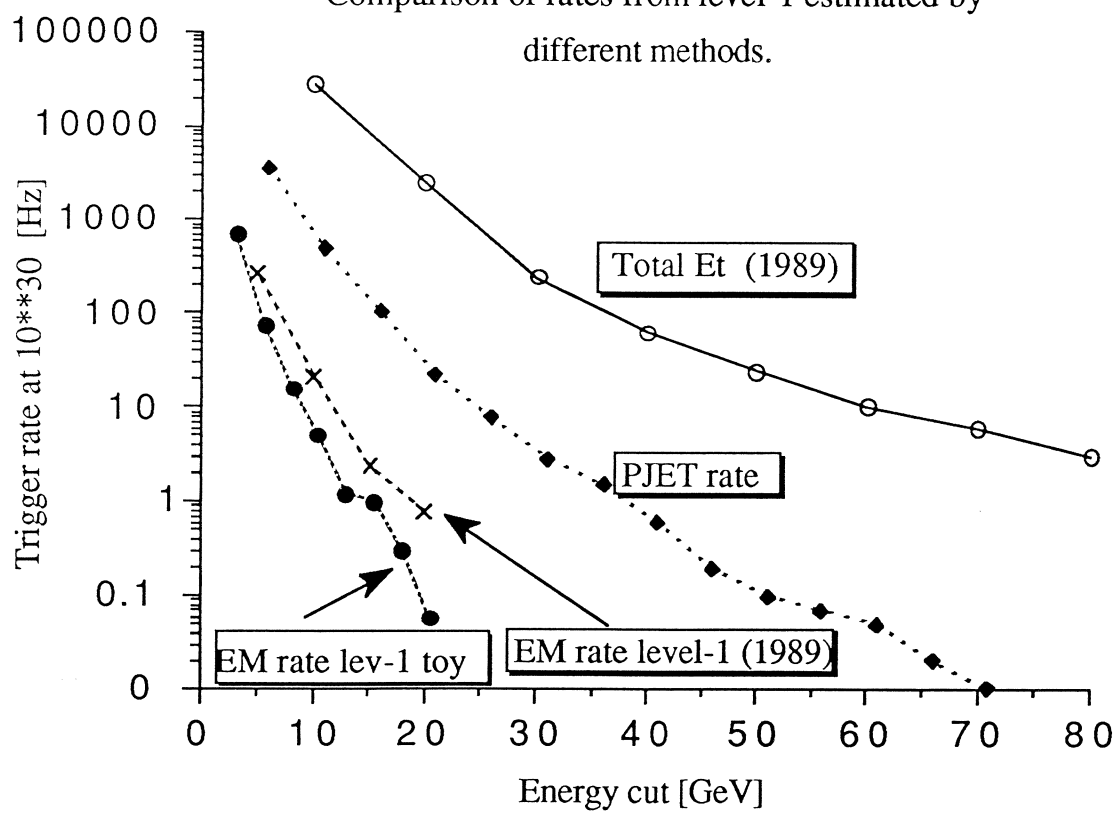
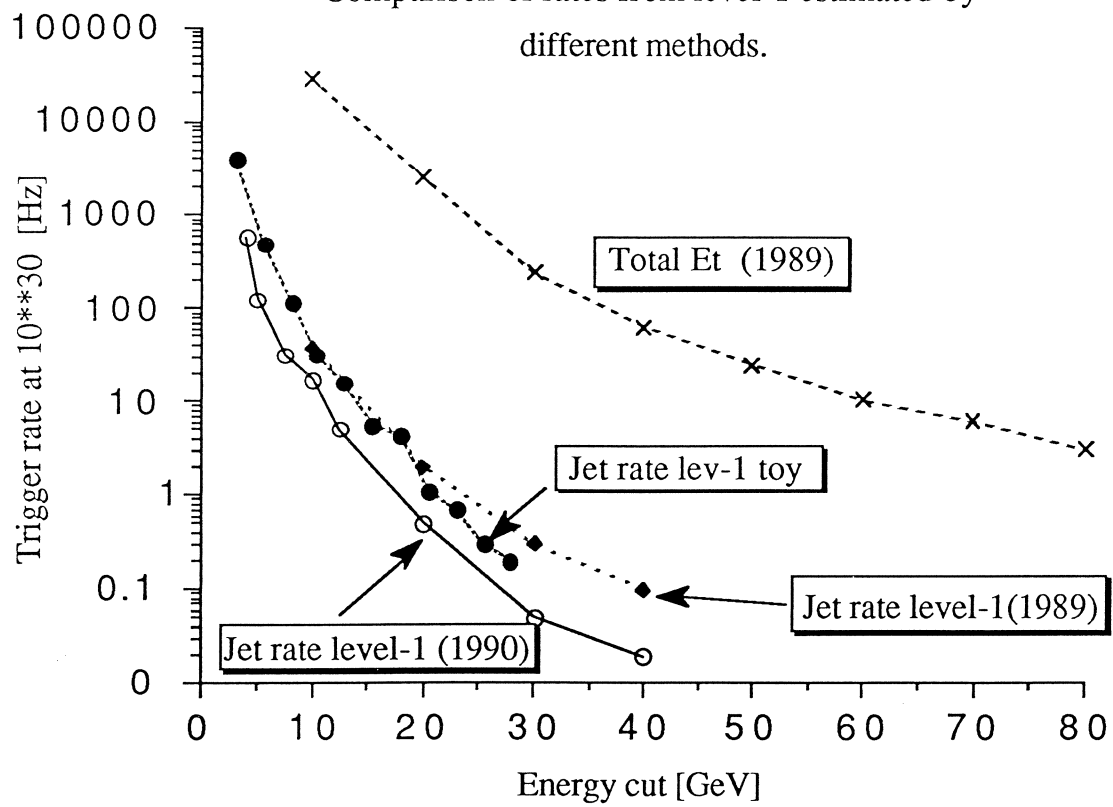




Figure A3

Comparison of rates from level-1 estimated by  
different methods.



CAZ

## Nonuniformity in charge collection efficiency of the ECEM calorimeter

### 1 Introduction

We have studied nonuniformity in charge collection efficiency due to irregularities in the electric field in the liquid Argon gap of ECEM. The charge collection efficiency deviates from its nominal value at the boundaries of segmented pads, at the crack between two resistive-coat sheets which form a disk and at the crack in the Uranium disk. We have calculated the size of the nonuniformity in these areas using ANSYS[1] program.

The formulae[2] for induced charges on pads can be derived using Green's reciprocal theorem:

$$\sum q'V = \sum V'q,$$

where  $q$  and  $V$  correspond to a set of charges and potentials in a system of conductors and  $q'$  and  $V'$  correspond to another set of charges and potentials in the same system. First we consider a set of charges and potentials to give the induced charge to be determined. A charge  $q$  is positioned at a point  $P$  in the liquid Argon gap. Absorber plates are grounded. Pads are also grounded through low input-impedance amplifiers. The induced signal on a pad in question is  $Q_{ind}$ . Table 1 shows the first set of charges and potentials. The other set of charges and potentials can be chosen so that all electrodes are at zero potentials except the pad in question. Table 2 shows this second set.

Table 1

Charge	Potential	Location
$q$	$V_P$	a point $P$ in LAr gap
$Q_{ind}$	$V_0 = 0$	a pad in question
$Q_{ind}^{others}$	0	other pads
$Q_{abs}$	0	an absorber plate

Table 2

Charge	Potential	Location
$q' = 0$	$V'_P$	a point $P$ in LAr gap
$Q'_{ind}$	$V'_0$	a pad in question
$Q'_{ind}^{others}$	0	other pads
$Q'_{abs}$	0	an absorber plate

From these two sets of charges and potentials Green's reciprocal theorem yields:

$$Q_{ind} = -\frac{V'_P}{V'_0}q.$$

This shows that the induced charge on a pad in question is obtained if the potential at the location of charge  $q$  is determined applying unity voltage at the pad and leaving all other electrodes grounded. By differentiating the above expression by time  $t$  we obtain the current induced on a pad by an drifting electron ( $-e$ ) at a point  $s(t)$  ( $s$  is the coordinate along the drift path) in the liquid Argon gap as:

$$i(t) = -(-e)\vec{v}(t) \cdot \vec{E}_w(s(t)). \quad (1)$$

Here  $\vec{v}(t)$  is the drift velocity of an electron.  $\vec{E}_w(s(t))$  is the electric field at  $s(t)$  calculated applying unity voltage on the pad and zero on all other electrodes. This field is sometimes called the weighting field.

An electron drifts along the electric field established to collect the charge:

$$\frac{\vec{v}(t)}{v(t)} = \frac{\vec{E}_d(s(t))}{E_d(s(t))}. \quad (2)$$

In our calorimeter this drift field  $\vec{E}_d(s(t))$  is established by applying positive voltage ( $\sim +2300\text{V}$ ) on the resistive coat while absorber (Uranium and steel) plates are grounded. The total induced charge  $Q(t)$  from  $t = 0$  to  $t = t$  is obtained by integrating the equation (1). Changing the variable from  $t$  to  $s$  and using the relation  $ds/dt = v(s)$ , we obtain:

$$\begin{aligned} Q(t) &= e \int_{s(0)}^{s(t)} \vec{v}(s) \cdot \vec{E}_w(s) \frac{ds}{v(s)} \\ &= e \int_{s(0)}^{s(t)} \frac{\vec{E}_d(s) \cdot \vec{E}_w(s)}{E_d(s)} ds. \end{aligned} \quad (3)$$

This equation (3) is our master equation to calculate charge collection efficiency.

## 2 Nonuniformity at the pad boundary

The geometry considered in this section is shown in Fig.1. Each pad is 20 mm wide. The gap width between two pads is 1 mm. Because the resistive coat is uniform in this geometry, the drift field is also uniform as  $E_{d-x} = 0$  and  $E_{d-y} = 2300\text{V}/2.3\text{mm} = 1000\text{V/mm}$ . Therefore the equation (3) is reduced as:

$$\begin{aligned} Q(t) &= e \int_{s(0)}^{s(t)} E_{w-y}(s) ds \\ &= e \int_{y(0)}^{y(t)} E_{w-y}(y) dy. \end{aligned} \quad (4)$$

We have calculated the weighting field using ANSYS. In the calculation the first pad is held at 1 V while the second pad and the absorber plate are left grounded. Figure 2

shows the calculated weighting field lines. The field is uniform up to  $x = 18$  mm or so. Some field lines originating from the edge land on the second pad. Assuming ionized electrons are deposited uniformly along the charged particle trajectory, perpendicular to the pad, we can calculate the total induced charge by the line of charge. Figure 3 shows the total induced charge on the first pad as a function of position ( $x$ ) of the line of charge. The value is normalized by the nominal value obtained in the area where the weighting field is uniform. Near the edge of the pad we observe the overshoot above 1 and, then, the undershoot below 0. The former corresponds to the dense area where the weighting field becomes stronger than the nominal. The amount of the induced charge is larger than the nominal. The latter corresponds to the field lines landing on the second pad. Because the weighting field is reversed, the net induced charge on the first pad becomes negative. After a few mm away from the edge the positive field and the negative field cancel each other. Therefore, the total induced charge on the first pad becomes zero.

We define the charge collection efficiency as:

$$\text{charge collection efficiency}(x) \equiv \frac{Q^{total}(1st) + Q^{total}(2nd)}{Q^{total}(nominal)}(x),$$

where  $x$  is the position of line of charge,  $Q^{total}(1st)$  and  $Q^{total}(2nd)$  are the total induced charges on 1st and 2nd pads, respectively, and  $Q^{total}(nominal)$  is the nominal total charge obtained if there is no gap between the pads. Figures 4(a) and 4(b) show the charge collection efficiency as a function of  $x$ . Dotted lines show where the pad boundaries are. Figures 5(a) and 5(b) show the plots for the narrower gap (0.5 mm) in between two pads. This is the case for the pads within the same multilayer board. Figures 6(a) and 6(b) show the plots for the wider gap (1.5 mm). This is the case for the gap between two edge pads on two adjacent multilayer boards. As is shown the loss of the efficiency is less than 10% for 0.5 mm gap. However, the inefficiency in the 1.5mm-wide gap can be as large as 50%.

We further studied the effect of the nonuniform efficiency taking into account the transverse shape of the electromagnetic shower. Figure 7 shows the transverse shape (i.e. energy deposited versus lateral coordinate) of 50 GeV electron shower summed over all layers of ECEM. Here we only consider a 2-dimensional problem. From the shower shape we can immediately tell the effect of the nonuniformity is the minimum when the shower peaks at the center of the pad while it is the maximum when the shower peaks at the middle of two pads. Therefore we plot the following quantity as a measure of the efficiency:

$$\epsilon(x) \equiv \frac{\text{total energy collected when the shower peaks at } x \text{ mm away from the pad center}}{\text{total energy collected when the shower peaks at the pad center}}.$$

Figure 8 shows  $\epsilon(x)$  for 50 GeV electron shower. The pad width is 20 mm and the gap between adjacent pads is 0.5 mm wide. The pad boundaries are shown by dotted lines. The inefficiency is less than 1%, negligibly small. Figures 9 and 10 show the plots for 1.0 mm and 1.5 mm gaps. The peak inefficiencies are  $\sim 3.5\%$  and  $\sim 7\%$ , respectively. These values are larger than the intrinsic energy resolution of ECEM. In particular, the 1.5 mm gaps of multilayer boards are all in line over all layers. We would expect to see this efficiency loss of  $\sim 7\%$  in the data. We hope we can correct for this inefficiency using the test beam data.

### 3 Nonuniformity at the crack in the resistive-coat sheet

Figures 11(a) and 11(b) show the geometries considered here. The gap between two resistive-coat sheets is 1.5 mm wide. The gap is filled with the epoxy in Fig.11(b), while it is not in Fig.11(a). Figures 12 and 13 show the drift and weighting field lines, respectively, for the case of Fig.11(a). Because both drift and weighting fields are distorted and have  $x$  components around the crack, the equation (3) can be rewritten as:

$$Q(t) = e \int_{s(0)}^{s(t)} \frac{E_{dx}E_{wx} + E_{dy}E_{wy}}{\sqrt{E_{dx}^2 + E_{dy}^2}} ds. \quad (5)$$

The integration is done over the electron drift path.

We define the charge collection efficiency as:

$$\text{charge collection efficiency}(x) \equiv \frac{Q^{total}(crack)}{Q^{total}(nominal)}(x, T),$$

where  $x$  is the position of the line of charge,  $Q^{total}(crack)$  and  $Q^{total}(nominal)$  are the total induced charges with and without a crack, respectively, and  $T$  is the total integration time. It takes longer than the nominal collection time for electrons deposited at the crack to reach the resistive-coat surface. In the simulation program electrons are drifted with the velocity given by[3]:

$$v_d(\text{cm/sec}) = 2.1 \times 10^4 \times \sqrt[3]{E_d(\text{V/cm})}. \quad (6)$$

For a field of 1000 V/mm, this gives  $v_d = 4.5 \times 10^{-3}$  mm/nsec. The total drift time for a 2.3 mm gap is  $\sim 510$  nsec. Figure 14 shows the drift velocity versus the drift field given by the above equation.

The calculated charge collection efficiencies are shown in Fig.15 for four different integration (or charge collection) times ( $T=550, 600, 650$  and  $700$  nsec). As is shown if the collection time is longer than 700 nsec the inefficiency is negligible. Figure 16 shows the same plots for the narrower gap (1 mm), which is the case for ECEM. Again the inefficiency is negligible if we collect electrons for more than 700 nsec.

Figures 17(a) and 17(b) show the drift and weighting field lines, respectively, for the geometry shown in Fig.11(b). Here the 1.5mm-wide gap is filled with the epoxy. The drift field is distorted while the weighting field is uniform. Figure 18 shows the same plots as in Figs.15. Again the inefficiency is negligible when we integrate the charge for 700 nsec or longer. Since the standard integration time for D0 calorimeter is more than 2  $\mu\text{s}$ , we conclude the inefficiency of charge collection due to the crack in the resistive-coat sheet is negligibly small.

### 4 Nonuniformity at the crack in the Uranium disk

Because ECEM Uranium disk is made of three plates, we have  $\sim 1$  mm gap between two Uranium plates as is shown in Fig.19. Both drift and weighting fields are distorted as is shown Figs.20(a) and 20(b). They are distorted in the same way. Again we define

the charge collection efficiency as:

$$\text{charge collection efficiency}(x) \equiv \frac{Q^{total}(crack)}{Q^{total}(nominal)}(x, T),$$

where  $x$  is the position of the line of charge,  $Q^{total}(crack)$  and  $Q^{total}(nominal)$  are the total induced charges with and without a crack, respectively, and  $T$  is the total integration time. Figure 21 shows the efficiencies for  $T=500, 600, 700$  nsec and  $1 \mu\text{sec}$ . The efficiency becomes more than 1 in the gap because of the extra contributions from electrons deposited in LAr between  $y=3.5$  and  $5.5$  mm. If we consider contributions only from electrons deposited in LAr between  $y=1.1$  and  $3.4$  mm (i.e. nominal LAr gap), the efficiency looks like Figure 22. This efficiency is independent of the integration time longer than 500 nsec. This is because the  $y$  component of the weighting field ( $E_{wy}$ ) in the gap is smaller than the nominal value and the integration of  $E_{wy}$  gives the smaller value than the nominal one.

Because the crack in the Uranium disk distorts not only the charge collection efficiency but also the longitudinal and lateral developments of the shower, it will require Monte Carlo studies in detail to understand how these results reflect to the uniformity of ECEM response.

## 5 Conclusion

We have studied the nonuniformity in charge collection efficiency due to irregularities in the electric field using ANSYS. Three cases studied are 1) the boundaries of segmented pads 2) the crack in the resistive-coat sheet and 3) the crack in the Uranium disk. For the first case we have found that the inefficiency is less than 10% even for the electrons deposited in the middle of the 0.5mm-wide gap between two pads within the same multilayer board. When we take into account the transverse shape of the electromagnetic shower, the inefficiency due to this gap is less than 1%, which is negligible compared with the intrinsic energy resolution. However, the 1.5mm-wide gap between multilayer boards causes the nonnegligible inefficiency, which is  $\sim 7\%$  after averaging over the transverse shower shape. For the second case we have found the effect is negligible because our charge integration time is much longer than the drift time of electrons. For the third case the charge collection efficiency will be largely distorted. How it will affect the uniformity of ECEM response needs to be studied by the shower (e.g. EGS) Monte Carlo programs.

## References

1. The ANSYS general purpose finite element analysis computer program, Swanson Analysis Systems Inc.
2. A.H.Walenta, Nucl. Instr. and Meth. **151** (1978) 461.
3. J.Engler et al., Nucl. Instr. and Meth. **120** (1974) 157.

## Figure captions

1. The pad boundary. Each pad is 20 mm wide and the gap between two pads is 1 mm wide. The distance between the pad plane and the ground plane is 0.5 mm. The resistive-coat sheet surface is 0.6 mm above the pad plane. The liquid Argon gap between the resistive-coat surface and the absorber plate is 2.3 mm.
2. The weighting field lines calculated applying +1 V on the 1st pad while the 2nd pad, an absorber plate and the ground plane are grounded. The field lines towards the ground plane are not shown.
3. The total induced charge observed on the 1st pad, normalized by the nominal value obtained in the area where the weighting field is uniform. It is plotted as a function of position (mm) of the line of charge.
4. (a) The charge collection efficiency as a function of the position (mm) of the line of charge. The gap between two pad is 1 mm wide as shown by the dotted line.  
(b) The detail around the pad boundary.
5. (a) The charge collection efficiency as a function of the position (mm) of the line of charge. The gap between two pads is 0.5 mm wide as shown by the dotted line.  
(b) The detail around the pad boundary.
6. (a) The charge collection efficiency as a function of the position (mm) of the line of charge. The gap between two pads is 1.5 mm wide as shown by the dotted line.  
(b) The detail around the pad boundary.
7. The transverse shape of 50 GeV electron shower summed over all layers of ECEM. The unit is mm.
8.  $\epsilon(x) \equiv (\text{total energy collected if shower maximum is } x \text{ mm away from the pad center}) / (\text{total energy collected if the shower maximum is at the pad center})$  for 50 GeV electron shower. The pad width is 20 mm and the gap between adjacent pads is 0.5 mm wide.
9.  $\epsilon(x) \equiv (\text{total energy collected if shower maximum is } x \text{ mm away from the pad center}) / (\text{total energy collected if the shower maximum is at the pad center})$  for 50 GeV electron shower. The pad width is 20 mm and the gap between adjacent pads is 1.0 mm wide.
10.  $\epsilon(x) \equiv (\text{total energy collected if shower maximum is } x \text{ mm away from the pad center}) / (\text{total energy collected if the shower maximum is at the pad center})$  for 50 GeV electron shower. The pad width is 20 mm and the gap between adjacent pads is 1.5 mm wide.
11. (a) A crack in a resistive-coat sheet. The crack is at the center of 20 mm wide pad. The crack is 1.5 mm wide. (b) Same as above, with the crack filled with the epoxy.
12. The drift field lines calculated applying +2.3 kV on a resistive-coat surface, leaving pads and the absorber plate grounded. Here the 1.5mm-wide crack is not filled with the epoxy.



13. The weighting field line calculated applying +1 V on a pad, leaving the absorber plate grounded. Here the 1.5mm-wide crack is not filled with the epoxy.
14. The electron drift velocity versus the drift field in liquid Argon [3].
15. The charge collection efficiency as a function of the position (mm) of the line of charge for four different charge collection times ( $T=550, 600, 650$  and  $700$  nsec). The crack is 1.5 mm wide as shown by the dotted line. The crack is not filled with the epoxy.
16. The charge collection efficiency as a function of the position (mm) of the line of charge for four different charge collection times ( $T=400, 500, 600$  and  $700$  nsec). The crack is 1 mm wide as shown by the dotted line. The crack is not filled with the epoxy.
17. (a) The drift field lines calculated applying +2.3 kV on a resistive-coat surface, leaving pads and the absorber plate grounded. (b) The weighting field line calculated applying +1 V on a pad, leaving the absorber plate grounded. Here the 1.5mm-wide crack is filled with the epoxy.
18. The charge collection efficiency as a function of the position (mm) of the line of charge for four different charge collection times ( $T=550, 600, 650$  and  $700$  nsec). The crack is 1.5 mm wide as shown by the dotted line. The crack is filled with the epoxy.
19. A crack in the Uranium disk. The gap between two Uranium plates is 1.0 mm wide.
20. (a) The drift field lines calculated applying +2.3 kV on a resistive-coat surface, leaving pads and the absorber plate grounded. (b) The weighting field line calculated applying +1 V on a pad, leaving the absorber plate and the other pads grounded.
21. The charge collection efficiency as a function of the position (mm) of the line of charge for four different charge collection times ( $T=500, 600, 700$  nsec and  $1 \mu\text{sec}$ ). The crack is 1 mm wide as shown by the dotted line.
22. The charge collection efficiency for electrons deposited between  $y=1.1$  and  $3.4$  mm (i.e. nominal LAr gap).

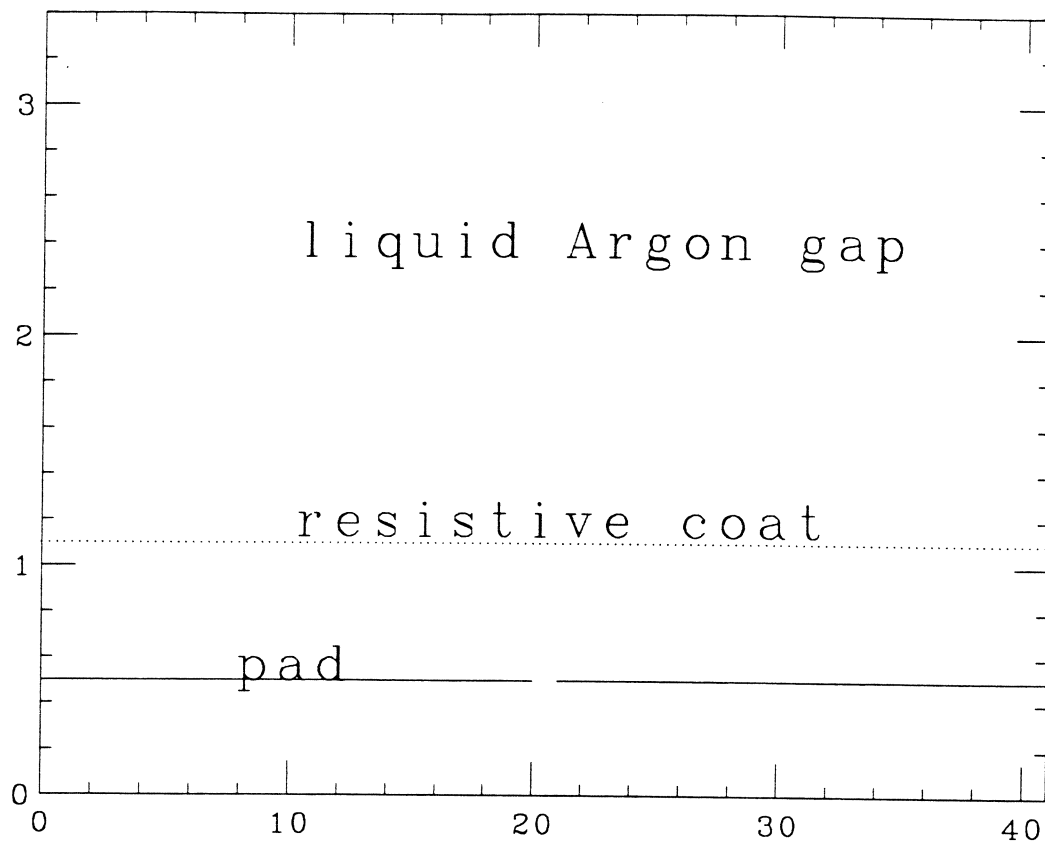
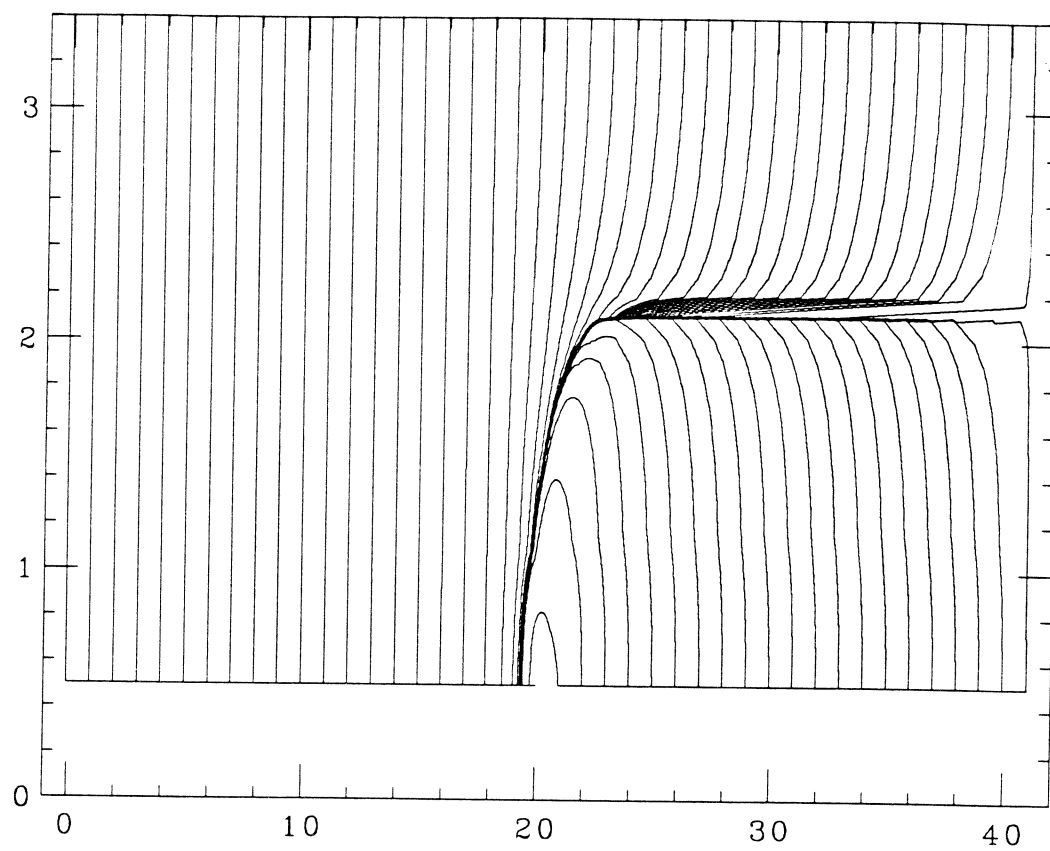


Figure 1



Weighting field lines

Figure 2

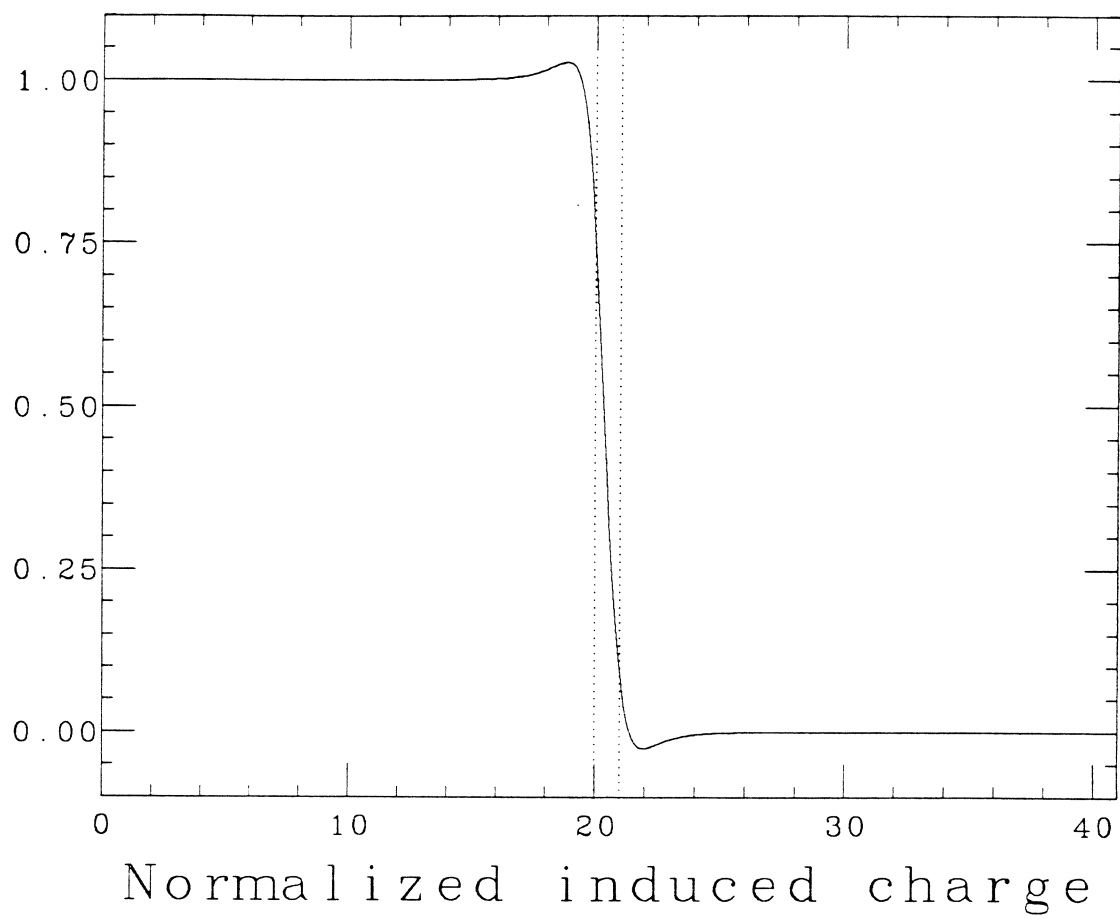


Figure 3

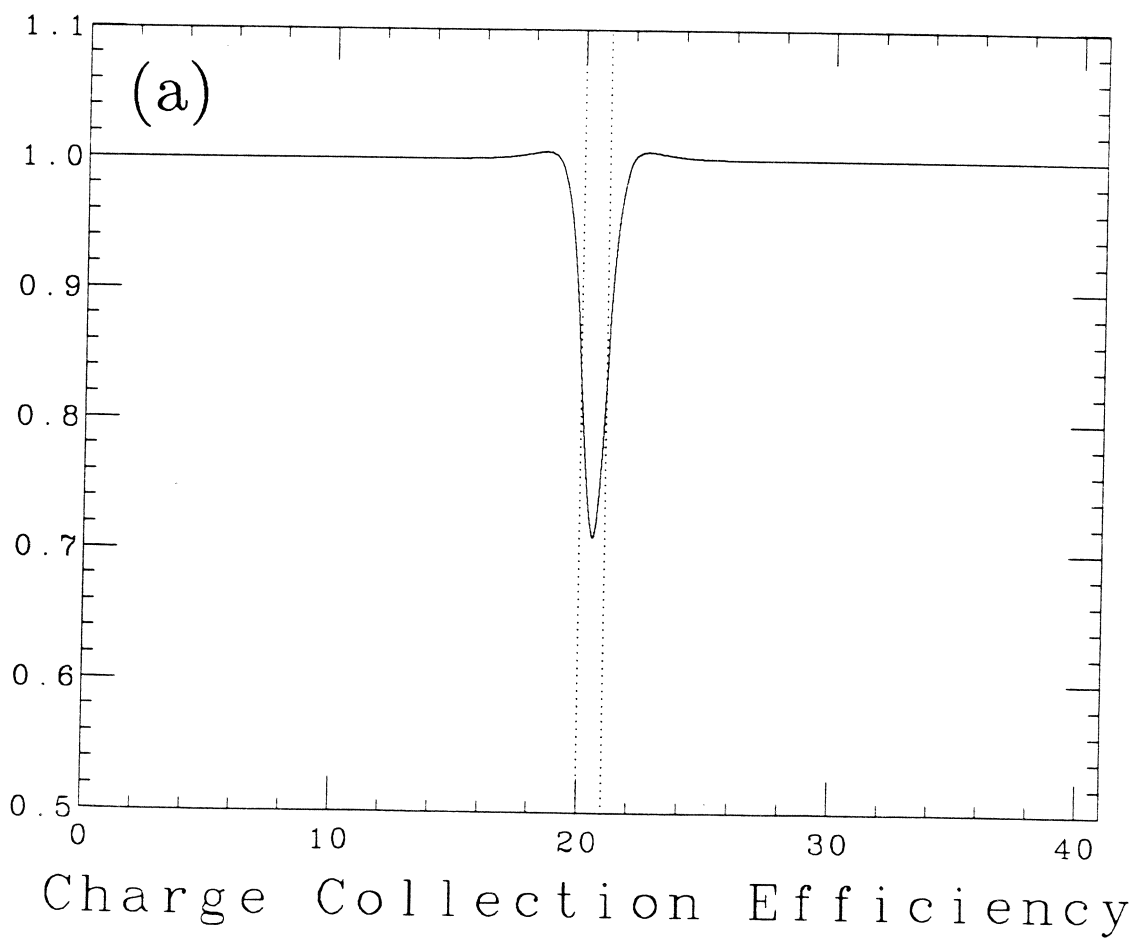
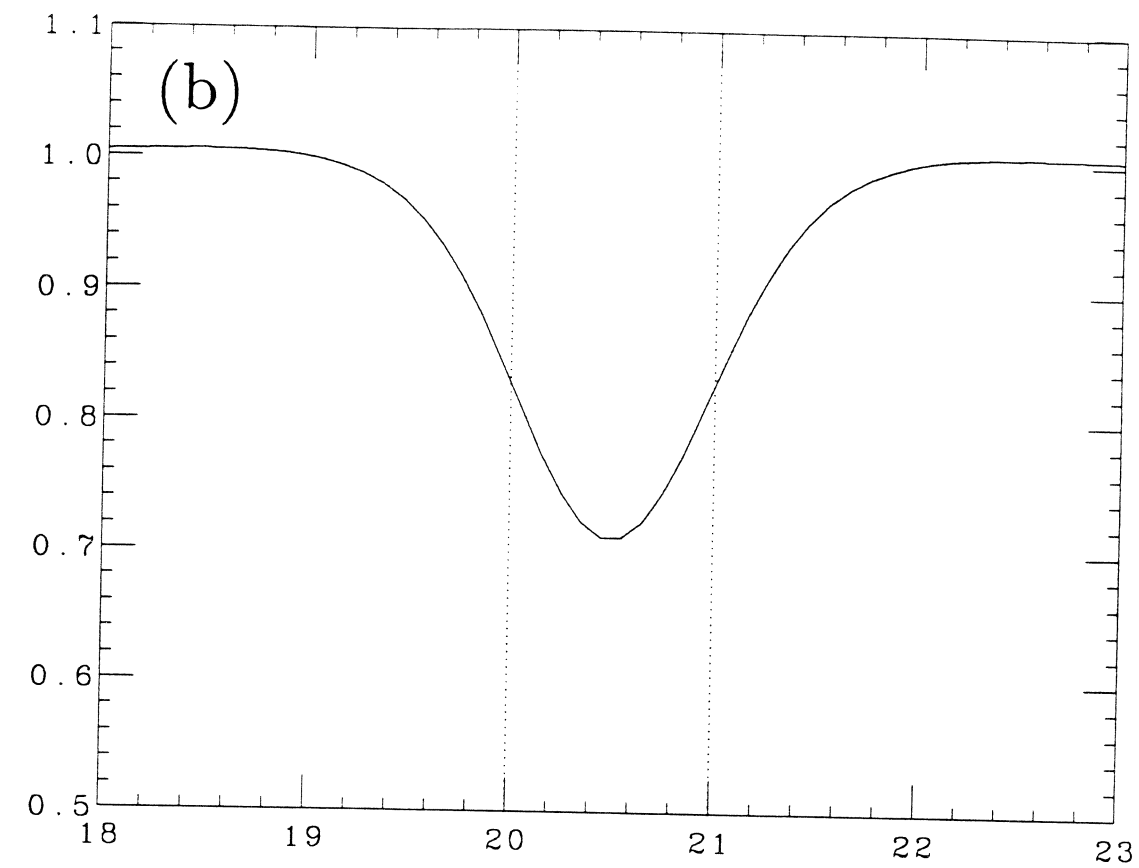


Figure 4

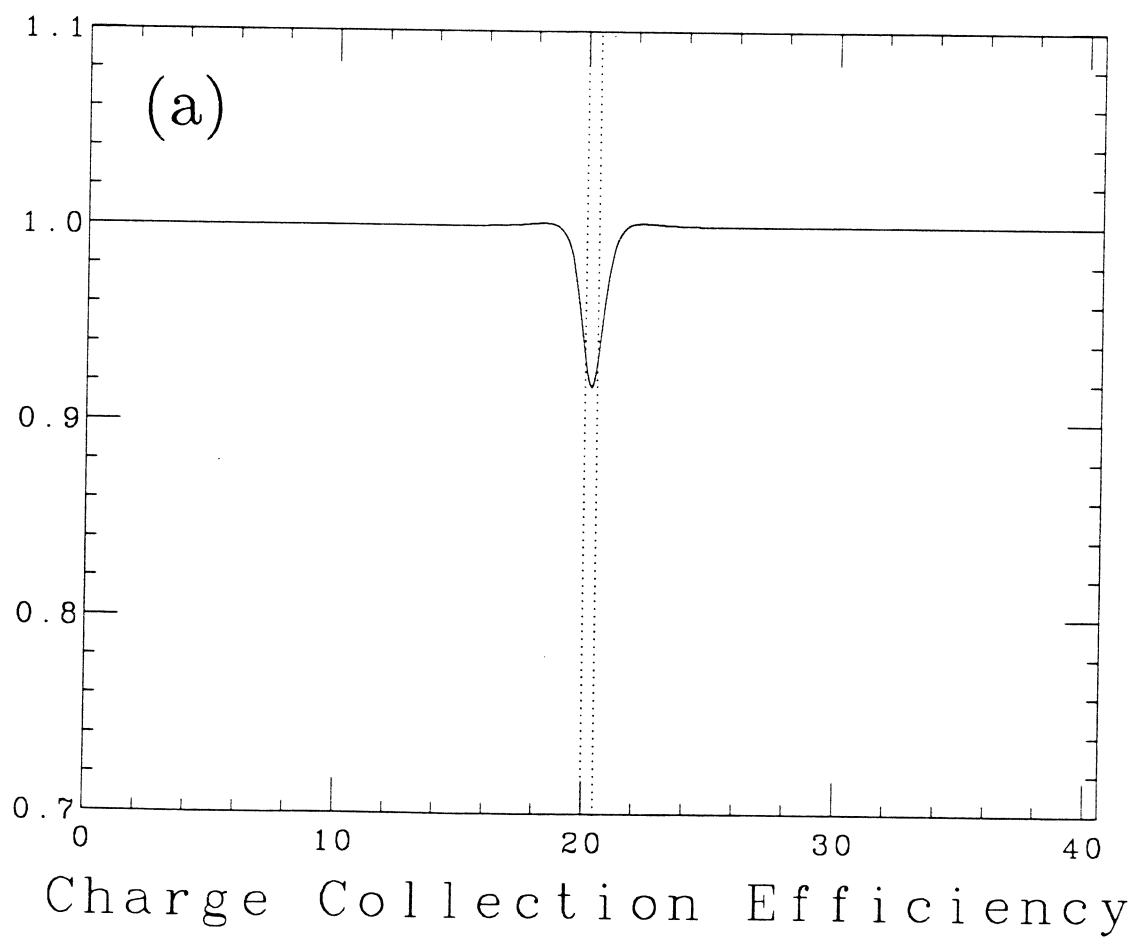
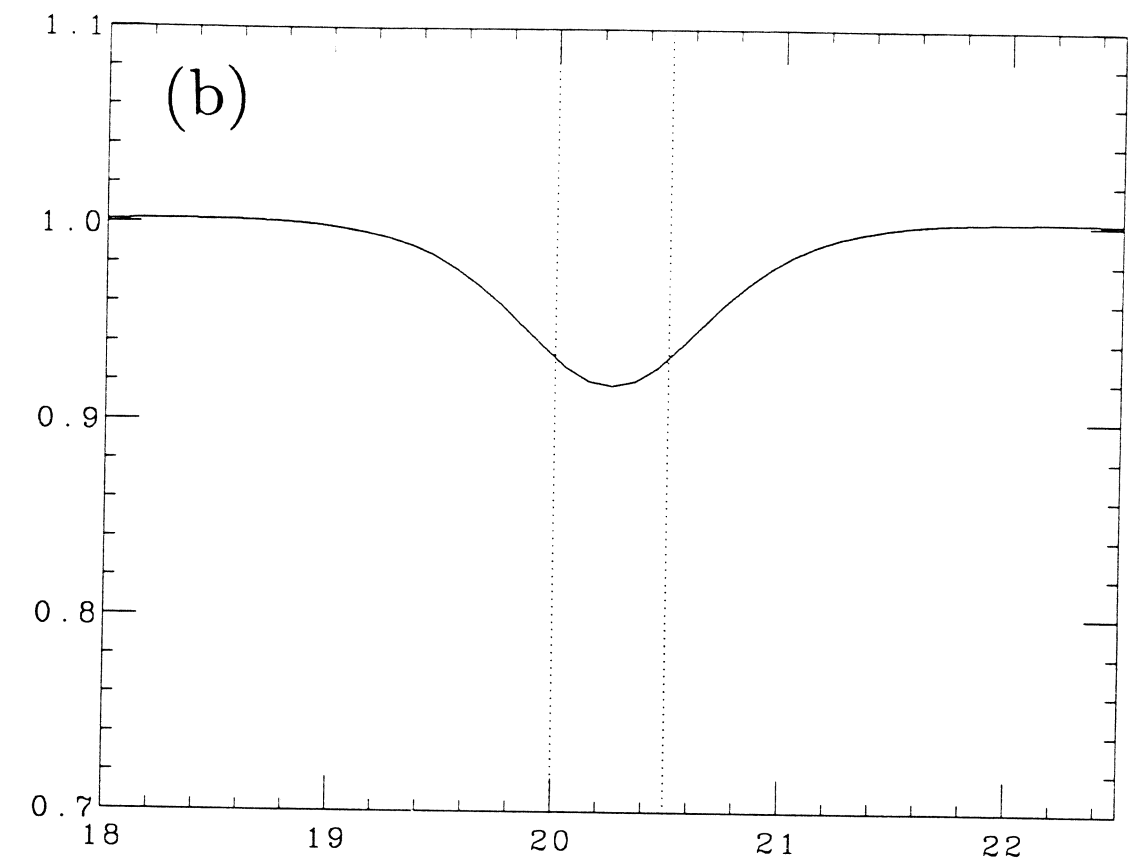


Figure 5

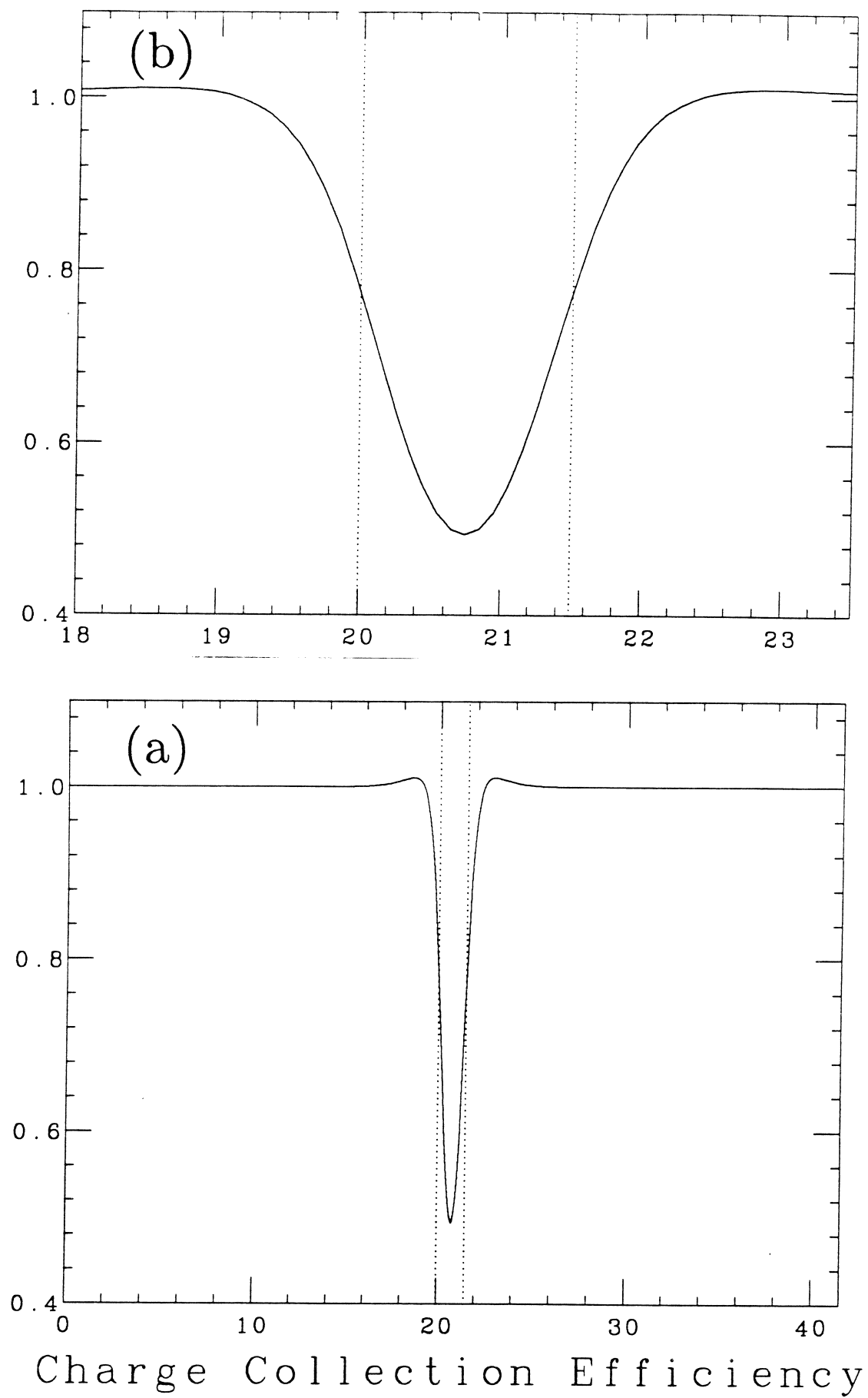


Figure 6

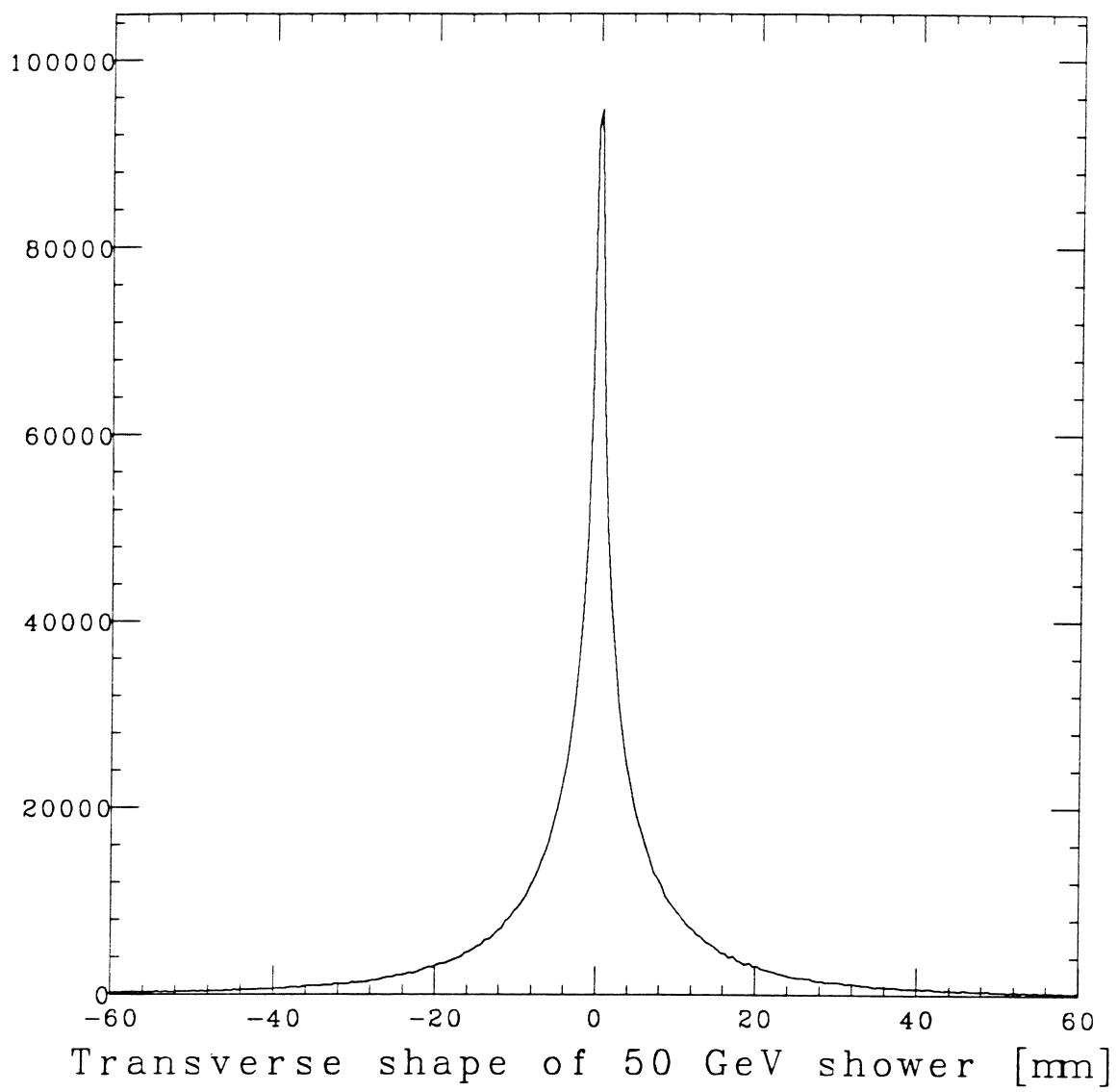


Figure 7



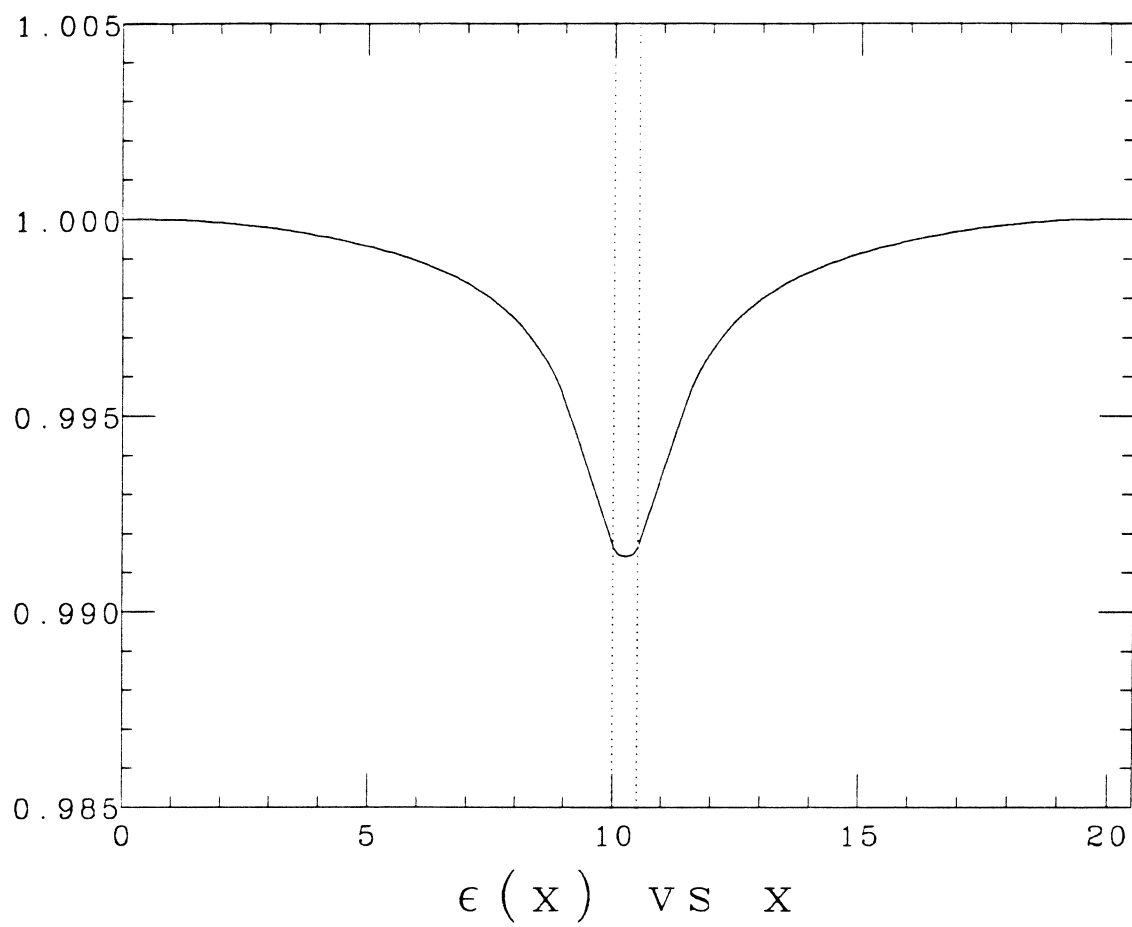


Figure 8

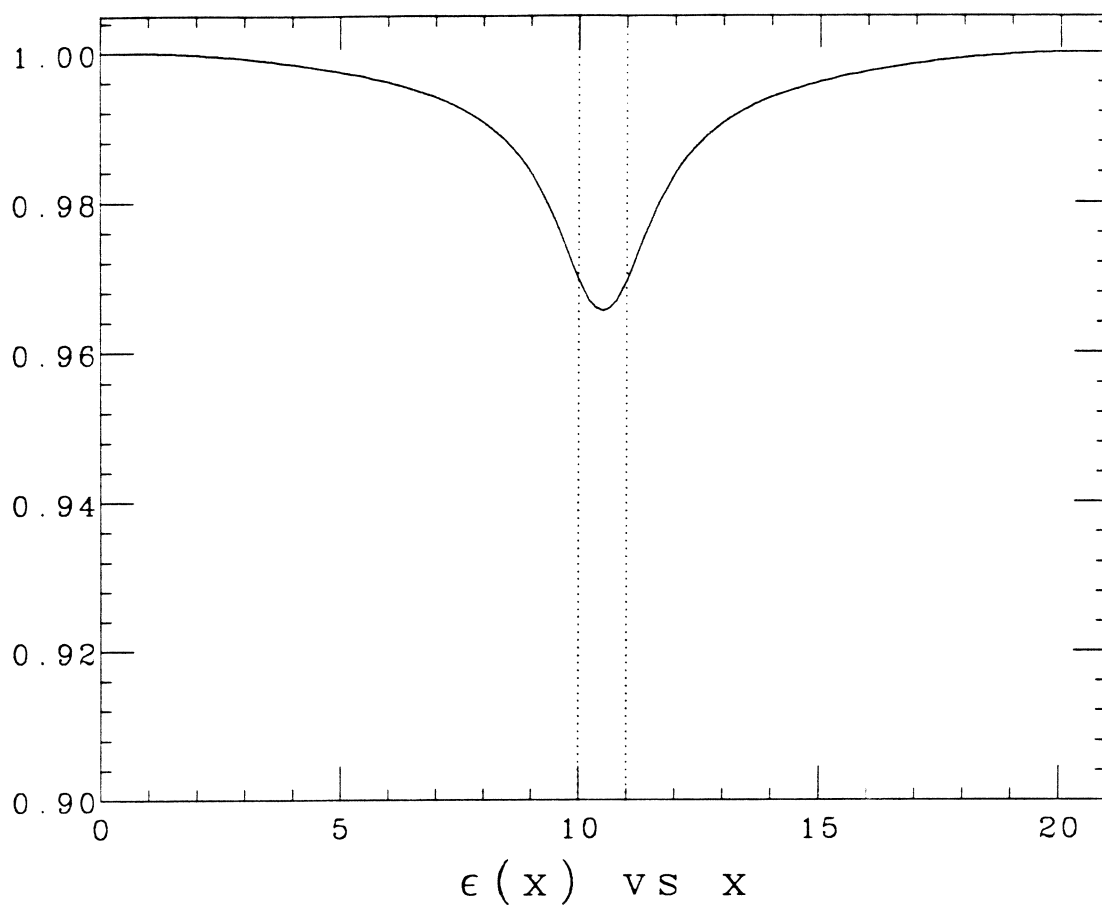


Figure 9

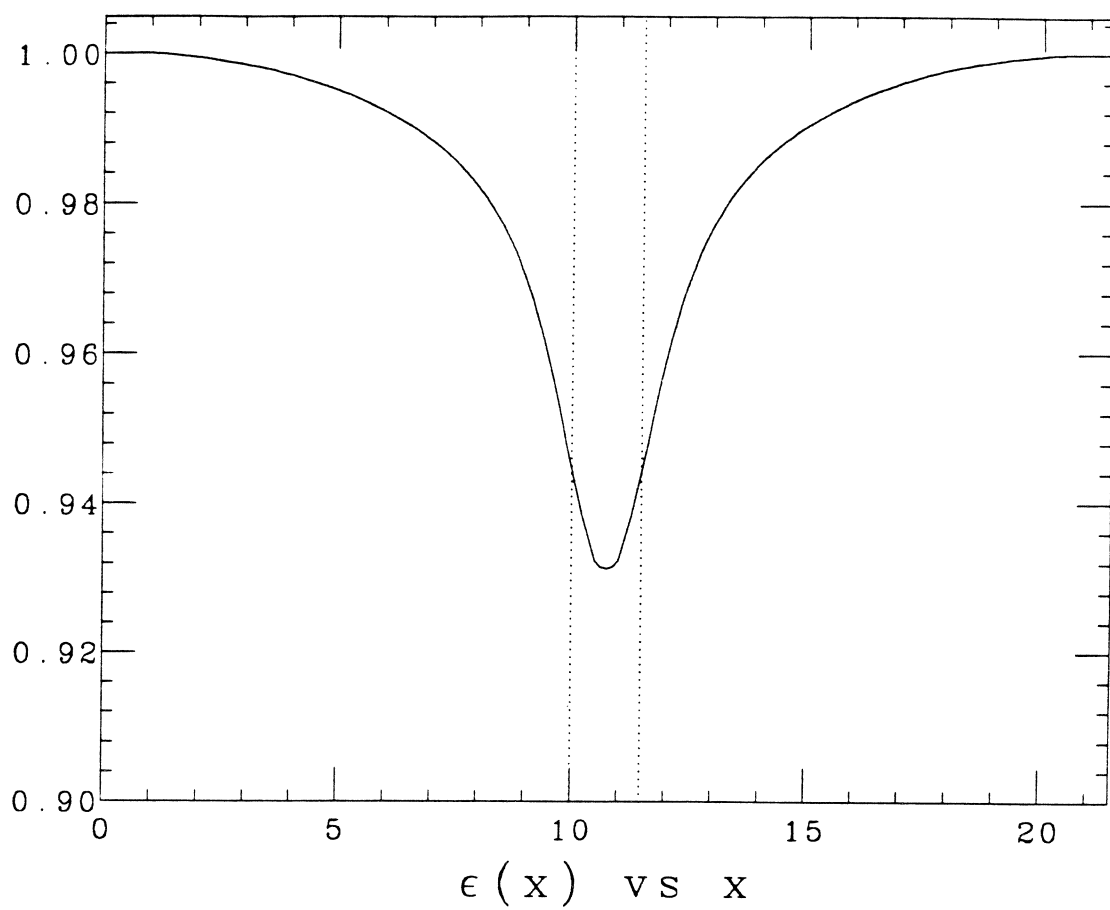


Figure 10

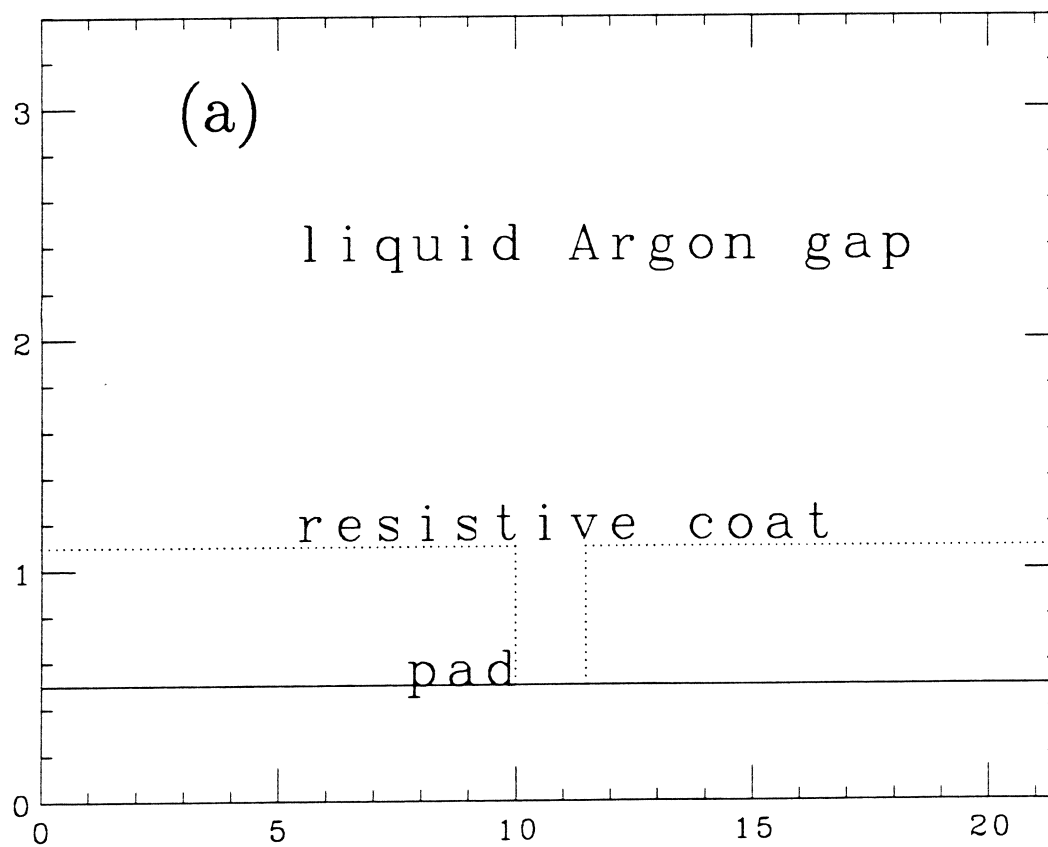
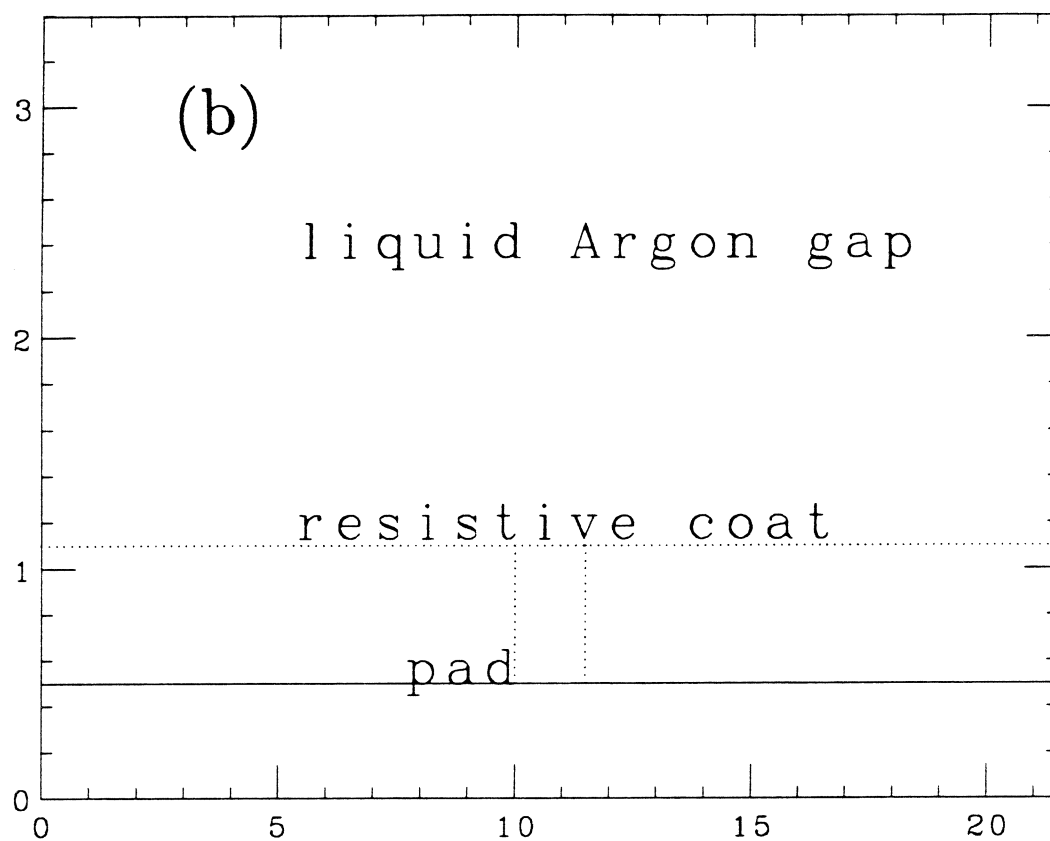
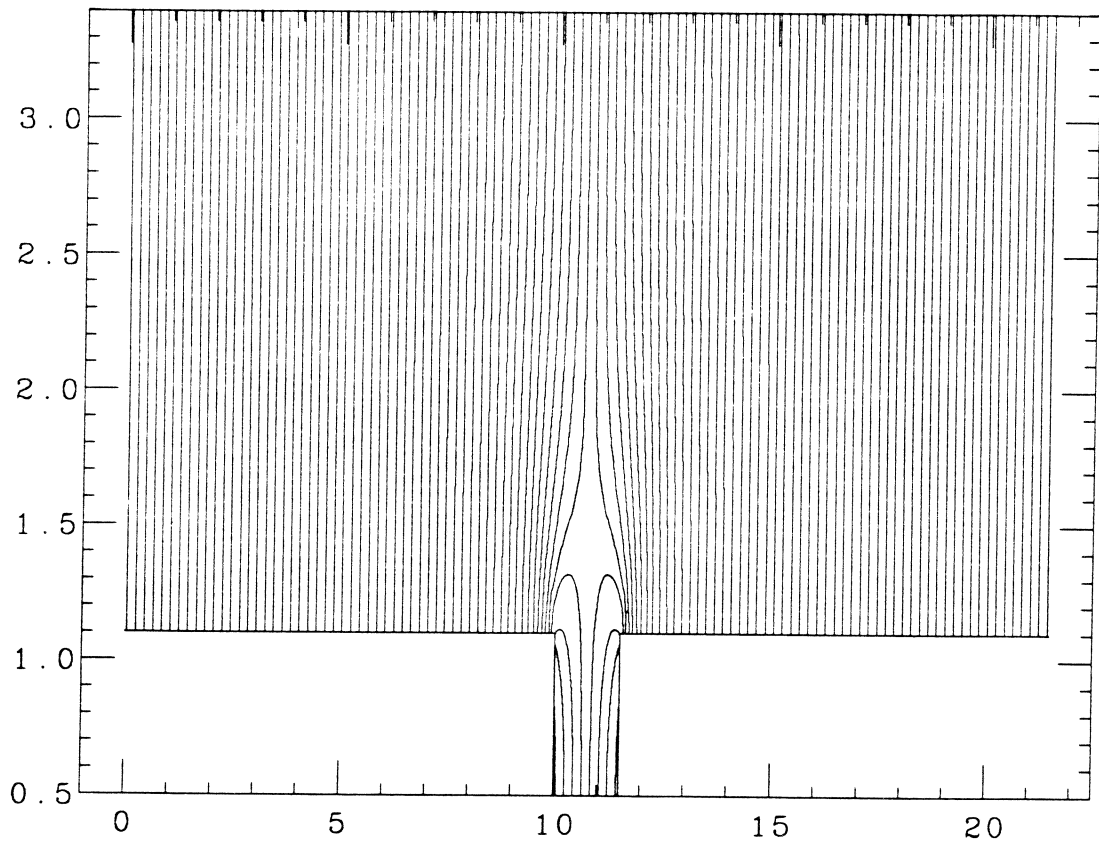
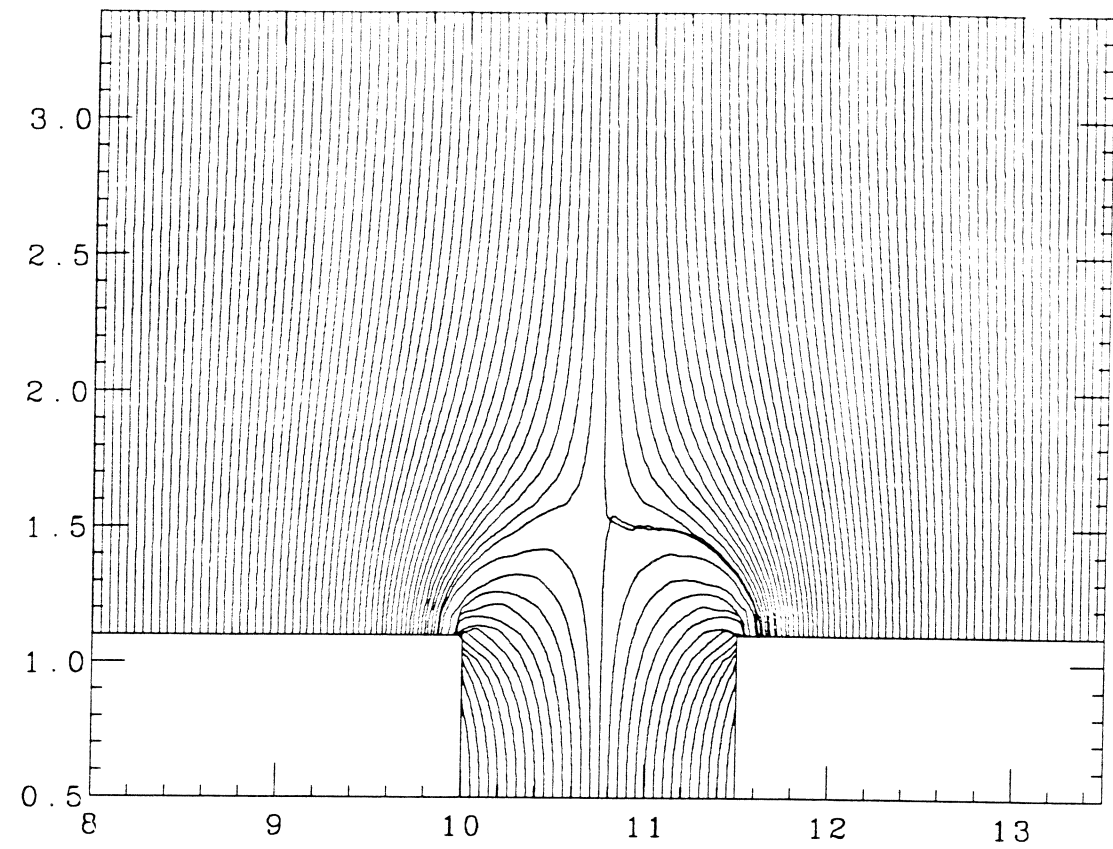


Figure 11



Drift field lines

Figure 12

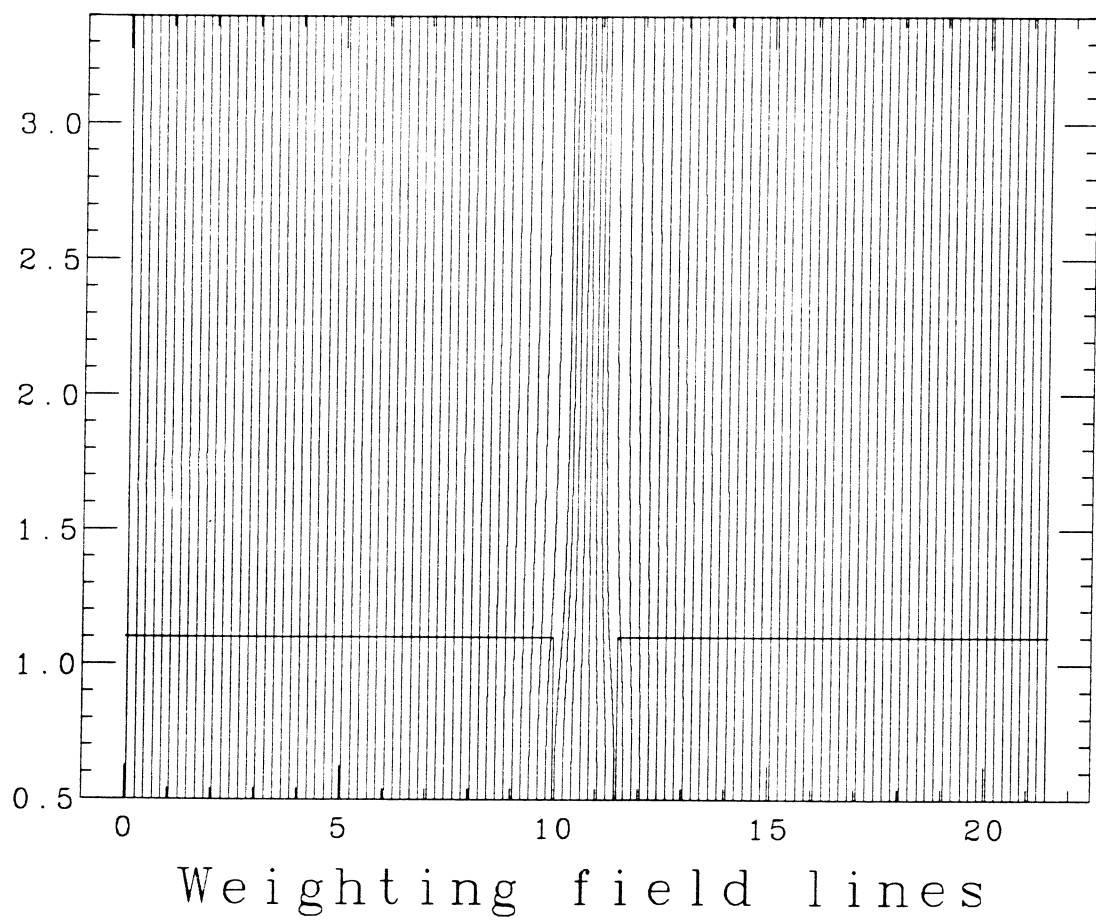
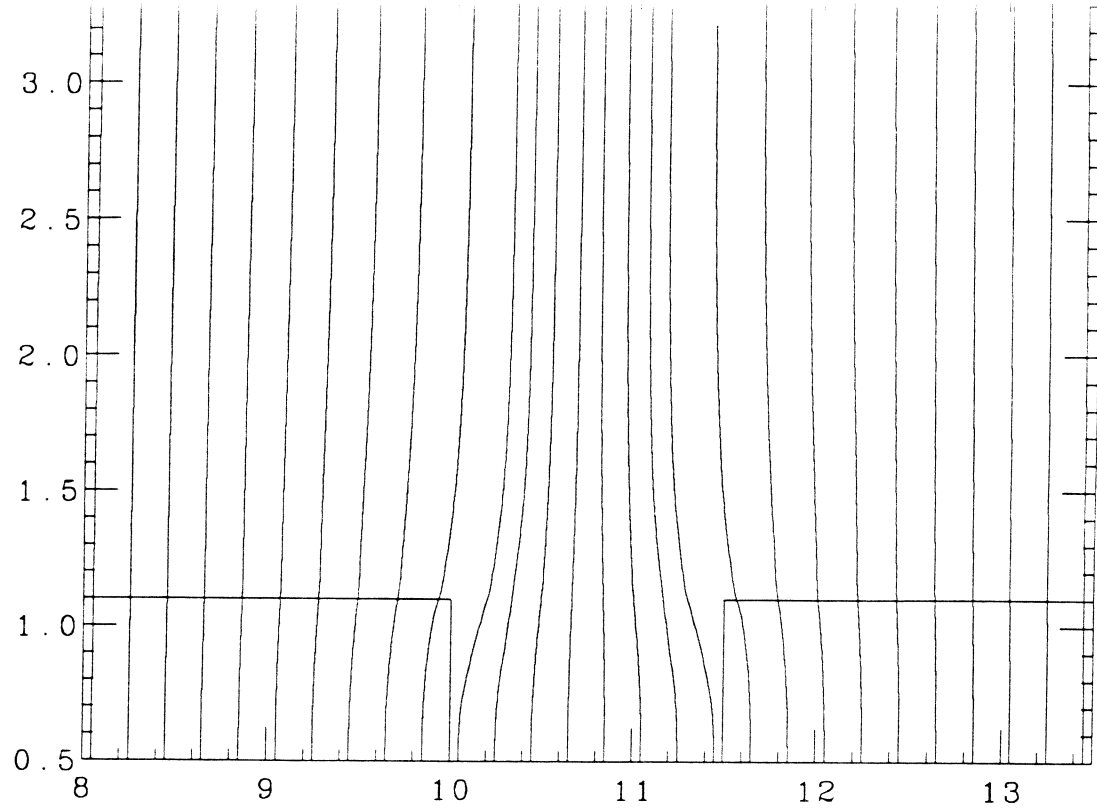


Figure 13

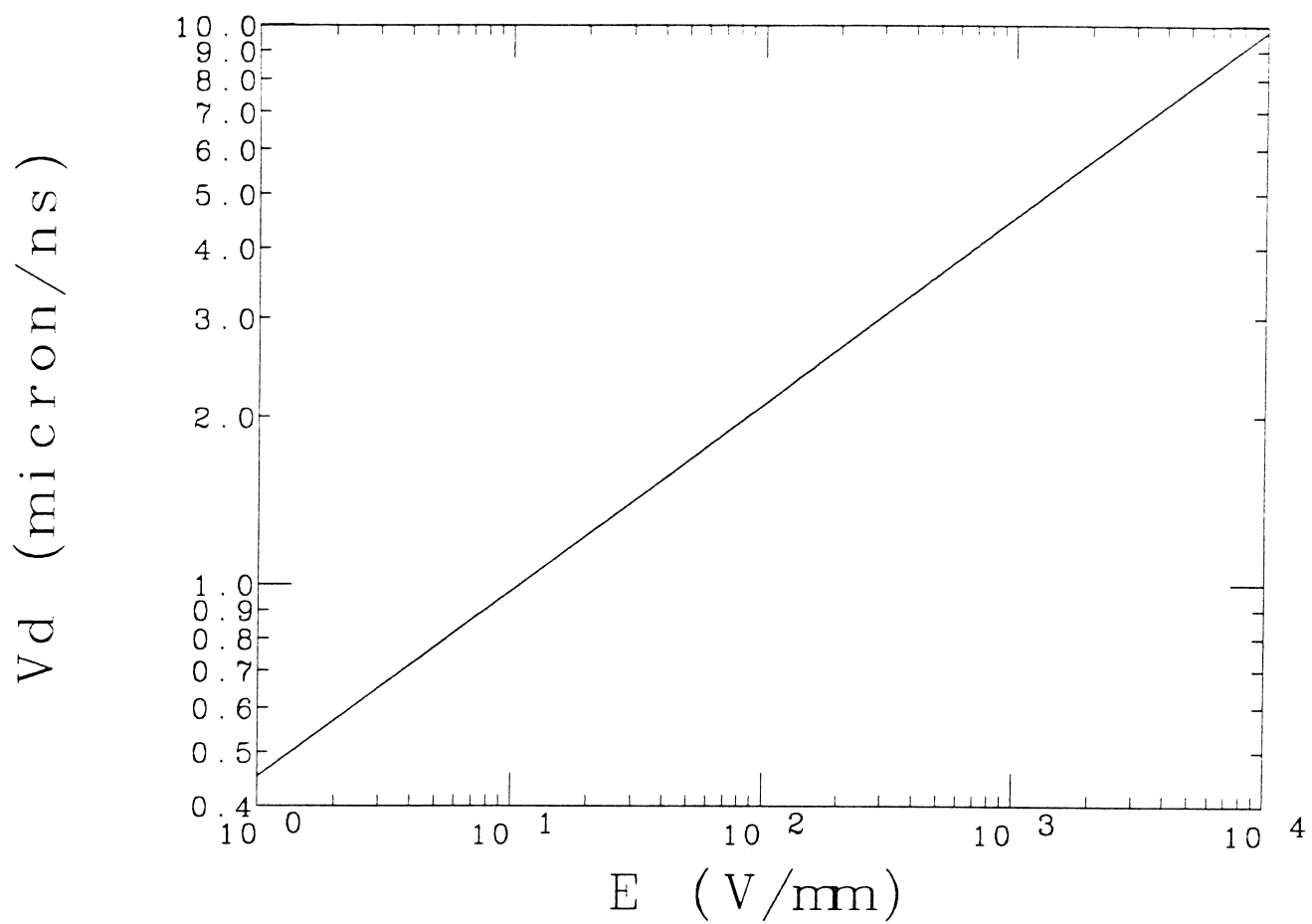
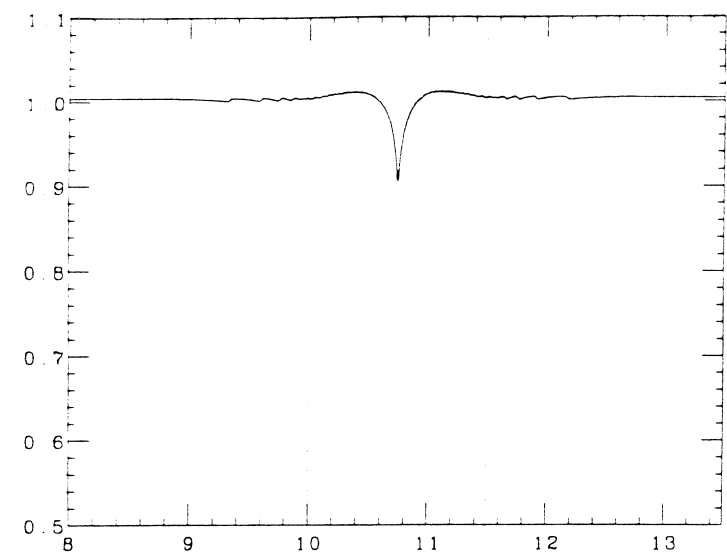
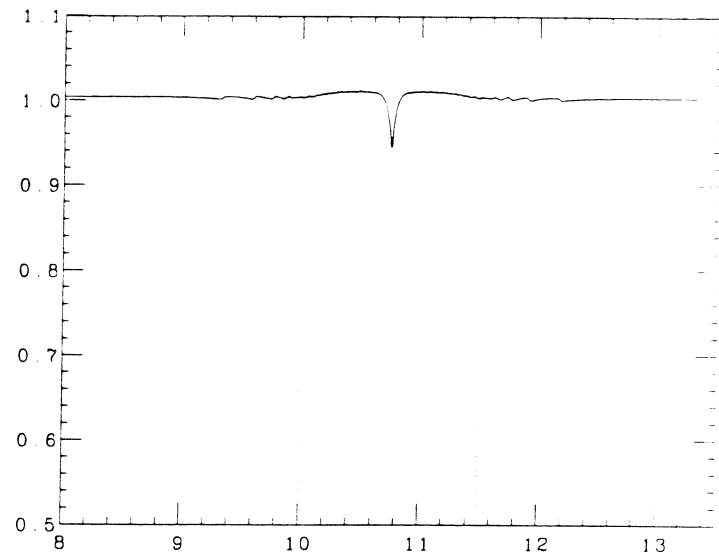


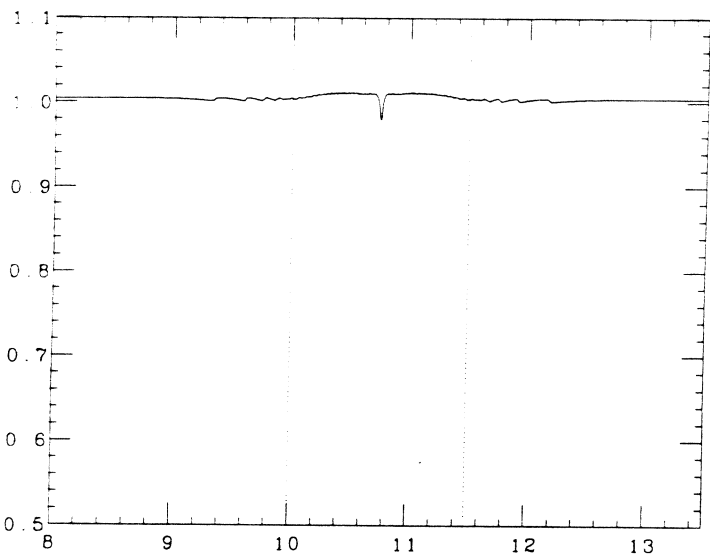
Figure 14



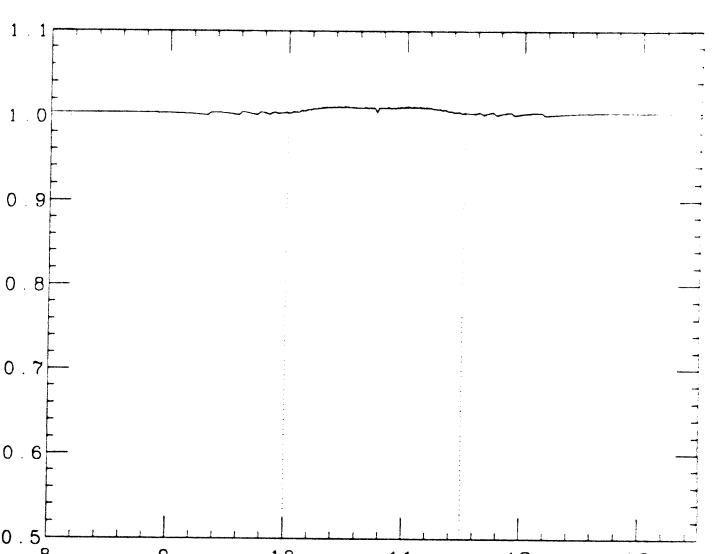
charge collection time = 550 ns



charge collection time = 600 ns



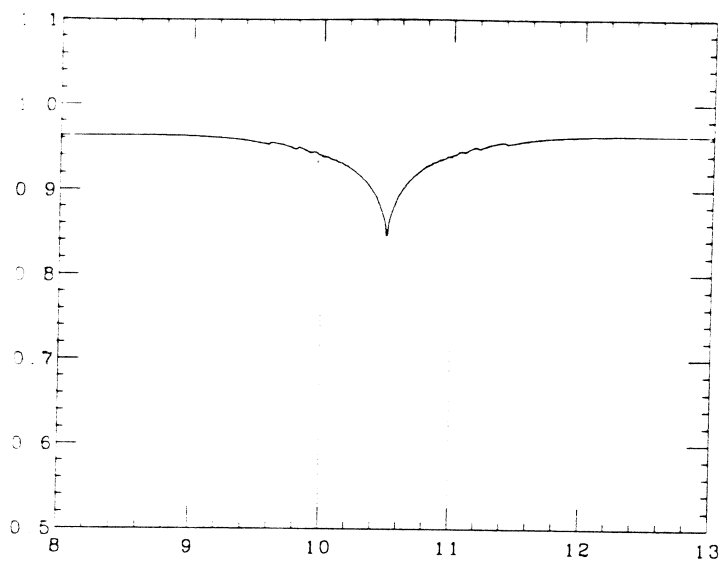
charge collection time = 650 ns



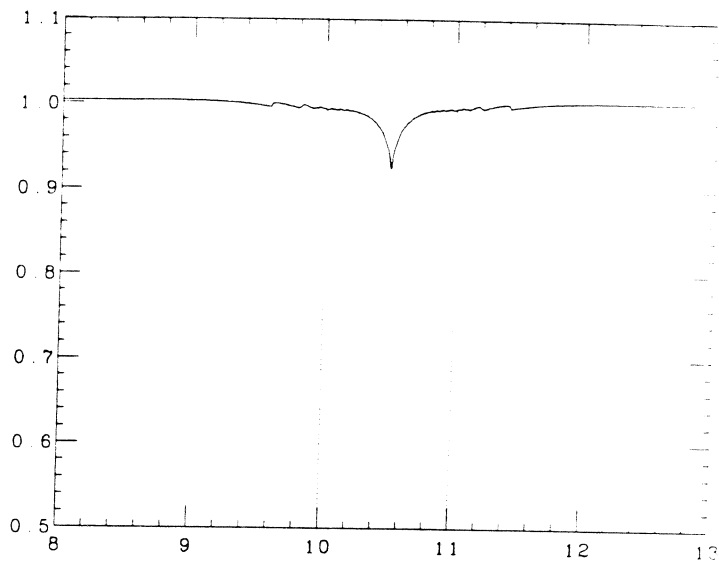
charge collection time = 700 ns

Figure 15

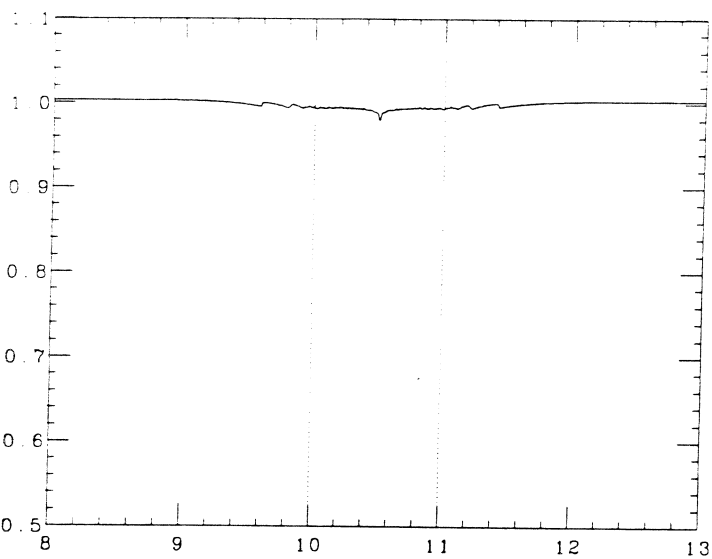




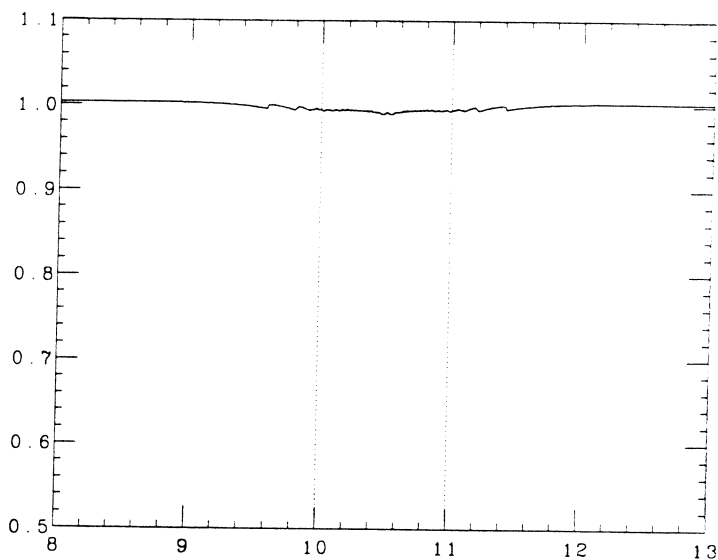
charge collection time = 400 ns



charge collection time = 500 ns



charge collection time = 600 ns



charge collection time = 700 ns

Figure 16

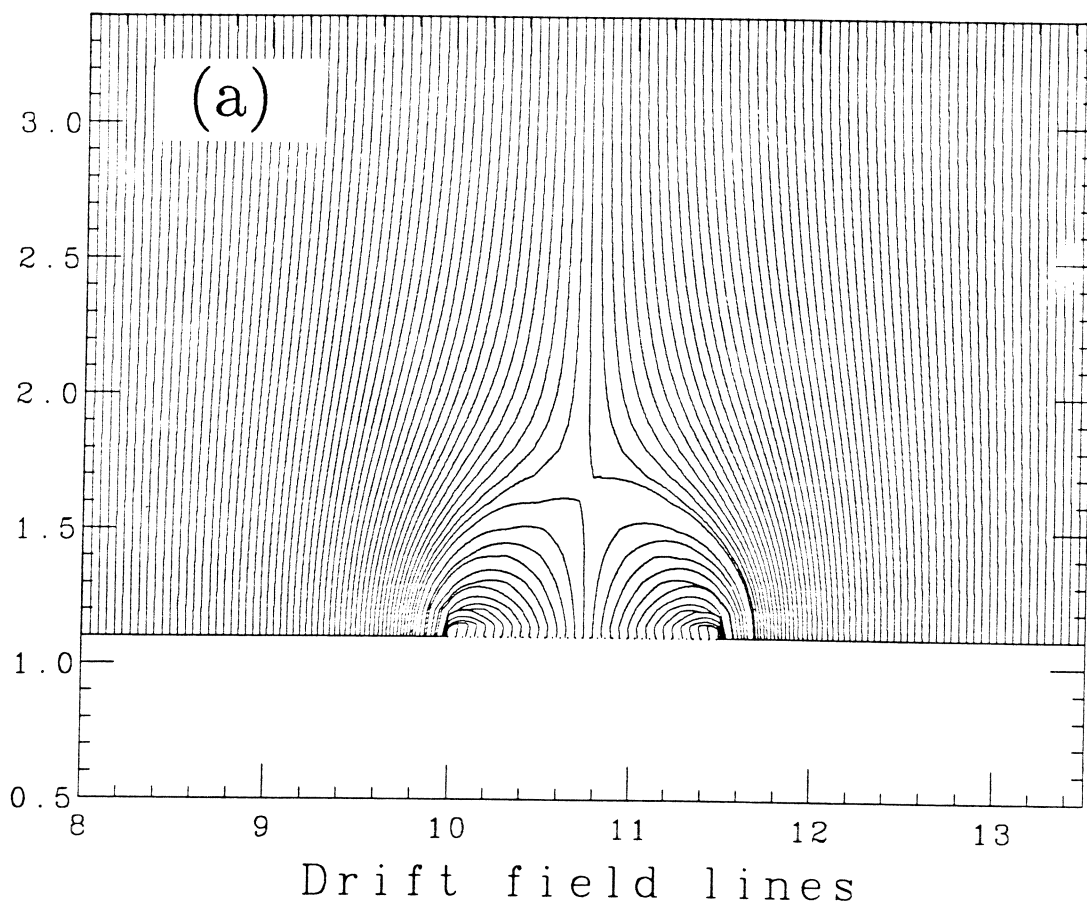
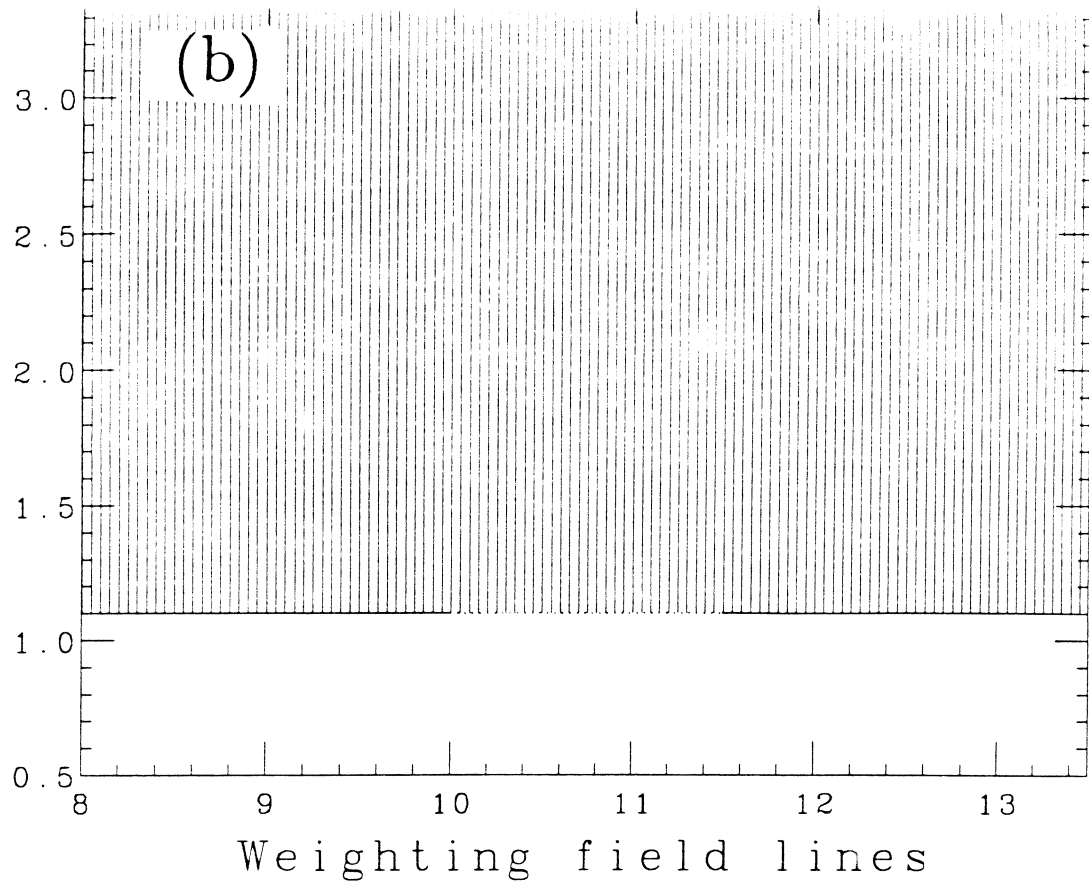


Figure 17

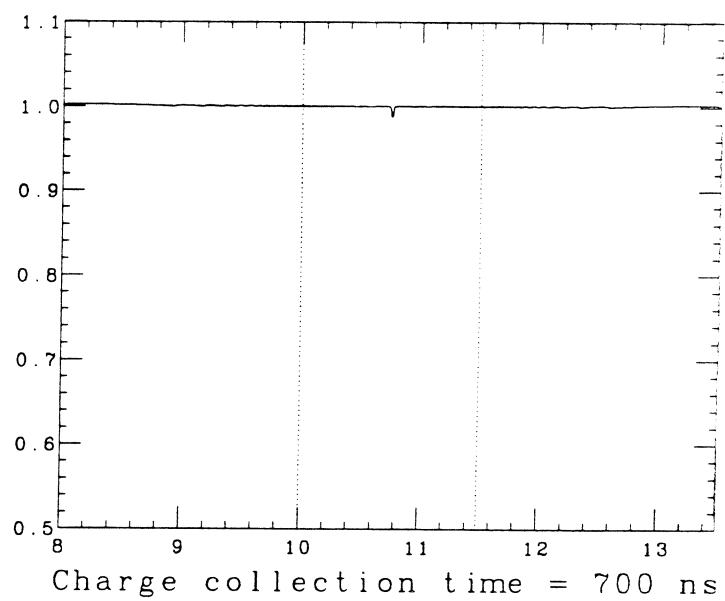
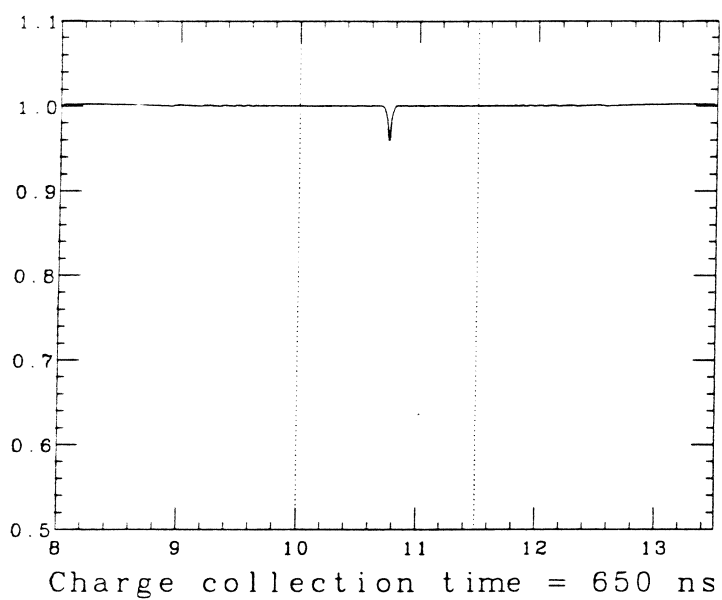
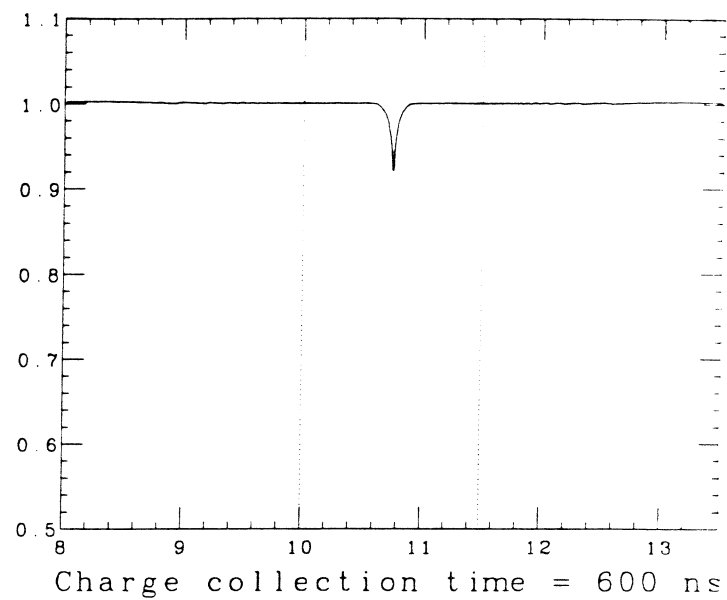
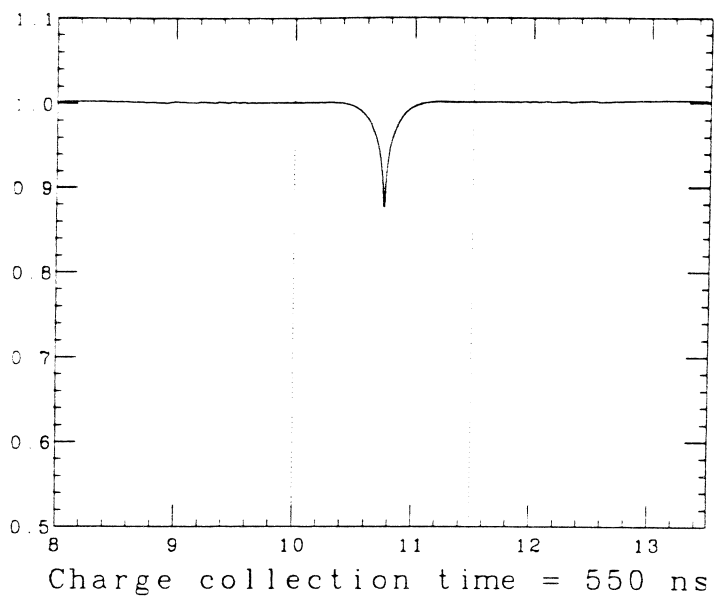


Figure 18

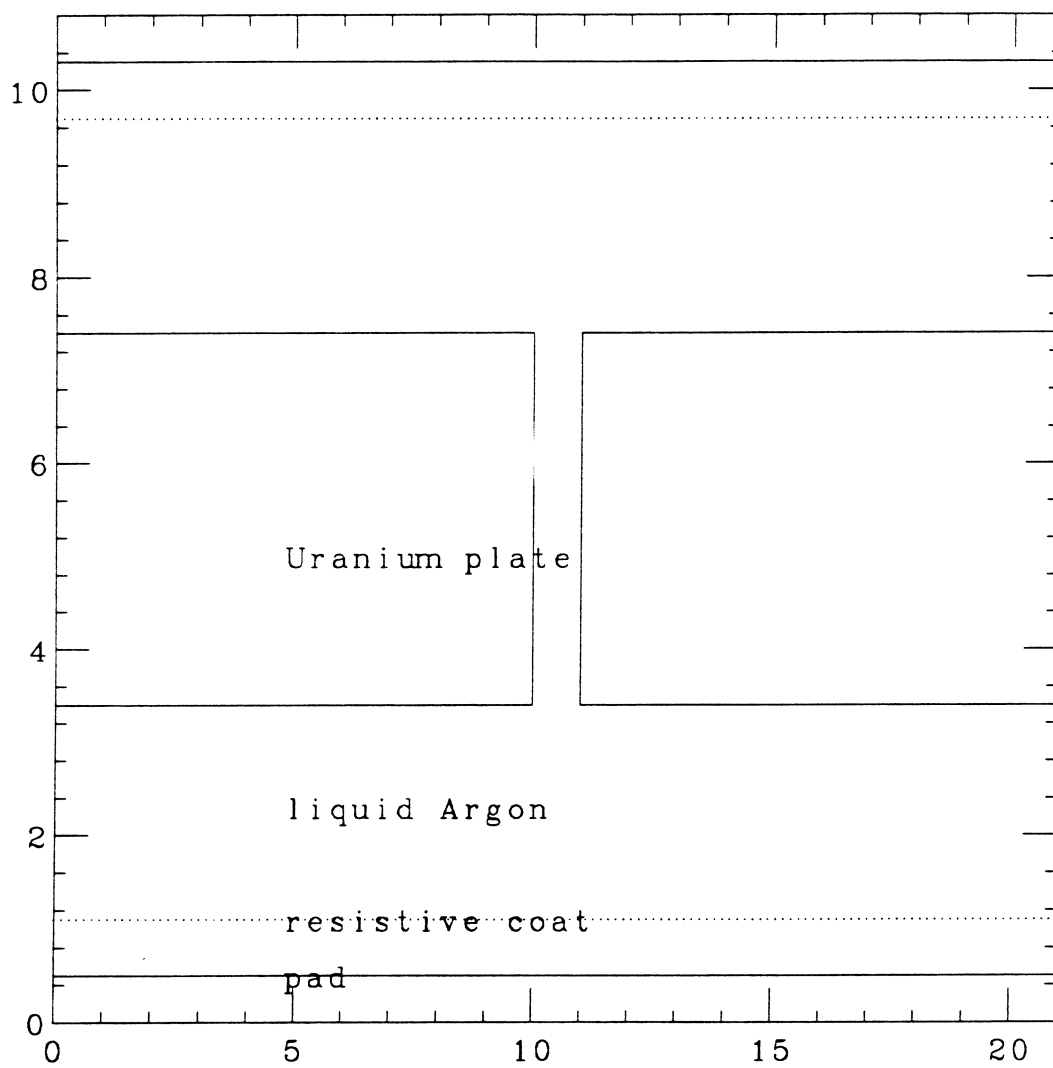


Figure 19

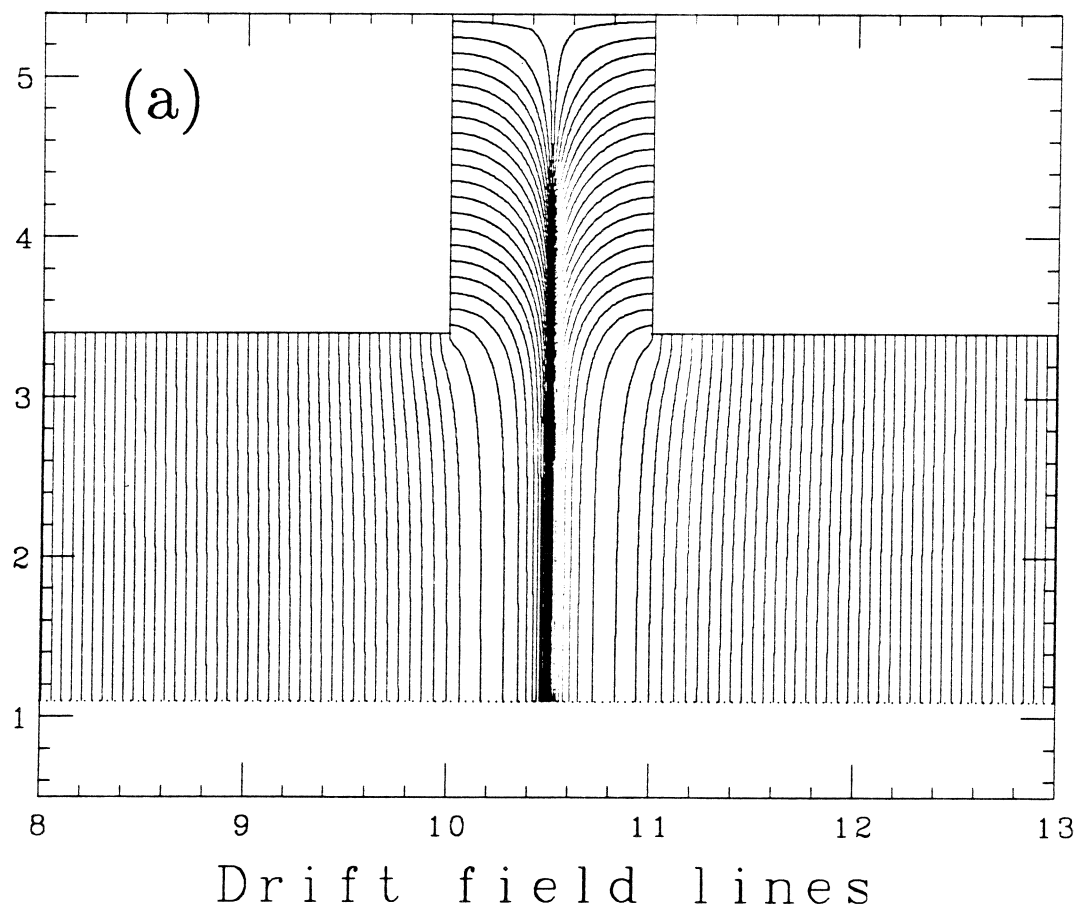
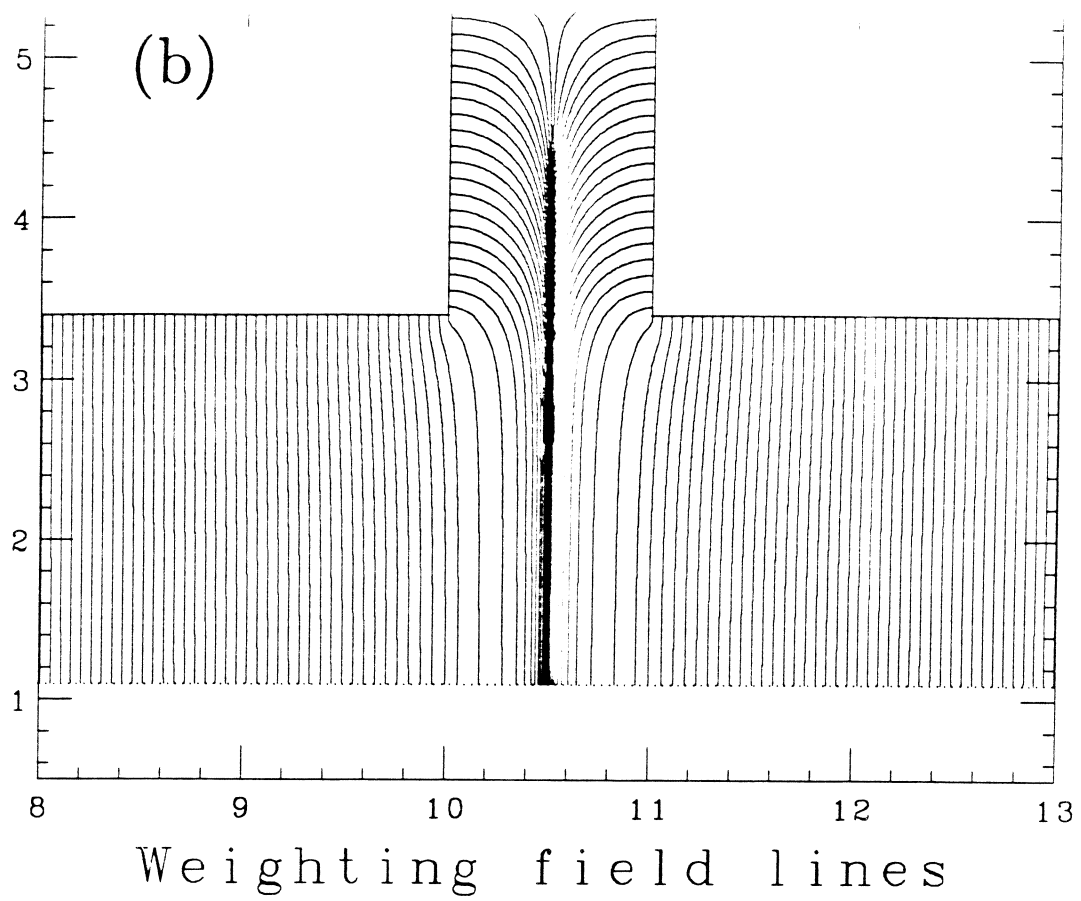


Figure 20

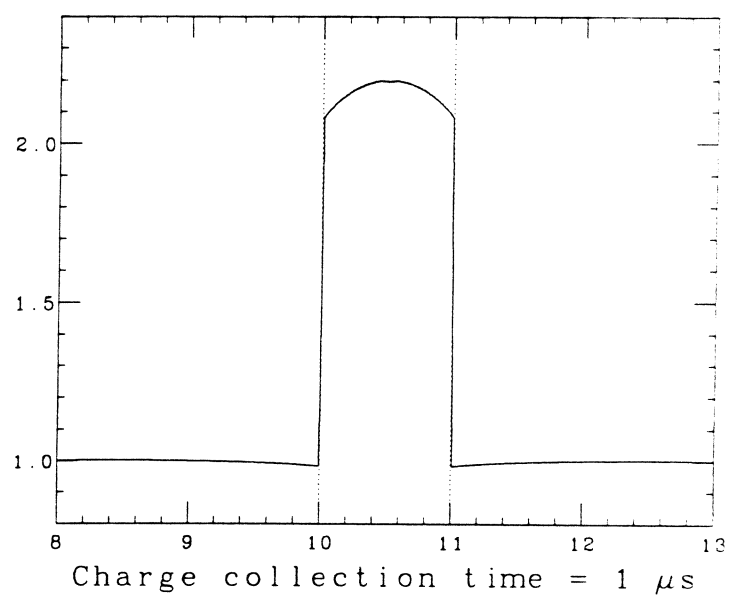
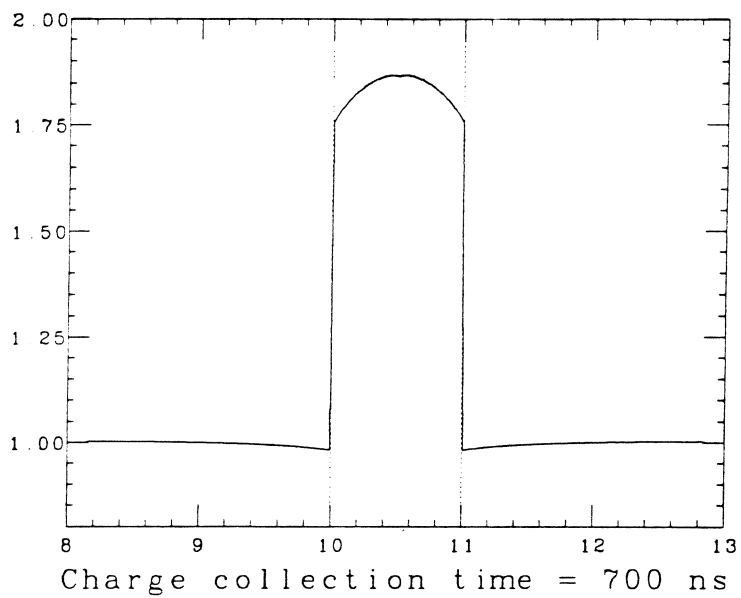
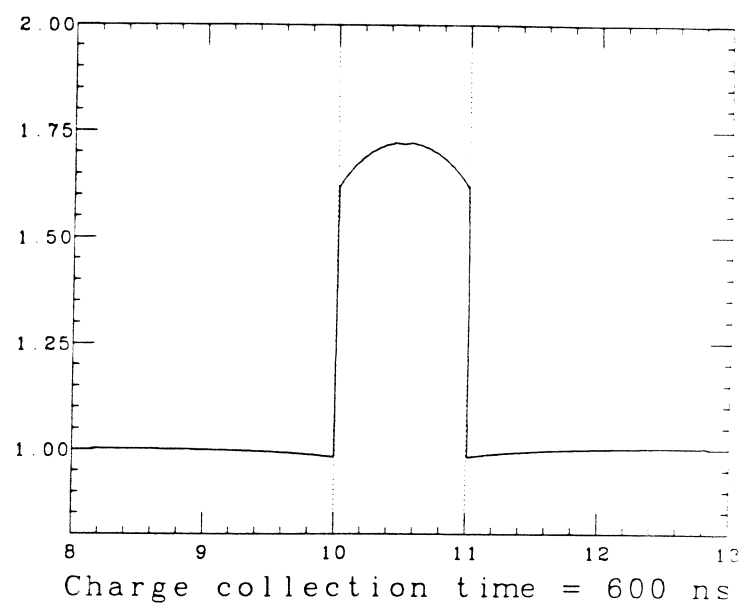
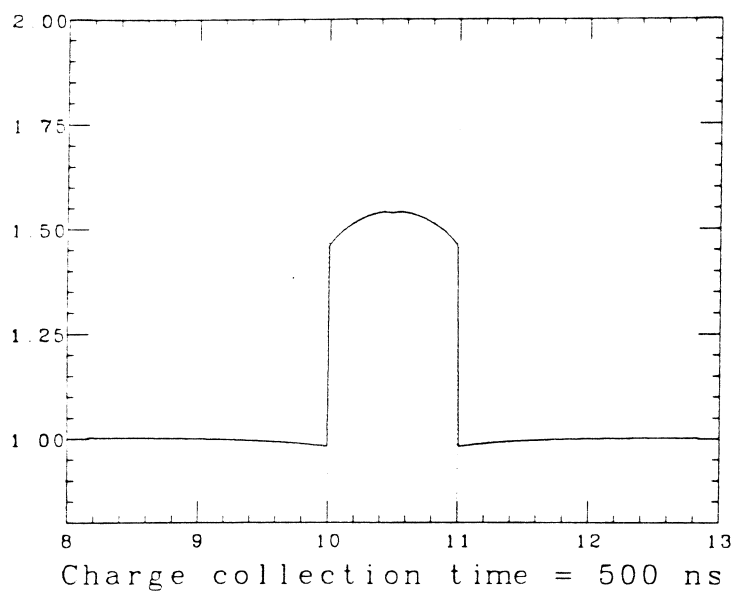


Figure 21

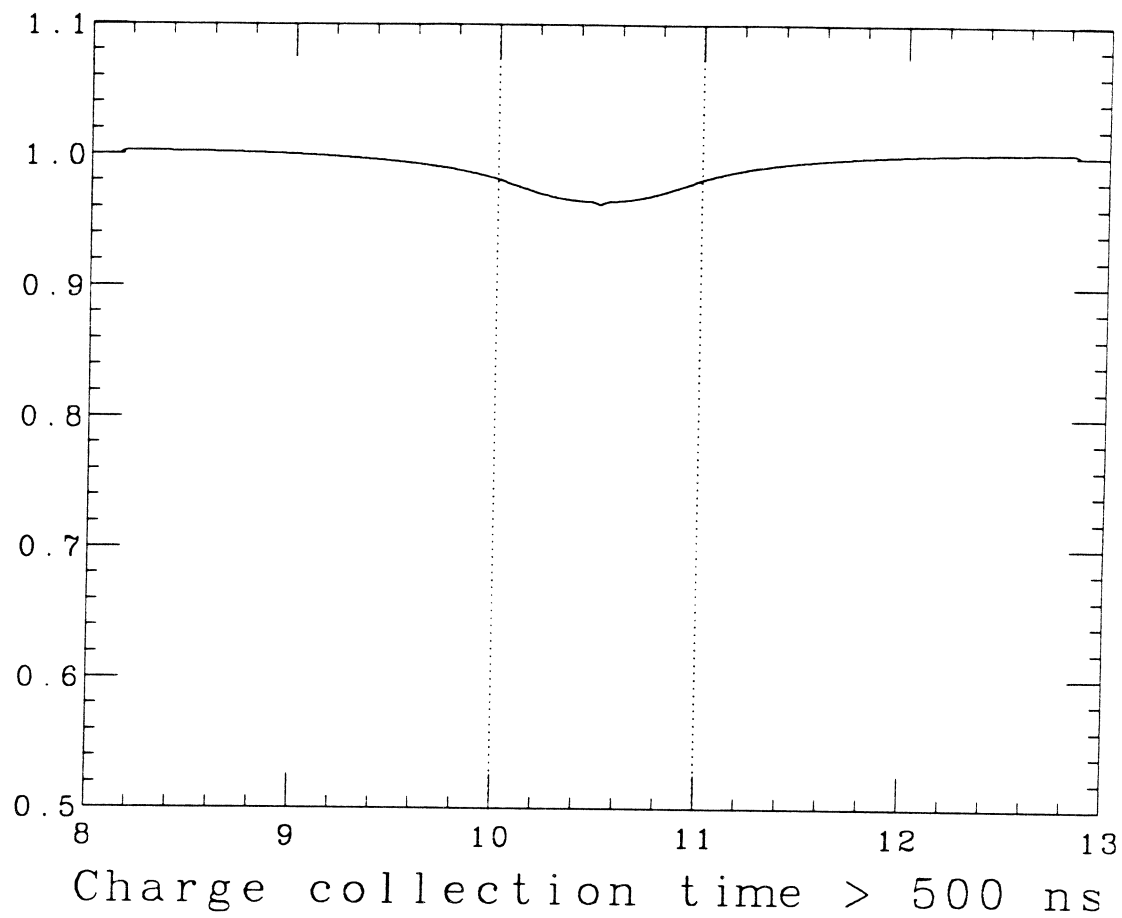


Figure 22

# Jet Energy Scale using Test Beam Data

Andy Milder

Rich Astur

December 15, 1992

## Abstract

The test beam single particle responses have been applied to various parton fragmentation schemes to derive an energy correction for jets in the central calorimeter. This correction accounts for particle responses that are significantly below 100% for low energy particles ( $< 10$  GeV.) A nominal jet energy scale is produced as well as an upper and lower limit based on the estimated test beam data errors.

## 1 Introduction

The jet energy scale is very important for almost every jet measurement and analysis made at D-zero. Errors in jet  $E_T$  result in amplified cross-section errors so that a premium is placed upon accuracy of the energy scale in order to do precision jet measurements or tests of QCD. As a rule of thumb, A 1% error in jet  $E_T$  corresponds to a 6% error in the single-jet inclusive cross



section.

The method described here is an attempt to use the test beam data to obtain a jet energy response that one can use to correct collider data. The test beam single particle responses were used to simulate the calorimeter response to a jet. A jet was generated using a given event generator Monte Carlo (either Pythia, Herwig, or ISAJET) and each particle's energy was multiplied by the appropriate test beam response and summed. The sum of response-altered particle energies divided by the sum of unaltered particle energies is the jet energy response. No detector simulations were used in this study.<sup>1</sup> This limits our ability to study several less important detector effects such as out-of-cone corrections and zero-suppression.

## 2 Method

### Test Beam data

The test beam data used in this note is shown in Figures 1 and 2<sup>2</sup>. The response is defined as the fraction of the incoming particle's energy which is measured by the calorimeter. The data at and below 10 GeV was obtained from a special low-energy beamline setup. The responses shown are from the benchmark point of  $\eta = 0.05$ ,  $\phi = 31.6$ .

---

<sup>1</sup>D0Geant was not used in this study.

<sup>2</sup>Data courtesy Bob Hirosky, Pushpa Bhat.

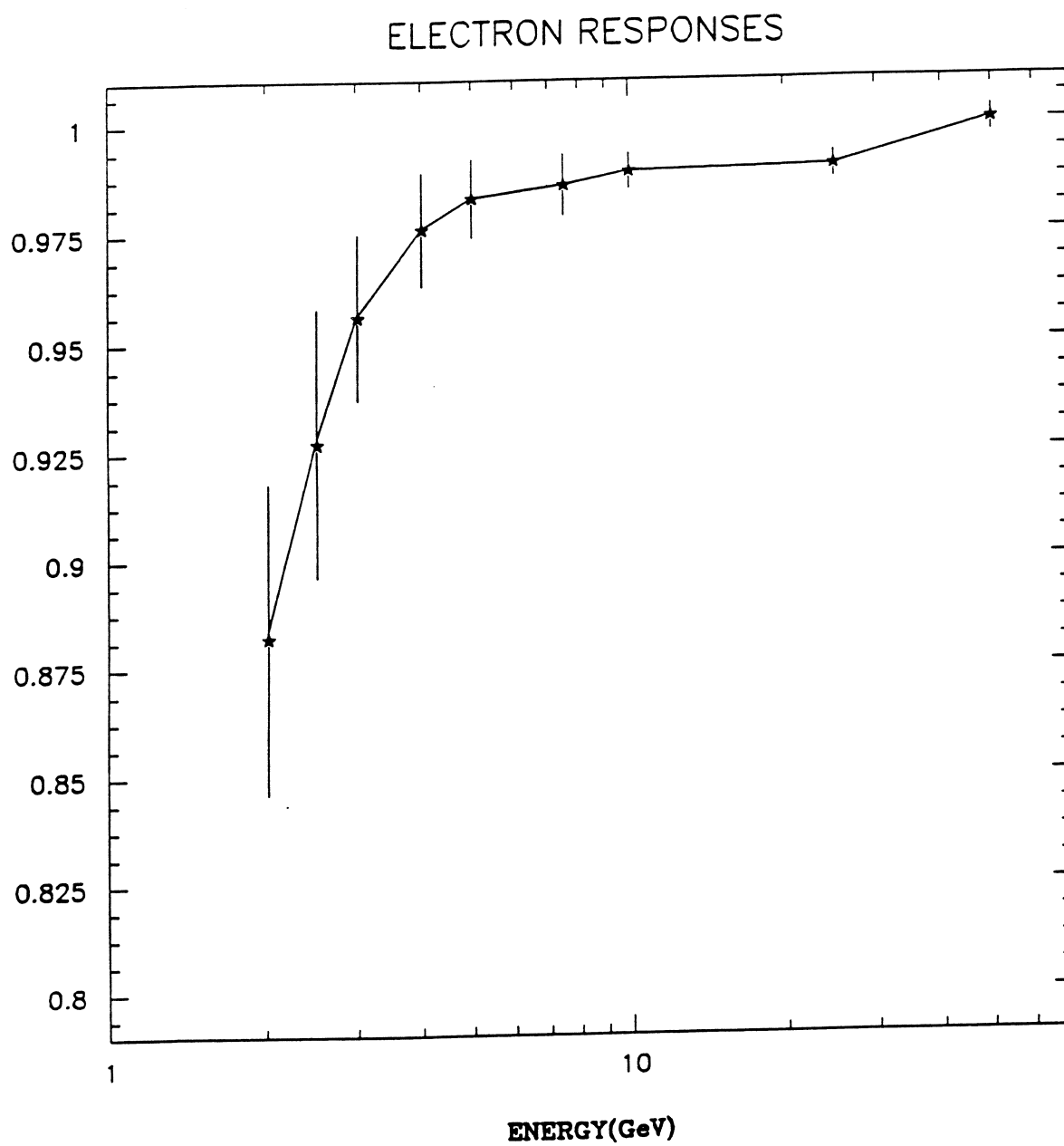


Figure 1: Test beam responses for electrons.

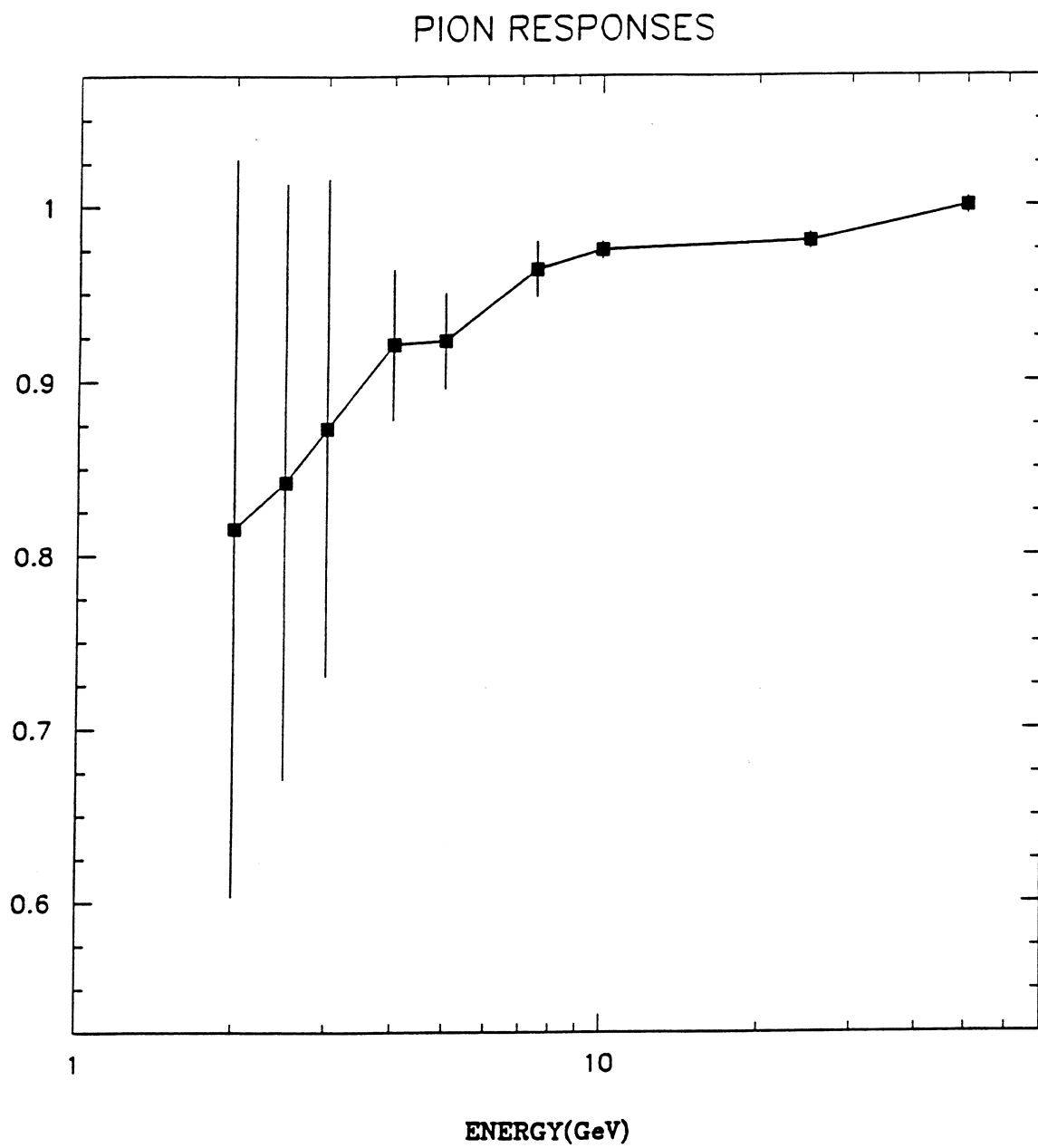


Figure 2: Test beam responses for pions.

The pion response drops a great deal at low energies, and this is the dominating effect when considering the jet energy scale. The shape of the jet energy scale depends mostly on the shape of the pion response curve and, to a lesser extent, the shape of the electron response curve (assuming a given jet fragmentation.)

Since there is no test beam data below 2 GeV, a (somewhat arbitrary) choice was made to use the 2 GeV point for all particle energies below 2 GeV. In effect, the response was chosen to be constant below 2 GeV. This was done for both pions and electrons and the ramifications of this choice are explored in section 3.

The detector response is not uniform in  $\phi$  due to the segmentation into 32 CCEM modules and 16 CCFH modules. Since the test beam responses used here were taken at a value of  $\phi$  away from these module/module cracks, a further correction must be applied in order to make the simulation more realistic. CCEM  $\phi$  crack effects were simulated using data from 25 GeV electrons at  $\eta = 0.025$ <sup>3</sup>. The data in Figure 3 shows the drop in response at the location of the  $\phi$  crack itself (dead material) as well as the increase in response nearby due to a gaps between absorber plates and the module wall. These effects average out and the result is a negligible difference in jet response when the CCEM  $\phi$  crack is included.

Cracks also exist between CCFH modules and effect hadronic response adversely. Data from 25 GeV pions near the CCFH  $\phi$  cracks is shown in

---

<sup>3</sup>Data from Welanthantri Dharmaratna.

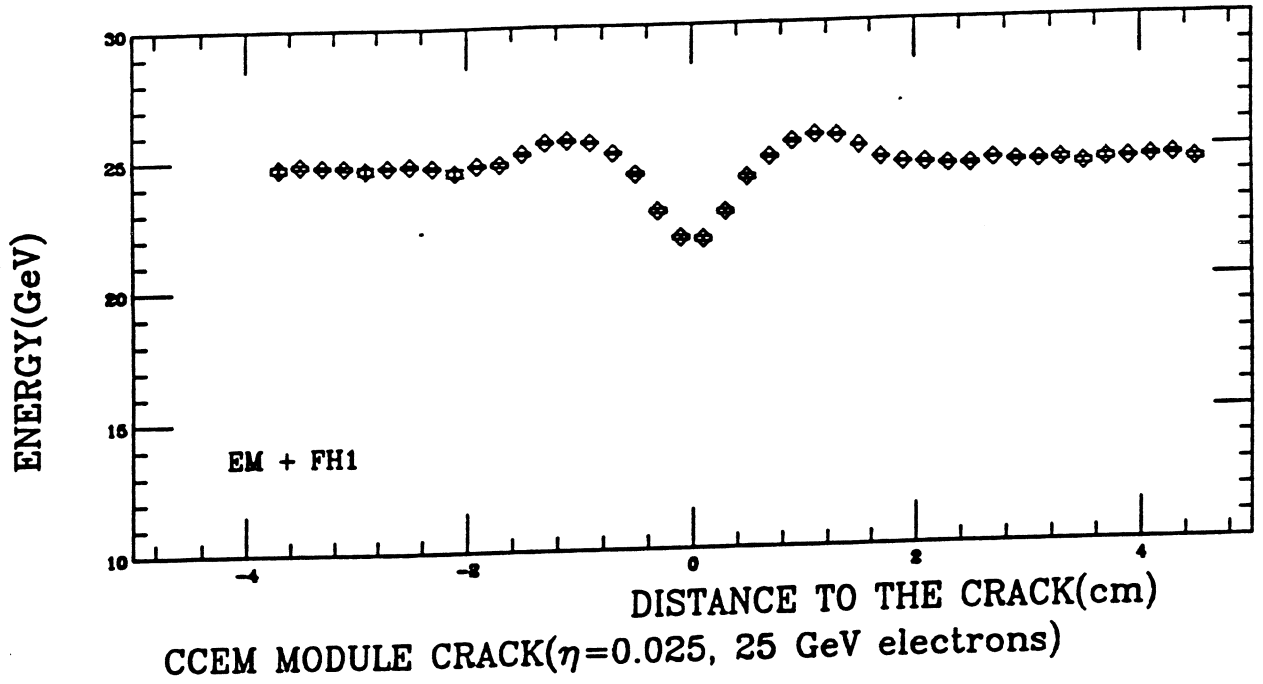


Figure 3: Response for 25 GeV electrons near a CCEM  $\phi$  crack.

Figure 4<sup>4</sup>. Using this data to simulate the effects of the cracks on hadronic response results in about a 1% decrease in the jet response. Pions in the test beam were seen to be insensitive to CCEM cracks and likewise electron response was independent of CCFH crack position.

## Event Generator Monte Carlo data

The jet simulation was accomplished using one of three event generators; Pythia, Herwig, or ISAJET. The Pythia jets do not include underlying event or initial state radiation while the Herwig and ISAJET results do. The use of three different event generators allows one to estimate the size of the errors

<sup>4</sup>Data from Welanthantri Dharmaratna.

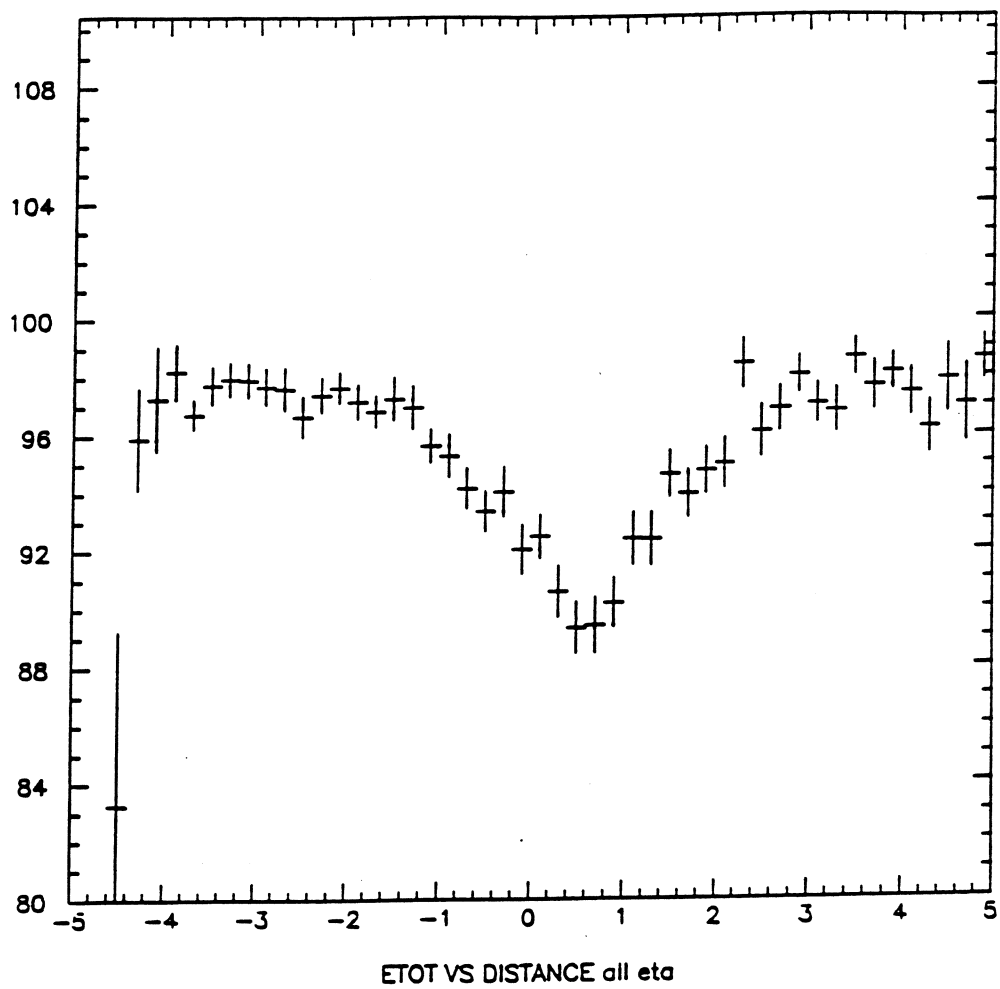


Figure 4: Response for 25 GeV pions near a CCFH  $\phi$  crack.

due to uncertainties in jet fragmentation and hadronization.

Jets were defined using the PJET jet finder which simply forms an energy-weighted  $\eta, \phi$  centroid from the particles inside a cone of a given radius. Iterations are made using the new centroid until a stable solution is obtained. A cone size of .7 was used. Also, the jets were required to be free of overlap with other jets found in the same event in order to minimize algorithm dependent biases.

Figures 5 and 6 show the particle energy composition of 50 GeV and 150 GeV jets, respectively. Electromagnetic and hadronic contributions from Pythia-produced jets are shown separately. The Figures show the importance of low energy responses; for 50 GeV jets, 67% of the total jet energy comes from particles with energies below 5 GeV. Even for 150 GeV jets this percentage is still substantial at 40%

## Jet Energy Scale Derivation

To generate a jet energy scale the particles in the jet cone were multiplied by the test beam response according to particle type. Electrons and photons were multiplied by the response from electrons at the test beam. In order to make the simulation more accurate,  $\pi^0$ 's and  $\eta^0$ 's were treated as if they decayed into two photons, each with half the energy of the original particle. All other particles were considered to be hadronic and were multiplied by the response from pions at the test beam. Since at the test beam the responses

## 50 GeV JET COMPOSITION

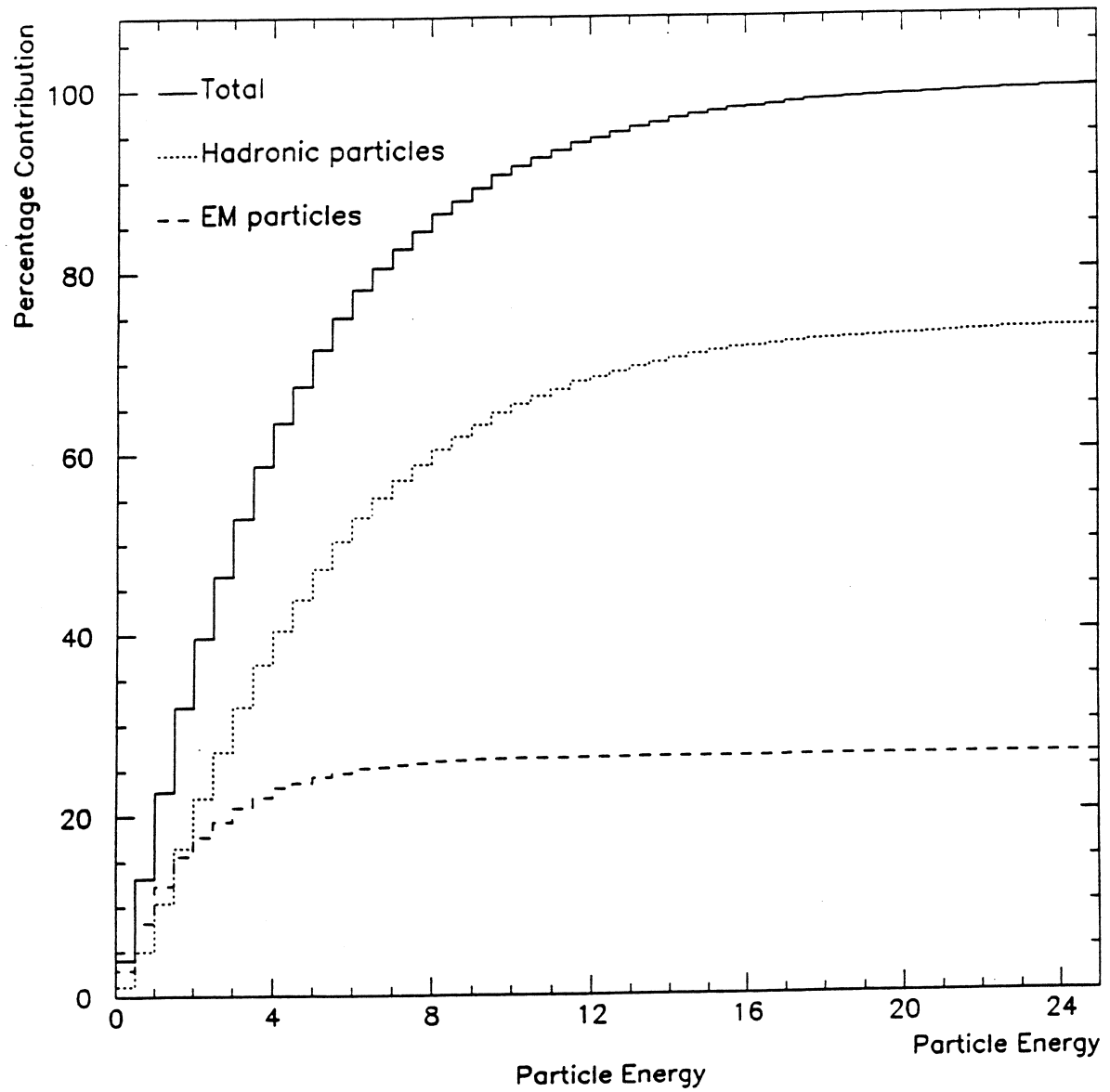


Figure 5: Particle composition of 50 GeV jets.



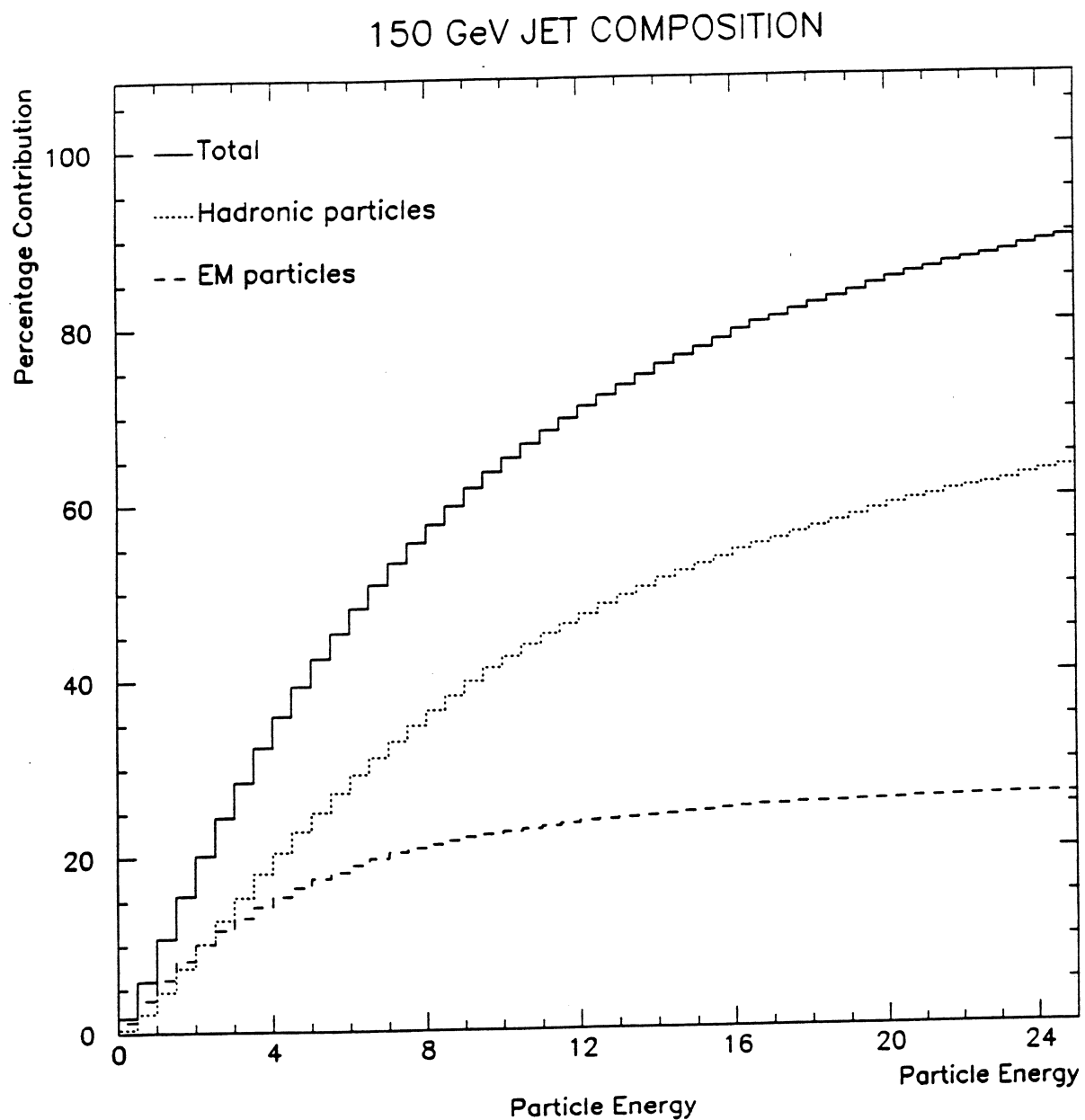


Figure 6: Particle composition of 150 GeV jets.

were measured at discrete values of particle energy, and the event generator gives a continuous spectrum of particle energies, the responses were calculated by interpolating between test beam data points. As mentioned above, below the lowest data point the response and error was taken to be constant equal to the response and error at 2 GeV for both pions and electrons. In order to incorporate  $\phi$  cracks the distance of each electromagnetic particle to the nearest CCEM  $\phi$  crack was calculated and the response degraded accordingly (see Figure 3.) The CCFH cracks are handled in a similar manner. The distance of each hadronic particle to the nearest CCFH crack was used to reduce the response according to Figure 4.

### 3 Results

#### Jet Energy Scale

The above method was used to derive a nominal energy scale as well as upper and lower limits. The nominal scale was generated using the nominal test beam response values. To get the upper limit, the upper points of the error bars in Figures 1 and 2 were used as well as an additional 2% for electrons and 5% for pions to reflect the overall scale uncertainty that occurs when transferring the test beam results to the D-Zero calorimeter. The lower limit was obtained in a similar way, by using the lower points on the error bars minus 2% for electrons and 5% for pions.

The simulated response curves were then fit to the following polynomial:

Table 1: Results of fitting  $E_{measured}$  versus  $E_{actual}$

$E_{measured} = A_0 + A_1 E_{actual} + A_2 E_{actual}^2$			
Fit Data	$A_0$	$A_1$	$A_2$
Nominal	-1.666	0.896	0.000239
High Response	-0.822	0.949	0.000142
Low Response	-2.177	0.843	0.000316

$E_{measured} = A_0 + A_1 E_{actual} + A_2 E_{actual}^2$ . The fits obtained agreed with the data curve to within .5%. The values of  $A_i$  are shown in Table 1 for the 3 fits. In Figure 7 we show  $E_{measured}/E_{actual}$ , the jet energy response in the calorimeter. The nominal curve ranges from 84% at 25 GeV to 93% at 200 GeV. The errors on the response are seen to range from 10% at 25 GeV to 4% at 200 GeV. Also note that the response is still somewhat less than 100% even for 200 GeV jets. This is due to the fact that low energy particles make up a substantial portion of the jet energy even for 200 GeV jets. The shape of the response curve is due to both the variation of the test beam results with particle energy (Figures 1 and 2) as well as the change in particle energy composition of jets with jet energy (Figures 5 and 6.)

The jet energy correction factor can be obtained using the fits shown in Table 1. Figure 8 shows  $E_{actual}/E_{measured}$  versus  $E_{measured}$ . This shows the correction factor the measured jet energy must be multiplied by in order to get the correct energy. In terms of the  $A_i$ , this factor is calculated by inverting the quadratic polynomial above to get:

$$\frac{E_{actual}}{E_{measured}} = \frac{-A_1 + \sqrt{A_1^2 + 4A_2(E_{measured} - A_0)}}{2A_2 E_{measured}}$$

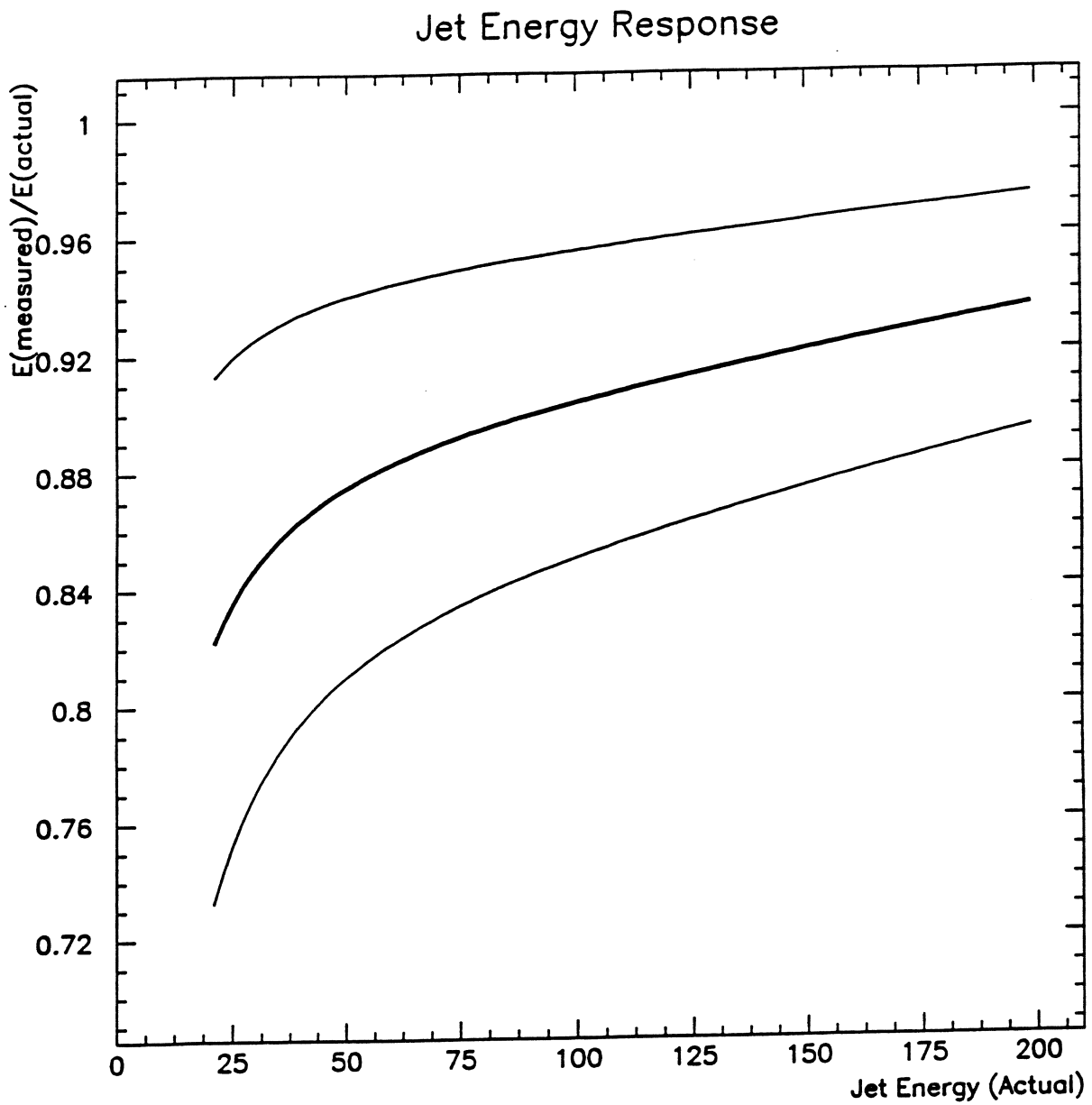


Figure 7: Nominal jet energy scale and limits of errors. The thick line is the nominal response and the thin lines are the upper and lower limits.

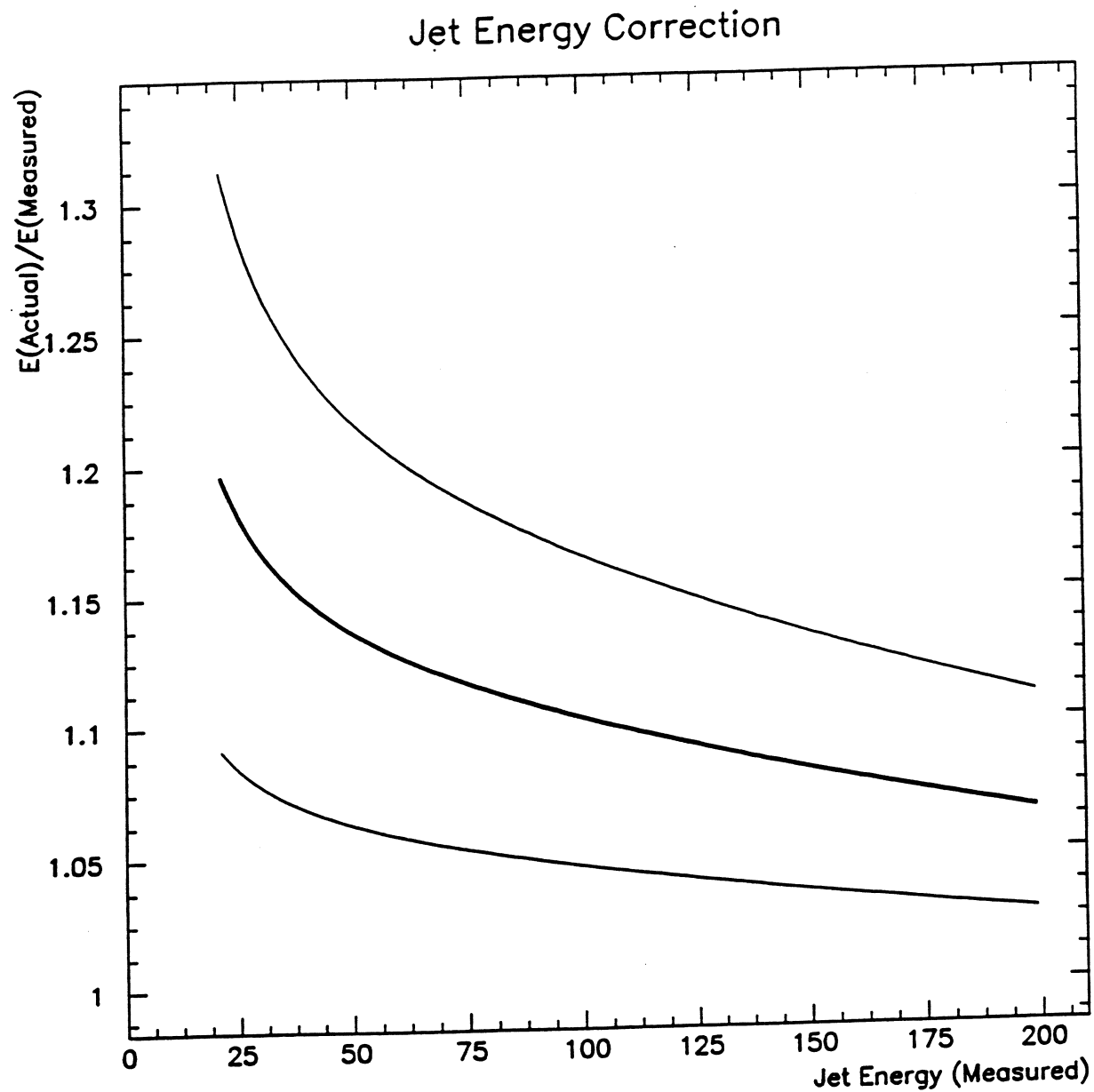


Figure 8: Jet energy correction (thick line) and errors (thinner lines.)

## Differences between Event Generators

The above results were calculated using Pythia jets which were free of both underlying event and initial state radiation. The jet energy response was also calculated using the Herwig and ISAJET Monte Carlo event generators, which include both of the above-mentioned effects. Despite this, the results were seen to agree with the Pythia results to within 1.5%. The Herwig and ISAJET results are compared to each other in Figure 9 and are seen to agree to within 1.5%. This gives an estimate of the systematic error due to the uncertainty in jet fragmentation and hadronization, but it is so much smaller than the errors due to test beam uncertainties that it has been ignored up to now.

## Effects of Varying Response Below 2 GeV

Since there is no reliable test beam data below 2 GeV, the response in that energy region is not known. In this study the response below 2 GeV, both for pions and electrons, was taken to be the same as the response used at 2 GeV. The question of how the jet response curve changes using other reasonable choices of single particle responses below 2 GeV are explored below. The response shift listed here are estimated using Figures 5 and 6. All the hypothetical very-low-energy response scenarios systematically shift the jet response curve as well as change its shape.

For electrons one could ask what would happen if the response continued

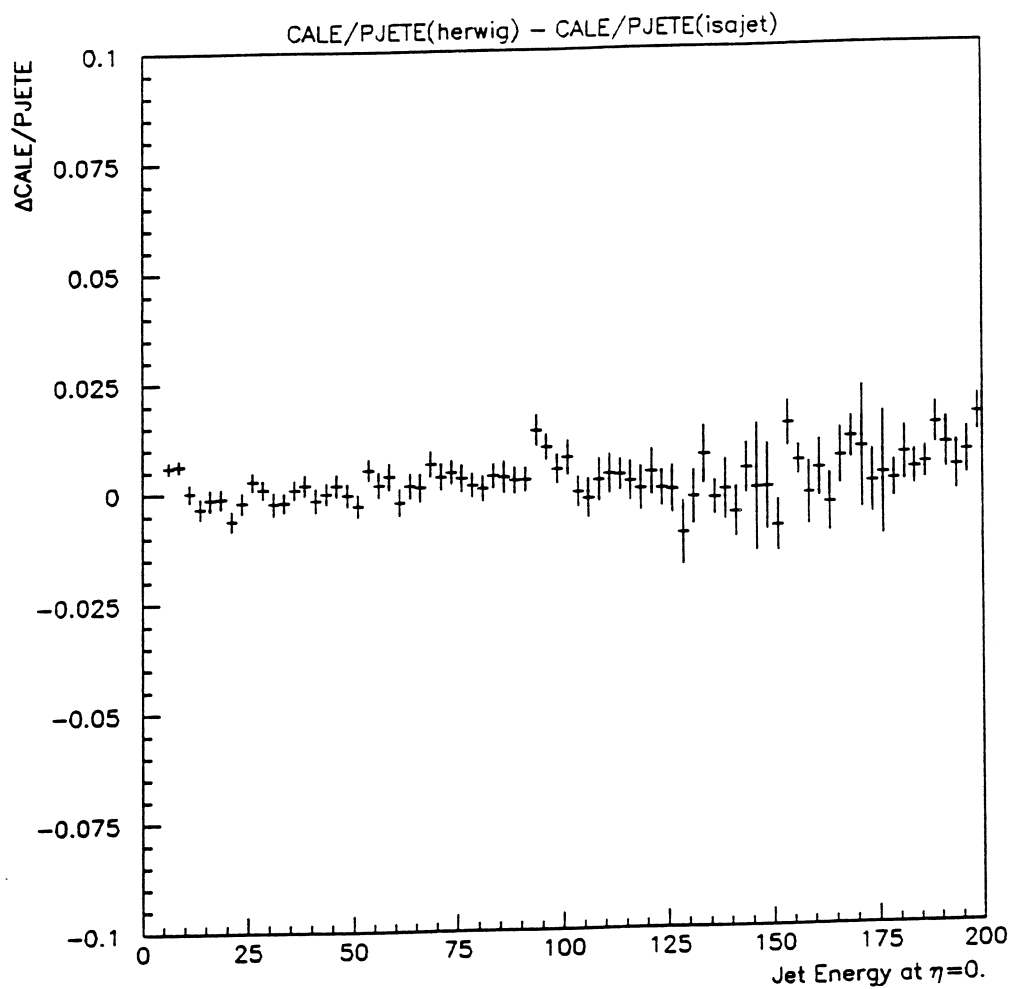


Figure 9: Difference in jet energy response between Herwig and ISAJET.

to drop as an extrapolation of the test beam data. In this case, the jet response would be 2% lower for 50 GeV jets and 1% lower for 150 GeV jets.

The pion response is expected to increase at very low energy. Assuming it increases to 100% at 1 GeV increases the response by 2% for 50 GeV jets and .5% for 150 GeV jets. If, on the other hand, the pion response continues to decrease as an extrapolation of test beam data, then the jet response decreases by 2% for 50 GeV jets and 1% for 150 GeV jets.

## 4 Summary

Using the test beam data and errors, along with estimates for CCEM and CCFH  $\phi$  crack effects, a jet energy scale correction has been generated. The correction ranges from 18% at 25 GeV to 6% at 200 GeV. The errors on the jet energy are approximately 10% at 25 GeV to 4% at 200 GeV. The shape of the energy scale is seen to depend greatly on the shape of the single particle response curve and, to a lesser extent, the jet fragmentation scheme that is used.

This method cannot be used to estimate effects due to out-of-cone showering or zero-suppression. These effects require knowledge of how the particles interact inside the calorimeter, namely shower width and cell energy distribution, that is not available for this simulation. These effects may amount to as much as a 2% decrease in the jet energy response.



At the time of writing the test beam results are in a state of flux. As a consequence the results presented here should *not* be considered as the final word on jet energy scales from test beam data. However, the method used is valid and much can be learned from its application.

# *Resolution Bias in Jet Response Measurement*

Bob Kehoe

University of Notre Dame

South Bend, IN 46617

February 8, 1994

## **Abstract:**

Response of the DØ calorimeter to particles in jets causes jet energies to differ from those of the partons that produce them. The response of jets is determined from calculation of the Missing  $E_T$  Projection Fraction (MPF) using direct photon candidates in the Central Calorimeter. Biases in the MPF method due to the energy resolution of the jet and photon are discussed. A revised MPF method which overcomes these biases is presented. A small bias has also been avoided resulting from event topologies where the photon and leading jet are not back-to-back in  $\phi$ .

Theoretical calculations of high energy physics processes give event kinematics in terms of parton energies. Experimentally, we reconstruct jets from energy deposition in the calorimeter using a fixed-cone algorithm where the cone is defined by its radius,  $\Delta R = (\Delta\eta^2 + \Delta\phi^2)^{1/2}$ . Several effects determine our measurement of jet energy including calorimeter response to the particles in the jet. The DØ Calorimeter has been designed to be both linear and compensating in its response to particles of different energies. Nevertheless, analysis of test beam data measured low energy pion response to be nonlinear, and  $e/\pi$  was found to be around 1.03 at 10 and 100 GeV<sup>1</sup>. Particles of widely varying energies comprise a jet so that the cumulative effect is to lower jet response from 100%, even for higher energy jets<sup>2</sup>.

The response of a jet,  $R_j$ , refers explicitly to the effective global response to the energy of all  $\pi$ 's, K's, etc. produced by fragmentation inside and outside of the jet cone. There are other effects which degrade our ability to measure the jet energy such as energy leakage outside of the jet cone,  $C_o$ , and energy deposited within the cone from the underlying event and from uranium noise,  $U_e$ . It is undesirable for our response measurement to be susceptible to these effects which are distinct phenomena and can be more accurately measured elsewhere.

In order to obtain a correction for jet response we calculate the Missing  $E_T$  Projection Fraction for jets in the Central Calorimeter (CC) using direct photon candidate events classified according to the leading jet energy,  $E_j$ . The primary issue of this paper is to discuss biases in this measurement due to the energy resolution of the jet and photon. A somewhat historical approach is taken to fully describe the impact of resolution on jet response measurement. The studies described motivate an alteration of the analysis. Therefore, in addition to the above method a new method classifying events by the photon  $E_T$ ,  $E_{\gamma T}$ , is presented and an argument is made in favor of this method due to its ability to overcome resolution bias.

# 1. The Method

The MPF method used to obtain a measurement of jet response was developed by CDF and first used at DØ on  $\Delta R = 0.7$  cone size jets by Andy Milder<sup>3</sup>. Direct photon events fully contained within the CC are used to calibrate calorimeter response to jets. Essentially, we assume the missing transverse energy,  $\vec{E}_T$ , in the event is dominated by the mismeasurement of the energy of the jet which balances the photon. We calculate the quantity MPF as

$$MPF = \frac{\vec{E}_T \cdot \hat{n}_{jT}}{E_{jT}} \quad \text{Eq. 1}$$

where  $\hat{n}_{jT}$  is the transverse jet unit vector and  $E_{jT}$  is the jet transverse energy. This gives a response,

$$R_j = \frac{1}{(1 + MPF)} \quad \text{Eq. 2}$$

which has been shown to give the jet response with respect to the EM scale<sup>3</sup>.

Although MPF and  $R_j$  are calculated using transverse quantities, the resulting response measurement is strictly speaking a function of the jet energy. Thus we calculate  $R_j$  and plot it directly vs.  $E_j$ .

There are three requirements that must be satisfied for the MPF method to work. So that it is a good indicator of the parton  $E_T$  of the event, the 'photon' must have a well measured response and its energy resolution must be good (say,  $\sigma_{em} \leq 0.3/\sqrt{E_j}$ ). Also, the  $\vec{E}_T$  must be an indicator of the energy in the jet which was not measured due to its response. To the extent that events with jets fragmenting to isolated  $\pi^0$ 's satisfies these requirements, the method is not compromised by the large contamination of the direct photon sample by  $\pi^0$ 's.

This method has good, although not complete, immunity from  $C_0$  and  $U_e$  contamination which only come into Eq. 1 via  $E_{jT}$ . Any change in  $E_{jT}$  will have a corresponding effect on MPF and thus on the disparity of  $R_j$  from 100%. For instance, a simple system with one jet and one photon back-to-back in  $\phi$  at  $\eta = 0.0$  has  $MPF = (E_{\gamma T}/E_{jT}) - 1$ . If  $MPF = 0.2$  and the cumulative affect of  $C_0$  and  $U_e$  is to increase  $E_{jT}$  by 10% then the measured value of  $MPF = 0.18$  and  $R_j$  changes by ~2% in this extreme case.

## 2. Event Selection

I obtain an event sample by first requiring one of the direct photon triggers given in Table 1 with offline cuts on the photons given in the last column.

Table 1: Level 2 and offline  $E_T$  thresholds for photons

<i>trigger</i>	<i>L2 threshold</i>	<i>photon <math>E_T</math> cut</i>
GAM_LOW_ISO	6 GeV	7 GeV
GAM_MED_ISO	14 GeV	15 GeV
GAM_HIGH_ISO	30 GeV	30 GeV

One photon is required and it must have isolation  $< 0.15$  where isolation, defined to be  $(E_{\text{tot}}(\Delta R=0.4) - E_{\text{em}}(\Delta R=0.2))/E_{\text{em}}(\Delta R=0.2)$ , is the percent hadronic plus electromagnetic energy in an annular cone around the photon direction from  $\Delta R = 0.2$  to  $\Delta R = 0.4$ . Photons are further required to be more than .01 radians from a CC EM crack. The  $|\eta|$  (detector eta) of the photon must be less than 0.9.

Considering the importance of  $\vec{E}_T$  to this method, I select events passing the following criteria to remove those where  $\vec{E}_T$  is not representative of  $R_j$  alone. To avoid events with  $\vec{E}_T$  being due to Main Ring activity, the event is rejected if the microblank bit is set. Events having photons due to hot EM cells are rejected by requiring  $\vec{E}_T$  to be less than 90% of the  $E_T$  of the photon,  $E_{\gamma T}$ . The  $z$  of the vertex must be within 70 cm of  $z = 0$  in order to avoid events in which the vertex and hence  $E_T$ 's are poorly measured.

There must be at least one and at most two jets in addition to the photon. I require these jets to satisfy good jet cuts which are defined as having the Coarse Hadronic fraction of their energy be less than 40%, an EM fraction between 5% and 95%, and the ratio of  $E_T$ 's of the leading and second-leading cells in the jet be less than 10.0. Any jet failing these cuts results in rejection of the event. The  $|\eta|$  (detector eta) of the leading jet must be less than 0.7 to avoid jets in which significant energy is deposited outside the CC.

Although all the results reported have been examined for 0.3, 0.5, 0.7, and 1.0 cone jets, all data presented here is for events reconstructed with 0.5 cone jets only. The results discussed do not qualitatively depend on this choice.

### 3. Topological Concerns

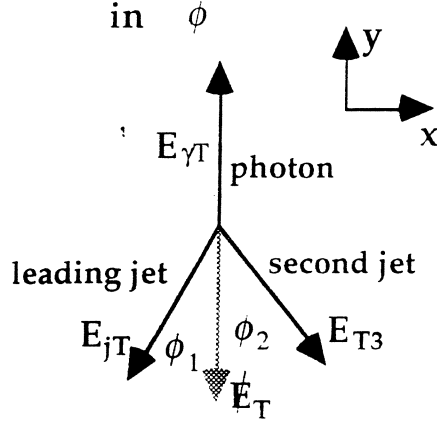
A third jet or unreconstructed energy cluster can cause the photon and leading jet not to be back-to-back in  $\phi$ . In such event topologies the  $\vec{E}_T$  is on average not due to only the leading jet. MPF has been designed to limit biases due to such energy deposition via the dot product of the  $\vec{E}_T$  with the jet direction.

Despite this, biases can still occur if a third energy cluster causes the photon and leading jet not to be back-to-back or if its  $E_T$  is comparable to the leading jet. This occurs because an implicit assumption of the method is that the  $\vec{E}_T$  in the event is due to any disparity between jet and photon responses. More specifically, MPF requires a back-to-back topology because the dot product preserves information about a second energy cluster if that cluster is not  $90^\circ$  in  $\phi$  from the leading jet. Consider the system shown in Figure 1 constrained to the  $x$ - $y$  plane in which there is no transverse boost to the event. In this situation, the  $x$ -

coordinates of the leading jet  $E_T$ ,  $E_{jT}$ , and second leading jet  $E_T$ ,  $E_{T3}$ , cancel. From this we get the expression:

$$\vec{E}_T \cdot \hat{n}_{jT} = E_{jT} \cos \phi_1 - E_{jT} \cos^2 \phi_1 - E_{T3} \cos \phi_1 \cos \phi_2 \quad \text{Eq. 3}$$

**Figure 1: Event not back-to-back**



If  $\Delta\phi$  between the two 'jets' is  $< 90^\circ$  we underestimate the response while we overestimate  $R_j$  if  $\Delta\phi > 90^\circ$ . The latter case is more likely for the second jet in the CC due to the effects of merging and splitting in the jet reconstruction. Second leading jets in the EC will also have an affect on  $\vec{E}_T$  and thus on MPF. Looking in direct photon candidates in data, we find that below 50 to 60 GeV jets, systematic shifts of 2% to 3% to higher response occur if we do not require a back-to-back topology.

Because of this, I stringently demand that the leading jet and photon be closely back-to-back and that any second jet have very low transverse energy relative to the leading jet. No second jets are allowed if  $E_{jT}$  is less than 50 GeV to remove events where the  $\vec{E}_T$  is due to both jets. Furthermore,  $\Delta\phi$  between the leading jet and photon is required to be within  $15^\circ$  of  $\pi$ . This requirement is loosened to allowing the  $E_T$  of the second leading jet,  $E_{T3}$ , up to 10 GeV for leading jets above 50 GeV because such a low energy second jet has no effect on MPF for these events. The  $\Delta\phi$  cut is loosened further. For events with jets above 100 GeV, the  $E_{T3}$  and  $\Delta\phi$  cuts are loosened still further. The values used for the current analysis are given in Table 4. Tighter cuts than these have no effect on the response curve indicating this bias has been eliminated.

**Table 2:  $\Delta\phi$  and  $E_{T3}$  cuts**

$E_{jT}$ range (GeV)	$E_{T3}$ (GeV)	$\Delta\phi$ (radians)
8. to 50.	$< 8.$	$\pi \pm 0.19$
50. to 100.	$< 10.$	$\pi \pm 0.34$
100. and up	$< 15.$	$\pi \pm 0.64$

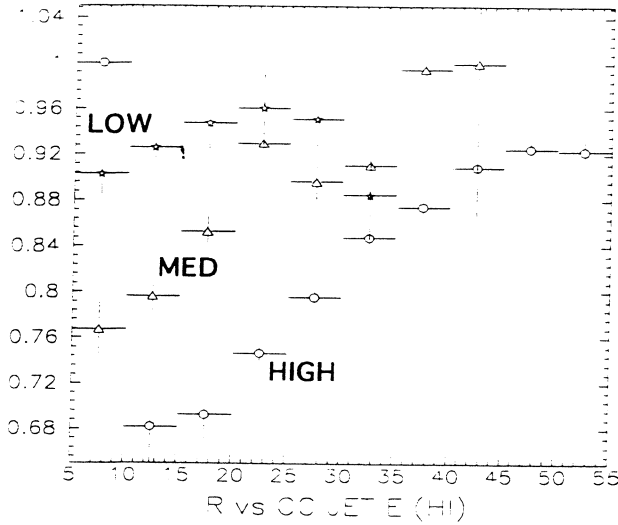
These cuts must also be performed in the MPF method discussed in Section 6.

## 4. Resolution Bias and Event Classification

The implementation of the method described in Section 1 turns out to suffer badly due to the jet resolution. Large fluctuations in  $E_{jT}$  mean the jet is a poor measure of the actual parton  $E_T$  scale of an event. As a result, the  $R_j$  measured is susceptible to bias when selections are performed on the  $E_T$ 's of the

photon or jet. The resolution affects our measured response via three routes: the jet reconstruction threshold, photon trigger thresholds, and the rapidly falling direct photon cross section.

**Figure 2: Response vs.  $E_j$  for direct photon triggers**



We will discuss these effects using a standard event. Unless otherwise noted, this consists of one photon and one jet back-to-back in  $\phi$ , at  $\eta = 0$ , and with  $U_e = C_o = 0$ . Let us assume that the photon response is 95% and the jet response is 90% with respect to the photon (ie.  $0.9 \times 0.95 = 0.855$ ). Furthermore, the jet and photon resolutions are:

$$\sigma_{em}/E_\gamma = 0.15/\sqrt{E_\gamma}$$

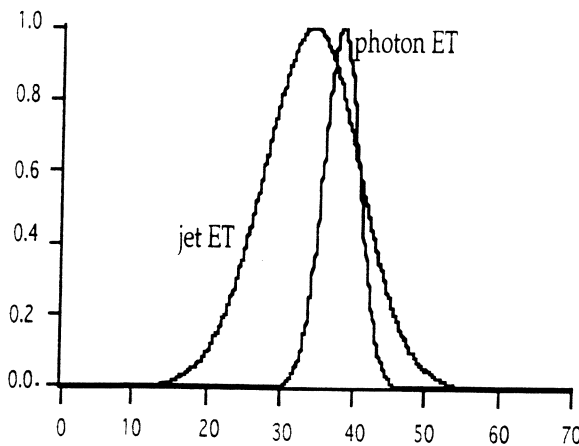
Eq. 4

$$\sigma_j/E_j = 0.80/\sqrt{E_j}$$

Eq. 5

For reasons that will be discussed later, we take the direct photon cross section to be constant in  $E_{\gamma T}$ .

**Figure 3: Photon and Jet ET distributions for an ensemble of 40 GeV ET parton events**



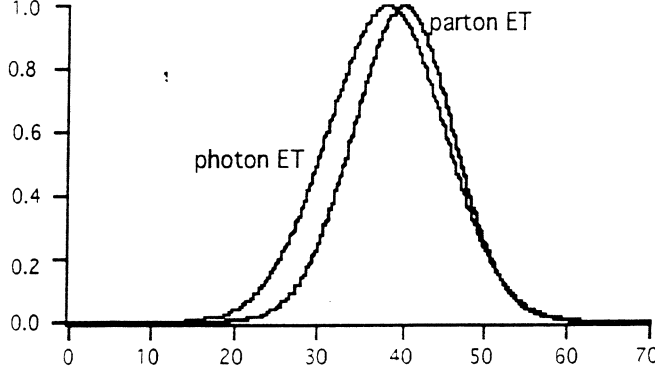
shown in Figure 3. On average MPF ( $= (E_{\gamma T}/E_{jT}) - 1$ ) would give a response (relative to the photon) of 90% for the mean jets having  $E_{jT} = 34.2$  GeV which is what we assumed.

Instead of considering 40 GeV partons, let us now consider looking at events by classifying (ie. 'binning') them in terms of the jets as we do in the

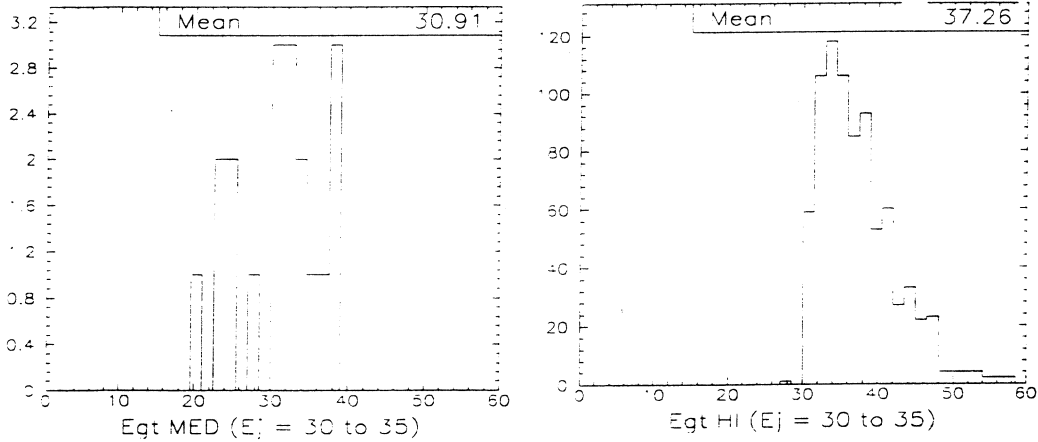
First let us discuss the resolution bias caused by the direct photon triggers by plotting  $R_j$  vs  $E_j$  for each. Figure 2 shows the response curves derived from the three direct photon triggers mentioned in Table 1. As we can see, our response curve changes with the trigger used. To understand the differences we take an ensemble of direct photon events with 40 GeV  $E_T$  partons. After passing thru the calorimeter, this will result in the distributions

analysis. For instance, take events with a leading jet having 34.2 GeV of  $E_T$ . Due to the jet resolution, the parton that the jet actually comes from would have an energy spectrum shown as the rightmost curve in Figure 4. The photon, because of its good resolution and response, approximates the parton  $E_T$  on an event by event basis causing its spectrum to look like the left curve in Figure 4.

**Figure 4: Photon and parton spectra for 34.2 GeV jets**



essentially a selection on a higher mean parton  $E_T$ . This is therefore a selection on a lower mean  $R_j$  for a given jet energy. **Figure 5: Photon spectra for GAM\_MED\_ISO and GAM\_HIGH\_ISO triggers.**



Looked at another way, near and below the direct photon triggers we exclude events where the jet fluctuated high into the  $E_j$  region we are considering. This skews the  $\vec{E}_T$  high by removing part of its normal distribution and this results in measuring a lower  $\langle R_j \rangle$ .

In our sample of standard events with 34.2 GeV jets, instead of  $\langle E_{jT} \rangle$  being 38 GeV it will now be  $\sim 42$  GeV so that  $R_j = E_{jT}/E_{jT} = 81\%$  rather than the actual value of 90%. If we look at events in which the GAM\_MED\_ISO trigger fired then we have  $\langle E_{jT} \rangle = 38$  GeV and the jet response is measured correctly.

A study of  $E_{jT}$  spectra in  $E_j$  bins indicate the trigger-dependent and cone-size -dependent cuts on  $E_{jT}$  in Table 3 are necessary for the method described in Section 1 to overcome this resolution bias. The cone size dependence occurs

because the larger cone jets have larger fluctuations in energy due to underlying event and other factors.

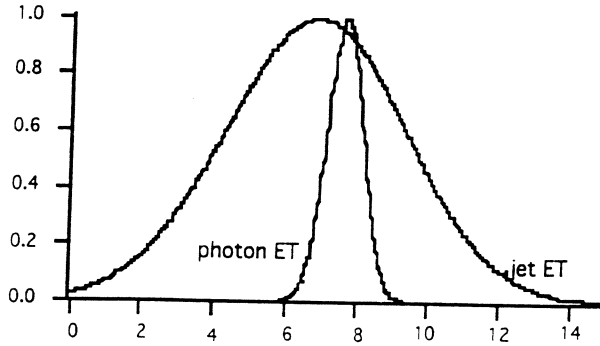
Table 3: Required  $E_{jT}$  thresholds for direct photon triggers for four cone sizes

cone size	LOW	MED	HIGH
.3	12 GeV	22 GeV	42 GeV
.5	15	22	45
.7	17	25	50
1.0	20	27	55

In the region near these cuts adjacent triggers give similar responses. On the other hand, the cuts produce a great loss in statistics.

Another manifestation of resolution bias occurs near the threshold for jet reconstruction. Jets in all events are reconstructed if their  $E_T \geq 8$  GeV. Let us take an ensemble of direct photon events with 8 GeV  $E_T$  at the parton level. In such a sample we take the same responses and resolutions as above and so we expect the distributions shown in Figure 6.

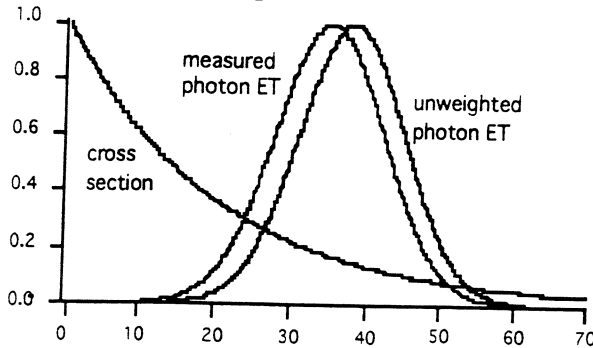
Figure 6: Photon and Jet  $E_T$  distributions for ensemble of 8 GeV parton  $E_T$  events.



After jet reconstruction, though, our jet spectrum is cut off at 8 GeV so that  $\langle E_j \rangle \sim 9$  GeV. In a way analogous (but oppositely directed) to the resolution bias from the triggers, this causes us to estimate  $\langle R_j \rangle$  to be artificially high in the  $E_j$  region out to about 12 to 20 GeV jets depending on the cone-size. Unfortunately, our ability to measure the jet energy scale below 15 GeV is not directly feasible with this method because

of this bias. All of our data, however, is reconstructed with the 8 GeV cut and so our MPF curve should give a reasonable description of the response of reconstructed jets.

Figure 7: Effect of direct photon cross section on photon distributions.



A third bias encountered when directly binning response in terms of  $E_j$  is due to the direct photon cross section,  $\sigma_\gamma$ . We now take our standard events to adhere to the direct photon cross section -- a rapidly falling distribution in  $E_{\gamma T}$ . As described above, when we classify ("bin") events according to  $E_j$  we accept events of widely varying parton  $E_T$  scales. The lower  $E_T$  parton events are

much more likely to be produced than higher  $E_T$  events in a given  $E_j$  bin. This shifts the mean of the  $E_{\gamma T}$  (ie. parton  $E_T$ ) distribution to a lower value than it should be as is shown in Figure 7. The degree to which this shift occurs depends on how steeply  $\sigma_\gamma$  falls. Nevertheless, the jet resolution itself becomes wider (in



% of  $E_j$ ) as the jet energy gets lower. Thus for a typical cross-section the  $E_{\gamma T}$  spectrum extends over a larger drop in  $\sigma_\gamma$  and the bias gets worse as we go lower in  $E_j$ .

The biases discussed above are summarized in Table 4.

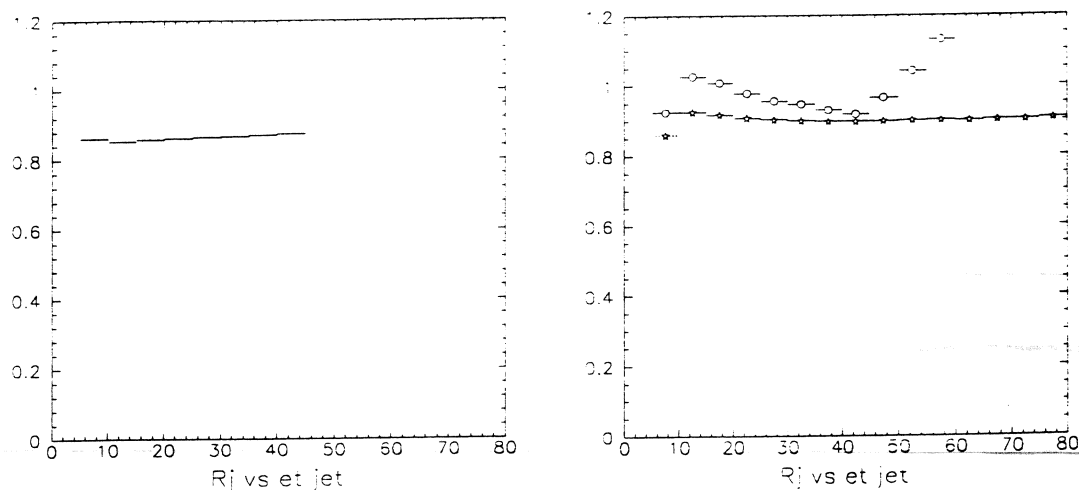
Table 4: Summary of Resolution Biases

Agent	Mechanism	Effect
photon trigger thresholds	cut on photon raises $\langle E_{\gamma T} \rangle$	lowers measured $R_j$ in region of trigger
jet reconstruction threshold	cut on jets raises $\langle E_{\gamma T} \rangle$	raises measured $R_j$ for jets with $E_T < 15$ GeV
direct photon cross section	weight lower $E_{\gamma T}$ over higher ones	raises measured $R_j$ over whole $E_j$ range

## 5. Event Simulation:

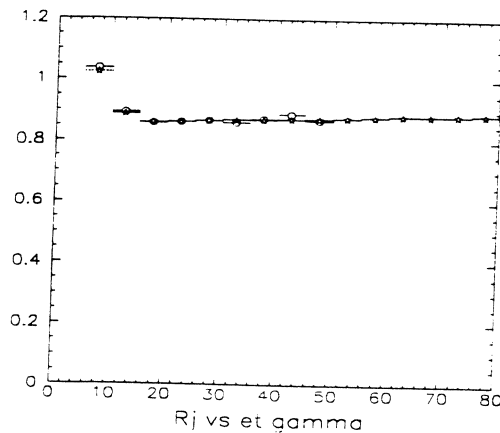
The cross section bias is difficult to estimate so an event simulator, originally written by Rich Astur, is used to generate events weighted by the  $E_T$  dependence of the direct photon cross section and smear the jet with its resolution. This has been modified to include photon resolution, the 8 GeV jet reconstruction threshold, and an 8 GeV photon trigger threshold. Response of the jet can be input.

Figure 8:  $R_j$  vs  $E_j$  for events with perfect jet and photon resolution



An illustration of the effect of the cross section bias is given in Figures 8 thru 9. The response function used for this was  $R_j = 0.85 + 0.0005 \cdot E_{jT}$  and otherwise the events conform to the standard defined in Section 4. Figure 8 shows  $R_j$  vs  $E_j$  for jets and photons with perfect resolution and a cross-section falling as  $1/E_T^5$ . Figure 9 adds jet resolution and two different cross-sections are shown: the stars (lower curve) are for an  $1/E_T^2$  dependence and the circles (upper curve) are for an  $1/E_T^5$  dependence. As we can see, the jet resolution skews the MPF measurement very badly and the bias is worse for steeper cross-sections. The dominant problem is the jet resolution -- smearing the photon has almost no effect.

The detailed shape of the curves in Figure 9 can be understood. For conciseness, consider the  $1/E_T^5$  curve. The decrease in measured response below 15 GeV is due to a lessening of the impact of the cross-section bias because there are no photons below 8 GeV. Above about 15 GeV,  $R_j$  is consistently several percent above the input value due to the cross section bias. As expected, the bias lessens as  $E_{jT}$  increases. The reason the plots increase in response at the highest  $E_{jT}$  is because the jet resolution allows the jet to fluctuate much higher than the photon can in a region in which the cross-section contributes no partons.



The cross-section resolution bias can be eliminated by binning the response as a function of  $E_{jT}$  instead of  $E_j$  directly. This is because we are classifying events with a quantity which is known better and is representative of the original partonic  $E_T$ . Figure 10 illustrates that, for both cross-sections mentioned above, we obtain a response curve which agrees much better with the input value. The close correspondence between the curves from the two cross-sections indicates we also obtain a cross-section independent

measurement from this method. The rise in  $R_j$  at low energy is due to the jet reconstruction bias.

For an ensemble of direct photon events with a photon in a given  $E_T$  range, the jets fluctuate in a way consistent with their resolution. We can see that no further biases are incurred by looking at these events in the following way. The photon represents the parton which gave rise to the jet before detector resolution caused its energy to vary widely. The jet represents itself -- the parton after detector resolution -- and is distributed in a symmetric gaussian unweighted by the cross section for each photon bin. In this case the mean jet  $E_T$  in each  $E_{jT}$  bin is unbiased and accurately indicates the response.

## 6. New MPF Method

Rich Astur, Jae Yu and myself have worked out the details of a new method to obtain a useful response curve for jets<sup>4</sup>. The quantities MPF and  $R_j$  are now defined to be

$$MPF = \frac{\vec{E}_T \cdot \hat{n}_{\gamma T}}{E_{\gamma T}} \quad \text{Eq. 6}$$

$$R_j = 1 + MPF \quad \text{Eq. 7}$$

Although we want to plot response vs. a well defined quantity such as  $E_{\gamma T}$ , we need to plot it vs. a quantity which reflects the actual jet energy that would be observed in an event. The procedure we use is the following. We calculate the quantity

$$E'_j = E_{\gamma T} \cosh(\eta_j) \quad \text{Eq. 8}$$

which represents an estimate of the jet energy without the affects of  $R_j$ ,  $U_e$ , and  $C_o$  (ie. the parton's *energy*). It fulfills the role played by  $E_{\gamma T}$  in Section 5. This is possible due to the good energy resolution and response of the photon and the good position resolution of the jet. Plotting the raw measured  $E_j$  vs  $E'_j$  provides a correction function representing the unbiased correspondence between  $E_j$  and  $E'_j$  and we apply this function to  $E'_j$ , giving  $E_j^{corr}$ . On average  $E_j^{corr} = E_j$  but now it has the photon resolution, not the jet's. Finally, we plot  $R_j$  vs  $E_j^{corr}$ .

Figure 11: Actual  $E_j T$  vs corrected  $E_j T$  using old method

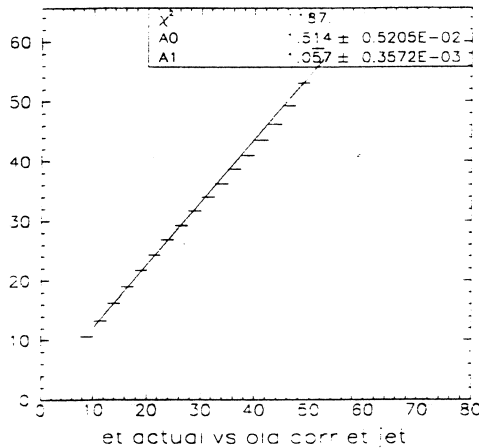
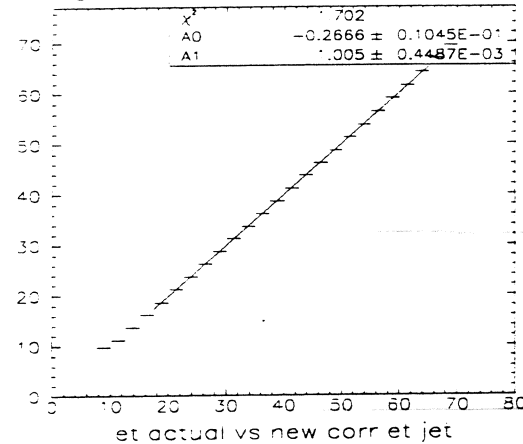
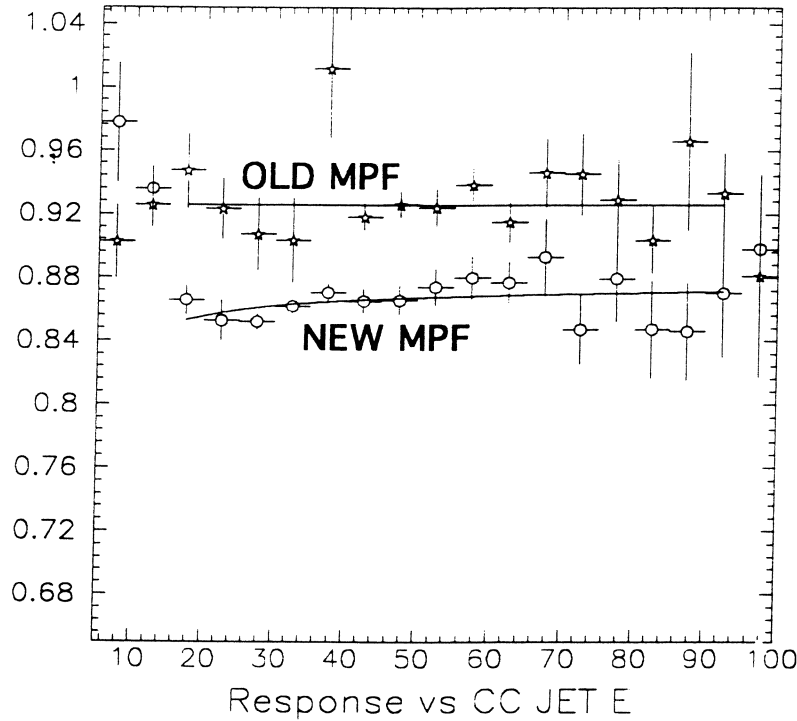


Figure 12: Actual  $E_j T$  vs corrected  $E_j T$  using new method



This method has been simulated and the corrections derived from a fit ( $0.848 + 0.0006 \cdot E_{\gamma T}$  above 15 GeV) were applied to see how well the corrected  $E_{\gamma T}$  matches the parton value. Figures 11 and 12 give the actual jet energy before

**Figure 14: Measured jet response vs  $E_j$  using old and new method**



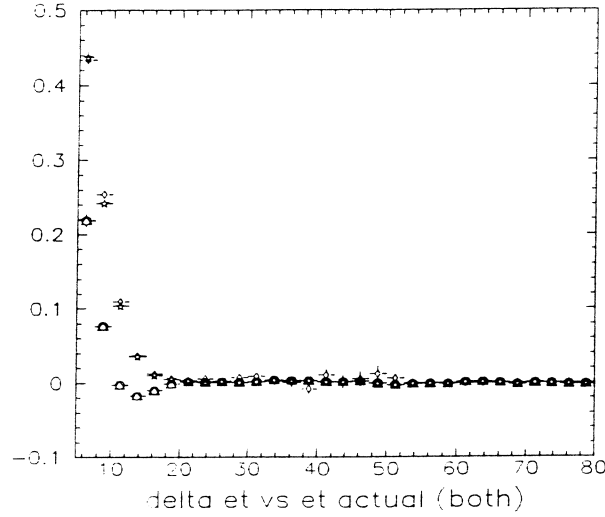
Response plots for jets reconstructed with 0.5 cone-size in collider data are shown in Figure 14 for the scheme where events are classified via jets ('Old' method) and in terms of the photons ('New' method). The change in shape at low energies is due to the jet reconstruction bias. The overall drop in response is due to the elimination of the cross-section bias.

## 7. Conclusion

The effects of jet and photon resolution on the measurement of jet response has been studied and the MPF method has been explored using events classified in terms of  $E_j$  and  $E_{\gamma T}$ . Large biases are seen when classifying events directly in terms of the leading jet because it is not a good indicator of the parton  $E_T$  scale of an event. We can overcome these biases if MPF is derived by classifying events in terms of the photons. A new method for determination of  $R_j$  based on this idea which is robust against resolution bias is briefly presented. It also gives a correction independent of the cross-section of the sample used to generate it. There is one resolution bias at the lowest jet energies due to the jet reconstruction threshold which is still problematic but has nearly been

response vs. the corrected energy. A perfect correction will give a plot with zero offset and slope of 1.0.

**Figure 13: Percent Discrepancy of Corrected Jet**



Although indirect, the new method has an improved slope, offset, and  $\chi^2$  compared with the old method. The large  $\chi^2$  for the old method is due to forcing a straight line fit to a non-linear plot; the nonlinearity being due to applying the wrong correction to the jets. Application of a correction derived from a fit of the low energy  $R_j$  curve results in a slight worsening of Figure 11 and slight improvement in Figure 12.

To get a better idea of how well we are doing in the low  $E_j$  region, we plot  $(E_{T\text{corrected}} - E_{T\text{parton}})/E_{T\text{parton}}$  vs.  $E_{T\text{parton}}$  in Figure 13. Four curves are given. The two highest curves at low  $E_j$  are for the two cross-sections mentioned above and all  $E_j$  are corrected with the curve obtained above 15 GeV and extrapolated at lower energies. These two agree very well and the large discrepancy at low  $E_j$  indicates the bias incurred if we do not fit the low energy part of our response curve. The bottom two curves in Figure 13 are also for the two cross-sections with the low energy correction applied. A large improvement in the agreement of corrected jet and parton is evident. A rapidly increasing discrepancy still occurs at the very lowest energies due to problems in binning and fitting a rapidly changing correction.

The most important advantage to the new method is its immunity from resolution bias. However, an additional benefit is that we can retain more statistics since we do not have to cut on the jet energy as is necessary if binning in  $E_j$ . We merely need to cut on  $E_{T\gamma}$  at the values given in Table 1 to get rid of any trigger bias from the photon's resolution. Because  $E_{T\gamma}$  does not enter into Eq.'s 6 thru 8, the calculated  $R_j$  now has no contamination from  $U_e$  or  $C_o$ . This also means we can study the region affected by the reconstruction bias since we do not have to explicitly require a jet.

eliminated. A comparatively small bias due to events diverging from a topology of back-to-back in  $\phi$  has also been removed.

Several people were helpful in this project. I am, however, most grateful to Jae Yu, Meena Narain, and especially Rich Astur for their patience and insight.

## 8. References:

1. R. Hirosky, "Response of D-ZERO U-LAr Calorimeters at Low Energies and the Effect of Oxygen Contamination on Observed Signals". U. of Rochester. Dissertation. 1992.
2. A. Milder, R. Astur. "Jet Energy Scale Using Test Beam Data". DØnote # 1595. 1992.
3. A. Milder. "Dijet Angular Distributions at  $s^{1/2} = 1800$  GeV Using the DØ Detector". U. of Arizona. Dissertation. 1993.
4. B. Kehoe, R. Astur, J. Yu. "Jet Response from the Missing  $E_T$  Projection Fraction". DØnote (upcoming) # 2053. 1994.



## Position Biases and Resolutions in Jet Measurements

Changlyong Kim  
*Korea University*

Terry C. Heuring  
*Florida State University*

Soon Yung Jun  
*Northwestern University*

### ABSTRACT

An accurate determination of the jet position is very important for many physics analyses. The pseudorapidity of the reconstructed jet is biased due to the detector structure and the jet reconstruction algorithm. The azimuthal angle of jets also shows an overall shift. As the extension of DØnote # 2173,<sup>1</sup> the jet  $\eta$  and  $\phi$  biases and their resolutions were determined as a function of the jet energy and detector pseudorapidity. HERWIG 4.6 was used to generate the jet events which were GEANTed and reconstructed using a fixed cone algorithm with a radius of 0.7. The result is valid for jets in  $|\eta| < 4.0$

### 1. Introduction

QCD physics measurements depend on the ability of the detector to properly determine the energy and position of a jet. Ideally, we would build a parton detector with perfect resolution and response and never worry about correcting biases or unsmearing resolution effects. To our knowledge, no such detector exists for jet measurements and as impressive as the DØ detector is, it is not perfect. The combination of many factors such as detector design and jet reconstruction algorithm leads to mismeasurements of physical quantities.

Unlike an electromagnetic shower produced by an electron or a photon, the calorimeter shower of a jet is initiated by many particles which are spread over a certain opening angle and a wide range of energy. Due to these characteristics, a test beam study of a jet is inapplicable. Therefore, we have to rely on Monte Carlo simulations to model the effects of fragmentation, hadronization and detector smearing. Specifically, we used HERWIG 4.6 and DØ GEANT to understand the position resolution and biases in measuring jets in the DØ detector.



## 2. Measurement Biases

Any bias in the position determination is expected to depend on the jet shape which is strongly related to hadronization. We used HERWIG to model these effects since it provides jets with the most realistic shape.<sup>2</sup> PJETS at the parton and particle level and CAJETS at the calorimeter level were reconstructed using the DØ standard reconstruction algorithm with a cone of radius  $\Delta R(= \sqrt{\Delta\eta^2 + \Delta\phi^2}) = 0.7$  and a minimum transverse energy of  $E_T^{min} = 8\text{GeV}$ . QCD  $2 \rightarrow 2$  parton event samples were generated at the vertex position  $z = 0$ , so that the detector pseudorapidity,  $\eta_d$ , which is same with the physics  $\eta$  was used throughout this note. Assuming perfect position resolution, the  $\eta$  of a jet would be:

$$\eta_d^{parton} = \eta_d^{reco} + \delta(E_{jet}^{reco}, \eta_d^{reco}) \quad (1)$$

where  $\eta_d^{reco}$  is a reconstructed calorimeter jet  $\eta$  and  $\delta$  is the bias which must be extracted from the Monte Carlo.  $\delta(E_{jet}^{reco}, \eta_d^{reco})$  is the average of  $\eta_d^{parton} - \eta_d^{reco}$  where a matching condition was used to associate parton jets with reconstructed jets. The two jets were matched if a reconstructed jet was within a cone of 0.7 around a parton jet. If there were two jets in the cone, then the matching cone size was reduced to 0.5. If there was only one reconstructed jet in that reduced cone, the jets were matched. If there were still two jets, the reconstructed jet with  $E_t$  closest to the parton jet  $E_t$  was selected. If no jet was found in the cone, there was no matching. Only isolated calorimeter jets were used by requiring the merge/split flag to be zero. If any of the calorimeter jets in an event was merged or split, the event was skipped. In other words, only simple jets were used in this study.

### 2.1. $\eta$ Bias

The tower size in the calorimeter is a function of pseudorapidity. Since the central calorimeter towers are physically larger than their forward counterparts, more energy may be deposited in the smaller  $\eta$  towers of a jet than the high  $\eta$  ones. Since the energy and polar angle  $\theta$  of each tower are used for calculating the centroid of a jet, it is natural that the center of the jet shifts toward the smaller  $\eta$ . In other words, the pseudorapidity dependence of the calorimeter tower size together with jet algorithm are mainly responsible for the tendency to shift the reconstructed jet  $\eta$  to the central region.

The average of  $\eta_d^{parton} - \eta_d^{reco}$  as a function of  $\eta_d^{reco}$  for all energies is shown in Fig. 1. Figure 2 shows the same quantity in various energy bins. The bias in  $|\eta_d| \in [1.0, 1.6]$  might be due to lower energy response in the IC region. The increase in the bias for  $|\eta| > 2.0$  might be due to the rapid increasing physical size ratio between two neighboring towers as a function of  $\eta$ . It shows that more energetic jets have less bias. This may be due to the tendency for higher energy jets to be more collimated.

The  $\eta$  bias between a parton jet and the matching particle jet was extracted in the same way and is shown in Fig. 3. Since there is no detector showering simulation, this represents only the effects due to the DØ jet reconstruction algorithm involved in particle jet reconstruction. As can be seen, there is a little bias due to the particle

spread during the hadronization. And, there is no IC region bump as we saw in the detector simulation.

## 2.2. $\phi$ Bias

The azimuthal angle bias study was conducted in the same way as the  $\eta$  study. There is no reason to expect a bias in the azimuthal angle because the calorimeter tower structure is symmetric in  $\phi$ . The average of  $\phi^{parton} - \phi^{reco}$  as a function of  $\eta_d$ , as shown in Fig. 4, indicates the overall shift toward the negative  $\langle \phi^{parton} - \phi^{reco} \rangle$  for both positive and negative  $\eta_d$  and that the size of the shift is on the order of -0.01. This kind of a distinct bias was not seen between a parton and the matching particle jet. Any bias introduced by this effect will be small for the physics analysis because all jets are systematically shifted in the same direction. For example, the relative angle between 2 jets will be useful for the physics analysis rather than the  $\phi$  position itself of a jet. Therefore  $\delta_\phi$  correction factor is assumed to be zero for now. On the other hand, we are still looking for the reason of the shift.

## 2.3. $\eta$ bias correction

The methodology we used to determine a correction function for the  $\eta$  bias is the same as that done by Daniel Elvira.<sup>1</sup> Since the bias seems to be symmetric in  $\eta$ , and to decrease our statistical errors, the bias from the negative side was projected onto the positive side with a reversed sign and is divided into 6 energy bins as shown in Fig. 2. A third degree polynomial was used to fit the range  $|\eta_d| \in [0., 1.8]$  for each histogram. A quadratic function was used for the range  $|\eta_d| \in [1.8, 3.0]$ . As an extension of Daniel Elvira's study, we used a third degree polynomial for the region  $|\eta_d| > 2.4$ . The parameterization functions are as follows.

$$\delta(E_{jet}^{reco}, \eta_d^{reco}) = A + Bx + Cx^2 + Dx^3 \text{ for } |\eta_d| \in [0.1, 1.8] \quad (2)$$

$$= A + Bx + Cx^2 \text{ for } |\eta_d| \in [1.8, 3.0] \quad (3)$$

$$= A + Bx + Cx^2 + Dx^3 \text{ for } |\eta_d| > 2.4 \quad (4)$$

$A, B, C$  and  $D$  are coefficients for the parameterization. They are shown in table 1, 2 and 3. The overlap between  $|\eta_d| \in [1.8, 3.0]$  and  $|\eta_d| > 2.4$  was used to guarantee the continuity of the parameterization. To cross check the correction parameterization, we applied this correction to the reconstructed jets. Solid crosses in Fig. 5 show the bias before the correction, whereas the dashed crosses indicate the bias after the correction. No distinct  $\eta$  bias is observed after the correction was applied.

## 3. Measurement of Position Resolutions

Once the bias is parameterized, the  $\eta_d$  of the calorimeter jet can be corrected to the initial parton jet  $\eta_d$  value. Although the average of  $\eta_d^{parton} - \eta_d^{reco}$  is zero, the overall distribution follows a gaussian distribution due to the finite calorimeter position resolution. The variance,  $\sigma_\eta(E_{jet}^{parton}, \eta)$ , of the gaussian distribution was taken as the

jet  $\eta$  resolution. The data was binned with energy boundaries at 20, 40, 70, 100, 200, 300 and 400 GeV. In Figs. 6 and 7 we plot the  $\eta$  and  $\phi$  resolutions as a function of the average energy in each bin. As can be seen, the nominal resolution varies from 0.01 to 0.07. The quantity  $\sigma_\eta(E_{jet}^{parton}, \eta)$  was obtained in seven  $\eta$  bins and was parameterized as a function of jet energy as follows.

$$\sigma_\eta(E, \eta) = A + \frac{B}{E} + \frac{C}{E^2} \quad (5)$$

The same method is used for the  $\phi$  resolution study. The parameterization coefficients are listed in the table 4 and 5 for  $\eta$  and  $\phi$ , respectively.

#### 4. Conclusions

We have studied the position biases and resolutions in simple jet measurement. The  $\eta$  bias was extracted from the GEANTed HERWIG Monte Carlo. After the bias correction, the position resolution has been calculated. The  $\eta$  position resolution shown in Fig. 6 is almost same with the result of DØ note # 2173 although the parameterized coefficients are a little different. And, the nominal resolution for  $\eta$  and  $\phi$  is around 0.03.

#### References

1. Victor Daniel Elvira *DØnote 2173* (1994)
2. Brad Abbott, Kathleen Streets *DØnote 2176* (1994)

	20-40(GeV)	40-70	70-100	100-200	200-300	300-500
A	0.003	0.00161	0.000469	0.000465	-0.000952	-0.000939
B	-0.0214	-0.00109	-0.00356	0.00737	0.00685	0.0162
C	0.0791	0.0426	0.0385	0.00953	0.0101	-0.00858
D	-0.0359	-0.0224	-0.0205	-0.00722	-0.00765	0.000533

Table 1.  $\eta$  bias parameterization for  $|\eta_d| \in [0.1, 1.8]$

	20-40(GeV)	40-70	70-100	100-200	200-300	300-500
A	-0.0591	-0.0717	0.0464	0.00553	0.0123	0.00592
B	0.0436	0.0470	-0.0770	-0.0257	-0.0266	-0.0188
C	0.	0.	0.0295	0.0141	0.0117	0.00888

Table 2.  $\eta$  bias parameterization for  $|\eta_d| \in [1.8, 3.0]$

	20-40(GeV)	40-70	70-100	100-200	200-300	300-500
A	0.0	0.0	-1.09	-0.770	-1.89	-1.04
B	0.0	0.0	1.15	0.760	1.86	1.02
C	0.0	0.0	-0.398	-0.244	-0.605	-0.333
D	0.0	0.0	0.0473	0.0272	0.0662	0.0369

Table 3.  $\eta$  bias parameterization for  $|\eta_d| > 2.4$

$\eta$	A	B	C
0.0-0.5	0.006663	0.7727	2.130
0.5-1.0	0.005418	1.164	1.230
1.0-1.5	0.005667	1.826	-5.847
1.5-2.0	0.003866	2.693	-13.84
2.0-2.5	0.0004306	5.578	-116.2
2.5-3.0	0.004273	8.637	-328.4
3.0-3.5	-0.01897	19.64	-1241.

Table 4. Parameterization of the jet  $\eta$  resolution

$\eta$	A	B	C
0.0-0.5	0.007554	0.5897	3.452
0.5-1.0	0.007105	0.8484	5.042
1.0-1.5	0.005567	1.836	-10.80
1.5-2.0	0.006334	2.296	-15.85
2.0-2.5	0.003316	4.787	-101.4
2.5-3.0	-0.001437	8.534	-346.7
3.0-	-0.01897	26.59	-2301.

Table 5. Parameterization of the jet  $\phi$  resolution

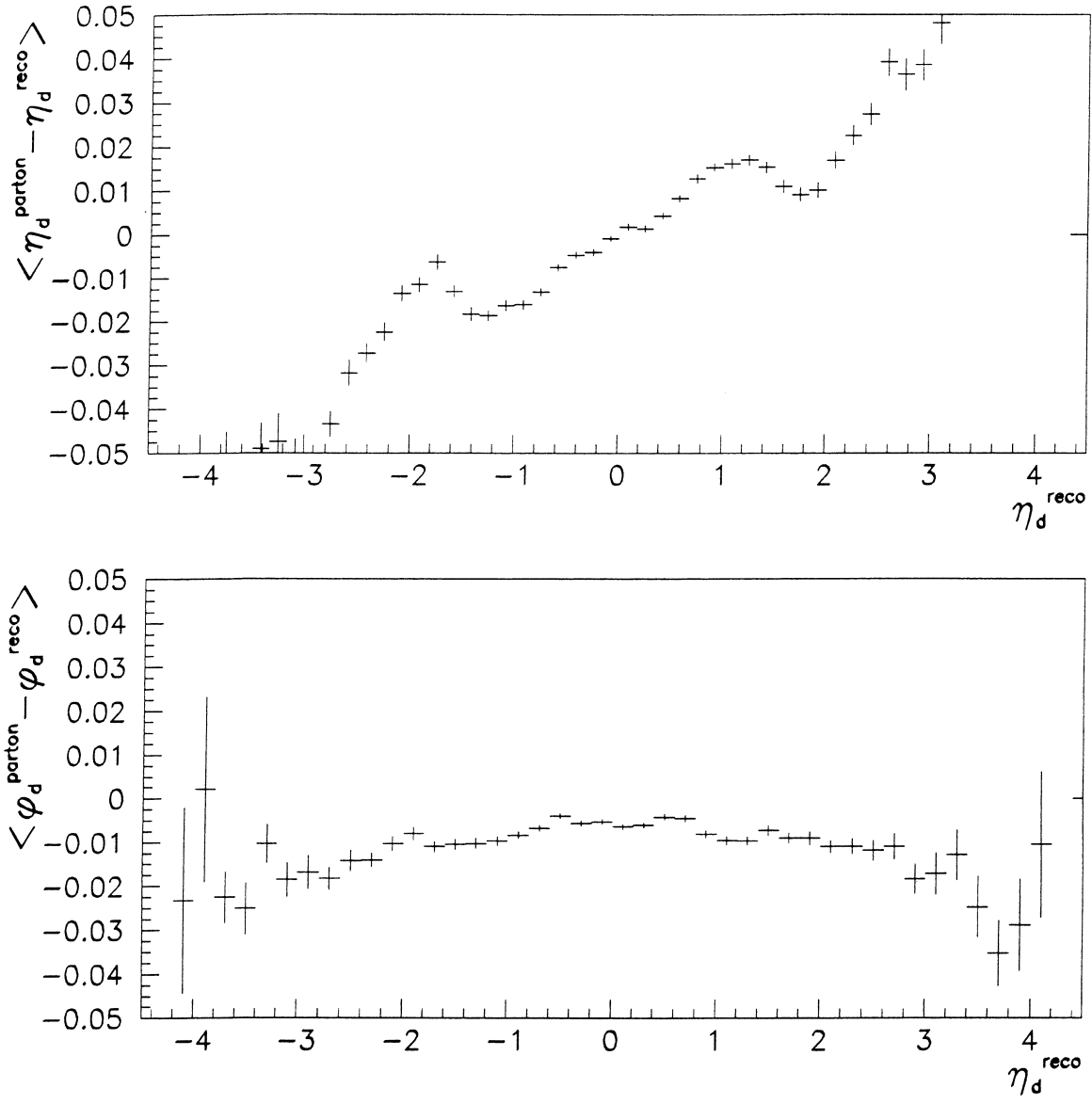


Fig. 1. HERW1G Monte Carlo simulation of the  $\eta$  &  $\phi$  biases for all jet energies(GeV) as a function of  $\eta_d^{reco}$ .

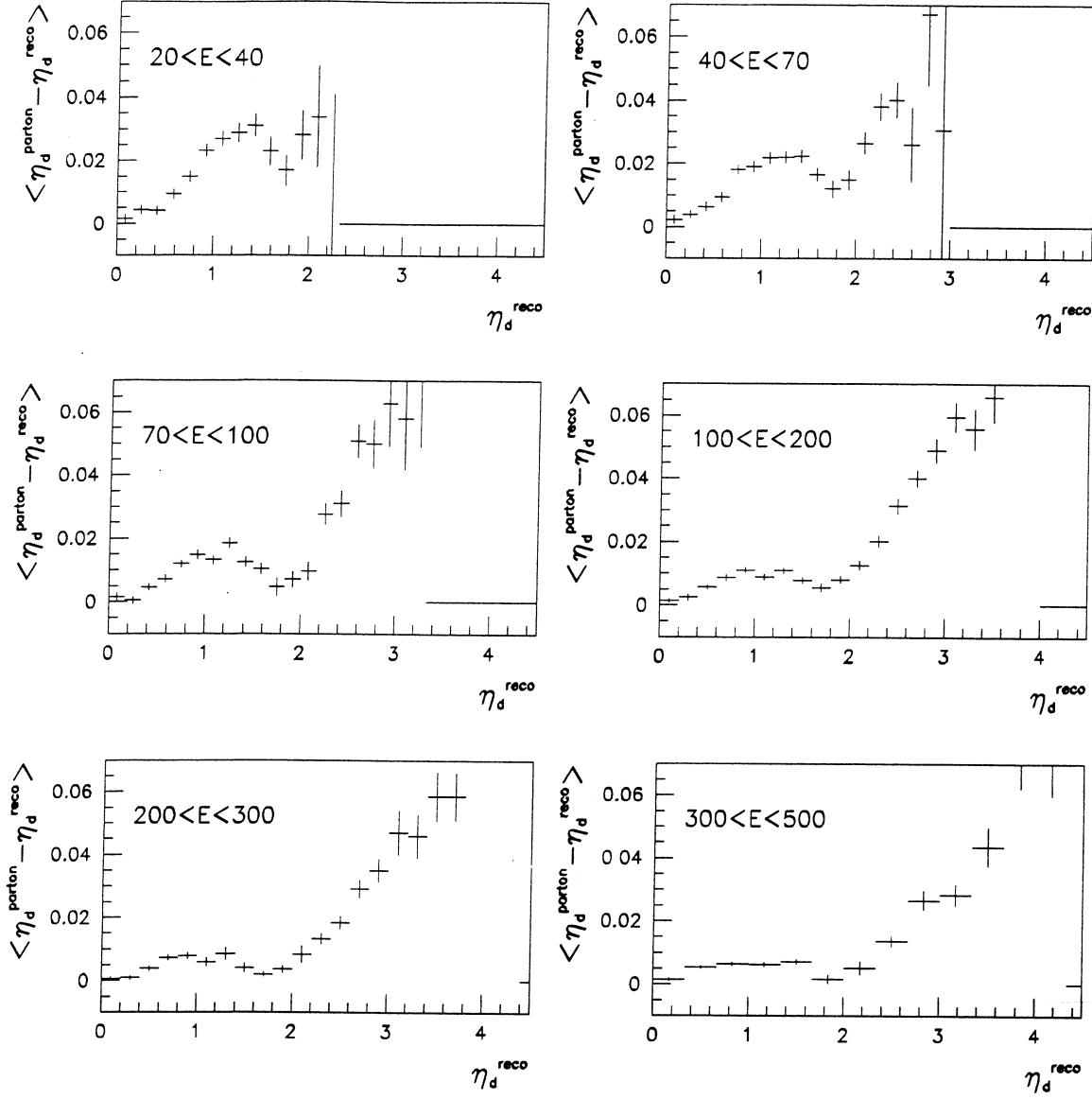


Fig. 2. HERWIG Monte Carlo simulation of the  $\eta$  bias as a function of  $\eta_d^{\text{reco}}$  and energies(GeV).

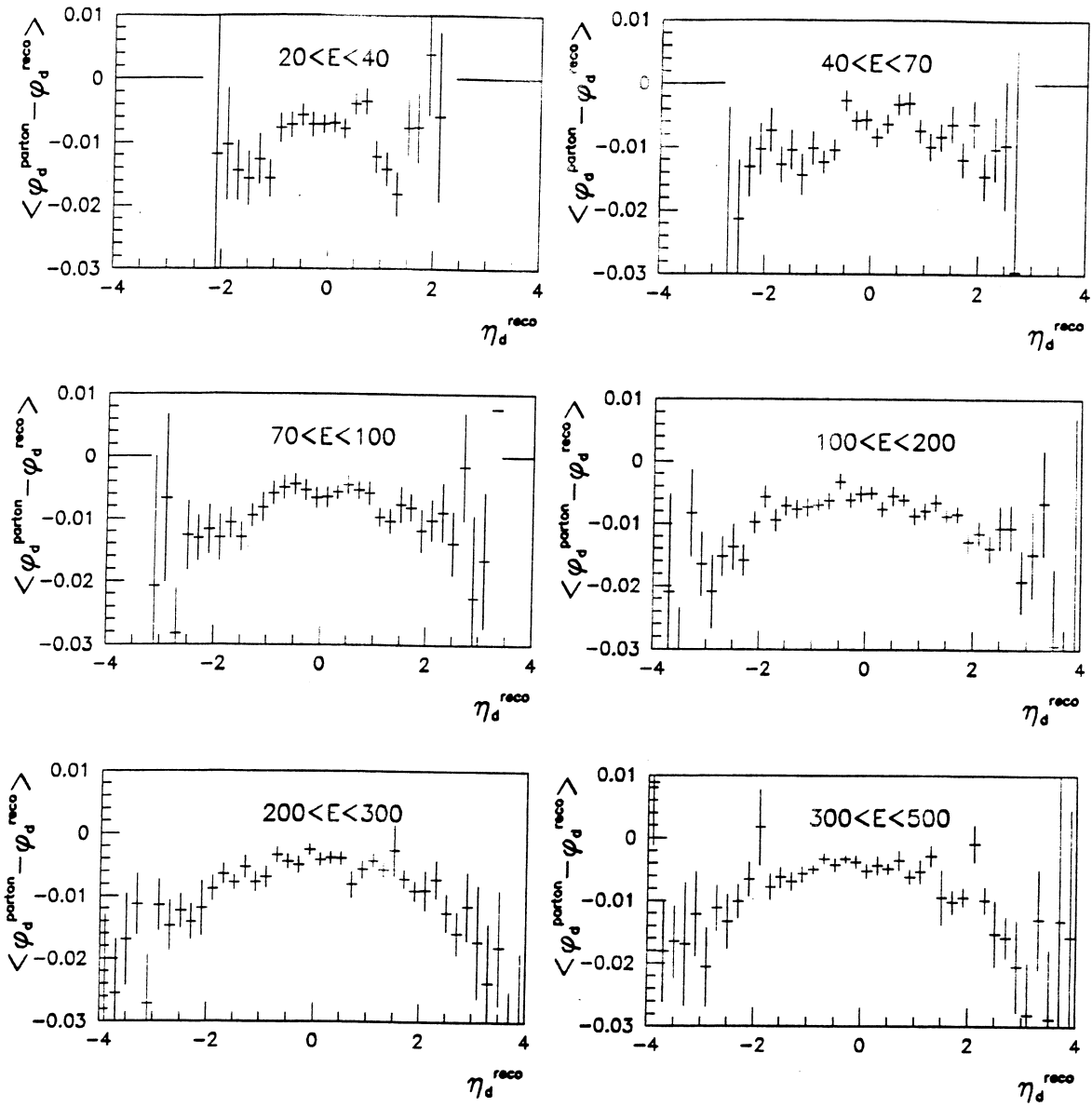


Fig. 4. HERWIG Monte Carlo simulation of the  $\phi$  bias between parton jets and calorimeter jets as a function of  $\eta_d^{\text{reco}}$  and energies(GeV)





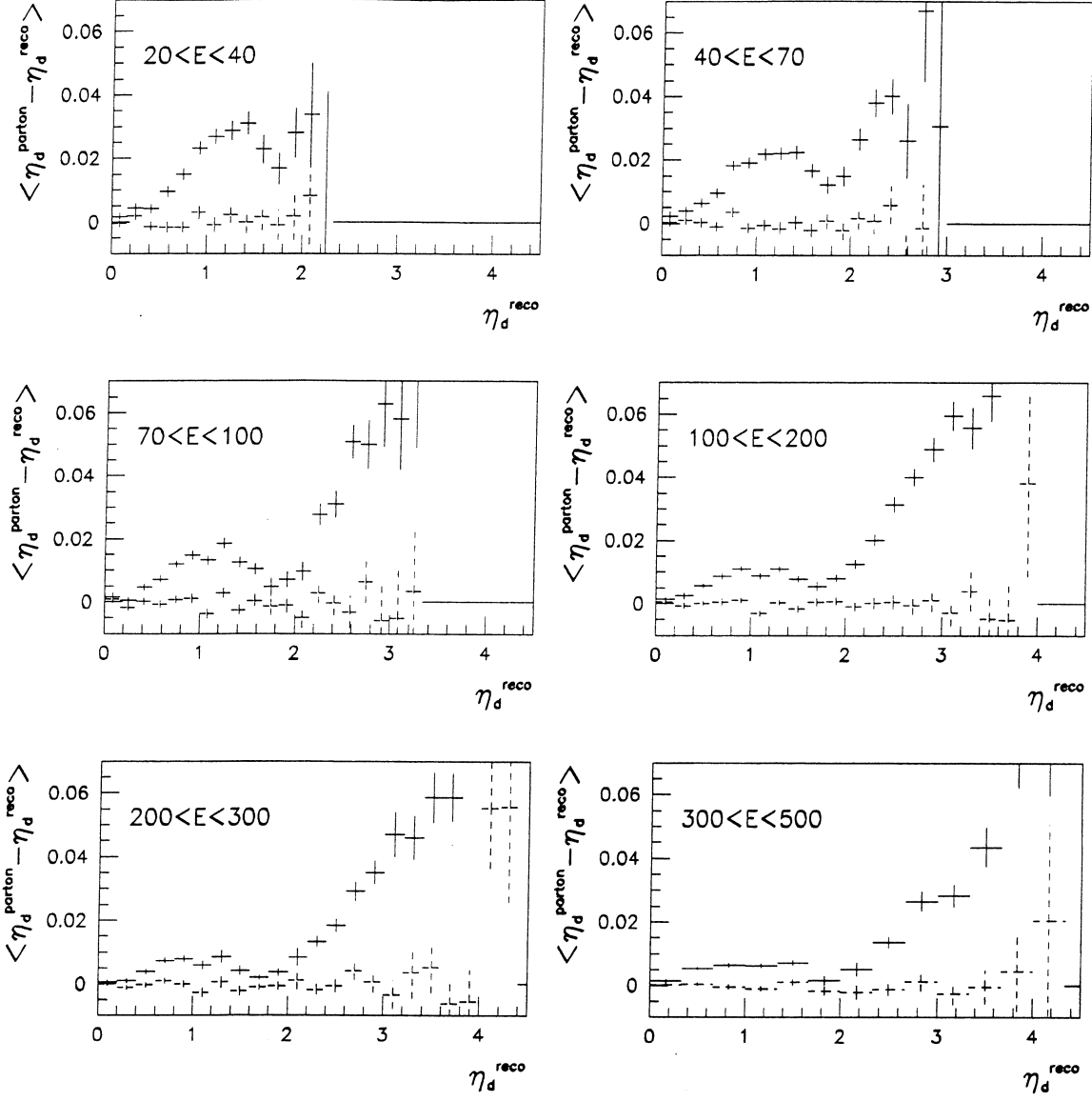


Fig. 5. HERWIG Monte Carlo simulation of the  $\eta$  bias.  $\langle \delta(E_{jet}^{\text{reco}}, \eta_d^{\text{reco}}) \rangle$  before the correction is plotted as a solid line, and the dotted line represents the bias after the correction.

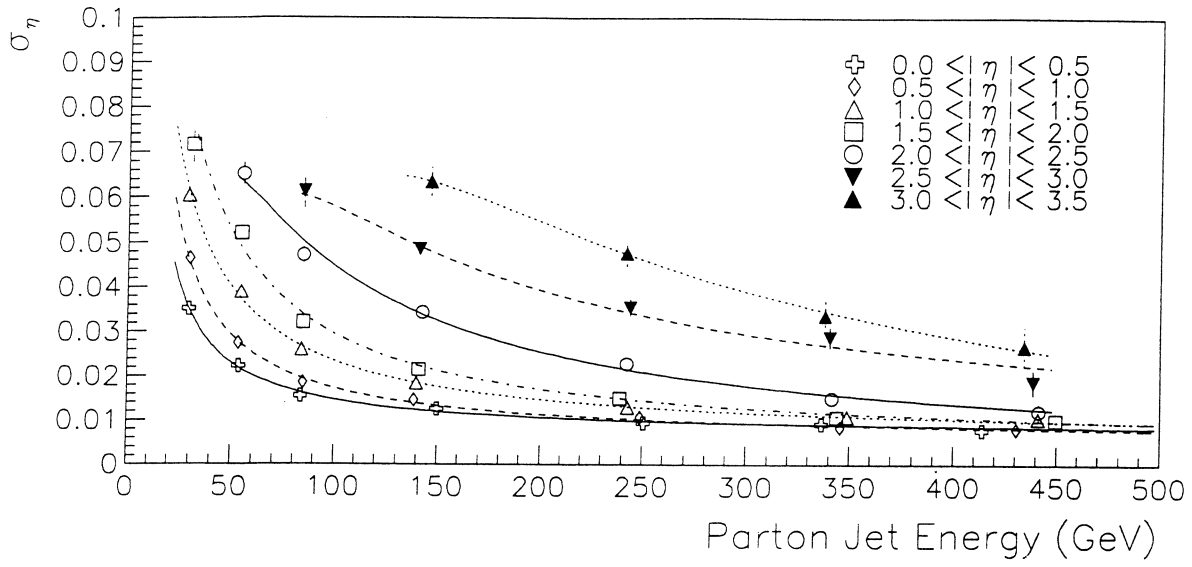


Fig. 6. The  $\eta$  resolution from HERWIG Monte Carlo simulation

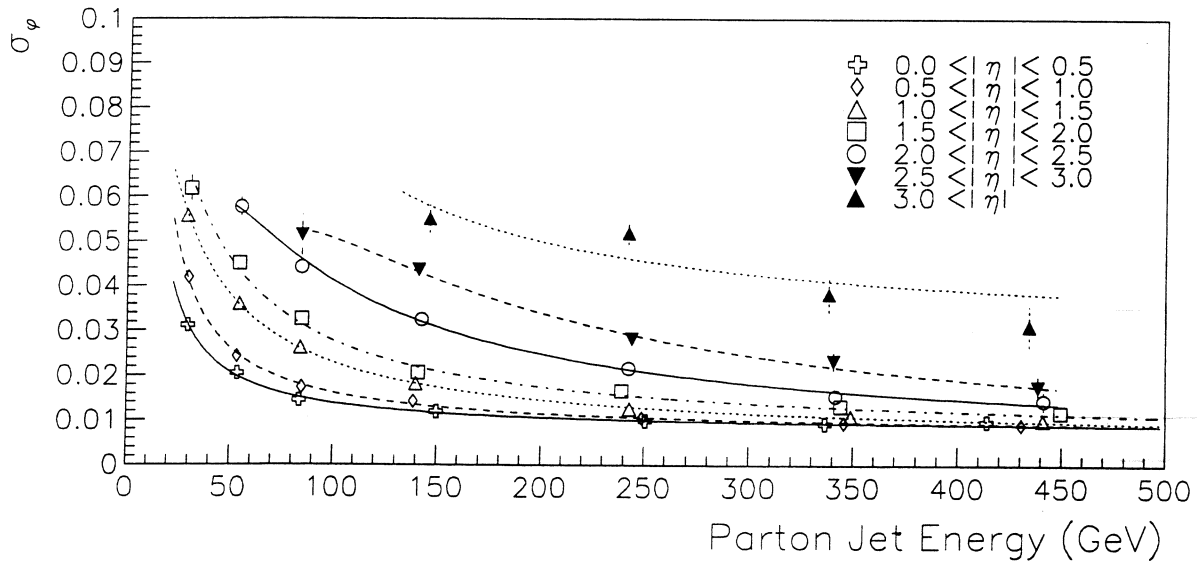


Fig. 7. The  $\phi$  resolution from HERWIG Monte Carlo simulation

DØ note #2769  
November 10, 1995

# Effects of $\eta$ and $\phi$ Definitions on Reconstructing Jets

Brad Abbott  
New York University

## Abstract

The effects of changing the  $\eta$  and  $\phi$  definition of jets from the standard DØ method to the Snowmass definition are investigated.

# 1 Introduction

Large effects in NLO parton calculations due to the definition of  $\eta$  and  $\phi$  were discovered by calculating the theoretical jet shape. This prompted some theorists to investigate the cause of this large effect. Their studies showed problems at NLO using the standard DØ  $\eta$  and  $\phi$  definitions and that these definitions should not be used at NLO. The effects of the different  $\eta$  and  $\phi$  definitions were studied in DØ data and are presented in this note.

## 2 Reconstructing jets at DØ

The process of reconstructing jets consists of a series of iterative processes. First, towers with transverse energy of 1.0 GeV or more are used as seed towers for finding preclusters, which are formed by adding neighboring towers within a radius of  $R_{\eta\phi} = 0.3$  to seed towers. We define  $R$  as

$$\sqrt{(\eta_{jet} - \eta_t)^2 + (\phi_{jet} - \phi_t)^2} \leq R$$

where  $(\eta_t, \phi_t)$  is the center of a calorimeter tower. The  $\eta$  of each tower is calculated with respect to the interaction vertex, which is determined from the tracking system.

Next, a fixed cone radius  $R$  is drawn around each precluster centered at  $(\eta_{jet}, \phi_{jet})$ . A new jet center  $(\eta_{jet}, \phi_{jet})$  is then calculated using the Snowmass accord.

$$\eta_{Snowmass} = \frac{\sum_i E_{Ti} \eta_i}{\sum_i E_{Ti}}$$

$$\phi_{Snowmass} = \frac{\sum_i E_{Ti} \phi_i}{\sum_i E_{Ti}}$$

where the sum over  $i$  is over all towers that are within the jet radius  $R$ .

Using this new jet center, this process is then repeated until a stable jet center is found. After a stable jet center is found,  $\eta_{jet}$  and  $\phi_{jet}$  are recalculated using the DØ algorithm for determining  $\eta_{jet}$  and  $\phi_{jet}$ .

$$\eta_{jet} = -\ln(\tan(\theta_{jet}/2))$$

$$\phi_{jet} = \tan^{-1} \frac{\sum_i E_{yi}}{\sum_i E_{xi}}$$

where

$$\theta_{jet} = \tan^{-1} \frac{\sqrt{(\sum_i E_{xi})^2 + (\sum_i E_{yi})^2}}{\sum_i E_{zi}}$$

$$E_{xi} = E_i \sin(\theta_i) \cos(\phi_i)$$

$$E_{yi} = E_i \sin(\theta_i) \sin(\phi_i)$$

$$E_{zi} = E_i \cos(\theta_i)$$

The transverse energy of a jet is defined as the sum of the transverse energy within each calorimeter tower which is located within the jet cone.

$$E_{Tjet} = \sum_i E_{Ti}$$

$$E_{Ti} = E_i \sin(\theta_i)$$

After the preliminary set of jets has been found, overlapping jets can be merged into a single jet or the energy apportioned to two individual jets. Two jets are merged into one jet if more than 50% of the lower energy jet's  $E_T$  is contained in the overlap region. The center of the new jet is defined as the vector sum of the original two jet centers, and the energy of the merged jet is the sum of the energy of the original two jets. If less than 50% of the lower energy jet's  $E_T$  is contained in the overlap region, the jets are classified as split. In this case, the energy of each cell in the overlap region is assigned to the nearest jet, and the jet directions are recalculated.

### 3 Jets at NLO

Because of the large effects due to different  $\eta$  and  $\phi$  definitions at NLO, Nigel Glover and David Kosower investigated the reason for these large effects [1]. Two quantities were studied to investigate these discrepancies. The event's "jet momentum fraction" is defined as:

$$x_{jet} = \max_{\sigma=\pm} \sum_{jetsj} E_T e^{\sigma\eta_j}$$

and the fractional energy defect for each jet is

$$\Delta\epsilon = (E_{jet} - \sum_{i \in jet} E_i) / \sum_{i \in jet} E_i$$

At NLO  $x_{jet}$  is strictly less than 1 ( $x_{jet} = \max(x_1, x_2)$ ). Events with  $x_{jet} > 1$  will have large higher order corrections, since they are forbidden at lowest order. Their studies show that the DØ recombination scheme can produce events with  $x_{jet} > 1$ , potentially causing large higher order corrections. In contrast, the Snowmass algorithm contained no events with  $x_{jet} > 1$ .

The energy defect in the central region was shown to be negative for both the Snowmass and DØ clustering methods. Because of the rapidly falling jet cross section, jets with negative energy defect will cause little effect due to their lower weight. In the forward region, the Snowmass clustering was also shown to have a negative energy defect. The DØ method, however, can produce a positive energy defect, potentially causing problems at NLO due to their larger weight.

## 4 Effect of $\eta$ and $\phi$ on DØ data

This theoretical study prompted DØ to investigate the effects of the two different  $\eta$  and  $\phi$  definitions in data. Two identical data sets were reconstructed; one using the standard DØ method and the other using the Snowmass angles for all steps of the reconstruction. All triggers were accepted and all jets with a cone radius of 0.7 were studied.

Figures 1 and 2 show the effects on the reconstructed jet's  $\phi$  due to changing the reconstruction algorithm from DØ to Snowmass. Very little change in the  $\phi$  distributions occur. Since the jet's  $\phi$  is unaffected, jets were matched event by event in  $\phi$  to compare the effects of the different clustering algorithms on both  $E_T$  and  $\eta$ .

Figures 3 - 10 show the effects on both  $E_T$  and  $\eta$  due to changing the reconstruction method from standard DØ to Snowmass. Little effects in the jet  $E_T$  occur. Small effects in the reconstructed jet's  $E_T$  are expected since only the  $\eta$  and  $\phi$  of the jets were changed. Two sources can produce a change in the jet's  $E_T$ . The first arising from the splitting and merging of jets, and the second due to the  $\eta$  dependence of CAFIX.

In the central region ( $|\eta| < 1$ ), the change in  $\eta$  is less than 0.02, with the Snowmass definition producing more central jets. In the forward region ( $2 < |\eta| < 3$ ), the change in  $\eta$  is much larger. Changes of 0.05 occur on average, again with Snowmass producing more central jets.

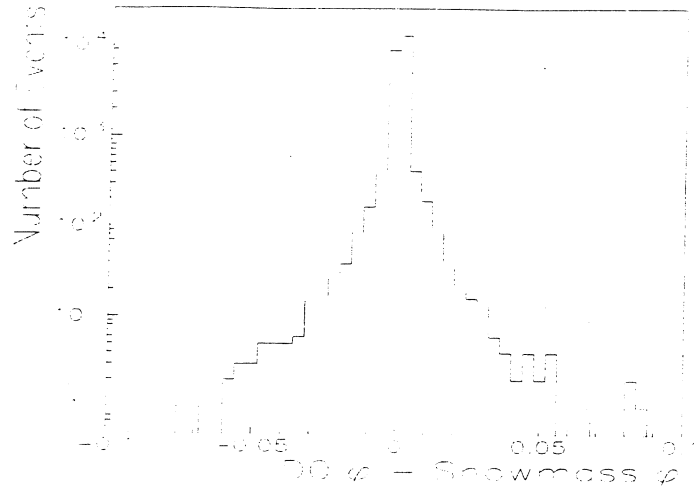


Figure 1: The difference in the jet's  $\phi$  due to changing the reconstruction algorithm from DØ to Snowmass.

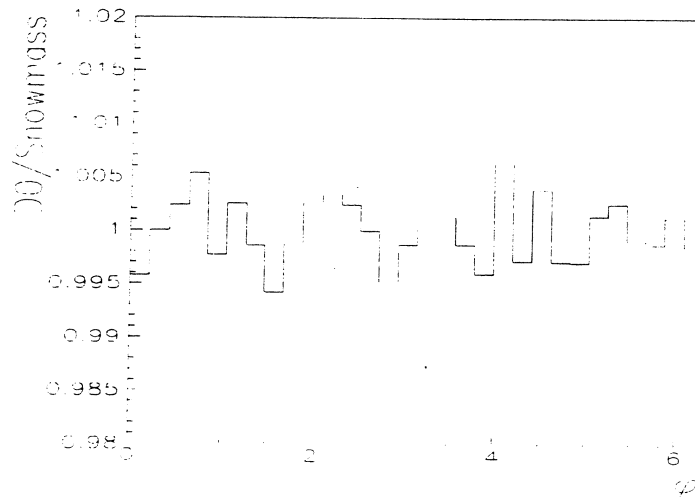


Figure 2: The average variation in  $\phi$  due to changing the reconstruction algorithm from DØ to Snowmass.



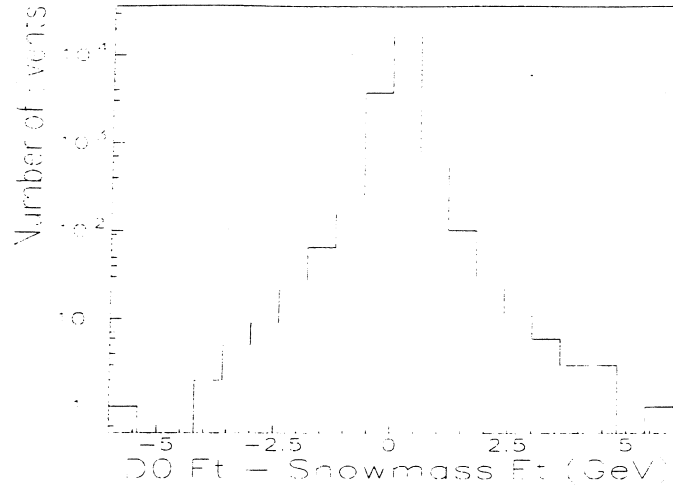


Figure 3: The change in the reconstructed jet's  $E_T$  due to changing the reconstruction algorithm from the standard DØ method to Snowmass.

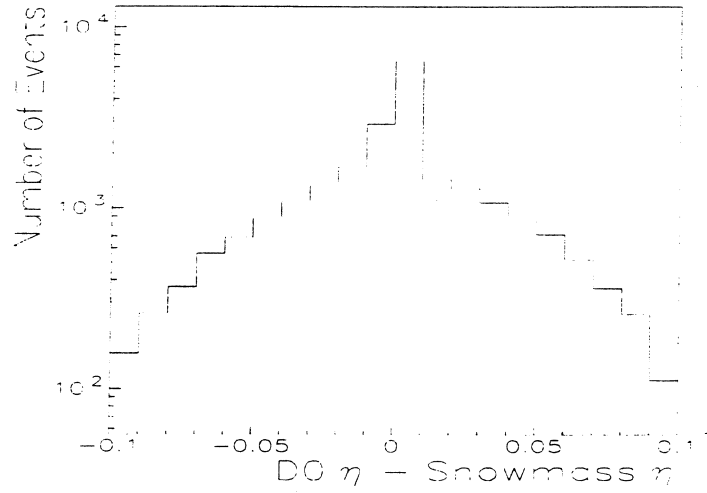


Figure 4: The change in the reconstructed jet's  $\eta$  due to changing the reconstruction algorithm from the standard DØ method to Snowmass.

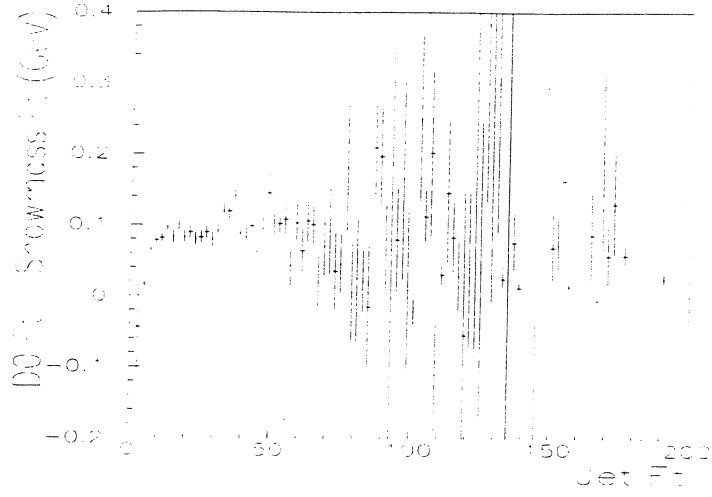


Figure 5: The change in the reconstructed jet's  $E_T$  as a function of  $E_T$  due to changing the reconstruction algorithm from the standard DØ method to Snowmass.

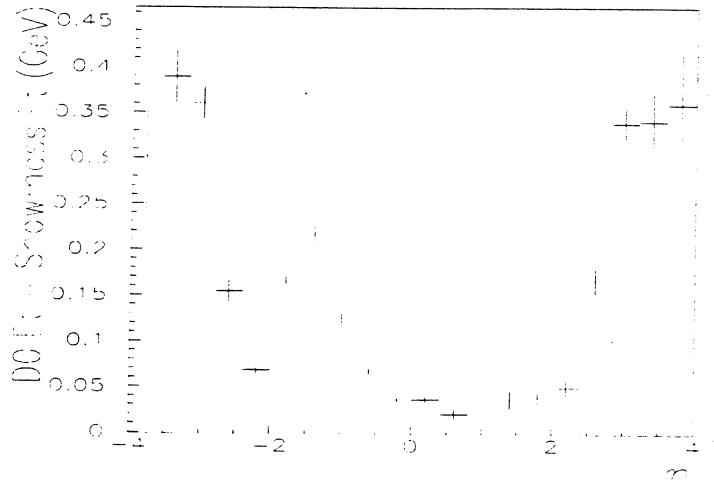


Figure 6: The change in the reconstructed jet's  $E_T$  as a function of  $\eta$  due to changing the reconstruction algorithm from the standard DØ method to Snowmass.

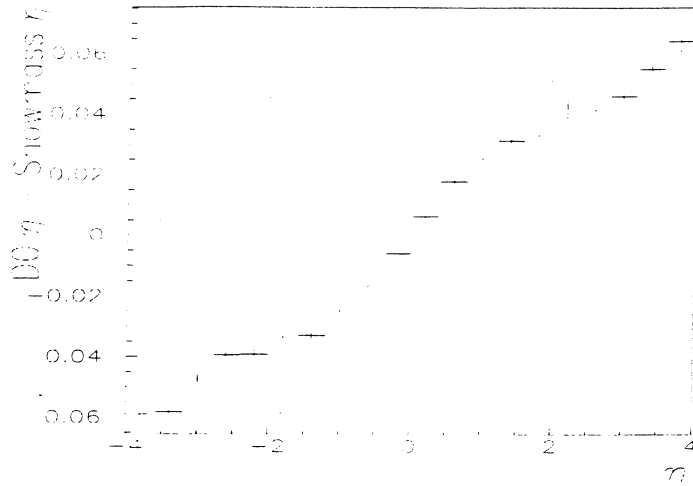


Figure 7: The change in the reconstructed jet's  $\eta$  as a function of  $\eta$  due to changing the reconstruction algorithm from the standard DØ method to Snowmass.

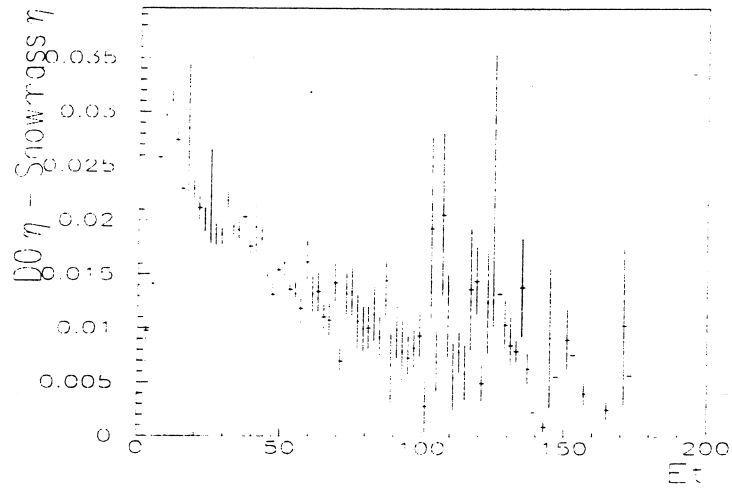


Figure 8: The change in the reconstructed jet's  $\eta$  as a function of  $E_T$  due to changing the reconstruction algorithm from the standard DØ method to Snowmass.

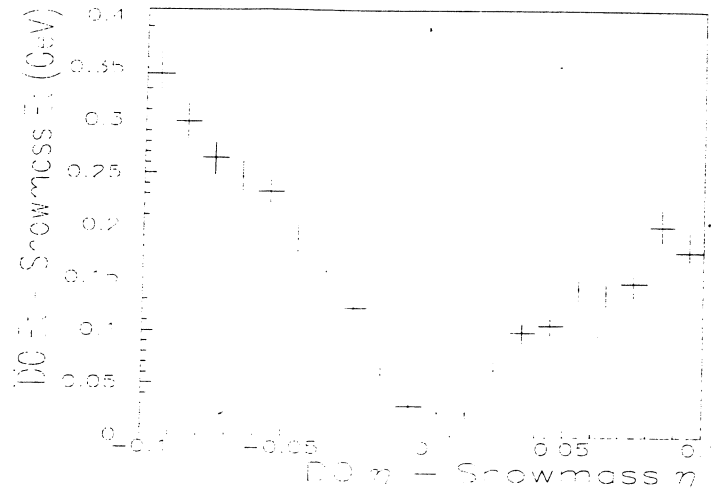


Figure 9: The change in the reconstructed jet's  $E_T$  as a function of the change in  $\eta$  due to changing the reconstruction algorithm from the standard DØ method to Snowmass.

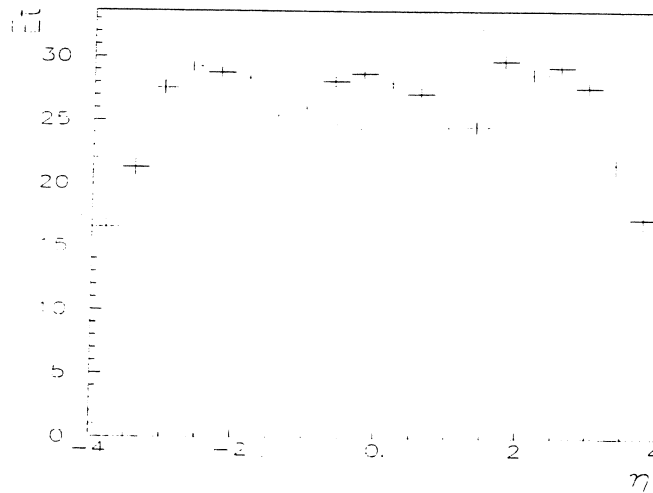


Figure 10: The average jet  $E_T$  as a function of  $\eta$ .

## 5 Conclusions

There exist large effects in the jet shape at NLO due to the definition of  $\eta$  and  $\phi$ . The standard DØ jet algorithm has been shown to potentially cause large higher order effects at NLO. The Snowmass definition of  $\eta$  and  $\phi$  does not show such behavior.

The data shows little sensitivity to the two different algorithm choices. The average change in  $\phi$  is less than 0.5%. The  $E_T$  of jets typically changed by less than 100 MeV. The largest change measured was  $\sim 5$  GeV, presumably due to merging and splitting effects.

The  $\eta$  of the jets shows the most sensitivity. Snowmass produces more central jets than DØ on average by about 0.01-0.03 for jets located in the central region and up to 0.06 on average for far forward jets.

## References

- [1] E.W.N. Glover and D.A. Kosower, *Recombination Methods for Jets in  $p\bar{p}$  Collisions*, Saclay/SPhT-T95/122

# Why You Probably Don't Understand Jet Kinematics as Well as You Think You Do

or

## Why Sometimes Small is Big

D. Lincoln

*University of Michigan, Ann Arbor, Michigan 48109, USA*

This note explores the differences between two, nominally identical, methods of measuring the kinematics of jets: Snowmass and 4-momentum. Given an identical object, the two methods report substantially different kinematics. The comparison for a 'realistic jet' is given. An argument is made for the use of the 4-momentum method.

### 1 Introduction

One of the most fundamental and important measurements that needs to be made in a hadronic environment is the kinematics of individual jets. For almost all analyses, the ability to infer the kinematics of post-collision partons is crucial. To this end, I have tried to understand what is truly necessary to accomplish this task. In this note, I explore different measuring algorithms and attempt to argue for those that are the most consistent.

The earliest physical principles taught to physics students are the nature of energy and momentum and their conservation laws. Momentum is a vector, energy is a scalar. Momentum has directional components. Energy does not.

We often talk about the 'transverse energy' of a jet. This is a nonsense concept. It stems, of course, from a tacit assumption that an entity (particle, jet, etc.) is massless and thus  $E = |p|$  (in units of  $c = 1$ ). The roots of this assumption come from two sources:

- (i) In the old days, calculations were done only to leading order, where the initial and final state partons were explicitly assumed to be massless, and
- (ii) We assume that we work at such high energies that the approximation  $E = |p|$  is valid.

A recent paper [1] has shown that earlier choices made by DØ for measuring jet kinematics had some undesirable properties. It underscored the fact that small effects, which are

commonly assumed to be zero, can cause substantial differences.

In this note, I compare the kinematics of identical objects, determined by two methods of determining jet kinematics: Snowmass and 4-momentum. I show that given the same object (i.e. after jet finding), the two algorithms give substantially different results. In order to demonstrate this, I give analytic calculations for four special cases, the most interesting being given in section A.4. The other cases are simpler and are given because they are easier to analyze and, through their simplicity, illustrate the salient points better. I follow this comparison with my opinion on why the Snowmass algorithm is probably inadequate and  $D\bar{O}$  should go entirely to the 4-momentum approach.

I should note that an investigation into this effect has been done earlier [2]. However, in this earlier investigation, no attempt to understand the mathematical, algorithmic causes for the observed discrepancies. This current note explains all observed effects.

## 2 Definitions

### 2.1 General Kinematics of Nearly-Massless Particles

To begin with, several definitions need to be made. If you have a massless particle with transverse momentum (incorrectly denoted  $E_\perp$ , in order to keep with common conventions) at direction  $(\eta, \phi)$

$$E = E_\perp \cosh \eta \tag{1}$$

$$p_x = E_\perp \cos \phi \tag{2}$$

$$p_y = E_\perp \sin \phi \tag{3}$$

$$p_z = E_\perp \sinh \eta \tag{4}$$

$$p_\perp = \sqrt{p_x^2 + p_y^2} = E_\perp \tag{5}$$

$$p = \sqrt{p_x^2 + p_y^2 + p_z^2} = E \tag{6}$$

$$\theta = \arccos(p_z/p) = \arccos(\tanh \eta) \tag{7}$$

$$\phi = \arccos(p_x/p_\perp) = \phi \tag{8}$$

$$\eta = -\ln[\tan(\theta/2)] \tag{9}$$

Jets are formed of many (essentially) massless particles. For the rest of this note, I assume massless objects go into making jets.

## 2.2 Vector Sum Algorithm (a.k.a. 4-vectors)

In order to determine the kinematics of an extended object containing a number of massless objects, each having kinematics  $(E_{\perp,i}, \eta_i, \phi_i)$ , one combines them in the strictly correct manner (i.e. scalar and vector arithmetic). Thus:

$$E^{(vs)} = \sum E_{\perp,i} \cosh \eta_i \quad (10)$$

$$p_x^{(vs)} = \sum E_{\perp,i} \cos \phi_i \quad (11)$$

$$p_y^{(vs)} = \sum E_{\perp,i} \sin \phi_i \quad (12)$$

$$p_z^{(vs)} = \sum E_{\perp,i} \sinh \eta_i \quad (13)$$

$$p_{\perp}^{(vs)} = \sqrt{p_{x,(vs)}^2 + p_{y,(vs)}^2} \quad (14)$$

$$p^{(vs)} = \sqrt{p_{x,(vs)}^2 + p_{y,(vs)}^2 + p_{z,(vs)}^2} \quad (15)$$

$$m^{(vs)} = \sqrt{E_{(vs)}^2 - p_{(vs)}^2} \quad (16)$$

$$\theta^{(vs)} = \arccos(p_z^{(vs)} / p^{(vs)}) \quad (17)$$

$$\phi^{(vs)} = \arccos(p_x^{(vs)} / p_{\perp}^{(vs)}) \quad (18)$$

$$\eta^{(vs)} = -\ln[\tan(\theta^{(vs)}/2)] \quad (19)$$

$$y^{(vs)} = \frac{1}{2} \ln \left[ \frac{E^{(vs)} + p_z^{(vs)}}{E^{(vs)} - p_z^{(vs)}} \right] \quad (20)$$

$$E_{\perp}^{(vs)} = E^{(vs)} \sin \theta^{(vs)} \quad (21)$$

Note that since  $\eta$  is only a concept appropriate for massless kinematics,  $\eta^{(vs)}$  is hard to understand for a massive jet. Rapidity should be used in this case.

## 2.3 Snowmass Algorithm

The Snowmass algorithm [3] implicitly assumes that a jet is massless (which is the same thing as saying that all of the particles contained in a jet are collinear). This algorithm almost certainly does not reflect reality. Its strength stems from its manifest Lorentz invariance. Only three things are calculated with the Snowmass algorithm:  $(E_{\perp}^{(sn)}, \eta^{(sn)}, \phi^{(sn)})$ .

$$E_{\perp}^{(sn)} = \sum E_{\perp,i} \quad (22)$$

$$\eta^{(sn)} = \frac{\sum \eta_i E_{\perp,i}}{\sum E_{\perp,i}} \quad (23)$$

$$\phi^{(sn)} = \frac{\sum \phi_i E_{\perp,i}}{\sum E_{\perp,i}} \quad (24)$$



The rest of the kinematic variables are inferred:

$$p_x^{(sn)} = E_{\perp}^{(sn)} \cos \phi^{(sn)} \quad (25)$$

$$p_y^{(sn)} = E_{\perp}^{(sn)} \sin \phi^{(sn)} \quad (26)$$

$$p_z^{(sn)} = E_{\perp}^{(sn)} \sinh \eta^{(sn)} \quad (27)$$

$$E^{(sn)} = E_{\perp}^{(sn)} \cosh \eta^{(sn)} \quad (28)$$

$$\theta^{(sn)} = 2 \arctan(e^{-\eta^{(sn)}}) \quad (29)$$

$$p^{(sn)} = E^{(sn)} \quad (30)$$

$$p_{\perp}^{(sn)} = E_{\perp}^{(sn)} \quad (31)$$

$$y^{(sn)} = \eta^{(sn)} \quad (32)$$

$$m^{(sn)} = 0. \quad (33)$$

### 3 Comparison

As will be made clear in the ensuing discussion, there are substantial differences between these two algorithms. My primary approach was to take a specific collection of particles and compute the various kinematic variables for the two algorithms. Note that this approach side-steps the effect of the jet finding. The effect investigated here *solely* reflects mathematics, the nature of the non-linear transformation between  $\theta$  and  $\eta$  and the transverse size of the jet. The general case mathematics are listed in the previous section, but in order to better understand the scope of the effect, I calculated special cases. The results of these cases are given in Appendix A and are the following:

**Case 1** Two massless particles, each carrying transverse momentum  $E_{\perp}$ , at coordinates  $(\eta + \Delta_{\eta}, \phi)$  and  $(\eta - \Delta_{\eta}, \phi)$ .

**Case 2** Two massless particles, each carrying transverse momentum  $E_{\perp}$ , at coordinates  $(\eta, \phi + \Delta_{\phi})$  and  $(\eta, \phi - \Delta_{\phi})$ .

**Case 3** Four massless particles, each carrying transverse momentum  $E_{\perp}$ , at coordinates  $(\eta + \Delta_{\eta}, \phi)$ ,  $(\eta - \Delta_{\eta}, \phi)$ ,  $(\eta, \phi + \Delta_{\phi})$  and  $(\eta, \phi - \Delta_{\phi})$ .

**Case 4** A two-dimensional gaussian distribution, with RMS'  $(\sigma_{\eta}, \sigma_{\phi})$  and integrated area  $E_{\perp}$ .

Case 4 is clearly the most ‘real’ case, but the first three cases illustrate the sensitivities. The most used quantities in jet physics are transverse energy (momentum) and pseudo-rapidity. To this end, I have plotted the the quantities  $[\eta(4 - \text{momentum}) - \eta(\text{Snowmass})]/\eta(\text{Snowmass})$ ,  $\eta(4 - \text{momentum}) - \eta(\text{Snowmass})$  and  $[E_{\perp}(4 - \text{momentum}) - E_{\perp}(\text{Snowmass})]/E_{\perp}(\text{Snowmass})$ . Figures 1-7 show these quantities for Case 4. Figure 1 shows the absolute difference in  $\eta$  determined by the two methods. This figure reflects information contained in equation A.60. This equation shows that the  $\eta$  and  $\phi$  width contribute symmetrically. Figure 2 shows the  $\eta$  difference in terms of a fraction. This result was observed in an earlier DØNote [2], as seen

in figure 5. Figure 3 shows the fractional  $E_\perp$  difference as a function of  $\eta$ . This figure reflects information contained in A.59 and also demonstrates that the two widths ( $\sigma_\eta$  and  $\sigma_\phi$ ) do *not* contribute symmetrically. If one compares the difference between  $p_\perp^{(vs)}$  and  $E_\perp^{(sn)}$ , one sees that there is a constant difference, which is independent of  $\eta$ , and is only dependent on the  $\phi$  width variable. For instance, for Case 4,  $[p_\perp^{(vs)} - E_\perp^{(sn)}]/E_\perp^{(sn)} = e^{\frac{\sigma_\phi^2}{2}} - 1$ .

Figures 4-7 demonstrate the sensitivity of these differences and ratios as a function of the jet width. Typical jet widths are of the order 0.2-0.3 [4] and we thus see that the differences between the two algorithms for these important variables are of the order 5-10%. These differences are of sufficient magnitude to be important.

Figures 8-10 show similar plots for the simple geometries of Cases 1-3. The behaviors are similar and underscore that the shape of the  $E_\perp$  distribution does not strongly change the underlying effect.

### 3.1 Determining the Width from an $E_\perp$ Distribution

Determining (for Case 4) variables  $\sigma_\eta$  and  $\sigma_\phi$  is not as trivial as it would appear. These variables are the second moment (in a particular direction) from the first moment  $\eta$  or  $\phi$ . These can be different from  $\eta^{(vs)}$  and  $\phi^{(vs)}$ . However, as seen in Appendix A, we see that  $y^{(vs)} = \eta$  and  $\phi^{(vs)} = \phi$ . Thus one may find the best approximation

$$\sigma_\eta^{(vs), \text{ best approximation}} = \sqrt{\frac{\sum_i (\eta_i - y^{(vs)})^2 E_{\perp,i}}{\sum_i E_{\perp,i}}} \quad (34)$$

$$\sigma_\phi^{(vs), \text{ best approximation}} = \sqrt{\frac{\sum_i (\phi_i - \phi^{(vs)})^2 E_{\perp,i}}{\sum_i E_{\perp,i}}} \quad (35)$$

where  $(E_{\perp,i}, \eta_i, \phi_i)$  are individual massless particles/partons/etc. that go into a jet. For Cases 1-3, the approach is different, but the use of  $y^{(vs)}$  (or alternatively  $\eta^{(sn)}$ ) is important.

## 4 Deep Insights

The above discussion clearly shows that there is a substantial difference between jet kinematics determined by the 4-momentum vs. the Snowmass algorithm. What is not demonstrated is the relative merits of the two algorithms. In this section, I will argue for the 4-vector algorithm.

The strength of the Snowmass algorithm is its explicit Lorentz invariance. However, its weakness is the definition of  $E_\perp$ . Implicit in the definition is the assumption that  $E = |p|$ .

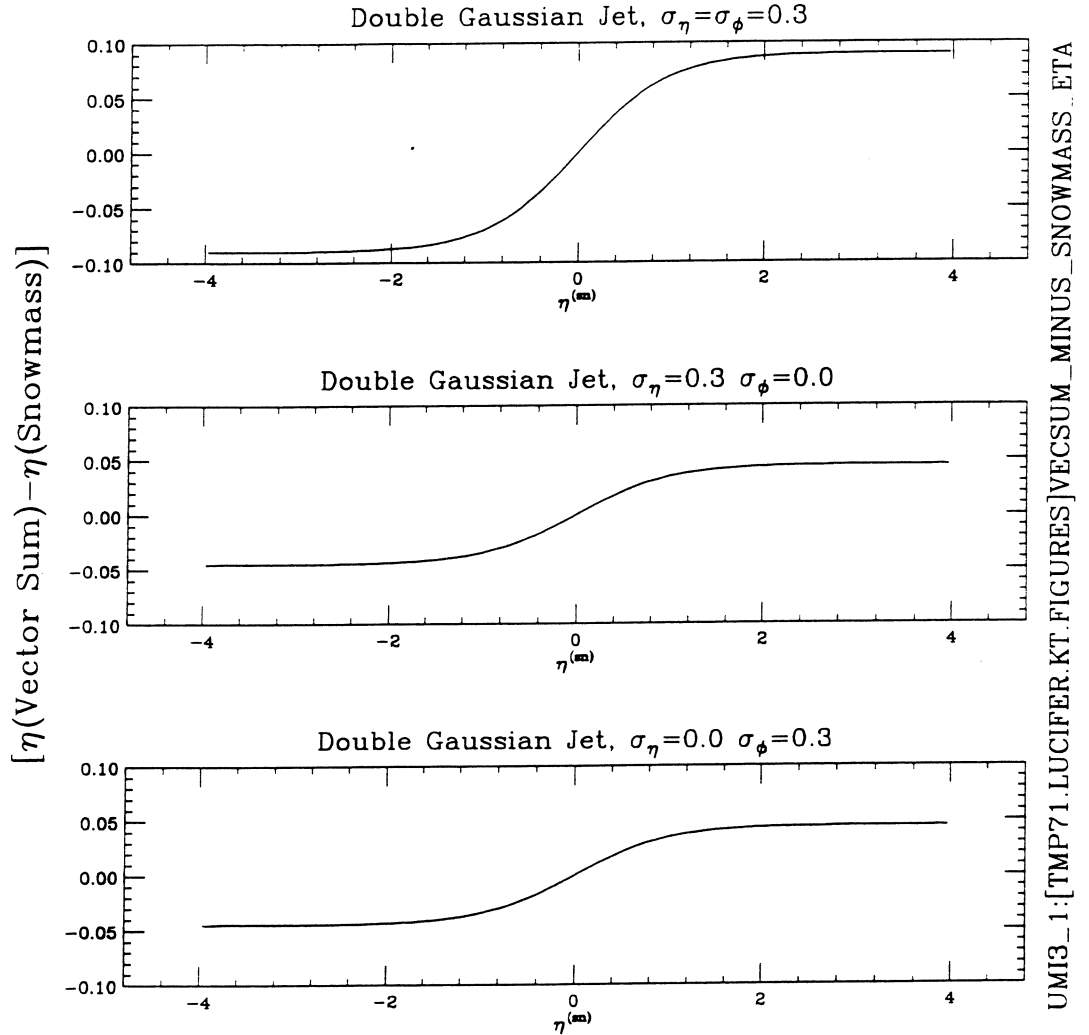


Fig. 1. This figure shows the absolute  $\eta$  difference between 4-vector and Snowmass algorithms for realistic jet shapes. The width in the  $\eta$  and  $\phi$  direction are different. The widths are given in the figure titles.

As we will see momentarily, this assumption is not valid at the  $\sim 5\%$  level.

Since the point of doing jet measurements is to relate jets to partons, the question arises: ‘Which quantities are preserved through the fragmentation process?’ This is a thornier question than it first appears. The total energy must be preserved before and after fragmentation, as must be the total momentum.

As an illustrative example, consider the simple process  $e^+e^- \rightarrow q\bar{q}$ . At leading order, two (essentially) massless quarks exit the collision. Kinematically, it is impossible to produce jets in this case. Massless particles can not produce particles with a component of momentum transverse to the initial particle’s direction. This point is discussed in [5]. Since we know that jets do contain such particles, something else must be going on. The two possibilities are:

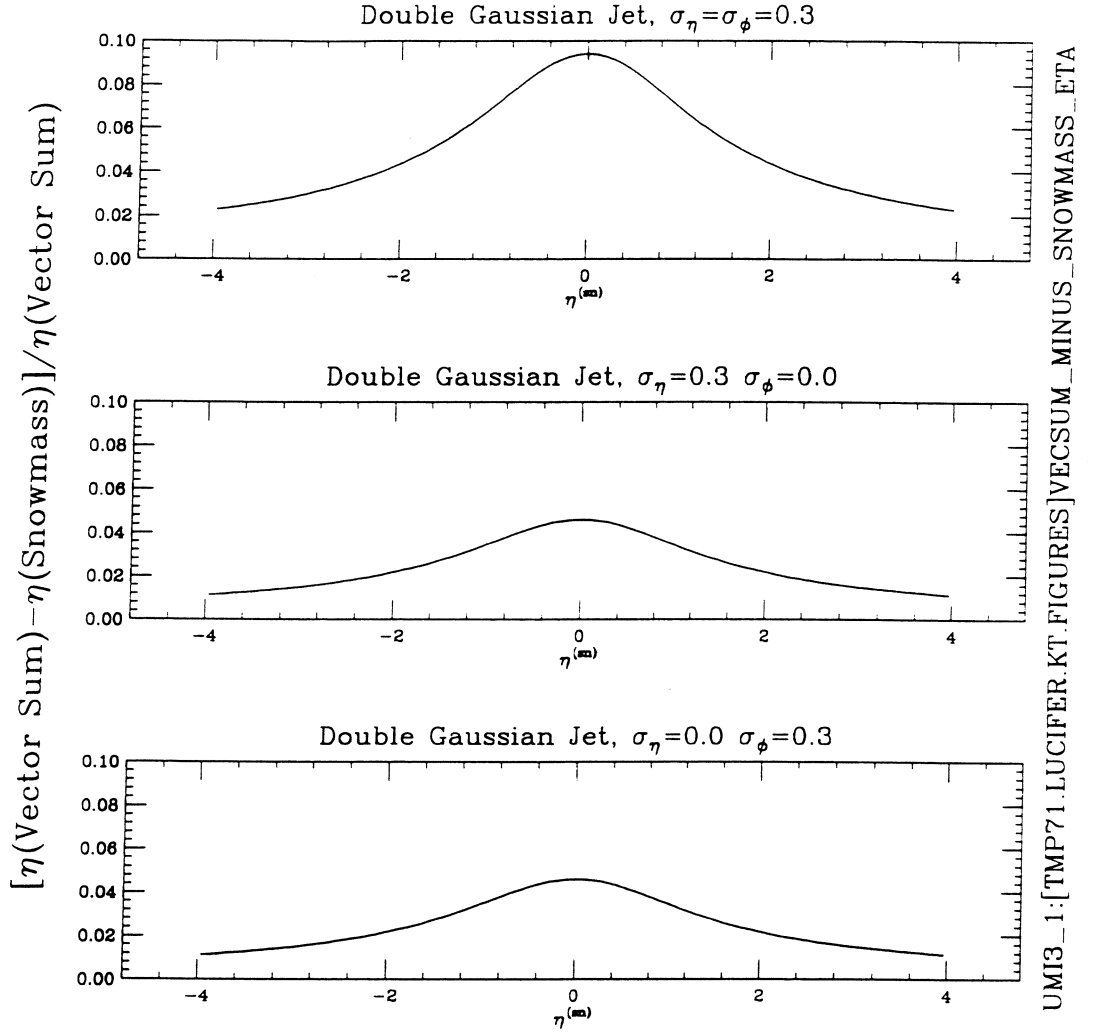


Fig. 2. This figure shows the fractional  $\eta$  difference between 4-vector and Snowmass algorithms for realistic jet shapes. The width in the  $\eta$  and  $\phi$  direction are different. The widths are given in the figure titles.

- (i) The quarks exit the collision without mass, but post-collision interactions (fragmentation) cause the  $E-p$  difference. As the quarks exit the collision, they feel a color force between them. The quarks slow as they separate and the kinetic energy is changed into the potential energy stored in the color field between them (like a rubber band stores energy). When the energy density in the color field becomes  $\sim 1 \text{ GeV/fm}$ , the vacuum breaks down, and  $q\bar{q}$ 's are produced. It is worth noting that this process conserves global energy and *net* momentum. Immediately after the collision, the net momentum is zero. After fragmentation, the net momentum is still zero. Taken to a kinematic extreme, the quarks could conceivably 'decay' into two very massive particles at rest.
- (ii) The quarks could be produced in a 'virtual' state. That is, due to the Heisenberg Uncertainty Principle, massless quarks could be produced such that  $E \neq |p|$  and thus have a large (but virtual) mass. Kinematics allows this virtual mass to be converted

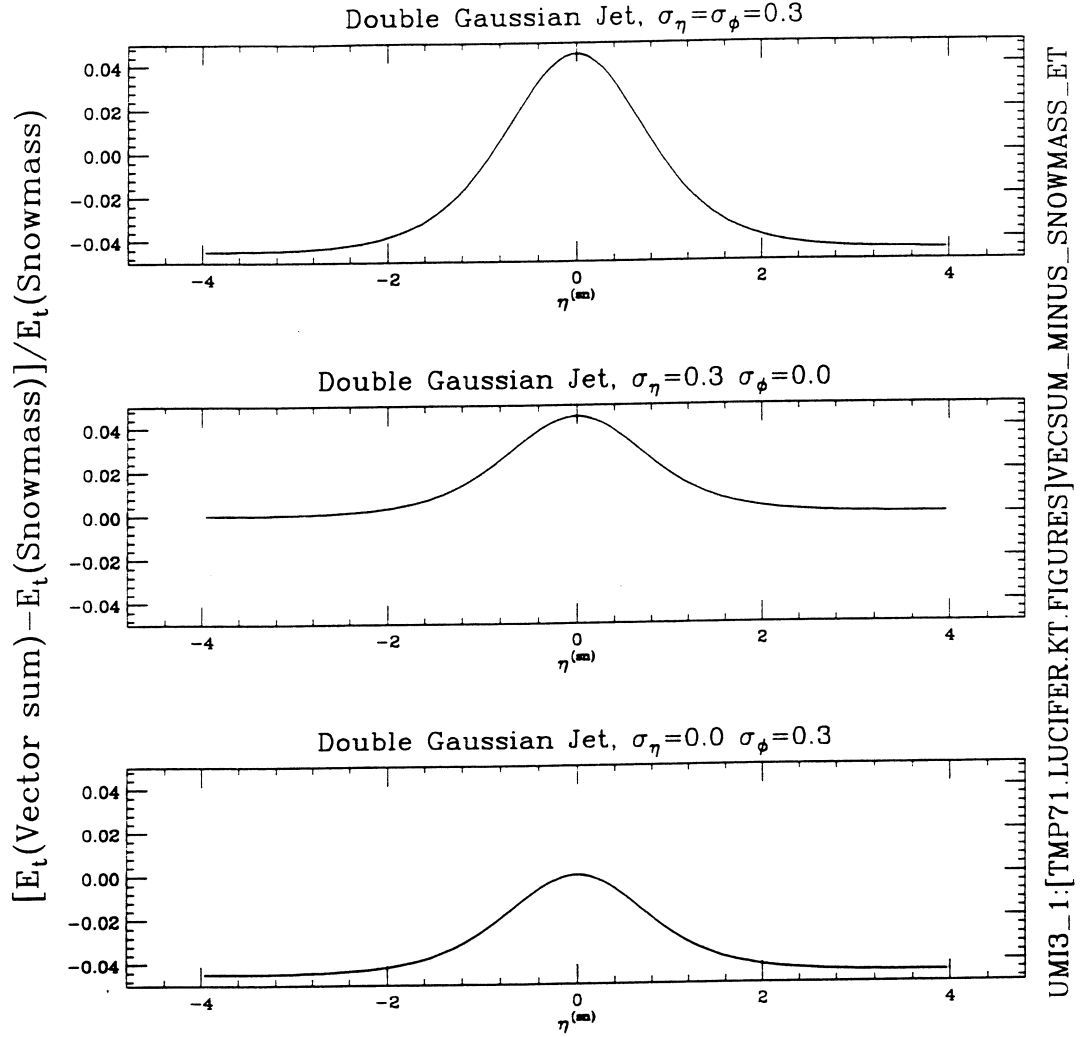


Fig. 3. This figure shows the fractional  $E_\perp$  difference between 4-vector and Snowmass algorithms for realistic jet shapes. The width in the  $\eta$  and  $\phi$  direction are different. The widths are given in the figure titles.

into energy transverse to the original quark's direction.

What actually occurs is unknown, but probably includes both effects. The distinction is, in part, an artifact of fixed order theory. In leading order theory, case (i) must be the case, as the quarks are treated as massless. At higher orders, both effect are possible, as the final quarks exiting the collision have (essentially) no mass (ignoring for the moment the heavy quarks). However, if a parton-level jet-finding algorithm is run which can combine nearby non-collinear partons, the combination of the partons can not have  $E = |p|$ . Thus the parton nearer the hard collision (which fragmented into the two quarks which were subsequently combined) would have to have a virtual mass.

These observations argue that the things that must be preserved across the fragmentation barrier are energy and angles. The reasoning is the following. In the simple  $e^+e^-$  case, all

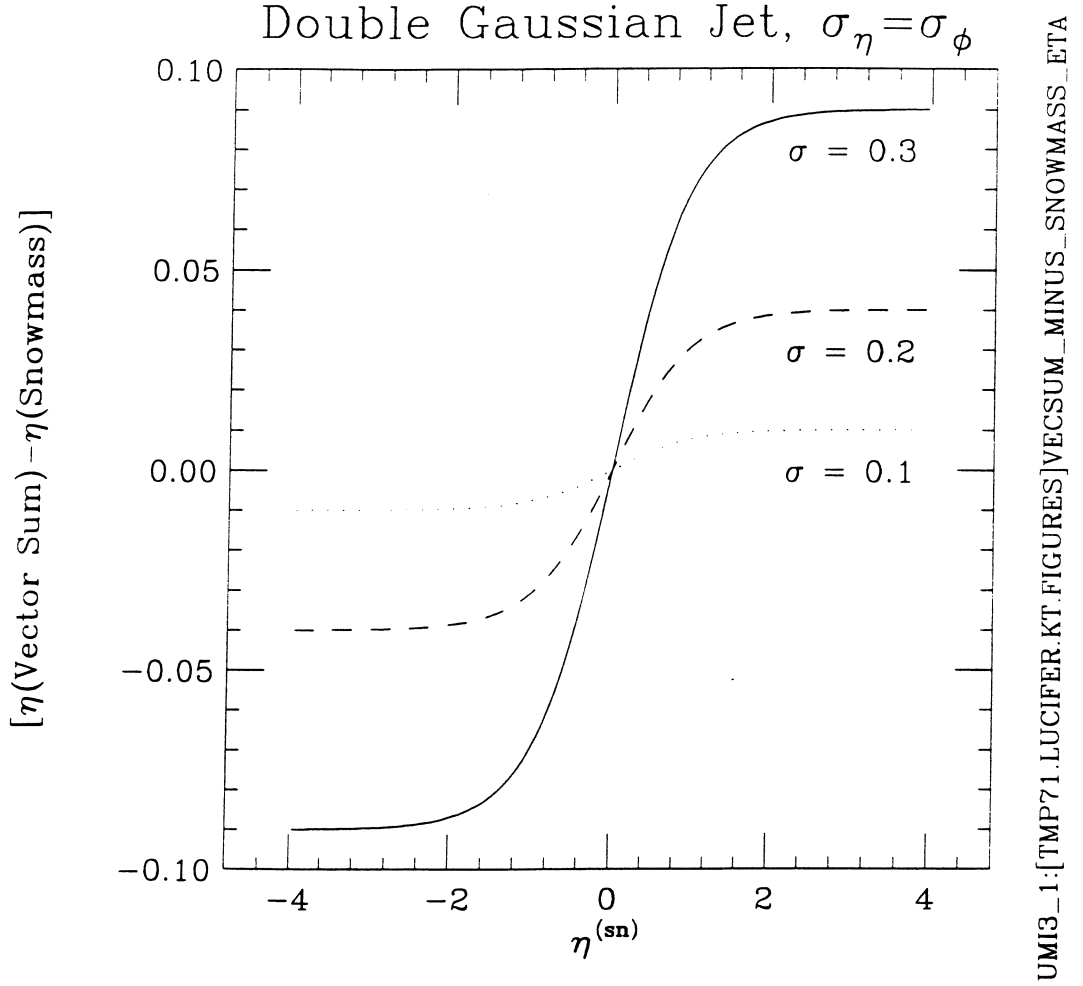


Fig. 4. This figure shows the absolute  $\eta$  difference between 4-vector and Snowmass algorithms for realistic jet shapes. The width in the  $\eta$  and  $\phi$  direction are the same, but the different curves show the different widths.

particles are contained in jets. The energy of a particular jet can be high compared to the parent parton, but the other must compensate by fluctuating low. By symmetry, the average must be preserved. Similarly, there is no preferred direction. A jet direction may fluctuate away from a parton direction, but since there is no preferred direction, on average there can be no offset.

Note that momentum does not have to be preserved within a jet. For instance, in case (i), the jet can have very much less momentum than the initial massless (Born level) quark. On the other hand, the kinematically correct thing to balance is  $p_\perp$  and not  $E_\perp$ . This is further demonstrated when one calculates the  $E_\perp$  after an arbitrary boost. Defining, as we have,  $E_\perp = E \sin \theta$  and similarly  $E'_\perp = E' \sin \theta'$ , boosting  $E$  and  $\theta$  separately, one can find the

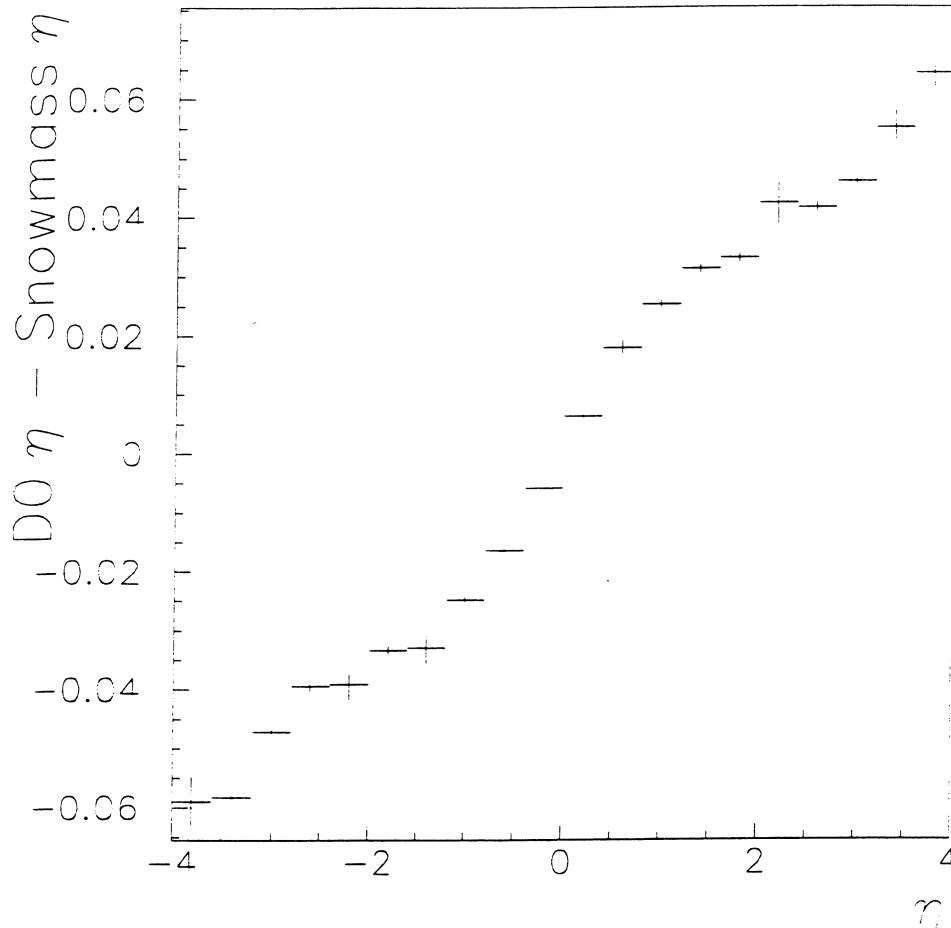


Fig. 5. This figure shows the absolute  $\eta$  difference between 4-vector and Snowmass algorithms for  $D0$  data. It suggests that a jet width of 0.2 is valid for central  $\eta$ , but this jet width grows at larger  $\eta$ .

following:

$$\frac{E'_\perp}{E_\perp} = \frac{\gamma(1 - \beta \frac{p}{E} \cos \theta)}{\sqrt{\sin^2 \theta + \gamma^2(\cos \theta - \beta \frac{E}{p})^2}} \quad (36)$$

where  $\beta$  &  $\gamma = 1/\sqrt{1 - \beta^2}$  are the usual Lorentz boost variables. A little arithmetic will show that this ratio is unity only if  $E = p$ . This implies that if one wishes to define  $E_\perp = E \sin \theta$ , then one must further define  $E = p$  in order to force that the  $p_\perp$  Lorentz invariance of the massless partons be reflected in the jet.

Figure 11 shows the ratio  $E'_\perp/E_\perp$  for the specific ratio  $E/p = 1.05$ . The ratio is near unity except for the poles  $(\beta, \theta) = (1, 0)$  and  $(-1, \pi)$ . Figure 12 shows the same plot, but with

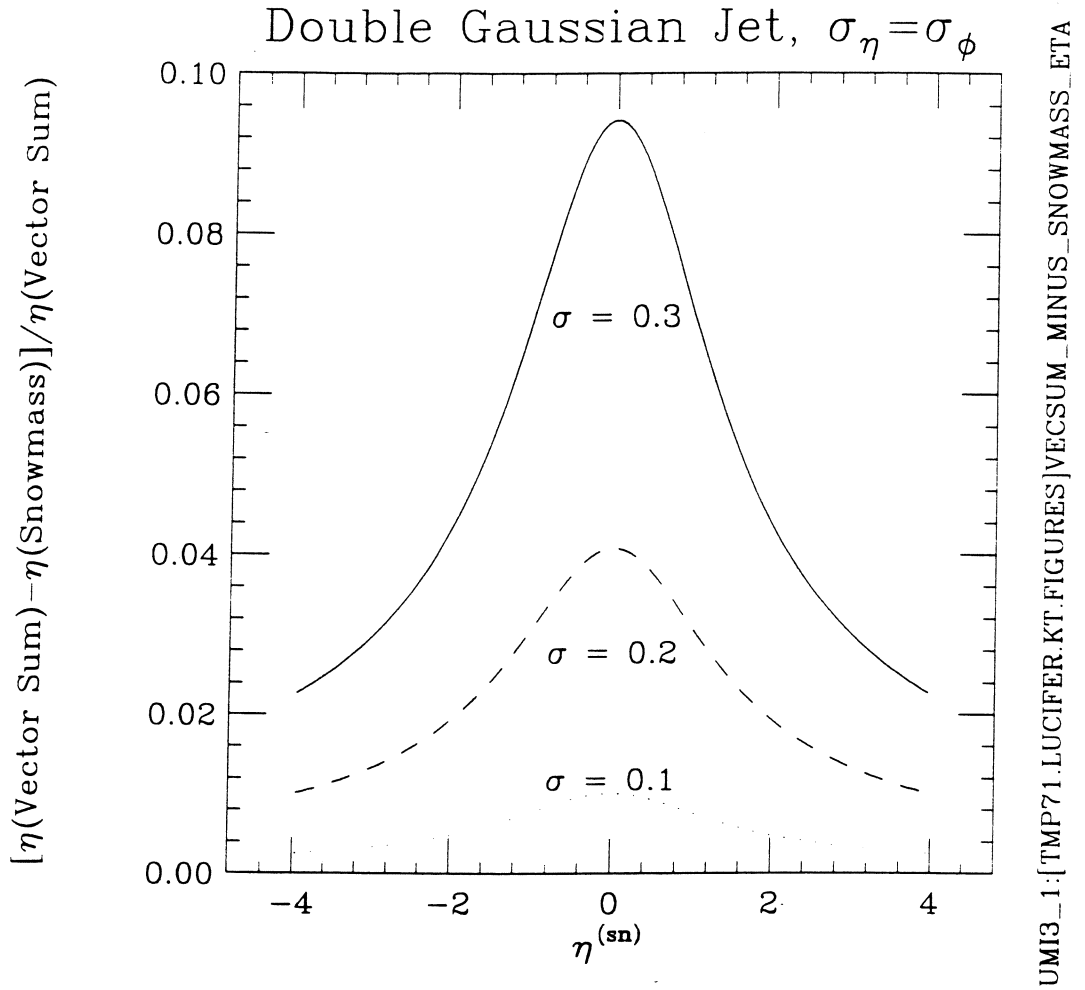


Fig. 6. This figure shows the fractional  $\eta$  difference between 4-vector and Snowmass algorithms for realistic jet shapes. The width in the  $\eta$  and  $\phi$  direction are the same, but the different curves show the different widths.

the truncation  $|\beta| < 0.4$ . The non-Lorentz invariance is substantial. The choice of  $E/p$  used is justified by figure 13. This plot is a Monte Carlo (HERWIG) in which dijet events are generated, with partons in the  $E_\perp$  range of 15-500 GeV. Over this entire range, the mean of the  $E/p$  ratio is about 1.05. Data looks very similar. The jet-finder in this example is the  $k_\perp$  jet finder with  $D = 1$ . This gives results similar to the more common  $(\eta, \phi)$  cone jet finder with  $R = 0.7$ .

## 5 Summary and Conclusions

In this note I have tried to understand the differences between two jet-kinematic measuring algorithms. I have argued that one algorithm is intrinsically flawed (Snowmass), but that the other has its own problems. The  $\eta$  bias in many of the variables is not a real problem,



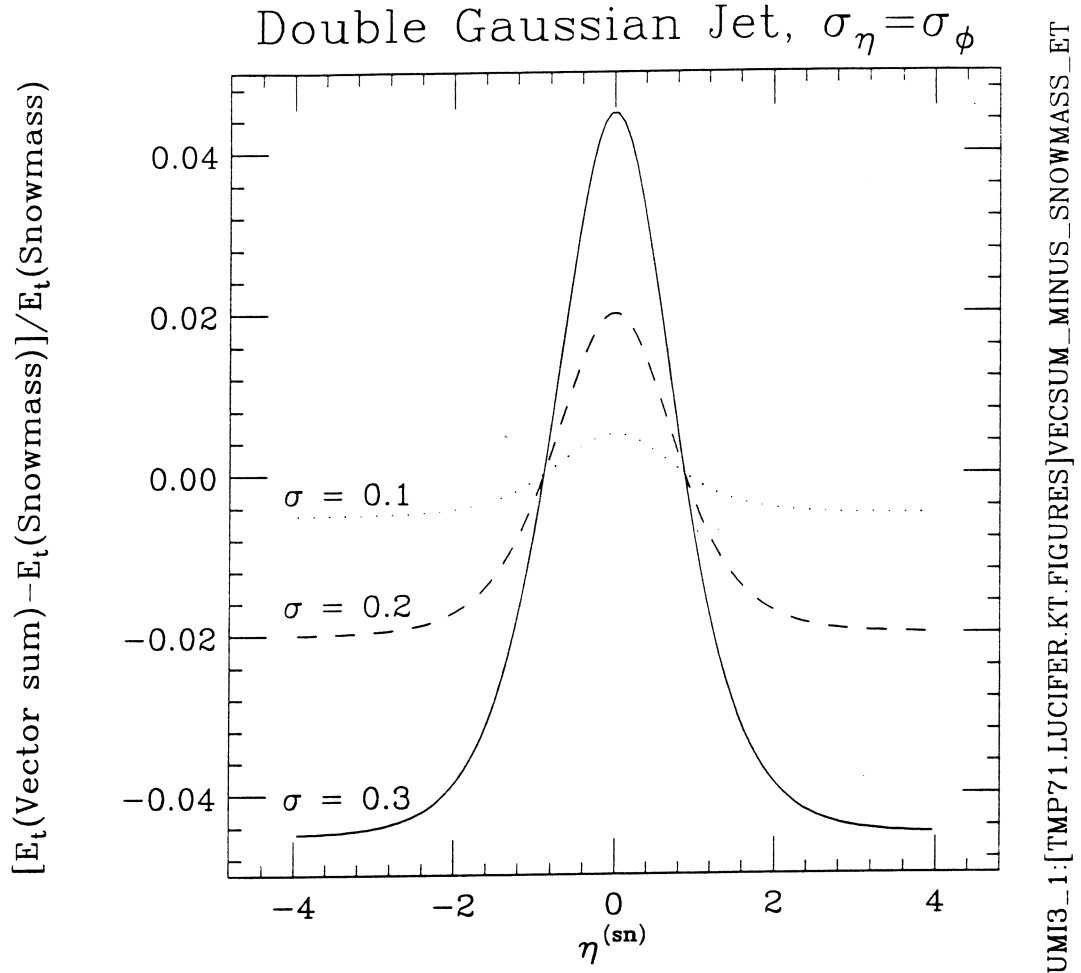


Fig. 7. This figure shows the fractional  $E_\perp$  difference between 4-vector and Snowmass algorithms for realistic jet shapes. The width in the  $\eta$  and  $\phi$  direction are the same, but the different curves show the different widths.

since we do an  $\eta$ -dependent correction anyways. It is possible that ~~some of that~~ correction reflects this algorithm effect. It is possible that the additional insight that the width of the jet affects the size of the correction may be used to improve jet resolution.

To recap, I believe that 4-vector kinematics are the best ones to use. They are defensible on very basic physics grounds and involve no approximations. The implications are if one uses  $E_\perp^{(vs)} = E^{(vs)} \sin \theta^{(vs)}$ , then it is necessary to assign a zero mass to the jet in order to get a comparable Lorentz invariance to the zero-mass parton. My own opinion is this is also a flawed idea. The thing that we measure is the simple 4-vector of the jet  $p^\mu$ . The fact that the theory is not capable of predicting this 4-vector with great accuracy is a theoretical problem, not an experimental one. We can compare the jet cross-section as a function of  $p_\perp$  with the (nominally) identical cross-section of the parton. Since the jet has an  $E$ - $p$  misbalance that is not reflected in leading order partons, they will not agree. However, this difference is physics and I believe that we should highlight this point.

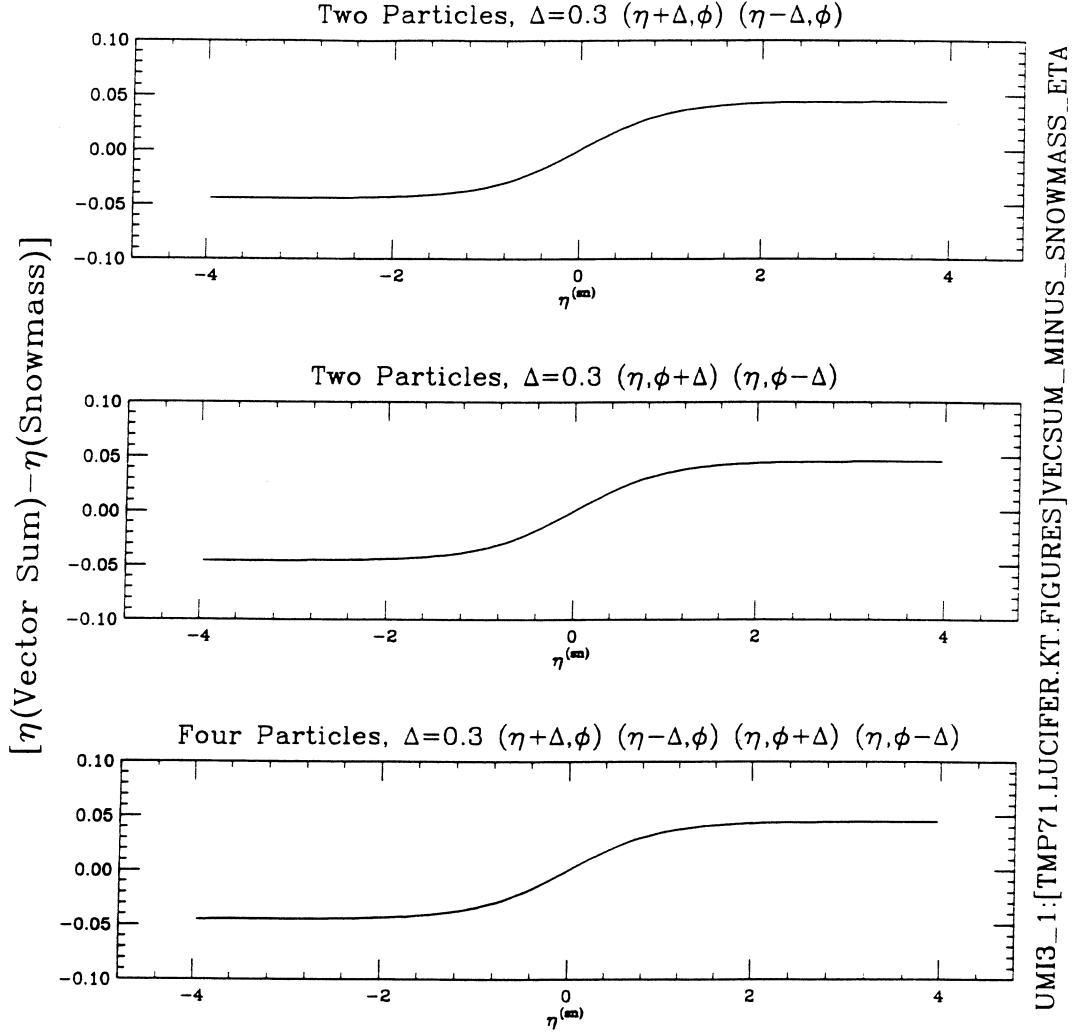


Fig. 8. This figure shows the absolute  $\eta$  difference between 4-vector and Snowmass algorithms. The figures reflect several simple geometries which include 2 or 4 particles. The width in the  $\eta$  and  $\phi$  direction are the same, but the different curves show the different geometrical combinations.

As a final note, these kinematic biases have been noted before in different contexts [6]. This earlier paper shows how showering in the calorimeter alters the reported kinematics of a single particle. This is kinematically similar to the jet width effects discussed here.

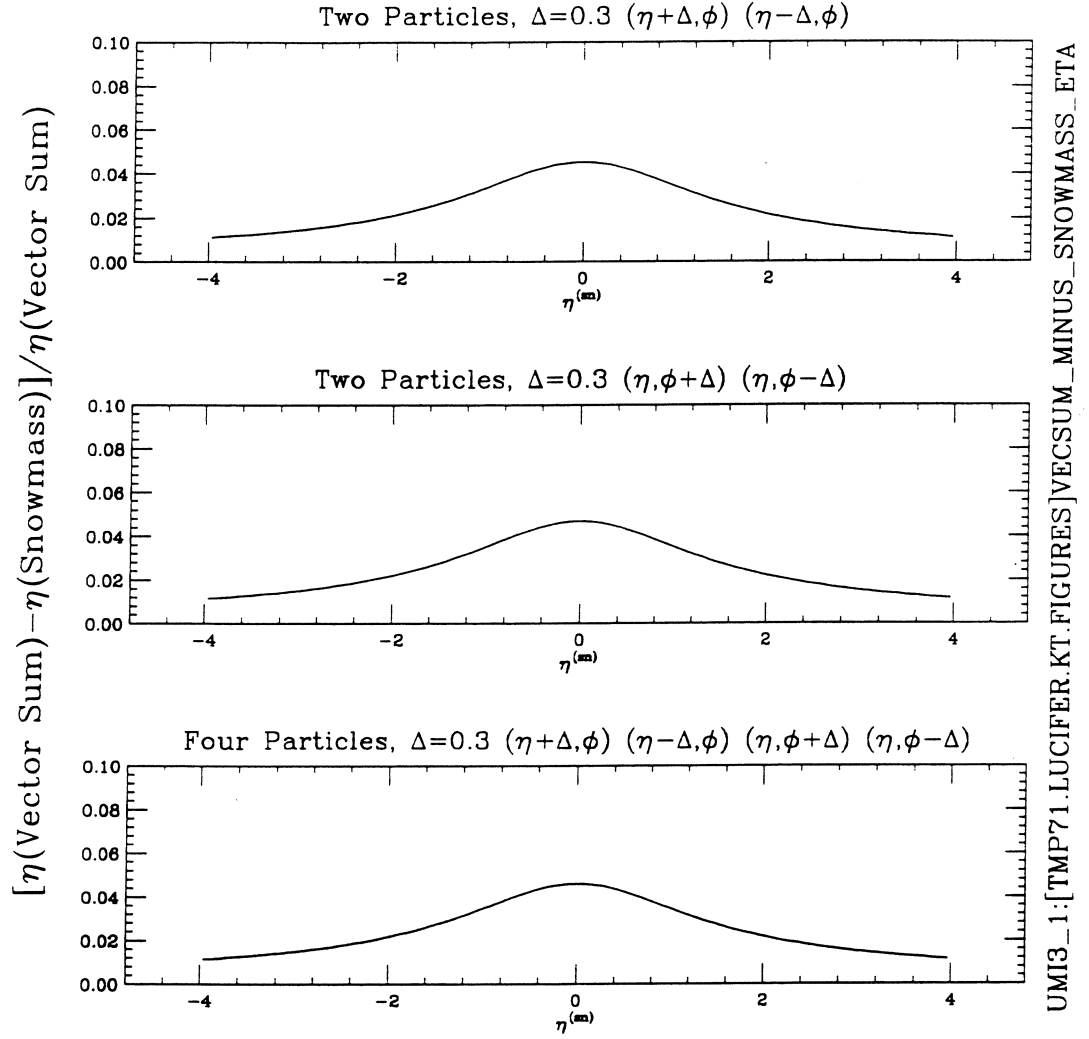


Fig. 9. This figure shows the fractional  $\eta$  difference between 4-vector and Snowmass algorithms. The figures reflect several simple geometries which include 2 or 4 particles. The width in the  $\eta$  and  $\phi$  direction are the same, but the different curves show the different geometrical combinations.

## A Special Cases

In this section, I give the formulas that allow a comparison between the measured kinematics for both the Snowmass and 4-momentum algorithms.

### A.1 Case 1: Two particles separated in $\eta$

Assume you have two massless particles, each with transverse energy (momentum)  $E_{\perp}$ , at coordinates  $(\eta + \Delta_{\eta}, \phi)$  and  $(\eta - \Delta_{\eta}, \phi)$ . One can calculate 4-vector quantities:

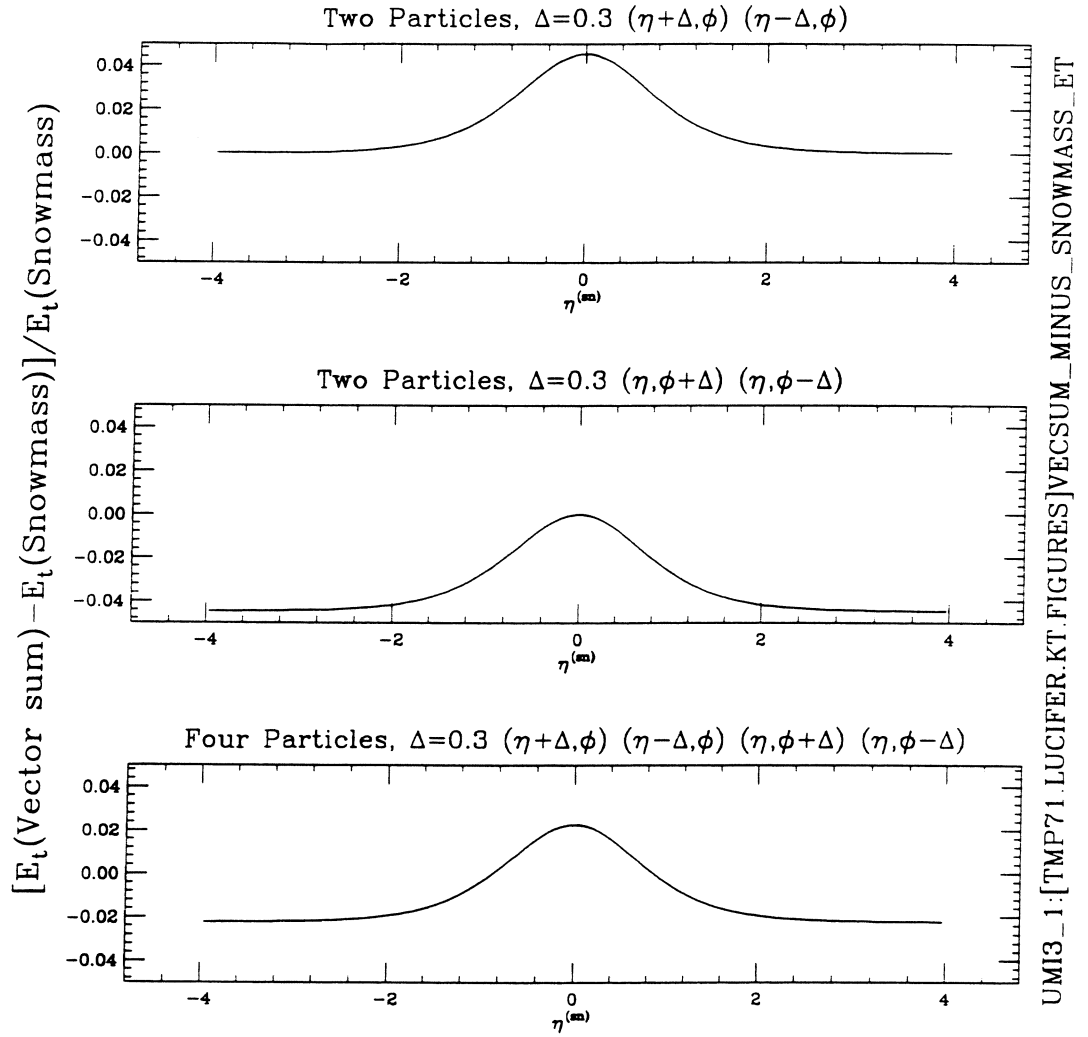


Fig. 10. This figure shows the fractional difference between 4-vector and Snowmass algorithms. The figures reflect several simple geometries which include 2 or 4 particles. The width in the  $\eta$  and  $\phi$  direction are the same, but the different curves show the different geometrical combinations.

$$E^{(vs)} = 2E_{\perp} \cosh \eta \cosh \Delta_{\eta} \quad (\text{A.1})$$

$$p_x^{(vs)} = 2E_{\perp} \cos \phi \quad (\text{A.2})$$

$$p_y^{(vs)} = 2E_{\perp} \sin \phi \quad (\text{A.3})$$

$$p_z^{(vs)} = 2E_{\perp} \sinh \eta \cosh \Delta_{\eta} \quad (\text{A.4})$$

$$p_{\perp}^{(vs)} = 2E_{\perp} \quad (\text{A.5})$$

$$p^{(vs)} = 2E_{\perp} \sqrt{1 + \sinh^2 \eta \cosh^2 \Delta_{\eta}} \quad (\text{A.6})$$

$$\sin \theta^{(vs)} = \frac{1}{\sqrt{1 + \sinh^2 \eta \cosh^2 \Delta_{\eta}}} \quad (\text{A.7})$$

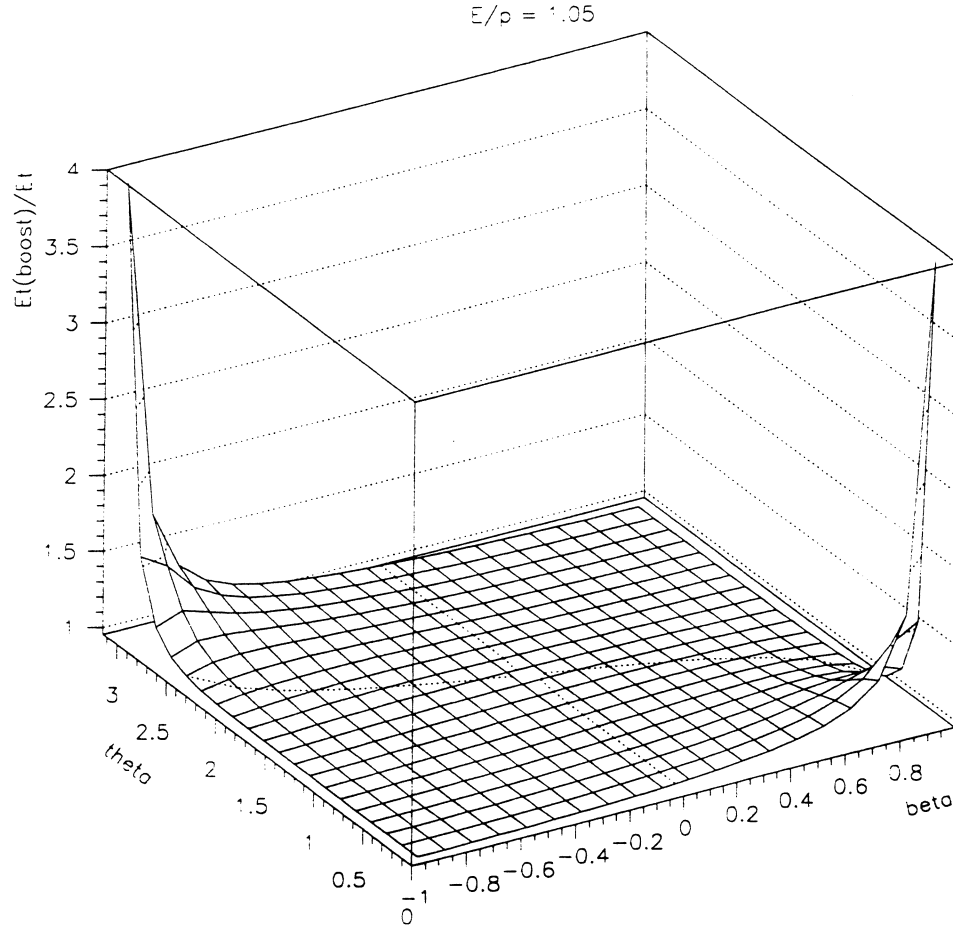


Fig. 11. This plot shows the ratio  $E'_\perp/E_\perp$  as a function of  $\theta$  in the unboosted frame and the boost  $\beta$ . For this plot, the specific choice  $E/p = 1.05$  was made.

$$E_\perp^{(vs)} = \frac{2E_\perp \cosh \eta \cosh \Delta_\eta}{\sqrt{1 + \sinh^2 \eta \cosh^2 \Delta_\eta}} \quad (\text{A.8})$$

$$y^{(vs)} = \eta \quad (\text{A.9})$$

$$\eta^{(vs)} = -\ln[\sqrt{1 + (\sinh^2 \eta)(\cosh^2 \Delta_\eta)} - (\sinh \eta)(\cosh \Delta_\eta)] \quad (\text{A.10})$$

$$\phi^{(vs)} = \phi \quad (\text{A.11})$$

$$m^{(vs)} = 2E_\perp \sinh \Delta_\eta \quad (\text{A.12})$$

Snowmass quantities

$$E_\perp^{(sn)} = 2E_\perp \quad (\text{A.13})$$

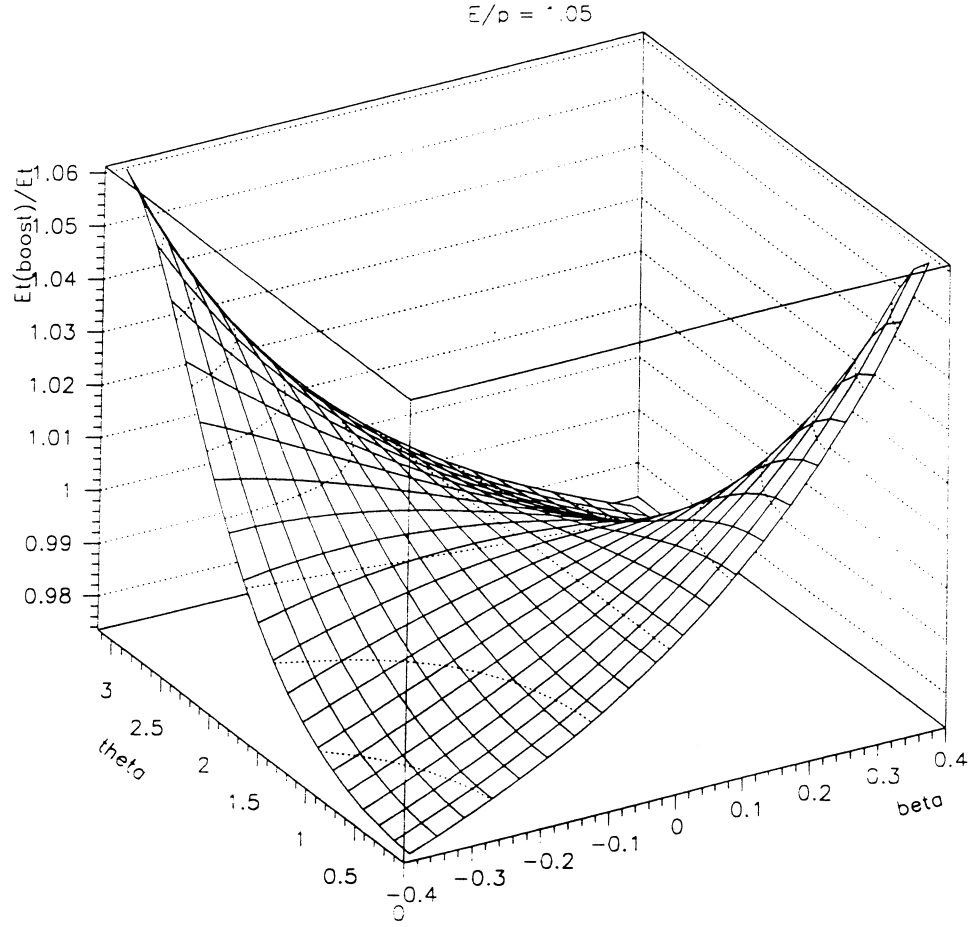


Fig. 12. This plot shows the ratio  $E'_\perp/E_\perp$  as a function of  $\theta$  in the unboosted frame and the boost  $\beta$ . For this plot, the specific choice  $E/p = 1.05$  was made. In addition, the truncation  $|\beta| < 0.4$  was made in order to better see the near-unity behavior.

$$\eta^{(sn)} = \eta \quad (\text{A.14})$$

$$\phi^{(sn)} = \phi \quad (\text{A.15})$$

### A.2 Case 2: Two particles separated in $\phi$

Assume you have two massless particles, each with transverse energy (momentum)  $E_\perp$ , at coordinates  $(\eta, \phi + \Delta_\phi)$  and  $(\eta, \phi - \Delta_\phi)$ . One can calculate 4-vector quantities:

$$E^{(vs)} = 2E_\perp \cosh \eta \quad (\text{A.16})$$

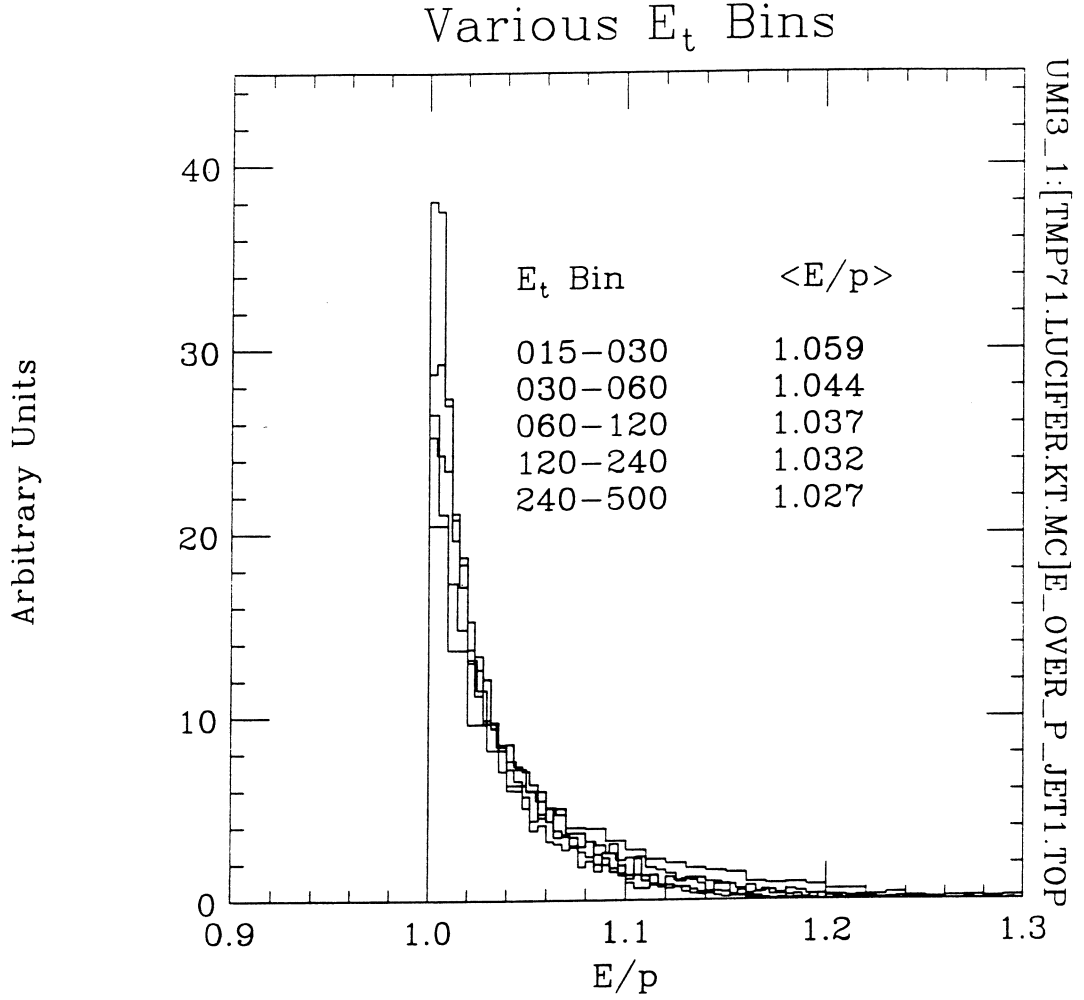


Fig. 13. This plot shows the distribution  $E/p$  ratio for different generated parton  $p_\perp$  bins. The Monte Carlo is HERWIG, generating dijet events. Data looks very similar. Listed on the plot are the generated  $p_\perp$  bins and the mean of the  $E/p$  ratio.

$$p_x^{(vs)} = 2E_\perp \cos \Delta_\phi \cos \phi \quad (\text{A.17})$$

$$p_y^{(vs)} = 2E_\perp \cos \Delta_\phi \sin \phi \quad (\text{A.18})$$

$$p_z^{(vs)} = 2E_\perp \sinh \eta \quad (\text{A.19})$$

$$p_\perp^{(vs)} = 2E_\perp \cos \Delta_\phi \quad (\text{A.20})$$

$$p^{(vs)} = 2E_\perp \sqrt{\cos^2 \Delta_\phi + \sinh^2 \eta} \quad (\text{A.21})$$

$$\sin \theta^{(vs)} = \frac{\cos \Delta_\phi}{\sqrt{\cos^2 \Delta_\phi + \sinh^2 \eta}} \quad (\text{A.22})$$

$$E_\perp^{(vs)} = \frac{2E_\perp \cosh \eta \cos \Delta_\phi}{\sqrt{\cos^2 \Delta_\phi + \sinh^2 \eta}} \quad (\text{A.23})$$

$$y^{(vs)} = \eta \quad (\text{A.24})$$

$$\eta^{(vs)} = -\ln\left[\frac{\sqrt{(\cos^2 \Delta_\phi) + (\sinh^2 \eta)} - \sinh \eta}{\cos \Delta_\phi}\right] \quad (\text{A.25})$$

$$\phi^{(vs)} = \phi \quad (\text{A.26})$$

$$m^{(vs)} = 2E_\perp \sin \Delta_\phi \quad (\text{A.27})$$

Snowmass quantities

$$E_\perp^{(sn)} = 2E_\perp \quad (\text{A.28})$$

$$\eta^{(sn)} = \eta \quad (\text{A.29})$$

$$\phi^{(sn)} = \phi \quad (\text{A.30})$$

### A.3 Case 3: Four particles separated in $\eta$ and $\phi$

Assume you have four massless particles, each with transverse energy (momentum)  $E_\perp$ , at coordinates  $(\eta + \Delta_\eta, \phi)$ ,  $(\eta - \Delta_\eta, \phi)$ ,  $(\eta, \phi + \Delta_\phi)$  and  $(\eta, \phi - \Delta_\phi)$ . One can calculate 4-vector quantities:

$$E^{(vs)} = 2E_\perp (\cosh \eta)(1 + \cosh \Delta_\eta) \quad (\text{A.31})$$

$$p_x^{(vs)} = 2E_\perp (1 + \cos \Delta_\phi) \cos \phi \quad (\text{A.32})$$

$$p_y^{(vs)} = 2E_\perp (1 + \cos \Delta_\phi) \sin \phi \quad (\text{A.33})$$

$$p_z^{(vs)} = 2E_\perp (\sinh \eta)(1 + \cosh \Delta_\eta) \quad (\text{A.34})$$

$$p_\perp^{(vs)} = 2E_\perp (1 + \cos \Delta_\phi) \quad (\text{A.35})$$

$$p^{(vs)} = 2E_\perp \sqrt{(1 + \cos \Delta_\phi)^2 + (\sinh^2 \eta)(1 + \cosh \Delta_\eta)^2} \quad (\text{A.36})$$

$$\sin \theta^{(vs)} = \frac{(1 + \cos \Delta_\phi)}{\sqrt{(1 + \cos \Delta_\phi)^2 + (\sinh^2 \eta)(1 + \cosh \Delta_\eta)^2}} \quad (\text{A.37})$$

$$E_\perp^{(vs)} = \frac{2E_\perp (\cosh \eta)(1 + \cosh \Delta_\eta)(1 + \cos \Delta_\phi)}{\sqrt{(1 + \cos \Delta_\phi)^2 + (\sinh^2 \eta)(1 + \cosh \Delta_\eta)^2}} \quad (\text{A.38})$$

$$y^{(vs)} = \eta \quad (\text{A.39})$$

$$\eta^{(vs)} = -\ln\left[\frac{\sqrt{(1 + \cos \Delta_\phi)^2 + (\sinh^2 \eta)(1 + \cosh \Delta_\eta)^2} - (\sinh \eta)(1 + \cosh \Delta_\eta)}{1 + \cos \Delta_\phi}\right] \quad (\text{A.40})$$

$$\phi^{(vs)} = \phi \quad (\text{A.41})$$

$$m^{(vs)} = 2E_\perp \sqrt{(1 + \cosh \Delta_\eta)^2 - (1 + \cos \Delta_\phi)^2} \quad (\text{A.42})$$

Snowmass quantities



$$E_{\perp}^{(sn)} = 4E_{\perp} \quad (\text{A.43})$$

$$\eta^{(sn)} = \eta \quad (\text{A.44})$$

$$\phi^{(sn)} = \phi \quad (\text{A.45})$$

#### A.4 Case 4: A double-gaussian distribution of massless $E_{\perp}$

Assume you have a jet which consists of smoothly distributed massless particles with  $E_{\perp}$  distribution:

$$\frac{dE_{\perp}(\eta, \phi)}{d\eta d\phi} = \frac{E_{\perp}}{2\pi\sigma_{\eta}\sigma_{\phi}} e^{-\frac{(\eta-\eta_0)^2}{2\sigma_{\eta}^2}} e^{-\frac{(\phi-\phi_0)^2}{2\sigma_{\phi}^2}} \quad (\text{A.46})$$

One can calculate 4-vector quantities:

$$E^{(vs)} = E_{\perp}(\cosh \eta_0) e^{\frac{\sigma_{\eta}^2}{2}} \quad (\text{A.47})$$

$$p_x^{(vs)} = E_{\perp} e^{-\frac{\sigma_{\phi}^2}{2}} \cos \phi_0 \quad (\text{A.48})$$

$$p_y^{(vs)} = E_{\perp} e^{-\frac{\sigma_{\phi}^2}{2}} \sin \phi_0 \quad (\text{A.49})$$

$$p_z^{(vs)} = E_{\perp}(\sinh \eta_0) e^{\frac{\sigma_{\eta}^2}{2}} \quad (\text{A.50})$$

$$p_{\perp}^{(vs)} = E_{\perp} e^{-\frac{\sigma_{\phi}^2}{2}} \quad (\text{A.51})$$

$$p^{(vs)} = E_{\perp} \sqrt{(\sinh^2 \eta_0) e^{\sigma_{\eta}^2} + e^{-\sigma_{\phi}^2}} \quad (\text{A.52})$$

$$\sin \theta^{(vs)} = \frac{e^{-\frac{\sigma_{\phi}^2}{2}}}{\sqrt{(\sinh^2 \eta_0) e^{\sigma_{\eta}^2} + e^{-\sigma_{\phi}^2}}} \quad (\text{A.53})$$

$$E_{\perp}^{(vs)} = E_{\perp} \frac{(\cosh \eta_0) e^{\frac{\sigma_{\eta}^2 - \sigma_{\phi}^2}{2}}}{\sqrt{(\sinh^2 \eta_0) e^{\sigma_{\eta}^2} + e^{-\sigma_{\phi}^2}}} \quad (\text{A.54})$$

$$\eta^{(vs)} = -\ln[\sqrt{(\sinh^2 \eta_0) e^{\sigma_{\phi}^2 + \sigma_{\eta}^2} + 1} - (\sinh \eta_0) e^{\frac{\sigma_{\phi}^2 + \sigma_{\eta}^2}{2}}] \quad (\text{A.55})$$

$$y^{(vs)} = \eta_0 \quad (\text{A.56})$$

$$\phi^{(vs)} = \phi_0 \quad (\text{A.57})$$

$$m^{(vs)} = E_{\perp} \sqrt{e^{\sigma_{\eta}^2} - e^{-\sigma_{\phi}^2}} \quad (\text{A.58})$$

Because this is a natural example, I have derived linearized formulas for  $E_{\perp}^{(vs)}$  and  $\eta^{(vs)}$  in order to better address one's intuitions. The linearized formulas are

$$E_{\perp}^{(vs)} = E_{\perp} \{1 + \frac{1}{2}[\sigma_{\eta}^2 - (\tanh^2 \eta_{\circ})(\sigma_{\eta}^2 + \sigma_{\phi}^2)]\} \quad (\text{A.59})$$

$$\eta^{(vs)} = \eta_{\circ} + \frac{\sigma_{\phi}^2 + \sigma_{\eta_{\circ}}^2}{2}(\tanh \eta_{\circ}) \quad (\text{A.60})$$

**Snowmass quantities**

$$E_{\perp}^{(sn)} = E_{\perp} \quad (\text{A.61})$$

$$\eta^{(sn)} = \eta_{\circ} \quad (\text{A.62})$$

$$\phi^{(sn)} = \phi_{\circ} \quad (\text{A.63})$$

## References

- [1] E.W.N. Glover and D. Kosower, 'Recombination methods for jets in  $p\bar{p}$  collisions', Phys. Lett. B 367 (1996) 369.
- [2] B. Abbott, 'Effects of  $\eta$  and  $\phi$  Definitions on Reconstructing Jets', DØNote #2769, Nov. 1995, Unpublished.
- [3] J. Huth, et al., 'Toward a Standardization of Jet Definitions', FERMILAB-CONF-90-249-E, Published in Snowmass Summer Study 1990, p. 134-136.
- [4] S. Ahn et al., 'First Observation of Quark-Jet and Gluon-Jet Differentiation in DØ Data', DØNote #2977, June 1996, in preparation.
- [5] D. Lincoln, 'On Determining  $x_{Bj}$  from Jet Measurements', in the proceedings of DPF92, p. 926-928.
- [6] P. Draper, S. Durston, N. Amos, 'Eta-dependent Effects Due to Shower Size', DØNote #1162, Nov. 1991, Unpublished.

# On Correcting Jets by Correcting the Electromagnetic and Hadronic Calorimeters Separately

Richard V Astur

May 23, 1995

## 1 Introduction

The purpose of this document is to describe the results of an initial investigation of the jet energy scale group into a different method for calibrating jets. This other method involves correcting energy contained in the electromagnetic calorimeter by the electromagnetic scale and then calibrating the hadronic calorimeter relative to the electromagnetic calorimeter. The results were sufficiently discouraging that no further work on this method is being attempted by us, however the issue could be revisited should solutions be found to the problems described below. This document is by no means meant to discourage members of the experiment from investigating this or similar calibration methods; it is simply meant as an explanation as to why the jet scale group itself has stopped work on it.

## 2 Description of the proposed method

It is known that electrons/photons have a generally higher response in our calorimeter relative to those of 'hadrons'. Since jets are comprised of both types of particles, calibration of such is complicated by the relatively unknown makeup of the jet on an event by event basis and further complicated by nonlinearities of hadron response. Since the EM calorimeter will largely

contain incident photons/electrons, it makes sense that it might also contain the electromagnetic portion of the showers of other particles such as charged pions. One would then have a situation where the EM calorimeter holds the 'electromagnetic' portion of the jet while the slowly interacting 'hadronic' portions of the jet might be contained only by the hadronic calorimeter. Since DØ has an established set of corrections for electrons which comes from the measurement of the Z boson, one could go ahead and correct the EM calorimeter with these numbers (thereby automatically getting the Z mass right to a high percentage). One would then use the usual photon+jet candidate event sample to determine the energy response of the hadronic calorimeter, we denote this as  $\mathcal{R}_{HAD}(E)$ . The energy dependence of the hadronic calorimeter would allow for nonlinearities in hadronic response.

### 3 Nutshell explanation of the method's flaw

The assumption is that the energy measured in the EM calorimeter came from the 'electromagnetic' portion of the jet shower and that the hadronic calorimeter then contains the 'hadronic' portion of the jet. First, the electromagnetic portions of late developing showers do reach the hadronic layers. We know that photons/electrons deposit energy in the hadronic calorimeter at the 1-5% level. Late developing showers would deposit even more in the hadronic layers. Secondly, the hadronic portions of low energy hadrons deposit a significant fraction of their energy into the EM layers. Thus the 'electromagnetic' and 'hadronic' components of the shower are mixed and not separated out into the 'electromagnetic' and 'hadronic' layers. Since jets are comprised of many low energy particles, the situation is made worse for jets. Finally, it seems that even the 'electromagnetic' and 'hadronic' portions of single pions do not separate into the electromagnetic and hadronic layers of the calorimeter. Without this identification, the method breaks down.

## 4 Discussion and results

### 4.1 Monte Carlo Jet Response

Previous Monte Carlo studies [1] with ISAJET+mixture GEANT have shown that jets which have a higher percentage of electromagnetic particles (neutral

mesons, photons and electrons) do indeed have a higher response. The response for 40 GeV Monte Carlo jets increases linearly with this percentage. Jets made up entirely of these particles have approximately a 15% higher response than jets made up entirely of non-electromagnetic particles. (The ratio of jet to electron response in this Monte Carlo was roughly 15%.) These numbers ignore the fact that charged pions shower partially electromagnetically. This would only make the non-electromagnetic jets respond better than if they truly showered in a purely hadronic manner.

However, when one considers the response versus jet electromagnetic fraction (the fraction of the jets energy which is contained in the electromagnetic layers of the calorimeter), this correlation is lost for jets. The same reference shows that now both high and low emfraction jets respond high while jets with average emfractions (from .5 to .8) respond low. Presumably, the high emfraction jets contain leading photons, low emfraction jets contain leading charged pions (or other hadrons) and the average emfractions contain leading particles mixed with low energy pions which have a lower response.

This is still okay, because this shape is predicted if one assumes a nonlinear hadronic response. If we assumed that:

$$\mathcal{R}_{\mathcal{EM}}(E) = 1.0 \quad (1)$$

$$\mathcal{R}_{\mathcal{HAD}}(E) = aE \quad (2)$$

That is, the EM calorimeter has perfect response and the hadron calorimeter has a response that increases as energy. This assumption is extreme, but would give the shape shown in the Monte Carlo since the response for a 40 GeV jet as a function of EMF (electromagnetic fraction) would then be:

$$\mathcal{R}(EMF) = EMF + 40a(1 - EMF)^2 \quad (3)$$

This response function starts at  $40a$ , falls and then rises to 1.0 when  $EMF=1.0$ . Thus we see that if we fix the scale of the EM calorimeter, we need an energy dependent response for the hadronic calorimeter to explain this Monte Carlo curve (which matches the data curves shown later). This is a reasonable result.

## 4.2 Results from photon + jet balancing

Assuming for a minute that one goes ahead and uses this procedure, it will not change the fact that one finds from photon-jet balancing in the central calorimeter that 20 GeV jets must be corrected by an average 25% [2] to get the event to balance. The data also shows that 20 GeV jets have on average 60% of their energy in the electromagnetic section. When we now fix the electromagnetic calorimeter correction to the roughly 5% correction needed to get the Z mass to the correct place, one sees that the remaining hadronic energy would have to be corrected by a whopping 55%! Thus  $\mathcal{R}_{HAD}(E)$  at 8 GeV must be at least  $1./1.55 = .65$ . We will see in the next section that 30 GeV jets which have EMF=0. have roughly the same response as EMF=1 jets, implying that  $\mathcal{R}_{HAD}(E)$  goes from .65 to 1 as the hadronic energy goes from 8 to 30 GeV. This is extremely non-linear behavior. Conversely, single pions in test beam data and monte carlo change their response by less than 10% in this region.

## 4.3 Results from Data

Figure 1 shows the relative response versus jet emfraction for jets of various transverse energies. All of them have the same shape as in the Monte Carlo. These curves are derived from inclusive QCD triggers. The full description of how this curve is derived is described elsewhere. [3] The study requires two central jets and further requires that one jet (the trigger jet) satisfy completely all of the trigger conditions. This makes the other one (the probe jet) completely unbiased. By definition the trigger jet tends to have a higher  $E_T$  on average than the probe jet. One then plots the quantity:

$$\mathcal{R}_{EMF}(EMF) = 1 + \frac{\cancel{E}_T \cdot E_T^{trigger}}{E_T^{trigger}} \quad (4)$$

$\mathcal{R}_{EMF}(EMF)$  is a function of the EMF of the probe jet.  $\mathcal{R}_{EMF}(EMF)$  is 1 when the  $\cancel{E}_T$  is uncorrelated with the probe jet. However since the trigger jet tends to have higher  $E_T$  by definition, the  $\mathcal{R}_{EMF}(EMF)$  values tend to be less than 1. Thus the absolute scale is not meaningful, but the relative change in the response of the probe jet is meaningful and is measured by  $\mathcal{R}_{EMF}(EMF)$ . We see that in the 30 GeV jet sample, the response of jets with 30 GeV of hadronic energy is as good (better) than jets with 30 GeV of

electromagnetic energy. This implies that  $\mathcal{R}_{HAD}(E)$  at 30 GeV is near 1. But now when we look at 80 GeV jets, 30 GeV of hadronic energy corresponds to an EMF of about .6 which clearly has a lower response than jets with 80 GeV of hadronic energy. The two plots contradict each other under the assumption and the only way out is to assume that the electromagnetic scale itself is nonlinear. Further contradictions by example can be drawn by comparing the different plots to each other. Each curve implies that the hadronic scale is approaching the electromagnetic scale at different energies: 20,30,50 and 80 GeV, if one were to assume that there is a universal response function ( $\mathcal{R}_{HAD}(E)$ ) for hadronic energy and that the EM scale is fixed.

#### 4.4 Test Beam pion results

We can look at something even simpler to test out the assumption that the 'electromagnetic' and 'hadronic' components of the shower separate out into the corresponding electromagnetic and hadronic layers. Figure 2 shows results for both 4 and 50 GeV testbeam lead II pions. We see from their electromagnetic fraction distributions that the 50 GeV pions are much more peaked at the low emfractions than 4 GeV pions. That is, the lower energy pions deposit more energy in the EM calorimeter. Considering that the electromagnetic content of a hadronic shower is supposed to increase with energy, it seems clear that the EM fraction of the pions is not a good measure of the electromagnetic component of the pion shower. Also shown are plots of the pion response as a function of pion emfraction. The response is defined as simply the total measured energy divided by the beam momentum. The emfraction of the pion is simply the fraction of the measured pion's energy which was found to be in the electromagnetic layers. We see that pions with low emfraction respond better than pions with a high emfraction at 4 GeV and is relatively insensitive at 50 GeV. This contradicts the assumption that the portion of the pion shower which is contained by the electromagnetic calorimeter is entirely from electromagnetic showers which would have the best response.

#### 4.5 Monte Carlo pion results

Figure 3 shows the same type of plots as described in figure 2, but this time for 10 GeV pions from both the test beam and as generated in the mixture



Monte Carlo. Again, we see clearly that pions which shower entirely in the EM calorimeter have generally lower response than those that shower in the hadronic calorimeter. This trend is followed to a lesser extent in the Monte Carlo.

## 5 Conclusions

Energy found in the EM calorimeters from single pions or jets does not seem to have the same energy scale as that of 'electromagnetic' particles. Thus calibrating the EM calorimeters by the EM scale found for Z electrons and then correcting separately the energy in the hadronic calorimeter is inappropriate.

However, this doesn't mean that the measured EM fraction of a jet should be ignored. We can see from figure 2 that a (possibly energy dependent) jet correction based on EM fraction or some other variable [3] can work nicely. This method is being used currently by the jet scale group.

## References

- [1] R. Astur (Ph.D. thesis) pp 88.
- [2] e.g. See DØ notes 2052,2053,2089 on photon-jet balance.
- [3] R. Astur, R. Kehoe, A. Milder, *Determination of Hadronic Energy Scale Corrections for the DØ Experiment* (draft)

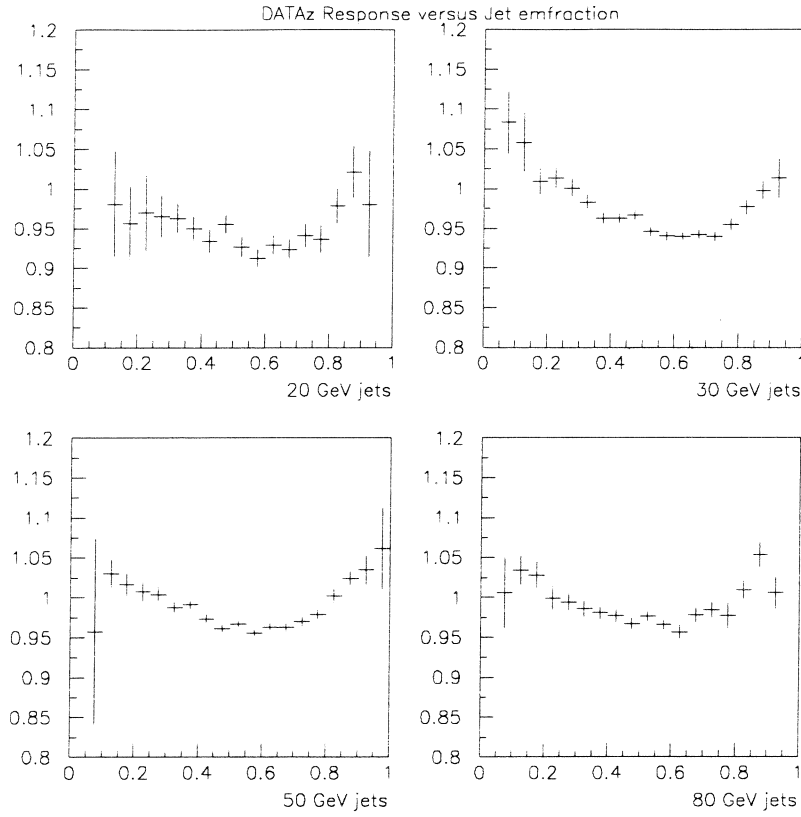


Figure 1: Relative hadronic response as a function of jet electromagnetic fraction for probe jets in various  $E_T$  ranges.

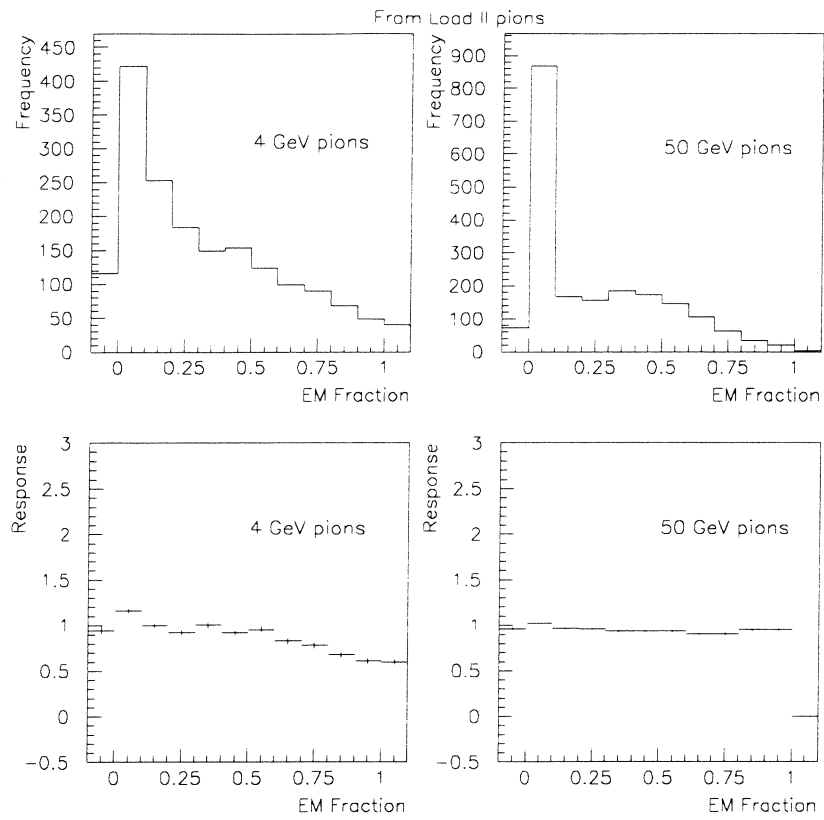


Figure 2: top: Distribution of the EM fraction for both 4 and 50 GeV pions. bottom: Ratio of measured energy over beam momentum for 4 and 50 GeV pions versus pion emfraction as seen at Load II testbeam.

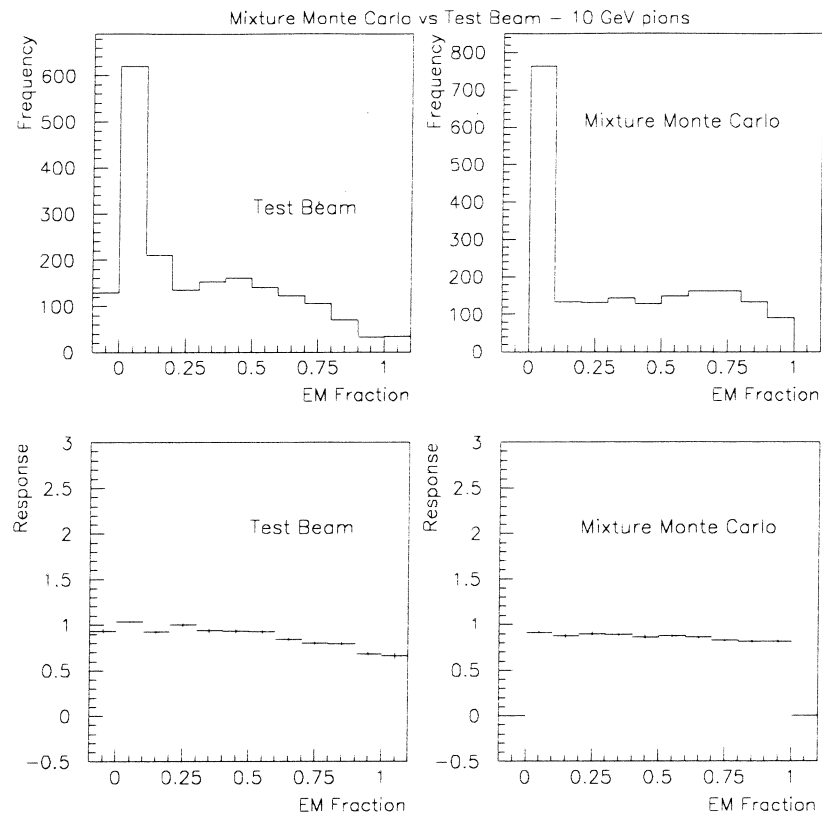


Figure 3: Ratio of measured energy over beam momentum for 10 GeV pions versus emfraction both from the testbeam and from mixture Monte Carlo.



## EM Calorimeter Calibration for the D0 Upgrade

John Womersley  
*Fermi National Accelerator Laboratory, Batavia, IL 60510*

### ABSTRACT

It is not anticipated that there will be a calorimeter test beam between Run 1B and Run 2. In the light of this, potential calibration techniques using Monte Carlo and in situ data for the DØ EM calorimeters in the upgrade configuration are described.

### 1. Introduction

It will be necessary to recalibrate the sampling weights used for the CCEM and ECEM calorimeters for Run 2. This is because:

- The material upstream will have changed — there will be the magnet coil, lead absorber and central preshower (CPS) detector in front of the CCEM, while there will be reduced chamber endplate material in front of the ECEM;
- The magnetic field will sweep some low-energy shower particles out of the cluster;
- The CPS energy measurement must be included in the optimized weights for the CCEM.

A two stage strategy may be imagined to determine the new weights: firstly one will start with the present weights and adjust them according to Monte Carlo estimation of the *changes* expected in the new geometry. Secondly, one will use collider data, with the magnetic momentum measurement, to optimize the sampling weights in situ.

## 2. Monte Carlo calculation

The simulations described here were run by Taka Yasuda (Northeastern University). The goal was to determine how much the sampling weights would be expected to change from Run 1B to Run 2 geometry, and how much a given error in the sampling weight would affect the electron energy scale.

Between 3000 and 10,000 single electrons were generated for each configuration of transverse momenta  $p_T^e = 10, 30, 50$  GeV, and pseudorapidity  $\eta^e = 0.05, 0.55, 1.05$ . The UPG\_GEANT Monte Carlo was used to simulate both Run 2 geometry (with coil and CPS) and Run 1B geometry (with the coil and CPS replaced by air). Only the CCEM was considered as the changes to ECEM weights would be expected to be much less. In each case the set of sampling weights which minimized the energy resolution was found.

Figure 1 (a)–(c) show the optimal EM1 weights for Run 1 and Run 2 geometries as a function of electron  $p_t$ , for  $\eta^e = 0.05, 0.55$ , and  $1.05$ . The weights are normalized to the current RECO weight (which is energy and  $\eta$  independent) as determined from the Load 2 testbeam data. It will be seen that at large  $\eta$  the Monte Carlo predicts an increase in EM1 weight of about 10% will be required in Run 2, while for  $\eta = 0.55$  the weight is unchanged. For  $\eta = 0.05$  the situation is unclear, as the weights are not very well-determined by the fitting program. This is because, as will be seen later, the reconstructed energy is insensitive to the EM1 weight in this region.

It will be noted that in all cases the optimized weights for the Run 1 configuration are larger than the RECO weights currently used, by factors of 1.1–1.2. It is not known where this discrepancy arises from. The Monte Carlo has been shown to model the Load 2 data imperfectly but it is not clear whether this originates in some feature of the testbeam data or in some inaccuracy of the modelling. In any case, the Monte Carlo should predict the change from Run 1 to Run 2 much better than it predicts the absolute value of the Run 1 weights. A reasonable first guess to the Run 2 weights would therefore be:

$$w_\beta = w_\alpha^{RECO} \cdot \frac{w_\beta^{MC}}{w_\alpha^{MC}}$$

where the subscripts  $\alpha$  and  $\beta$  denote Run 1 and Run 2 respectively.

Figure 1 (d) shows the optimized preshower weights for the Run 2 configuration. The predicted weights appear rather stable and energy-independent except for the lowest energy point at  $\eta = 0.05$ , where, once again, the optimization is somewhat suspect because the reconstructed energy is not sensitive to the weight.

Figure 2 shows the effect of using erroneous EM1 sampling weights in reconstructing the shower energy. In Fig. 2(a) the effect of a 10% error in the EM1 weight is shown. The choice of 10% is not completely arbitrary since this is the approximate level of uncertainty on our present (Run 1) determination of the weight from the testbeam. Figure 2(b) shows

the effect of using the EM1 weight appropriate to Run 1 on simulated data from Run 2 (the correct Run 2 preshower weight is still used). This represents very much of a “worst case” scenario on EM1 weight, but even so the reconstructed energy is shifted everywhere by less than 0.6%. This value is the absolute energy shift, assuming no renormalization of the mean energy. The effect on energy resolution is also small: an increase of about 0.5% in the constant term in the resolution at  $\eta = 1.05$  may be expected if the Run 1 EM1 weights are used. This would increase the single electron resolution from 1.68% to 1.75% for 50 GeV  $p_T$ .

To summarize, the changes in EM1 sampling weights between Run 1 and Run 2 are small, and expected to be predicted by Monte Carlo. Even using the Run 1 weights during Run 2 (a worst case scenario), the nonlinearities and resolution broadening which is introduced is very small.

### 3. In-situ Determination of Weights

The present (Run 1) EM weights were determined<sup>1</sup> using Load 1 and Load 2 testbeam data, by minimizing the function:

$$\sum_j \left( \frac{(\sum_i w_i E_{ij} - p_j)^2}{\sigma_E^2(p_j)} \right)$$

where this sum is over all events at all beam momentum settings. Here  $w_i$  is the weight of layer  $i$  ( $w_3 = 1$ ),  $E_{ij}$  is the energy measured in layer  $i$  for event  $j$ ,  $p_j$  is the momentum measured in the beamline PWC's for that event, and  $\sigma_E^2(p_j) = 0.15^2/p_j$  is an estimate of the variance on the calorimeter energy measurement. In load 1 and 2 we had a few thousand events at each of about 5 energies between 10 and 150 GeV; approximately 15k events in total. The calorimeter resolution was  $15\%/\sqrt{E}$ , i.e. about 2% at 50 GeV.

This method could simply be extended to *in situ* calibration using  $W \rightarrow e$  events in Run 2. In Run 1a (20 pb<sup>-1</sup> delivered) we have about 10k  $W$ 's, with approximately equal numbers of electrons in the CC and EC. In Run 2 with 1 fb<sup>-1</sup> delivered, we would therefore expect 200k in CC and 200k in EC. The same procedure would be used, except that the momentum measurement would come from the central tracker rather than from beam momentum counters. The weights would be determined by minimizing:

$$\sum_j \left( \frac{(\sum_i w_i E_{ij} - p_j)^2}{\sigma_j^2} \right)$$

where the sum is now over  $W \rightarrow e$  events and  $\sigma_j^2$  now represents the variance on the energy-momentum match  $E - p$ . At  $W \rightarrow e$  transverse momenta this is dominated by the resolution of the tracker, rather than that of the calorimeter. For the CCEM, the tracker resolution at 50 GeV  $p_T$  is about 8%. This is four times worse than that of the calorimeter, and so  $4^2 = 16$  times more events than were available in the testbeam would be needed to obtain comparable precision on the weights. The statistics available in Run 2 should be close to this and therefore should permit an *in situ* weight determination once all the data are taken.



It will still be possible to check the overall energy scale and perform other consistency checks with much lower statistics. For example, in several week's data (a few tens of  $\text{pb}^{-1}$ ), a few hundred good  $Z \rightarrow ee$  events will be obtained in each of the CCEM and ECEM's. These will allow the relative energy scales in each cryostat to be checked at the level of a few tenths of one percent. The same sample should contain of the order of ten thousand  $W \rightarrow e$  events in the CCEM. With these electrons, module-to-module uniformity checks at the level of 0.5% can be made. (Any uncertainty in the magnetic field as a function of  $\phi$  must also be considered, of course, but this should be small).

For the ECEM, the tracker resolution is worse; for  $\eta = 2$  the momentum resolution is likely to be about 25% at  $p_T = 50 \text{ GeV}$ . Here, 1.5 million electrons would be required to obtain a weight determination at the same precision as the testbeam, which is not possible. Testing the uniformity of energy response across the module will still be straightforward, however, using the copious  $W \rightarrow e$  and  $Z \rightarrow ee$  data.

An additional *in situ* constraint on calorimeter sampling weights will be obtainable from  $Z$  events. In  $1 \text{ fb}^{-1}$  we expect 40k reconstructed  $Z \rightarrow ee$  events. It should be possible to minimize:

$$\sum_j \left( \frac{2(\sum_i w_i E_{ij}^1)(\sum_k w_k E_{kj}^2)(1 - \cos \theta_j^{12}) - m_Z^2}{\sigma_j^2} \right)$$

where  $E^1$  and  $E^2$  are the two electron energies,  $\theta_j^{12}$  is the angle between them, and  $\sigma_j^2$  is an estimate of the variance on the invariant mass measurement. This minimization may be computationally hard as the function is quadratic in the weights, but as we have good starting values from Run 1 it should be possible to expand the function in the form of a Taylor series around these values and thus linearize its dependence on changes in the weights.

#### 4. Summary and Conclusions

- GEANT has been used to estimate the changes in EM1 weight required to minimize electron energy resolution going from Run 1 to Run 2.
- A worst case estimate of the effect of using the incorrect EM1 weight (using Run 1 weights on Run 2 data) gives response errors everywhere less than 0.6% and negligible worsening of EM resolution.
- There will be sufficient  $W \rightarrow e$  and  $Z \rightarrow ee$  data, after even a few weeks' running, to permit *in situ* tests of absolute energy scale and module-to-module nonuniformity.
- Using the whole run 2 dataset it will be possible to redetermine the CCEM sampling weights with comparable precision to that obtained in the testbeam.

#### References

1. H. Aihara *et al.*, *Nucl. Instr. and Meth.* **A325** (1993) 393.

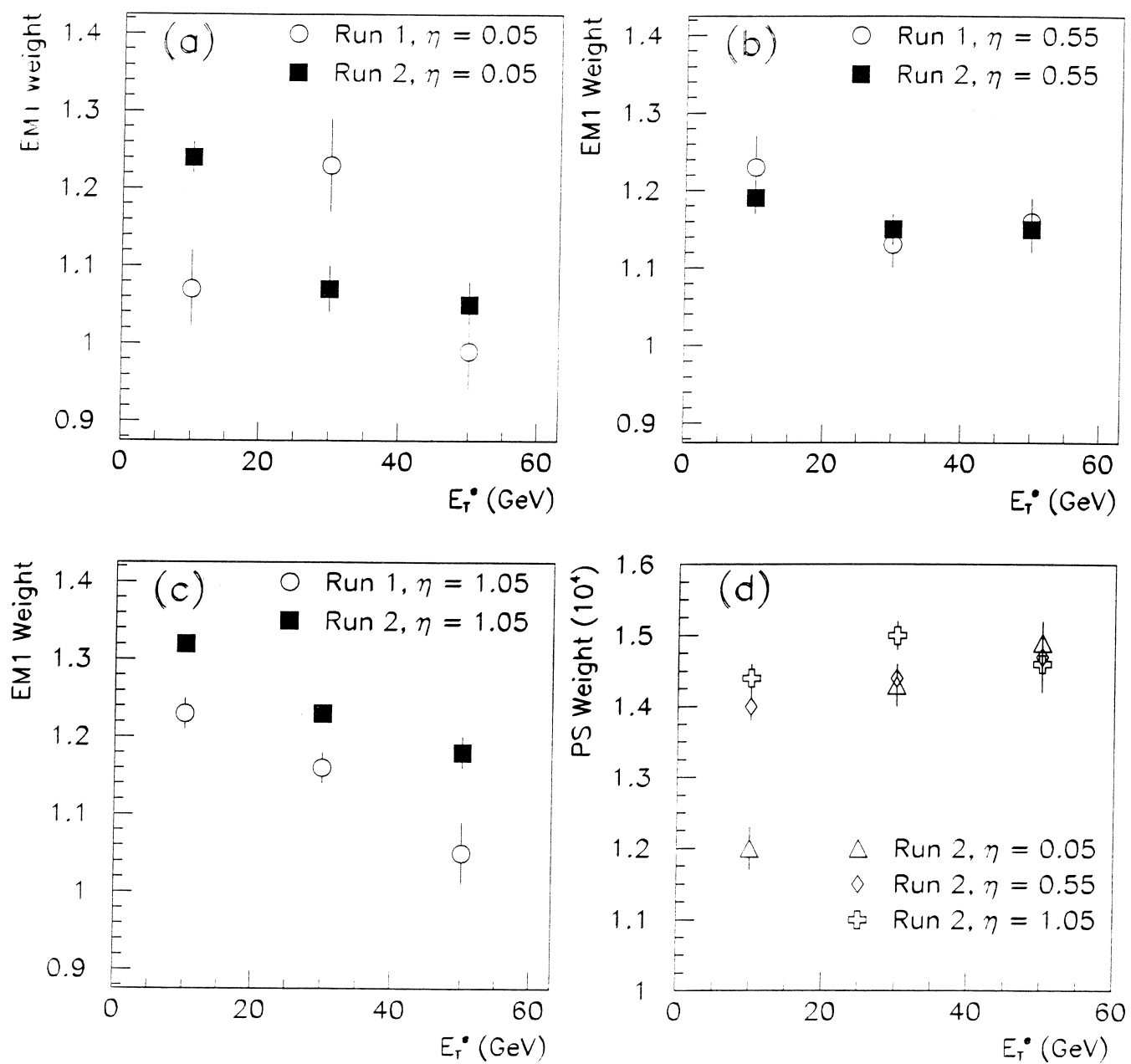


Figure 1

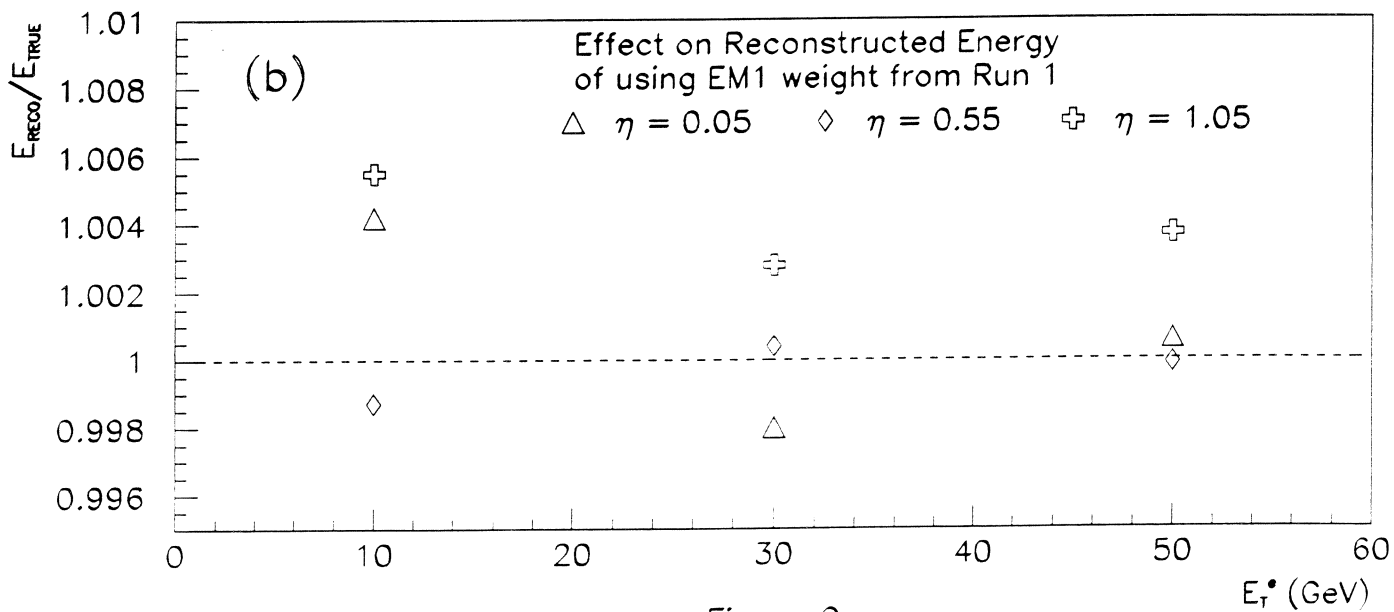
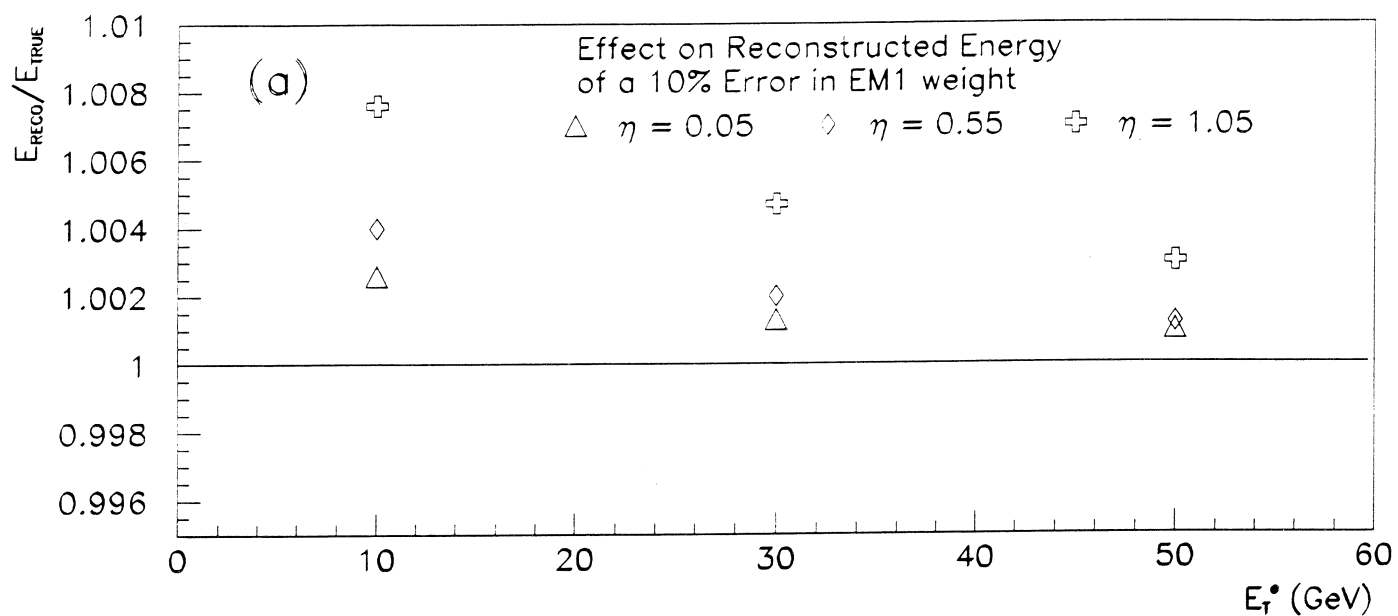


Figure 2

# Observation of $J/\psi \rightarrow ee$ decays at DØ and calibration of the central calorimeter electromagnetic energy scale

Ian Adam, Claudia Bormann, Heriberto Castilla, Nina Denisenko,  
Eric Flattum, Alberto Sanchez, Mike Tartaglia

October 3, 1994

## 1 Introduction

The observation of  $J/\psi \rightarrow ee$  decays at DØ can provide a constraint on the electromagnetic response of the central calorimeter. The  $J/\psi$  mass has been measured very precisely at  $e^+e^-$  machines and has a negligible width compared to the resolution at DØ. The PDG values are [1]:

$$M_{J/\psi} = (3.09693 \pm 0.00009) \text{ GeV}$$

$$\Gamma_{J/\psi} = (86 \pm 6) \text{ keV}$$

Combined with the  $Z \rightarrow ee$  resonance, the  $J/\psi$  provides a measurement of the scale,  $\alpha$ , and offset,  $\beta$ , in the electron energy response, which is assumed to have the form [2, 3]:

$$E^{true} = \alpha E^{measured} + \beta$$

For simplicity of notation, variables with a tilde will represent measured quantities and corresponding variables without tildes will represent the corresponding true quantity (e.g.,  $E^{true}$  will be written as  $E$  and  $E^{measured}$  as  $\tilde{E}$ .) The uncertainty in  $\beta$  is an important systematic uncertainty in the  $M_W/M_Z$  mass ratio. The offset  $\beta$  can be measured using the “binned  $Z$ ” method [4, 5]. However, the  $J/\psi$  gives a measurement of  $\beta$  with a smaller

uncertainty, hence the observation of the  $J/\psi$  is a useful input to the  $W$  mass measurement.

The  $J/\psi$  is produced in  $p\bar{p}$  collisions principally by two processes: via intermediate  $\chi_c$  states and via  $B$  decays [6, 7]. The cross section in either case depends strongly on  $P_T(\psi)$ . For  $P_T(\psi) > 5\text{ GeV}$ , the cross sections from  $B$  decays and from  $\chi_c$  states are each about  $200\text{ nb}$  from leading order diagrams [6]. The branching ratio for  $J/\psi \rightarrow ee$  is 6.3% [1], so  $\sigma \cdot B$  is about  $15\text{ nb}$  for either process. However, CDF and DØ  $J/\psi \rightarrow \mu\mu$  data favor a larger cross section than that predicted by the LO theory, and recent calculations indicate that  $J/\psi$  production via fragmentation may dominate LO mechanisms. Although the fragmentation calculations are not in good agreement with CDF  $\psi'$  data, they indicate that  $\sigma \cdot B$  is probably higher than the previous estimate [7].

## 2 Data sample

The data were collected in a set of special runs at the end of run Ia and at the beginning of run Ib. The level 1 trigger required two EM towers above  $2.5\text{ GeV}$  with less than  $1\text{ GeV}$  in the corresponding hadronic towers. At level 2, two L2EM objects above  $3\text{ GeV}$  were required. Different quality cuts were applied in several different filters. The only unrescaled filter required both objects to have isolation less than 0.4 in a cone of radius 0.4 in  $\eta$ - $\phi$  space. In order to have a consistent dataset, only data reconstructed with RECO v12.09 were used. The integrated luminosity of the sample used was approximately  $100\text{ nb}^{-1}$ . The standard software (CORRECTEM) was used to apply the same energy corrections to EM clusters as were applied to the  $W \rightarrow e\nu$  and  $Z \rightarrow ee$  samples [8]. Duplicate events were removed.

## 3 Backgrounds

### 3.1 Fake electrons

The dominant background to the  $J/\psi \rightarrow ee$  process is contributed by pairs of fake electrons. The main sources of fake electrons at low energies are  $\pi^0 \rightarrow \gamma\gamma$  and  $\eta \rightarrow \gamma\gamma$  decays, in which the two photons are not resolved into separate clusters and a track is associated with the cluster, because of

a random track overlap or a conversion of one of the photons. These will be referred to generically as  $\pi^0$ s. Other fakes, which are much less important, include charged hadrons which fluctuate in showering to deposit most of their energy in the EM layers of the calorimeter, single photons which convert, and multiparticle jets.

### 3.2 Physics backgrounds

There are two main processes other than  $J/\psi \rightarrow ee$  decays which are expected to produce low mass electron pairs, namely Drell-Yan production and heavy quark ( $b$  and  $c$ ) decays to electrons. The latter can be divided into three mechanisms: sequential  $b$  quark decays, parallel decays of pairs of heavy quarks, and decays of heavy quark pairs produced by gluon splitting. Electron pairs from the Drell-Yan process and parallel decays tend to be back to back. These events do not contribute to the low mass region because of the  $E_T$  cut on the electrons.

Sequential decays and decays of quark pairs from gluon splitting produce electrons which originally come from one parton, so that the pair tends to have a small opening angle, and hence small invariant mass. However, these electrons tend to be non-isolated and do not contribute much. The contribution from  $\psi'$  decays is negligible [9].

## 4 Selection criteria

Most of the analysis was performed using a “daughter sample”, i.e., a sample of manageable size ( $\approx 35k$  events) selected with loose cuts from the large ( $> 600k$  events) special run dataset. The daughter sample was selected by requiring two central, isolated electromagnetic clusters, at least one of which had a track in the road in the CDC. A cluster is electromagnetic if more than 90% of its energy is in the EM layers and more than 60% of its energy in a single tower. An EM cluster is a PELC if it has a track in its road, else it is a PPHO. A PELC or PPHO is defined to be central if its hottest calorimeter tower has  $\eta$  index  $|i\eta| \leq 12$ . Isolation is defined in section 4.2.1 below.

## 4.1 $\Delta R$

For a pair of clusters with direction coordinates  $(\eta_1, \phi_1)$  and  $(\eta_2, \phi_2)$  the distance in  $\eta - \phi$  space,  $\Delta R$ , between them is given by:

$$\Delta R = \sqrt{(\eta_1 - \eta_2)^2 + (\phi_1 - \phi_2)^2}$$

where the  $\phi$  difference is in radians modulo  $2\pi$ . The  $\Delta R$  of a cluster pair is correlated with the mass of the pair. The data (figure 1) shows two components to the background invariant mass distribution, which can be separated by a  $\Delta R$  cut, which essentially corresponds to a soft invariant mass cut. The low mass component corresponds to cluster pairs which are correlated in direction. It is the low mass component which is an important background to the  $J/\psi$ . Although  $J/\psi \rightarrow ee$  decays have small values of  $\Delta R$ , no cut was made to the data sample used to fit the  $J/\psi$  mass, since it removes background in an unimportant mass region. However, it is important to distinguish between the two components. Drell-Yan and upsilon production are both expected to contribute isolated electrons in the high mass region, so that the QCD background normalization cannot simply be taken from the high mass region.

## 4.2 Electron identification cuts

### 4.2.1 Isolation

The isolation (or isolation fraction) of an EM cluster (PELC or PPHO) is defined as the ratio

$$\frac{E\_TOT(0.4) - E\_EM(0.2)}{E\_EM(0.2)}$$

Where  $E\_TOT(R)$  and  $E\_EM(R)$  are the total and electromagnetic energies in a cone of size  $R$  in  $\eta - \phi$  space centered on the cluster direction. It is useful to require electron candidates to have low isolation fractions because hadron jets typically are much wider than electrons so that the isolation cut improves the signal to background ratio. An isolation requirement also selects well measured electrons by rejecting clusters which have large overlapping energy from other nearby particles. A cut of isolation  $< 0.4$  was applied to reinforce the cut applied at the level 2 trigger, which is necessary because the reconstructed clusters may be different from the level 2 EM objects.

#### 4.2.2 CDC Ionization

Conversions, which occur mainly in the TRD, can be rejected using the ionization measured in the CDC, since  $\gamma \rightarrow e^+e^-$  will typically deposit twice as much charge as a single MIP. A cut on the CDC ionization  $< 1.5 \text{ MIP}$  is used to reject conversions in the signal sample. Cutting on  $> 1.5 \text{ MIP}$  defines a background sample.

#### 4.2.3 Number of tracks

Requiring the number of tracks in the PELC road to be exactly one removes some QCD background, from jets with several charged particles. This cut also rejects low energy conversions in which the tracks separate. It selects well measured electrons, since it removes electron candidates with another charged particle in the electron road which adds energy to the electron cluster. Since the invariant mass is calculated from the tracking angles, this requirement should also improve the mass resolution.

#### 4.2.4 Spread

Spread is a variable originated by the direct photon group. The spread of a PELC or PPHO is a measure of the width of the cluster, and is expected to be higher for  $\pi^0$  clusters formed from two photons than for single electron or photon clusters. Distributions of spread for plate-level Monte Carlo electrons and  $\pi^0$ s with full noise simulation indicate that it is useful for  $\pi^0$  rejection. Cuts on spread also improve the resolution in the Monte Carlo sample. A detailed study of this variable applied to low energy electron identification is available [10].

## 5 Fits and error estimation

A tight sample was used to fit the resonance mass. Although with tight cuts reduce the number of events in the peak, there is a significant improvement in resolution, the underlying event correction becomes less important and the dependence of the fit on the background shape is reduced, so that imposing the tight cuts improves the result. The  $E_T$  cut is important because it affects the average  $f$  value (see section 7.) The cut is chosen so that the level 2



threshold does not bias the computation of  $f$ . The tight sample was derived from the daughter sample with the following cuts, each applied to the two leading  $E_T$  PELC objects:

- $E_T > 3 \text{ GeV}$
- $|i\eta| \leq 12$
- isolation  $< 0.4$
- exactly one track in the road
- ionization  $dE/dx < 1.5$
- spread  $< 0.7$

The invariant mass spectrum with these cuts shows a clear peak near the  $J/\psi$  mass (figure 2), with a width comparable to widths expected from monte carlo samples. The statistical significance of the peak is about  $6\sigma$ . The background shape was measured from the data using events in which there are two EM clusters without tracks, which are expected to be dominantly  $\pi^0$ s. The cuts applied to this PPHO-PPHO sample were

- $E_T > 3 \text{ GeV}$
- $|i\eta| \leq 12$
- isolation  $< 0.4$

The distribution of the invariant mass of these cluster pairs was fit with a 6th degree polynomial (figure 3). This polynomial was taken to be the measured background shape. A binned fit was performed using a gaussian signal shape added to the measured background shape with a floating background normalization. This fit is shown superimposed on figure 2.

Since the signal sample contains a small number of events, an unbinned maximum likelihood fit was also performed. A mass window from  $2.0 \text{ GeV}$  to  $4.1 \text{ GeV}$  was imposed on the data. The likelihood function was taken as a sum of signal plus background as a function of invariant mass. The signal shape was a gaussian of floating normalization, mass and width. The background shape was the measured shape from the PPHO-PPHO sample.

Figure 4 shows 2-dimensional likelihood contours for the mass and width. The result for the uncorrected mass fit and statistical error is

$$M_{J/\psi}^{uncorrected} = (3.102 \pm 0.035(stat)) GeV$$

The fitted width is  $(115 \pm 25) MeV$ .

The main correction to be applied is the shift in the reconstructed electron energies from the underlying event. In any  $p\bar{p}$  process there are soft particles in the final state from spectator partons, which can overlap with the electron clusters reconstructed in the calorimeter. For  $J/\psi$  events the situation is complicated by the presence of additional activity close to the electrons. In the case of  $B \rightarrow J/\psi$  production, particles are produced close to the  $J/\psi$  by both the fragmentation of the  $b$  quark and the decay of the  $B$  meson or baryon into the  $J/\psi$  plus other particles. In the case of  $\chi_c \rightarrow J/\psi + \gamma$  production, the photon from the  $\chi_c$  decay is close to the  $J/\psi$ . Although the effects of the underlying event from spectator partons can be estimated using either minimum bias events or a monte carlo model of the soft spectator processes, the effect of the correlated activity can most easily be studied using the monte carlo samples. The contribution from both sources is affected by the quality cuts, and the correlation between the correction and the cuts is modelled using the monte carlo.

The correction was determined by fitting two monte carlo samples. One was generated with the full ISAJET  $p\bar{p}$  event, figure 5. The other sample consisted of the same events with only the  $e^+e^-$  pair from the  $J/\psi$ , figure 6. The relevant cuts were applied to both samples. The difference between the two fitted masses was taken as the correction to be applied to the data fit. The error assigned was the value of the correction:

$$\delta M_{J/\psi}^{underlying\ event} = (0.080 \pm 0.080) GeV$$

This correction depends on the monte carlo model. However, a constraint is provided by the width of the peak, which is close to that expected from the sampling resolution. A large underlying event contribution would widen the peak.

No cut was applied to ensure that the electrons were far from the cracks between the CCEM modules. The effect of the cracks was investigated by applying crack distance cuts of 0.01 and 0.02. The fitted mass increased by  $10 MeV$  with the 0.01 cut (the standard cut, based on testbeam crack scans)

<i>Source of error</i>	<i>Uncertainty (MeV)</i>
statistical	35
background and fitting	8
crack	10
underlying event	80
linearity	170
total	190

Table 1: Errors in the  $J/\psi$  fitted mass

and by  $20\text{MeV}$  with the 0.02 cut. Both are within statistical error. The fitted mass was corrected by  $+10\text{MeV}$ . This correction was conservatively assigned an error of  $\pm 10\text{MeV}$ . A cut was not applied directly to the data because the distance between an electron candidate and the nearest crack is computed from the calorimeter centroid of the shower, which is not well understood at low energies.

The final corrected value is

$$M_{J/\psi}^{\text{corrected}} = (3.032 \pm 0.035(\text{stat}) \pm 0.190(\text{sys})) \text{ GeV}$$

The systematic errors are shown in table 1.

The largest error comes from the lack of constraint on the linearity at low energy from the test beam. Residuals in linear fits to the energy response of test beam electrons show peak to peak excursions of the order of  $300\text{MeV}$ , which could be interpreted as indicating nonlinearity. The uncertainty can be estimated conservatively by taking the maximum excursions from the fit as the linearity error on the measured energies [3, 11].

## 6 Consistency checks

The width of the peak is completely determined by the measurement resolutions. For comparison, a toy monte carlo was used to generate the electron pair at the 4-vector level. The energies were smeared with a sampling term of  $0.13/\sqrt{E_T}$ , a constant term of 0.01 and an exponentially distributed underlying event term of  $90\text{MeV}$ . The resulting width was  $153\text{MeV}$ . This

was checked with plate level GEANT samples, which give a width of about 140  $MeV$ . The measured width of  $(115 \pm 25)MeV$  is therefore consistent with expectations.

The expected number of events depends on the efficiencies of the selection cuts. From monte carlo samples with noise simulation, the number of events expected was estimated to be between 5 and 50. This is an order of magnitude check only, since there are large uncertainties in the efficiencies and in the theoretical cross sections at this time.

The background invariant mass shape from the PPHO-PPHO sample was checked by using the PELC-PPHO sample as well as the PELC-PELC sample where one PELC is required to have  $dE/dx > 1.5 MIP$ . All these spectra were consistent. The estimated normalization of the background was calculated to be  $0.012 \pm 0.004$  from the probability that an isolated  $\pi^0$  is reconstructed as a PELC (determined to be  $0.3 \pm 0.05$  from the conversion and random track overlap probabilities) and from the rejections of the  $dE/dx$ , number of tracks and spread cuts determined from the inclusive PELC sample. The normalization from the fit was 0.0116, which is consistent with the prediction.

Other checks were performed, including tightening the isolation and  $E_T$  cuts on the PELCs, replacing the spread cut with a track match significance cut, and checking kinematic distributions ( $E_T$ ,  $P_T^{ee}$ ,  $\eta$  vs.  $\phi$ , etc.)

All checks indicated that the observed mass peak is consistent with expectations from  $J/\psi$  production.

## 7 Extraction of calibration constants

The scale,  $\alpha$ , and offset,  $\beta$ , are determined from the fitted  $Z$  and  $J/\psi$  resonance positions and from the mean  $f$  values for each resonance [12]:

$$f = \frac{(\tilde{E}_1 + \tilde{E}_2)(1 - \cos \theta)}{\tilde{M}_{ee}}$$

$$\alpha = \frac{M_Z f_\psi - M_\psi f_Z}{\tilde{M}_Z f_\psi - \tilde{M}_\psi f_Z}$$

$$\beta = \frac{\tilde{M}_Z M_\psi - \tilde{M}_\psi M_Z}{\tilde{M}_Z f_\psi - \tilde{M}_\psi f_Z}$$

<i>Source of error</i>	<i>Uncertainty (MeV)</i>
$M_{J/\psi}^{stat}$	75
$M_{J/\psi}^{sys}$	400
$M_Z^{FIT}$	15
$f_\psi$	20
$f_Z$	15
total	410

Table 2: Errors in  $\beta$

The distributions of  $f$  for the  $Z$  and  $J/\psi$  samples used in the mass fits are shown in figure 7. The mean values are  $f_Z = 1.82 \pm 0.1$  and  $f_\psi = 0.56 \pm 0.1$ . The mean  $f$  can be affected by background, so the appropriate  $f$  for each resonance can be determined more accurately by adding an offset  $\beta_0$  to the electron energies in the data and refitting the resonance position  $M(\beta_0)$ .  $f$  is then determined as  $dM(\beta_0)/d\beta_0$ . This approach gives  $f_\psi = 0.61 \pm 0.1$  [13]. Each  $f$  is conservatively assigned a systematic error of 0.1 which reflects the uncertainty due to the background and the effect of kinematic cuts. This uncertainty has a minimal effect on the measurement of  $\beta$ . The  $Z$  masses used were  $M_Z = 91.19 \text{ GeV}$  and  $\tilde{M}_Z = (87.17 \pm 0.18) \text{ GeV}$  [1, 5].

Table 2 shows the error in the calculated value of  $\beta$  from uncertainties in  $M_\psi, M_Z, f_\psi$  and  $f_Z$ .

The final result is

$$\alpha = 1.049 \pm 0.009$$

$$\beta = (-130 \pm 410) \text{ MeV}$$

## 8 Implications for the $W$ mass measurement

The error on  $\beta$  is the dominant source of the systematic component of the energy scale error in the  $W$  mass. The  $W$  mass is measured as a ratio of  $M_W/M_Z$  which is then scaled to  $M_Z^{LEP}$ . Any error in the scale  $\alpha$  completely cancels in the  $M_W/M_Z$  ratio, provided that  $\beta$  is zero. The effect of non-zero

$\beta$  is summarized in the formulas:

$$M_W^{D0}(\beta = 0) = \frac{M_W^{FIT}}{M_Z^{FIT}} M_Z^{LEP}$$

$$M_W^{D0}(\beta = \beta_0) = \frac{M_W^{FIT}}{M_Z^{FIT}} M_Z^{LEP} + f \frac{\beta_0}{\alpha} \frac{M_Z - M_W}{M_Z M_W}$$

The first formula is a special case of the second, and represents the case of a pure scale. The second formula quantifies the effect of an error in the assumption of a pure scale. The superscript *FIT* refers to a numerical fitted value using the nominal testbeam calibration. The error on the first term is the sum in quadrature of the errors on  $M_Z^{LEP}$ ,  $M_W^{FIT}$  and  $M_Z^{FIT}$  propagated into the ratio, all including statistical and systematic non-scale errors on each fit. The error on  $M_Z^{FIT}$  is dominated by statistics. The statistical error on  $M_Z^{FIT}$  can be considered as a scale error with respect to a measurement of  $M_W$  or a statistical error with respect to an  $M_W/M_Z$  measurement. The error on  $\beta$  introduces an additional component to the error on  $M_W$  which is properly systematic. This error can be propagated by varying  $\beta$  by its error and using the above formula to obtain the spread of values obtained for  $M_W^{D0}$ . This variation added to the error on  $M_Z^{FIT}$  in quadrature is what is called the scale error. The error in  $M_W$  using the  $J/\psi$  with the  $Z$  is  $190 \text{ MeV}$ , which should be compared to  $255 \text{ MeV}$ , which is the current error from the binned  $Z$  method.

## 9 Conclusion

A  $J/\psi \rightarrow ee$  signal has been observed at  $D0$ . In spite of the poor detection and reconstruction efficiency, the signal provides a useful calibration point for the electromagnetic energy scale. Even with the small data sample used, the error on the electron energy offset  $\beta$  is systematics limited. The offset is consistent with zero.

## References

- [1] Particle Data Group, *Phys. Rev. D* **45** (1992)
- [2] W. Dharmaratna, DØ Note 1731
- [3] N. Graf, DØ Note 2313 (in preparation.)
- [4] U. Heintz and I. Adam, DØ Note 2314 (in preparation.)
- [5] I. Adam, in DØ Note 2128 (WZ transparencies from APS 94)
- [6] E.W.N. Glover, A.D. Martin and W.J. Stirling, *Z. Phys. C* **38** 473 (1988)
- [7] E. Braaten et al., FERMILAB-PUB-94/135-T
- [8] See WZ\$\_{HROOT}\$:[WMASS]CORRECTEM.RCP
- [9] From UA1 results. S. Wimpenny, DØ Note 1254
- [10] C. Bormann, DØ Note 2297
- [11] N. Denisenko, DØ Note 1852
- [12] U. Heintz, DØ Note 1819
- [13] I. Adam, in DØ Note 2301 (transparencies from the WZ meeting Sept 7, 1994)

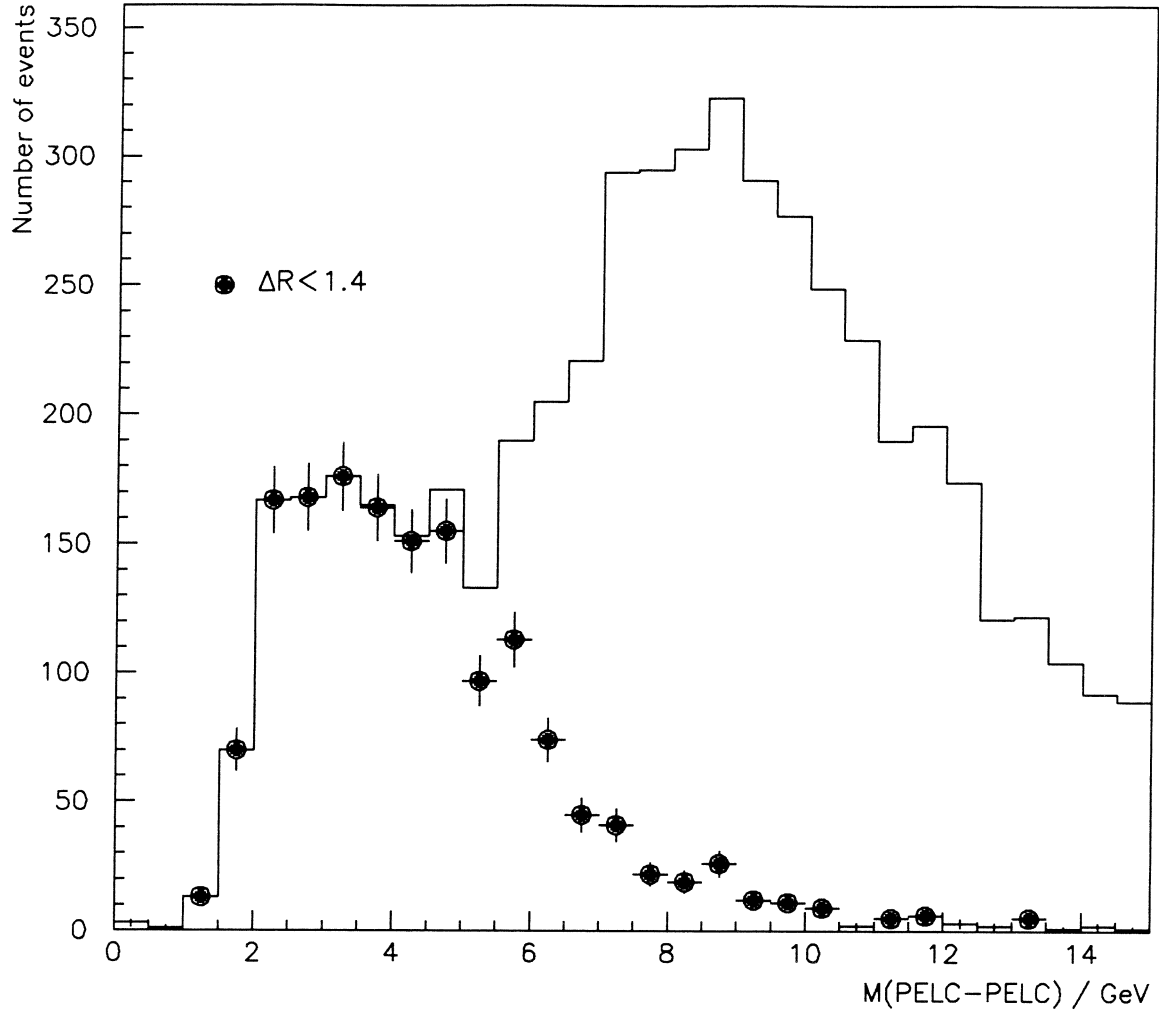


Figure 1: The pair invariant mass distributions for PELC-PELC pairs in the  $J/\psi \rightarrow ee$  special run data and correlation with  $\Delta R$ .



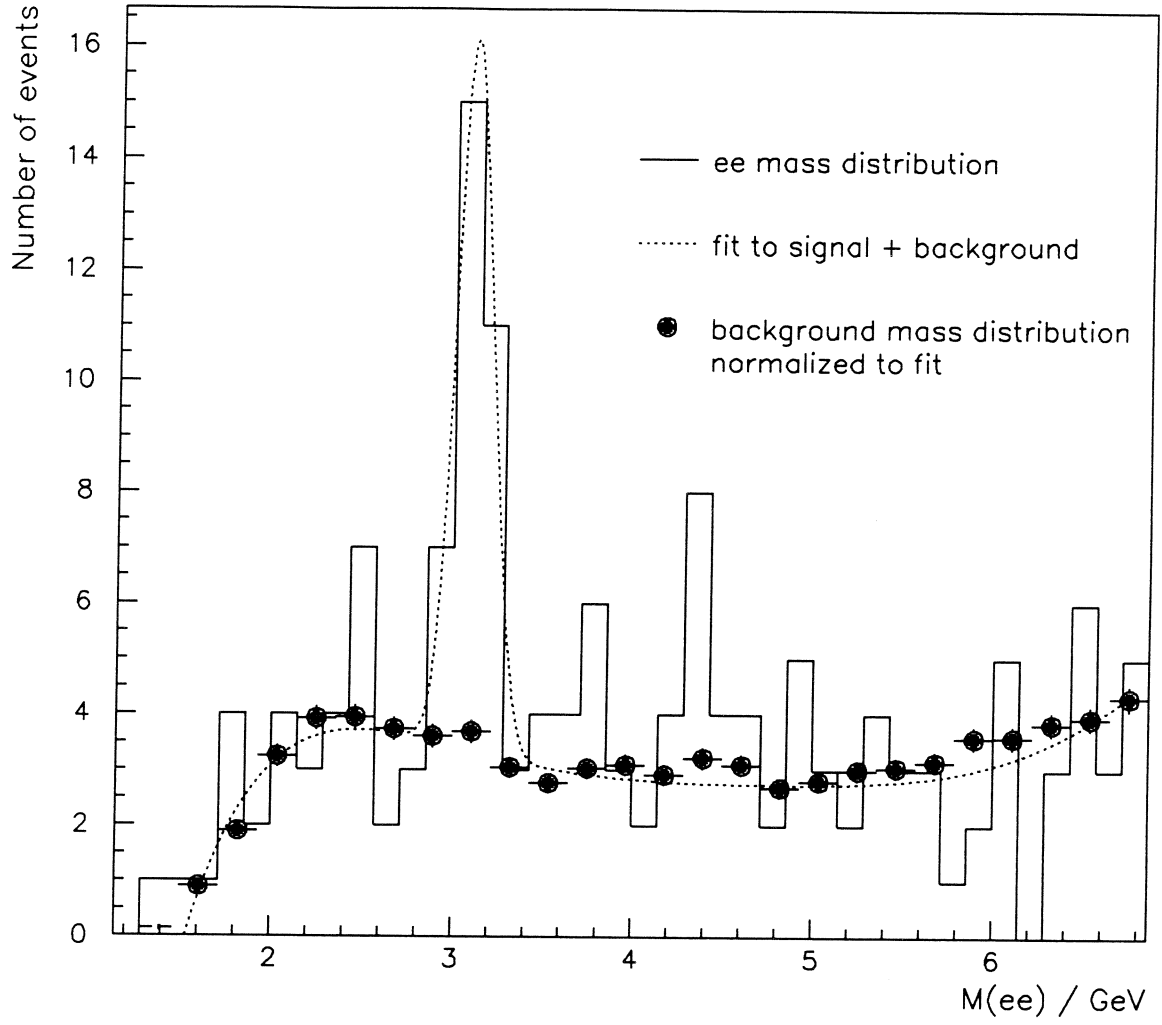


Figure 2: The PELC-PELC invariant mass distribution with quality cuts.

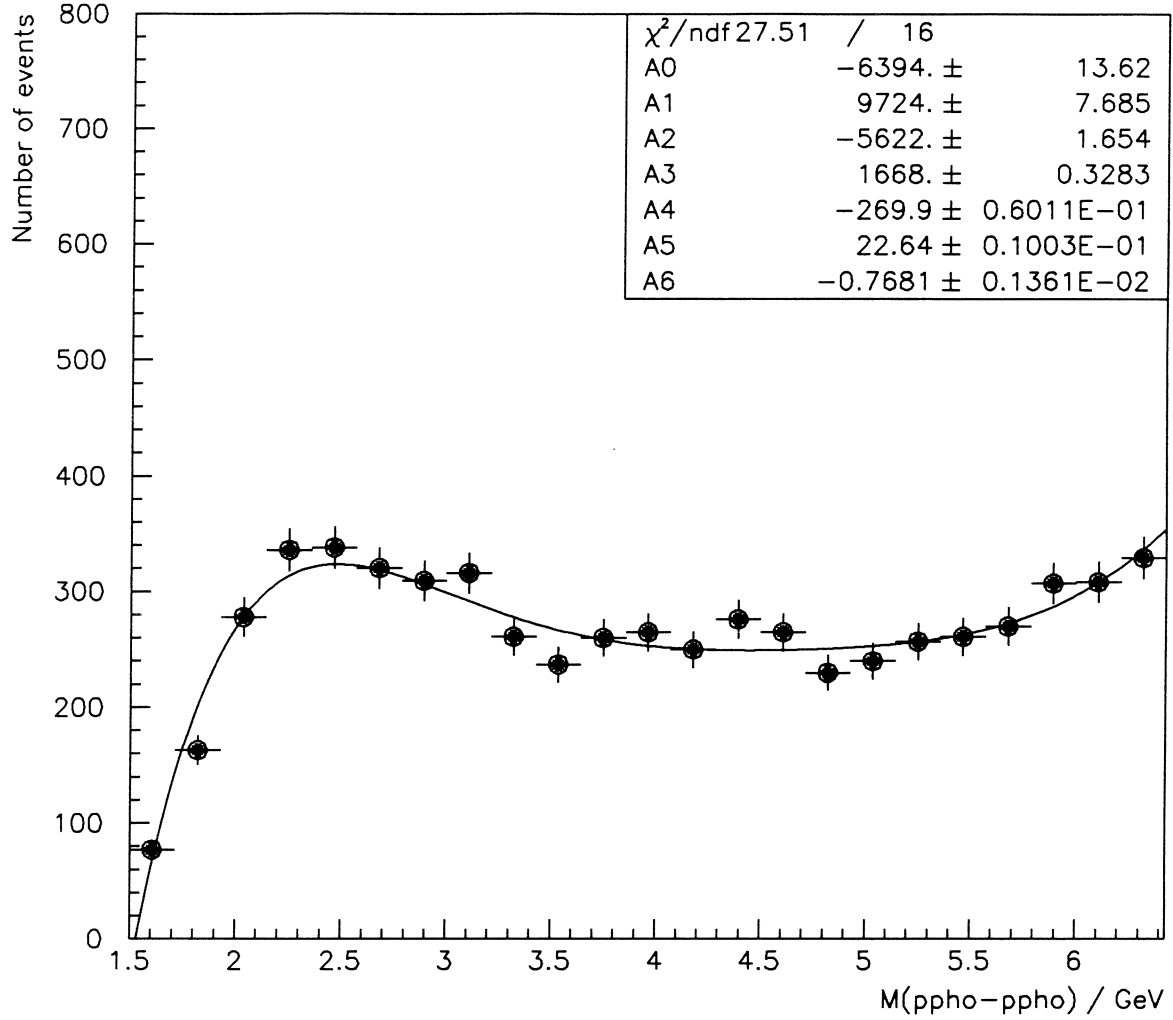


Figure 3: The PPHO-PPHO invariant mass distribution used to define the background shape.

Maximum likelihood fit : 1 and 2  $\sigma$  contours

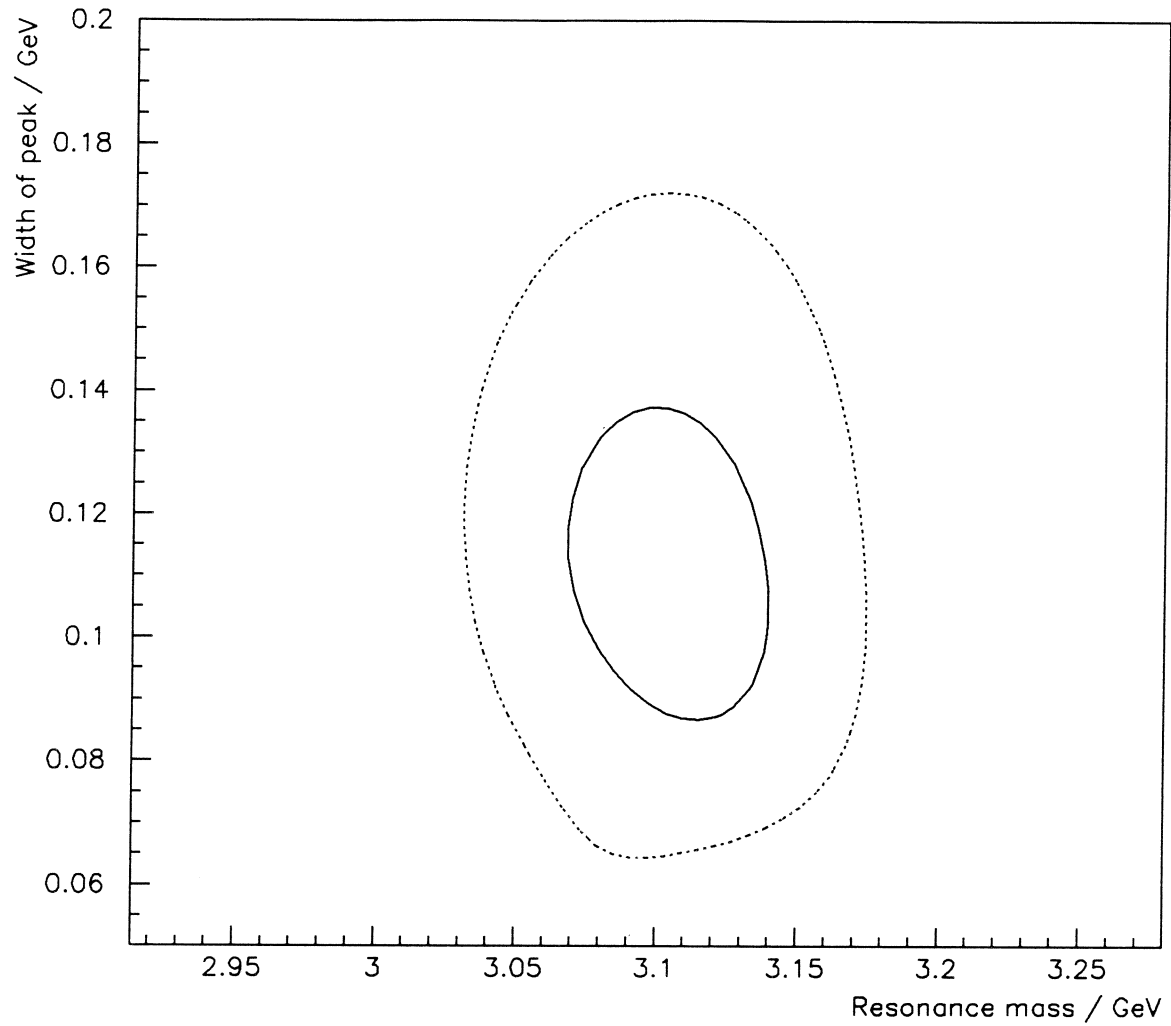


Figure 4: 1 and 2  $\sigma$  likelihood contours for the mass and resolution of the  $J/\psi$  resonance.

$B \rightarrow \psi \rightarrow ee$  Plate Monte Carlo

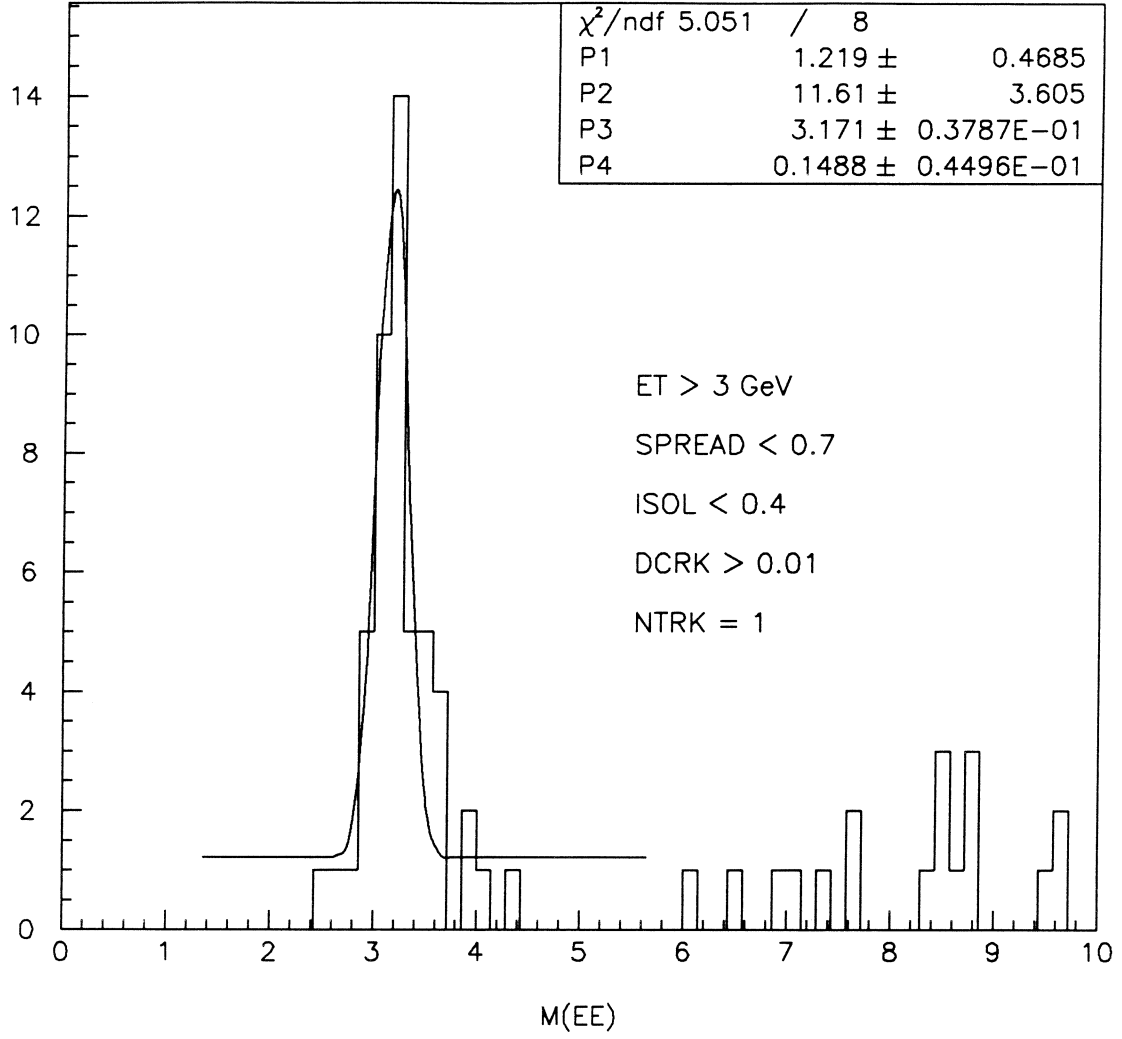


Figure 5: The PELC-PELC invariant mass distribution from monte carlo data with quality cuts.

$B \rightarrow \psi \rightarrow ee$  leptons only

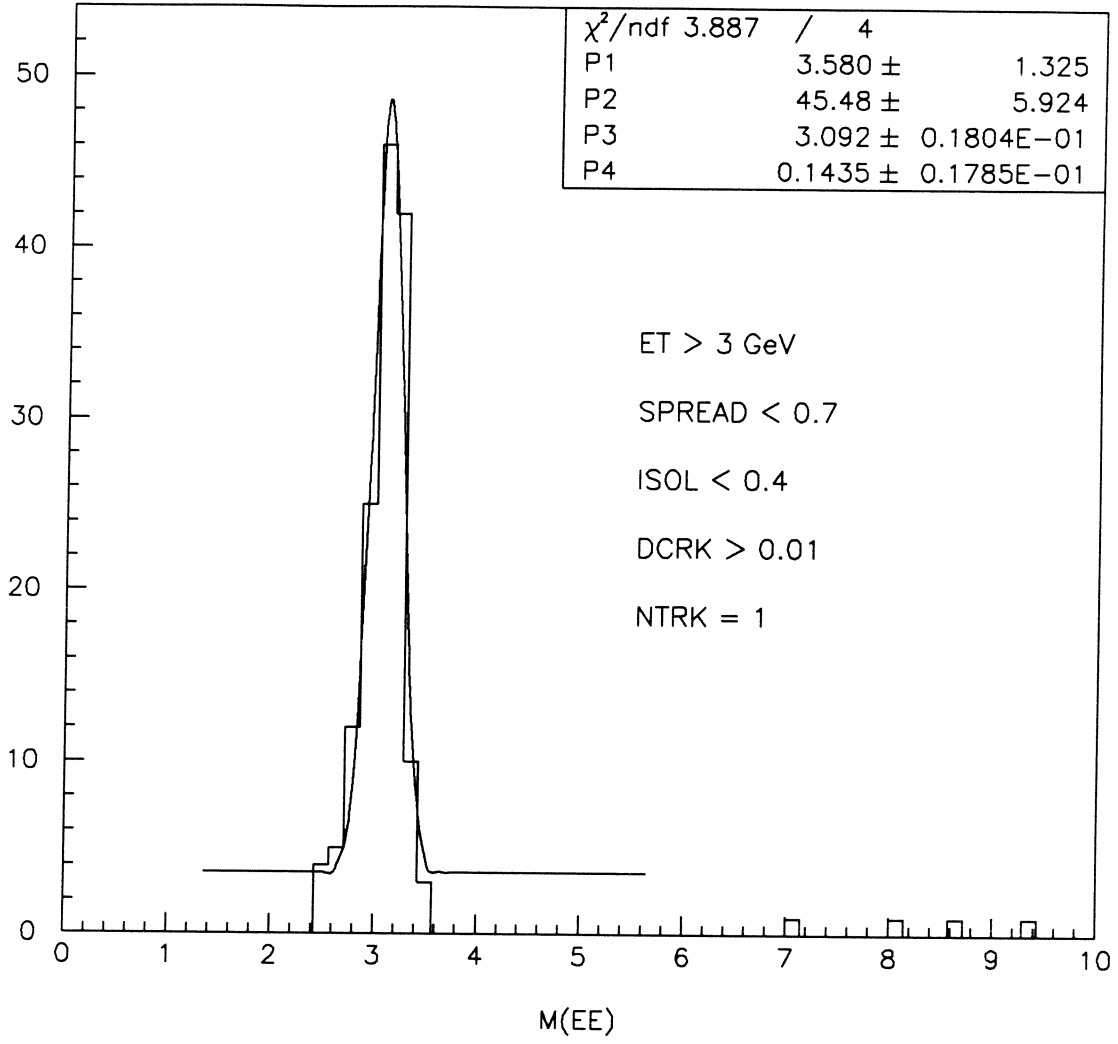


Figure 6: The PELC-PELC invariant mass distribution from monte carlo data without underlying event.

$\langle f \rangle$  from data

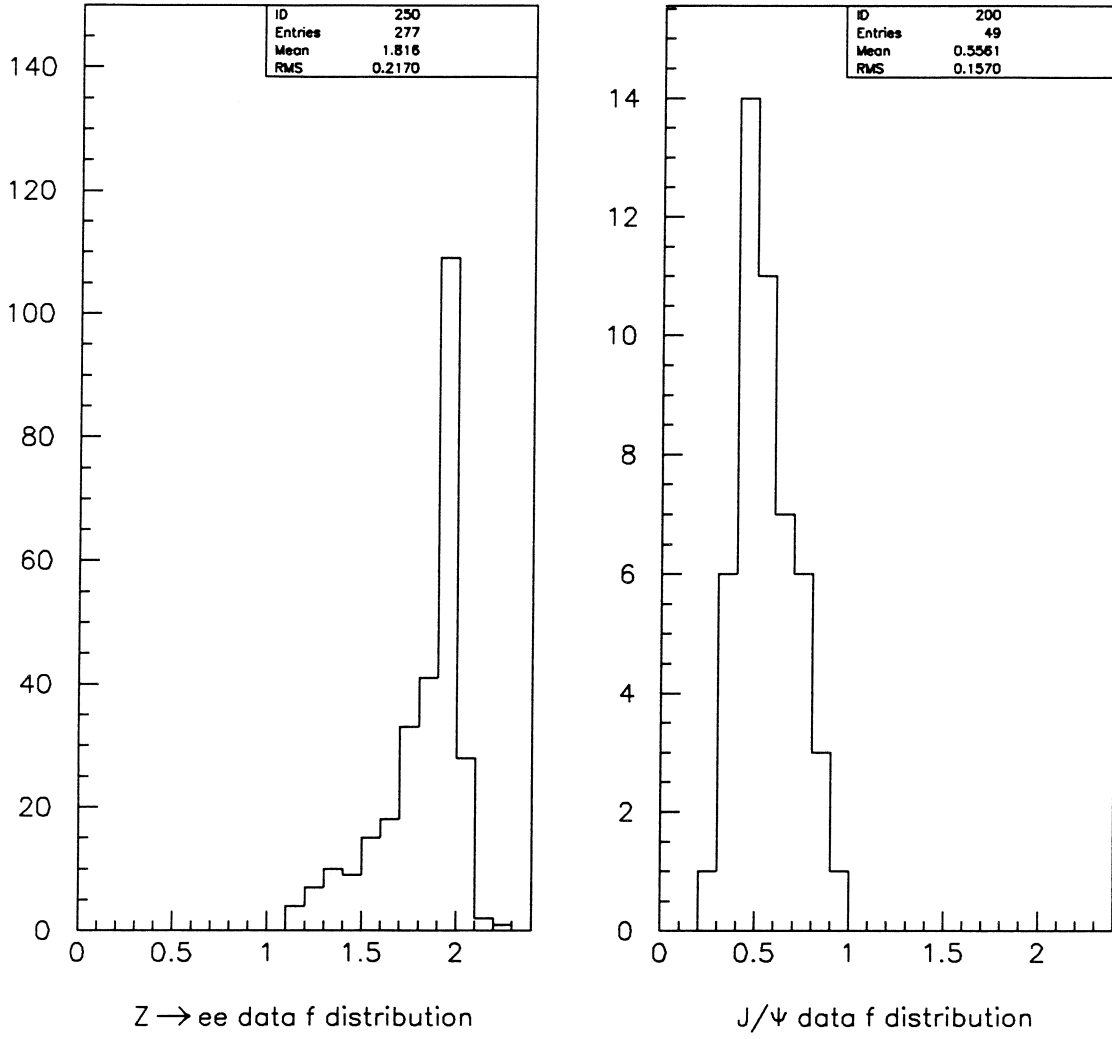


Figure 7: The  $f$  distributions obtained from  $Z \rightarrow ee$  and  $J/\psi \rightarrow ee$  candidates from collider data.



# Optimizing Jet Energy Resolution with Jets Simulated from Test-Beam Data

John P. Borders

Restrictions introduced in the optimization of the energy response of the DØ calorimeter to hadrons worsen hadron energy resolution by a total of about 6% for the sampling term  $S$  over that found using an unrestricted optimization.<sup>[1]</sup> The worst degradation occurs when the weights for the electromagnetic layers are fixed to values that provide the best resolution for single electrons. Another restriction that produces a clear loss in resolution is when the weights are required to be independent of the energy of the incident particle. These restrictions can produce similar or perhaps even more detrimental effects on jet resolution. Finally, the somewhat intuitive prediction that the Default Set of weights would be best for jet resolution leads to a loss in single hadron resolution of about 9-11% in the sampling term  $S$ . Without a detailed knowledge of the composition of jets, it is difficult to predict the impact of such restrictions. Unfortunately, jets of precise energy cannot be produced in test beams, and consequently cannot be studied in a calorimeter.

However, production of jets can be modeled using Monte Carlo generation based on QCD theory. The individual hadronic fragments of such jets can be taken from a library of data obtained in the test beam, summed to form a jet, and then propagated through the detector to simulate the response of the DØ calorimeter to jets. In this analysis, we use such simulations to study the effects that the restrictions placed on single-hadron optimization produce on jet resolution. In particular, we study the effects on jet response using the default weights from previous analysis,<sup>[1]</sup> and investigate possible alternate schemes for improving jet resolution.

## 1 Generating Test Beam Jets

The Particle Library, based on data from the test beam, was formed to provide the individual particles needed for generating jets.<sup>[2]</sup> The Particle Library contains both electron and hadron data over the full range of energies studied at the test beam, but only at the position corresponding to  $\eta=0.05$  and  $\phi=3.16$  in the DØ calorimeter. Extrapolations, also described in Appendix B, are performed to shift the scales and locations of particles to the appropriate energies and positions of specified jet constituents. These particles are then superimposed to form complete jet events which mimic DØ events on a cell-by-cell level.

To specify the structure of the jets to be built by the Particle Library, partons were generated at minimum transverse energies of 20, 30, 40, 50, 63, 80, 100, 120, 150, 175, and 200 GeV, using the Isajet program. After fragmentation and radiation, the jet with the highest  $p_T$  from the collision was selected and stored in a file specifying the energy, type, and the  $\eta$



and  $\phi$  for each constituent. For each specified minimum energy, this process produced a group of jets distributed around the minimum energy. The specified set of minimum energies had been selected so that, taken all together, the Isajet events had a broad range of energies with essentially uniform distribution between about 15 and 225 GeV. We will refer to these seed events as "Isajet events", to distinguish them from the test-beam jet events ("TB jets"), which are constructed using the Isajet events.

For each Isajet event, the Particle Library was used to create TB jets that are similar to jets seen in the DØ detector. Because the library is limited to particles at  $\eta=0.05$ , only central jets could be simulated accurately (see Appendix B for a discussion of the differences between the assembled jets and DØ jets). For each specified Isajet event, 200 TB jets were constructed from data randomly selected from the Particle Library).<sup>[2]</sup>

## 2 Parameters of Jet Response

Because a non-linearity in the energy response of calorimeters to jets can, in principle, be easily corrected, we will concentrate on issues relevant to the resolution of the DØ calorimeters in optimizing TB jets. The jet resolution was fitted to the same generic equation that was used for parametrizing the energy resolution of single particles.<sup>[1]</sup> However, because the noise term in the jet cannot be simply the sum over the noise of individual hadrons, the  $N$  parameter must be handled differently for TB jets.

For the resolution of hadrons in single-particle test beam data, the noise term  $N$  was equated to the expected standard deviation of an appropriate pedestal distribution, and thereby the number of degrees of freedom in the fit was reduced.<sup>[1]</sup> When the contributions from individual particles are added together to form TB jets, the magnitude of the noise in a typical TB jet will usually be far greater than for a single particle, and will increase with the multiplicity of the jet. Since the multiplicity of a jet also depends upon jet energy, the noise in TB jets will have a dependence upon incident jet energy. This is an artificial feature of building jets from individual particles, and does not reflect the true noise of the calorimeter.

Noise in TB jets was estimated by merging data for inspill pedestal events on a cell-by-cell basis, using the same correction algorithms that were applied to the cells occupied by

the particles in a TB jet, using the following procedure. First, an inspill-pedestal library was created in parallel with the Particle Library: this contained inspill pedestal events from the test beam. For each initial Isajet event that had been used to create TB jets, we then created a jet-pedestal event by adding events from the pedestal library for all individual particles in the Isajet event. Essentially, a TB jet was built, but with cells containing only pedestal signals, rather than ionization energy. This procedure overestimates the noise seen in a DØ jet-pedestal event by an amount equivalent to that in a TB jet relative to a real (DØ) jet, providing a dependence of the standard deviation of a jet-pedestal event on incident jet energy. The mean value of the jet-pedestal events is, of course, still zero. A plot of the  $N$  parameter (i.e., the average width of the jet-pedestals) vs. incident jet energy, in 5 GeV intervals, is shown in Fig. 1. A fit to the energy dependence is also shown in the figure, and is given by:

$$N(E) = P_1 + P_2 \ln(E) \quad (1)$$

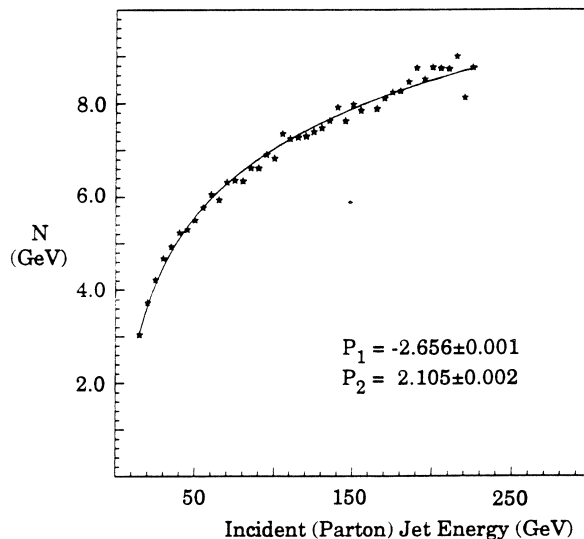


Figure 1 Standard deviation of "artificial" inspill pedestals (jet-pedestal events) as a function of incident jet energy

Due to the way the data in the Particle Library are scaled for low incident energies (see Appendix B), the noise for a single particle ( $\approx 1.9$  GeV) does not have to correspond exactly to the noise at smallest jet energy in Fig. 1. Also, the same scaling techniques cause the

above fit to become non-physical at energies less than about 10 GeV (for example,  $N(5 \text{ GeV}) \approx 0$ ). Since the particle library is only used down to 15 GeV, this will not present a problem.

Using Eq. 1 in the standard expression for resolution,<sup>[1]</sup> we obtain a modified form that we can use to extract the other parameters of the fractional resolution:

$$\left(\frac{\sigma(E)}{\mu(E)}\right)^2 = C^2 + \frac{S^2}{E} + \frac{\left[P_1 + P_2 \ln(E)\right]^2}{E^2} \quad (2)$$

Single hadron analysis indicated that the default weights should be used for building jets. Here we will examine the jet properties found using these weights.<sup>[1]</sup> Figure 2(a) gives a plot of the reconstructed jet energy vs. the incident jet energy, including a linear fit through the data, and the parameters for the fit (the statistical errors on these are very small). In Fig. 2(b) we show the result of the linear fit compared to the fractional energy difference.

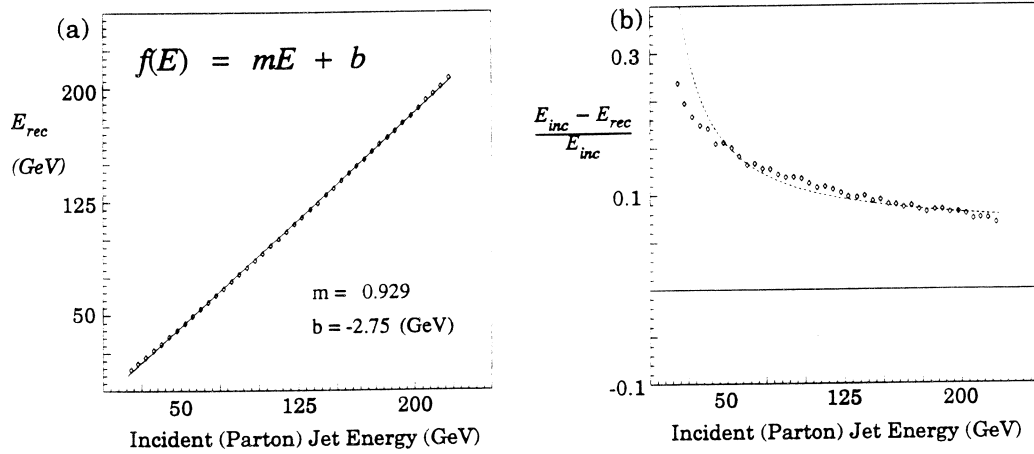


Figure 2 Reconstructed energies obtained using default weights at  $\eta=0.45$

As seen in Fig. 2, the response of the calorimeter to energy is not completely linear, and has both a large offset and a slope that differs significantly from 1.0. In order to correct for these effects, a simple second-order polynomial can be fitted to the response, and the reconstructed energy can be corrected using the resulting function. In this chapter we correct all energies in this manner. The corrected energy for the default weights, in terms of the plot

of fractional energy differences, is given in Fig. 3(a), and the relative resolution is shown in Fig. 3(b).

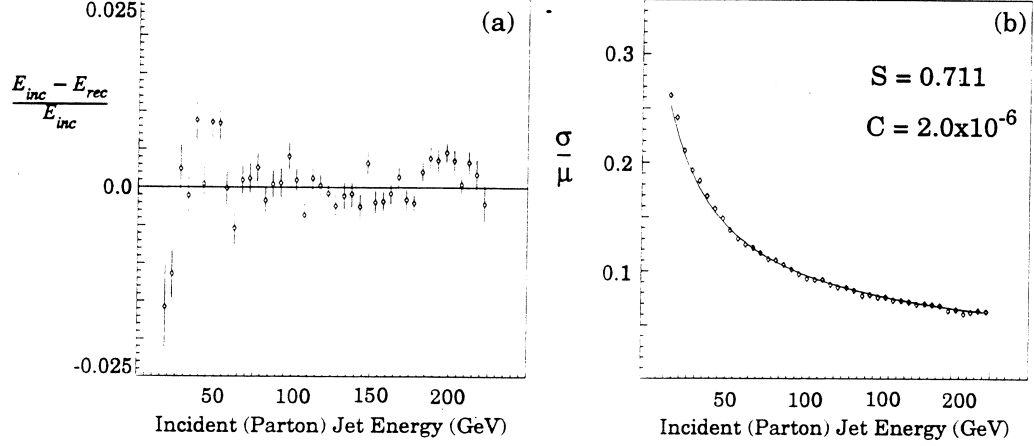


Figure 3 (a) Relative differences and (b) relative resolution for corrected reconstructed jet energies  
The fit that corresponds to the corrected data in Fig. 3 is:

$$E_{rec}^{corr} = P_1 + P_2 E_{rec} + P_3 E_{rec}^2 \quad (3)$$

with  $P_1 = 2.42$  GeV,  $P_2 = 1.13$ , and  $P_3 = -3 \times 10^{-4} \text{ GeV}^{-1}$ , and where  $E_{rec}$  is the uncorrected reconstructed energy shown in Fig 2.

Figure 3 shows that the data at the lower end of the energy range have more scatter than at the central region. This is due to the fact that the simulation of  $D\bar{O}$  jets becomes less accurate at the lowest energies. This breakdown of the simulation is mainly due to the scaling of the lowest energy particles, and an arbitrary cutoff of low-energy jet constituents used when building the TB jets.<sup>[2]</sup>

The Isajet jets in this analysis were required to be in the central region of the calorimeter at the Isajet generation stage. However, due to the way the particle library produces the coordinates of TB jets by shifting the particles at  $\eta=0.05$  to the appropriate coordinates, TB jets will not vary in structure, regardless of pseudo-rapidity of the Isajet jet.

### 3 Optimization of Jet Resolution

All results in the following optimizations will be presented in terms of sampling factors, relative to the default weights. (The default weights correspond to  $dE/dx$  weights for the hadronic layers, and EM-layer weights chosen to optimize the response to electron).

Five different optimization schemes (OS) were implemented to try to improve the energy resolution of TB jets. OS-1 simply varies the relative scales between the EM and hadronic layers, and otherwise uses the default weights. OS-2 allows all weights to vary, and provides a single constant offset  $\delta$  for the simultaneous optimization of all jet energies. OS-3 admits weights that depend on the reconstructed jet energy, and OS-4 allows weights that depend on the fraction of total reconstructed jet energy deposited in the electromagnetic layers (EM fraction). Finally, OS-5 implements a sequential optimization of energy-dependent and EM fraction-dependent variations. A summary of the various optimization schemes is included in Table 1, and the details of the separate optimizations are given below.

**Table 1 Summary of optimization schemes (OS)**

OS	Parameters allowed to vary	# parameters	constant offset $\delta$
1	scale factors describing relative contributions of EM and hadronic sections	2	set to zero
2	energy-independent weights describing the relative contributions of all layers	8	varies
3	parameters describing the energy-dependence of 8 layer weights	16	set to zero
4	parameters describing the EM fraction-dependence of 8 layers weights and a constant offset $\delta$	18	varies
5	parameters describing the EM fraction-dependence and energy-dependence of 8 layer weights and a constant offset $\delta$	8	varies for EM dependence set to zero for energy-dependence

#### 3.1 Optimization of Relative Electromagnetic and Hadronic Scales (Scheme

**OS-1)**

Just as in the case of single hadrons, the relative scales of the signals from the electromagnetic and hadronic sections were varied, keeping the default weights for the individual layers in the two sections. The reconstructed jet energy ( $E_{rec}^k$ ) is found from:

$$E_{rec}^k = \alpha_{em} E_{em}^k + \alpha_{had} E_{had}^k \quad (4)$$

where  $E_{rec}^k$  is the reconstructed energy for TB jet event  $k$ ,  $E_{em}^k$  and  $E_{had}^k$  are the sums of the energies found in the electromagnetic and hadronic layers, respectively (calculated using the default weights), and  $\alpha_{em}$  and  $\alpha_{had}$  are parameters that are varied using our standard optimization routine for all TB jet events (all energies). The resultant values of  $\alpha_{em}$  and  $\alpha_{had}$  are given in Table 2. Uncertainties on these values are not included: since the scales are found through the optimization procedure used to find sampling weights, the uncertainties are of little use in evaluating the results, due to the correlations between them.

**Table 2 Optimized relative scales (OS-1)**

$\alpha_{em}$	1.25
$\alpha_{had}$	0.98

### 3.2 Full Optimization Without Energy Dependence (Scheme OS-2)

The TB jet resolution was optimized simultaneously over the full range of energies, resulting in the set of 8 sampling factors and the constant offset  $\delta$ , given in Table 3. This scheme assumes that the weights are independent of jet energy.

**Table 3 Fully optimized, energy-independent sampling factors (OS-2)**

Calorimeter Layer	Sampling Factors
EM1	2.443
EM2	1.163
EM3	0.856
EM4	1.335
FH1	1.006
FH2	0.895
FH3	0.839
CH	0.758
$\delta$ (GeV)	3.325

### 3.3 Sampling Factors as a Function of Reconstructed Jet Energy (Scheme OS-3)

The energy-dependent weights were found as follows:

1. The default reconstructed energy ( $E_{def}$ ) was calculated using the default weights in Eq. 5.9.
2. The events were divided into 5 GeV bands of  $E_{def}$ .
3. A set of sampling factors were obtained for each band  $E_{def}$ .
4. The sampling factors were fitted to a linear function of  $E_{def}$ .

A constant offset  $\delta$  is not allowed in this optimization, since such an offset is not suitable for optimizations over small energy ranges. The calculated sampling weights, along with the linear fits to  $E_{def}$  are shown as a function of reconstructed energy in Fig. 4. All eight fits are superimposed in Fig. 4(i) to demonstrate the correlations between the weights as a function of energy, along with a line at unity. The parameters for these functions, along with the statistical uncertainties on them, are given in Table 4.



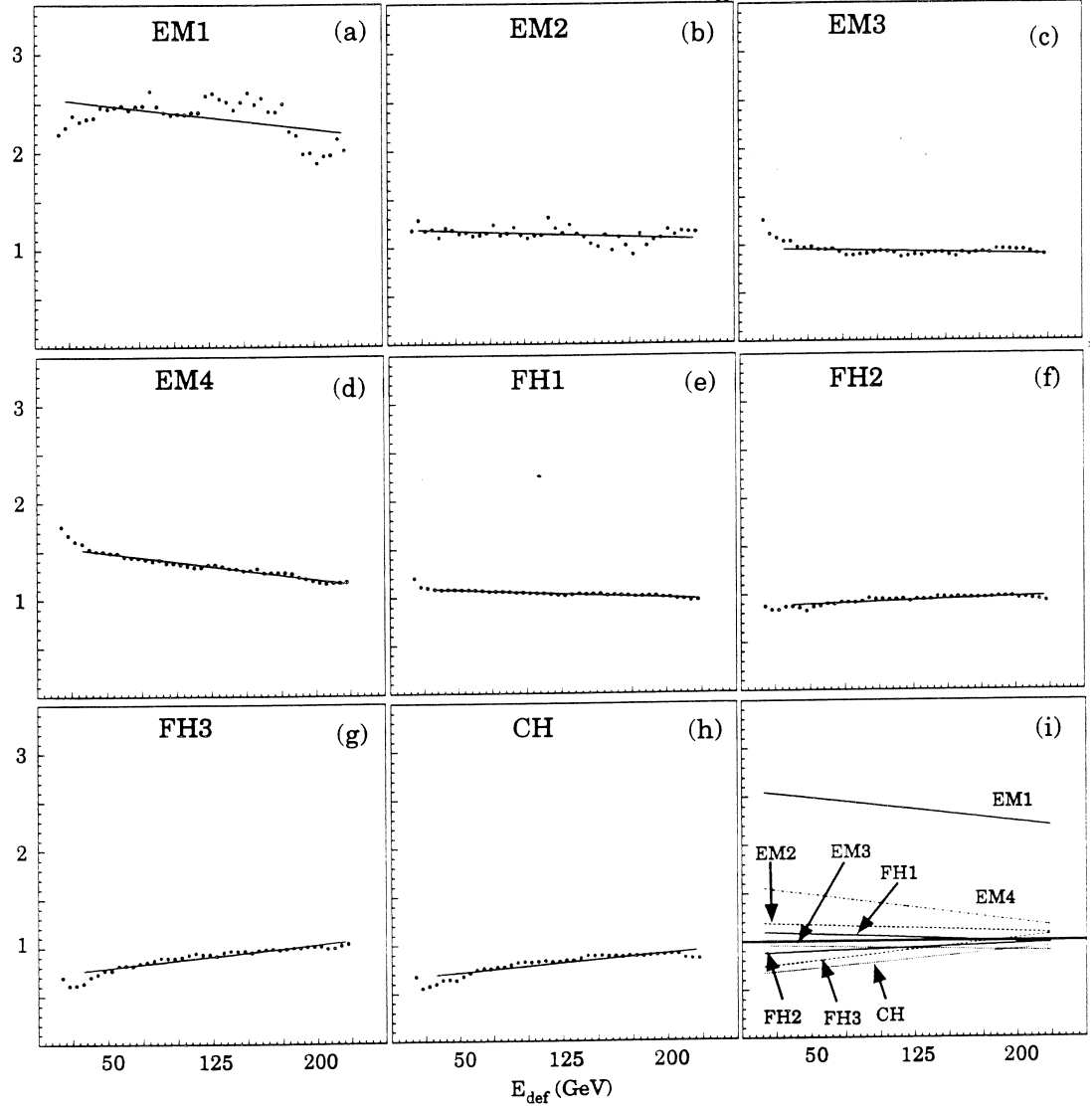


Figure 4 Sampling factors as a function of reconstructed energy (OS-3). The fits are to linear functions of the form  $P_1 + P_2 E_{def}$  (see Table 4).

As can be seen in Fig. 4, the sampling factors at the extreme ranges of the energy scales do not seem to follow the trend observed in the center regions. By changing the ranges for the fits, we have determined that restricting the fits to the trend established by the central energy regions results in the best overall resolutions. The functions in the figures are plotted only over the energy ranges used in the fits.

It can also be seen from Fig. 4 that some of the sampling factors do not seem to depend linearly on energy. We have tried to fit the sampling factors with a more complex energy dependence, but found that using a linear fit provides similar overall resolution, and produces a more linear energy response. We have consequently chosen the simplest parameterization for this study.

**Table 4 Parameters describing energy-dependence of sampling factors (OS-3)**

	$P_1$	$P_2$ ( $\times 10^{-3}$ ) ( $\text{GeV}^{-1}$ )
EM1	$2.571 \pm 0.003$	$-1.69 \pm 0.02$
EM2	$1.195 \pm 0.003$	$-0.51 \pm 0.02$
EM3	$0.963 \pm 0.004$	$-0.33 \pm 0.03$
EM4	$1.579 \pm 0.004$	$-1.88 \pm 0.03$
FH1	$1.104 \pm 0.004$	$-0.56 \pm 0.03$
FH2	$0.870 \pm 0.004$	$0.49 \pm 0.03$
FH3	$0.714 \pm 0.004$	$1.56 \pm 0.03$
CH	$0.652 \pm 0.004$	$1.28 \pm 0.03$

It is interesting that all weights appear to approach unity at highest energies, as shown in Fig. 4(i). This would suggest that these weights should provide the greatest improvement in reconstructed energy resolution at lowest energies.

### 3.4 Sampling Factors that Depend on Jet EM Fraction (OS-4)

The weights that depend on EM fraction were found as follows. Starting out with the default  $E_{def}$  values, as discussed in Section 3.3, we defined  $F_{EM}$  as the fraction of the energy in a TB jet that was reconstructed in the EM section. The  $F_{EM}$  values for all events were divided in bands of 0.04 width, to obtain a set of sampling factors (and a constant offset  $\delta$ ) for all events (independent of energy) within each band of EM fraction. These factors were then fitted as a function of  $F_{EM}$ .

The sampling factors as a function of EM fraction in a TB jet are shown in Fig. 5, along with the linear functions used in the fit. The parameters for these functions, along with their statistical errors, are given in Table 5.

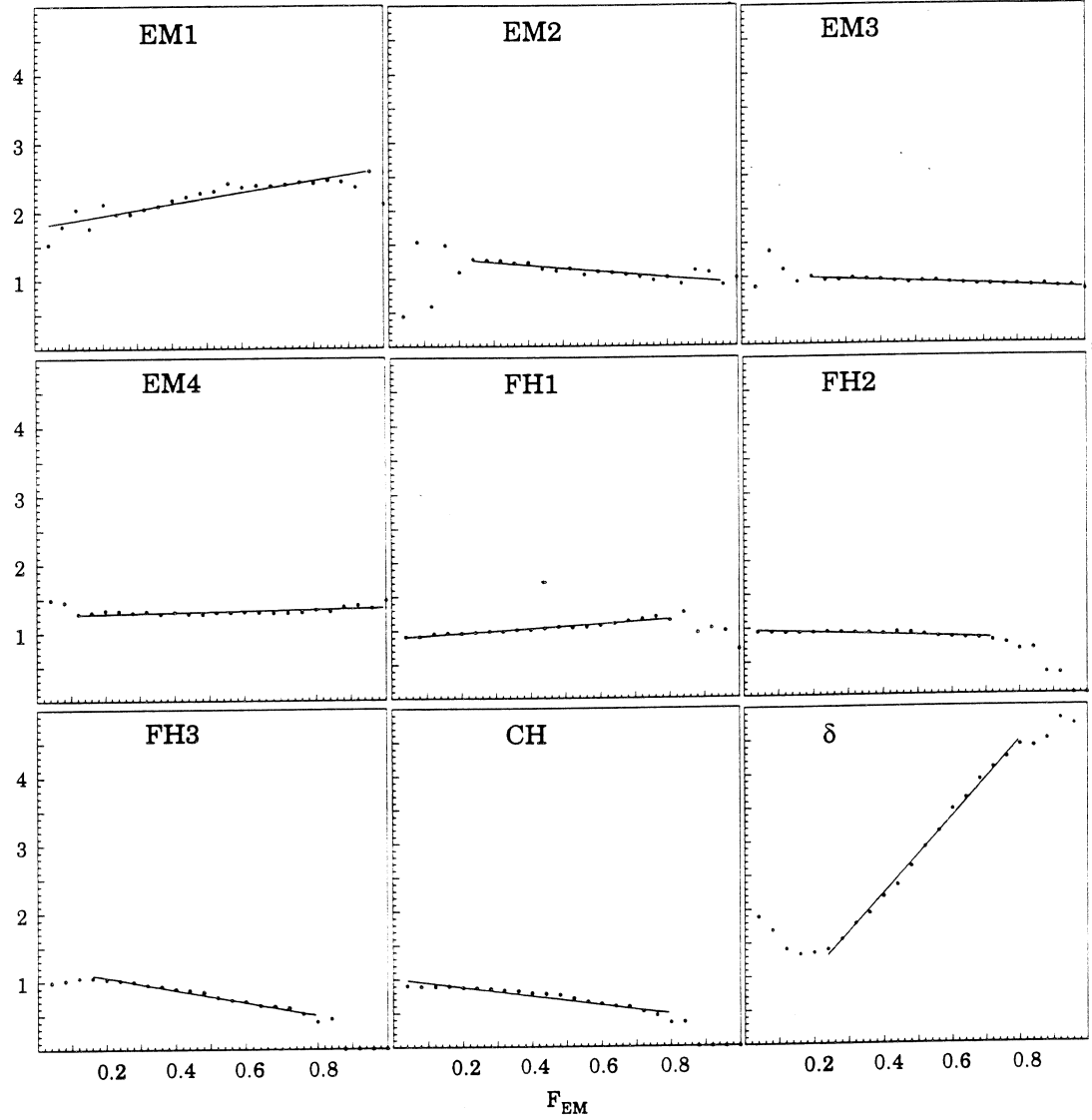


Figure 5 Sampling factors as a function of the fraction of the reconstructed energy in a TB jet that is deposited in the EM section. The fits are to linear functions of the form  $P_1 + P_2 F_{EM}$  (see Table 5)

As seen in Fig. 5, the sampling factors for  $F_{EM} \leq 0.2$  and  $F_{EM} \geq 0.8$ , (especially for  $\delta$ ) show marked deviations from the trend established in the rest of the range. This is caused primarily by the characteristic patterns of energy deposition for jets in these regions. For example, a jet with more than 90% of its energy in the electromagnetic section, will have little energy in CH that could be used to sharpen the CH sampling factor. Also, it should be

recognized that jets usually deposit  $\approx 0.5$  of their energy in the EM section, so the low incidence of jets with  $> 0.9$  of the total energy in either section makes the optimizations in these regions statistically inadequate (the statistical uncertainties on these points are connected to the correlations between weights, so these uncertainties are not shown in the plots).

**Table 5 Energy-independent sampling factors (OS-4) obtained from linear fits to the EM energy fraction in TB jets (with statistical uncertainties from the fits)**

	$P_1$	$P_2 (\times 10^{-1} \text{ GeV}^{-1})$
EM1	$1.788 \pm 0.004$	$8.37 \pm 0.07$
EM2	$1.370 \pm 0.007$	$-4.47 \pm 0.1$
EM3	$1.016 \pm 0.006$	$-2.11 \pm 0.09$
EM4	$1.263 \pm 0.005$	$0.96 \pm 0.08$
FH1	$0.896 \pm 0.005$	$3.34 \pm 0.09$
FH2	$0.977 \pm 0.005$	$-1.99 \pm 0.1$
FH3	$1.247 \pm 0.006$	$-9.40 \pm 0.1$
CH	$1.011 \pm 0.005$	$-6.60 \pm 0.1$
$\delta$	$-0.057 \pm 0.001$	$56.9 \pm 0.1$

### 3.5 Sampling Factors that Depend on both EM Fraction and Reconstructed Energy (Scheme OS-5)

In order to exploit information about both the energy of the TB jet and its EM fraction, optimizations were carried out that included both dependences. First, the factors found in Sec. 3.4 (for OS-4) were applied to data, and then sampling factors were recalculated as a function of reconstructed energy as was done in Sec. 3.3. However, the reconstructed energy for this optimization was taken as the corrected energy  $E_{EM}$  found using the parameters discussed in Sec. 3.4, rather than  $E_{def}$ .

Plots of the final factors as a function of  $E_{EM}$  are shown Fig. 6, and the parameters for fits to a linear dependence on  $E_{EM}$  are shown in Table 6. We see in Fig. 6 that after correcting for the EM fraction, the sampling factors are all close to unity over our entire energy range, indicating that applying both energy-dependent and EM fraction-dependent corrections is not significantly more useful than using only one of these corrections.

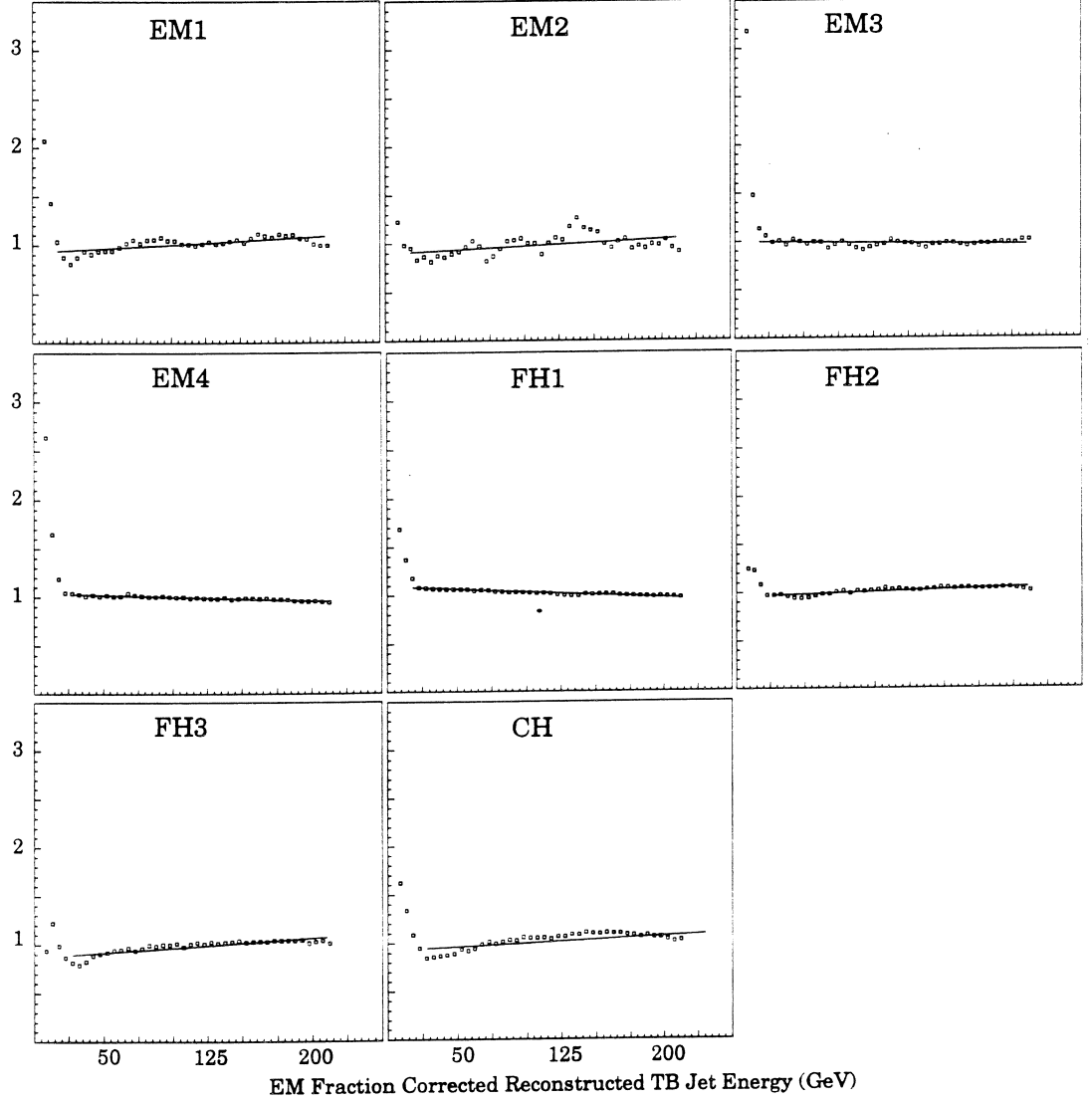


Figure 6 Sampling factors as a function of EM-fraction corrected reconstructed energy (OS-5). The fits are to linear functions of the form  $P_1 + P_2 E_{rec}$  (see Table 6).

We also see in Fig. 6 that the sampling weights for the lowest energies show a marked difference from those for the higher energies. This indicates that using both EM fraction and energy-dependent corrections should have a negative impact on lowest-energy jets.

**Table 6** Energy dependent sampling factors obtained from linear fits to the energy after EM-fraction corrections (OS-5) (with statistical uncertainties from the fits)

	$P_1$	$P_2$ ( $\times 10^{-4}$ GeV $^{-1}$ )
EM1	$0.927 \pm 0.003$	$7.65 \pm 0.02$
EM2	$0.898 \pm 0.003$	$7.29 \pm 0.02$
EM3	$0.998 \pm 0.003$	$-1.75 \pm 0.02$
EM4	$1.042 \pm 0.004$	$-4.17 \pm 0.03$
FH1	$1.094 \pm 0.003$	$-6.07 \pm 0.02$
FH2	$0.957 \pm 0.004$	$4.57 \pm 0.03$
FH3	$0.869 \pm 0.004$	$9.71 \pm 0.03$
CH	$0.927 \pm 0.004$	$6.90 \pm 0.03$

### 3.6 Corrections to Reconstructed Energies

As stated in Sec. 2, all reconstructed TB jet energies for the default as well as for the optimized parameters were corrected using a second-order polynomial in  $E_{rec}$  (Eq. 3). The plots of the nominal parton energies vs. reconstructed energies are given in Fig. 7, and the parameters for the fits indicated are given in Table 7.

**Table 7** Parameters from fits of second-order polynomial in reconstructed TB jet energy to the incident parton energy (with statistical errors from the fits)

OS-#	$P_1$ (GeV)	$P_2$	$P_3$ ( $\times 10^{-4}$ GeV $^{-1}$ )
Default	$2.41 \pm 0.02$	$1.13 \pm 0.01$	$-3.12 \pm 0.03$
1	$2.22 \pm 0.02$	$1.02 \pm 0.01$	$-2.16 \pm 0.02$
2	$-1.96 \pm 0.02$	$1.04 \pm 0.01$	$-0.96 \pm 0.02$
3	$1.37 \pm 0.02$	$0.97 \pm 0.01$	$1.70 \pm 0.02$
4	$-2.07 \pm 0.02$	$1.05 \pm 0.01$	$1.53 \pm 0.02$
5	$-1.97 \pm 0.02$	$1.04 \pm 0.01$	$-1.03 \pm 0.02$

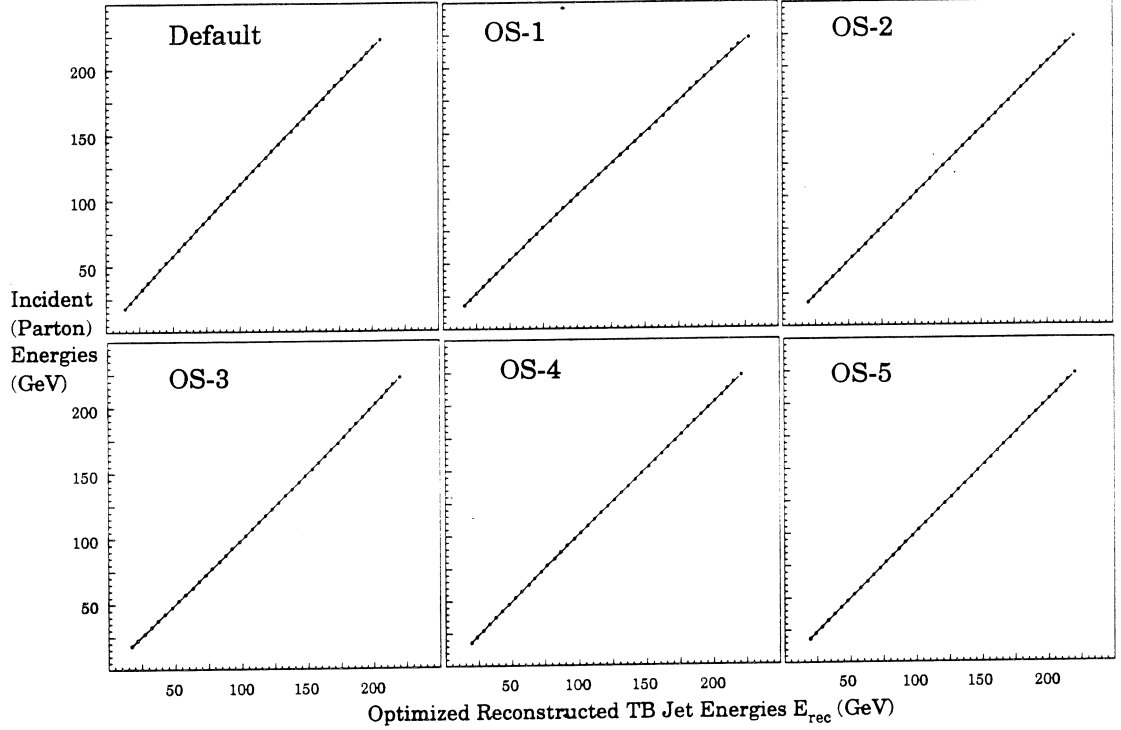


Figure 7 Nominal parton energy as a function of reconstructed TB jet energy for various optimizations. The fits are to second-order polynomial functions of  $E_{rec}$ .

These plots give little indication of the differences between the different response distributions. The parameters in Table 7 give greater detail about the differences between the various optimizations.

## 4 Judging the Success of the Optimization Schemes on Resolution

To investigate the effect of the optimization schemes on reconstructed TB jet energy resolution, a separate set of data, consisting of 218,500 events, was generated from the Particle Library. The corrections obtained from the optimization schemes were then applied as follows:

1. For each event, we calculated the default reconstructed TB jet energy  $E_{def}$  using the default weights.
2. Choosing some optimization scheme, the appropriate sampling factors were determined for any given  $E_{def}$

3. These factors were then applied to the layer energies to find the optimized reconstructed energies  $E_{opt}^i$ , for any given optimization scheme  $i$ .
4. Finally, the corrections to the reconstructed TB jet energy, based on Table 7, were applied to determine the final energies  $E_{corr}^i$ .

These corrected and optimized energies were then compared with the parton energies to determine the jet resolution as a function of incident energy, as explained here. The reconstructed energies  $E_{corr}^i$  were separated into bands of 5 GeV. In parallel with the rescaling of energies of singles hadrons that was based on the measurements using PWCs, we also rescaled all the values of  $E_{corr}^i$  to the mean parton energy in the band. This eliminated any smearing in  $E_{corr}^i$  due to the spread in parton energies. We then calculated the standard deviation  $\sigma(E)$  and mean  $\mu(E)$  for each band of  $E_{corr}^i$  energies. The parameters of the resolution were then extracted by fitting Eq. (2) to the values of  $\sigma/\mu$ . The parameters  $S$  and  $C$  from the fits, and their statistical uncertainties, are given in Table 8, and the corrected data for the various schemes with the fitted functions are shown in Fig. 8.

**Table 8 Parameters describing resolution of reconstructed and corrected TB jet energies**

OS-#	S (%/ $\sqrt{E}$ )	C (%)
Default	71.15 $\pm$ 0.004	0.002 $\pm$ 0.003
1	58.18 $\pm$ 0.01	1.98 $\pm$ 0.002
2	48.19 $\pm$ 0.01	2.32 $\pm$ 0.002
3	43.42 $\pm$ 0.01	2.76 $\pm$ 0.001
4	37.03 $\pm$ 0.01	3.32 $\pm$ 0.002
5	35.18 $\pm$ 0.01	3.40 $\pm$ 0.001



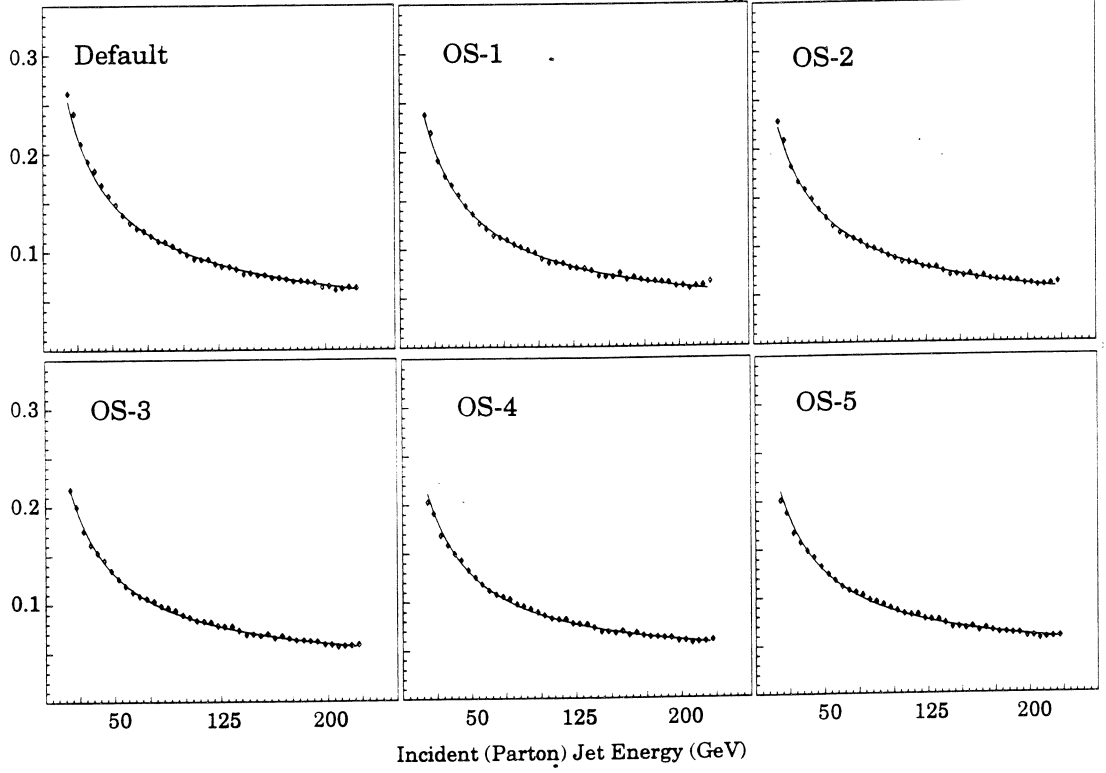


Figure 8 Fractional resolutions for TB jets as a function of incident energy for the various optimization schemes. Fits of the data are to Eq. 2

To show a simple example of the improvement in resolution given by the optimization, we include a plot of the distribution of a single jet energy peak ( $E=150$  GeV) for both the default weights and the OS-5 weights in Fig. 9.

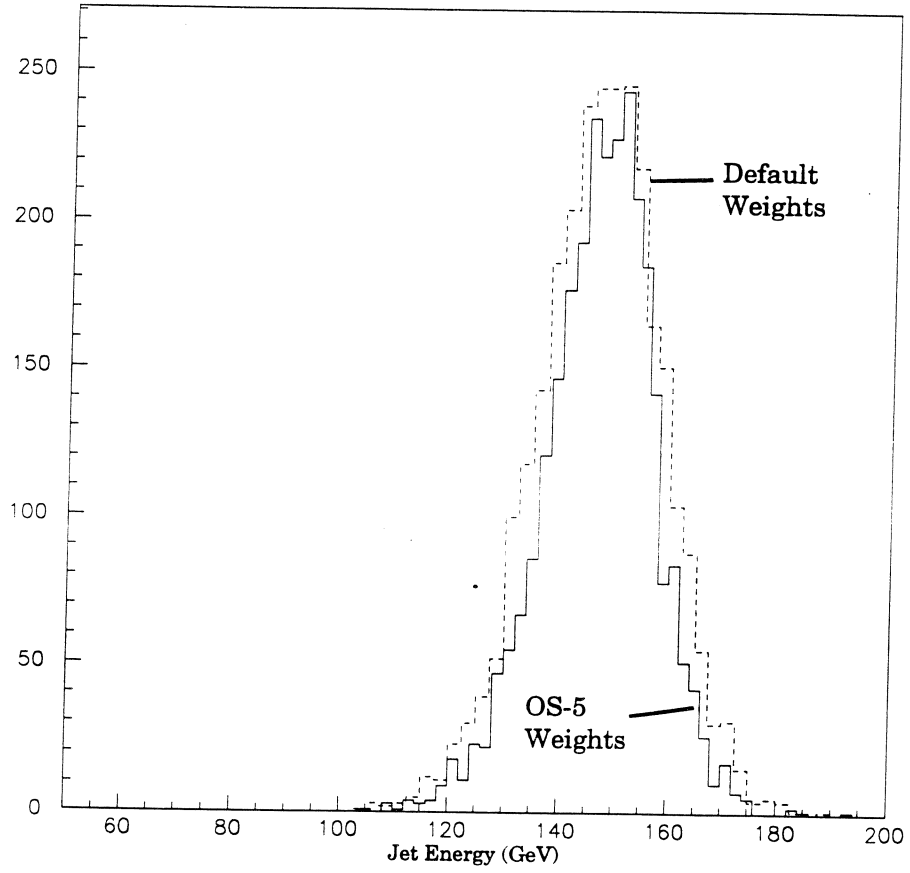


Figure 9 150 GeV Jet Response Distribution for Default Weights and OS-5 Weights

Because of the similarity of the plots in Fig. 8, and the fact that an increase in  $C$  can be compensated by a decrease in  $S$  in Table 8, it is difficult to gauge any improvement in jet energy resolution from the different optimization schemes. We therefore provide in Fig. 10 a comparison of the resolutions for the various schemes relative to the case using the default parameters.

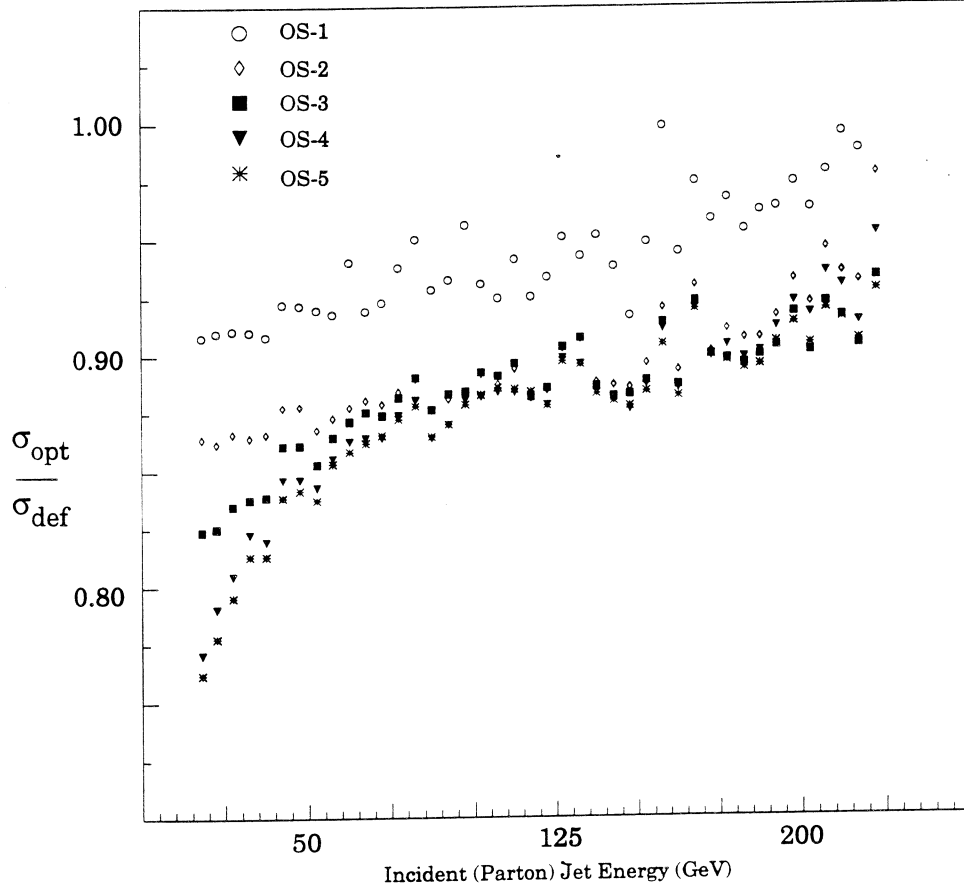


Figure 10 Ratio of optimized TB jet resolutions to the default values as a function of jet parton energy.

From Fig. 10, we see that while OS-1 improves the resolution over the default scheme, it is not as marked an improvement as those using the other schemes. The improvements for OS-2 to OS-5 are only slight at the highest energies, but more apparent at the lower energies. The OS-4 and OS-5 schemes appear to provide the best overall resolution.

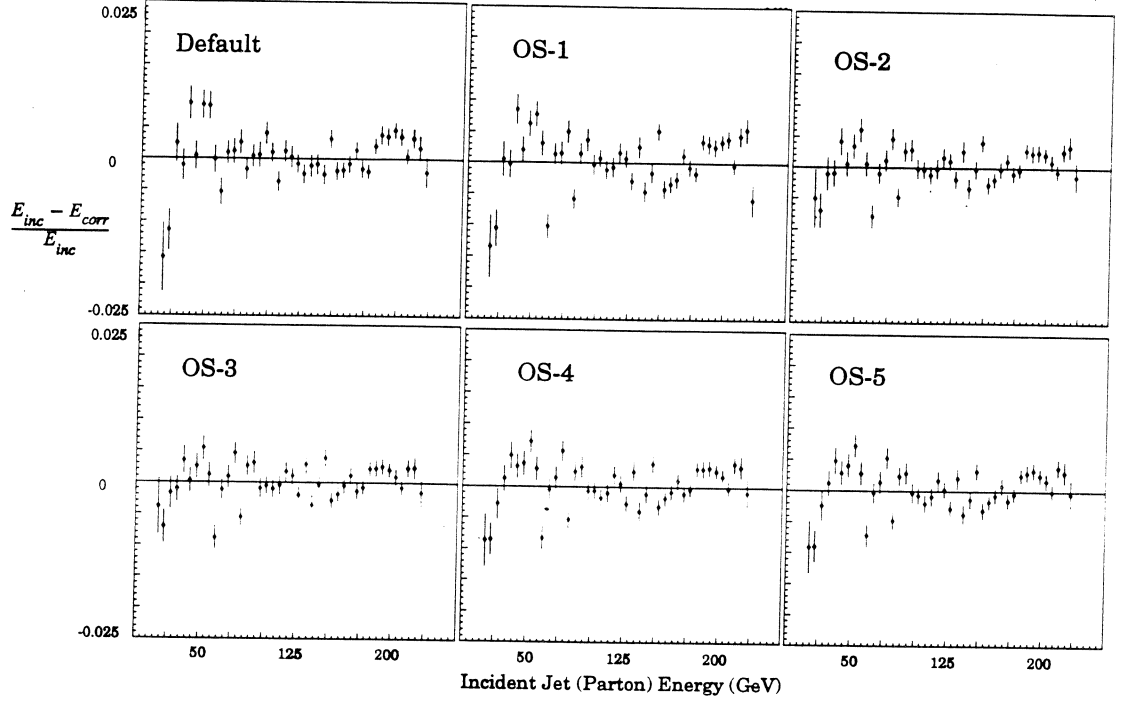


Figure 11 Fractional differences between the corrected reconstructed TB jet energies and incident parton energies, for different optimization schemes.

Fractional energy differences for the various optimization schemes are shown in Fig. 11. As can be seen in the figure, the fractional differences are all very similar, as expected, since all energy responses were corrected using a second-order polynomial in  $E_{rec}$ , (see Sec. 3.6). Nevertheless, these plots verify that the corrections are reasonable. (As we mentioned previously, when the sampling factors in Sections 3.3, 3.4, and 3.5 were fitted to third or fourth-order polynomials in  $E_{rec}$ , these fractional differences were not as well-behaved.)

From the results of this analysis, we see that the energies of TB jets more closely reflect the original parton characteristics (as shown by jet energy resolution) when we implement our optimization schemes. Thus, the weights suggested by single-particle optimization can be improved upon by applying a more detailed knowledge of jet structure to test beam data.

## References:

1. J. Borders, *Using Single Hadron Data to Optimize the Response of DØ Central Calorimeters for the Measurement of Hadronic Jet Energies*, DØ Note #1502 (1994).
2. J. Borders, *Structure of the DØ Particle Library and How it is Used to Simulate Jets*, DØ Note #2078 (1994).

DØ note #2469  
February 13, 1995

# Effects of Zero Suppression and Underlying Event on the Measured Jet Energies

Brad Abbott  
New York University

## Abstract

The effects of both underlying event and zero suppression artificially increase the measured jet energies at DØ. For centrally located jets this increase can be as large as 3 GeV for jets reconstructed with a 0.7 cone. This note describes the corrections needed to remove the effects of both underlying event and zero suppression.

## 1 Introduction

In addition to the jet energy deposited from the fragmentation of the hard scattered partons in collisions at DØ, there are two additional sources of energy in an event. The first, known as zero suppression, is due to the detector. It occurs even in the absence of a particle flux, and is due to the decay of uranium nuclei, the electronic shaping technique and the hardware pedestal cut. The second correction, known as the underlying event, is due to interactions amongst the spectator partons, those which do not participate in the hard scattering but scatter energy into the

detector. The energy contributions due to the underlying event and zero suppression were measured using minimum bias runs. The energy contribution due to the underlying event was found to be constant in  $E_T$ , while the energy due to zero suppression was assumed to be constant in energy.

## 2 Underlying Event

The transverse energy due to the underlying event was found to be constant in  $\eta$  and  $\phi$  with a measured value  $\frac{dE_T}{d\eta d\phi} = 0.55 \pm 0.1$  GeV. Since the energy due to the underlying event is constant in  $E_T$ , the amount of transverse energy in each jet due to spectator interactions is simply the product:  $(\frac{dE_T}{d\eta d\phi} \times \text{jet cone area})$ . As the number of multiple interactions increases, the energy deposited in the calorimeter due to spectator interactions also increases. To remove this extra energy, the underlying event correction should be doubled if a multiple interaction occurred.

## 3 Zero Suppression

The energy due to the zero suppression was parameterized to be constant in  $\eta$  and  $\phi$  with a value  $\frac{dE}{d\eta d\phi} = 1.36 \pm 0.2$  GeV. The energy due to the zero suppression, however, must be treated differently because it is a constant in energy, not  $E_T$ . In order to determine the amount of transverse energy due to zero suppression, an integration over  $\eta$  and  $\phi$  within each jet cone is performed.

Because of the large number of cells in the calorimeter, the data is not readout unless the absolute value of the energy in

each cell is greater than twice the pedestal width,  $\sigma$ . This means a cell can record a negative energy value because the average value of the pedestal has been defined as zero within the hardware. Mathematically, before data suppression the pedestal distribution is composed of three parts, whose sum on average is zero.

$$N_{-2\sigma}E_{-2\sigma} + N_{2\sigma}E_{2\sigma} + N_{+2\sigma}E_{+2\sigma} = 0 \quad (1)$$

Where  $E_{-2\sigma}$ ,  $E_{2\sigma}$ , and  $E_{+2\sigma}$  are the average energy of the calorimeter cells within each interval, and  $N_{-2\sigma}$ ,  $N_{2\sigma}$ , and  $N_{+2\sigma}$  are the average number of calorimeter cells within each interval for a sample of minimum bias events, (see Figure 1).

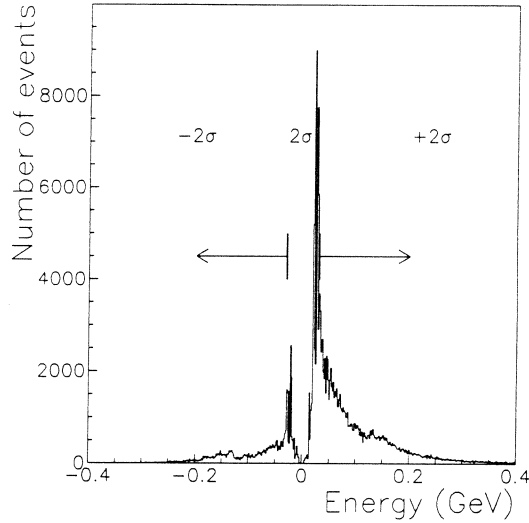


Figure 1: Energy distribution of calorimeter cells for a sample of minimum bias events. The  $2\sigma$  region has been set to zero in hardware before being readout.

Without the hardware suppression, the uranium noise on average would not contribute energy to the measurement. How-



ever, due to the decay of the uranium and the electronic shaping technique, the pedestal distribution is asymmetric around zero with a larger positive side tail. Therefore, after each cell is hardware suppressed, on average there is a net positive signal remaining. The data must be corrected for this effect.

The hardware data suppression sets all calorimeter cells within  $\pm 2\sigma$  of the pedestal to zero, forcing  $E_{2\sigma} \equiv 0$  at readout. After suppression the pedestal distribution contributes on average a net energy to each cell. Equation 1 now becomes

$$N_{-2\sigma}E_{-2\sigma} + N_{+2\sigma}E_{+2\sigma} = \frac{dE}{d\eta d\phi} = -N_{2\sigma}E_{2\sigma}. \quad (2)$$

Before suppression it is found that  $E_{2\sigma} < 0$ , so in effect the zero suppression unphysically raises the jet's energy. One can think of zero suppression as artificially adding positive energy to each suppressed cell in order to increase each suppressed cell's energy to 0.

The amount of pedestal energy to be subtracted from a given jet depends upon the energy distribution of the cells within the jet. Consider a jet of energy  $E_{jet}$  in which all cells within the jet contain sufficient energy such that no cells are suppressed. The measured jet energy,  $E_{measured}$ , is

$$E_{measured} = E_{jet} + N_{-2\sigma}E_{-2\sigma} + N_{2\sigma}E_{2\sigma} + N_{+2\sigma}E_{+2\sigma} \quad (3)$$

which by equation 1 yields

$$E_{measured} = E_{jet}. \quad (4)$$

In other words, no pedestal suppression has occurred so no correction is necessary for these cells.

On the other hand, if the jet contains  $M_{2\sigma}$  cells which have been suppressed, the measured jet energy is

$$E_{measured} = E_{jet} - M_{2\sigma}E_{2\sigma}. \quad (5)$$

Which by equation 2 yields on average  $E_{measured} > E_{jet}$ , so energy must be removed.

Equation 2 shows that the average energy remaining after suppression depends upon the number of cells,  $M_{2\sigma}$ , that have been hardware suppressed. The number of suppressed cells should be taken into account when removing the energy caused by the hardware pedestal suppression.

There are two methods available to remove the effects of the hardware suppression. The first is to correct each jet on an event by event basis. The number of suppressed cells within a jet can be measured and a correction can be applied to each jet. A second method is to measure the average number of cells suppressed for a given sample as a function of  $E_T$  and  $\eta$  and then apply this average correction to each jet. For this method, the average number of cells suppressed in both the hard scatter data and the minimum bias sample need to be compared. Note the jet cone radius used in this study is  $R=1.0$ .

The fraction of cells with energy outside the suppression value for a sample of minimum bias events is shown in Figure 2. The fraction of cells not suppressed in the minimum bias data is approximately 5% in the central region and 7% in the forward region.

The percentage of cells in a hard scatter event with energy outside the suppression value is shown in Figure 3. The fraction of cells not suppressed within jets in hard scatter events is approximately 12% in the central region and approximately

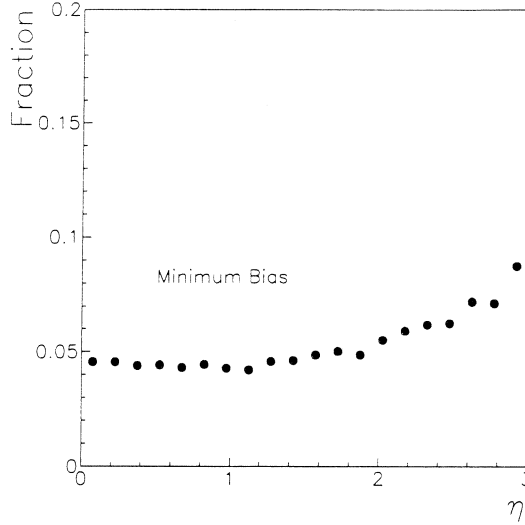


Figure 2: The fraction of cells within a cone radius  $R = 1.0$  with non-zero energy outside the hardware suppression value for a sample of minimum bias data vs  $\eta$ .

15% in the forward region. The difference in the fraction of cells suppressed between the hard scatter data and the minimum bias sample is  $\sim 8\%$ . Therefore, applying the zero suppression correction determined from the minimum bias sample introduces an error of approximately 8% on this correction. This is within the error of  $\sim 15\%$  on the measured value of the zero suppression correction.

The percentage of cells with energy outside the suppression value was also measured as a function of distance from the jet center. The jet cone was divided into 10 subcones around the jet axis with radii varying from 0.1 to 1.0 in  $\Delta r=0.1$  increments. In the center of a jet, the percentage of cells with energy outside the suppression value can be greater than 80%, see Figure 4. In the center of a jet, the zero suppression value from the minimum bias

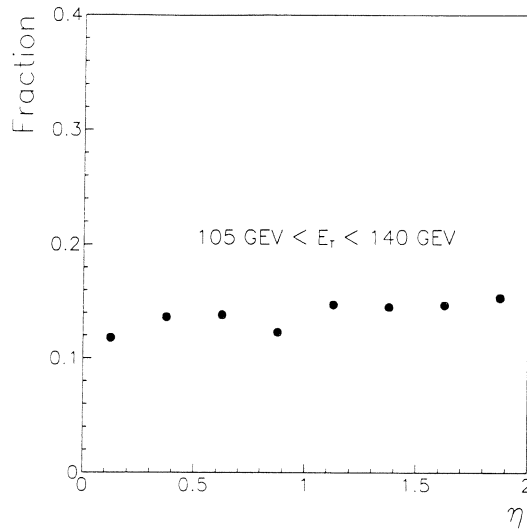


Figure 3: The fraction of cells within a cone radius  $R = 1.0$  with non-zero energy outside the hardware suppression value for jets between 105 and 140 GeV vs  $\eta$ .

sample introduces an error larger than the 15% error on the zero suppression value. Therefore, the zero suppression value should be corrected for the percentage of cells suppressed within each subcone.

The transverse energy correction due to the hardware data suppression can be written as:

$$\text{zero supp. correction} = A(\eta, E_T, r) \int_{\text{cone}} \frac{dE}{d\eta d\phi} \frac{1}{\cosh\eta} d\eta d\phi \quad (6)$$

where  $A(\eta, E_T, r)$  is a correction factor which takes into account the differences between the number of calorimeter cells suppressed between the minimum bias sample and the hard scatter data. ( $A = 1 - (.87 - .05) = .18$  for the first subcone for jets with transverse energy between 105 and 140 GeV, see figures 2 and

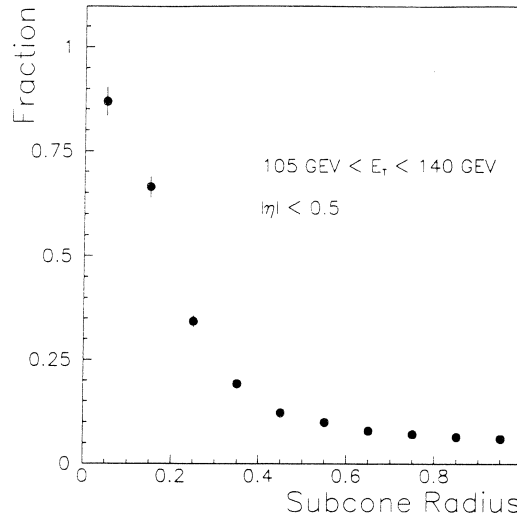


Figure 4: The fraction of cells with non-zero energy outside the hardware suppression value for jets between 105 and 140 GeV vs subcone radius.

4.)

## 4 Conclusions

The effects of underlying event on the measured jet energy can be corrected by multiplying the underlying event value of 0.55 GeV  $\times$  the jet cone area. This correction should be doubled if a multiple interaction has occurred.

The energy due to the zero suppression must be treated differently because it is a constant in energy, not  $E_T$ . The amount of transverse energy due to zero suppression can be found by calculating

$$1.36 \text{ GeV} \int_{\text{cone}} \frac{1}{\cosh \eta} d\eta d\phi. \quad (7)$$

Within errors, one can ignore the difference in the number of cells suppressed between minimum bias and the hard scatter data. This will introduce an error of  $\sim 8\%$  on the zero suppression correction, within the  $15\%$  assigned error.

The effects of ignoring the fraction of suppressed cells is small because in the center of the jet, where the number of suppressed cells is low, the area is small and so there is little effect due to zero suppression. At the edge of a jet where the area is larger, the number of cells suppressed is similar to the minimum bias sample and so ignoring the fraction of suppressed cells causes little error.



# A Measurement of the Calorimeter Response using $\pi^0$ Decays

Ulrich Heintz

*Columbia University, New York*

## Abstract

Using a sample of reconstructed  $\pi^0$  decays I study the  $\eta$  dependence of the response of the central EM calorimeter and constrain a possible offset in the electron energy scale, which reduces the error due to the energy scale calibration in the  $W$  mass measurement to 185 MeV.

## 1. Introduction

In the DØ detector  $\pi^0$  decays can be reconstructed if both photons pair-convert before the central drift chamber<sup>[1]</sup>. The observed  $\pi^0$  signal can be used to measure the response of the EM calorimeter. The relatively large number of reconstructed  $\pi^0$  decays allows subdivision of the sample to study the uniformity of response over the calorimeter. A good understanding of the asymmetric line shape of the  $m_{sym}$  distribution from  $\pi^0$  decays is required to extract the calorimeter response. In the following I will first describe the data selection, and models for signal and background shapes. Then I will use the model to fit the data in order to measure the calorimeter response and help calibrate the energy scale for the  $W$  mass measurement.

## 2. Selection Criteria

For this note  $\pi^0$  candidates have been selected from the special run data by requiring a PELC bank with

$$\begin{aligned} &\geq 2 \text{ tracks in the road with } dE/dx > 1.0; \\ &\geq 1 \text{ track in the road with } dE/dx > 1.5; \\ &R < 20 \text{ cm.} \end{aligned} \tag{2.1}$$

The data set and the variable  $R$  are defined in reference 1. These are the same cuts as used in reference 1. For response measurements I also apply the following fiducial cuts to restrict the sample to the CC fiducial region away from cracks and edges:

$$\begin{aligned} &\text{tower } \eta \text{ index} \leq 11; \\ &\Delta\phi(\text{crack-shower}) > 0.01. \end{aligned} \tag{2.2}$$



To reconstruct the mass I use the variable

$$m_{sym} = \sqrt{\frac{E^2(1 - \cos\alpha)}{2}}, \quad (2.3)$$

where  $E$  is the energy of the cluster and  $\alpha$  is the angle defined by the event vertex and the centers of gravity of the two tracks in the road with the highest ionization.

### 3. Signal Model

To measure the calorimeter response I need a model that predicts the  $\pi^0$  line shape in the  $m_{sym}$  distribution as a function of the calorimeter response. The first step is to create a sample of reconstructed  $\pi^0$  decays with full DØGEANT simulation to which such a model can be tuned. Unfortunately the reconstruction efficiency for  $\pi^0$  decays is very small. Out of a sample of 2000  $\pi^0$  decays generated with DØGEANT at  $\theta = \frac{\pi}{2}$  only 7 pass the cuts given in equation (2.1). The CPU time required to generate enough  $\pi^0$ s to obtain a sizable reconstructed sample is prohibitive, unless a preselection can be made before the GEANT simulation is completed. Figure 1 shows the pair-conversion points for the photons from the 2000  $\pi^0$  decays in a coordinate system in which the  $z$  axis is along the beam and the  $R$  axis is transverse to the beam. The stars mark the conversion points for the photons in the 7 events that passed the cuts. Almost all of them lie before the CDC. To generate a sample of double converted  $\pi^0$  decays in the most efficient fashion I follow the path of each photon from the  $\pi^0$  decay in GEANT and abort simulation of the event if one of them escapes into the CDC volume without pair-converting. In this way it is possible to generate a large sample of reconstructed  $\pi^0$  decays with reasonable CPU time expenditure. Table 1 summarizes the generated samples of double converted  $\pi^0$  decays. All were generated with plate geometry and reconstructed after smearing of the CDC hits to make the CDC resolution agree with collider data<sup>[2]</sup>. The calorimeter energies were reweighted using sampling fraction set 5 from reference 3 with CORRECTEM, which was modified to perform this operation on Monte Carlo events. The number of reconstructed  $\pi^0$ s is given without the  $dE/dx$  cuts. Not applying the  $dE/dx$  cut to the DØGEANT sample increases the number of reconstructed events. The number of events reconstructed with the full selection cuts from equation (2.1) is given in brackets.

To verify that the tracking resolution in the DØGEANT events agrees with the collider data, I compare the distributions of  $R$  and  $\Delta z$  for events that pass the signal selection cuts.  $\Delta z$  is the distance along the beam between the points on the two tracks that are closest to the beam. Figure 2 shows that there is agreement between the data and the DØGEANT simulation.

The directions of the two photons are given by the event vertex and the centers of gravity of the two tracks. The measurement of the opening angle  $\alpha$  between them is best characterized by the resolutions in azimuthal ( $\phi$ ) direction and in the beam ( $z$ ) direction at a fixed radius  $R_{CDC}$ , because these resolutions are not correlated with other variables.  $R_{CDC} = 62$  cm is the mean radial distance of the CDC sense wires from the beam. The

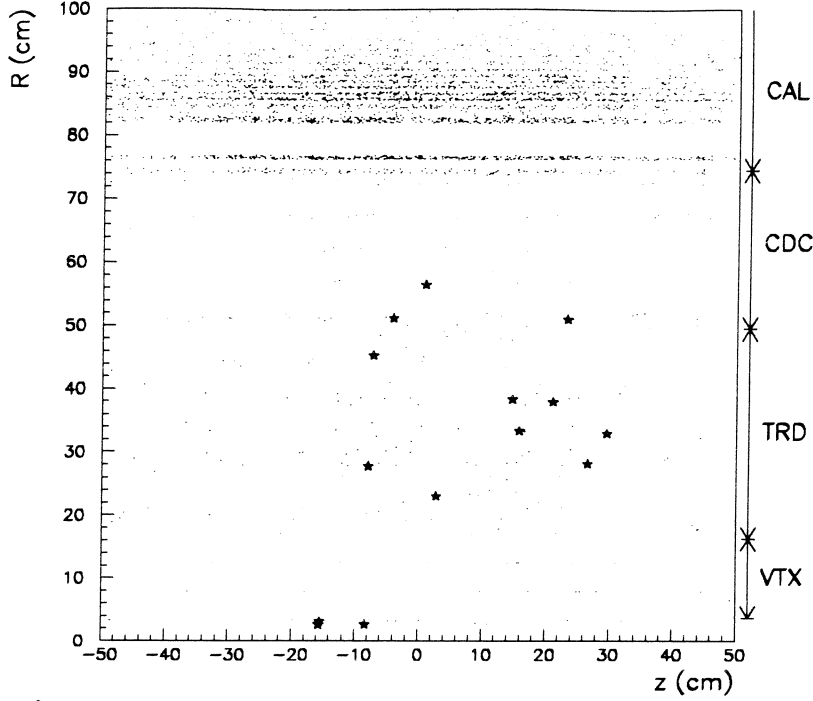


Fig. 1. Conversion points of photons in DØGEANT simulation.

Table 1. Double converted  $\pi^0$  DØGEANT samples.

$E_T$	$\eta$	# tried	# generated	# reconstructed
2 GeV	0.00	60,000	322	96 (29)
3 GeV	0.00	70,000	424	191 (119)
5 GeV	0.00	128,479	745	466 (319)
10 GeV	0.00	72,687	461	269 (220)
2 GeV	0.45	40,000	286	80 (38)
3 GeV	0.45	50,769	361	153 (92)
5 GeV	0.45	100,528	763	400 (293)
10 GeV	0.45	50,000	413	211 (165)
2 GeV	0.85	40,000	531	66 (34)
3 GeV	0.85	50,000	725	164 (105)
5 GeV	0.85	90,676	1360	430 (306)
10 GeV	0.85	34,666	545	177 (138)

opening angle is given by

$$\cos\alpha = \frac{R_{CDC}^2 \cos\Delta\phi + z^2 - \frac{1}{4}\Delta z^2}{\sqrt{R_{CDC}^2 + z^2 - z\Delta z + \frac{1}{4}\Delta z^2} \sqrt{R_{CDC}^2 + z^2 + z\Delta z + \frac{1}{4}\Delta z^2}}, \quad (3.1)$$

where  $\Delta\phi$  is the azimuthal separation  $\Delta\phi$  of the two tracks,  $\delta z$  their separation and  $z$  their mean coordinate in  $z$ -direction at radius  $R_{CDC}$ . The deviations between generated

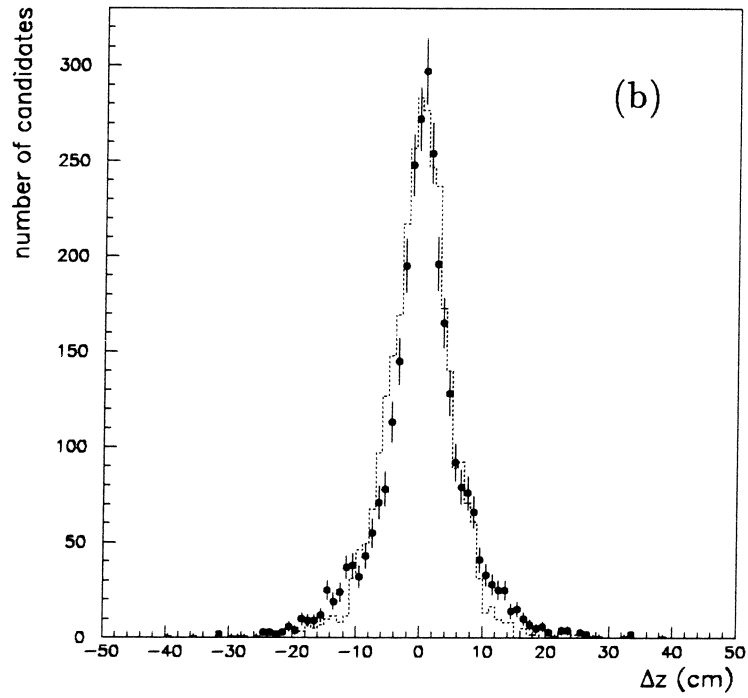
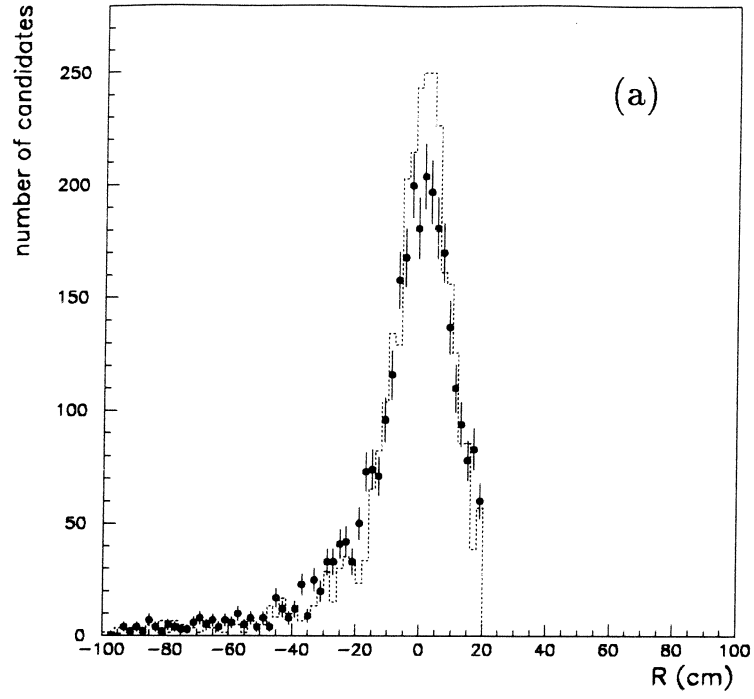


**Fig.2.** Comparison of  $R$  (a) and  $\Delta z$  (b) from special run data (points) and DØGEANT (dashed line).

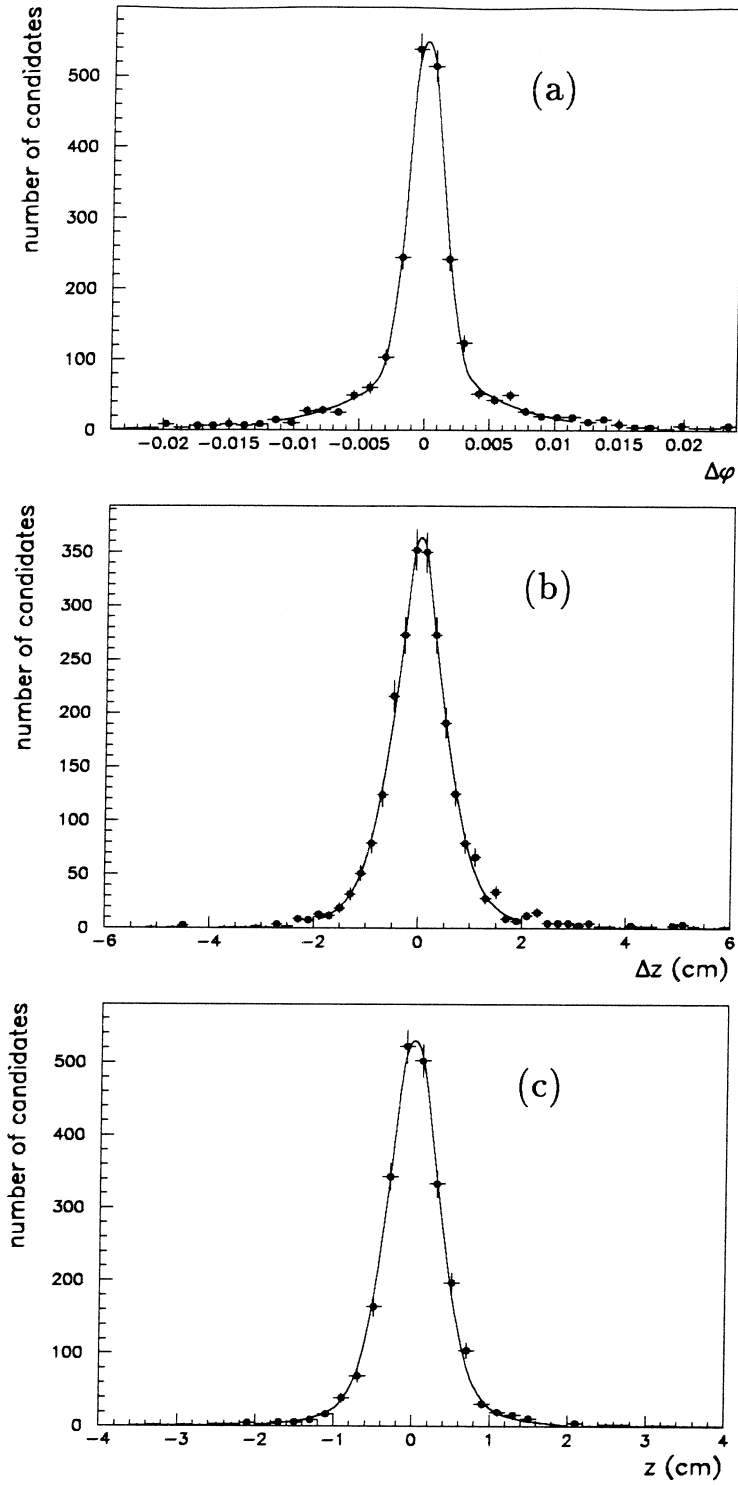


**Fig. 3.** Resolution functions for  $\Delta\phi$  (a),  $\Delta z$  (b), and  $z$  (c) for DØGEANT  $\pi^0$ s.

and measured values for these three variables for the DØGEANT  $\pi^0$  samples are shown in figures 3(a)-(c). The superimposed curves are fits to the data with the function

$$f(x) = \frac{f}{\sqrt{2\pi}\sigma} e^{-\frac{1}{2}\frac{x^2}{\sigma^2}} + \frac{b(1-f)}{2} e^{-b|x|}. \quad (3.2)$$

The following table summarizes the fitted values of the parameters  $f$ ,  $\sigma$ , and  $b$ .

variable	$f$	$\sigma$	$b$
$\Delta\phi$	0.50	0.0012	210.
$\delta z$	0.40	0.52 cm	$1.78 \text{ cm}^{-1}$
$z$	0.59	0.33 cm	$2.30 \text{ cm}^{-1}$

Soft photons are less likely to be reconstructed as 2-mip tracks after conversion, because the electrons are likely to separate due to multiple scattering. This reduces the reconstruction efficiency for very asymmetric decays and reduces the tail in the  $m_{sym}$  distribution. Figure 4 shows the reconstruction efficiency of DØGEANT  $\pi^0$ s as a function of the energy of the softer photon. The curve is the parametrization used in the model.

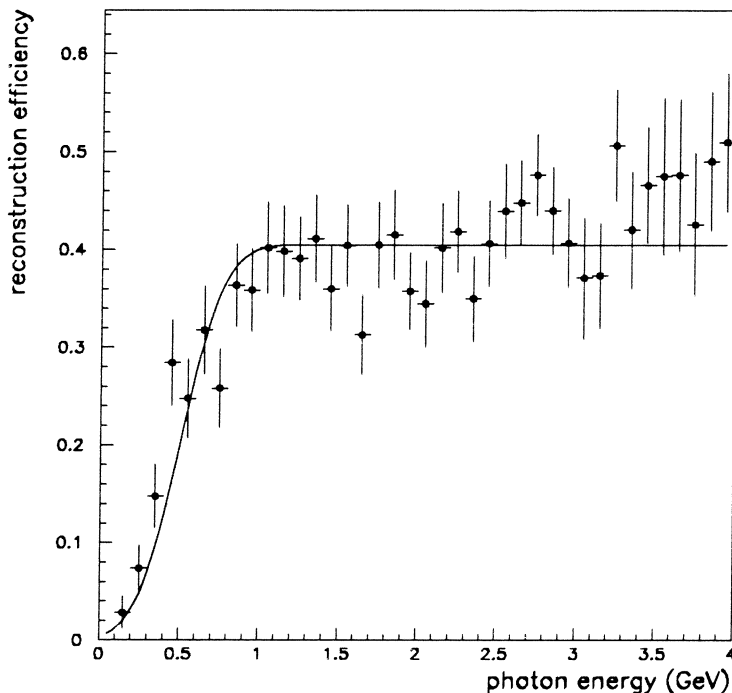


**Fig. 4.** Reconstruction efficiency as a function of photon energy.

Figure 5 shows the azimuthal separation between the two tracks measured in the  $\pi^0$  candidates from the special run data (points) and for DØGEANT  $\pi^0$ s (dashed line). If the separation is below  $\approx 0.0056$  the two tracks are not resolved in the CDC.

The energy resolution of the central EM calorimeter is

$$\left(\frac{\sigma_E}{E}\right)^2 = \left(\frac{0.13}{\sqrt{E_T}}\right)^2 + 0.005^2. \quad (3.3)$$

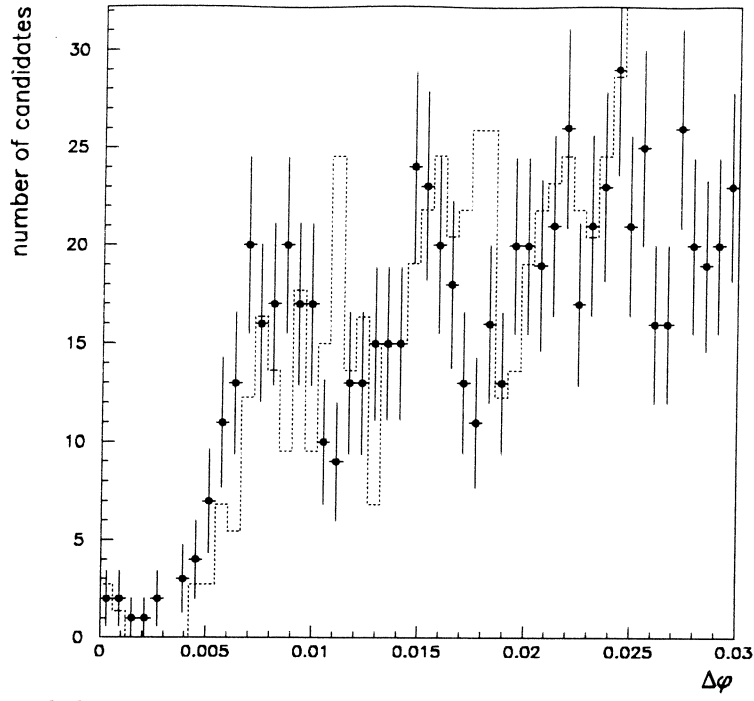


**Fig. 5.** Azimuthal separation between tracks for data (points) and DØGEANT (dashed line).

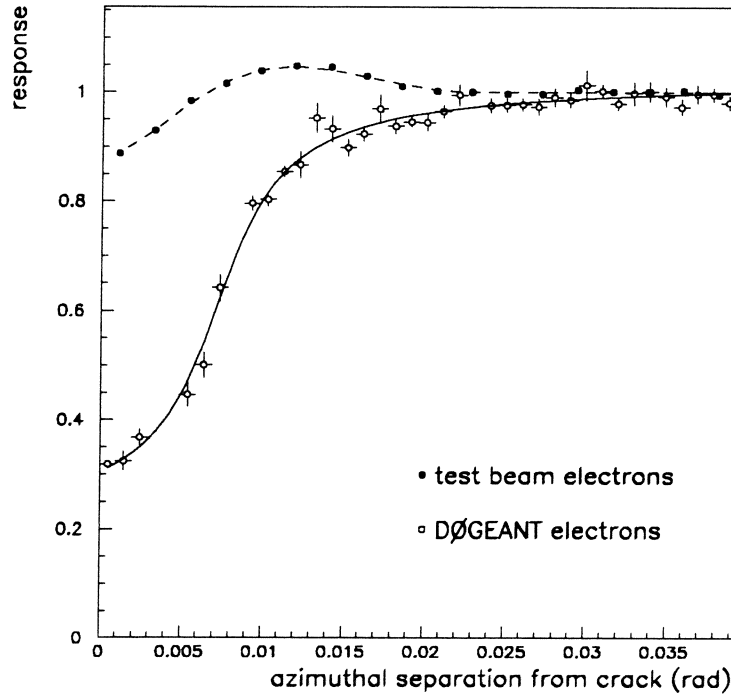


**Fig. 6.** Response near crack for DØGEANT and test beam electrons.

The sampling term was determined in test beam measurements<sup>[3][4]</sup> and the constant term from  $Z \rightarrow ee$  decays<sup>[5]</sup>. To correctly reproduce the energy response for  $\pi^0$  decays, the response for photons that hit one of the azimuthal cracks between CC modules must be parametrized. Since the separation between the photons is on the order of the tower size it is not possible to completely eliminate these events by making a cut on the separation of the cluster centroid from the cracks. Figure 6 shows the response as a function of azimuthal separation from the crack for single electrons generated with DØGEANT with plate geometry and for test beam electrons<sup>[6]</sup>. The smooth curves are parametrizations of the responses.

Now I can build the model to describe the  $\pi^0$  line shape as a function of the calorimeter response:

- generate  $\pi^0$  4-momentum from an input  $E_T$  and  $\eta$  distribution and isotropically in  $\phi$ .
- reject the event if the distance between the  $\pi^0$  and a crack, smeared by 0.0065 radians, is less than 0.01 radians.
- let the  $\pi^0$  decay isotropically in its rest frame.
- impose parametrized photon reconstruction efficiency (see figure 4).
- multiply the photon energies by the parametrized crack response (see figure 6).
- multiply both photon energies by the assumed calorimeter response.
- smear the resulting  $\pi^0$  energy by the energy resolution (equation (3.3)).
- smear  $\Delta\phi$ ,  $\delta z$ , and  $z$  by the resolutions given in the table above
- smear vertex  $z$  position by 0.6 cm (for collider data only).
- reject the event if the smeared  $\Delta\phi < 0.0056$  (see figure 5).
- compute  $m_{sym}$

This model produces histograms of  $\pi^0$  energy response and  $m_{sym}$  for values of the calorimeter response between 0.85 and 1.15 in 0.01 intervals. Figure 7 shows the line shape predicted by the model for unit response for different  $E_T$  values. There is no significant variation in the shape with  $\eta$ .

To fit the data for the best value of the calorimeter response, I perform a  $\chi^2$  fit for each value of the response with the normalization of the curve as the only free parameter and then fit a parabola to the minimized  $\chi^2$  values as a function of the response. The minimum of the parabola determines response for which the predicted shape fits best. For the DØGEANT sample of  $\pi^0$  decays this fit can be performed both to the  $m_{sym}$  and the energy response spectra. There is good agreement between the two response measurements for the  $\pi^0$  samples. Figure 8 displays the fitted responses versus  $\eta$  for three different values of  $E_T$ . Also plotted is the response for DØGEANT electrons at the same  $\eta$  and  $E_T$ , which is systematically higher than for  $\pi^0$ s. Figures 9(a) and (b) show the fitted  $m_{sym}$  and energy response distributions for  $E_T = 5$  GeV and  $\eta = 0$ .

The measured response to  $\pi^0$ s has to be corrected for the difference in response between electrons and double converted  $\pi^0$ s. The response to double converted  $\pi^0$ s is lower

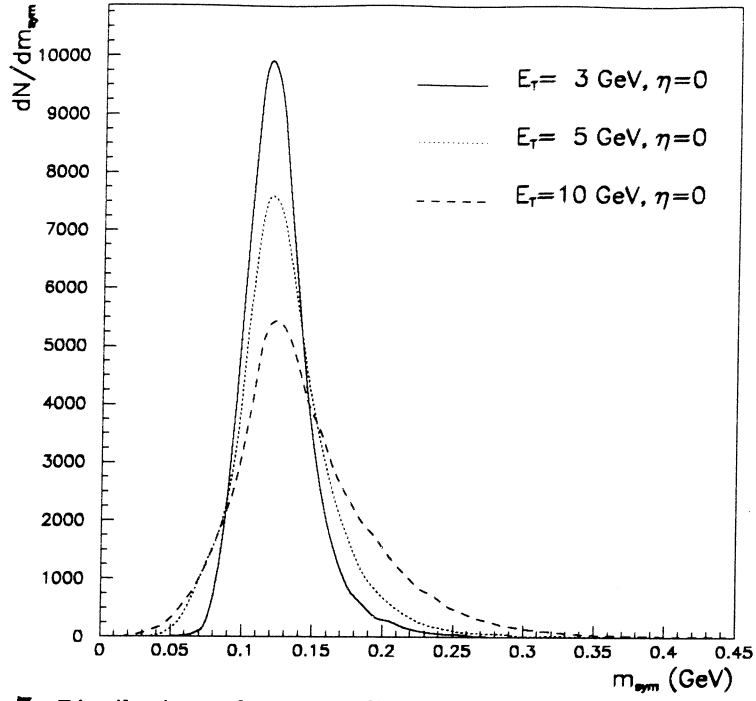


Fig. 7. Distributions of  $m_{sym}$  predicted by the model for different  $E_T$  values.

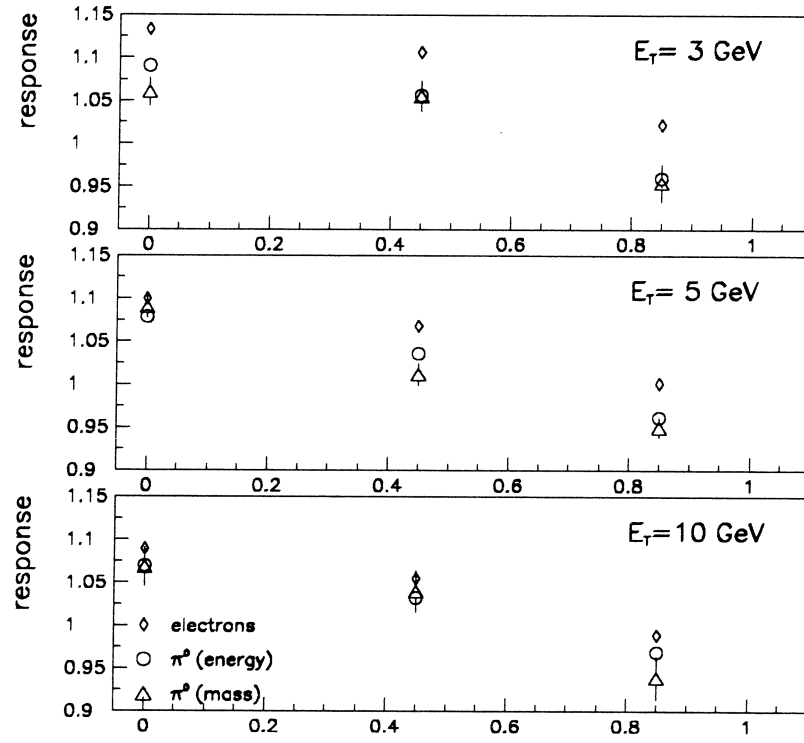
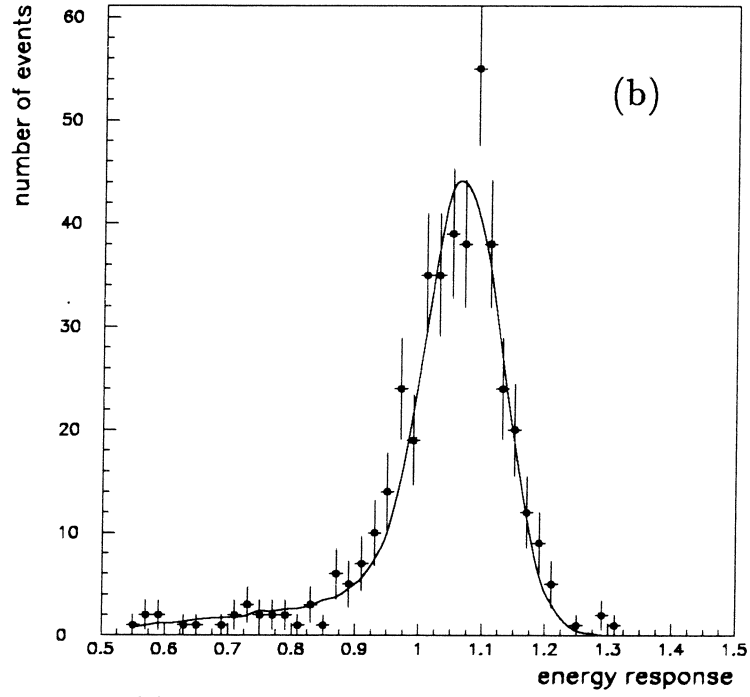
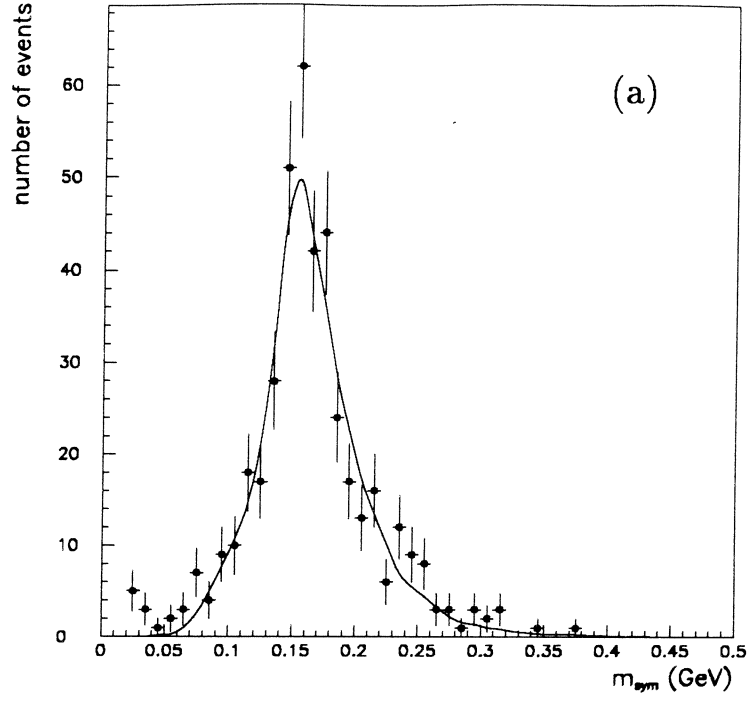


Fig. 8. Response from fits to DØGEANT  $\pi^0$  samples.  $\eta$





**Fig. 9.** Fits to  $m_{sym}$  (a) and energy response (b) distributions for  $E_T = 5$  GeV and  $\eta = 0$ .

than to electrons because the  $\pi^0$  shower starts earlier (when the conversions occur) and therefore the  $\pi^0$ s loose more energy when traversing the central detector and the cryostat than electrons. Table 2 lists the mean energy loss for DØGEANT  $\pi^0$ s and electrons in these regions. The event samples were selected so that no electron or photon was closer than 0.025 radians to a crack. The energy losses are consistent with the difference in reconstructed energies implied by the fitted responses for  $\pi^0$ s and electrons, which is also listed in the table. As a correction I choose an offset of  $(185 \pm 90)$  MeV, which is the average over the three  $\eta$  points for  $E_T = 5$  GeV, the peak of the  $E_T$  spectrum for the data sample. The error spans the full range of differences.

**Table 2.** Energy loss before the EM calorimeter for DØGEANT electrons and  $\pi^0$ s.  $E_{CD}$  is the energy lost in the central detector and  $E_{cryo}$  is the energy lost in the inner cryostat tube. The column marked “fitted response” tabulates the difference between the fitted responses times the generated energy for comparison. All energies are given in MeV.

$E_T$	$\eta$	electrons		$\pi^0$ s		fitted response
		$E_{CD}$	$E_{cryo}$	$E_{CD}$	$E_{cryo}$	
3 GeV	0.00	17	71	54	175	126
5 GeV	0.00	19	82	54	197	105
10 GeV	0.00	22	95	68	234	200
3 GeV	0.45	21	92	83	233	165
5 GeV	0.45	23	100	84	259	182
10 GeV	0.45	26	124	95	320	254
3 GeV	0.85	35	171	93	370	257
5 GeV	0.85	39	199	93	422	270
10 GeV	0.85	47	256	94	527	277

## 4. Background Model

The shape of the background can be determined directly from the data. Backgrounds can be due to single conversions, which are removed by the cut on  $R^{[1]}$ , and to random overlaps of two uncorrelated tracks. The latter background should not be correlated with the ionization of the tracks and its shape can therefore be determined from a control sample of PELC banks with

$$\begin{aligned} &\geq 2 \text{ tracks in the road with } dE/dx < 1.0; \\ &R < 20 \text{ cm,} \end{aligned} \tag{4.1}$$

and the same fiducial cuts as for the signal sample. The  $E_T$  spectrum of this control sample is softer than that of the signal sample. Therefore I weight every event such that the weighted  $E_T$  spectrum agrees with that of the signal sample. The shape of the weighted  $m_{sym}$  distribution agrees well with the background in the signal sample. This is true for any subset of the signal sample selected by making fiducial or kinematic cuts as long as

the same cuts are applied to the control sample. I normalize the control sample to the signal sample in the regions  $m_{sym} < 80$  MeV and  $m_{sym} > 400$  MeV. Figure 10 shows the  $m_{sym}$  distributions for the signal and control samples without any additional cuts. In the following I will use background subtracted  $m_{sym}$  distributions obtained by binwise subtraction of the renormalized background spectrum from the signal spectrum.

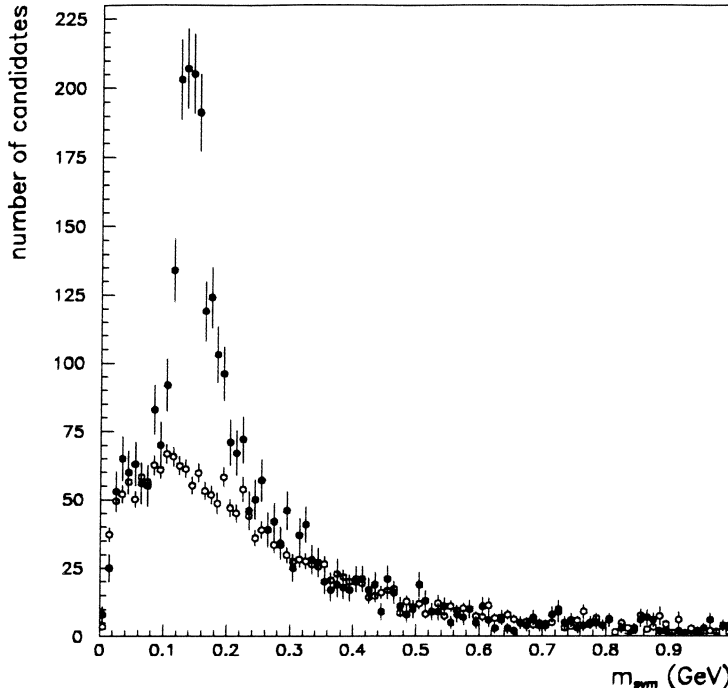


Fig. 10.  $m_{sym}$  distribution for signal sample (solid points) and for the control sample (open points).

## 5. Calorimeter Response

Now I use the model to fit the data. To generate the fitting functions I use the  $E_T$  and  $\eta$  spectra of the data sample to be fitted as inputs to the model. These spectra are shown in figures 10 and 11 of reference 1. The  $E_T$  spectrum does not vary significantly with  $\eta$ . The crack response from test beam is used as well as the  $z$  vertex smearing.

To study uniformity as a function of the  $z$  position of the point of incidence on the calorimeter I divide the sample of  $\pi^0$  candidates from the special run data into 11 sub-samples, which each populate two adjacent  $\eta$  towers of the central calorimeter. Figure 11 shows the response versus tower  $\eta$  index.

To study dependence on the incident angle I divide the sample into five  $\eta$  bins. Here  $\eta$  is defined by the  $z$  position of the vertex and the  $z$  position of the cluster centroid in the EM3 layer. The fits to these bins are shown in figure 12(a) and the fitted response is plotted versus  $\eta$  in figure 12(b). For comparison the response to DØGEANT electrons and  $\pi^0$ s is also shown. Both Monte Carlo and collider data show an  $\eta$  dependence of the response, but the dependence in the data is flatter, except for the last bin.

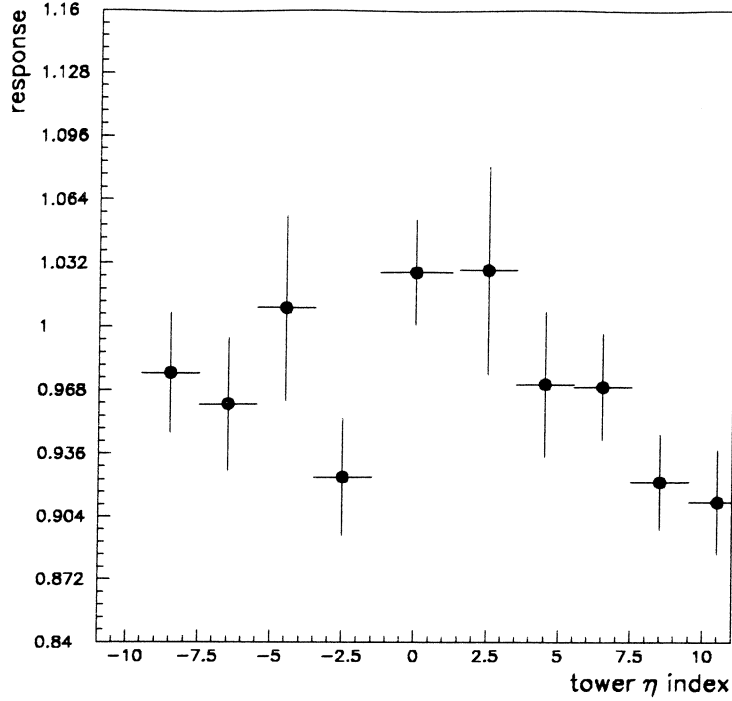


**Fig. 11.** Response versus tower  $\eta$  index.

The  $\eta$  distribution for electrons from  $Z \rightarrow ee$  decays is quite different from that of the reconstructed  $\pi^0$  sample. To measure an average response for the calorimeter I weight the events in signal and background samples so that the weighted  $\eta$  distribution agrees with that for  $Z \rightarrow ee$  decays. Table 3 gives the number of reconstructed  $\pi^0$ s (from the area under the fit), the  $\eta$  distribution of electrons from  $Z \rightarrow ee$  decays (normalized to the  $|\eta| < 0.3$  bin), the weights and the fitted responses for the five  $\eta$  bins. Errors are statistical only. The fit to the  $\eta$  weighted spectrum is shown in figure 13.

**Table 3.** Fitted response as a function of  $\eta$ .

$\eta$ region	number of $\pi^0$ s	$\eta$ distribution for $Z \rightarrow ee$	$\eta$ weight	$\pi^0$ response
$<0.3$	202	1.00	1.00	$1.012 \pm 0.021$
$0.3-0.6$	178	0.92	1.04	$0.983 \pm 0.021$
$0.6-0.8$	162	0.56	0.70	$0.969 \pm 0.021$
$0.8-1.0$	150	0.46	0.62	$0.948 \pm 0.024$
$>1.0$	257	0.37	0.29	$0.880 \pm 0.015$
full $\eta$ range	949			
unweighted				$0.958 \pm 0.009$
$\eta$ weighted				$0.980 \pm 0.012$

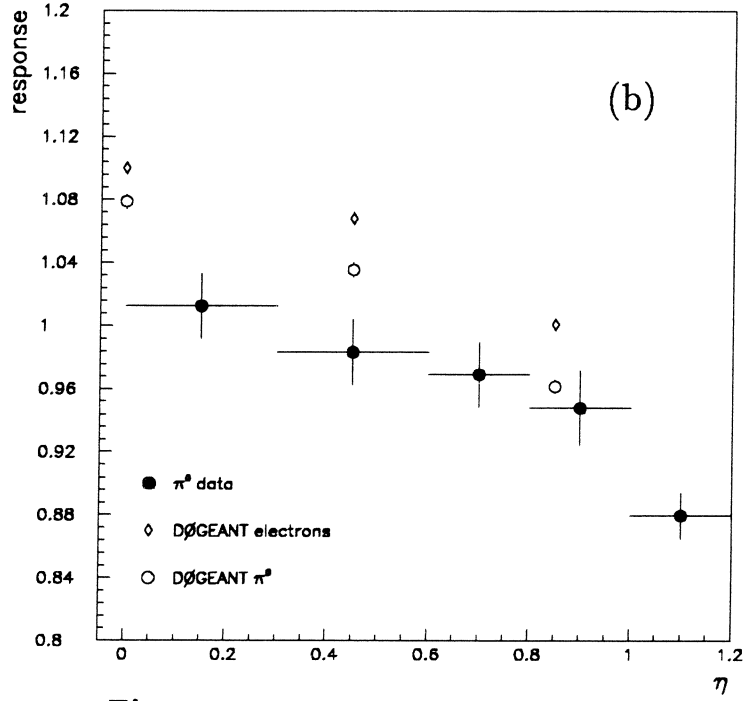
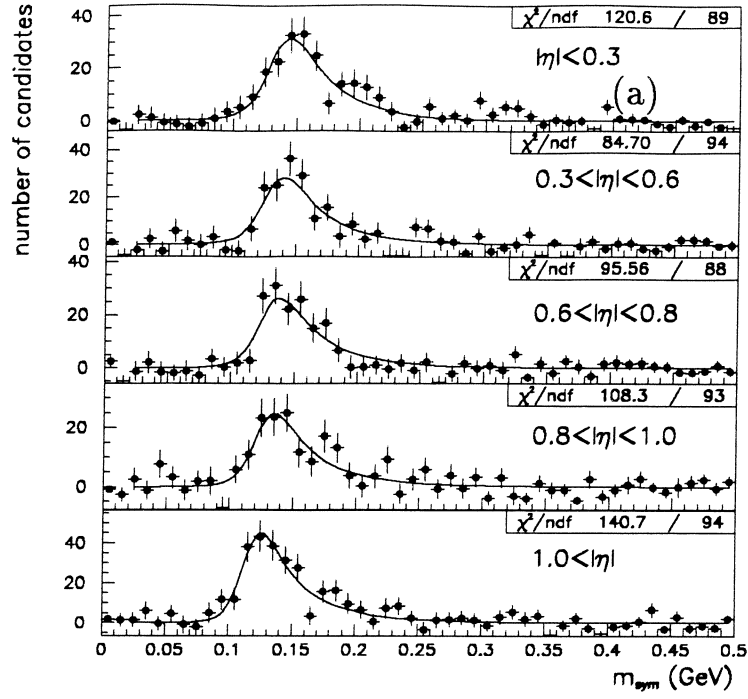


**Fig. 12.** Fits to the special run data in  $\eta$  bins.

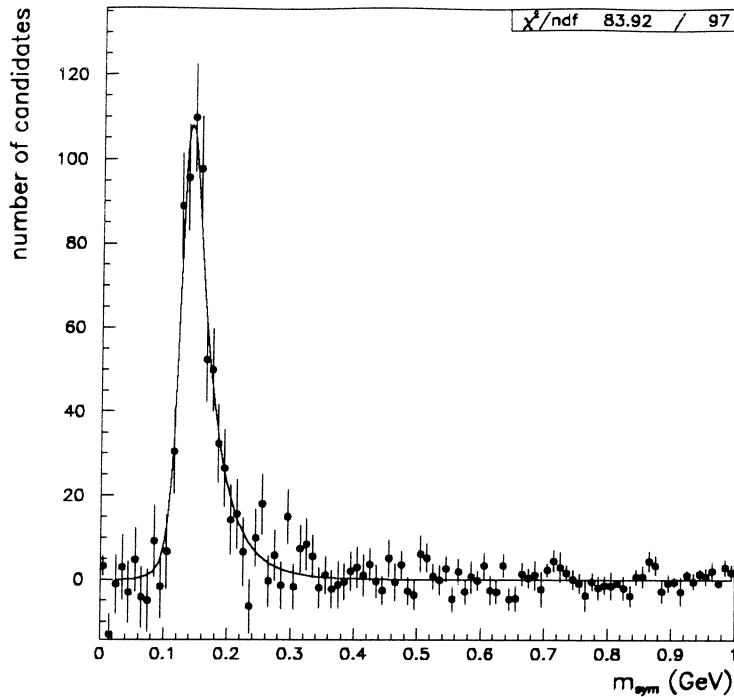


Fig. 13. Fit to  $\eta$  weighted  $m_{sym}$  distribution.

## 6. Calibration of Energy Scale

For an absolute calibration of the calorimeter energy scale, I have to estimate any systematic effects that may bias the response measurement in the previous section and correct for them as well as assign appropriate errors. Systematic errors due to uncertainties in the model parameters, like crack response, resolutions etc., affect this result at the 1% level. The measured response has to be corrected for the difference in electron and  $\pi^0$  energy response. Energy leakage into the cluster from the underlying event may lead to an overestimate of the cluster energy. I estimate this effect from the EM energy in a cone of  $\Delta R = 0.4$  around the cluster. On the average there is 1 GeV of energy in this cone, excluding the cells that comprise the cluster. The cone has approximately 450 cells of which on the average 31 are part of the cluster. If the energy density is uniform over the cone this implies a leakage of approximately 75 MeV into the cluster. The actual effect may be somewhat smaller because the zero suppression of the calorimeter readout enhances the positive tail from the uranium noise in the pedestal distributions and therefore leads to an overestimate of small energy depositions. I therefore assign an error of 75 MeV to this correction. In order to estimate the sensitivity of the response to this offset I introduce an offset into the cluster energy used to compute  $m_{sym}$  in the data and refit for the response. The measured response changes by  $\pm 4.5\%$  for offsets of  $\pm 200$  MeV. The following table summarizes these corrections and systematic errors.

source	correction to energy	correction to response	error
model parameters	—	—	$\pm 1\%$
electron- $\pi^0$ response difference	185 MeV	+4%	$\pm 2\%$
underlying event	75 MeV	-1.7%	$\pm 1.7\%$

After all corrections the calorimeter response is  $1.003 \pm 0.028$ . This corresponds to a  $\pi^0$  mass measurement of  $(135.4 \pm 3.8)$  MeV.

Using the formalism defined in reference 7 I combine this measurement with the measurement of the  $Z$  mass to limit a possible offset in the calorimeter energy scale. This formalism assumes that the calorimeter response is completely described by a scale  $\alpha$  and an offset  $\beta$ . Analyses of low energy test beam data<sup>[8]</sup> show that this is not the case. Deviations from a straight line fit of up to 300 MeV are observed. I assign an error due to this nonlinearity by treating the deviation as an offset in the  $\pi^0$  energy measurement. This provides an upper limit on the uncertainty due to nonlinearities seen in the test beam data. In the future we may come to a more detailed understanding of this effect which might allow us to reduce this error. A 300 MeV offset causes a mismeasurement of the response by 6.8% or, correspondingly, an error in the measured  $\pi^0$  mass of 9.2 MeV which is added in quadrature with the error quoted above.

The following table summarizes the input values for the energy scale calibration.

resonance	$f$	mass	measured mass
$\pi^0$	0.03	135 MeV	$(135.4 \pm 10.0)$ MeV
$Z$	1.8	91.19 GeV	$(87.17 \pm 0.18)$ GeV <sup>[9]</sup>

This gives for scale  $\alpha$  and offset  $\beta$

$$\alpha = 1.051 \pm 0.008 \quad \text{and} \quad \beta = (-245 \pm 314) \text{ MeV}. \quad (6.1)$$

The following table gives the error on the  $W$  mass measurement for a measured  $W$  mass of 76.3 GeV from the uncertainties in the energy scale calibration. The values of observed  $Z$  and  $W$  masses that I use are our present preliminary results.

source of error	error on $M_W$
$Z$ mass measurement	163 MeV
$\pi^0$ response	37 MeV
nonlinearity of response	79 MeV
total	185 MeV

## 7. Conclusion

Using a sample of reconstructed  $\pi^0$  decays I have measured the response of the central EM calorimeter. There is evidence for a slight  $\eta$  dependence of the response. This measurement of the response to  $\pi^0$  decays constrains a possible offset in the energy scale and reduces the error in the  $W$  mass measurement due to the uncertainty in this offset. The final energy scale error in the measured  $W$  mass is 185 MeV, dominated by the number of  $Z \rightarrow ee$  events and the uncertainty from the nonlinearity of the response at low energies.

## REFERENCES

1. Ulrich Heintz, DØnote 2209
2. Ulrich Heintz, DØnote 2267.
3. W. G. D. Dharmaratna, DØnote 1731.
4. Qiang Zhu, Ph. D. thesis, p.64ff.
5. Marcel Demarteau...
6. W. G. D. Dharmaratna, DØnote 1501.
7. Ulrich Heintz, DØnote 1819.
8. Nina Denisenko, DØnote 1852, Norm Graf...
9. Ian Adam, APS meeting, April 1994.





## B<sub>c</sub> Decays

B. Gómez, J.P. Negret, M. Zanabria  
Universidad de los Andes

The B<sub>c</sub> meson has not yet been observed, but its mass is expected to be around 6.3 GeV/c<sup>2</sup>. There are motivations for the study of the B<sub>c</sub> system. It is a nonrelativistic system intermediary between charmonium and bottomonium and the study of the B<sub>c</sub> family of mesons would serve as a test of the applicability of potential models for describing the properties of heavy quark systems. Similar to ordinary B mesons with a light quark, B<sub>c</sub> is expected to have a long life (of the order of 5 x 10<sup>-13</sup> s), since its decays are due to the weak interaction.

The available estimates [1-5] for the B<sub>c</sub> production cross section at the Tevatron are of the order of  $\sigma(B_c)/\sigma(b\bar{b}) \approx 1 - 4 \times 10^{-3}$ . For an integrated luminosity of 50 pb<sup>-1</sup>, this means that several million B<sub>c</sub> are produced, making observation possible at D0. The estimated ratio for inclusive J/Ψ in the B<sub>c</sub> decay (B<sub>c</sub> → J/Ψ X) is large, around 24%, and this should be exploited.

A measurement of the B<sub>c</sub> mass would be possible looking for the invariant mass of the J/Ψ π system in the B<sub>c</sub> → J/Ψ + π decay, which has a branching ratio of the order of 2 x 10<sup>-3</sup>. The combined branching ratio for B<sub>c</sub> → J/Ψ + π, followed by J/Ψ → l<sup>+</sup> + l<sup>-</sup> is about 3 x 10<sup>-4</sup> (l is a lepton).

Lusignoli et al [4] have estimated the p<sub>T</sub> and η distributions of the B<sub>c</sub><sup>+</sup> at the Tevatron. They find that the average p<sub>T</sub> is 4.7 GeV/c, that the average η for B<sub>c</sub><sup>+</sup> is -0.5 and that the root mean square η is 1.8. There is a slight asymmetry in the η distribution, because the B<sub>c</sub><sup>+</sup> go preferably in the direction of the p<sub>bar</sub>. The produced B<sub>c</sub><sup>+</sup> with |η| < 1.5 have a total energy typically less than 17 GeV and will be therefore hard to detect.

The clearest signature at D0 would be the decay B<sub>c</sub> → J/Ψ + μ + ν, with the subsequent decay J/Ψ → μ<sup>+</sup> + μ<sup>-</sup>. This has an estimated branching ratio of the order of 0.5%. We would see three muons coming from the same vertex, two of them reconstructing a J/Ψ and some missing p<sub>T</sub>.

A simulation program was written to learn more about the topology of this decay for  $B_c^+$ . The  $p_T$  and  $\eta$  distributions predicted for the  $B_c^+$  by Lusignoli et al (Figure 1) were used. One lets the  $B_c^+$  decay as a three body decay ( $J/\Psi - \mu - \nu$ ). Possible polarization or other dynamical effects were not included. The mass of the  $B_c^+$  was assumed to be  $6.27 \text{ GeV}/c^2$ . (See reference [3],[4]).

The simulation starts by choosing a mass for the  $\mu$ - $\nu$  system and generating (isotropically) the  $\mu$  and the  $\nu$  in the frame of the  $\mu$ - $\nu$  system. This single muon is positively charged as the  $B_c$ . With this, the  $J/\Psi$  was generated in the frame of the  $B_c^+$ , and the variables for the  $\mu$  and  $\nu$  were transformed to the  $B_c^+$  frame. The  $J/\Psi$  was allowed to decay into a  $\mu^+ - \mu^-$  pair. At the end, all the relevant variables for each final particle (energy, momentum,  $\Phi$  and  $\eta$ ) were transformed to the laboratory frame.

Background events were simulated by generating a  $J/\Psi$  plus a single muon. The  $p_T$  distribution used for generating the inclusive  $J/\Psi$  events included the following effects:  $J/\Psi$  direct production,  $J/\Psi$  coming from B mesons other than the  $B_c$ ,  $J/\Psi$  coming from charmonium excited states. The  $p_T$  and  $\eta$  distributions for the inclusive  $J/\Psi$  were taken from distributions given by CDF and D0 [6]. The  $J/\Psi$  was allowed to decay into two muons. Similarly the  $p_T$  and  $\eta$  distributions for the inclusive single muon were taken from CDF and D0 publications [7], [8].

Several thousands of signal events were generated, and without cuts in  $p_T$ , in  $\eta$ , or any other kind, the following average values of  $p_T$  were found:  $2.9 \text{ GeV}/c$  for the the  $J/\Psi$ ,  $2.0 \text{ GeV}/c$  for a muon coming from a  $J/\Psi$ ,  $1.5 \text{ GeV}/c$  for the single muon, and  $1.2 \text{ GeV}/c$  for the neutrino. (A simulated effect due to the muon chambers of a 20% smearing for the momentum of each final muon was included). These average values in  $p_T$  would make it difficult if not impossible to detect the  $B_c$  using missing  $p_T$  techniques. Figure 2 shows the  $p_T$  distributions for these particles.

In order to enhance the simulation of the D0 detector upon the signal and background events, two effects were introduced, namely: a) the efficiency of the level 1.5 trigger as a function of the transverse momentum for each final state muon, and b) the minimum momentum of the muons to exit the toroids as a function of the polar angle theta, and c) the three layers geometric acceptance [7]. After applying these effects (one could call them hardware cuts) upon the generated signal events, the combined overall efficiency of the cuts a and b was found to be 0.6%. And if applied upon the background

events the combined efficiency was 1.1%. This means that in order to have a meaningful sample of signal and background events to analyze, a statistical sample of more than 35000 events was created.

Topological cuts that would discriminate between signal and background events were searched. For that purpose several parameters were studied and compared. For example one studied: the transverse momentum distribution for each of the three final state muons, the transverse momentum distribution of the  $J/\Psi$ , the invariant mass of the  $J/\Psi$ , the invariant mass of the  $J/\Psi$ -single muon system, the angle made by the  $J/\Psi$  and single muon, the angle made by the two muons coming from the  $J/\Psi$ , the  $\eta$  distribution of each of the final state muons, scatter plot of the square of the mass for the  $\mu^+ \mu^-$  system versus the square of the mass for the  $\mu^+$  and single muon system, etc.

The  $J/\Psi$  was identified by looking at the invariant mass of each pair of opposite charge muons. The mass range for the  $J/\Psi$  was selected to be from  $2.0 \text{ GeV}/c^2$  to  $4.0 \text{ GeV}/c^2$ . From the comparison of the parameters for signal and background distributions, the invariant mass for the  $J/\Psi$  - single muon system was selected as the main topological cut. An optimal value for this cut was searched, and as a consequence, a window for the invariant mass of the  $J/\Psi$ -single muon system was selected to be from  $3.25 \text{ GeV}/c^2$  to  $7.0 \text{ GeV}/c^2$ . This window cut alone (hardware cuts not included) rejects more than 90% of the background events. If the three hardware cuts plus the topological cut were combined the overall efficiency for signal events was 0.012%, while for background events was 0.0017%.

Figure 3 shows the invariant mass distribution for the  $J/\Psi$ -single muon system as well as the angular distribution between the reconstructed  $J/\Psi$  and the single muon. Figure 3a shows these distributions for the  $B_c$ , and Figure 3b for the background events (for convenience these figures do not include the hardware cuts).

For run 1a, the D0 experiment required a minimum value of  $p_T$  of  $3 \text{ GeV}/c$  for all the final state muons but the average value of  $p_T$  for the muons coming from the  $B_c$  is around  $1.8 \text{ GeV}/c$ , thus the minimum value of  $3 \text{ GeV}/c$  wipes out most of the signal events. Thus the events that pass the requirement in  $p_T$  plus the topological cuts were the events that populate the exponential tail of the  $p_T$  distribution of each final state muon. As a consequence, any increase in the minimum value of  $p_T$  would have little effect over the final number of detectable  $B_c$  mesons. For signal events it was also found that the angle in the laboratory system made between the  $J/\Psi$  and the single muon

was of the order of a few degrees, while for background events this angle could cover the full range from 0 to 180 degrees.

The events that pass the hardware cuts plus the topological cuts were used to study efficiencies for signal and background events when the requirements in minimum  $p_T$  and maximum  $\eta$  for each muon were varied.

In order to compute the number of observed  $B_c^+$  events, the following parameters were used: an integrated luminosity of  $50 \text{ pb}^{-1}$ , a cross section for producing  $b\bar{b}$  of  $50 \mu\text{b}$ , a 0.4% branching ratio for the  $B_c$  decaying into  $\mu^+ + \mu^- + \mu^+ + \nu$ . The geometric acceptance was included selecting a value of 0.6 for each final state muon, and a value of 0.216 was used for this case of three final state muons. We also considered the increase in  $\Delta p_T/p_T$  as a function of the momentum of the muon, as measured in the muon chambers [9]. This means that if we take  $\Delta p_T/p_T = 0.5$  as the maximum reasonable value, we have to discard events with muons of momentum greater than 60 GeV/c. This is going to wipe out almost all the remaining events, because they typically have very large momentum.

Table 1 shows the number of expected  $B_c$  mesons as a function of the minimum value in  $p_T$  and maximum value of  $\eta$  when a cut for the uncertainty in the transverse momentum was not included. Table 2 shows the number of expected  $B_c$  but this time with a cut for  $p > 60 \text{ GeV/c}$  in order to have  $\Delta p_T/p_T$  less than 0.5. These numbers have an uncertainty of the order of 70%. We would expect similar numbers for the  $B_c^-$ .

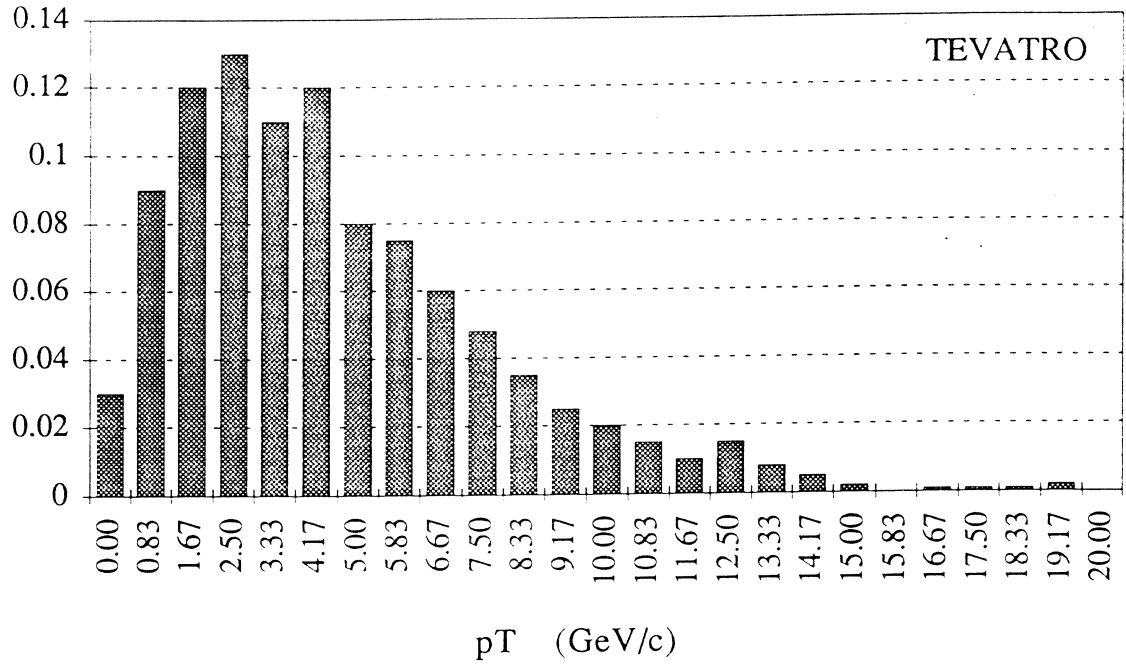
There are other efficiencies and cuts that could make this exercise more realistic, but that were not included in the evaluation of the expected number of events. For example, other detector inefficiencies, trigger cuts, reconstruction efficiencies, the uncertainty due to missidentification of particles, impact parameter cuts and cuts to find "good" muons, etc.

This work was supported in part by a grant from Colciencias in Colombia.

- [1] Semileptonic  $B_c$  Decays. V.V. Kiselev, A.K. Likhoded, A.V. Tkabladze. Preprint-IHEP 92-138, (1992), submitted to Yad. Fiz.
- [2] Production Cross Section and Spectroscopy of  $B_c$  Mesons. S.S. Gershtein et al. Yad. Fiz. 48, 515-524 (August 1988).
- [3]  $B_c$  Decays. M. Lusignoli, M. Masetti. Z. fur Physik C 51, p. 549-555 (1991).
- [4]  $B_c$  Production. M. Lusignoli, M. Masetti, S. Petrarca. Physics Letters B 266, p. 142-146 (1991).
- [5]  $B_c$  Meson Production at Hadron Colliders by Heavy Quark Fragmentation.

- K. Cheung. Physics Review Letters, Vol. 71,21 (November 1993).
- [6]  $J/\Psi$  Production in ppbar. R. Meng, D0 internal notes.
  - [7] Inclusive Single Muon Production With The D0 Detector. K. Bazizi, D0 note # 1539, Nov. 1992.
  - [8] Measurements of Bottom Quark Production in 1.8 TeV ppbar Collisions using Semileptonic Decay Muons. F. Abe et al, CDF Collaboration, Fermilab-Pub. 93/145-E
  - [9] Muon Momentum Resolution from D0. C. Gerber, P. Quintas, D0 note #1985.

Normalized pT distribution of Bc+ produced in hadronic collisions.



Normalized rapidity distribution of Bc+ produced in hadronic collisions.

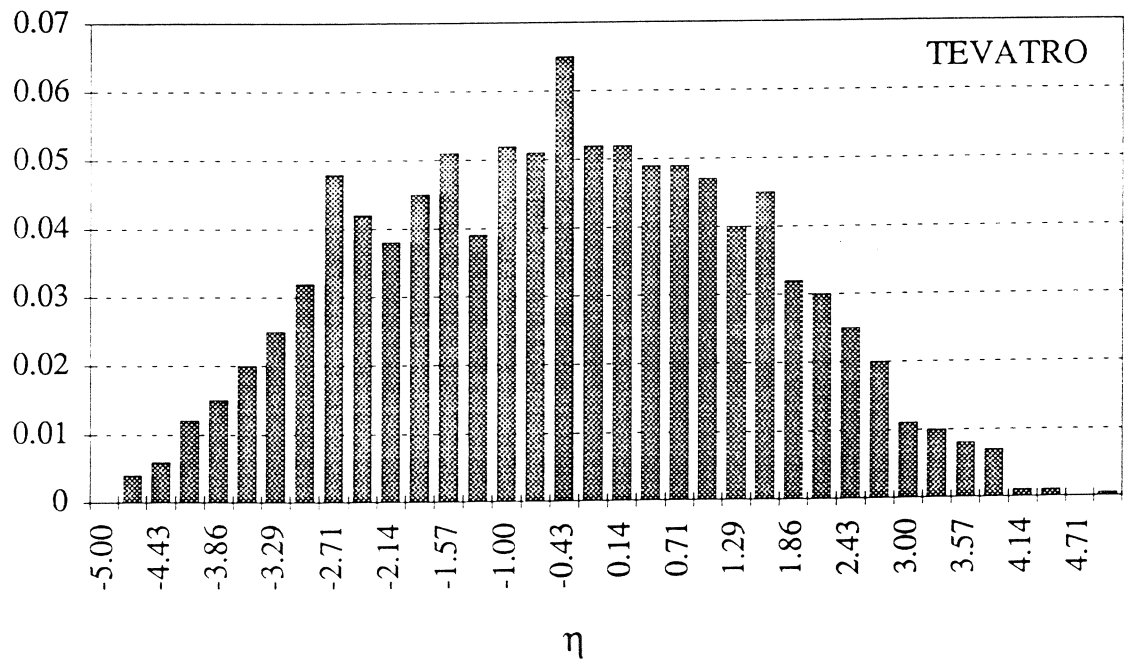


Figure 1

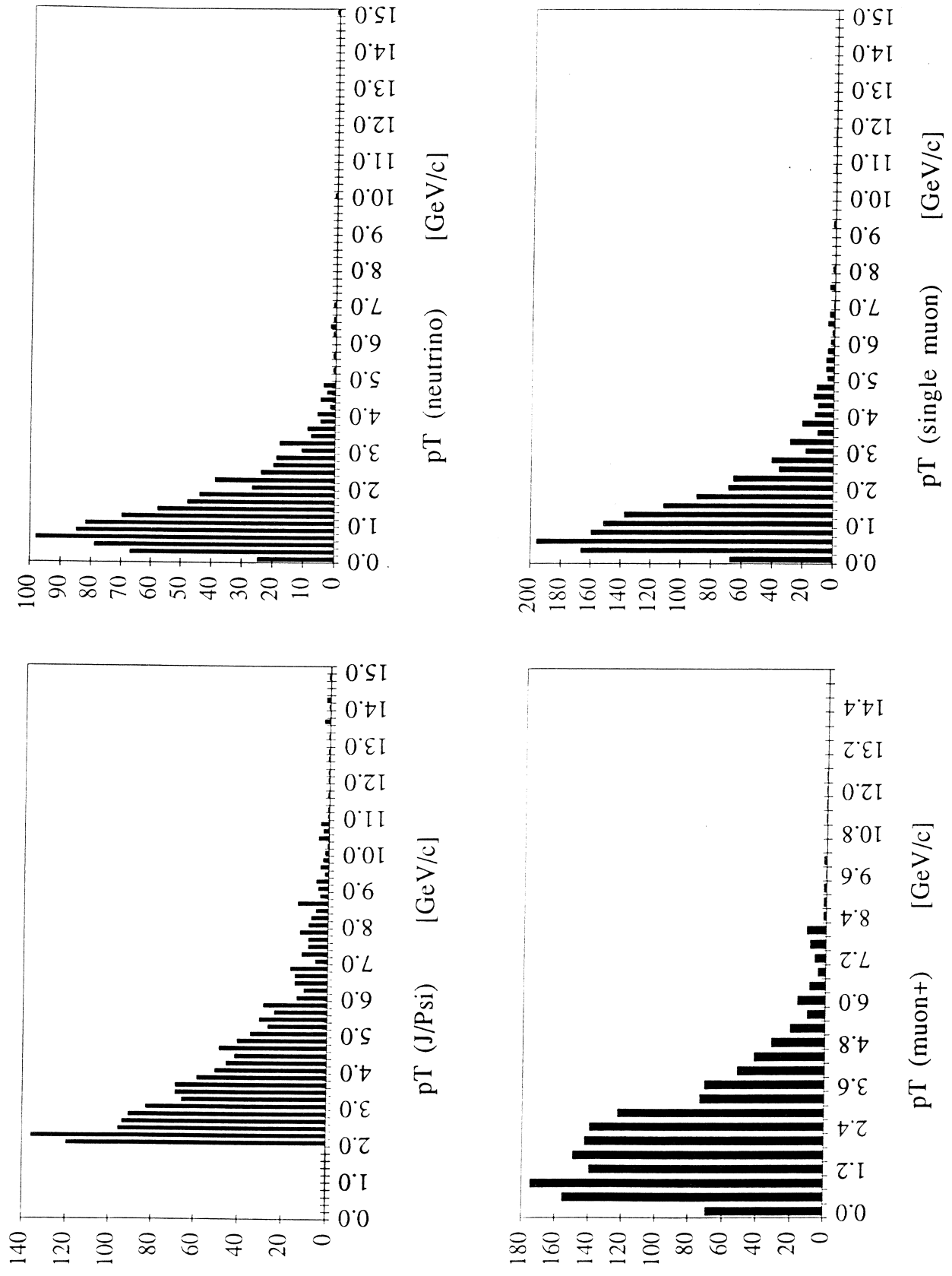


Figure 2



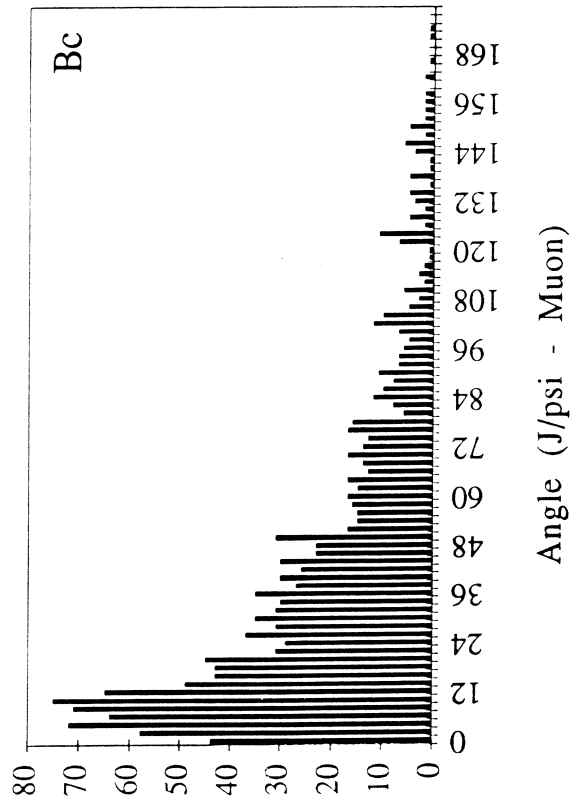
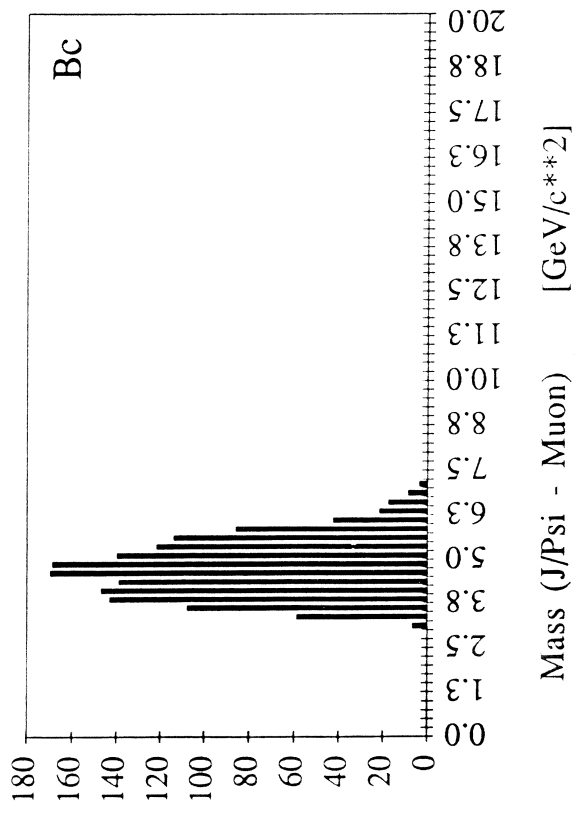


Figure 3a.

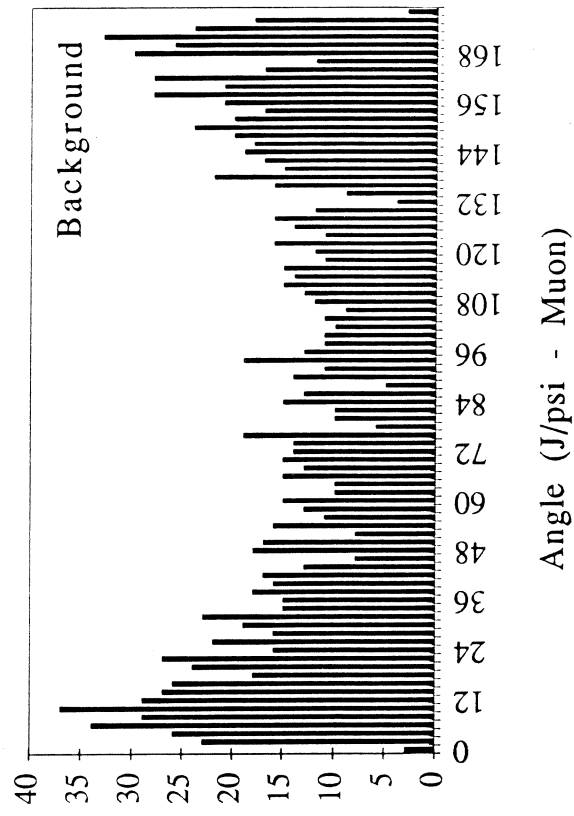
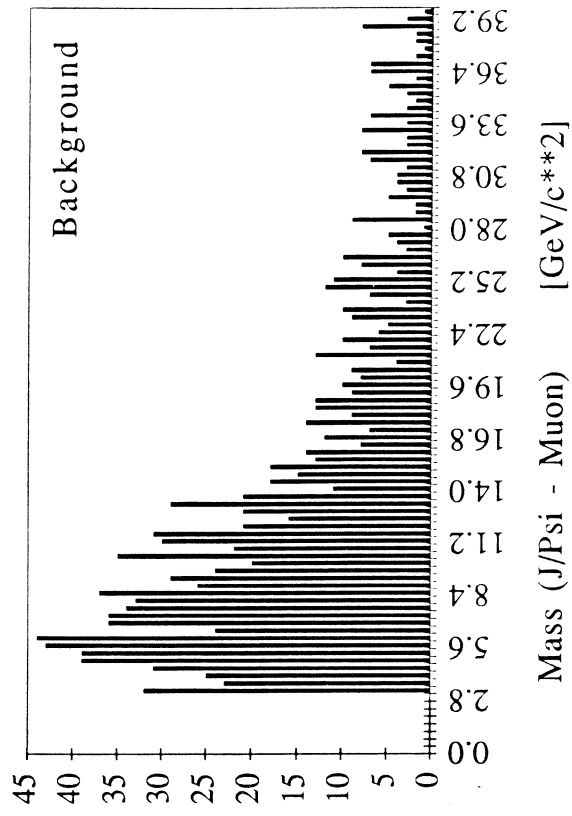


Figure 3b.

TABLE 1

$\eta \longrightarrow$

**pT**  
(GeV/c)

$\downarrow$

	3,5	3,0	2,5	2,0	1,5	1,0
3	35	35	34	32	29	27
4	34	34	32	32	28	26
5	34	34	32	32	28	26
6	34	34	32	31	28	26
7	34	33	32	31	27	26
8	34	33	32	31	27	26
9	33	33	32	31	27	25
10	33	33	32	31	27	25

TABLE 2

$\eta \longrightarrow$

**pT**  
(GeV/c)

$\downarrow$

	3,5	3,0	2,5	2,0	1,5	1,0
3	1.2	1.2	1.2	0.9	0.9	0.9
4	0.5	0.5	0.5	0.5	0.5	0.5
5	0.5	0.5	0.5	0.5	0.5	0.5
6	0	0	0	0	0	0
7	0	0	0	0	0	0
8	0	0	0	0	0	0
9	0	0	0	0	0	0
10	0	0	0	0	0	0



# Punchthrough in the Central Calorimeter

James Jaques  
University of Notre Dame

February 14, 1994

## 1 Introduction

The D0 calorimeter was designed to contain hadronic showers. However, particles other than muons do occasionally punch through the back of the calorimeter, resulting in a systematically low measurement of the particle energy. This effect can be significant for jets, as both the jet energy and position measurements depend upon an accurate measurement of a large ensemble of particles.

High energy jets are particularly susceptible to the loss of measured energy, or punchthrough, and are the main focus of this study. Errors in jet energy measurement lead directly to errors in the inclusive jet cross section. This is especially important in the high energy range where statistics are low and the inclusive cross section becomes a measure of quark compositeness. Studies involving energy flow can also be affected since accurate calorimetry is normally required for these types of studies.

This study is an attempt to characterize the punchthrough effect and find correlations between punchthrough and known jet quantities. These correlations can then be used to derive a correction to the overall jet energy.

## 2 Method and Data Sample

Just beyond the calorimeter cryostat is the first layer of muon system PDT's. Punchthrough particles escaping the cryostat pass through this layer, called the A-layer, and register as hits. The effect is easily seen in jet events, where particle multiplicity is high. Figure 1 shows the muon hit distribution for a two-jet event. The circles represent the jet projections onto the A-layer of

the muon system. Here, punchthrough is indicated by clusters of hits in the A-layer of the muon system that fall within the jet cone.

In a dijet event, the effect contributes to an overall  $E_T$  imbalance between the jets. This imbalance can be reduced by applying a correction to all jets exhibiting punchthrough. Due to time and disk space constraints, and the scarcity of high energy dijet events from the collider, the study focused on a large sample of Herwig Monte Carlo dijet events. A smaller sample of collider events was used to confirm the Monte Carlo results. The Monte Carlo sample consisted of the following:

- 2000 events                      Leading jet  $E_T \rightarrow 350\text{GeV to } 400\text{GeV}$
- 2000 events                      Leading jet  $E_T \rightarrow 250\text{GeV to } 300\text{GeV}$
- 2000 events                      Leading jet  $E_T \rightarrow 150\text{GeV to } 200\text{GeV}$
- 2000 events                      Leading jet  $E_T \rightarrow 100\text{GeV to } 150\text{GeV}$

The gap in the  $E_T$  ranges are due to a lack of available data, but this is partially compensated for by the lower  $E_T$  of the second jet. The collider sample consisted of:

- 400 events                      Leading jet  $E_T > 200\text{GeV}$

Standard quality cuts were applied to the data, with the exception of the coarse hadronic fraction cut, which would remove jets that have the best chance for exhibiting punchthrough (due to late showering). Additionally, the following restrictions were imposed:

- $|\eta| < 1.0$                       (first two jets)
- $|\phi_1 - \phi_2| - \pi < 0.7$
- $E_{T_3} < 15\% \text{ of } E_{T_2}$                       (if third jet is present)
- $3.93 < \phi_{1,2} < 5.5$

where the subscripts indicate the jet number, ordered in decreasing  $E_T$ . The first cut ensures that the two leading jets are centrally located. This assures uniform calorimeter response. The second and third cuts help define a dijet event. The fourth cut removes all events with a jet located at the bottom of the detector, where muon coverage is poor due to structural supports.

### 3 Analysis

Of the original 8000 Monte Carlo events, 2350 pass all of the cuts. With the remaining data, a count was made of the number of A-layer hits associated with each jet, that is, hits whose coordinates satisfy the inequality,

$$\sqrt{(\eta_{Hit} - \eta_{Jet})^2 + (\phi_{Hit} - \phi_{Jet})^2} < 0.7$$

The hits were extracted from a routine, written by Bob Kehoe, that reads the MUOH bank and returns the wire address and Cartesian coordinate of each hit. Definite correlations were found between the number of punchthrough hits and jet energy, EM fraction, and missing  $E_T$ . These correlations imply three separate possible corrections to the jet energy. A correction based on the EM fraction, however, was rejected because it would have altered the systematics of the calorimeter energy measurement. A correction based on the missing  $E_T$  was also discarded because the missing  $E_T$  has many sources other than punchthrough.

Figure 2 shows the average number of punchthrough hits per event as a function of jet energy. The data suggest a linear relationship between jet energy and the number of punchthrough hits. The number of hits can be considered as a final calorimetric sample of the jet, so that each hit represents a fixed amount of energy lost.

In estimating this fixed amount, however, consideration was made for another form of jet energy correction, the missing  $p_T$  fraction (MPF), in which a jet is balanced with a direct photon. This correction includes contributions from punchthrough, but was measured only for jets less than 100 GeV. Therefore, the average number of punchthrough hits per event at 100 GeV was reduced to 0.0 to remove the possibility of redundant corrections. Additionally, the MPF correction was assumed to be constant beyond 100 GeV. Therefore, the reduction in punchthrough hits at 100 GeV was applied to the entire spectrum of punchthrough hits per event. The result is shown in Figure 3. The straight solid line represents the amount of punchthrough accounted for by the MPF correction, while the diamonds represent the spectrum of punchthrough hits after subtracting this amount from each bin. The asteriks are the original values, for comparison.

A correction to the jet energy can be approximated by

$$E_{Corr} = E_{Jet} + cN_{Hits}$$

where  $E_{Jet}$  is the calorimeter measurement,  $N_{Hits}$  is the number of punchthrough hits, and  $c$  is a constant to be determined. That is, each

hit adds  $c$  GeV to the jet energy. A corrected  $E_T$  can then be calculated from  $E_{Corr}$ . MINUIT was employed to determine a best value for  $c$ , using the above correction and the  $E_T$  imbalance, represented by

$$I_{E_T} = \frac{E_{T_1} - E_{T_2}}{E_{T_1} + E_{T_2}}$$

The SIMPLEX minimization was used to minimize  $I_{E_T}$  by correcting the energy of all jets exhibiting punchthrough and substituting the corrected  $E_T$  for the measured  $E_T$  in the above expression.

The calculated value of  $c$  is  $2.25 \pm 0.07$  (error given by MINOS), with an average  $\chi^2$  of 5.1 for the fit. Figure 4 shows  $I_{E_T}$  for selected events where one jet exhibited punchthrough. The solid line represents the corrected distribution, while the dashed line represents the uncorrected distribution. Figure 5 shows the corrected and uncorrected  $I_{E_T}$  distributions for all events. For both plots, the width of the uncorrected distribution is not significantly greater than the width of the corrected distribution. This indicates no significant reduction in the overall  $E_T$  imbalance with the application of the punchthrough correction. One likely reason for this is that punchthrough does not occur in a large percentage of jets, particularly jets below 200 GeV. Another likely reason is that the  $E_T$  imbalance is a result of other effects that punchthrough cannot account for.

Figures 6 and 7 depict the magnitude of the punchthrough correction as a function of the uncorrected jet energy. In particular, Figure 7 indicates that the punchthrough contribution to jet energies is on the order of two or three percent. In the absence of a definitive correction factor, this may be taken as the error applied to jet energies due to punchthrough.

Figures 8, 9, 10, and 11 show the relevant plots for the 96 collider data events that passed all cuts. The punchthrough hit subtraction above 100 GeV was made for these events as it was for the Monte Carlo data, and the same correction factor (2.25) was applied to the punchthrough jets. It should be noted that the SIMPLEX minimization was applied to the collider data in an attempt to determine an independent correction factor, but unphysical results were returned.

Figure 8 shows the corrected and uncorrected  $I_{E_T}$  distribution for selected events with one-jet punchthrough, while Figure 9 shows the same for all of the events. Again, the solid line represents the corrected  $I_{E_T}$  distribution. The lack of statistics makes it difficult to definitively assess the effectiveness of the punchthrough correction on these events. Figures 10

and 11, however, confirm that the punchthrough effect is on the order of two percent of the jet energy.

Based on these observations, the recommendation is to apply the fractional energy added to the jets as a contribution to the overall error in jet energy measurement for high-energy jets.

Many thanks to Jerry Blazey and Bob Kehoe for their aid in this study.



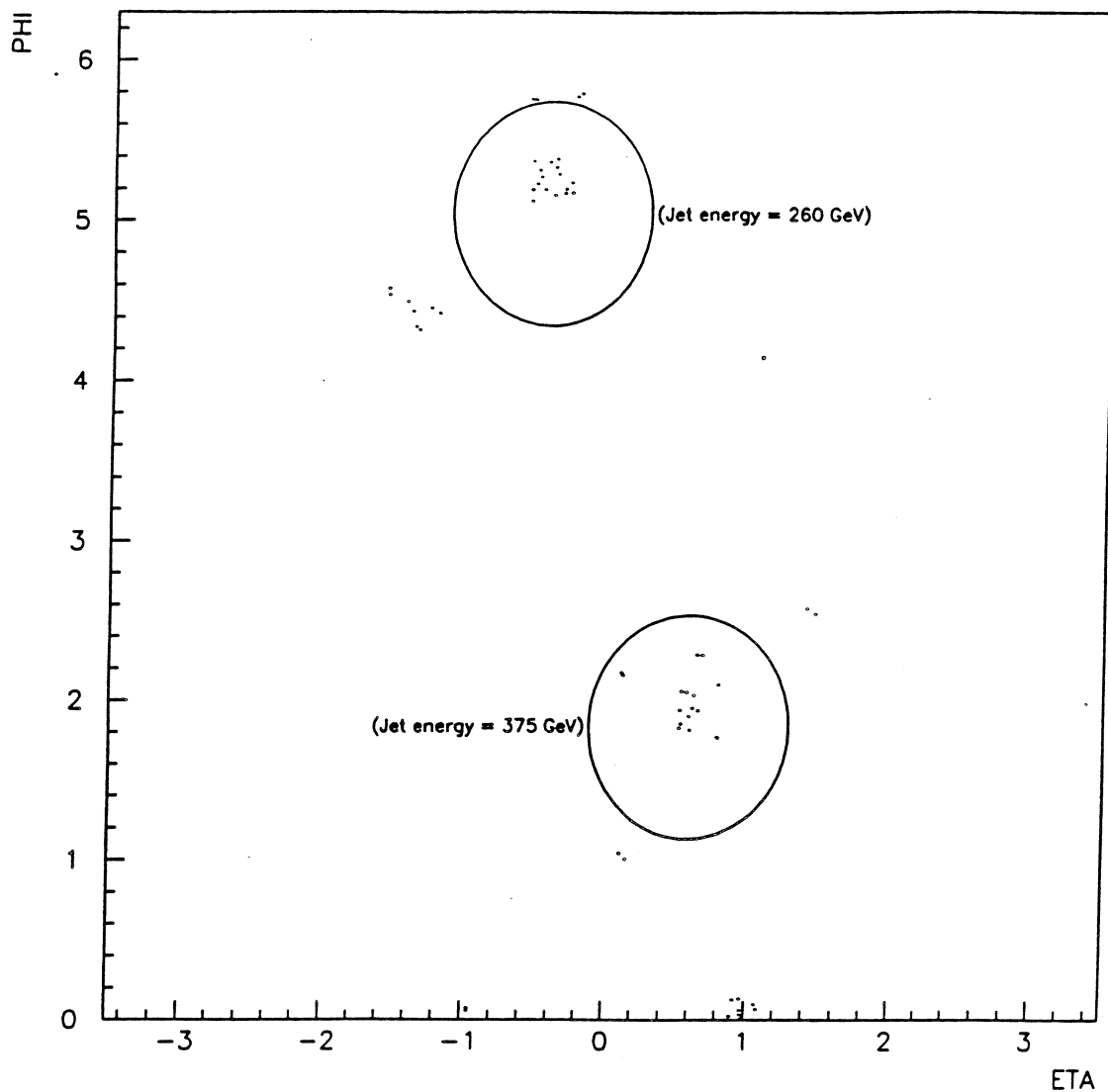


Figure 1. Muon A-layer hits

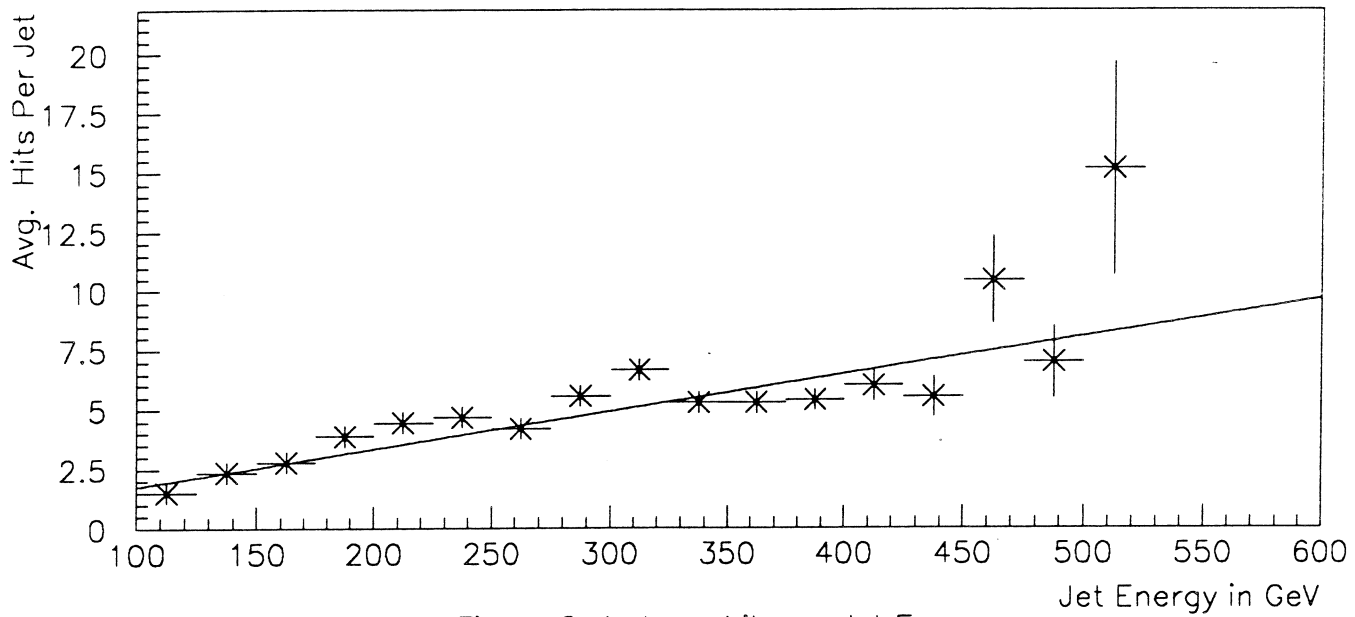


Figure 2. A-layer hits vs. Jet Energy

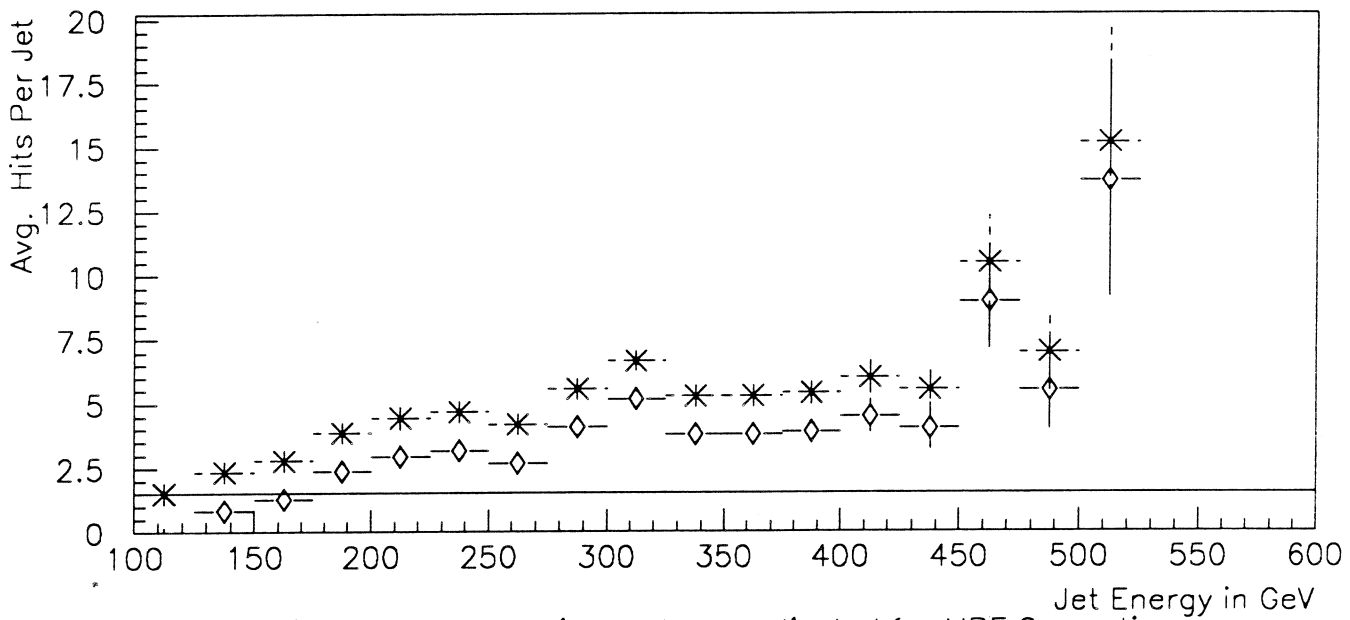


Figure 3. A-layer hit spectrum, adjusted for MPF Correction

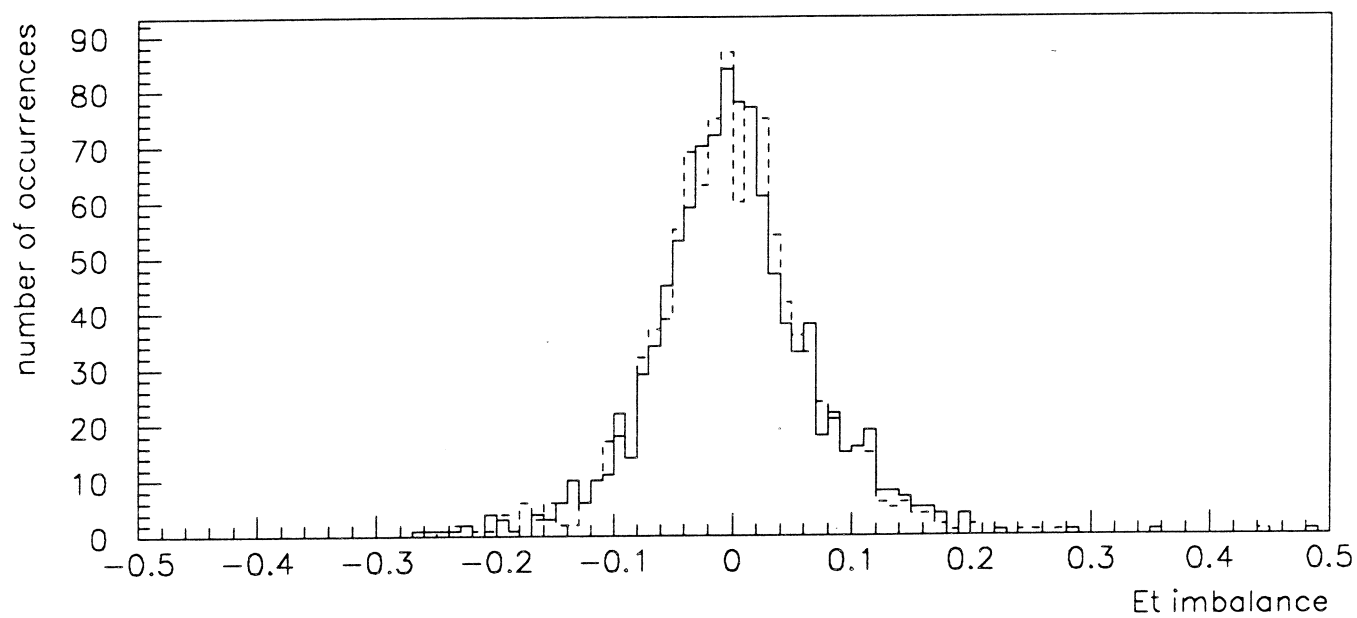


Figure 4. Et imbalance for selected events

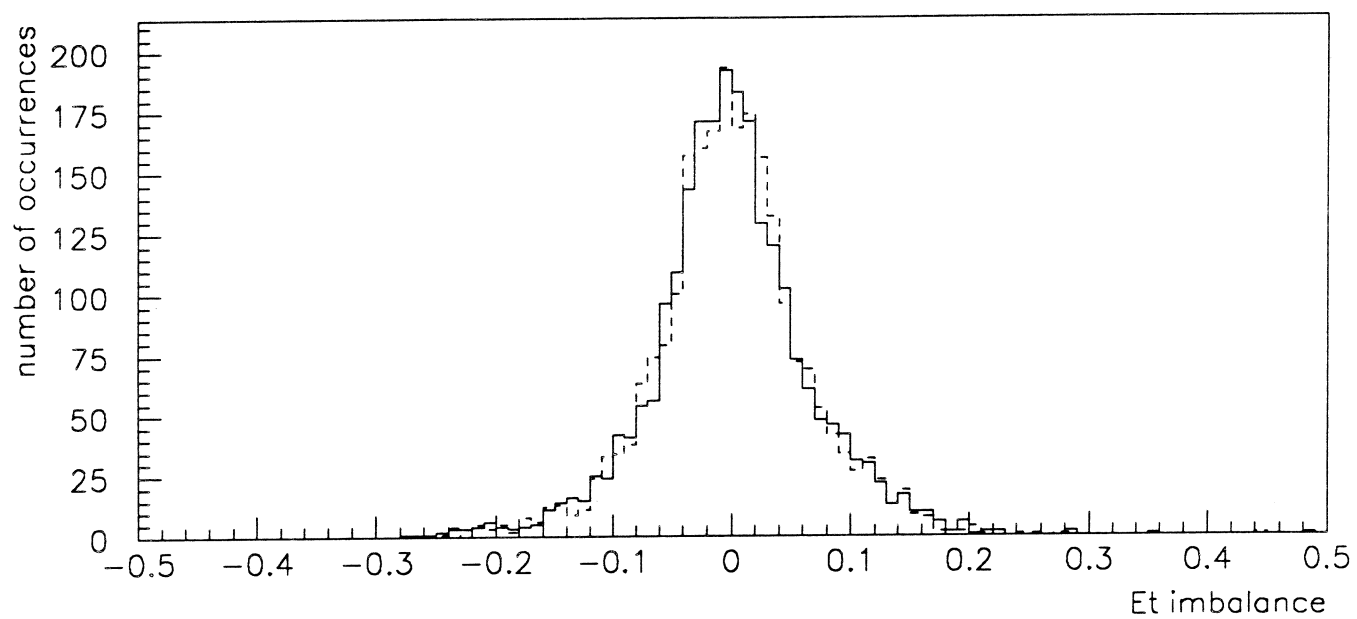


Figure 5. Et imbalance for all events

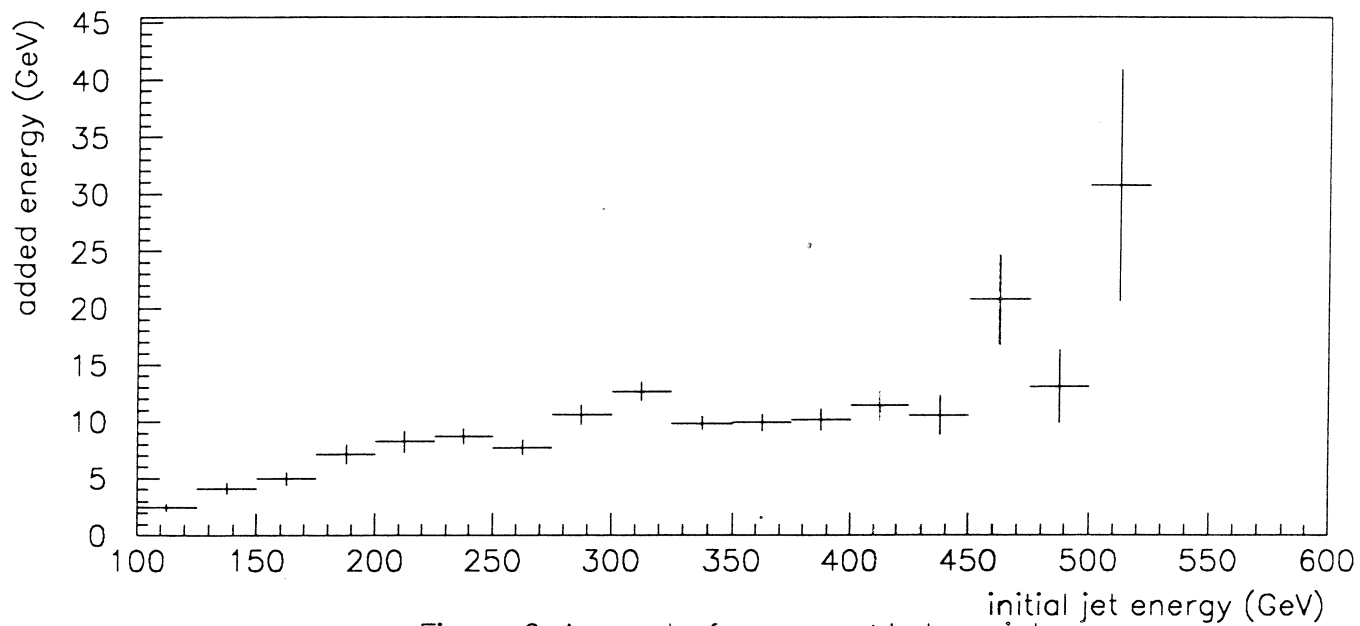


Figure 6. Amount of energy added per jet

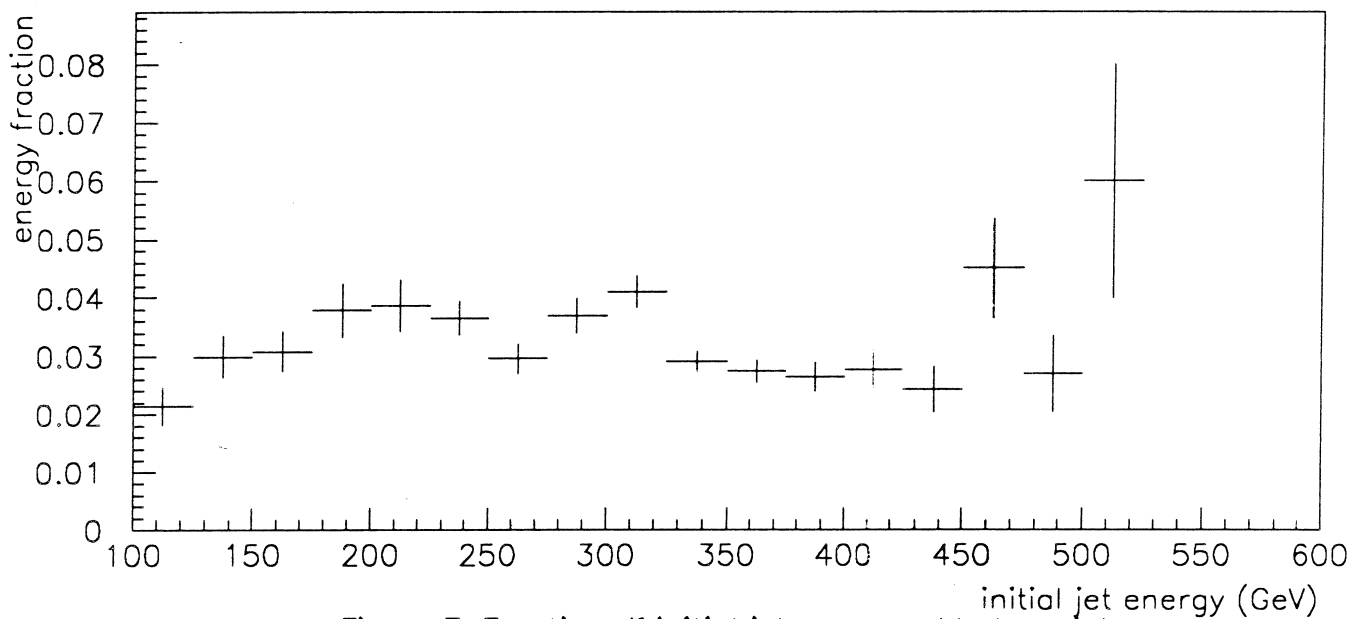


Figure 7. Fraction of initial jet energy added per jet

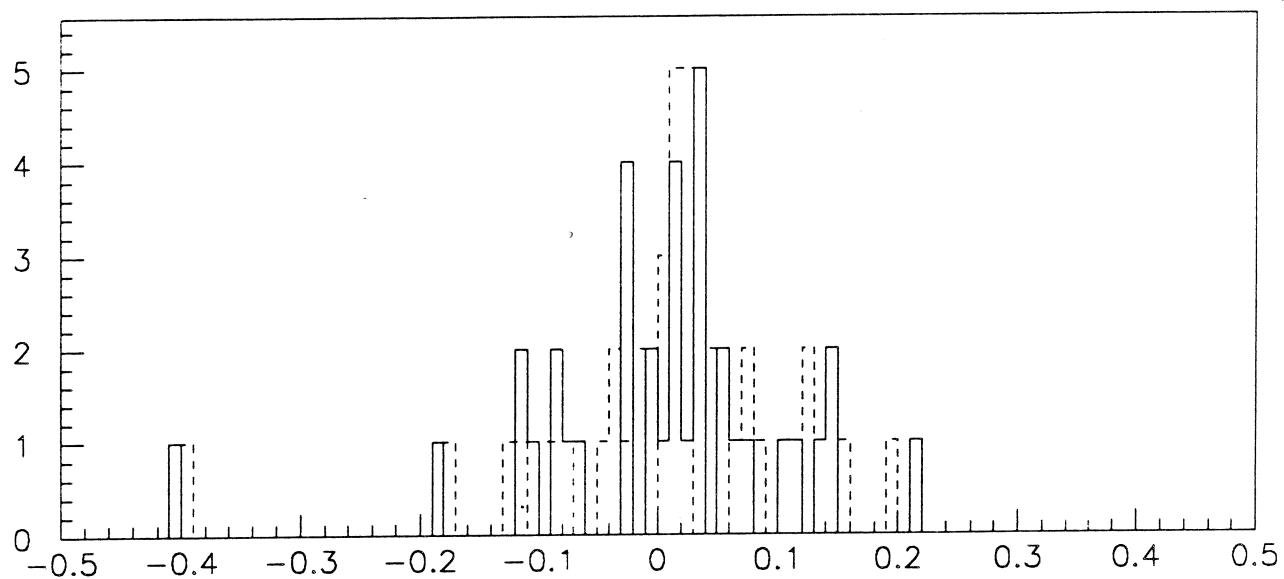


Figure 8. Et imbalance for selected events

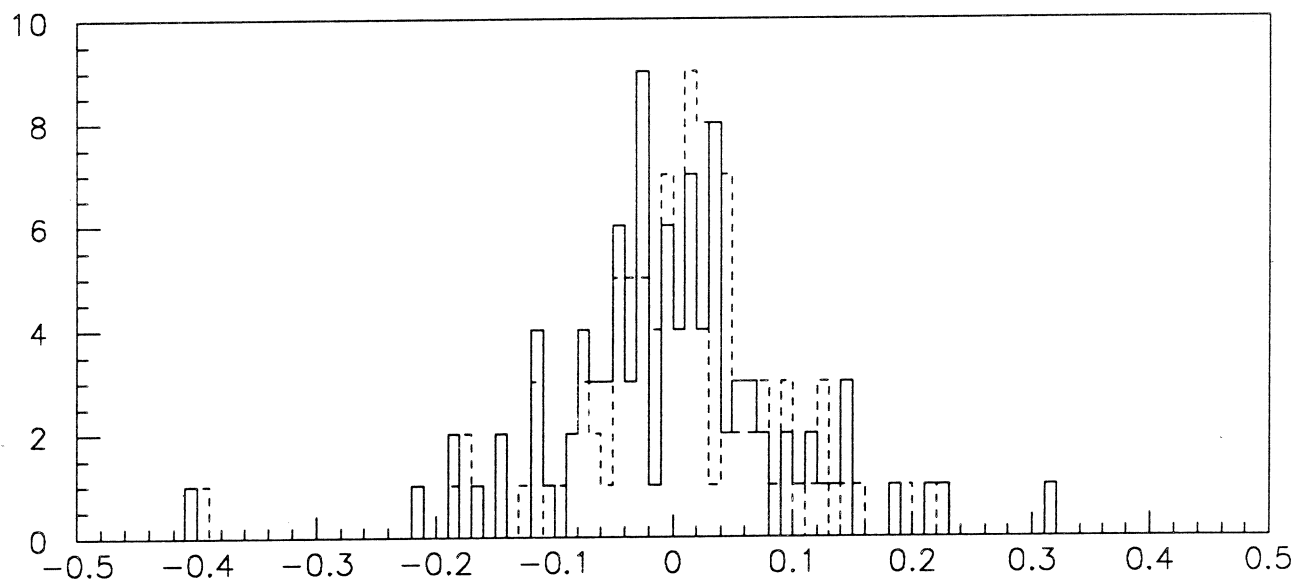


Figure 9. Et imbalance for all events

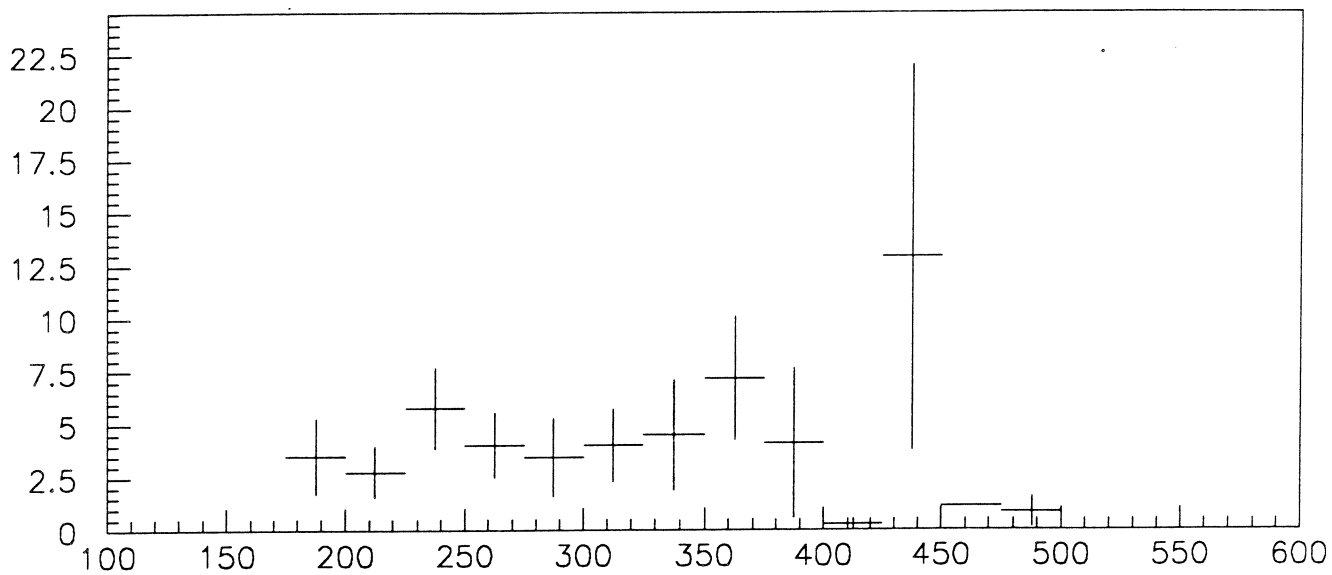


Figure 10. Amount of energy added per jet

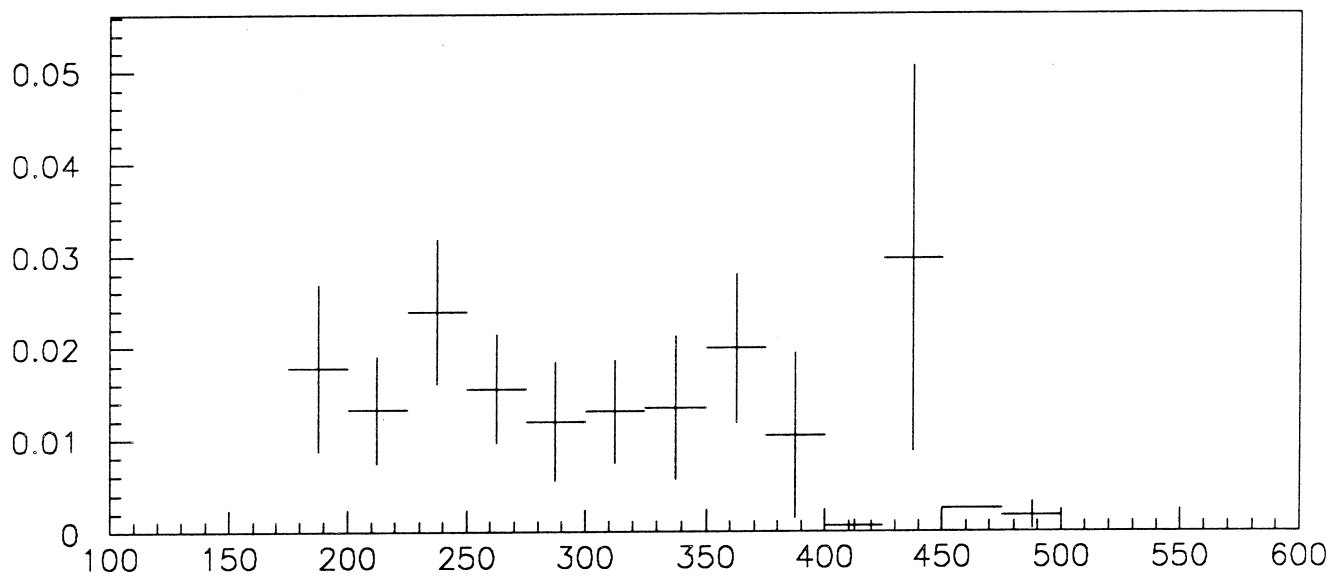


Figure 11. Fraction of initial jet energy added per jet



# EFFECT OF DEAD MATERIALS ON CALORIMETER RESPONSE AND MONTE CARLO SIMULATION.

W. G. D. Dharmaratna

*Department of Physics, Florida State University  
Tallahassee, Florida 32306*

## ABSTRACT

The DØ calorimeter system, cylindrical central calorimeter and two end calorimeters, is constructed with minimal cracks and dead regions in order to provide essentially hermetic coverage over the full solid angle. The effect of the existing few construction features which could perturb the uniformity of the calorimeter is studied in detail with beam tests. The results with the correction algorithms are presented. A comparison with the Monte Carlo simulation is made.

## 1. Introduction

The uranium liquid argon calorimeter system of the DØ detector[1], which recently started its operation at the Tevatron Proton-Antiproton collider at the Fermi National Accelerator Laboratory, consists of a central calorimeter and two end calorimeters covering the full solid angle down to within  $1^\circ$  of the beamline. The calorimeter system is designed with minimal cracks and dead materials in order to provide essentially hermetic coverage over the full range of pseudo-rapidity( $\eta$ ) and azimuthal angle( $\phi$ ).

The uniformity in the region between the central and the end calorimeters, where the effect of the dead material(end plates, support walls and cryostat walls) is most significant, is preserved by using an inter-cryostat detector and massless gaps (see[2] for test results). The remaining few construction features within each calorimeter, module cracks, notches etc., which could perturb the uniformity of the calorimeter are studied with beam tests. In this paper we will present beam test results on the effect of the cracks and dead materials with correction mechanisms to preserve the uniformity when necessary and will demonstrate the ability to reproduce the effect in the Monte Carlo simulations. Sections 2 and 3 will discuss the effects in the electromagnetic section of the central calorimeter(CCEM) and the end calorimeter(ECCEM) respectively. Section 4 will discuss the Monte Carlo simulation.

## 2. Cracks and Dead Materials in CCEM

The cylindrical central calorimeter consists of the inner electromagnetic section surrounded by the fine hadronic(CCFH) section and the outer coarse hadronic section(CCH) covering the full azimuthal angle. As shown in Fig.1(a), there are



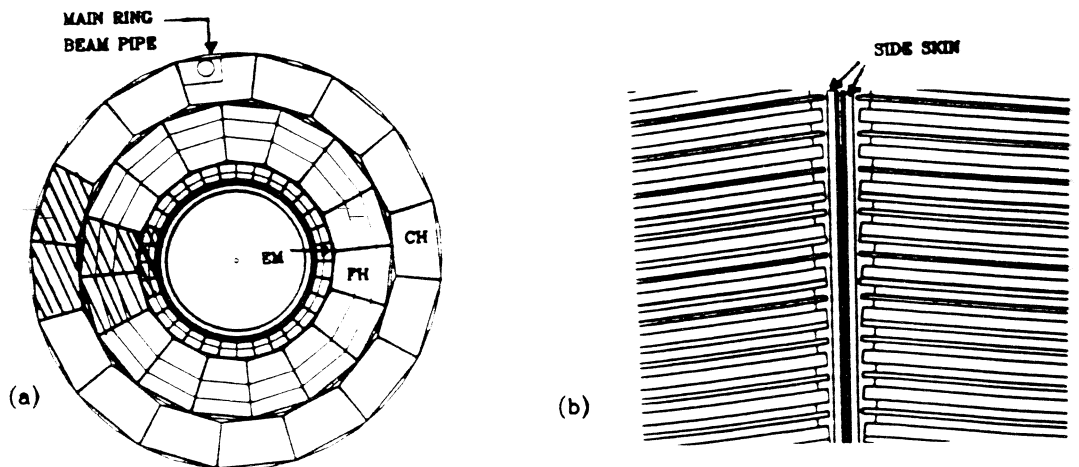


Figure 1: (a)  $\phi$  view of the central calorimeter. (b) Section of a CCEM module crack.

32, 16 and 16 modules (therefore module cracks) in CCEM, CCFH and CCCH respectively, which are placed so that the module cracks from different sections do not align with each other. Each module covers the full  $\eta$  region of the central calorimeter. The first layer of the fine hadronic section is about twice as thick in radiation lengths (40.4) as the total electromagnetic section (20.1). Therefore, any electromagnetically interacting particle, at energies of interest, passing through a CCEM crack will be fully contained in the first layer of the CCFH section.

A section of a side view of a module crack, edges of the uranium plates and signal boards and side skins of the modules, is shown in Fig.1(b). The space between the edges of the uranium plates is about 1.4 cm and the stainless steel side skins are about 2 mm each. All the other structural features in CCEM, spacers, connectors and keys, are positioned at the edge of the module at several positions in  $\eta$  so that they overlap with the module cracks minimizing the dead regions of the calorimeter.

### 2.1. The effect of the module cracks

An assembly of modules (identical to those installed in DØ) corresponding to the shaded area in Fig.1(a) was used during the 1991 test beam run, to study the calorimeter response in the central and the inter-cryostat region[3]. In order to understand the effect of the module cracks, they were scanned in  $\phi$  with  $e^-$  and  $\pi^-$  beams of 10, 25, 50 and 100 GeV at several  $\eta$  locations.

The response of the calorimeter to 25 GeV electrons is shown in Fig.2(a)-(b). The variation of the measured mean energy with the "arc length" is given. Arc length is defined as the distance from the center of the crack to the intersection point of the cylindrical mid surface of the third layer and the projected track from the beam line PWC's. As expected a significant fraction of the energy is collected from the first layer of the CCFH when the particle goes through the crack. There is a net energy loss (maximum of 15–18%) if the particle goes between the edges of

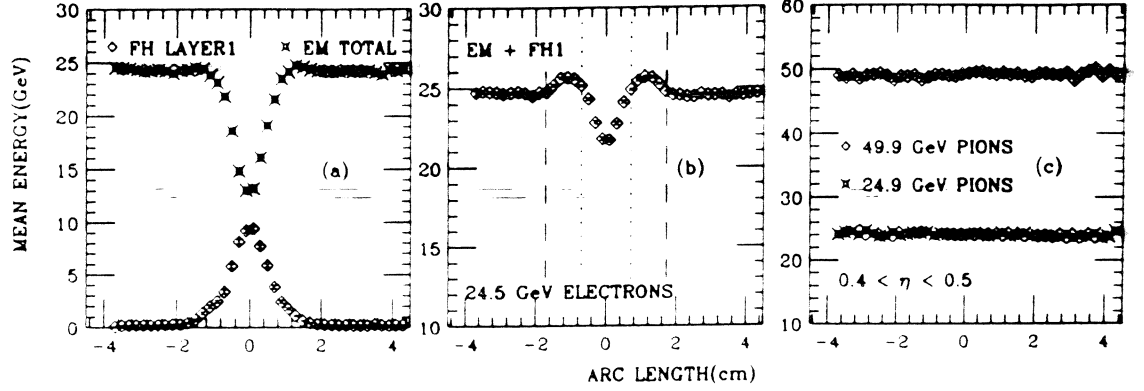


Figure 2: Measured mean energy vs arc length, (a)-(b) for  $e^-$  and (c) for  $\pi^-$ , in the vicinity of the CCEM module crack.

the pads as indicated by the dotted lines. An excess energy of 4–7% is observed if the particle trajectory is next to the pad edge. In this particular case, where some of the connector notches (uranium removed) is included in the scanned region, the excess energy is observed up to the boundary of the connector notch as indicated by the dashed line. The reason for the increase in signal is due to the locally increased sampling fraction in the calorimeter because of the absence of the uranium in this region. From this measurement, we estimate that only about 6% of the active area of the CCEM is affected by more than 4% of the mean signal. The uniformity of the calorimeter to  $\pi^-$  is not affected by the CCEM module cracks as shown in Fig.2(c). This is not surprising since most of the energy is deposited in the hadronic calorimeter.

## 2.2 The correction mechanism

Once the effect is known, it is straightforward to have a mechanism to correct for it. We have developed a general method of correction for energy of an isolated particle going through a module crack. Our main goal here is to have a correction for isolated  $e^-/e^+$ s if they are passing in the vicinity of the CCEM module cracks, but the model can be used even for neutral particles. The only restriction is the crack has to be symmetric around its center as is the case in DØ. The approach made here is to parametrize the dead energy by using only the energy measured in the calorimeter.

By knowing the calorimeter cell energies for an isolated electron, one can find the total energy on each side of the crack, for example the energy on the left side ( $E_l$ ) and the right side ( $E_r$ ). These two quantities are used in the parametrization as follows.

$$\alpha = \frac{E_l - E_r}{E_l + E_r} \quad E_{dead} = F(\alpha) E_{obs}$$

The parameter  $\alpha$  determines the path of the particle with respect to the center of

the crack.  $E_{obs} = E_l + E_r$  and  $E_{dead}$  is the dead energy. When  $\alpha = -1(1)$  the particle is on the right(left) side of the crack with no significant effect of the crack. The function  $F(\alpha)$  is determined from the test beam data. Here,  $E_{dead}$  equals the energy of the incoming particle minus  $E_{obs}$ .

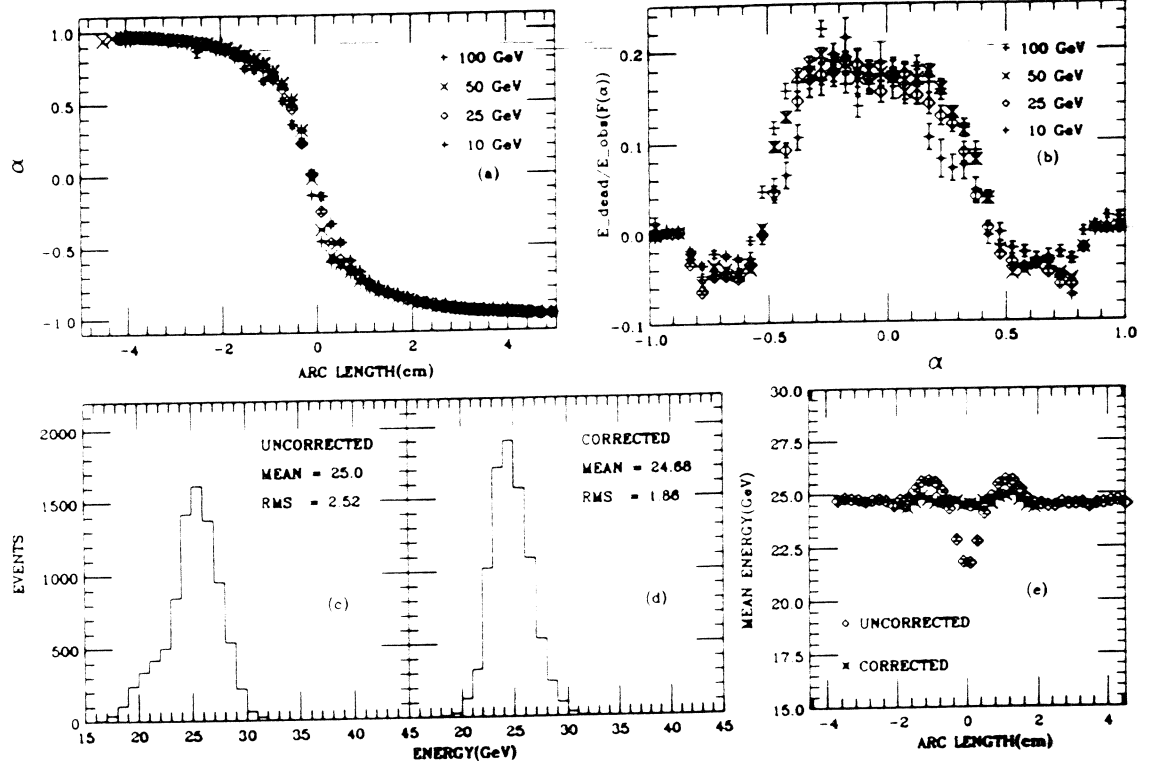


Figure 3: (a)  $\alpha$  vs arc length. (b)  $E_{dead}/E_{obs}$  vs  $\alpha$ . Uncorrected (c) and corrected (d) energy spectra(24.5 GeV  $e^-$  beam). (e) Mean energy vs arc length before and after the correction.

The parameter  $\alpha$  has the expected behaviour as illustrated in Fig.3, where the average values for 10, 25, 50 and 100 GeV  $e^-$  are included. Most importantly, both  $\alpha$  (Fig 3(a)) and  $F(\alpha) = E_{dead}/E_{obs}$  (Fig 3(b)) are approximately independent of the energy for the range studied. Note that the parameter  $\alpha$  expands the central region of the crack, where the variation is most significant. The correction function  $F(\alpha)$  is obtained by fitting a polynomial in  $\alpha$  to the curve in Fig.3(b). The calorimeter response before and after the correction is compared in Fig.3(c)-(d). The uniformity is better than 2% for most of the region and the resolution is improved significantly by the correction.

### 3. Cracks and Dead Materials in ECEM

One of the two identical end calorimeters was studied[4] in a test beam at Fermilab during the 1990 run before its installation in the DØ detector. The construction and performance of the electromagnetic section is described in detail in

a separate publication[5]. Each of the ECEM modules is constructed as a monolithic unit by assembling signal boards and uranium plates into disks to minimize the energy loss in cracks.

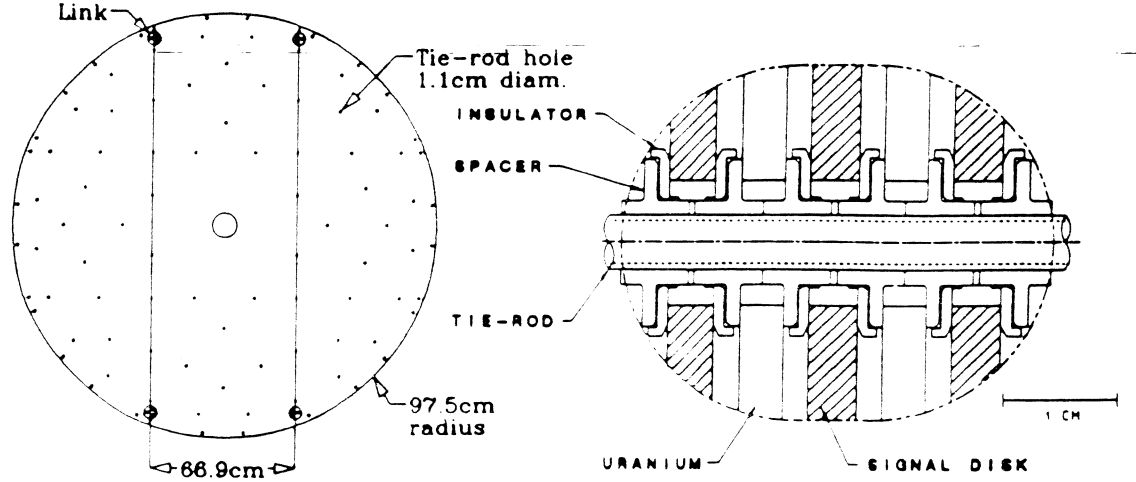


Figure 4: (a) An EM3 uranium disk assembly. (b) A section of a tie-rod assembly.

Fig.4 illustrates the two construction features that perturb the uniformity in the ECEM. They are the two small gaps( 1mm each at  $z = \pm 33.5$  cm) in uranium disks (made with a central plate and two side plates) and the 96 titanium tie-rods(4.8 mm diameter) that penetrate the module to maintain the spacing of the liquid argon gaps and the flatness of the uranium plates. The tie-rods are arranged in an eight-fold symmetric pattern. Both the uranium gap and the tie-rods are parallel to the beam axis and hence they are not projective relative to the interaction region.

### 3.1. The Effect of the Uranium gaps and the Tie-rods

The effect of these features has been studied during beam tests. The mean calorimeter response to 100 GeV electrons in the vicinity of the uranium gap (Fig.5(a)) as a function of the  $z$  coordinate of the shower, and of the tie-rod as a function of  $\phi$  (Fig.5(b)) and the polar angle( $\theta$ )(Fig.5(c)) are shown. The effect of the uranium gap is to increase the response, maximum of 5% with a full width at half maximum of 1.4 cm. As in the case of the CCEM module cracks, the increase in the signal can be explained by a local increase in the sampling fraction. The effect of the two uranium gaps is that 2.5% of the active area of the ECEM module has an increase in signal  $\geq 1\%$ . In the vicinity of the tie-rod, a loss of signal (maximum of 15%) is observed when the particle passes through the area where the high voltage bearing resistive coat has been removed from the signal boards as indicated by the dotted lines in Fig.5(b) & (c). The effect of the tie-rods is that 8%(1.5%) of the active area of the ECEM has a loss of signal greater than 1%(5%).

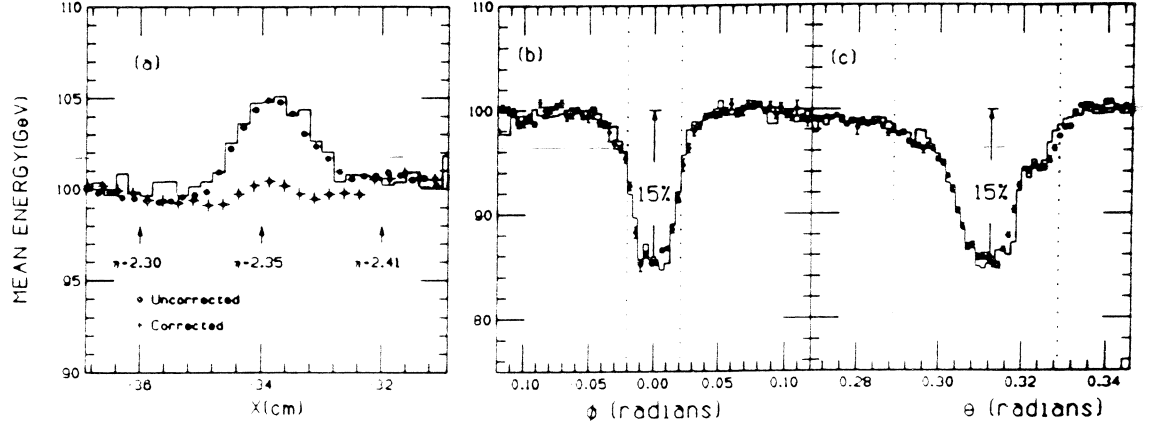


Figure 5: Calorimeter response to 100 GeV  $e^-$ s. (a) Mean energy vs  $x$  before and after the correction in the vicinity of the uranium gap. (b) Mean energy vs  $\phi$  and (c) Mean energy vs  $\theta$  in the vicinity of the tie-rod. The points are the data and the histograms are from the Monte Carlo simulation.

### 3.2 The correction mechanism

The parametrization of the response function at the uranium gap is done by using a gaussian in  $x$ , but due to the non-projective nature of the uranium gap the form is more complex than for the CCEM cracks. The functional form used is:

$$E_{obs} = E_{corr}(1 + F(x)) \quad F(x) = F_{peak} e^{-\frac{(x-x_0)^2}{2\sigma^2}}$$

where

$$F_{peak} = F_0(z_{em3} - z_{int})/z_{em3} \quad x_0 = x_{crack} + x_{offset} + \delta x$$

$$\delta x = -\tan(x) \quad z_{\delta x} \quad \ln(E_{corr}/E_{\delta x}) \quad \tan(x) = x_{crack}/(z_{em3} - z_{int})$$

here  $E_{obs}$  and  $E_{corr}$  are the observed and corrected energies.  $z_{int}$  and  $z_{em3}$  are the  $z$ -coordinates at the interaction position and at the center of EM layer 3.  $x_{crack}$  is the position of the crack ( $\pm 33.5$  cm). All other parameters are determined from a fit to the test beam data. When using the correction function we may use  $E_{obs}$  instead of  $E_{corr}$  in forming  $\delta x$  since this produces no significant effect. The corrected response, which is included in Fig.5(a), shows better than 1% uniformity. Work is in progress to obtain the correction algorithm for the effect due to tie-rods.

## 4. Monte Carlo Simulation

A comprehensive effort was made to setup up the DØ Monte Carlo(MC) system to simulate the detector response. Excellent agreement between the MC and the test beam data for the end calorimeter has been obtained[4][5] by using the version 3.14 of the CERN MC program GEANT[6]. The geometry of the calorime-

ter (individual uranium plates, argon gaps and signal boards) and the materials upstream of the calorimeter including the cryostat walls are modelled in detail.

The effect of the dead materials in ECEM (uranium gap and tie-rods) are modelled in the MC simulation. The response in the vicinity of the uranium gap is modelled by including a 0.9mm (instead of 1mm) gap in the MC and summing all energy deposited in the argon in to the signal. This reproduces the calorimeter response very well as shown in Fig.5(a). The structure of the tie-rod is more complicated as shown in Fig.4(b). However, by using a model which approximates all components, spacers, insulators and dead argon etc., we were able to simulate the effect very well as shown in Fig.5(b)-(c). It is interesting to point out that the model is capable of simulating the response on individual layers as well (Fig.6). The dotted lines in the figure indicate the boundary within each section of the 20 mm diameter zone where the resistive coat has been removed from the signal disk.

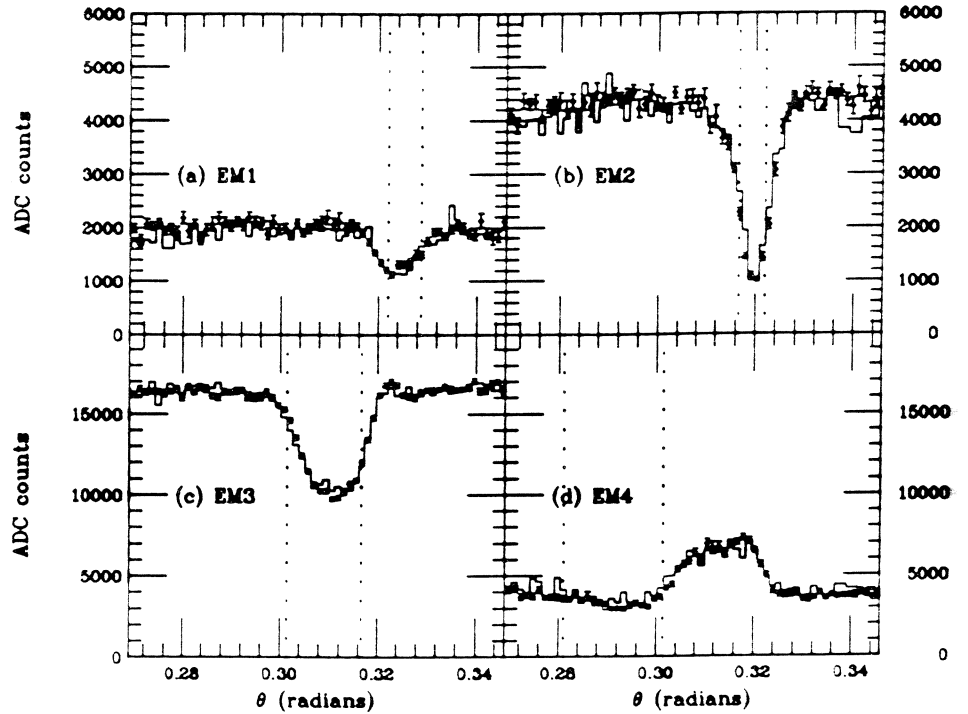


Figure 6: Mean pulse height vs polar angle( $\theta$ ) for individual layers. The points are the data and the histograms are from the Monte Carlo simulation.

## 5. Summary

We have been successful in understanding, in correcting when necessary and in simulating, the effect of the cracks and dead materials in the electromagnetic section of the DØ calorimeter. While the effect of these structural features are as large as 15%–20% at the maximum, we are able to correct most of the affected area to have the response uniform to better than 2%. This will certainly help to improve

the accuracy of our forth-coming physics results.

## 6. Acknowledgements

I would like to thank H. Aihara, O. Dahl and A. Spadafora, who did the studies of the ECEM, for their contribution to this report. Thanks to R. Raja for his initiation on the crack correction model of the CCEM and to E. Clark and D. Stewart for their help in analysing CCEM data. I would also like to thank D. Owen and H. Wahl for careful reading of this paper. This work was supported by the U.S. Department of Energy and the National Science Foundation.

## References

1. J. Christenson, These proceedings.
2. K. Streets, "The DØ Inter-Cryostat Detector. Massless Gaps and Missing  $P_t$ ", These proceedings.
3. Kaushik De, "Test of the DØ Calorimeter Response in 2-150 GeV Beams", to be published in XXVI International Conference on High Energy Physics, Aug. 6-12, 1992.
4. A. Abachi *et al.*, FNAL-PUB-92/162, submitted to Nucl. Instr. and Meth.
5. H. Aihara *et al.*, LBL-31378 UC-414, submitted to Nucl. Instr. and Meth.
6. R. Brun *et al.*, CERN-DD/EE/84-1, May 1986.

\* This paper will be published in the proceedings of the "III International Conference on Calorimetry in High Energy Physics", Sep 29 - Oct 2, 1992, Corpus Christi, Texas.

# Using Single Hadron Data to Optimize the Response of DØ Central Calorimeters for the Measurement of Hadronic Jet Energies

John P. Borders

University of Rochester, Rochester, NY\*

This note presents a discussion of the sampling weights used for reconstructing energies of hadronic showers in the DØ calorimeter. The weights are chosen with the goal of optimizing the response of the DØ detector to jets in the central calorimeter. The analysis is presented in four parts. First, we describe an appropriate optimization technique that is intended to improve the resolution of the response of the DØ detector to single-particles by varying the sampling weights of the various DØ calorimeter layers. Second, without considering the detailed structure of jets, we discuss constraints that can be imposed upon sampling weights in order to achieve an improvement in the overall jet resolution. Third, we perform optimizations, applying the chosen constraints, in order to gauge their impact on single-hadron resolution. Finally, we examine if the restricted optimization produces single-hadron response that will, in fact, provide improved resolution for jets relative to that obtained using essentially default ( $dE/dx$ ) weights.

The data used for this analysis consist of two high-energy scans, both at an azimuth of  $\phi=3.16$  (3.10 radians), and at pseudo-rapidities of  $\eta=0.05$  and  $\eta=0.45$ . Since processed low-energy data (from 2-5 GeV) was not available for  $\eta=0.45$ , only high energy data (7.5-150.0 GeV) were used for the analysis.

## 1 The Process of Optimizing Sampling Weights

The sampling weights and scale factor for the CC were obtained from the test beam using the following steps.

1. An initial estimate of the relative energy deposited in the various layers was found by choosing a set of default weights, which are inversely proportional to the  $dE/dx$  sampling fractions. (These weights are referred to as  *$dE/dx$  weights*).
2. An initial estimate of the scale factor  $\alpha$  was found by normalizing the observed response of the calorimeter to electrons at 100 GeV.
3. A set of optimized electron weights was found for the electromagnetic layers of the CC, using the full range of energies for data at  $\eta=0.05$ ,  $\eta=0.45$ , and  $\eta=1.05$ .<sup>[1]</sup>
4. A set of best weights for hadrons was then found by optimizing the hadron response, subject to certain constraints imposed with the goal of improving jet resolution.

This note is concerned with Step 4 of this process, that is, with determining the weights for the

\* Research Supported by the Department of Energy



hadronic layers that can provide the best jet resolution. In this section, we describe a suitable procedure for use in the optimization of sampling weights for electrons, hadrons, and jets. This optimization procedure is identical to the one used for extracting electron weights.<sup>[1]</sup>

The hadron data from the test beam consist of data taken at different energies and positions in the calorimeter. For any particular event  $k$  in a data set, we can write:

$$E^k = \alpha \sum_i^X \beta_i L_{ik} \quad (1)$$

here,  $X$  is the total number of longitudinal layers of the calorimeter,  $\alpha$  is our conversion factor from ADC counts to GeV,  $\beta_i$  are the sampling weights,  $L_{ik}$  are the observed signals in ADC counts in the various calorimeter layers for event  $k$ , and  $E^k$  is the reconstructed energy for event  $k$ .

To compensate for any possible energy-independent offsets to the overall energy scale, a constant  $\delta$  can be introduced as an *ad hoc* parameter in Eq. 1.

$$E^k = \alpha \sum_i^X \beta_i L_{ik} + \delta \quad (2)$$

Such an offset is only useful in examining individual particles, as when, for example, dealing with single electrons. For studies of single hadrons, this offset will be set to zero, since a non-zero offset will be difficult to use for reconstructing jets. Nevertheless, we introduce this offset into the formalism in order to maintain consistency with the procedure used to obtain single-electron weights.<sup>[1]</sup>

For simplicity,  $\alpha$  can be incorporated into the  $\beta$ s to get new sampling weights  $\gamma_i = \alpha\beta_i$ . Also,  $\delta$  can be defined as a  $(X+1)^{st}$  layer, with  $\gamma_{X+1} = \delta$ , and  $L_{(X+1)k} = 1.0$ . Thus,  $\delta$  will have units of GeV, and  $\gamma_i$  will have units of GeV/ADC counts. Finally, for any incident energy, we can write:

$$E^k = \sum_i^Y \gamma_i L_{ik} \quad (3)$$

where  $Y$  is the number of layers + 1.

The parameters  $\gamma_i$  are obtained by minimizing the following  $\chi^2$  function with respect to the  $\gamma_i$ :

$$\chi^2 = \sum_{k=1}^T \frac{(E_{inc}^k - \sum_{i=1}^Y \gamma_i L_{ik})^2}{(\sigma_{inc}^k)^2} \quad (4)$$

here  $E_{inc}^k$  is the known incident energy (obtained from PWC information), and the sum is for all  $T$  events included in the optimization (it can be limited to a single energy set, or to events from different energies and calorimeter positions). For  $\sigma_{inc}^k$  we use approximate values for  $S$ ,  $N$ , and  $C$  in Eq. 5:

$$\sigma_{inc}^2 \approx S^2 E_{inc}^2 + C^2 E_{inc}^2 + N^2 \quad (5)$$

$S$  is typically 0.50 for hadrons and 0.15 for electrons, and  $C$  is typically 0.04 for hadrons and 0.01 for electrons.  $N$  is determined by the pedestal noise (primarily due to radiation emitted by the uranium absorber) at the appropriate location in the calorimeter, and is approximately 1.6-2.0 GeV. For this analysis,  $N$  is determined from inspill pedestals at the appropriate calorimeter positions.

The  $\chi^2$  can be minimized using a fitting routine,<sup>[2]</sup> or, instead, the parameters can be found directly by taking the partial derivatives of the  $\chi^2$  with respect to the  $\gamma_i$  and setting them to zero, as shown:

$$\frac{\partial \chi^2}{\partial \gamma_j} = -2 \sum_{k=1}^T \frac{1}{(\sigma_{inc}^k)^2} \left[ E_{inc}^k - \sum_{i=1}^Y \gamma_i L_{ik} \right] L_{jk} = 0 \quad (6)$$

First, considering the sum over  $k$ , we can take an average of Eq. 6 over all events, and obtain:

$$\left\langle \frac{E_{inc} L_j}{\sigma^2} \right\rangle = \sum_{i=1}^Y \gamma_i \left\langle \frac{L_i L_j}{\sigma^2} \right\rangle \quad (7)$$

where the products of all variables within the brackets in Eq. 7 are averaged over all the  $T$  events.

If we define a correlation matrix  $M_{ij} = \langle L_i L_j / \sigma^2 \rangle$ , we can solve for the weights  $\gamma_j$  as follows:

$$\gamma_i = \sum_{j=1}^Y \left\langle \frac{E_{inc} L_j}{\sigma^2} \right\rangle (M^{-1})_{ij} \quad (8)$$

Finally, the parameters for Eq. 2 can be extracted from the  $\gamma_i$ , and used to calculate the total energy observed in an event (the *reconstructed* energy):

$$E_{obs} = \alpha \sum_i^X \beta_i L_i + \delta \quad (9)$$

Uncertainties on the weights can be found by calculating the second derivative of  $\chi^2$  with respect to  $\gamma_k$ , diagonalizing the resulting matrix  $(D_{ij})$  to find the eigenvalues  $\lambda_i$ , and finding the uncertainties  $\Delta_i = 1/\sqrt{\lambda_i}$ . Upon taking the derivative of Eq. 6 with respect to  $\gamma_m$ , we find that  $D_{mj} = 2M_{mj}$ . However, due to correlations between the energy deposited in the various layers, just the diagonal uncertainties are of little use in evaluating the results of an optimization. Instead, the resolution on the reconstructed energy provides the best indication of the results of the optimization.

A simple modification of Eq. 4 provides a flexibility to fix certain of the weights in the optimization and allow others to vary. We can write:

$$\chi^2 = \sum_{k=1}^T \frac{(E_{inc}^k - \sum_{j=1}^F \psi_j L_{jk} - \sum_{i=1}^V \gamma_i L_{ik})^2}{(\sigma_{inc}^k)^2} \quad (10)$$

Here  $F$  is the number of number of layers with fixed weights, and  $V$  is the number of layers that are varied. The resultant solution for the varied weights is similar to what we obtained before:

$$\gamma_i = \sum_{j=1}^V \left\langle \frac{(E_{inc} - E_{fix}) L_j}{\sigma^2} \right\rangle (M^{-1})_{ij} \quad (11)$$

where  $E_{fix}$  is the mean energy deposited in the layers with the fixed weights, which is related to the sum over  $F$  in Eq. 10.

This optimization technique finds sampling weights based upon correlations between the energy deposited among the various layers. It is equivalent to using a 1-dimensional H-matrix approach.<sup>[3]</sup>

## 2 Restricting the Optimization of Hadronic Weights to Produce the Best Jet Resolution

To provide a set of sampling weights for the CC hadronic layers that provide the best possible jet response, the following assumptions were incorporated in the analysis:

1. Because electromagnetically and hadronically-interacting particles cannot be distinguished within a jet, the weights must be chosen to be independent of particle type.
2. Because the energies of particles within a jet cannot be measured individually, the weights must be independent of the energies of the particles in a jet.
3. Because the locations and trajectories of particles within a jet cannot be measured individually, the weights should not depend upon the trajectories of particles within the jet.

To make the weights independent of particle type within a jet, a decision was made to choose the weights so that the response to electrons was optimized, even at the possible expense of hadron resolution. The rationale for this was that, since the fractional

electron energy resolution is far better than the hadronic energy resolution (at best,  $0.15/\sqrt{E}$  vs.  $0.4/\sqrt{E}$ ), a small change in the sampling weights for the electromagnetic layers could result in a big change in the electron energy resolution, but would result in only a slight improvement in the hadron energy resolution. (The actual effect of this restriction upon hadronic energy resolution will be investigated later in this note). Since electrons deposit almost their entire energy in the electromagnetic layers of the calorimeter, the weights for these layers are fixed to those found from the electron optimization.<sup>[1]</sup>

To make the weights independent of the distribution of particle energies within a jet, the sampling weights were chosen by optimizing the weights over a wide range of incident particle energies. This procedure is based upon an assumption that the response of the detector has a linear dependence upon the energy of incident hadrons. In other words, that the sampling weights  $\beta_i$  and the scale factor  $\alpha$  can be expressed as energy-independent constants. Consequently, any energy dependence of the weights has to be ignored when jet response is derived from the response to individual hadrons.

Finally, hadronic response was optimized over two beam positions in the calorimeter, using the same procedures as in electron optimization.<sup>[1]</sup> However, although the electromagnetic weights were optimized over the entire range of the data in the CC, namely at  $\eta=0.05$ ,  $\eta=0.45$ , and  $\eta=1.05$ , the hadronic weights were only optimized at  $\eta=0.05$  and  $\eta=0.45$  (because hadrons are not fully contained in the CC at  $\eta=1.05$ ).

### 3 Characterizing Results of Weight Optimizations

In order to investigate the effects of the constraints on optimization discussed in Section 2, the data will be optimized in several ways, beginning with an unrestricted optimization, and then applying the restrictions in sequence. These results will be compared to a control set, which relies on reconstruction of energy using a set of default weights, and thereby used to judge the improvement, if any, produced by the optimization.

### 3.1 The Default Sampling Weights

The default (starting) sampling weights for this analysis (corresponding to  $\beta_i$  in Eq. 9, with  $\delta = 0$ ) consist of the optimized electron weights for the electromagnetic sections (layers 1-4),<sup>[1]</sup> and  $dE/dx$  weights for the hadronic layers (layers 5-8). In the following analysis, the original optimized electromagnetic weights (and scale factor  $\alpha$ ) have all been renormalized so that the weight for the third electromagnetic layer (EM3) is 0.75, or  $\beta_i(3) = 0.75$ , in order to maintain the previous relative electromagnetic layer weights. The overall scale factor will not vary throughout all the analysis, and is fixed so that  $\alpha = 0.00394$  (which is, again, consistent with previous optimization of electron data). Unless otherwise specified, results of all optimizations will be compared with those obtained using this default set of weights. The default weights are shown in Table 1.

**Table 1 Default sampling weights, with  $\alpha = 0.00394$  and  $\delta = 0$**

Calorimeter Layer	Sampling Weights
EM1	0.981 $\pm$ 0.006
EM2	0.639 $\pm$ 0.005
EM3	0.750
EM4	0.734 $\pm$ 0.003
FH1	1.354 $\pm$ 0.04
FH2	1.293 $\pm$ 0.04
FH3	1.295 $\pm$ 0.05
CH	6.135 $\pm$ 0.18

In order to simplify comparisons between the default weights and any optimized weights, the optimized sampling weights will be presented as factors that are to multiply default set. To prevent confusion, such factors will be listed as *sampling factors*. Consequently, all the sampling factors for the default weights equal unity.

### 3.2 Characteristics of the Response of the Calorimeter to Single Hadrons

The two important characteristics of the response of a calorimeter are the linearity and the resolution. The resolution is found from a fit of Eq. 12 to the reconstructed data

as a function of energy.

$$\left(\frac{\sigma(E)}{\mu(E)}\right)^2 = C^2 + \frac{S^2}{E} + \frac{N^2}{E^2} \quad (12)$$

Here  $E$  are the nominal energies of the beam settings (found from PWC momentum measurement, and renormalized as discussed in Sec. 4.4), and  $\sigma(E)$  and  $\mu(E)$  are obtained from Gaussian fits (see Eq. 4.3) to distributions of the reconstructed energies at the various settings (as shown in Fig. 4.5). Figure 1 shows a plot of the fractional resolution for the default weights (see Table 1) at  $\eta=0.45$ . In the fit, the noise term  $N$  is fixed to the standard deviation of the appropriate inspill-pedestal distribution. The parameters of the fit are given in the figure.

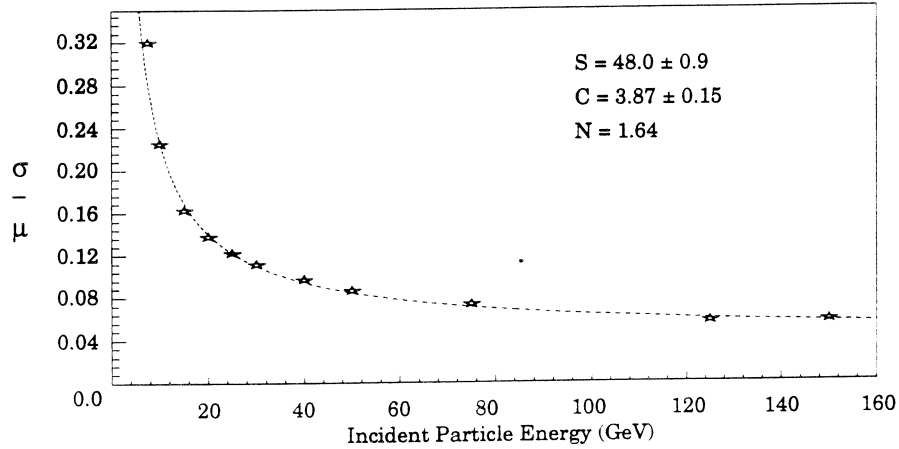


Figure 1 Fractional resolution obtained when using default weights at  $\eta=0.45$

Linearity of response of the calorimeter to single particles is an important characteristic of the detector because it also affects jet resolution. (Linearity refers to the degree to which the reconstructed energy is linearly related to the incident energy.) A plot of the detector response to hadrons at  $\eta=0.45$ , using the default sampling weights is shown in Fig. 2(a), along with a linear fit through the data. The residuals, or the fractional differences between the data and the results of the fit, are shown in Fig. 2(b), along with the parameters obtained from the fit to a straight line.

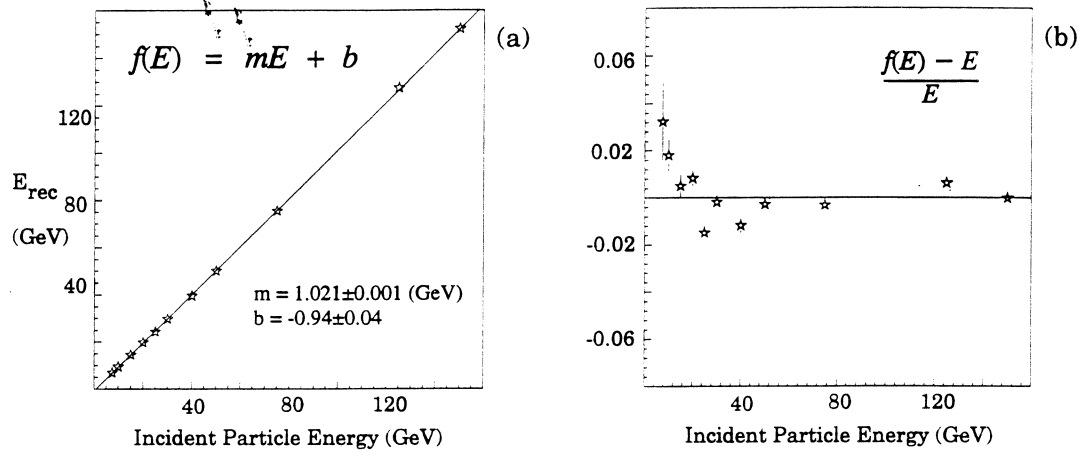


Figure 2 Reconstructed energies obtained using default weights at  $\eta=0.45$

From the statistical errors given in Fig. 2(b), it is clear that the fit to a straight line is poor, and that there is a sizeable intercept. At this point, it is important to stress the fact that such a linear fit is of little use when optimizing jet resolution, since individual particle energies within a jet cannot be corrected through such a fit (because the individual energies cannot be unfolded from the total jet energy). Nonlinearities of the detector can be characterized, however, by the fractional difference between the reconstructed and incident energy, as shown in Fig. 3. The dashed curve corresponds to the previous linear fit to the data.

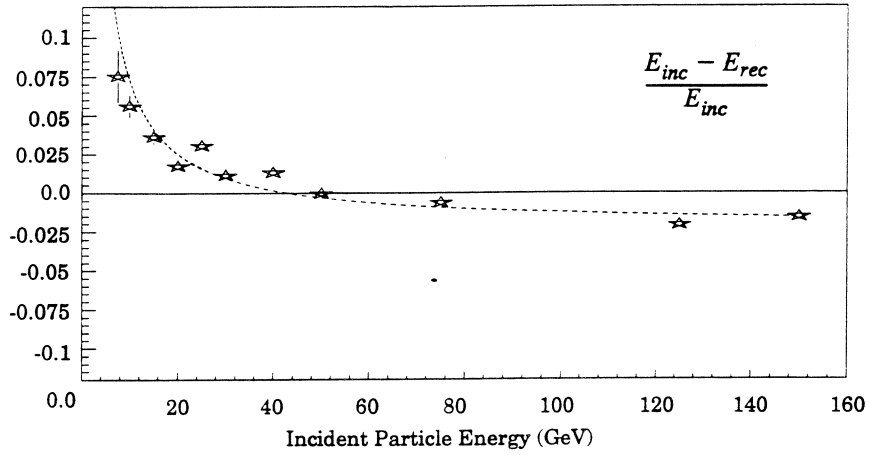


Figure 3 Fractional difference between incident and reconstructed energy using default weights at  $\eta=0.45$



For a detector with a truly linear response, the differences would all be consistent with zero (within statistical uncertainty). Clearly, this is not the case for the default response, especially at the lower energies. It is important to note that the response to electrons in DØ is essentially linear,<sup>[1]</sup> so that the plot of the fractional differences in the response to hadrons provides almost a direct measure of the difference in the relative electron/hadron response of DØ calorimeters. Thus, Fig. 3 shows that, for energies  $> 50$  GeV, the relative electron/hadron response is greater than unity. Remember that the relative electron/hadron response is not the same as  $e/h$ .

## 4 Optimizing Single-Hadron Response While Applying Restrictions Aimed at Improving Jet Resolution

In this section, we will investigate the detector resolution and linearity for single hadrons under different restrictions on the optimizations of the sampling weights  $\gamma_i$ . We will consider energy and position-dependent weights, allowing the weights to vary for the electromagnetic layers as well as for the hadronic layers. Then, we will restrict ourselves to energy-independent weights. After that, data from the two  $\eta$  positions in the detector will be optimized simultaneously to find a single set of position-independent weights. Finally, the weights for the electromagnetic layers will be fixed to those considered best for electrons (the default), to obtain a set of weights that is optimized simultaneously for electrons and hadrons. In this manner we hope to learn which restrictions produce the greatest degradation in resolution and linearity for hadrons, as well as deduce whether the final optimized weights (applying all restrictions) are likely to produce better jet-energy resolution.

The optimized sampling weights can be divided into sets that correspond to different restrictions in the optimization of hadronic response. These sets are defined in Table 2. For this study we use only the data corresponding to the high-energy beam configuration at  $\phi = 3.16$ , thus optimizing over an energy range of 7.5-150 GeV. Also, the optimization for Sets 1 and 2 were performed over each energy individually, resulting in a different set of weights for each energy, while the other sets were optimized for all energies simultaneously, as shown in the table. The entire data sample for this optimiza-

tion consists of the two high-energy sets, one set taken at  $\eta=0.05$ , and one at  $\eta=0.45$ , both at  $\phi=31.6$

The results from the various optimizations will be presented solely for gauging the effect of the various restrictions on single-hadron response. For application in DØ, all restrictions must be imposed upon any final set of weights, therefore only the results of the optimization using Set 6 will be compared to the default set to decide which of the sampling factors would be best for the DØ detector. However, in Chapter 6 we will be investigating ways to reduce the impact any of the restrictions through alternate implementations, so it is useful to study the relative magnitudes of the effects that the different constraints have on the energy resolution of individual hadrons.

**Table 2 Definitions of sets of hadronic weights**

Set	$\eta$ Value	EM Weights	Energy Points
1	0.05	allowed to vary	individual
2	0.45	allowed to vary	individual
3	0.05	allowed to vary	simultaneous
4	0.45	allowed to vary	simultaneous
5	0.05,0.45	allowed to vary	simultaneous
6	0.05,0.45	fix at default	simultaneous

#### 4.1 Results of Hadronic Optimizations

The sampling factors found for Sets 1 and 2 for each available energy are presented in Tables 3 and 4, respectively. As stated earlier, correlations between layers make any uncertainties cited on purely the sampling factors difficult to interpret. Therefore, no uncertainties are given. Instead, the resolution of the reconstructed energies will be used to provide an indication of the quality of the results.

**Table 3 Sampling Factors for Set 1**

Energy (GeV)	EM1	EM2	EM3	EM4	FH1	FH2	FH3	CH
7.5	1.98	1.55	1.03	1.28	0.98	0.73	0.66	0.51
10.0	1.81	1.58	1.12	1.19	0.93	0.93	0.80	0.63
15.0	1.68	1.34	0.89	1.24	0.94	0.88	0.95	0.78
20.0	1.97	1.28	0.94	1.20	0.96	0.92	0.91	0.87
25.0	2.30	1.34	0.94	1.21	0.96	0.95	0.98	0.88
30.0	2.18	1.29	0.95	1.19	0.95	0.95	1.02	0.87
40.0	1.91	1.79	0.88	1.22	0.95	0.94	0.96	0.95
50.0	2.98	1.30	0.87	1.17	0.94	0.95	1.02	0.90
75.0	2.58	1.39	0.87	1.15	0.96	0.91	1.02	0.95
100.0	2.16	1.80	0.86	1.15	0.94	0.93	1.04	0.92
150.0	2.41	2.21	0.75	1.13	0.92	0.93	1.00	0.91

**Table 4 Sampling Factors for Set 2**

Energy (GeV)	EM1	EM2	EM3	EM4	FH1	FH2	FH3	CH
7.5	1.20	0.96	0.98	1.45	0.85	0.70	0.72	0.22
10.0	2.01	0.58	1.07	1.23	0.97	0.89	0.85	0.74
15.0	1.89	1.03	0.94	1.27	0.95	0.94	0.91	0.85
20.0	2.24	1.07	0.93	1.21	0.94	0.93	0.96	0.85
25.0	1.99	1.28	0.99	1.18	0.97	0.93	0.98	0.88
30.0	1.72	1.55	0.97	1.17	0.96	0.90	1.00	0.87
40.0	1.94	1.43	0.98	1.17	0.94	0.92	1.02	0.93
50.0	2.19	1.34	0.94	1.18	0.94	0.95	1.01	0.90
75.0	2.23	1.31	0.94	1.16	0.93	0.94	1.04	0.93
125.0	2.97	1.47	0.98	1.11	0.93	0.94	1.02	0.94
150.0	2.77	1.00	0.93	1.12	0.93	0.95	1.02	0.92

These tables show that the weights vary somewhat with energy, but do not display any clear trend. Also, due to correlations between layers, the significance of the observed variations is quite uncertain.

Table 5 gives the sampling factors for the other optimizations. The weights are consistent overall, except for the EM weights for Set 6, which, of course, are fixed to the

default values. The hadronic weights are virtually the same for all optimizations.

**Table 5 Sampling Factors for Sets 3, 4, 5, and 6**

Set	EM1	EM2	EM3	EM4	FH1	FH2	FH3	CH
3	2.24	1.63	0.87	1.16	0.94	0.93	1.00	0.90
4	2.11	1.13	0.96	1.15	0.94	0.93	1.01	0.91
5	2.16	1.34	0.92	1.15	0.94	0.94	1.01	0.91
6	1.00	1.00	1.00	1.00	0.98	0.94	1.01	0.91

Tables 6 and 7 provide the parameters characterizing the optimizations for the data sets at  $\eta=0.05$  and  $\eta=0.45$ , respectively. Although the character of the results for Sets 1 through 5 are not grossly different, Sets 1 and 2, which allow an energy dependence, provide the best results overall. The results using Set 6 show a larger degradation in resolution and linearity than the other sets, indicating that restricting the EM weights to those that are best for electrons has the biggest detrimental effect on the hadron response.

**Table 6 Parameters from optimizations at  $\eta=0.05$**

Set	Fits to $\sigma(E)/E$		Fits to straight line	
	S (%)	C (%)	Slope	Intercept (GeV)
Default	51.1 $\pm$ 1.0	3.56 $\pm$ 0.21	1.022 $\pm$ 0.001	-0.84 $\pm$ 0.04
1	39.8 $\pm$ 0.9	2.84 $\pm$ 0.17	1.004 $\pm$ 0.001	-0.51 $\pm$ 0.03
3	42.7 $\pm$ 0.9	2.45 $\pm$ 0.21	0.999 $\pm$ 0.001	-0.41 $\pm$ 0.03
5	43.8 $\pm$ 0.9	2.31 $\pm$ 0.21	1.000 $\pm$ 0.001	-0.49 $\pm$ 0.03
6	47.2 $\pm$ 0.9	3.30 $\pm$ 0.20	0.995 $\pm$ 0.001	-0.75 $\pm$ 0.03

**Table 7 Parameters from optimizations at  $\eta=0.45$**

Set	Fits to $\sigma(E)/E$		Fits to straight line	
	S (%)	C (%)	Slope	Intercept (GeV)
Default	48.0 $\pm$ 0.9	3.87 $\pm$ 0.16	1.021 $\pm$ 0.001	-0.94 $\pm$ 0.04
2	39.1 $\pm$ 0.8	2.57 $\pm$ 0.15	1.000 $\pm$ 0.001	-0.21 $\pm$ 0.03
4	40.2 $\pm$ 0.8	2.38 $\pm$ 0.17	1.001 $\pm$ 0.001	-0.34 $\pm$ 0.03
5	41.2 $\pm$ 0.8	2.22 $\pm$ 0.18	1.000 $\pm$ 0.001	-0.30 $\pm$ 0.03
6	45.9 $\pm$ 0.9	3.51 $\pm$ 0.16	0.994 $\pm$ 0.001	-0.81 $\pm$ 0.04

Fig. 4 shows the fits to the fractional resolutions for the various optimizations. These fits were used to extract the values of  $C$  and  $S$  presented in Tables 6 and 7. The plots confirm that the best resolution is obtained using energy-dependent weights, and that restrictions worsen the resolution. However, the energy-independent weights (Sets 3 and 4), and the energy-independent and position-independent weights (Set 5) produce only slightly worse resolution at lower energies, and equivalent resolution at higher energies, indicating that requiring the weights to be independent of energy and position does not have a great effect on the resolution.

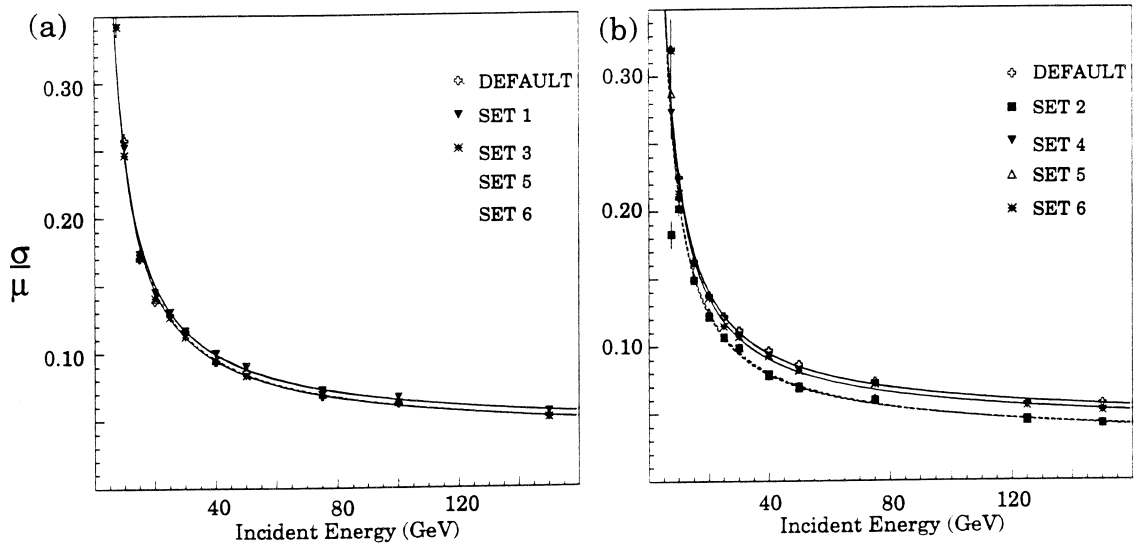


Figure 4 Fractional resolutions for hadrons at (a)  $\eta=0.05$ , and (b)  $\eta=0.45$

Figure 5 gives the fractional differences in the energies (between reconstructed and incident) for  $\eta=0.05$  and  $\eta=0.45$ , for the various optimizations. As can be seen, the default set of weights produce reconstructed energies that are, on average, symmetric around zero for the range of incident energies. However, optimized results appear to provide less absolute spread over the entire range of energies. It is important to recognize that the fractional differences for all sets other than Set 6 (and the Default) could be renormalized (with an overall scale factor) so that they would be symmetric about the zero. Since the purpose of these optimizations is just to show the effect of the vari-

ous restrictions, we will not perform such a renormalization. It should be pointed out that the factors for Set 6 are constrained by the requirement of best electron resolution, and cannot be rescaled.

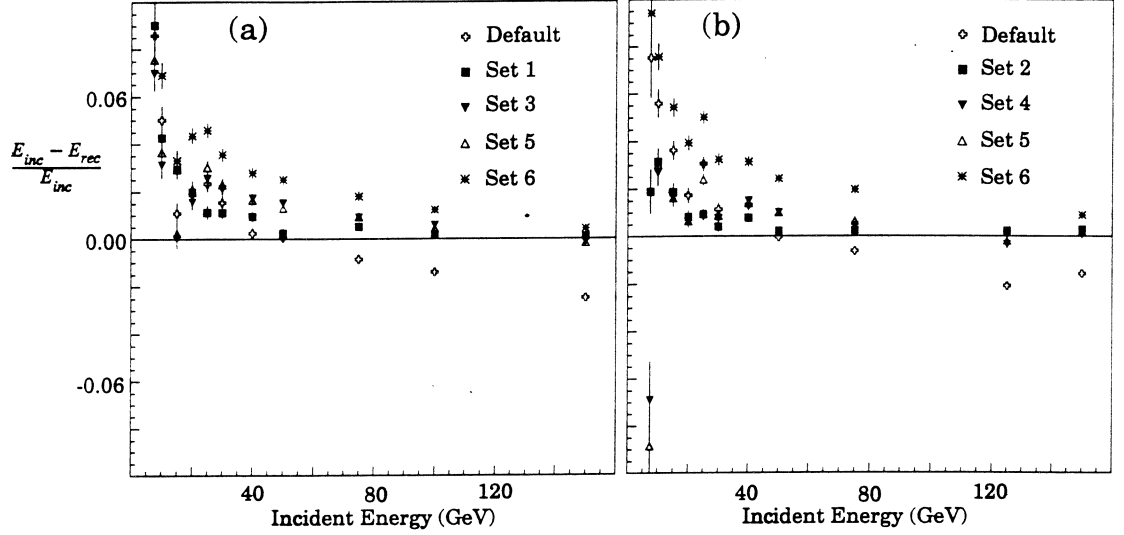


Figure 5 Deviation plots for (a)  $\eta=0.05$ , and (b)  $\eta=0.45$

From these results, we conclude that optimization improves the single-hadron energy resolution. However, it is also clear that the successively imposed restrictions tend to worsen the resolution relative to that obtained using the unrestricted optimization. All of the sets of sampling factors do indeed produce resolutions somewhat better than that found for the Default Set (including Set 6). However, because the Default Set provides reconstructed energies that are more evenly distributed around the incident energies than Set 6 does, it is not clear which one would best optimize jet energy resolution.

#### 4.2 Varying only Relative Scales on the Default Set ("Shifted Set")

Hadronic resolution can also be improved by simply changing the relative scales used for the hadronic and electromagnetic sections. That is, the reconstructed energy can be described by:

$$E^k = \alpha E_{em}^k + \alpha' E_{had}^k \quad (13)$$

where  $E^k$  is the reconstructed energy for event  $k$ ;  $\alpha$  is the scale factor appropriate for electromagnetic layers;  $E_{em}^k$  is the sum over layers 1-4 in Eq. 1; and  $E_{had}^k$  is the sum over layers 5-8 in Eq. 1, using the Default Set of sampling weights; and  $\alpha'$  is the scale for the hadronic layers, nominally equal to  $\alpha$ . It is interesting to see how a change in the relative value of  $\alpha$  and  $\alpha'$  affects the response of the detector to single hadrons.

**Table 8 Results from varying only the relative hadronic scale,  $\alpha'$**

Weights	$\eta$	Fits to $\sigma(E)/E$		Fits to straight line	
		S (%)	C (%)	Slope	Intercept (GeV)
Default	0.05	51.1 $\pm$ 1.0	3.56 $\pm$ 0.21	1.022 $\pm$ 0.001	-0.84 $\pm$ 0.04
Set 6	0.05	47.2 $\pm$ 0.9	3.30 $\pm$ 0.20	0.995 $\pm$ 0.001	-0.75 $\pm$ 0.03
Default (shifted)	0.05	47.2 $\pm$ 0.9	3.33 $\pm$ 0.20	0.996 $\pm$ 0.001	-0.75 $\pm$ 0.03
Default	0.45	48.0 $\pm$ 0.9	3.87 $\pm$ 0.16	1.021 $\pm$ 0.001	-0.94 $\pm$ 0.04
Set 6	0.45	45.9 $\pm$ 0.9	3.51 $\pm$ 0.16	0.994 $\pm$ 0.001	-0.81 $\pm$ 0.04
Default (shifted)	0.45	46.3 $\pm$ 0.9	4.13 $\pm$ 0.16	1.020 $\pm$ 0.001	-0.83 $\pm$ 0.04

Table 8 compares the results for the Default Set and the fully optimized weights of Set 6 (both also given in Tables 6 and 7) with the results when  $\alpha'$  is shifted from 1.000 to 0.965, an amount chosen arbitrarily to produce results close to the optimized set. We refer to the shift in the Default Set as the Shifted Set of sampling factors. As can be seen, within errors, the results using optimized and shifted weights are essentially identical.

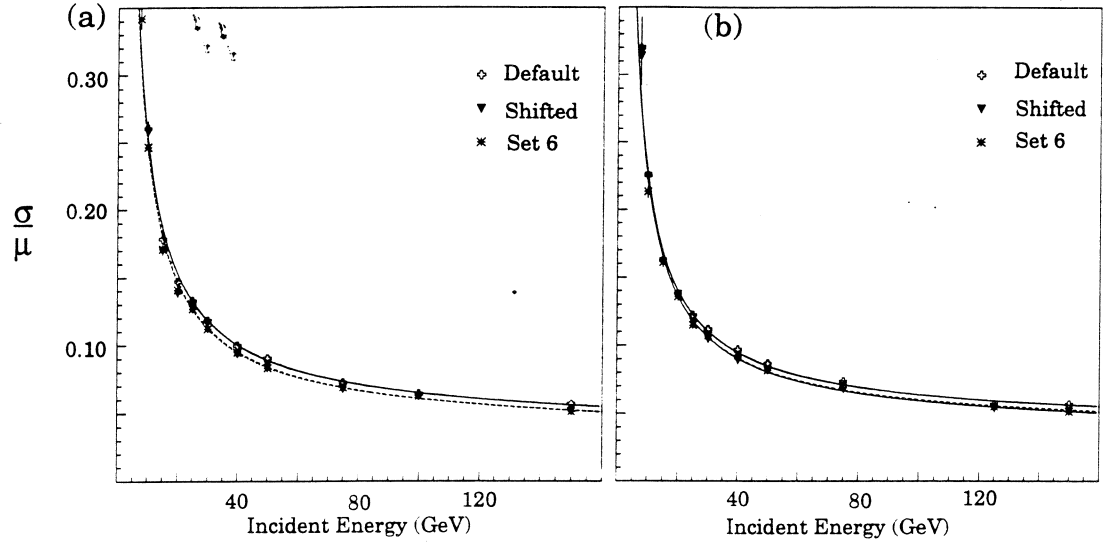


Figure 6 Resolution plots for (a)  $\eta=0.05$ , and (b)  $\eta=0.45$

Figure 6 displays the energy resolution of the detector for our three cases, and Fig. 7 shows the plot of the fractional differences in energy. Again, the results for a shift in  $\alpha'$  to 0.965 are essentially identical to those already found for Set 6. The response using the Shifted Set is virtually identical to that for Set 6, and significantly different from that using the Default Set.

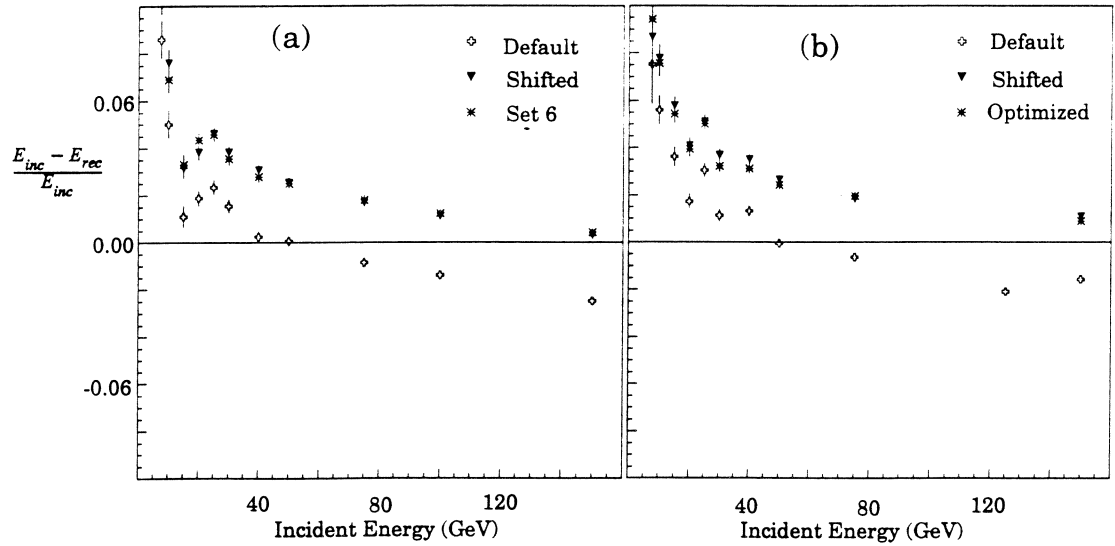


Figure 7 Fractional energy deviations for (a)  $\eta=0.05$ , and (b)  $\eta=0.45$



The results of this section suggest that the small improvement in resolution and linearity gained through optimization of layer weights can also be achieved by simply changing the relative scale between the electromagnetic and hadronic modules. Such a simplification of the optimization procedure is reasonable because differences in the relative responses between different portions of the calorimeter can have a negative impact on resolution. Thus, reducing these differences, as is done by changing the relative scale here, can improve the resolution. Since the optimization routine is designed to improve the resolution, the primary impact of the restricted optimization may well have arisen out of such a variation between the electromagnetic and the hadronic scales. The results of this section seem to have verified that this is the case.

### 4.3 Quality of the Response of the Calorimeter to Hadrons

As we have discussed before, the goal of any optimization of the response of a calorimeter to single hadrons is to improve the measurement of jet energy. However, without a detailed knowledge of the structure of jets, and without the means to implement any such knowledge in the optimization, it is, of course, difficult to determine which weights produce the best jet resolution. We have therefore examined the response to single hadrons in order to estimate the features of the calorimeter response that are likely to have the greatest impact on jet energy resolution.

Three characteristics of energy deposition for single hadrons that come to mind involve the resolution, linearity with energy, and the relative electron/hadron response. Improving resolution is desirable because it leads to more precise measurement of energies of single particles, and thereby, hopefully, to a more precise measurement of the energy of a jet. Also, increasing linearity of response to incident-particle energy is important for minimizing variations in the reconstructed energy of a jet that may depend upon the energies of its individual particles. Finally, it is important to ensure that the mean response of the detector is the same for electromagnetically and hadronically interacting particles, since differences in response to different types of particles can lead to large *a priori* variations in the energies of reconstructed jets.

From previous arguments,<sup>[4]</sup> it appears that the relative electron/hadron response has the greatest impact upon jet resolution (see Sec. 2.1.3). Since jets of a given energy

can exhibit wide fluctuations in the types of their constituents, there is no simple way to correct for effects of a large electron/hadron response ratio. Thus, the principle requirement for improving jet resolution through a variation in the response to single hadrons is making the average hadron response as close to electron response as possible. The issue of linearity is also very important, but since the energy of jets is the sum of the energies of individual particles, corrections can be based upon overall jet energy. Therefore, after settling the electron/hadron issue, linearity can also be improved.

Finally, while it is useful to have good single-particle resolution, the degradation of jet resolution due to variations in the response to different jet constituents at a given jet energy is far more important. Thus, improving single-hadron resolution of calorimeters is not a primary concern in collider environments. It should be recognized that the overall optimization procedures discussed in this chapter tend to equalize the response of the hadronic layers and of the electromagnetic layers (thus improving resolution). Because the DØ calorimeter is not completely compensating (that is,  $e/h \approx 1.05$  and not 1.00), the optimization therefore decreases the reconstructed energies, which has the unfortunate effect of worsening the linearity, while improving resolution.

Since the Default Set of weights produces a hadron response that is, on average, more symmetric relative to the electron response (which, as stated before, is essentially linear with incident hadron energy), the default weights would seem to be better suited for use in improving jet resolution. (Although the optimized weights improve both the resolution and the linearity of response for hadrons, these improvements have less impact on the jet resolution.) Thus, based upon the results of this chapter, the DØ experiment decided to use the default weights for reconstructing jet energies.

It is clear that the methods for determining the appropriate restrictions upon the optimized weights, as well as the rationale for deciding which weights are best, are only qualitative. As we have emphasized, a detailed knowledge of jet structure is needed to determine quantitatively which weights are best for jet resolution. In a future DØnote, we introduce a method for simulating jets using a Monte Carlo program for jet fragmentation, which, when coupled with data from the test beam, can provide a more rigorous procedure for optimizing jet energy resolution.

**References:**

1. W. G. D. Dharmaratna (DØ Collaboration), "Reconstruction of the Calorimeter Response- Test Beam Load 2", DØ Internal Notes, #1731 (1993).
2. CERN Program Library, CERN document 1989.05.30 (1989).
3. D. Kewley, G. Blazey, J. Chiu, T. Ferbel, "Improving Energy Resolution of Calorimeters Using a Covariance Matrix Approach", *Nucl. Instr. and Meth.*, **A280**, 36 (1989).
4. R. Wigmans, "Advances in Hadron Calorimetry." *Annu. Rev. Nucl. Part. Sci* **41**, 133-85 (1991)